Yuanfang Chen
Trung Q. Duong (Eds.)

LNICST 221

Industrial Networks and Intelligent Systems

3rd International Conference, INISCOM 2017
Ho Chi Minh City, Vietnam, September 4, 2017
Proceedings

EAI
Springer

Lecture Notes of the Institute for Computer Sciences, Social Informatics and Telecommunications Engineering 221

Editorial Board

Ozgur Akan
Middle East Technical University, Ankara, Turkey

Paolo Bellavista
University of Bologna, Bologna, Italy

Jiannong Cao
Hong Kong Polytechnic University, Hong Kong, Hong Kong

Geoffrey Coulson
Lancaster University, Lancaster, UK

Falko Dressler
University of Erlangen, Erlangen, Germany

Domenico Ferrari
Università Cattolica Piacenza, Piacenza, Italy

Mario Gerla
UCLA, Los Angeles, USA

Hisashi Kobayashi
Princeton University, Princeton, USA

Sergio Palazzo
University of Catania, Catania, Italy

Sartaj Sahni
University of Florida, Florida, USA

Xuemin Sherman Shen
University of Waterloo, Waterloo, Canada

Mircea Stan
University of Virginia, Charlottesville, USA

Jia Xiaohua
City University of Hong Kong, Kowloon, Hong Kong

Albert Y. Zomaya
University of Sydney, Sydney, Australia

More information about this series at http://www.springer.com/series/8197

Yuanfang Chen · Trung Q. Duong (Eds.)

Industrial Networks and Intelligent Systems

3rd International Conference, INISCOM 2017
Ho Chi Minh City, Vietnam, September 4, 2017
Proceedings

Springer

Editors
Yuanfang Chen
Hangzhou Dianzi University
Hangzhou
China

Trung Q. Duong
Queen's University Belfast
Belfast
UK

ISSN 1867-8211 ISSN 1867-822X (electronic)
Lecture Notes of the Institute for Computer Sciences, Social Informatics
and Telecommunications Engineering
ISBN 978-3-319-74175-8 ISBN 978-3-319-74176-5 (eBook)
https://doi.org/10.1007/978-3-319-74176-5

Library of Congress Control Number: 2017964222

© ICST Institute for Computer Sciences, Social Informatics and Telecommunications Engineering 2018
This work is subject to copyright. All rights are reserved by the Publisher, whether the whole or part of the material is concerned, specifically the rights of translation, reprinting, reuse of illustrations, recitation, broadcasting, reproduction on microfilms or in any other physical way, and transmission or information storage and retrieval, electronic adaptation, computer software, or by similar or dissimilar methodology now known or hereafter developed.
The use of general descriptive names, registered names, trademarks, service marks, etc. in this publication does not imply, even in the absence of a specific statement, that such names are exempt from the relevant protective laws and regulations and therefore free for general use.
The publisher, the authors and the editors are safe to assume that the advice and information in this book are believed to be true and accurate at the date of publication. Neither the publisher nor the authors or the editors give a warranty, express or implied, with respect to the material contained herein or for any errors or omissions that may have been made. The publisher remains neutral with regard to jurisdictional claims in published maps and institutional affiliations.

Printed on acid-free paper

This Springer imprint is published by Springer Nature
The registered company is Springer International Publishing AG
The registered company address is: Gewerbestrasse 11, 6330 Cham, Switzerland

Preface

We are delighted to introduce the proceedings of the 2017 European Alliance for Innovation (EAI) International Conference on Industrial Networks and Intelligent Systems (INISCOM). This conference brought together researchers, developers, and practitioners from around the world who are leveraging and developing industrial networks and intelligent systems.

The theme of INISCOM 2017 was "Industry Inspired Future Technologies: A more intelligent industrial system".

The technical program of INISCOM 2017 consisted of 31 full papers in oral presentation sessions during the main conference tracks. The conference tracks were: Track 1—Telecommunications Systems and Networks; Track 2—Industrial Applications of Intelligent Systems; Track 3—Intelligent Systems and Applications; Track 4—Information Processing and Data Analysis; Track 5—Signal Processing; Track 6—Hardware and Software Design and Development; Track 7—Security and Privacy.

Apart from the high-quality technical paper presentations, the technical program also featured two keynote speeches, and two invited talks.

The two keynote speeches were by Prof. Octavia A. Dobre from Memorial University, Canada, and Prof. Muhammad Imran from Glasgow College UESTC, UK. The invited talks were presented by Prof. Nguyen Van Thu from Ho Chi Minh City University of Transport, Vietnam, and Prof. Trung Q. Duong from Queen's University Belfast, UK.

Coordination with the steering chairs, Prof. Imrich Chlamtac, Prof. Lei Shu, Prof. Carlo Cecati, and Prof. Song Guo, was essential for the success of the conference. We sincerely appreciate their constant support and guidance. It was also a great pleasure to work with such an excellent Organizing Committee team for their hard work in organizing and supporting the conference. In particular, the Technical Program Committee, led by the co-chairs, Dr. Huu Khuong Nguyen, Dr. Xuan-Kien Dang, Dr. Nguyen-Son Vo, who completed the peer-review process of technical papers and created a high-quality technical program. We are also grateful to the conference manager, Lenka Bilska, and publications manager, Erika Pokorna for their support, and all the authors who submitted their papers to INISCOM 2017.

We strongly believe that the INISCOM conference provides a good forum for all researchers, developers, and practitioners to discuss all science and technology aspects that are relevant to intelligent systems. We also expect that future INISCOM conferences will be as successful and stimulating, as indicated by the contributions presented in this volume.

December 2017

Trung Q. Duong
Yuanfang Chen

Conference Organization

Steering Committee

Imrich Chlamtac	CREATE-NET, Italy
Lei Shu	Guangdong University of Petrochemical Technology, China
Carlo Cecati	University of L'Aquila, Italy
Song Guo	The University of Aizu, Japan

Organizing Committee

General Chair

Trung Q. Duong	Queen's University Belfast, UK

General Co-chair

Nguyen Van Thu	Ho Chi Minh City University of Transport, Vietnam

Technical Program Committee Co-chairs

Lei Shu	Guangdong University of Petrochemical Technology, China
Huu Khuong Nguyen	Ho Chi Minh City University of Transport, Vietnam
Xuan-Kien Dang	Ho Chi Minh City University of Transport, Vietnam
Nguyen-Son Vo	Duy Tan University, Vietnam

Workshops Chairs

Wei Liu	University of Sheffield, UK
Vincent Zhu	University of British Columbia, Canada

Publicity and Social Media Chairs

Tomohiko Taniguchi	Fujitsu Laboratories, Japan
Al-Sakib Khan Pathan	Islamic University in Madinah, Saudi Arabia

Sponsorship and Exhibits Chair

Narayan C. Debnath	Winona State University, USA

Publications Chair

Yuan-Fang Chen	Hangzhou Dianzi University, China

Panels Chair

Berk Canberk	Istanbul Technical University, Turkey

Tutorials Chair

Marco Di Renzo	SUPELEC, and the University of Paris–Sud XI, Paris, France

Demos Chair

Zoran Hadzi-Velkov	Ss. Cyril and Methodius University, Republic of Macedonia

Posters and PhD Track Chair

Daniel Benevides da Costa	Federal University of Cearas, Brazil

Local Chair

Phuong Cong Vo	Ho Chi Minh City University of Transport, Vietnam

Web Chair

Nguyen-Son Vo	Duy Tan University, Vietnam

Conference Manager

Lenka Bilska	European Alliance for Innovation (EAI)

Technical Program Committee

Yuanfang Chen	Hangzhou Dianzi University, China
Yu Zhang	University of Lincoln, UK
Gerhard Hancke	City University of Hong Kong, China
Xiaoling Wu	Guangzhou Institute of Advanced Technology (GIAT), Chinese Academy of Sciences (CAS), China
Kun Wang	Nanjing University of Posts and Telecommunications, China
Leandros Maglaras	De Montfort University, UK
Der-Jiunn Deng	NCUE
Jun-Hui Zhao	Beijing Jiaotong University, China
Zhenquan Qin	Dalian University of Technology, China
Jianwei Niu	Beihang University, China
Deze Zeng	CUG
Long Nguyen	Queen's University Belfast, UK
Toan Doan	Queen's University Belfast, UK
Chung Ho	Queen's University Belfast, UK
Sunyoung Lee	Queen's University Belfast, UK

Tiep Hoang	Queen's University Belfast, UK
Cong Trang Mai	Queen's University Belfast, UK
Sang Nguyen	Duy Tan University, Vietnam
Phong Nguyen	Queen's University Belfast, UK
Junqing Zhang	Queen's University Belfast, UK
Muhammad Azhar Iqbal	Capital University of Science and Technology
Nguyen-Son Vo	Duy Tan University, Vietnam
Thanh-Hieu	Nguyen Duy Tan University, Vietnam
Deze Zeng	China University of Geosciences, China

Contents

Telecommunications Systems and Networks

Swarm Intelligence Inspired Adaptive Traffic Control for Traffic Networks

Daxin Tian[1,3,4], Yu Wei[1,3,4], Jianshan Zhou[1,3,4], Kunxian Zheng[1,3,4], Xuting Duan[1,3,4(✉)], Yunpeng Wang[1,3,4], Wenyang Wang[2], Rong Hui[2], and Peng Guo[2]

[1] Beijing Advanced Innovation Center for Big Data and Brain Computing, Beihang University, XueYuan Road No. 37, Beijing 100191, China
231665217@qq.com

[2] China Automotive Technology and Research Center, Automotive Engineering Research Institute, East Xianfeng Road No. 68, Tianjin 300300, China

[3] Beijing Key Laboratory for Cooperative Vehicle Infrastructure Systems and Safety Control, School of Transportation Science and Engineering, Beihang University, XueYuan Road No. 37, Beijing 100191, China

[4] Jiangsu Province Collaborative Innovation Center of Modern Urban Traffic Technologies, Si Pai Lou. 2, Nanjing 210096, China

Abstract. The internet of Vehicles (IoV) technologies have boosted diverse applications related to Intelligent Transportation System (ITS) and Traffic Information Systems (TIS), which have significant potential to advance management of complex and large-scale traffic networks. With the goal of adaptive coordination of a traffic network to achieve high network-wide traffic efficiency, this paper develops a bio-inspired adaptive traffic signal control for real-time traffic flow operations. This adaptive control model is proposed based on swarm intelligence, inspired from particle swarm optimization. It treats each signalized traffic intersection as a particle and the whole traffic network as the particle swarm, then optimizes the global traffic efficiency in a distributed and on-line fashion. Our simulation results show that the proposed algorithm can achieve the performance improvement in terms of the queuing length and traffic flow allocation.

Keywords: Particle swarm optimization · Traffic signal control
Adaptive control

1 Introduction

Internet of vehicles (IoV) has boosted diverse applications with its rapid development. In the transportation network, IoV improves the communication abilities between vehicles, which can help avoid the collision accident, resulting a substantial increase in road safety [1]. Communications between vehicles can provide the real-time vehicle dynamic information [2]. With the rapid development of the city road network, the efficiency of the net-wide traffic system is more significant. IoV enhances the exchange of information between vehicles and the road network [3], and improves the Intelligent Transportation System (ITS) and Traffic Information Systems (TIS). Based on this, we

© ICST Institute for Computer Sciences, Social Informatics and Telecommunications Engineering 2018
Y. Chen and T. Q. Duong (Eds.): INISCOM 2017, LNICST 221, pp. 3–13, 2018.
https://doi.org/10.1007/978-3-319-74176-5_1

can get a better grasp of the real-time dynamic traffic information, and a novel adapted signal control is proposed. The management of the traffic signal control is essential for traffic operation, and numbers of profound research have been done in this hot area.

To ease the traffic pressure, Lin Cao and Bin Hu proposed a traffic signal control based on Action-Dependent Heuristic Dynamic Programming (ADHDP). It is specially adapted to the two intersections traffic model [4]. Daxin Tian and Jianshan Zhou proposed a adaptive signal control model based on the cellular attractor selection, and investigated the robustness and adaptivity of the model [5]. And an adaptive signal control scheme was put forward to prevent intersection traffic blockage [6]. To improve the traffic system performance, a set of algorithms on the traffic signal timing based on the deep neural network (DNN) were also proposed [7]. But with the extension of the city, the road network is becoming bigger, thus a concise and effective traffic signal control model is needed.

We propose a bio-inspired adaptive traffic signal control for the road network with multiple intersections [8, 9]. Due to the topology structure of the road network, inspired by particle swarm optimization, we consider the traffic signal control of an intersection as a particle and the control of the entire traffic network as a networking particle swarm [10, 11]. We propose a adaptive algorithm to improve the traffic conditions.

In this paper, the traffic dynamic model is displayed in the Sect. 2, and in the Sect. 3, we propose the new algorithm on the traffic signal control on the road network with multiple intersections. Section 4 presents the simulation we set up to test our model and discusses the results of it. Section 5 concludes the paper.

2 Traffic Flow Model

Initially, a single intersection is discussed. Considering the straight and left-turn movements, one direction of a intersection is divided into two kinds of flows. One crossroad's four directions are composed of 8 movements, which are controlled by 8 groups of signal lights labeled as Fig. 1 shows.

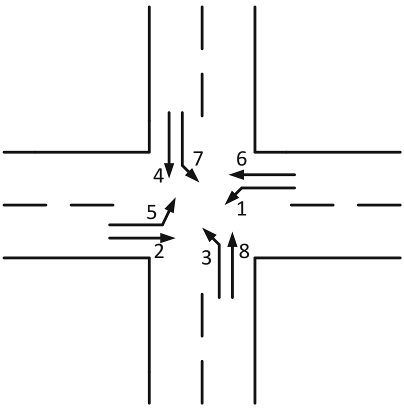

Fig. 1. Typical traffic intersection

Assuming that the signal phases switch with the equal time interval, we get each movement's state transition equation. The current queuing length of each movement is updated by the queuing length of the last time and the varying queuing length. The state of each alignment is updated with every same time interval, which is denoted as t.

$$A^i(t) = A^i(t-1) + \Delta A^i(t) \quad i = 1, 2, 3 \ldots 8 \tag{1}$$

The varying length of the alignment ΔA is the difference of the incoming flow and the output flow:

$$\Delta A^i(t) = A^i_{in}(t) - A^i_{out}(t) \tag{2}$$

The alignments in an intersection are denoted as the vector:

$$\boldsymbol{A(t)} = [A^1(t), A^2(t), A^3(t) \ldots A^8(t)]^{\mathrm{T}} \tag{3}$$

The incoming flow and output flow are expressed as:

$$\boldsymbol{A_{in}(t)} = [A^1_{in}(t), A^2_{in}(t), A^3_{in}(t) \ldots A^8_{in}(t)]^{\mathrm{T}} \tag{4}$$

$$\boldsymbol{A_{out}(t)} = [A^1_{out}(t), A^2_{out}(t), A^3_{out}(t) \ldots A^8_{out}(t)]^{\mathrm{T}} \tag{5}$$

The signal phase is denoted as an 8 dimensional binary vector $\boldsymbol{s(t)}$, $s^i(t) = 1$ represents that i^{th} signal light is green and the lane is released. $s^i(t) = 0$ represents that the signal light is red.

$$\boldsymbol{s(t)} = [s^i(t)]^{\mathrm{T}} \quad i = 1, 2, 3 \ldots 8 \tag{6}$$

The output flow rate is related to the current signal phase $\boldsymbol{s(t)}$ and the current queuing length $\boldsymbol{A(t)}$ which is denoted as:

$$\boldsymbol{A_{out}(t)} = f_{out}(\boldsymbol{s(t)}, \boldsymbol{A(t)}) \tag{7}$$

where the function f^j_{out} is expressed as:

$$f^j_{out} = \begin{cases} \min\left[A^j(t); \frac{\Delta t}{I}\right], & s^j(t) = 1, \\ 0, & s^j(t) = 0 \end{cases} \tag{8}$$

$$\boldsymbol{f_{out}(t)} = [f^j_{out}(t)]^{\mathrm{T}} \quad j = 1, 2, 3 \ldots 8 \tag{9}$$

The $A^j(t)$ stands for the current alignment length, I stands for the average passing time between two neighboring vehicles. Δt is denoted as the green light time. $s^j(t) = 1$ represents that the lane is released and $s^j(t) = 0$ represents that the lane is blocked.

Single intersection can be promoted to large road network. We put emphasis on discussing the four-intersection road network. There are $8 \times 4 = 32$ different movements controlled by signal lights which are labeled as the Fig. 2 shows:

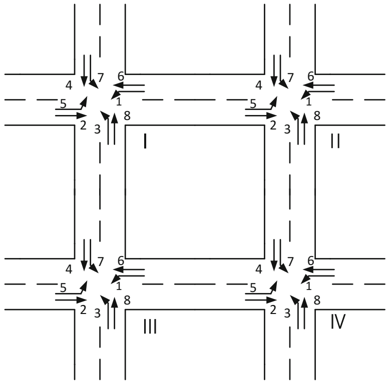

Fig. 2. Traffic network with four intersections

The traffic flow vectors of the four-intersection road network include:

$$\boldsymbol{s(t)} = [s_1(t), s_2(t), s_3(t), s_4(t)]^{\mathrm{T}} \tag{10}$$

$$\boldsymbol{A_{out}(t)} = [A_{out1}(t), A_{out2}(t), A_{out3}(t), A_{out4}(t)]^{\mathrm{T}} \tag{11}$$

$$\boldsymbol{A_{in}(t)} = [A_{in1}(t), A_{in2}(t), A_{in3}(t), A_{in4}(t)]^{\mathrm{T}} \tag{12}$$

$$\boldsymbol{A(t)} = [A_1(t), A_2(t), A_3(t), A_4(t)]^{\mathrm{T}} \tag{13}$$

The directions of the intersections can be categorized into two types:

External direction, which is connected with a node outside the system we consider.
Internal direction, which is connected with the intersection inside the system we consider.

For internal direction, the entering flow of the alignment is from the other three nodes in the road network. Taking intersection I for example, the entering flow of the movements labeled as 1^{st} and 6^{th} can only be from 3^{rd} and 6^{th} movements of the intersection II. So the increased queuing length of the intersection I is related to the queuing length and the signal control $s_2(t)$ of the intersection II. The flow transition equation of the movements can be expressed as:

$$A_{in\mathbf{1}}^{1,6}(t+1) = f_{in}(A_{\mathbf{2}}^{1,6}(t), s_2(t)) \tag{14}$$

3 Swarm Intelligent Inspired Adaptive Traffic Control Model

Based on the NEMA (National Electrical Manufacturers Association) 8-phase dual-ring control, the signal phases are classified into two types: the west/east direction and the south/north direction. In the real operation process, the green lights which control the release of the lane can only be lighted in one of the types. Additionally, the changing model of the signal lights is limited. According to the NEMA phase, the next-time signal control phase is related to the current phase. For example, if the current control phase $\boldsymbol{s}(\boldsymbol{t})$ is (1 0 0 0 1 0 0 0), which also can be denoted as *1 + 5,* the next-time signal phase $\boldsymbol{s}(\boldsymbol{t}+1)$ can only be selected from the *1 + 6*, *2 + 5* and *2 + 6*. Every intersection in a traffic network faces such choices. We treat this problem as a decision strategy problem (Fig. 3).

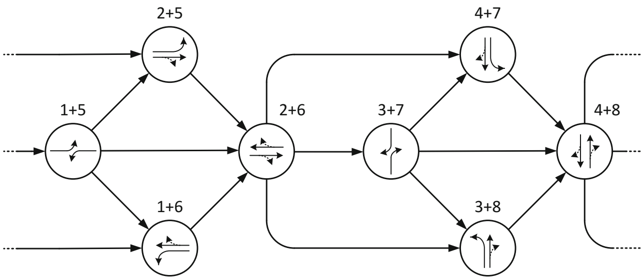

Fig. 3. Primary phasing options for 8-phase dual-ring control

For an eight-phase dual-ring signal control loop, there are four nodes needed to make the decision from three choices to select the next signal phase:

$$\begin{aligned} \boldsymbol{m}_1 &= \left[p_1^1, p_1^2, p_1^3\right]^{\mathrm{T}} \\ \boldsymbol{m}_2 &= \left[p_2^1, p_2^2, p_2^3\right]^{\mathrm{T}} \\ \boldsymbol{m}_3 &= \left[p_3^1, p_3^2, p_3^3\right]^{\mathrm{T}} \\ \boldsymbol{m}_4 &= \left[p_4^1, p_4^2, p_4^3\right]^{\mathrm{T}} \end{aligned} \tag{15}$$

$\boldsymbol{m}_1$, $\boldsymbol{m}_2$, $\boldsymbol{m}_3$, $\boldsymbol{m}_4$ respectively represent the probability vectors when going through the phases of *1 + 5*, *4 + 8*, *2 + 6* and *3 + 7* in the loop.

p^1, p^2 and p^3 respectively represent the probability value, which satisfying the function: $p^1 + p^2 + p^3 = 1$. If the current signal control is *1 + 5*, p_1^1, p_1^2, p_1^3 respectively represent the probability value of choosing the phase of *1 + 6*, *2 + 5* and *2 + 6* as the next-time signal phase. We choose the largest fraction $\max\left\{p_i^1, p_i^2, p_i^3,\right\}$ from the three choices as the next-time signal phase.

The complete loop of the NEMA phases can be expressed as:

$$\boldsymbol{x} = [\boldsymbol{m}_1, \boldsymbol{m}_2, \boldsymbol{m}_3, \boldsymbol{m}_4]^{\mathrm{T}} \tag{16}$$

The next time signal control transition is defined as:

$$\boldsymbol{s}(\mathbf{t}+\mathbf{1}) = f_s(\boldsymbol{s}(\boldsymbol{t}), \boldsymbol{x}) \tag{17}$$

Inspired by the foraging behavior of birds, we consider the signal selection strategy of one intersection a particle and the selections of the entire traffic network as a networking particle swarm, we map the sequential signal operations of each intersection to the iterative updates of the position and velocity of the corresponding virtualized particle induced by the particle swarm optimization (PSO). Every particle has its own corresponding function. Because the entire traffic is inflow-related, every particle has relation with other particle. Formulating the global objective to optimize the global traffic efficiency as a collection of individual objectives, we implement the iterative PSO in a distributed fashion over the network of particles, in which each particle can sense the surrounding real-time traffic state, share its own signal control and state information with other local particles, and coordinate its own signal control with other particles' controls to get a better traffic condition.

Based on the particle swarm intelligence algorithm, we set the velocity as:

$$\begin{aligned} \boldsymbol{n_1} &= \left[r_1^1, r_1^2, r_1^3\right]^{\mathrm{T}} \\ \boldsymbol{n_2} &= \left[r_2^1, r_2^2, r_2^3\right]^{\mathrm{T}} \\ \boldsymbol{n_3} &= \left[r_3^1, r_3^2, r_3^3\right]^{\mathrm{T}} \\ \boldsymbol{n_4} &= \left[r_4^1, r_4^2, r_4^3\right]^{\mathrm{T}} \end{aligned} \tag{18}$$

We initialize the fraction of the vector of the velocity as random value. During the process of interating, the values will have adaptive changes.

We can get the general vector of the velocity:

$$\boldsymbol{v} = [\boldsymbol{n_1}, \boldsymbol{n_2}, \boldsymbol{n_3}, \boldsymbol{n_4}]^{\mathrm{T}} \tag{19}$$

For the network with four intersections

$$\boldsymbol{x_1}, \boldsymbol{x_2}, \boldsymbol{x_3}, \boldsymbol{x_4} \in \boldsymbol{U_i} \tag{20}$$

The velocity $\boldsymbol{v}$ is updated as:

$$\boldsymbol{v_{i+1}}(\boldsymbol{t}+\mathbf{1}) = \boldsymbol{v_i}(\boldsymbol{t}) + \omega\left(\boldsymbol{x}_i^{best}(\boldsymbol{t}) - \boldsymbol{x_i}(\boldsymbol{t})\right) + (1-\omega)(\boldsymbol{x}_{U_i}^{best}(\boldsymbol{t}) - \boldsymbol{x_i}(\boldsymbol{t})) \tag{21}$$

$\boldsymbol{x}_i^{best}(\boldsymbol{t})$ stands for the optimal value of the single intersection, and $\boldsymbol{x}_{U_i}^{best}(\boldsymbol{t})$ represents the optimal value of the four intersections in the whole network. ω is the inertia coefficient.

Based on the particle swarm intelligence algorithm, $\boldsymbol{x}$ is updated as the sum of the old position $\boldsymbol{x}$ and the velocity $\boldsymbol{v}$. To satisfy $p^1 + p^2 + p^3 = 1$, we use $\boldsymbol{f_x}$ to correct the interation function:

$$\boldsymbol{x}'(\boldsymbol{t}+\mathbf{1}) = \boldsymbol{x}(\boldsymbol{t}) + \boldsymbol{v}(\boldsymbol{t}+\mathbf{1}) \tag{22}$$

$$\boldsymbol{x}(\boldsymbol{t}+\mathbf{1}) = \boldsymbol{f_x}(\boldsymbol{x}'(\boldsymbol{t}+\mathbf{1})) \tag{23}$$

We organize the formula and get the expression of the $\boldsymbol{x}(\boldsymbol{t}+\mathbf{1})$:

$$\boldsymbol{x}_i^j(\boldsymbol{t}+\mathbf{1}) = \left[\left(p_i^j + r_i^j\right) \Big/ \sum\nolimits_{j=1}^{3} (p_i^j + r_i^j)\right] \; i = 1,2,3,4 \quad j = 1,2,3 \tag{24}$$

Through interative computing, we hope to get a better condition of the road network which is quantificated as the fitness of the alignment. The fitness is defined as:

$$\text{fitness} = \max\left\{A^i(t)\right\} \quad i = 1,2,3\ldots8 \tag{25}$$

To avoid the congestion of the single direction in an intersection, we set the biggest current alignment length as the fitness value. In the process of iteration, the smaller fitness value is considered to be better.

During the iteration, $\boldsymbol{x}_{U_i}^{\boldsymbol{best}}$ continues to evolve, globally coordinating the signal phase control in the road network. The four intersection will achieve the coordinate and optimized traffic flow distribution.

The computational flow chart is showed in the Fig. 4:

4 Performance Evaluation

By using distributed interactions and PSO, the signal control strategies of the particles are induced co-evolutionary, self-organized, and self-adaptive to varying environmental conditions. Finally, simulation results have also been supplemented to show that our proposed method can better benefit the global traffic network than the conventional fixed-time control in term of robustness and traffic efficiency regardless of its large-scale complexity and dynamic nature.

We simulate our bio-inspired algorithm based on the road network with four intersections. To compare with the conventional fixed-time control, we set the same initial value and parameter for our algorithm. We initially set every movement as empty. For every movement, the maximum passing capacity is 3600 vehicles per hour. We differentiate the entering traffic flow to see the performance of the algorithm under different conditions. If the outflow rate is lower than the inflow rate, the condition is defined as unsaturated, and conversely it is defined as saturated.

For one single direction, the inflow of whole network with 4 intersections is differentiated as 1600, 2400, 3200, 4000, 4800 vehicles per hour. And we set the ratio of the flow rate in the left-turn movement and straight movement as 1.0 and 0.5 to test the

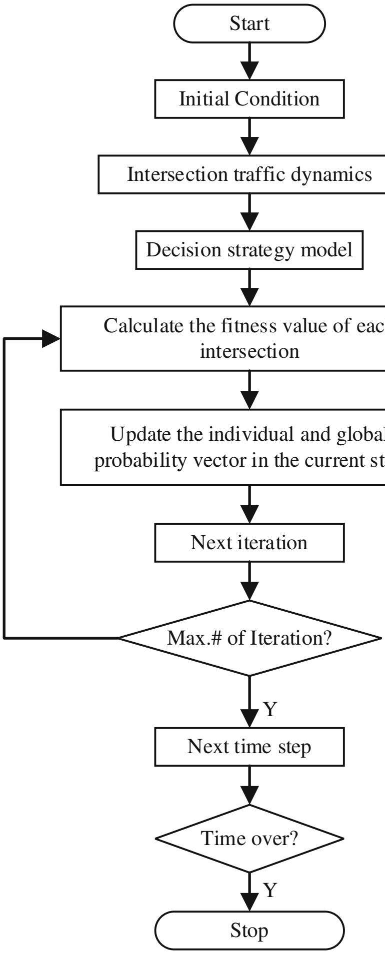

Fig. 4. Computational flow chart

algorithm under different conditions. We set the same time interval to be 30 s. Inertia coefficient $\omega = 0.3$.

Figure 5 shows the performance of the algorithm under Left-turn/straight = 1.0 condition:

In the unsaturated part where the inflow rate is relatively small, the conventional fixed-time control is capable to coordinate the traffic situations. We can see that the performance of the bio-inspired algorithm and the conventional control is relatively close. In the saturated part, we can see a good improvement compared with the conventional control. When the inflow rate reaches 4000 vehicles per hours, the algorithm can optimize the maximum queuing length for about 26%. When it reaches 4800 vehicles per hours, the improvement is more obvious.

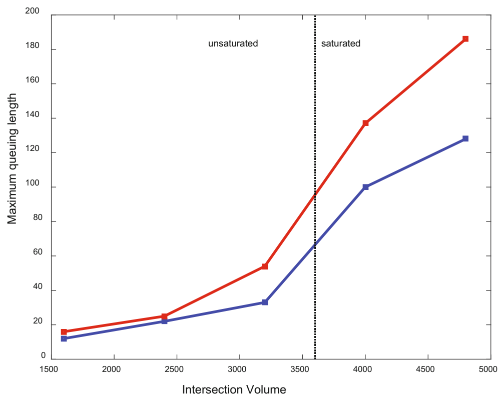

Fig. 5. Algorithm performance comparison

For the ratio of Left-turn/straight = 0.5 condition, generally both controls have better performances than the Left-turn/straight = 1.0 condition. Analogously we still can see that our bio-inspired algorithm has a good improvement on the traffic conditions (Fig. 6).

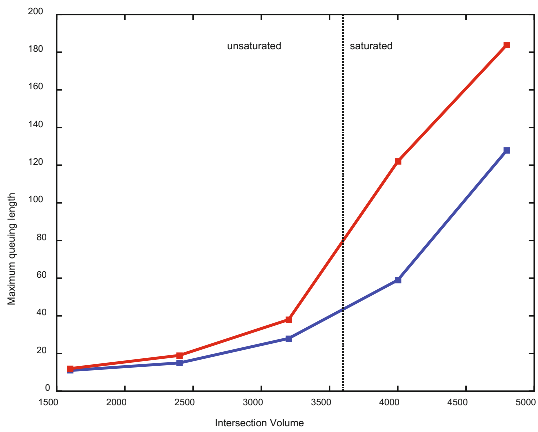

Fig. 6. Algorithm performance comparison

As for the general situation of the intersection, since we set the fitness as the maximum of the queuing length. As the algorithm trying to reduce the value of the maximum queuing length, the vehicles need to be distributed to the rest of the movements, which will greatly help to reasonably coordinate the traffic flows. We selected the inflow rate of the 3200 vehicles per hour situation to see the performance. We can see that the distribution of the traffic flow is more reasonable than the conventional control (Fig. 7).

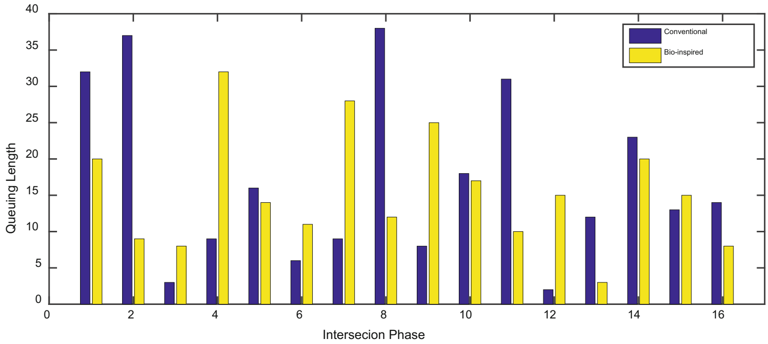

Fig. 7. Queuing length comparison

5 Conclusions

We use the particle swarm intelligent inspired algorithm to find the rational proportion of the signal lights, and map the sequential control way to promote the condition of the traffic intersection. We simulate the four-intersection situation in this paper. As the results show, the algorithm has a good progress under different situations. For larger road network, the algorithm will show good reliability and efficiency of the traffic control.

Acknowledgments. This research was supported by the National Key Research and Development Program of China (2017YFB0102500).

References

1. Tian, D., Zhou, J., Wang, Y., Sheng, Z., Xia, H., Yi, Z.: Modeling chain collisions in vehicular networks with variable penetration rates. Transp. Res. Part C Emerg. Technol. **69**, 36–59 (2016)
2. Tian, D., Zhou, J., Wang, Y., Xia, H., Yi, Z., Liu, H.: Optimal epidemic broadcasting for vehicular ad hoc networks. Int. J. Commun Syst. **27**(9), 1220–1242 (2014)
3. Tian, D., Zhou, J., Wang, Y., Lu, Y.: A dynamic and self-adaptive network selection method for multimode communications in heterogeneous vehicular telematics. IEEE Trans. Intell. Transp. Syst. **16**(6), 3033–3049 (2015)
4. Cao, L., Hu, B., Dong, X., et al.: Two intersections traffic signal control method based on ADHDP. In: IEEE International Conference on Vehicular Electronics and Safety. IEEE (2016)
5. Tian, D., Zhou, J., Sheng, Z., et al.: From cellular attractor selection to adaptive signal control for traffic networks. Sci. Reports **6**, 23048 (2016)
6. Ren, Y., Wang, Y., Yu, G., et al.: An adaptive signal control scheme to prevent intersection traffic blockage. IEEE Trans. Intell. Transp. Syst. **18**, 1519–1528 (2016)
7. Li, L., Lv, Y., Wang, F.Y.: Traffic signal timing via deep reinforcement learning. IEEE/CAA J. Autom. Sinica **3**(3), 247–254 (2016)

8. Geng, Y., Cassandras, C.G.: Multi-intersection traffic light control using infinitesimal perturbation analysis. IFAC Proc. **45**(29), 104–109 (2012)
9. Parker, M., Pursula, M., Egyháziová, E.: Evaluating off-peak traffic signal control strategies. Comput. Aided Civil Infrastruct. Eng. **14**(5), 379–383 (1999)
10. Duan, H., Sun, C.: Swarm intelligence inspired shills and the evolution of cooperation. Sci. Reports **4**(6), 5210 (2014)
11. Zhu, Y., Zhang, G., Qiu, J.: Network traffic prediction based on particle swarm BP neural network. J. Networks **8**(11), 2685–2691 (2013)

Energy-Efficient Data Collection Using Lossless Compression for Industrial Wireless Sensor Networks

Xiaolan Tang[1], Hua Xie[1], Wenlong Chen[1(✉)], and Jianwei Niu[2]

[1] College of Information Engineering, Capital Normal University, Beijing 100048, China
chenwenlong@cnu.edu.cn

[2] State Key Laboratory of Virtual Reality Technology and Systems, School of Computer Science and Engineering, Beihang University, Beijing 100191, China

Abstract. Industrial wireless sensor network is an important technology for precise monitoring in industrial systems. Sensors are deployed densely in various industry applications, where the high density of sensors results in large amounts of redundant data. Therefore, information aggregation is used to avoid forwarding redundant data and thus save limited resources. However, when decreasing transmission cost, existing aggregation schemes lead to low data accuracy and long delivery latency. In this paper, we propose an energy-efficient data collection solution using lossless compression for industrial wireless sensor networks, namely ECL, aiming for high energy efficiency and high information entropy. According to three aggregation rules, aggregation regions are constructed in a distributed way based on a preset threshold of sensing duplication rate. Therefore, the aggregated data are probably similar, and ECL has the original entropy through removing only the redundant data. Experiment results show that compared with other schemes, ECL keeps about 38% and 48% higher data accuracy and 12% and 25% shorter maximum end-to-end delay than EEUC and HEER, respectively, with a similar lifetime.

Keywords: Industrial wireless sensor networks · Sensing duplication rate · Data aggregation · Redundant data

1 Introduction

Industrial Wireless Sensor Network (IWSN) plays a vital role in creating a highly reliable and self-healing industrial system that rapidly responds to real-time events with appropriate actions. Machines are automatically controlled by using the obtained information to make an efficient production line [1]. In order to improve the stability and robustness of the entire network and the accuracy of gathered information, sensor nodes are usually densely deployed in industrial

© ICST Institute for Computer Sciences, Social Informatics and Telecommunications Engineering 2018
Y. Chen and T. Q. Duong (Eds.): INISCOM 2017, LNICST 221, pp. 14–27, 2018.
https://doi.org/10.1007/978-3-319-74176-5_2

areas [2]. However, more than enough sensors lead to a large amount of redundant data. Forwarding these redundancy further wastes the nodes' energies and bandwidths, which reduces energy efficiency and shortens network lifetime.

Data aggregation is widely utilized in IWSNs, aiming for reducing the transmissions of redundancy [3]. Specifically, in most aggregation protocols, the general network is divided into some areas/cells based on the geographical locations. A selected node gathers and aggregates all the obtained data in each area [4]. Since the data might be delivered to an aggregation node through several hops, the redundant information wastes a large amount of communication resources due to multi-hop relays. Meanwhile, multiple forwarding brings in a long latency for data aggregation [5,6]. In addition, because of the possible random distribution of nodes and several times of aggregation of the raw data, data accuracy is reduced, which affects the performance of data collection.

In this paper, we propose an energy-efficient data collection scheme using lossless compression for IWSNs, named ECL, to keep high data accuracy when aggregating data. Several sensors construct an aggregation region if their sensing duplication rate equals or is larger than a preset threshold. In this way, the data in an aggregation region are spatial correlated, and the contents are similar, which would be aggregated efficiently and accurately. Moreover, since there are only two levels of nodes in an aggregation region, it limits the hops of redundancy forwarding and decreases the transmission overhead as much as possible. Additionally, for further energy efficiency, a proper neighbor node could also be selected as an aggregation node. Through lossless compression algorithms, ECL keeps the original entropy by only deleting the repeated information in the collected data.

The contributions of ECL scheme are as follows. (1) Utilize the sensing duplication rates to construct aggregation regions. It helps to improve the accuracy of information and diminish the energy consumption. (2) Three aggregation rules are designed to support aggregating node selection from available parent nodes or appropriate neighbor nodes. Thus, it establishes an efficient and accurate data route for each sensor. (3) From lots of simulation experiments, ECL scheme shows high information accuracy, energy efficiency and fast collection of data.

The reminder of this paper is organized as follows. Section 2 introduces related work on data aggregation. After discussing on aggregation rules used in ECL in Sect. 3, the implementation of ECL is illustrated in Sect. 4. Experimental results are analyzed in Sect. 5, and Sect. 6 concludes this paper.

2 Related Work

In IWSNs, data aggregation helps to remove the same information from several collected packets and thus reduce the resource consumption when delivering information from sensor nodes to the sink. In specific, data aggregation schemes are classified into three categories, i.e., tree-based aggregation [7,8], hybrid aggregation [9], and cluster-based aggregation [10–13].

Cluster-based aggregation usually has better scalability and higher energy efficiency than tree-based and hybrid aggregation [10,11]. Since the cluster heads which are closer to the sink, relay more data than others, they are easy to run out of power. In an energy-efficient unequal clustering scheme (EEUC) [12], cluster heads are elected by localized competition, and the competition range becomes small when it is near the base station. Therefore, those clusters closer to sink have smaller cluster sizes than others, and the energy consumption of cluster heads is balanced. Even though, the cluster maintenance is somewhat difficult.

In order to deal with the cluster update problem, Yi and Yang design Hamilton energy-efficient routing protocol (HEER) [13]. A Hamilton path consists of members in a cluster, which take turns to be the unique cluster head. The first round of cluster construction is like LEACH and may result in energy hole problem. The assumption that all members in a cluster can communicate with each other is too strict, and data transmissions in turn along the Hamilton Path lead to a long delivery latency.

IWSNs are required to provide highly reliable and real-time transmissions. Shu et al. investigate the routing performance of TPGF in CKN-based duty-cycled IWSNs with radio irregularity, in terms of the number of explored routing paths as well as the lengths of the average and shortest routing paths. They prove that the cross-layer optimized version of TPGF finds reliable transmission paths with low end-to-end delay [14]. Considering the resource constraint in IWSNs, a cross-layer optimization scheme named Adjusting the Transmission Radius (ATR) is proposed. In EC-CKN-based WSNs, it solves two important problems, namely, the death acceleration problem and the network isolation problem [15].

Present data aggregation researches construct clusters based on preset geographical scale. If the preset scale is too large, the collected data from member nodes have low similarity, which results in low accuracy after aggregation; if the preset area is too small, data aggregation does not function well. To combine the advantages of data aggregation and high accuracy, we attempt to remove redundant data efficiently by using the threshold of sensing duplication rate to construct aggregation regions.

3 Network Model and Aggregation Rules

In an IWSN we focus on, all sensor nodes have the same sensing radius, denoted by R_S; the communication radius is the same, denoted by R_C, and $R_C > 2R_S$ [16]; the size of data collected from each sensor is d. Table 1 lists the main symbols used in ECL.

Definition 1. *Transfer topology L: The topology is a directed acyclic diagram of all the sensors, which indicates communication relations and levels.*

For the adjacent levels in the topology, the level with a smaller value is called upper-level (L_i) and that with a higher value is called lower-level ($L_i + 1$). Since a node may link with more than one up-level nodes, L is similar to but not the same with a tree structure. In a dense network we focus on, it is assumed that all the sensor nodes can communicate with the sink by one hop or multi-hop transfers. Therefore, all the nodes are included in the transfer topology.

Table 1. Symbols.

Symbol	Description
R_S	Sensing radius of a sensor node
R_C	Communication radius of a sensor node
SDR	Sensing duplication rate, which indicates the ratio of two nodes' sharing sensing area to each one's own sensing range
SDR_T	Threshold of sensing duplication rate, which is utilized to select the aggregation nodes
AR_i	Aggregation region with the aggregation node v_i, in which the collected information are aggregated by the node v_i
AN	Aggregation node, which aggregates data collected in an aggregation area and transfers the aggregated to sink
AVL_AN_i	Available aggregation node set of v_i, where the nodes have the privilege to be aggregation node
MN	Member node, which sends its data to the aggregation node in its aggregation region
AVL_P_i	Available parent node set of v_i, which is comprised of all the upper-level nodes that could communicate with v_i directly
N_i	Neighbor node set of v_i, including all the nodes in the same level that could communicate with v_i directly
IN	Independent node, which has a low sensing duplication rate with its available parent nodes and neighbor nodes, and sends its data to sink without data aggregation
L	Level, which represents the hierarchy value of the sensor node and $L \geq 0$
S_C	The overlapping sensing area of two nodes

An example of transfer topology is illustrated in Fig. 1. There are m nodes in the network. Node 0 (v_0) is the sink, and the edges show the possible communication probabilities among nodes. In particular, the parent-child relations are shown by solid lines, while the neighbor relations are indicated by dotted lines.

Definition 2. *Sensing duplication rate, SDR: The ratio of the sensing duplication area to the sensing range of each node ($\pi {R_S}^2$). Thus the nodes sharing the sensing duplication area have the same sensing duplication rate.*

Since each sensor monitors its whole sensing area, we assume that the amount of collected data from a sensor is proportional to the area of sensing range. Therefore, a larger SDR implies a larger amount of duplicated information. ECL scheme only removes duplicated data, and retains the entropy of all the original data. It works as a lossless compression algorithm with the sensing duplication rate as its compression ratio.

For the sake of data accuracy, a threshold of sensing duplication rate, denoted by SDR_T, is introduced for aggregation node selection. The specific value of

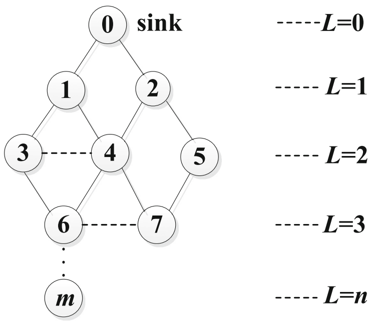

Fig. 1. Transfer topology.

SDR_T influences the performance of data aggregation. A small SDR_T may result in large aggregation regions, where the collected data from members have low similarity; otherwise, the larger SDR_T is, the smaller aggregation regions leads to low energy efficiency. Selecting a suitable value for SDR_T requires comprehensive analysis.

Definition 3. *Aggregation region, AR: An aggregation region is an area consisting of an aggregation node and several member nodes. A aggregation node gathers and aggregates all the data in a region and then forwards the results to the sink, while a member node only sends its data to its aggregation node.*

An aggregation region with node v_i as aggregation node and $v_j, \ldots, v_k$ as member nodes is presented with $AR_i = (v_i, \{v_j, \ldots, v_k\})$. Note that one node is included in at most one aggregation region; $AR_i \bigcap AR_j = \emptyset (i \neq j)$. If node v_k does not join in an aggregation region, v_k works as an independent node, $AR_k = (v_k, \emptyset)$. If a node v_m is not an aggregation node, we call v_m non-aggregation node. In the initial phrase, no aggregation regions exist, and all the nodes are free nodes.

Definition 4. *Available aggregation node set of v_i, AVL_AN_i: A set consists of all the nodes having the privilege to be the aggregation node for v_i.*

Definition 5. *Available parent node set of v_i, AVL_P_i: A set consists of those nodes at level $L_i - 1$ which could directly communicate with v_i (level L_i).*

Definition 6. *Neighbor nodes set of v_i, N_i: A set is composed of those nodes at level L_i which could directly communicate with v_i (level L_i).*

Figure 2 shows a transfer topology, which has three aggregation regions. v_3, v_6 and v_7, as the member nodes, transmit their data to the aggregation node v_4 directly, therefore $AR_4 = (v_4, \{v_3, v_6, v_7\})$. Similarly, aggregation node v_2 receives the data from v_5 and aggregates these data, $AR_2 = (v_2, \{v_5\})$. v_1 transmits its data to sink directly, expressed as $AR_1 = (v_1, \emptyset)$.

There are three rules to guide aggregation node selection and data routing in ECL.

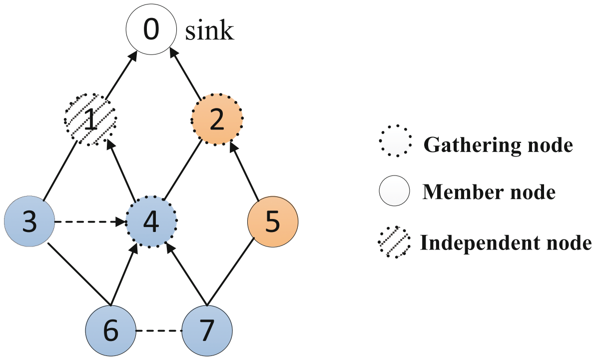

Fig. 2. An instance with three aggregation region.

Rule 1. *In an aggregation region, the available parent nodes have priorities to be chose as aggregation nodes.*
Rule 2. *After all the lower-level nodes joined an aggregation region, the free nodes in the upper-level prefer to find their aggregation nodes from the available parent nodes, and then the neighbor nodes are taken into account.*
Rule 3. *Sensor data are aggregated at most once. In the phase of relay node selection, the non-aggregation nodes are first choice and then the available parent node with most power is considered.*

4 Implementation of ECL Scheme

The transfer topology of sensor network is established through broadcasting hello messages among nearby nodes. Hello message has the sender's identifier, location, remaining power and the level in transfer topology. The nodes that could communicate directly at the same level are included in the neighbor node set, while the upper-level nodes communicating directly are added to the available parent node set. In initialization phase, the level of sink is set to 0, and that of sensors is infinity. Sink sends its hello message, and then other nodes update their levels with the small values compared with receiving hello messages. In detail, upon receiving a hello message, v_i checks whether its current level value L_i is 1 plus the level in received hello message. If true, v_i updates L_i with the level in hello message plus 1, and then propagates hello message with the new level value; otherwise, if the level in received message is larger than L_i by 1, v_i adds the identifier in hello message to AVL_P_i; if the difference between the local level and the received level equals 0, v_i stores the identifier in hello message to N_i.

4.1 Aggregation Region Construction

After transfer topology is finished, sensor nodes begin to construct the aggregation region distributively. Aggregation region construction is sequencing activity which starts from free nodes in the lowest level and then to the upper-level layer by layer. The construction phase follows three rules in Sect. 3. A free node might be picked as an aggregation node to construct an new aggregation region, or join in an aggregation region as a member node, or work as an independent node to deliver data to sink directly. Take v_i as an example, Algorithm 1 shows the aggregation region construction phase, and finding available aggregation nodes is described in Algorithm 2.

Algorithm 1. Aggregation region construction.

Input: the transfer topology, a free node v_i
Output: AR_i

if *several nodes M request to be members of AR_i* **then**
  construct aggregation region $AR_i = (v_i, M)$, and reply to M;
else
  if $L_i \neq 1$ **then**
    $AVL\_AN_i \leftarrow$ Algorithm 2;
    if $AVL\_AN_i = \emptyset$ **then**
      v_i is an independent node, $AR_i = (v_i, \emptyset)$;
    else
      select $v_t \in AVL\_AN_i$ with max E_t to be the aggregation node of v_i;
      send the request to be a member of AR_t;
    end
  else
    v_i is an independent node, $AR_i = (v_i, \emptyset)$;
  end
end
return AR_i;

In Algorithm 1, the residual energy of node v_i is denoted by E_i. At the first, complete transfer topology construction with $(n+1)$ levels for all the free nodes, and thus the nodes at level n begin aggregation region construction. Any node v_i with $L_i > 1$ calculates its sensing duplication rates related to nearby nodes, and updates its available aggregation node set by executing Algorithm 2 (finding available aggregation node set algorithm). If the available aggregation node set AVL_AN_i is empty, v_i turns into an independent node; otherwise, v_i selects the node v_t with the most remaining power in CG_i as its aggregation node, and sends a request to join the aggregation region AR_t. Regarding a free node v_j in level 1, it is invalid to take the sink as aggregation node. Meanwhile, its sensing duplication rate with any neighbor cannot be bigger than 2 (Rule 2). Thus, v_j becomes an independent node, and sends its data to the sink without aggregation.

Algorithm 2 returns the available aggregation node set of v_i. For every available parent node v_j of v_i, if $SDR_{i,j} \geq SDR_T$, v_j is inserted to the set AVL_AN_i. Only if no available aggregation node is picked from the available parent node

Algorithm 2. Finding available aggregation node set.

Input: AVL_P_i, N_i
Output: AVL_AN_i

initialize:$AVL\_AN_i \leftarrow \emptyset$;
for $\forall\ v_j \in AVL\_P_i$ **do**
    if $\exists\ SDR_{i,j} \geq SDR_T$ **then**
        $AVL\_AN_i \leftarrow AVL\_AN_i \cup \{v_j\}$;
    end
end
if $AVL\_AN_i = \emptyset$ **then**
    for $\forall\ v_k \in N_i$ **do**
        if $SDR_{i,k} \geq SDR_T$ *and* $SDR_{i,k}(2L_i - 1) > 2$ **then**
            $AVL\_AN_i \leftarrow AVL\_AN_i \cup \{v_k\}$;
        end
    end
end
return AVL_AN_i;

set, v_i considers the sensing duplication rate with its neighbors. If a neighbor v_k has $SDR_{i,k}(2L_i - 1) > 2$ and $SDR_{i,k} \geq SDR_T$, v_i stores v_k into AVL_AN_i.

4.2 Data Routing

In an aggregation region, member nodes only transfer their own data to the aggregation node by one hop transfer; the aggregation node collects and aggregates data from all the members in this region and transmits them to sink along energy-efficient paths; sensing data of independent nodes are sent to sink without any aggregation. Energy-efficient paths are selected according to Rule 3, in which the non-aggregation nodes have priority to forward data and then powerful available parent nodes are picked to be relays.

Take Fig. 1 as an instance. Its construction of aggregation regions and data routing are depicted in Fig. 3. Suppose that v_4 has more energy left than v_3, $SDR_{3,4} = 0.7$. At the highest level, there are two nodes, v_6 and v_7, which obtain the sensing duplication rates with their available parent nodes v_4, v_5 and v_3. Suppose that $SDR_{4,6} > SDR_{3,6} > SDR_T$, $SDR_{4,7} > SDR_T > SDR_{5,7}$, thus $CG_6 = \{v_3, v_4\}$, $CG_7 = \{v_4\}$. Due to $E_4 > E_3$, v_6 and v_7 both choose v_4 as their aggregation node, $GA_4 = (v_4, \{v_6, v_7\})$. Since no free nodes exist in level 3, v_3 and v_5 in level 2 start to find their aggregation regions. Considering the available parent nodes, suppose that $SDR_{1,3} < SDR_T$, $SDR_{2,3} < SDR_T$ and $SDR_{2,5} = SDR_T$. Thus, at the moment, $CG_3 = \emptyset$, and $CG_5 = v_2$. In this way, v_5 chooses v_2 as it aggregation node, $GA_2 = (v_2, \{v_5\})$. Since $CG_3 = \emptyset$, v_3 further considers its neighbor node v_4, and gets $SDR_{3,4} \times (2L_3 - 1) = 0.7 \times 3 > 2$. Since v_4 is the only neighbor of v_3, v_3 selects v_4 to be its aggregation node ($AVL\_AN_3 = \{v_4\}$). Until then, $AR_4 = (v_4, \{v_3, v_6, v_7\})$, and no free nodes are in level 2. According to previous analysis, all free nodes in level 1 should be independent nodes. Thus, v_1 turns into independent node. The aggregation region construction is completed here. For the data routing, nodes v_3, v_6 and v_7 transfer their own data to v_4, which aggregates all the data in AR_4. Then v_4 selects v_1 (non-aggregation node) as relay node to sink. Node v_5 sends data to its aggregation node v_2, which transfers data to sink directly, while v_1 delivers its data to sink without aggregation.

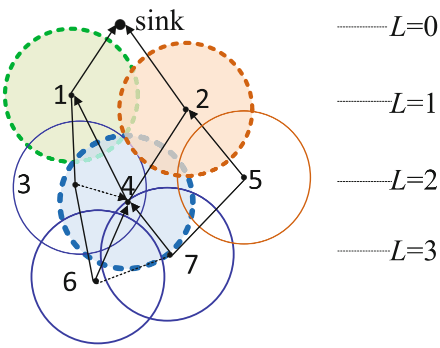

Fig. 3. An example of ECL implementation.

4.3 Complexity Analysis

In the Algorithm 2 (finding available aggregation node set), if each node v_i visits all the nodes in AVL_P_i and N_i, the computation complexity is $O(\max_{\forall i \in [1,m]} (|AVL\_P_i| + |N_i|))$ in the process of finding the available aggregation node set AVL_AN_i. Correspondingly, the computation complexity of Algorithm 1 (aggregation region construction) is $O(\max_{\forall i \in [1,m]} |AVL\_AN_i|)$. Because the number of nodes in AVL_P_i, N_i and AVL_AN_i are all smaller than m (the number of sensors), the computing complexity of algorithms is $O(m)$.

With regard to transfer topology establishment, sink broadcasts the control message firstly and other nodes update and resend it out after reception, in which the control message complexity is m. In order to set aggregation regions, node v_i sends requests to its potential aggregation nodes, and after receiving acceptance messages, v_i replies with a response message to join in an aggregation region. In this phase, control message cost is $3m$. In conclusion, message complexity of ECL is $O(m)$.

With respect to additional information, every node only carries its level, remaining energy, available parent set and neighbor set, and thus the storage complexity is $O(m)$. The message complexities of HEER and EEUC both are $O(m)$, while HEER has exponential computation complexity. Overall, ECL has relatively low computation complexity and requires small storage spaces.

5 Performance Evaluation

5.1 Network Configurations

For accurate analysis, we analyze the performance of ECL scheme on OPNET Modeler [17] network simulation platform. Table 2 lists the network configurations. Note that sensor nodes are distributed in the target field with common density. In scenario, the nodes are deployed in a pyramid field, of which the top is the sink. In the experiments, for the adequate power of sink, only the energy of sensor nodes are taken into account. Since data transmission and reception cost most of the energy, small consumptions in data processing are ignored. Besides, the energy consumption of sensing is fixed, because every node collects the same size of data. Therefore only the transmission overhead is focused on.

Table 2. Simulation parameters.

Parameter	Value
Scenario (m^2)	100×100
Number of sink	1
Number of sensors	40, 80, 120, 160 and 200 (nodes)
Sensing radius (m)	25
Communication radius (m)	52
Data collection cycle (s)	60
SDR_T	0.5

In the simulation experiments, we compare the proposed scheme ECL with a latest data collection scheme HEER and a typical aggregation scheme EEUC. HEER uses Hamilton Path to realize data routing and forms clusters in a similar way with LEACH. Specifically, Hamilton Path is designed for the sequence of data transfers, as analyzed in Sect. 2. In another compared scheme EEUC, cluster heads are elected by localized competition in a distributed way. In the cluster construction phase, a competition range is calculated according to the distance to the base station, and is used to control the sizes of clusters. The final cluster heads are elected by several tentative nodes. After the cluster heads have been decided, accordingly ordinary nodes request to be members of their closest cluster heads. In order to see the different performances of aggregation node selection algorithms, we also regard a variation of ECL, ECL-CP, as a compared scheme. In ECL-CP, the aggregation nodes are only selected from available parent nodes. In other words, neighbor nodes cannot be picked as aggregation nodes.

It is noteworthy that, in different data collection schemes, the sizes of aggregation output packets are not the same. In ECL, when an aggregation node aggregates x data packets, it gets $p(0 < p < x \cdot d)$ amount of data thereafter, where p is decided by sensing duplication rate in this aggregation region. Because

ECL uses lossless compression algorithm, which only deletes repetition of sensing duplication areas, the general information received by sink is correct and lossless. While in compared schemes, aggregation function is compressing x data packets into a fixed packet whose size is d.

For the performance analysis, four following metrics are introduced. First, information accuracy [18] is the proportion of the information entropy gathered by sink in all the generated data in the scenario. Second, network lifetime is the period of time from the start of data collection to the time when a sensor runs out of battery. Third, the longest path to sink is the longest path from sensors to sink in the network lifetime. A larger value for the longest path to sink indicates a longer delay for the sink to gather the sensing data from all the sensors deployed in the target monitoring field, and thus it represents the data collection latency. Fourth, transmission overhead is the number of data transmitted in one round of data transfer. It implies the energy consumption of data transfer and reception by all the sensors.

5.2 Experiment Results

In this subsection, we discuss the simulation results of all the schemes mentioned above, i.e., ECL, ECL-CP, EEUC and HEER, and the results are illustrated in Fig. 4.

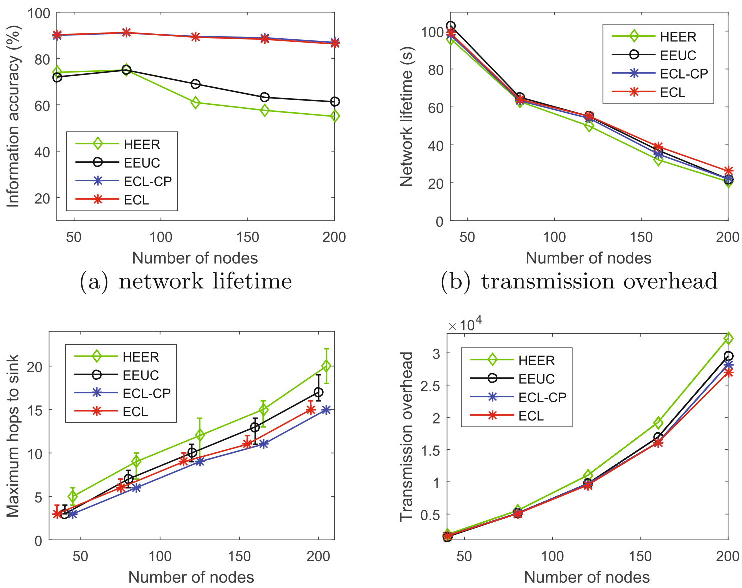

(a) network lifetime (b) transmission overhead

(c) maximum hops to sink (d) information accuracy

Fig. 4. Experiment results.

As Fig. 4(a) depicts, the data correctness in ECL is about 88%, which is the highest compared with other three comparisons. It is very similar to ECL-CP and has 38% and 48% higher ratio than EEUC and HEER respectively. It is obvious that aggregating a large amount of data into a small package easily introduces information loss. Moreover, regarding an original data packet generated by a sensor, multiple times of data aggregation further aggravate the information inaccuracy. On a Hamilton Path in HEER, the end node begins data transmission to its neighbor which is closer to cluster head. After that, the neighbor aggregates its obtained data into one package with a fixed size, and then send it to the next node on the path until arriving at the cluster head. As a result, the raw data may be aggregated multiple times at different forwarders. Every cluster, in EEUC, aggregates data from all members into one packet with a constant size, not considering different duplication ratios. In comparison, sensor data of ECL are required to be aggregated once, and keep the information entropy through lossless compression. Therefore, ECL keeps the most information compared with others. Because some nodes are not included in the transfer topology (in other words, they can not communicate with others), the information accuracy is not 100% in ECL.

In the Fig. 4(b), EEUC has the longest lifetime with 40 sensors deployed in the scenario, and the lifetime of ECL is the second longest. As the number of nodes increases, the lifetime of ECL which is longer than ECL-CP, gradually becomes longer than EEUC when there are over 120 nodes. Meanwhile, HEER has the shortest lifetime. EEUC has a single length-fixed packet as aggregation output in each cluster, and the fixed size is smaller than that in ECL. There are two primary reasons why ECL gradually has long lifetime. (1) The duplicated data are transferred for multiple hops in EEUC, but ECL only forwards the redundant information once. (2) The cluster heads of EEUC may be in lower levels of the cluster, while in ECL, almost all the aggregation nodes are from upper levels, which ensures that the data always go up along the transfer topology without loops.

Since the longest paths in several rounds of experiments for HEER are not stable, median values are calculated in Fig. 4(c). As the figure illustrates, ECL-CP has the shortest paths and the numbers of hops are relatively stable. In addition, ECL only has few cases with long paths to sink. The reason for that is all the aggregation nodes in ECL-CP are the upper-level nodes, and hence data are only transferred upwards; in ECL, a part of aggregation nodes are picked from neighbor nodes, which slightly prolongs the paths for data collection. When there are more sensors, the numbers of hops along the longest paths in EEUC and HEED have sharp rises and fluctuate. The paths are longer than those in ECL, especially for HEED. With the scale of 200 nodes, the longest paths in ECL are shorter than those in EEUC and HEER by 12% and 25%, respectively. Because members transfer data to their aggregation nodes directly in ECL and ECL-CP, which ensures the shortest distances to sink. However, multi-hop routing inside a cluster is common in EEUC, and the members, in HEER, forward their data to the cluster head according to the order of nodes on Hamilton Paths, which leads to a longer path to sink and a longer end-to-end latency.

As Fig. 4(d) shows, when the network scale is 80 nodes, the transmission overhead of one data collection round in ECL is a little smaller than those in ECL-CP and EEUC schemes. When the number of nodes increasing, the transmission overhead of HEER, EEUC and ECL-CP are increasing quicker than ECL. In the 200 nodes scenario, ECL has a smaller transmission overhead than ECL-CP, EEUC and HEER by about 4%, 11% and 18% respectively. However, HEER always has the biggest overhead among four comparisons.

To sum up, the proposed scheme ECL reaches a high data accuracy, and meanwhile maintains energy-efficient and fast data collection.

6 Conclusion and Future Work

In order to support precise control in industrial systems, IWSNs are highly required in modern industry, and require an energy-efficient and lossless data aggregation protocol. In this paper, we propose an energy-efficient data collection scheme using lossless compression for IWSNs, named ECL. In the transfer topology, a threshold SDR_T is introduced for aggregation node selection from available parent nodes and neighbor nodes, which guarantees that sensors in an aggregation region keep a high correlation of collected information. Only cleaning redundant data does not reduce the data accuracy and ensures energy efficiency. Member nodes only forward data to their aggregation nodes by one hop transmission, and then the aggregation nodes aggregate sensor data immediately, which maintains a short collection latency. Simulation experiments on OPNET platform show that ECL scheme achieves a much higher data accuracy and a shorter latency than EEUC and HEER schemes, when working for a similar lifetime.

Moreover, network density is a significant factor for the proper assignment of SDR_T, which requires further study. Meanwhile, the energy-efficient data collection solution with a high accuracy for several concurrent events [19] also needs indepth explorations in the future.

Acknowledgments. We gratefully acknowledge the support from the National Natural Science Foundation of China (61502320, 61373161, 61173009 & 61572060), Science & Technology Project of Beijing Municipal Commission of Education in China (KM201410028015), Youth Backbone Project of Beijing Outstanding Talent Training Project (2014000020124G133), 973 Program (2013CB035503), CERNET Innovation Project (NGII20151004, NGII20160316), Beijing Advanced Innovation Center for Imaging Technology, and Cultivation Object of Young Yanjing Scholar of Capital Normal University.

References

1. Gungor, V.C., Hancke, G.P.: Industrial wireless sensor networks: challenges, design principles, and technical approaches. IEEE Trans. Industr. Electron. **56**(10), 4258–4265 (2009)
2. Tang, X., Juhua, P., Gao, Y., Xiong, Z., Weng, Y.: Energy-efficient multicast routing scheme for wireless sensor networks. Trans. Emerg. Telecommun. Technol. **25**(10), 965–980 (2014)

3. Zhang, X., Liang, W., Haibin, Y., Feng, X.: Optimal convergecast scheduling limits for clustered industrial wireless sensor networks. Int. J. Distrib. Sens. Netw. **2012**, 1319–1322 (2012)
4. Kumar, A., Baksh, R., Thakur, R.K., Singh, A.P.: Data aggregation in wireless sensor networks. Int. J. Sci. Res. **3**(3), 249–251 (2014)
5. Singh, S.P., Sharma, S.C.: A survey on cluster based routing protocols in wireless sensor networks. Comput. Sci. **45**(18), 687–695 (2015)
6. Zeb, A., Muzahidul Islam, A.K.M., Zareei, M., Al Mamoon, I., Mansoor, N., Baharun, S., Katayama, Y., Komaki, S.: Cluster analysis in wireless sensor networks: the ambit of performance metrics and schemes taxonomy. Int. J. Distrib. Sensor Netw. **12**(7) (2016)
7. Fasolo, E., Rossi, M., Widmer, J., Zorzi, M.: In-network aggregation techniques for wireless sensor networks: a survey. IEEE Wirel. Commun. **14**(2), 70–87 (2007)
8. Zhang, Y., Juhua, P., Liu, X., Chen, Z.: An adaptive spanning tree-based data collection scheme in wireless sensor networks. Int. J. Distrib. Sens. Netw. **2** (2015)
9. Manjhi, A., Nath, S., Gibbons, P.B.: Tributaries and deltas: efficient and robust aggregation in sensor network stream. Int. J. Distrib. Sens. Netw. **17**(1), 287–298 (2005)
10. Shukla, K.V.: Research on energy efficient routing protocol leach for wireless sensor networks. Int. J. Eng. **2**(3), 1–5 (2013)
11. Younis, O., Fahmy, S.: HEED: a hybrid, energy-efficient, distributed clustering approach for ad hoc sensor networks. IEEE Trans. Mob. Comput. **3**(4), 660–669 (2004)
12. Li, C., Ye, M., Chen, G., Wu, J.: An energy-efficient unequal clustering mechanism for wireless sensor networks. In: IEEE International Conference on Mobile Adhoc and Sensor Systems Conference, pp. 597–604 (2005)
13. Yi, D., Yang, H.: HEER-a delay-aware and energy efficient routing protocol for wireless sensor networks. Comput. Netw. **104**(C), 155–173 (2016)
14. Shu, L., Mukherjee, M., Hu, L., Bergmann, N., Zhu, C.: Geographic routing in duty-cycled industrial wireless sensor networks with radio irregularity. IEEE Access **4**, 9043–9052 (2016)
15. Shu, L., Wang, L., Niu, J., Zhu, C., Mukherjee, M.: Releasing network isolation problem in group-based industrial wireless sensor networks. IEEE Syst. J. **PP**(99), 1–11 (2015)
16. Juhua, P., Yu, G., Zhang, Y., Chen, J., Xiong, Z.: A hole-tolerant redundancy scheme for wireless sensor networks. Int. J. Distrib. Sens. Netw. **1550–1329**, 184–195 (2012)
17. George, T., Trevor, C.: Simulation tools for multilayer fault restoration. IEEE Commun. Mag. **47**(3), 128–134 (2009)
18. Villas, L.A., Boukerche, A., de Oliveira, H.A.B.F., de Araujo, R.B., Loureiro, A.A.F.: A special correlation aware algorithm to perform efficient data collection in wireless sensor networks. Ad Hoc Netw. **12**(1), 10–30 (2011)
19. Dong, M., Ota, K., Liu, A.: RMER: reliable and energy-efficient data collection for large-scale wireless sensor networks. IEEE IoT J. **3**(4), 511–519 (2016)

Outage Probability Analysis of Single Energy Constraint Relay NOMA Network

Sang Quang Nguyen(✉) and Dac-Binh Ha

Duy Tan University, Da Nang City, Vietnam
sangnqdv05@gmail.com, hadacbinh@duytan.edu.vn

Abstract. In this paper, we investigate energy harvesting decode-and-forward relaying non-orthogonal multiple access (NOMA) networks. Specifically, one source node wishes to transmit two symbols to its two desired destinations directly and via the help of an intermediate energy constraint relay node, and the NOMA technique is applied in the transmission of both hops (from source to relay and from relay to destinations). For performance evaluation, we derive the closed-form expressions for the outage probability (OP) at D_1 and D_2. Our analysis is substantiated via Monte Carlo simulation. The effect of several parameters, such as power allocation factors in both transmissions in two hops, the power splitting ratio, the location of relay node, to the outage performances at two destinations is investigated.

Keywords: Non-orthogonal Multiple Access · Energy harvesting
Power splitting · Decode-and-forward

1 Introduction

Due to the significantly growing number of users and wireless devices, the future 5G networks are required to support the demand for low-latency, low-cost and diversified services, yet at higher quality and a thousand-time faster data rate. In the quest for new technologies, non-orthogonal multiple access (NOMA) technique has emerged as one of the most prominent candidates in meeting these requirements. The use of NOMA can ensure a significant spectral efficiency as it takes advantage of the power domain to serve multiple users at the same time/frequency/code. In addition, compared with conventional multiple access, NOMA offers better user fairness since even users with weak channel state information (CSI) can be served in a timely manner.

NOMA in cooperative and cognitive radio networks has been pursued by research groups from Princeton University, USA (Ding et al.) and Queen Mary University of London, UK (Elkashlan et al.) with a focus on cooperative communication protocols and performance analysis of cooperative networks [1] and large-scale underlay cognitive radio networks [2] taking into account users? geographical distribution. Specifically, in [1], the authors analyzed the outage probability and diversity order under the assumption that users with better

© ICST Institute for Computer Sciences, Social Informatics and Telecommunications Engineering 2018
Y. Chen and T. Q. Duong (Eds.): INISCOM 2017, LNICST 221, pp. 28–39, 2018.
https://doi.org/10.1007/978-3-319-74176-5_3

channel conditions can decode the message for the others, and proposed a cooperative NOMA transmission protocol. The work in [2] presented the closed-form expression of outage probability to evaluate the system performance by using stochastic-geometry. Also in this research stream, Men and Ge (Xidian University, China) proposed a NOMA-based downlink cooperative cellular system, where the base station communicates with two paired mobile users through the help of a half-duplex amplify-and-forward (AF) relay [3]. To investigate the performance of the considered network, a closed-form expression of outage probability was derived and ergodic sum-rate was studied. By comparing NOMA with conventional multiple access, the authors showed that NOMA can offer better spectral efficiency and user fairness since more users are served at the same time/frequency/spreading code. Furthermore, J.-B. Kim and I.-H. Lee's research group has investigated NOMA in cooperative networks and derived exact and closed-form expressions of outage probability. The results showed that the system performance is improved significantly with NOMA. Their system model consists of one base station (BS) and two users, in which user 1 communicates directly to the BS while user 2 communicates with the BS through the help of user 1.

For NOMA with RF-EH, authors from Aristotle University have studied data rates optimization and fairness increase in NOMA systems with wireless energy harvesting based on time allocation [4]. The analytical and simulation results indicated that this proposed method is better than TDMA scheme. Moreover, the research group from Queen Mary University of London (UK) and Princeton University (USA) proposed NOMA scheme in simultaneous wireless information and power transfer (SWIPT) networks [5]. Specifically, near NOMA users that are close to the source act as energy harvesting relays to help far NOMA users. Furthermore, the authors investigated the performance of the considered systems by deriving the closed-form expressions for outage probability and system throughput under the random distribution of users' location. Analytical and simulation results showed that selecting users can reasonably reduce the outage probability. Moreover, by carefully choosing the parameters of the network such as transmission rate or power splitting coefficient, system performance can be guaranteed even if the users do not use their own batteries to power the relay transmission.

In this paper, we investigate energy harvesting DF NOMA relaying networks, in which one source nodes want to transmit its two symbols to two destinations directly and via the help of an energy constraint relay nodes. The relay harvests the energy and decode the radio frequency (RF) signal from the source and forward the encoded signal to two destinations. In addition, the NOMA technique is considered for transmission in both hops from the source to relay and from relay to destinations with two set of power allocation factor.

Notation: The notation $\mathcal{CN}(0, N_0)$ denotes a circularly symmetric complex Gaussian random variable (RV) with zero mean and variance N_0. $\mathcal{E}\{.\}$ denotes mathematical expectation. The functions $f_X(.)$ and $F_X(.)$ present the probability density function (PDF) and cumulative distribution function (CDF) of RV

X. The function $\Gamma(x, y)$ is an incomplete Gamma function (Eq. 8.310.1 of [6]). $C_b^a = \frac{b!}{a!(b-a)!}$. Notation Pr[.] returns the probability.

2 Network and Channel Models

As illustrated in Fig. 1, we consider a system model of a NOMA EH DF relaying network, where a source node S want to transmit its two symbols x_1 and x_2 to two destination nodes D_1 and D_2, respectively, directly and via the help of an intermediate EH relay nodes R. All nodes are equipped with single antenna operating in half-duplex mode. In Fig. 1, (h_1, d_1), (h_2, d_2), (h_3, d_3), (h_4, d_4), and (h_5, d_5) denote the Rayleigh channel coefficients over the distances for the links between S and R, R and D_1, R and D_2, S and D_1, and S and D_2, respectively. The corresponding channel gain $g_\Omega \triangleq |h_\Omega|^2$ is exponential random variable (RV) with parameter $\lambda_\Omega = (d_\Omega)^\beta$, with $\Omega \in \{1, 2, 3, 4, 5\}$ and β denote path-loss exponent. The channel state information (CSI) is assumed to be known at all nodes. The corresponding probability density function (PDF) and cumulative distribution function (CDF) of each RV is $f_{g_\Omega}(x) = \lambda_\Omega e^{-\lambda_\Omega x}$ and $F_{g_\Omega}(x) = 1 - e^{-\lambda_\Omega x}$, respectively. The power splitting architecture is apply at relay for harvesting the energy with power splitting ratio ρ and $(1-\rho)$ for decoding the source information.

The channels from S to R, from R to D_1, and from R to D_2 are denoted by h_1, h_2 and h_3, respectively. In the first phase, the source node S broadcast its signal containing two symbols x_1 and x_2 as a form $x = \sqrt{a_1 P} x_1 + \sqrt{a_2 P} x_2$, with $\mathcal{E}\left\{|x|^2 = 1\right\}$, P is a transmit power of source node, a_1 and a_2 respectively denote the power allocation coefficient for symbols x_1 and x_2, and $a_1 + a_2 = 1$, $a_1 \geq a_2$. The received signals at relay R and two destinations D_1 and D_2, respectively, given as

$$y_1 = h_1(\sqrt{a_1 P} x_1 + \sqrt{a_2 P} x_2) + n_1^a \tag{1}$$

$$y_4 = h_4(\sqrt{a_1 P} x_1 + \sqrt{a_2 P} x_2) + n_4^a \tag{2}$$

$$y_5 = h_5(\sqrt{a_1 P} x_1 + \sqrt{a_2 P} x_2) + n_5^a \tag{3}$$

where n_1^a, n_4^a, and $n_5^a \sim \mathcal{CN}(0, N_0)$ denote the additive white Gaussian noise (AWGN) at R, D_1, and D_2, respectively.

At relay R, the received signal y_1 in (1) is split into two parts for energy harvesting $(y_{1,eh})$ and information decoding $(y_{1,id})$:

$$y_{1,eh} = \sqrt{\rho} y_1 = h_1(\sqrt{\rho a_1 P} x_1 + \sqrt{\rho a_2 P} x_2) + \sqrt{\rho} n_1^a \tag{4}$$

$$y_{1,id} = \sqrt{(1-\rho)} y_1 = h_1(\sqrt{(1-\rho) a_1 P} x_1 + \sqrt{(1-\rho) a_2 P} x_2) + \sqrt{(1-\rho)} n_1^a \tag{5}$$

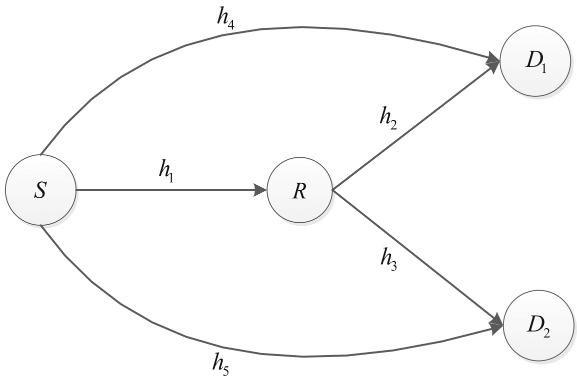

Fig. 1. Network model for NOMA energy constraint DF relaying.

The harvested power at R can be obtained from (4) as:

$$P_R = \eta\rho a_1 P|h_1|^2 + \eta\rho a_2 P|h_1|^2 = \eta\rho P|h_1|^2 = \eta\rho P g_1 \tag{6}$$

The received RF signals is sampled by RF-to-baseband conversion units. Thus, the signals in (2), (3) and (5) are added with the noise $n^c \sim \mathcal{CN}(0, \mu N_0)$, with $\mu > 0$, as

$$y_4^c = h_4(\sqrt{a_1 P}x_1 + \sqrt{a_2 P}x_2) + n_4^a + n_4^c \tag{7}$$

$$y_5^c = h_5(\sqrt{a_1 P}x_1 + \sqrt{a_2 P}x_2) + n_5^a + n_5^c \tag{8}$$

$$y_{1,id}^c = h_1(\sqrt{(1-\rho)a_1 P}x_1 + \sqrt{(1-\rho)a_2 P}x_2) + \sqrt{(1-\rho)}n_1^a + n_1^c \tag{9}$$

First, to decode symbol x_1, the relay R and two destinations D_1 and D_2 treat x_2 as noise. We obtain the signal to interference plus noise (SINR) for x_1 at R, D_1, and D_2, respectively, as

$$\gamma_1^{x_1} = \frac{a_1(1-\rho)P|h_1|^2}{a_2(1-\rho)P|h_1|^2 + (1-\rho+\mu)N_0} = \frac{a_1(1-\rho)\gamma_0 g_1}{a_2(1-\rho)\gamma_0 g_1 + (1-\rho+\mu)} \tag{10}$$

$$\gamma_4^{x_1} = \frac{a_1 P|h_4|^2}{a_2 P|h_4|^2 + (1+\mu)\,N_0} = \frac{a_1\gamma_0 g_4}{a_2\gamma_0 g_4 + 1 + \mu} \tag{11}$$

$$\gamma_5^{x_1} = \frac{a_1 P|h_5|^2}{a_2 P|h_5|^2 + (1+\mu)\,N_0} = \frac{a_1\gamma_0 g_5}{a_2\gamma_0 g_5 + 1 + \mu} \tag{12}$$

where $\gamma_0 \overset{\Delta}{=} \frac{P}{N_0}$ denote the transmit signal to noise (SNR).

Second, the relay R and destination D_2 decode symbol x_2 by cancelling x_1 with successive interference cancellation (SIC) from (9) and (8). The received SNRs for x_2 at R and D_2 are respectively given as

$$\gamma_1^{x_2} = \frac{a_2(1-\rho)P|h_1|^2}{(1-\rho)N_0 + \mu N_0} = \frac{a_2(1-\rho)\gamma_0 g_1}{1-\rho+\mu} \tag{13}$$

$$\gamma_5^{x_2} = \frac{a_2 P|h_5|^2}{(1+\mu)N_0} = \frac{a_2\gamma_0 g_5}{1+\mu} \tag{14}$$

In the second phase, after successfully decoded the symbols x_1 and x_2, relay R forwards them to D_1 and D_2 as a form $(\sqrt{b_1 P_R}x_1 + \sqrt{b_2 P_R}x_2)$ with the transmit power P_R in (6), with b_1 and b_2 denote the power allocation coefficient ($b_1 + b_2 = 1$, $b_1 \geq b_2$). The base-band received signals at D_1 and D_2 are expressed as

$$y_2 = h_2(\sqrt{b_1 P_R}x_1 + \sqrt{b_2 P_R}x_2) + n_2^a + n_2^c \tag{15}$$

$$y_3 = h_3(\sqrt{b_1 P_R}x_1 + \sqrt{b_2 P_R}x_2) + n_3^a + n_3^c \tag{16}$$

where $n_2^a, n_3^a \sim \mathcal{CN}(0, N_0)$, $n_2^c, n_3^c \sim \mathcal{CN}(0, \mu N_0)$.

D_1 decode its desired symbol (x_1) by treating x_2 as noise. From (15), the SINR for decoding x_1 at D_1 is given as

$$\gamma_2^{x_1} = \frac{b_1 P_R|h_2|^2}{b_2 P_R|h_2|^2 + (1+\mu)\,N_0} = \frac{b_1\eta\rho\gamma_0 g_1 g_2}{b_2\eta\rho\gamma_0 g_1 g_2 + 1 + \mu} \tag{17}$$

D_2 decode its desired symbol (x_2) after decoding x_1 (with SINR $\gamma_3^{x_1} = \frac{b_1 P_R g_3}{b_2 P_R g_3 + (1+\mu)N_0} = \frac{b_1\eta\rho\gamma_0 g_1 g_3}{b_2\eta\rho\gamma_0 g_1 g_3 + 1 + \mu}$) and cancelling it. The SNR for decoding x_2 at D_2 is given as

$$\gamma_3^{x_2} = \frac{b_2 P_R|h_3|^2}{(1+\mu)N_0} = \frac{b_2\eta\rho\gamma_0 g_1 g_3}{1+\mu} \tag{18}$$

3 Outage Probability Analysis

In this paper, the receiver decodes successfully the information if its SINR or SNR satisfies the pre-defined threshold γ_t. In this section, we will derive the outage probabilities at D_1, D_2 both cases of one relay and multiple relays under relay selection scheme.

3.1 Outage Probability at D_1

An outage event happens when D_1 unsuccessfully decodes the symbol x_1 both from S in the first phase and from R in the second phase. The outage probability at D_1 can be formulated as

$$\begin{aligned} OP_{D_1}^{1relay} &= \underbrace{\Pr\left[\min\left(\gamma_1^{x_1},\gamma_1^{x_2}\right)<\gamma_t,\gamma_4^{x_1}<\gamma_t\right]}_{OP_1} \\ &+ \underbrace{\Pr\left[\min\left(\gamma_1^{x_1},\gamma_1^{x_2}\right)\geqslant\gamma_t,\max\left(\gamma_4^{x_1},\gamma_2^{x_1}\right)<\gamma_t\right]}_{OP_2} \end{aligned} \tag{19}$$

Particularly, OP_1 is the outage event for the case that R can not decode successfully both x_1 and x_2 ($\min\left(\gamma_1^{x_1},\gamma_1^{x_2}\right)<\gamma_t$), leading to R does not forward the signal ($\sqrt{b_1P_R}x_1+\sqrt{b_2P_R}x_2$) to destinations, and the destination D_1 can not decode successfully symbol x_1 directly from S in the first phase ($\gamma_4^{x_1}<\gamma_t$). OP_2 is the outage event for the case that R decodes correctly both symbol x_1 and x_2 ($\min\left(\gamma_1^{x_1},\gamma_1^{x_2}\right)\geq\gamma_t$), but D_1 can not decodes successfully x_1 both from S and R in the first and second phase, respectively ($\max\left(\gamma_4^{x_1},\gamma_2^{x_1}\right)<\gamma_t$).

The term OP_1 and OP_2 can be obtain by substituting the SINRs and SNRs in (10), (13), (11) and (17) into (19) as follows

$$\begin{aligned} OP_1 &= \Pr\left[\min\left(\frac{a_1(1-\rho)\gamma_0 g_1}{a_2(1-\rho)\gamma_0 g_1+(1-\rho+\mu)},\frac{a_2(1-\rho)\gamma_0 g_1}{1-\rho+\mu}\right)<\gamma_t,\frac{a_1\gamma_0 g_4}{a_2\gamma_0 g_4+1+\mu}<\gamma_t\right] \\ &= \Pr\left[\frac{a_1\gamma_0 g_4}{a_2\gamma_0 g_4+1+\mu}<\gamma_t\right]\Pr\left[\min\left(\frac{a_1(1-\rho)\gamma_0 g_1}{a_2(1-\rho)\gamma_0 g_1+(1-\rho+\mu)},\frac{a_2(1-\rho)\gamma_0 g_1}{1-\rho+\mu}\right)<\gamma_t\right] \\ &= \Pr\left[g_4<\frac{(1+\mu)\gamma_t}{(a_1-a_2\gamma_t)\gamma_0}\right]\left\{1-\Pr\left[g_1\geqslant\frac{(1-\rho+\mu)\gamma_t}{(a_1-a_2\gamma_t)(1-\rho)\gamma_0},g_1\geqslant\frac{(1-\rho+\mu)\gamma_t}{a_2(1-\rho)\gamma_0}\right]\right\} \\ &= F_{g_4}\left(\frac{(1+\mu)\gamma_t}{(a_1-a_2\gamma_t)\gamma_0}\right)\times\begin{cases} F_{g_1}\left(\dfrac{(1-\rho+\mu)\gamma_t}{(a_1-a_2\gamma_t)(1-\rho)\gamma_0}\right) & if\ a_1-a_2\gamma_t<a_2 \\ F_{g_1}\left(\dfrac{(1-\rho+\mu)\gamma_t}{a_2(1-\rho)\gamma_0}\right) & if\ a_1-a_2\gamma_t\geqslant a_2 \end{cases} \\ &= \left(1-e^{-\frac{\lambda_4\omega_1\gamma_t}{(a_1-a_2\gamma_t)\gamma_0}}\right)\times\begin{cases} \left(1-e^{-\frac{\lambda_1\omega_2\gamma_t}{(a_1-a_2\gamma_t)\gamma_0}}\right) & if\ a_1<a_2(1+\gamma_t) \\ \left(1-e^{-\frac{\lambda_1\omega_2\gamma_t}{a_2\gamma_0}}\right) & if\ a_1\geqslant a_2(1+\gamma_t) \end{cases} \end{aligned} \tag{20}$$

where $\omega_1\triangleq 1+\mu$, $\omega_2\triangleq\frac{1-\rho+\mu}{1-\rho}$.

$$\begin{aligned} OP_2 &= \Pr\left[\begin{array}{l}\min\left(\dfrac{a_1(1-\rho)\gamma_0 g_1}{a_2(1-\rho)\gamma_0 g_1+(1-\rho+\mu)},\dfrac{a_2(1-\rho)\gamma_0 g_1}{1-\rho+\mu}\right)\geqslant\gamma_t, \\ \max\left(\dfrac{a_1\gamma_0 g_4}{a_2\gamma_0 g_4+1+\mu},\dfrac{b_1\eta\rho\gamma_0 g_1 g_2}{b_2\eta\rho\gamma_0 g_1 g_2+1+\mu}\right)<\gamma_t\end{array}\right] \\ &= \Pr\left[g_4<\frac{(1+\mu)\gamma_t}{(a_1-a_2\gamma_t)\gamma_0}\right]\Pr\left[\begin{array}{l} g_1\geqslant\dfrac{(1-\rho+\mu)\gamma_t}{(a_1-a_2\gamma_t)(1-\rho)\gamma_0},g_1\geqslant\dfrac{(1-\rho+\mu)\gamma_t}{a_2(1-\rho)\gamma_0} \\ \dfrac{b_1\eta\rho\gamma_0 g_1 g_2}{b_2\eta\rho\gamma_0 g_1 g_2+1+\mu}<\gamma_t\end{array}\right] \\ &\overset{(21.1)}{=}\left(1-e^{-\frac{\lambda_4(1+\mu)\gamma_t}{(a_1-a_2\gamma_t)\gamma_0}}\right) \\ &\times\begin{cases}\Pr\left[g_1\geqslant\dfrac{(1-\rho+\mu)\gamma_t}{(a_1-a_2\gamma_t)(1-\rho)\gamma_0},g_2<\dfrac{(1+\mu)\gamma_t}{(b_1-b_2\gamma_t)\eta\rho\gamma_0 g_1}\right] & if\ a_1-a_2\gamma_t<a_2 \\ \Pr\left[g_1\geqslant\dfrac{(1-\rho+\mu)\gamma_t}{a_2(1-\rho)\gamma_0},g_2<\dfrac{(1+\mu)\gamma_t}{(b_1-b_2\gamma_t)\eta\rho\gamma_0 g_1}\right] & if\ a_1-a_2\gamma_t\geqslant a_2\end{cases} \end{aligned}$$

$$\stackrel{(21.2)}{=} \left(1 - e^{-\frac{\lambda_4 \omega_1 \gamma_t}{(a_1 - a_2\gamma_t)\gamma_0}}\right)$$
$$\times \begin{cases} e^{-\frac{\lambda_1 \omega_2 \gamma_t}{(a_1 - a_2\gamma_t)\gamma_0}} - \sum\limits_{k=0}^{\infty} \frac{1}{k!}\left(-\frac{\lambda_1 \lambda_2 \omega_3 \gamma_t}{(b_1 - b_2\gamma_t)\gamma_0}\right)^k \Gamma\left(1-k, \frac{\lambda_1 \omega_2 \gamma_t}{(a_1 - a_2\gamma_t)\gamma_0}\right) & if\ a_1 < (1+\gamma_t)\, a_2 \\ e^{-\frac{\lambda_1 \omega_2 \gamma_t}{a_2\gamma_0}} - \sum\limits_{k=0}^{\infty} \frac{1}{k!}\left(-\frac{\lambda_1 \lambda_2 \omega_3 \gamma_t}{(b_1 - b_2\gamma_t)\gamma_0}\right)^k \Gamma\left(1-k, \frac{\lambda_1 \omega_2 \gamma_t}{a_2\gamma_0}\right) & if\ a_1 \geqslant (1+\gamma_t)\, a_2 \end{cases} \tag{21}$$

where $\omega_3 \triangleq \frac{1+\mu}{\eta\rho}$.

where (21.2) is obtained from (21.1) by using the result in Appendix A. Note that we allocate the power coefficients a_1, a_2, b_1, and b_2 that $(a_1 - a_2\gamma_t) > 0$ and $(b_1 - b_2\gamma_t) > 0$ for OP_1 and OP_2 not equal to 0.

Finally, a closed-form expression for $OP_{D_1}^{1relay}$ is derived by substituting (20) and (21) into (19) as

$$OP_{D_1}^{1relay} = \left(1 - e^{-\frac{\lambda_4 \omega_1 \gamma_t}{(a_1 - a_2\gamma_t)\gamma_0}}\right)$$
$$\times \begin{cases} 1 - \sum\limits_{k=0}^{\infty} \frac{1}{k!}\left(-\frac{\lambda_1 \lambda_2 \omega_3 \gamma_t}{(b_1 - b_2\gamma_t)\gamma_0}\right)^k \Gamma\left(1-k, \frac{\lambda_1 \omega_3 \gamma_t}{(a_1 - a_2\gamma_t)\gamma_0}\right) & if\ a_1 < (1+\gamma_t)\, a_2 \\ 1 - \sum\limits_{k=0}^{\infty} \frac{1}{k!}\left(-\frac{\lambda_1 \lambda_2 \omega_3 \gamma_t}{(b_1 - b_2\gamma_t)\gamma_0}\right)^k \Gamma\left(1-k, \frac{\lambda_1 \omega_3 \gamma_t}{a_2\gamma_0}\right) & if\ a_1 \geqslant (1+\gamma_t)\, a_2 \end{cases} \tag{22}$$

3.2 Outage Probability at D_2

In this paper, the desired symbol for destination is x_2, thus D_2 has to successfully decode x_1 first then using SIC to obtain x_2. There are two cases for outage happening at D_2 that (i) both x_1 and x_2 can not be decoded successfully from S and D_2 in the first time slot $\left(\left(\min\left(\gamma_1^{x_1}, \gamma_1^{x_2}\right) < \gamma_t, \min\left(\gamma_5^{x_1}, \gamma_5^{x_2}\right) < \gamma_t\right)\right)$, the probability for this event is denoted by OP_5; (ii) R detects correctly x_1 and x_2 transmitted from S in the first phase but D_2 does not from both S and R in the first and second phases, repsectively.

$\left(\Pr\left[\min\left(\gamma_1^{x_1}, \gamma_1^{x_2}\right) \geqslant \gamma_t, \min\left(\gamma_5^{x_1}, \gamma_5^{x_2}\right) < \gamma_t, \min\left(\gamma_3^{x_1}, \gamma_3^{x_2}\right) < \gamma_t\right]\right)$,this probability denoted by OP_6. The outage probability at D can be formulated by:

$$\begin{aligned} OP_{D_2}^{1\,relay} &= \underbrace{\Pr\left[\left(\min\left(\gamma_1^{x_1}, \gamma_1^{x_2}\right) < \gamma_t, \min\left(\gamma_5^{x_1}, \gamma_5^{x_2}\right) < \gamma_t\right)\right]}_{OP_5} \\ &+ \underbrace{\Pr\left[\min\left(\gamma_1^{x_1}, \gamma_1^{x_2}\right) \geqslant \gamma_t, \min\left(\gamma_5^{x_1}, \gamma_5^{x_2}\right) < \gamma_t, \min\left(\gamma_3^{x_1}, \gamma_3^{x_2}\right) < \gamma_t\right]}_{OP_6} \end{aligned} \tag{23}$$

The probabilities OP_5 and OP_6 can be obtained by substituting the SINRs and SINRs $\gamma_1^{x_1}$, $\gamma_1^{x_2}$, $\gamma_5^{x_1}$, $\gamma_5^{x_2}$, $\gamma_3^{x_1}$, and $\gamma_3^{x_2}$ into (23) as follows

$$\begin{aligned} OP_5 &= \underbrace{\Pr\left[\min\left(\frac{a_1(1-\rho)\gamma_0 g_1}{a_2(1-\rho)\gamma_0 g_1 + (1-\rho+\mu)}, \frac{a_2(1-\rho)\gamma_0 g_1}{1-\rho+\mu}\right) < \gamma_t\right]}_{OP_{5.1}} \\ &\quad \times \underbrace{\Pr\left[\min\left(\frac{a_1\gamma_0 g_5}{a_2\gamma_0 g_5 + 1 + \mu}, \frac{a_2\gamma_0 g_5}{1+\mu}\right) < \gamma_t\right]}_{OP_{5.2}} \end{aligned} \tag{24}$$

$$\begin{aligned} OP_6 &= \underbrace{\Pr\left[\min\left(\frac{a_1\gamma_0 g_5}{a_2\gamma_0 g_5 + 1 + \mu}, \frac{a_1\gamma_0 g_5}{1+\mu}\right) < \gamma_t\right]}_{OP_{6.1}} \\ &\quad \times \underbrace{\Pr\left[\begin{array}{l} \min\left(\dfrac{a_1(1-\rho)\gamma_0 g_1}{a_2(1-\rho)\gamma_0 g_1 + (1-\rho+\mu)}, \dfrac{a_2(1-\rho)\gamma_0 g_1}{1-\rho+\mu}\right) \geqslant \gamma_t, \\ \min\left(\dfrac{b_1\eta\rho\gamma_0 g_1 g_3}{b_2\eta\rho\gamma_0 g_1 g_3 + 1 + \mu}, \dfrac{b_2\eta\rho\gamma_0 g_1 g_3}{1+\mu}\right) < \gamma_t \end{array}\right]}_{OP_{6.2}} \end{aligned} \tag{25}$$

where $OP_{5.1}$ can be obtained from OP_1 as

$$OP_{5.1} = \begin{cases} \left(1 - e^{-\frac{\lambda_1\omega_2\gamma_t}{(a_1 - a_2\gamma_t)\gamma_0}}\right) & if \quad a_1 < a_2\left(1+\gamma_t\right) \\ \left(1 - e^{-\frac{\lambda_1\omega_2\gamma_t}{a_2\gamma_0}}\right) & if \quad a_1 \geqslant a_2\left(1+\gamma_t\right) \end{cases} \tag{26}$$

$OP_{5.2} = OP_{6.1}$ is expressed as

$$\begin{aligned} OP_{5.2} = OP_{6.1} &= 1 - \Pr\left[g_5 \geqslant \frac{(1+\mu)\gamma_t}{(a_1 - a_2\gamma_t)\gamma_0}, g_5 \geqslant \frac{(1+\mu)\gamma_t}{a_2\gamma_0}\right] \\ &= \begin{cases} F_{g_5}\left(\dfrac{(1+\mu)\gamma_t}{(a_1 - a_2\gamma_t)\gamma_0}\right) & if \ a_1 - a_2\gamma_t < a_2 \\ F_{g_5}\left(\dfrac{(1+\mu)\gamma_t}{a_2\gamma_0}\right) & if \ a_1 - a_2\gamma_t \geqslant a_2 \end{cases} \\ &= \begin{cases} \left(1 - e^{\frac{-\lambda_5\omega_1\gamma_t}{(a_1 - a_2\gamma_t)\gamma_0}}\right) & if \quad a_1 < a_2\left(1+\gamma_t\right) \\ \left(1 - e^{\frac{-\lambda_5\omega_1\gamma_t}{a_2\gamma_0}}\right) & if \quad a_1 \geqslant a_2\left(1+\gamma_t\right) \end{cases} \end{aligned} \tag{27}$$

$OP_{6.2}$ is derived from Appendix B as

$$OP_{6.2} = \begin{cases} e^{-\frac{\lambda_1\omega_2\gamma_t}{(a_1-a_2\gamma_t)\gamma_0}} - \sum\limits_{k=0}^{\infty}\frac{1}{k!}\left(-\frac{\lambda_1\lambda_3\omega_3\gamma_t}{(b_1-b_2\gamma_t)\gamma_0}\right)^k \Gamma\left(1-k,\frac{\lambda_1\omega_2\gamma_t}{(a_1-a_2\gamma_t)\gamma_0}\right), & if \begin{cases} b_1 < b_2(1+\gamma_t) \\ a_1 < a_2(1+\gamma_t) \end{cases} \\ e^{-\frac{\lambda_1\omega_2\gamma_t}{(a_1-a_2\gamma_t)\gamma_0}} - \sum\limits_{k=0}^{\infty}\frac{1}{k!}\left(-\frac{\lambda_1\lambda_3\omega_3\gamma_t}{b_2\gamma_0}\right)^k \Gamma\left(1-k,\frac{\lambda_1\omega_2\gamma_t}{(a_1-a_2\gamma_t)\gamma_0}\right), & if \begin{cases} b_1 \geqslant b_2(1+\gamma_t) \\ a_1 < a_2(1+\gamma_t) \end{cases} \\ e^{-\frac{\lambda_1\omega_2\gamma_t}{a_2\gamma_0}} - \sum\limits_{k=0}^{\infty}\frac{1}{k!}\left(-\frac{\lambda_1\lambda_3\omega_3\gamma_t}{(b_1-b_2\gamma_t)\gamma_0}\right)^k \Gamma\left(1-k,\frac{\lambda_1\omega_2\gamma_t}{a_2\gamma_0}\right), & if \begin{cases} b_1 < b_2(1+\gamma_t) \\ a_1 \geqslant a_2(1+\gamma_t) \end{cases} \\ e^{-\frac{\lambda_1\omega_2\gamma_t}{a_2\gamma_0}} - \sum\limits_{k=0}^{\infty}\frac{1}{k!}\left(-\frac{\lambda_1\lambda_3\omega_3\gamma_t}{b_2\gamma_0}\right)^k \Gamma\left(1-k,\frac{\lambda_1\omega_2\gamma_t}{a_2\gamma_0}\right), & if \begin{cases} b_1 \geqslant b_2(1+\gamma_t) \\ a_1 \geqslant a_2(1+\gamma_t) \end{cases} \end{cases} \tag{28}$$

The outage probability at D_2 in the case of one relay can be obtained by substituting the equations from (24) to (28) into (23) as

$$OP_{D_2}^{1\ relay} = \begin{cases} \left(1-e^{-\frac{\lambda_5\omega_1\gamma_t}{(a_1-a_2\gamma_t)\gamma_0}}\right)\left[1-\sum\limits_{k=0}^{\infty}\frac{1}{k!}\left(-\frac{\lambda_1\lambda_3\omega_3\gamma_t}{(b_1-b_2\gamma_t)\gamma_0}\right)^k \Gamma\left(1-k,\frac{\lambda_1\omega_2\gamma_t}{(a_1-a_2\gamma_t)\gamma_0}\right)\right], & if \begin{cases} b_1 < b_2(1+\gamma_t) \\ a_1 < a_2(1+\gamma_t) \end{cases} \\ \left(1-e^{-\frac{\lambda_5\omega_1\gamma_t}{(a_1-a_2\gamma_t)\gamma_0}}\right)\left[1-\sum\limits_{k=0}^{\infty}\frac{1}{k!}\left(-\frac{\lambda_1\lambda_3\omega_3\gamma_t}{b_2\gamma_0}\right)^k \Gamma\left(1-k,\frac{\lambda_1\omega_2\gamma_t}{(a_1-a_2\gamma_t)\gamma_0}\right)\right], & if \begin{cases} b_1 \geqslant b_2(1+\gamma_t) \\ a_1 < a_2(1+\gamma_t) \end{cases} \\ \left(1-e^{-\frac{\lambda_5\omega_1\gamma_t}{a_2\gamma_0}}\right)\left[1-\sum\limits_{k=0}^{\infty}\frac{1}{k!}\left(-\frac{\lambda_1\lambda_3\omega_3\gamma_t}{(b_1-b_2\gamma_t)\gamma_0}\right)^k \Gamma\left(1-k,\frac{\lambda_1\omega_2\gamma_t}{a_2\gamma_0}\right)\right], & if \begin{cases} b_1 < b_2(1+\gamma_t) \\ a_1 \geqslant a_2(1+\gamma_t) \end{cases} \\ \left(1-e^{-\frac{\lambda_5\omega_1\gamma_t}{a_2\gamma_0}}\right)\left[1-\sum\limits_{k=0}^{\infty}\frac{1}{k!}\left(-\frac{\lambda_1\lambda_3\omega_3\gamma_t}{b_2\gamma_0}\right)^k \Gamma\left(1-k,\frac{\lambda_1\omega_2\gamma_t}{a_2\gamma_0}\right)\right], & if \begin{cases} b_1 \geqslant b_2(1+\gamma_t) \\ a_1 \geqslant a_2(1+\gamma_t) \end{cases} \end{cases} \tag{29}$$

4 Result and Disscussion

This section provide result and discussion of the outage performance at both D_1 and D_2 in both cases of one and N relays via Monte Carlo simulation and theoretical results. In a two-dimensional plane, the corrdinates of the source S, the destinations D_1, D_2, and the cluster of relays are $(0,0)$, $(1,0.3)$, $(0.8,-0.3)$, and $(x_R,0)$, respectively. Hence, we obtain the normalize distances $d_1 = |x_R|$, $d_2 = \sqrt{(1-x_R)^2+0.3^2}$, $d_3 = \sqrt{(0.8-x_R)^2+0.3^2}$, $d_4 = \sqrt{1+0.3^2}$, $d_5 = \sqrt{0.8^2+0.3^2}$. We assume that the path-loss exponent $\beta = 3$, the target $\gamma_t = 1$, and $\mu = 1$.

In Fig. 2, the outage probabilities at D_1 and D_2 versus power splitting ratio $\rho \in (0.1, 0.9)$ (for relay located between source and destinations) are investigated. It can be seen that at ρ around 0.7, the outage performances of almost cases in this scenario are obtained the best performance because it is the optimal position for relay to decode information and harvest energy from source in the first phase and forward information to destination in the second phase. We note that D_2 locates nearer the source and relay than D_1 does, therefore the outage performance at D_2 is better than D_1 in the case of the power allocation for symbol x_2 and x_1 is nearly similar like $(a_1,a_2) = (b_1,b_2) = (0.6,0.4)$, but in the case that the power allocation for x_1 is much higher than that for x_2, the outage performance at D_1 is higher than that at D_2.

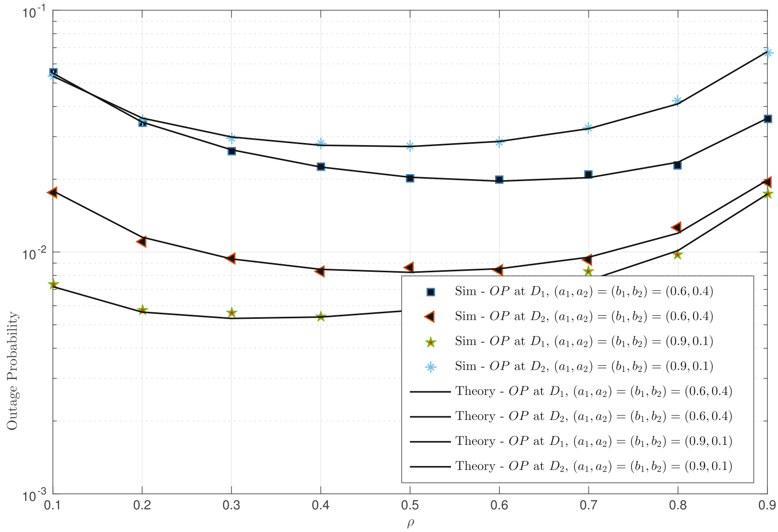

Fig. 2. Effect of power allocation a_1, a_2, b_1, and b_2 on the outage probability at D_1 and D_2 versus ρ, when $x_R = 0.4$, $\gamma_0 = 15$ dB, $\rho = 0.5$, and $\eta = 0.9$.

5 Conclusions

In this paper, we consider energy harvesting technique in the NOMA relaying networks. Partial relay selection scheme is applied to improve the system performance. The closed-form expressions of the outage probability are presented to evaluation and comparison of the performance at two destinations in both cases of single and multiple relays. These theoretical expressions are derived using the Monte Carlo simulation method. The theoretical results match the simulation results well.

A Appendix A: Finding the Closed-Form of Probability $\Pr\left[g_1 \geqslant u_1, g_2 < \frac{u_2}{g_1}\right]$

By using the PDF of RV g_1 and CDF of RV g_2, the probability $\Pr\left[g_1 \geqslant u_1, g_2 < \frac{u_2}{g_1}\right]$ can be obtained as

$$\begin{aligned}
&\Pr\left[g_1 \geqslant u_1, g_2 < \frac{u_2}{g_1}\right] = \int_{u_1}^{\infty} f_{g_1}(x) F_{g_2}\left(\frac{u_2}{x}\right) dx \\
&= \int_{u_1}^{\infty} \lambda_1 e^{-\lambda_1 x}\left(1 - e^{-\frac{\lambda_2 u_2}{x}}\right) dx \\
&= e^{-\lambda_1 u_1} - \underbrace{\int_{u_1}^{\infty} \lambda_1 e^{-\lambda_1 x} e^{-\frac{\lambda_2 u_2}{x}} dx}_{I_1}
\end{aligned} \tag{A.1}$$

To calculate the integral I_1, we first apply the Eq. 1.211 of [6]: $e^x = \sum_{k=0}^{\infty} \frac{x^k}{k!}$ to the term $e^{-\frac{\lambda_2 u_2}{x}}$ to obtain (A.2.1), then using Eq. 3.381.3 of [6]: $\int_u^{\infty} x^{v-1} e^{-\mu x} dx = \frac{1}{\mu^v} \Gamma(v, \mu u)$ to obtain (A.2.2) as follows

$$\begin{aligned}
I_1 &\overset{(A.2.1)}{=} \lambda_1 \sum_{k=0}^{\infty} \frac{1}{k!} (-\lambda_2 u_2)^k \int_{u_1}^{\infty} \frac{e^{-\lambda_1 x}}{(x)^k} dx \\
&\overset{(A.2.2)}{=} \sum_{k=0}^{\infty} \frac{1}{k!} (-\lambda_1 \lambda_2 u_2)^k \Gamma(1 - k, \lambda_1 u_1)
\end{aligned} \tag{A.2}$$

By substituting (A.3) into (A.1), we obtain:

$$\Pr\left[g_1 \geqslant u_1, g_2 < \frac{u_2}{g_1}\right] = e^{-\lambda_1 u_1} - \sum_{k=0}^{\infty} \frac{1}{k!} (-\lambda_1 \lambda_2 u_2)^k \Gamma(1 - k, \lambda_1 u_1) \tag{A.3}$$

B Appendix B: Proof of Eq. (28)

First, for the case of $a_1 < a_2(1 + \gamma_t)$, the probability $OP_{6.2}$ in (25) can be rewritten as

$$\begin{aligned}
&OP_{6.2}|_{a_1 < a_2(1+\gamma_t)} = \Pr\left[\begin{array}{l} g_1 \geq \frac{(1-\rho+\mu)\gamma_t}{(a_1 - a_2\gamma_t)(1-\rho)\gamma_0} \\ \min\left(\frac{b_1 \eta\rho\gamma_0 g_1 g_3}{b_2 \eta\rho\gamma_0 g_1 g_3 + 1 + \mu}, \frac{b_2 \eta\rho\gamma_0 g_1 g_3}{1+\mu}\right) < \gamma_t \end{array}\right] \\
&= \Pr\left[\begin{array}{l} g_1 \geq \frac{(1-\rho+\mu)\gamma_t}{(a_1 - a_2\gamma_t)(1-\rho)\gamma_0} \\ \frac{b_1 \eta\rho\gamma_0 g_1 g_3}{b_2 \eta\rho\gamma_0 g_1 g_3 + 1 + \mu} < \frac{b_2 \eta\rho\gamma_0 g_1 g_3}{1+\mu}, \frac{b_1 \eta\rho\gamma_0 g_1 g_3}{b_2 \eta\rho\gamma_0 g_1 g_3 + 1 + \mu} < \gamma_t \end{array}\right] \\
&+ \Pr\left[\begin{array}{l} g_1 \geq \frac{(1-\rho+\mu)\gamma_t}{(a_1 - a_2\gamma_t)(1-\rho)\gamma_0} \\ \frac{b_1 \eta\rho\gamma_0 g_1 g_3}{b_2 \eta\rho\gamma_0 g_1 g_3 + 1 + \mu} \geq \frac{b_2 \eta\rho\gamma_0 g_1 g_3}{1+\mu}, \frac{b_2 \eta\rho\gamma_0 g_1 g_3}{1+\mu} < \gamma_t \end{array}\right] \\
&= \underbrace{\Pr\left[\begin{array}{l} g_1 \geq \frac{(1-\rho+\mu)\gamma_t}{(a_1 - a_2\gamma_t)(1-\rho)\gamma_0} \\ g_3 > \frac{(b_1 - b_2)(1+\mu)}{(b_2)^2 \eta\rho\gamma_0 g_1}, g_3 < \frac{(1+\mu)\gamma_t}{(b_1 - b_2\gamma_t)\eta\rho\gamma_0 g_1} \end{array}\right]}_{OP_{6.2.1}} + \underbrace{\Pr\left[\begin{array}{l} g_1 \geq \frac{(1-\rho+\mu)\gamma_t}{(a_1 - a_2\gamma_t)(1-\rho)\gamma_0} \\ g_3 \leq \frac{(b_1 - b_2)(1+\mu)}{(b_2)^2 \eta\rho\gamma_0 g_1}, g_3 < \frac{(1+\mu)\gamma_t}{b_2 \eta\rho\gamma_0 g_1} \end{array}\right]}_{OP_{6.2.2}}
\end{aligned} \tag{B.1}$$

where $OP_{6.2.1}$ and $OP_{6.2.2}$ are given as

$$OP_{6.2.1} = \begin{cases} \int\limits_{\frac{\omega_2 \gamma_t}{(a_1 - a_2\gamma_t)\gamma_0}}^{\infty} f_{g_1}(x) \left[F_{g_3}\left(\frac{\omega_3 \gamma_t}{(b_1 - b_2\gamma_t)\gamma_0 x} \right) - F_{g_3}\left(\frac{(b_1 - b_2)\omega_3}{(b_2)^2 \gamma_0 x} \right) \right] dx, & if\ b_1 < b_2(1+\gamma_t) \\ 0 & if\ b_1 \geq b_2(1+\gamma_t) \end{cases} \tag{B.2}$$

$$\begin{aligned} OP_{6.2.2} &= \begin{cases} \Pr\left[\begin{array}{l} g_1 \geq \frac{\omega_2 \gamma_t}{(a_1 - a_2\gamma_t)\gamma_0} \\ g_3 \leq \frac{(b_1 - b_2)\omega_3}{(b_2)^2 \gamma_0 g_1} \end{array} \right] & if\ b_1 < b_2(1+\gamma_t) \\ \Pr\left[\begin{array}{l} g_1 \geq \frac{\omega_2 \gamma_t}{(a_1 - a_2\gamma_t)\gamma_0} \\ g_3 < \frac{\omega_3 \gamma_t}{b_2 \gamma_0 g_1} \end{array} \right] & if\ b_1 \geq b_2(1+\gamma_t) \end{cases} \\ &= \begin{cases} \int\limits_{\frac{\omega_2 \gamma_t}{(a_1 - a_2\gamma_t)\gamma_0}}^{\infty} f_{g_1}(x) \left[F_{g_3}\left(\frac{(b_1 - b_2)\omega_3}{(b_2)^2 \gamma_0 g_1} \right) \right] dx, & if\ b_1 < b_2(1+\gamma_t) \\ \int\limits_{\frac{\omega_2 \gamma_t}{(a_1 - a_2\gamma_t)\gamma_0}}^{\infty} f_{g_1}(x) \left[F_{g_3}\left(\frac{\omega_3 \gamma_t}{b_2 \gamma_0 g_1} \right) \right] dx, & if\ b_1 \geq b_2(1+\gamma_t) \end{cases} \end{aligned} \tag{B.3}$$

By substituting (B.2) and (B.3) into (B.1), and using the result in Appendix A, we obtain

$$\begin{aligned} & OP_{6.2}|_{a_1 < a_2(1+\gamma_t)} = OP_{6.2.1} + OP_{6.2.2} \\ &= \begin{cases} \int\limits_{\frac{\omega_2 \gamma_t}{(a_1 - a_2\gamma_t)\gamma_0}}^{\infty} f_{g_1}(x) \left[F_{g_3}\left(\frac{\omega_3 \gamma_t}{(b_1 - b_2\gamma_t)\gamma_0 g_1} \right) \right] dx, & if\ b_1 < b_2(1+\gamma_t) \\ \int\limits_{\frac{\omega_2 \gamma_t}{(a_1 - a_2\gamma_t)\gamma_0}}^{\infty} f_{g_1}(x) \left[F_{g_3}\left(\frac{\omega_3 \gamma_t}{b_2 \gamma_0 g_1} \right) \right] dx, & if\ b_1 \geq b_2(1+\gamma_t) \end{cases} \\ &= e^{-\frac{\lambda_1 \omega_2 \gamma_t}{(a_1 - a_2\gamma_t)\gamma_0}} - \begin{cases} \sum\limits_{k=0}^{\infty} \frac{1}{k!} \left(-\frac{\lambda_1 \lambda_3 \omega_3 \gamma_t}{(b_1 - b_2\gamma_t)\gamma_0} \right)^k \Gamma\left(1-k, \frac{\lambda_1 \omega_2 \gamma_t}{(a_1 - a_2\gamma_t)\gamma_0} \right), & if\ b_1 < b_2(1+\gamma_t) \\ \sum\limits_{k=0}^{\infty} \frac{1}{k!} \left(-\frac{\lambda_1 \lambda_3 \omega_3 \gamma_t}{b_2\gamma_0} \right)^k \Gamma\left(1-k, \frac{\lambda_1 \omega_2 \gamma_t}{(a_1 - a_2\gamma_t)\gamma_0} \right), & if\ b_1 \geq b_2(1+\gamma_t) \end{cases} \end{aligned} \tag{B.4}$$

Next, we can obtain the result for $OP_{6.2}$ in the case of $a_1 \geq a_2(1+\gamma_t)$ from (B.4) with replacing '$(a_1 - a_2\gamma_t)$' by 'a_2' as

$$OP_{6.2}|_{a_1 \geq a_2(1+\gamma_t)} = e^{-\frac{\lambda_1 \omega_2 \gamma_t}{a_2 \gamma_0}} - \begin{cases} \sum\limits_{k=0}^{\infty} \frac{1}{k!} \left(-\frac{\lambda_1 \lambda_3 \omega_3 \gamma_t}{(b_1 - b_2\gamma_t)\gamma_0} \right)^k \Gamma\left(1-k, \frac{\lambda_1 \omega_2 \gamma_t}{a_2 \gamma_0} \right), & if\ b_1 < b_2(1+\gamma_t) \\ \sum\limits_{k=0}^{\infty} \frac{1}{k!} \left(-\frac{\lambda_1 \lambda_3 \omega_3 \gamma_t}{b_2\gamma_0} \right)^k \Gamma\left(1-k, \frac{\lambda_1 \omega_2 \gamma_t}{a_2 \gamma_0} \right), & if\ b_1 \geq b_2(1+\gamma_t) \end{cases} \tag{B.5}$$

By combining (B.4) and (B.5), we finish the proof for Eq. (28).

References

1. Ding, Z., Peng, M., Poor, H.V.: Cooperative non-orthogonal multiple access in 5G systems. IEEE Commun. Lett. **19**(8), 1462–1465 (2015)
2. Liu, Y., Ding, Z., Elkashlan, M., Yuan, J.: Non-orthogonal multiple access in large-scale underlay cognitive radio networks (2016). http://arxiv.org/abs/1601.03613
3. Men, J., Ge, J.: Performance analysis of non-orthogonal multiple access in downlink cooperative network. IET Commun. **9**(18), 2267–2273 (2015)
4. Diamantoulakis, P.D., Pappi, K.N., Ding, Z., Karagiannidis, G.K.: Optimal design of non-orthogonal multiple access with wireless power transfer (2015). http://arxiv.org/abs/1511.01291
5. Liu, Y., Ding, Z., Elkashlan, M., Poor, H.V.: Coperative non-orthogonal multiple access with simultaneous wireless information and power transfer (2016). http://arxiv.org/abs/1511.02833
6. Gradshteyn, I.S., Ryzhik, I.M.: Table of Integrals, Series and Products, 7th edn. Academic Press, Orlando (2007)

SDN Based Content-Centric QoS-Guaranteed for Wireless Multimedia Sensor Networks

Gaolei Li, Jun Wu(✉), Jianhua Li, Kuan Wang, and Shan He

School of Electronic Information and Electrical Engineering, Shanghai Jiao Tong University, Shanghai 200240, China
{gaolei_li, junwuhn, lijh888, wangkuanfyfy, hszoe1995}@sjtu.edu.cn

Abstract. As the deployment of wireless multimedia sensor networks (WMSNs) increases sharply, the control granularity of traditional quality of service (QoS) technologies present weak assistance to satisfy the various application requirements. In this paper, we propose a novel architecture of software-defined network (SDN) based content-centric QoS-guaranteed (SCQG) for WMSNs. The SDN is an innovative network paradigm, which has capability to uniformly monitor and control the WMSNs' infrastructures automatically. In proposed architecture, we formulate proper priority for each content based on its popularity in WMSNs. And also, we extend the SDN controller to match the content and make flow tables each content requests. Besides, we design an k-nearest neighbor (KNN) based machine-learning algorithm to identify the popularity of different contents.

Keywords: Wireless multimedia sensor networks (WMSNs)
Software-defined network (SDN) · Content-centric QoS-guaranteed
Popularity · k-nearest neighbor (KNN)

1 Introduction

Wireless multimedia sensor networks (WMSNs) aims to provide more comfortable urban life, enriching data acquisition methods with videos, pictures and voices [1]. As the increasing deployment of WMSNs, the control granularity of traditional quality of service (QoS) technologies present weak assistance to support various future smart applications in smart city [2].

Recently, concept of software defined networks (SDN) has been considered as an innovative architecture with tremendous potential for utilization by the underlying infrastructures [3]. Firstly, SDN decouples control plane from data plane, breaking the vertical OSI model. States of all underlying infrastructures in the whole network are monitored and controlled centralizedlly. Secondly, to provide efficient information exchange between control plane and data plane, OpenFlow protocol, which has become the most popular southbound application programmable interface (S-API), defines a pipeline processing model [4, 5]. Rules of packets forwarding are handed out together with flow tables from SDN controller. When a packet arrives, switch will look up flow tables one by one. Once the corresponding flow table is matched, the packet will be

© ICST Institute for Computer Sciences, Social Informatics and Telecommunications Engineering 2018
Y. Chen and T. Q. Duong (Eds.): INISCOM 2017, LNICST 221, pp. 40–48, 2018.
https://doi.org/10.1007/978-3-319-74176-5_4

forwarded according to rules in the flow table. If there is no appropriate flow table, packet will be sent into SDN controller for analysis (such as routing path, firewall, and load balancing). In summary, centralized control and global forwarding optimization accelerate packet forwarding speed significantly [6–9]. However, the rules for packet forwarding are designed only relying on the information from layer1 (L1) to layer4 (L4) of OSI model so that control granularity of OpenFlow protocol is inadequate for provisioning quality of services (QoS) satisfactorily. Particularly, priority can not be configured for each traffic dynamically. Therefore, some important sessions especially for multimedia data delivery may be interrupted when congested. Thus, SDN needs a new traffic engineering technique that can see deeper into the packet and identifies behaviors of every traffic, then classifies traffic according to these diverse identified behaviors in a fine-grained way. Content-awareness is perceived as a very imperative technology to provision optimal QoS for communication networks [10–13]. However, different from matching the static information from L1 to L4 of OSI model of TCP/IP simply, huge overhead of traffic behavior identification may lead to sharp degradation of network performance in traditional network.

In this paper, we propose SDN based content-centric QoS-guaranteed (SCQG) architecture which incorporates content-aware capability into SDN. The behavior identification is based on deep packet inspection (DPI), which is a typical traffic engineering technique and this function is shifted into the control plane of SDN in a previous work [14]. The SCQG specify the priority for each content appropriately according to its popularity, mapping from behaviors and the real-time network states adaptively. Priority control relies on dynamical modification of flow table. We present the designation principles and discuss how the SCQG will facilitate the provision of QoS. Many significant advantages in network performance such as delay, delay variation (including jitter and drift), packet loss and throughput can be improved promissingly.

The main contributions of our work contain three aspects. Firstly, we formulate proper priority for each content based on its popularity in WMSNs rather than the information in packet header. Secondly, we extend the SDN controller to match the content and make flow tables each content requests. Finally, we design an k-nearest neighbor (KNN) based machine-learning algorithm to identify the popularity of different contents.

We push content-awareness to SDN controller that has the whole view of network. The controller identifies popularity of each content and the underlying infrastructures rewrites flow table to determine which action to use for a packet and which packets to drop when congested. The scheme allows us to configure priority for each packet dynamically according to the comprehensive analysis about users' demands.

The rest of this paper is organized as follows. Section 2 introduces the preliminaries. Section 3 describes the basic model and every component of SCQG architecture. Section 4 describes the designation principles and its work process. Ultimately, Sect. 5 concludes this paper.

2 Preliminaries

In this section, we consider the possible existing technologies that may be utilized to implement the proposed SDN based content-centric QoS-guaranteed (SCQG) architecture as follows.

2.1 OpenFlow Protocol

The emerge of OpenFlow protocol greatly accelerates the development of SDN. Now it has become a standardized communication protocol for interconnection between control plane and data plane of SDN. Flow table has been central to OpenFlow protocol and it consists of matches, actions and counters mainly. Intelligent functions separated from the underlying infrastructures are integrated into flow tables. When a packet arrives, switch will match its IP header (L1–L4) by looking up the local flow tables one by one fastly. If there is no appropriate flow table, this packet will be sent into SDN controller for further analysis. Otherwise, it will be forwarded according to actions defined in the flow table. In this process, packets can be classified rapidly according to information from L1 to L4 and routing path is selected through computing some statistical characteristics about states of communication links. OpenFlow makes it flexible to reconfigure network elements dynamically and improves network performance significantly [18].

2.2 Quality of Services and Priority Control

QoS refers to ability of a network that can use a variety of basic technology, to provide better services for the specified network communication. QoS is a kind of network security mechanism, and it is often used for solving the problem of network delay when congested [14]. It is very important for network stability ensuring to implement better QoS policy in time-critical network such as wireless sensor networks (WSNs) [15], Smart Grid [16] and multimedia networks [17]. Usually, different applications have different requirements for QoS in different networks. The more characteristics of traffic flows are recognized, the more fine grained rules for QoS services can be provided. Priority control is the most popular approach to provide QoS services. In IP based network, DSCP is originally designated to distinguish the priority of each packet but not adopted practically.

2.3 Content Popularity Awareness

In traditional network, content-awareness is commonly treated as behavior identification of users. Therefore, deep packet inspection (DPI) originally is designed to enhance the security of the network. It combines the functionality of intrusion detection system (IDS) and intrusion prevention system (IPS) with a stately traditional firewall. The basic concept of DPI contains content analysis of the captured packets as well as accurate and timely discrimination of the traffic generated by different Internet protocols. Nowadays, DPI has been the most widely used method for application-awareness [19, 20].

Implementing application-awareness allows network to provide fine-grained traffic control by inspecting packets and identifying their application behaviors.

In this paper, we treat content-awareness as investigating the content's popularity. Implementing this content-awareness capability in SDN has two additional benefits. Firstly, popularity based content-awareness enables privacy security by hiding the identity of each user. Secondly, popularity based content-awareness is flexible for network elements to reduce the overhead QoS management.

3 SDN Based Content-Centric QoS-Guaranteed

It is generally assumed that there are two elements that have affect on the QoS performances of a communication system: (1) users' demands, and (2) network resources allocation. SDN treats all contents from the same local network as a group. In the past, networking technology care more about the connection between hosts. Popularity of contents are not considered when users call for content processing services. QoS services provided by SDN is often implemented through network monitoring and control. Multi-path is an effective approach to provide QoS guarantees. However, for resource constrained and time-critical scenarios such as wireless multimedia sensor networks (WMSNs), scale of delivered data in real-time is so large that every node and link may be being occupied. To ensure non-interrupted of important sessions, the importance of priority control is highlighted again. Therefore, we propose SDN based content-centric QoS-guaranteed architecture, in which the SDN controller can identify popularity of each content and classify them according to their popularity, and then maps the popularity into priority to control the QoS performances.

3.1 Constrains and Assumptions

This section shows the motivation of this paper and the significance of our work. Constrains of the scene are described as follows.

- Multimedia data delivery. Data exchanged in the specified communication system is mixed with diverse types of information including texts, voices, pictures, flashes and videos. We assume that the priority is positively proportional to content popularity.
- Time-critical & fault-tolerance. To ensure stability and availability of the network, it is imperative to transmit content with high priority from one to anther precisely in real time.
- Costs optimization. Either energy, bandwidth or cache of each network node in WMSNs are limited respectively, Moreover, continual join and quit my lead to unavailability of multi-path because energy of each node can't be aware of in real time.

Besides, we also assume that the SDN control is a trusted control center, and this center is maintained by trusted operators. Actually, this scene can be found out in the real word easily.

3.2 Components Description

As illustrated in Fig. 1, the proposed architecture consists of four core modules including ***content requests monitoring module***, ***popularity identification module***, ***priority mapping module*** and ***QoS-guaranteed policy module***.

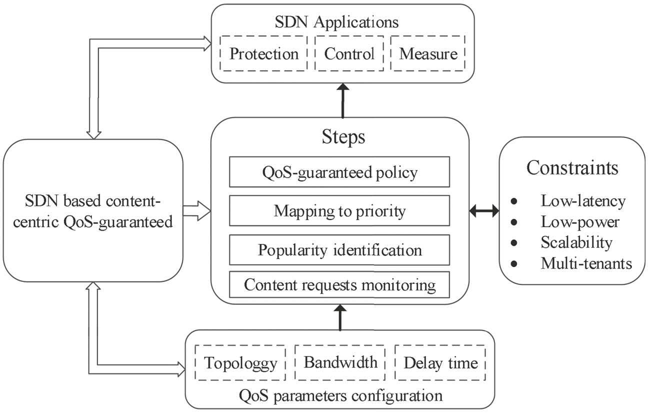

Fig. 1. The system model of SDN based content-centric QoS-guaranteed architecture.

Different from tradition network in which QoS requirements are mapped into differentiated service control protocol (DSCP) markings at the side of hosts, in our scheme QoS requirement of each content is identified by monitoring the popularity of diverse content. The priority-marking of each content coming from any user is set as zero initially. ***Content requests monitoring module*** consists of content requests collection, content inspection and information analysis. Content requests collection unit is designed to collect the content names which are the first time to enter into this network and must be sent to SDN controller for identification. This unit is deployed on the network elements in data plane. Content inspection unit is designed to identify application layer's information from the sent content. The application layer's information related to L7 visibility is provided as network services for orchestration of QoS guarantees. Information analysis unit is designed to provide an interface for synchronization between L7 information and states of whole network.

When the next same content arrives, priority-marking unit on the switch will match its priority-marking with flow tables one by one. If there is no corresponding flow table for this packet, it will be sent into traffic collection unit and then be sent into content inspection unit for identification. Applications of QoS guarantees unit in SDN converts these L7 information into a series of priority values, then priority control unit distributes them into data plane together with the corresponding flow table about forwarding. Rules in the flow table will contain policy about how to deal with the priority-markings. Therefore, the scheme allows us to configure priority for each content dynamically according to the comprehensive analysis about network states and users' QoS demands.

4 Design Principles

In SCQG scheme, the content popularity awareness is formulated to KNN algorithm. It allows priority for each content to be configured appropriately according to their popularity and the real-time network states automatically. Priority control also relies on dynamical modification of DSCP label. In this section, we will present the design principles and discuss how SCQG architecture to facilitate the provision of QoS in WMSNs. The main contribution of our work that hosts are the wrong place to map priority onto per-content will be introduced in detail. We push priority-mapping to SDN controller to identify popularity of each content. DSCP field is rewritten for determine which content to drop when congested and marking the identified contents. SCQG scheme enables inter-network priority-making. The proposed scheme makes it possible to dynamically configure priority for each content in a fine-grained way.

4.1 Priority-Mapping from Popularity

Forwarding policy for every content with a fixed priority is unelastic, priority marking defined by hosts can't be change in real-time with network states. As introduced in advance, the main contribution of our work is that hosts are the wrong place to map priority onto per-content. We push priority-mapping to a trusted SDN controller which has view of the whole network. Priority-marking of each packet coming from any host is set to zero initially.

The priority-mapping from popularity is based on KNN algorithm. The steps of KNN algorithm is showed as follows.

(1) Initialization of training set: We compute out the 42 different stochastic values in training set and compare them with many cautiousness in training set. We denote the eigen matrix in training set by $\mathrm{X} = \{X_1; X_2; \ldots; X_n\}$, in which X_i presents stochastic values with significant difference. Therein, n represents the total number of training set, and the stochastic values with significant difference in training set is denoted as $\mathrm{X}_i = \left\{x_1^i, x_2^i, \ldots, x_l^i\right\}$, $1 \leq l \leq 14$; $l, n \in N^+$. The $i-th$ training content is labeled with priority λ_i, $\lambda_i \in \{\text{'a'},\text{'b'}\}$.

(2) Initialization of testing set: We compute out the 42 different stochastic values in training set and compare them with many cautiousness in testing set. By comparing, we select 14 different eigen values, which are denoted by a matrix $Y = \{Y_1; Y_2; \ldots; Y_m\}$. Therein, m represents the total number of testing set; We denote the eigen matrix in testing set by $Y_j = \left\{y_1^j, y_2^j, \ldots, y_l^j\right\}$, $1 \leq l \leq 14$; $l, m \in N^+$.

(3) KNN based priority-awareness:
To complete the priority prediction of each content in testing set, we calculate the euclidean distance between vectors in training set and testing set $D_{ij} = d(X_i, Y_j) = \sqrt{\sum_i^n (x_l^i - y_l^j)^2}$. When we want to predict the priority of $j-th$ content,the contents in $j-th$ column of D_{ij} are ranked from high to low. We select K lowest values and their corresponding i, and re-label them as

$\{i_1, i_2, \ldots, i_K\}$. In the algorithm, the priority counter is initialized as $C_a = 0$ and $C_b = 0$ firstly; Then, we retrieve the $\{\lambda_{i_1}, \lambda_{i_2}, \ldots, \lambda_{i_K}\}$, if $\lambda_{i_k} = 'a'$, then $C_a = C_a + 1$; if $\lambda_{i_k} = 'b'$, then $C_b = C_b + 1$. Consequently, if $C_b > C_a$, then the priority label is set as 'b', otherwise, the priority label is set as 'a'. Recycling the above process can finish the priority prediction. Actually, by the classification of KNN algorithm, the most popular content will be configured as the highest priority.

4.2 Packet Matching

The priority configuration is implemented by setting the DSCP value. When content arrives in switch supporting OpenFlow protocol, DSCP field will be matched firstly, if it is equal to zero, this content will be mirrored into SDN controller through “Packet In” message, and then it will be inspected by content popularity aware module. If malicious behaviors are found, this content will be dropped. Therefore, there no doubt that our scheme also can prevent malicious programs stepping into the networks additionally. Otherwise, a new flow table with DSCP value representing for priority will be distributed into OpenFlow switches.

As defined in advance, if it is the first time for this content to step into network, DSCP field will be set to zero and there is no corresponding flow table for it. Hence, it will be sent to SDN controller through a secure channel for analysis. Steps of content matching related to IP priority on the OpenFlow switch are introduced as follows

(1) Check whether DSCP field are NULL (every bit is zero).
    If not, continue to match. Otherwise, go to step (5).
(2) Matching flow table one by one. If not found, go to step (5) Otherwise, continue.
(3) Forward content to the next switch.
(4) Execute instructions in action sets and update the counter.
(5) Send content to controller.

4.3 DSCP Field Marking

As introduced in advanced, the main contribution of our work is that hosts are the wrong place to map application behaviors onto per-content. In our scheme, application behaviors are identified by application-aware technology, and service priority are marked by set DSCP field. Moreover, DSCP field is filled out according to network states in real time dynamically by network operators rather than settled by hosts (users). Values of DSCP field are distributed together with the corresponding flow table through “Packet Out” message. Before this content is forwarded to the next switch, its DSCP field will be rewritten by the distributed values.

4.4 Optimization of Content-Awareness

Overhead of content-aware technology is very large and both efficiency and accuracy of it still need to be improved, in this paper we adopt three methods to optimize it as introduced in followings.

(1) DSCP field in the packet header is used to mark QoS priority of diverse applications uniquely. When a marked content arrives again, the corresponding flow table which has been formulated when the data content arrives for the first time is executed. In another word, content is inspected only when it arrives for the first time.
(2) A high-speed traffic collection unit is deployed in data plane to line the contents up, and this unit also set up an agent to pre-process and classify these contents. Both when and where the content arrives will be recorded and these records will be stored in a management information (MIB). They are also provided for diverse applications by the general interface.
(3) Content popularity-awareness is provided as services. Different application-aware instances can be allocated on demands. Scalability and efficiency of it can be improved significantly.

5 Conclusion

In this paper, a novel architecture with content-aware traffic control was proposed for WMSNs, popularity based priority configuration was integrated into the SDN controller. The global network view, status, flow patterns/characteristics and behaviors of the traffic flows were exploited to meet the diverse requirements of network applications for better stability, scalability and flexible scheduling. The proposed architecture contained content popularity aware module and the traffic control module. Besides, we adopted some mathematical models to quantitatively evaluate the performances of the proposed architecture. We designed an k-nearest neighbor (KNN) based machine-learning algorithm to identify the popularity of different contents.

Acknowledgments. This work was supported by the National Science Foundation of China (Grant No. 61401273 and 61431008) and Shanghai Science and Technology Committee (Grant No. 15PJ1433800 and 14DZ1104903).

References

1. Baccarelli, E., Chiti, F., Cordeschi, N., Fantacci, R., Marabissi, D., Parisi, R., Uncini, A.: Green multimedia wireless sensor networks: distributed intelligent data fusion, in-network processing, and optimized resource management. IEEE Wirel. Commun. **21**(4), 20–26 (2014)
2. Gaolei, L., Mianxiong, D., Kaoru, O., Jun, W., Jianhua, L., Tianpeng, Y.: Towards QoE named content-centric wireless multimedia sensor networks with mobile sinks. In: IEEE International Conference on Communication (ICC) (2017)
3. Kreutz, D., Ramos, F.M.V., Esteves Verissimo, P., Esteve Pothenberg, C., Azodolmolky, S., Uhlig, S.: Software-defined networking: a comprehensive survey. Proc. IEEE **103**(1), 14–76 (2015)
4. McKeown, N., Anderson, T., Balakrishnan, H., Parulkar, G., Peterson, L., Rexford, J., Shenker, S., Turner, J.: OpenFlow: enabling innovation in campus networks. ACM SIGCOMM Comput. Commun. Rev. **38**(2), 69–74 (2008)

5. Lara, A., Kolasani, A., Ramamurthy, B.: Network innovation using OpenFlow: a survey. IEEE Commun. Surv. Tutor. **16**(1), 493–512 (2014)
6. Akyildiz, I.F., Lee, A., Wang, P., et al.: A roadmap for traffic engineering in SDN-OpenFlow networks. Comput. Netw. **71**(4), 1–30 (2014)
7. Agarwal, S., Kodialam, M., Lakshman, T.V.: Traffic engineering in software defined networks. In: INFOCOM, 2013 Proceedings IEEE, pp. 2211–2219. IEEE (2013)
8. Yassine, A., Rahimi, H., Shirmohammadi, S.: Software defined network traffic measurement: current trends and challenges. Instrum. Meas. Mag. IEEE **18**(2), 42–50 (2015)
9. Yong, C., Shihan, X., Chunpeng, L., Stojmenovic, I., Minming, L.: Data centers as software defined networks: traffic redundancy elimination with wireless cards at routers. IEEE J. Sel. Areas Commun. **31**(12), 2658–2672 (2013)
10. Qazi, Z.A., Lee, J., Jin, T., et al.: Application-awareness in SDN. ACM SIGCOMM Comput. Commun. Rev. **43**(4), 487–488 (2013)
11. Zhenyun, Z., Tae-Young, C., Raghupathy, S., Aravind, V.: Application-aware acceleration for wireless data networks: design elements and prototype implementation. IEEE Trans. Mob. Comput. **8**(9), 1280–1295 (2009)
12. Amemiya, K., Abiru, K., Ishihara, T.: Application-aware traffic control for network-based data processing services. In: IEEE International Conference on Intelligence in Next Generation Networks (ICIN), pp. 142–147 (2012)
13. Jarschel, M., Wamser, F., Hohn, T., Zinner, T., Tran-Gia, P.: SDN based application-aware networking on the example of YouTube video streaming. In: 2013 Second European Workshop on Software Defined Networks (EWSDN), vol. 87, no. 92 (2013)
14. Gaolei, L., Mianxiong, D., Kaoru, O., Jun, W., Jianhua, L., Tianpeng, Y.: Deep packet inspection based application-aware traffic control for software defined networks. In: IEEE Global Communication Conference, pp. 1–6 (2017)
15. Chang-Su, M., Sun-Hyung, K.: A study on the integrated security system based real-time network packet deep inspection. Int. J. Secur. Appl. **8**(1), 113–122 (2014)
16. Al-Anbagi, I., Erol-Kantarci, M., Mouftah, H.T.: A survey on cross-layer quality-of-service approaches in WSNs for delay and reliability aware applications. IEEE Commun. Surv. Tutor. **18**(1), 525–552 (2016)
17. Kaulbars, D., Schweikowski, F., Wietfeld, C.: Spatially distributed traffic generation for stress testing the robustness of mission critical smart grid communication. In: IEEE Globecom Workshops (GC Wkshps) (2015)
18. Spachos, P., Toumpakaris, D., Hatzinakos, D.: QoS and energy-aware dynamic routing in wireless multimedia sensor networks. In: IEEE International Conference on Communications (ICC), pp. 6935–6940 (2015)
19. Kogan, K., Nikolenko, S., Culhane, W., et al.: Towards efficient implementation of packet classifiers in sdn/OpenFlo. In: Proceedings of the Second ACM SIGCOMM Workshop on Hot Topics in Software Defined Networking, pp. 153–154 (2013)
20. Dainotti, A., Pescape, A., Claffy, K.C.: Issues and future directions in traffic classification. IEEE Netw. **26**(1), 35–40 (2012)
21. Finsterbusch, M., Richter, C., Rocha, E., Muller, J.-A., Hanssgen, K.: A survey of payload-based traffic classification approaches. IEEE Commun. Surv. Tutor. **16**(2), 1135–1156 (2014)

Study on the Effect of the Sensor Array on the Source Localization Performance in Shallow Water

Phu Ninh Tran(✉) and Khanh Dang Trinh

Le Quy Don University, Hanoi, Vietnam
ninhphutran@gmail.com

Abstract. In the paper, we investigate the effect of the total number of sensors on the localization performance in a shallow water area. The source localization performance is evaluated by using the White Noise Constraint (WNC) matching field processing (MFP) algorithm in this paper. The obtained results demonstrate that the quantity of the sensors influences on the accuracy of the localization performance that is estimated for the case of the fixed target as well as for the case of the moving one. The effect of the amount of the sensors studied on this paper can be used as guidelines to design sensor arrays in a particular shallow water area for a passive sonar system.

Keywords: Matched field processing · Source localization
Shallow water

1 Introduction

Matching field processing (MFP) is a fundamental approach to localize source targets in shallow underwater [1,4,7,8]. In conventional MFP method, the ambiguity surface contains many sidelobes besides the mainlobe. A solution to overcome this drawback provides several adaptive MFP methods for an attempt to get higher resolutions and more robust to the environmental mismatch in comparison with the conventional MFP. Among variety of adaptive MFP methods, the Dialog Loading (DL) or White Noise Constraint (WNC), which uses an array of sensors vertically or horizontally and justify the parameter in the diagonal loading, is used to evaluate the localization performance in the paper. The reason for this selection is that WNC algorithm improves significantly the localization performance in terms of high resolution as well as the ability to resist to environmental mismatch. The localization performance obviously depends on inevitable mismatch problems that caused by environmental factors [2,3,9] and on the presence of the noise effects [10–12]. Further, the random sensor topology is considered as a factor that impacts on localization performance [5]. The localization performance depends on the positioning error that is varies according to the range error, the depth error and the peak background rate (PBR). In this

© ICST Institute for Computer Sciences, Social Informatics and Telecommunications Engineering 2018
Y. Chen and T. Q. Duong (Eds.): INISCOM 2017, LNICST 221, pp. 49–56, 2018.
https://doi.org/10.1007/978-3-319-74176-5_5

paper, the positioning error is based on the error criteria with the range error not higher than 40 m, depth error not higher than 4 m and the PBR higher than 2. In this paper, we evaluate the effect of sensor topologies in term of the number of the sensors on the localization performance in typical shallow water area. This analysis can be extended with respect to both the fixed target and the moving one. The presented results are intended to serves as guidelines for the design of the sensor array to get better performance.

The paper is organized as follows. In Sect. 2, we summarize the WNC-MFP algorithm which is used for localization in shallow underwater. In Sect. 3, the effects of the number of the sensors are demonstrated. Section 4, a discussion of simulation results can be found. Finally, the conclusion is presented in Sect. 5.

2 The WNC Algorithm

The output of MFP algorithm is calculated by [8]:

$$B = \mathrm{w}^H \mathrm{R} \mathrm{w} \tag{1}$$

Where R is the covariance matrix, which is calculated based on the spectral of received signal at the sensors. To improve the estimation, the data snapshot is averaged, leading to R expressed by:

$$R = \frac{1}{M} \sum_{m=1}^{M} p_m p_m^H \tag{2}$$

where p_m is the m^{th} snapshot.

The weight vector w of the MFP processor, which is equal to the replica vector ν, is calculated by applying an acoustic model. And, the weight vector is presented by:

$$\mathrm{w} = \nu = \frac{G\,(r,z)}{|G\,(r,z)|} \tag{3}$$

Where Green function (G) is calculated based on acoustic models. When applying the Normal Mode Method, Green function is calculated as following [6]:

$$G(r,z) = \frac{i}{\rho(z_s)\sqrt{8\pi r}} e^{-j\frac{\pi}{4}} \sum_{m=1}^{\infty} \Psi_m(z_s)\Psi_m(z) \frac{e^{jk_m r}}{\sqrt{k_m}} \tag{4}$$

Where r is the distance, z is the depth, ρ is the density, z_s is the depth of the source, Ψ_m is the mode amplitude and k_m is eigenvalue.

In the conventional MFP algorithm, the weight vector w is proportional to the replica vector ν, and many sidelobes come into existence next to the mainlobe. This presences motivate other adaptive methods should be proposed to suppress the sidelobes so that they are extremely lower than the mainlobe. The minimum variance directionless response (MVDR) MFP algorithm is developed to significantly improve the ability to localize the source with considerable resolutions. However, this remarkable resolutions capacity deals with the mismatch of the ocean condition. In this paper, the WNC-MFP algorithm is applied to investigate the localization performance since it not only keeps the advantage of the conventional MFP algorithm's wide mainlobe which makes the WNC MFP robust to environmental mismatch but also maintains the minimum variance directionless response (MVDR) MFP algorithm's high resolutions. The weight vector of the WNC method is the function of both the replica vector ν and the covariance matrix R, as well as the loading parameter ε:

$$\mathrm{w}_{wnc} = \frac{(R + \varepsilon I)^{-1}\nu}{\nu^H (R + \varepsilon I)^{-1}\nu} \tag{5}$$

The output of the WNC-MFP processor is presented as:

$$B_{wnc} = \mathrm{w}_{wnc}^H \mathrm{R} \mathrm{w}_{wnc} \tag{6}$$

The maximum of the output of the processor will locate the source position.

3 The Environmental Model

To evaluate the effect of the sensors on the performance of the system, the paper choose a typical shallow water area which contains environmental parameters as follows. The environmental model includes three layers: water layer, sand layer and bottom layer; each layer has its own parameters. In the water layer, the sound speed varies from 1522 to 1543 m depth, the density ρ is 1.024 g/cm^3, and the depth of the layer is 112 m. In the sand layer, the sound speed varies from 1520 to 1590 m depth, the density ρ is 1.75 g/cm^3, the absorption parameter is 0.2 dB/λ and the depth of the layer is 12 m. In the bottom layer, the sound speed is 1650 m/s, the density ρ is 1.9 g/cm^3, the absorption parameter is 0.5 dB/λ (Fig. 1).

4 Simulation Results

4.1 Input Parameters

The environmental model including particular parameters is described in Sect. 3. For the case of moving target, the source transmitted at 110 Hz is at the range of 2000 m and at the depth of 59 m. For the case of fixed target, the source transmitted at 110 Hz is at the range from 1000 m to 3000 m and at the depth of 59 m. The simulation is carried out in presence of the Gaussian noise that has signal to noise ratio (SNR) equal to −5 dB. The simulation evaluates the effect of the total of the sensors on the localization performance when applying WNC-MFP algorithm with diagonal loading parameter ε equal to 1. In this paper, the localization error is evaluated based on the error criteria with the range error not higher than $40m$, depth error not higher than 4 m and the PBR higher than 2.

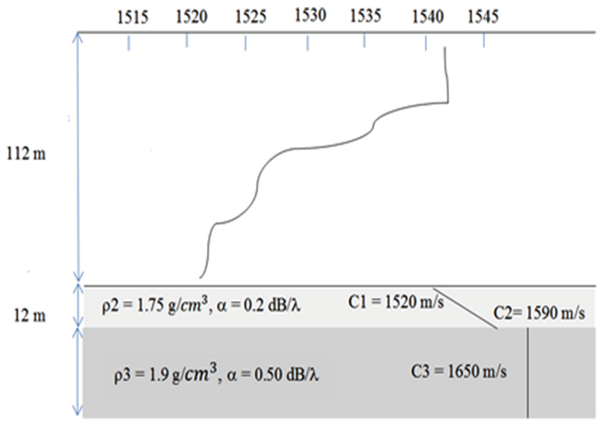

Fig. 1. Ocean model.

4.2 The Simulation with Different Number of Sensors for the Case of the Fixed Source Target

In Figs. 2, 3, 4 and 5 the localization results is presented when the source target is fixed. The simulation shows that the higher number of sensors is used, the better performance result is obtained. To be more specific, the source position is wrongly determined if only 4 sensors are used; in contrast the localization result becomes exact if 6 sensors are employed. In Fig. 5, when the total sensors are equal to 4, the ambiguity surface contains lots of sidelobes beside an undistinguishable mainlobe. The ability to distinct the mainlobe for the case of higher 6 sensors is better than one for the case of 4 sensors. The ambiguity surface for the case of 32 sensors gets higher resolutions in which high mainlobe could be considerably distinguishable beside other suppressed sidelobes in comparison to those for the remainder of the simulation cases.

4.3 The Simulation with Different Number of Sensors for the Case of the Moving Source Target

When the source target is a moving one, the simulation is presented in Figs. 6, 7 and 8. In Fig. 6, using 4 sensors could make the source target run out of its orbit. In Fig. 7, the target follows its orbit when using 6 sensors, however the mainlobe could not be distinguished clearly from the sidelobes. In Fig. 8, if 16 sensors are employed, the mainlobes not only follow their orbit but also play prominent places which could be distinguishable from other sidelobes. An increase of the number of the sensors, particularly higher than 6 sensors, makes the resolutions of the ambiguity surface better, leading to raise the ability to determine the target.

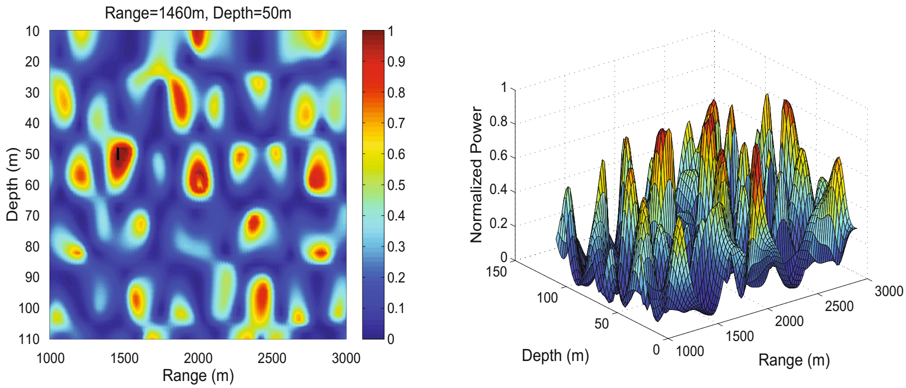

Fig. 2. The ambiguity surface for the case of fixed target with 4 sensors.

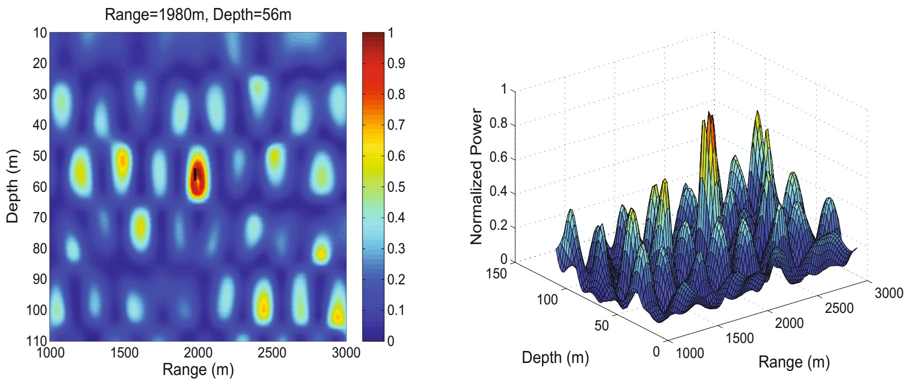

Fig. 3. The ambiguity surface for the case of fixed target with 8 sensors.

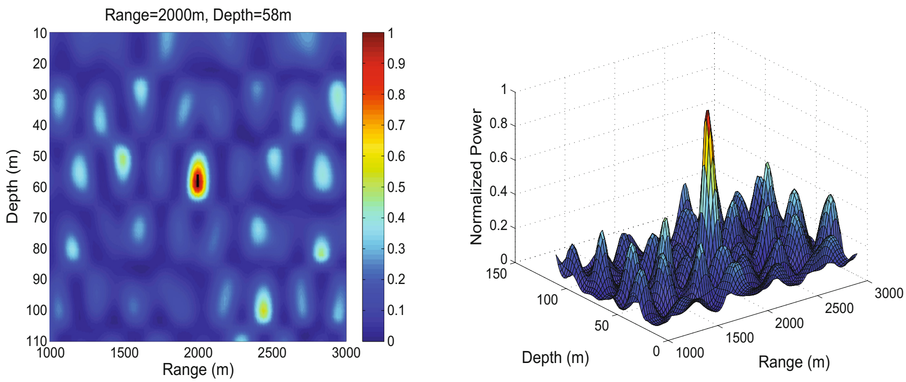

Fig. 4. The ambiguity surface for fixed target for the case of fixed target with 16 sensors.

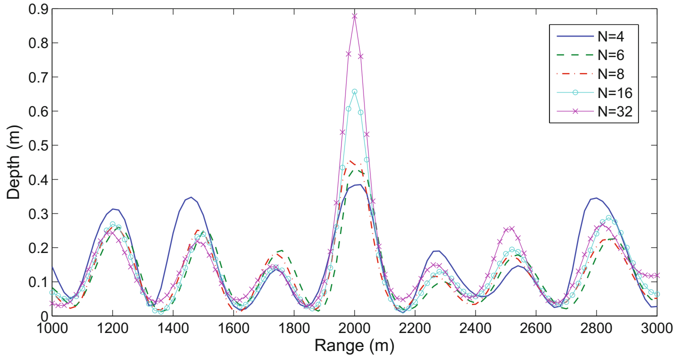

Fig. 5. The cross section of the ambiguity surface for fixed target with different sensor number.

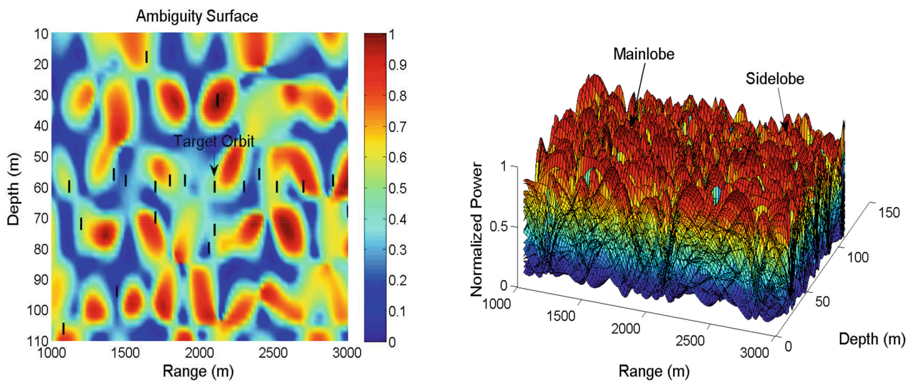

Fig. 6. The ambiguity surface for the case of moving target with 4 sensors.

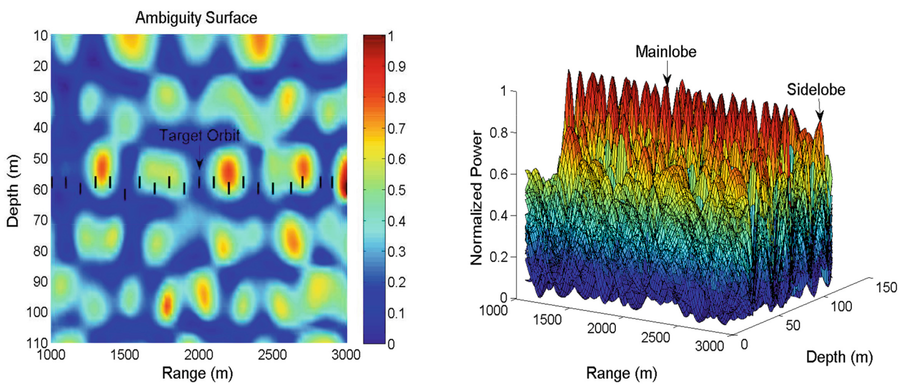

Fig. 7. The ambiguity surface for the case of moving target with 6 sensors.

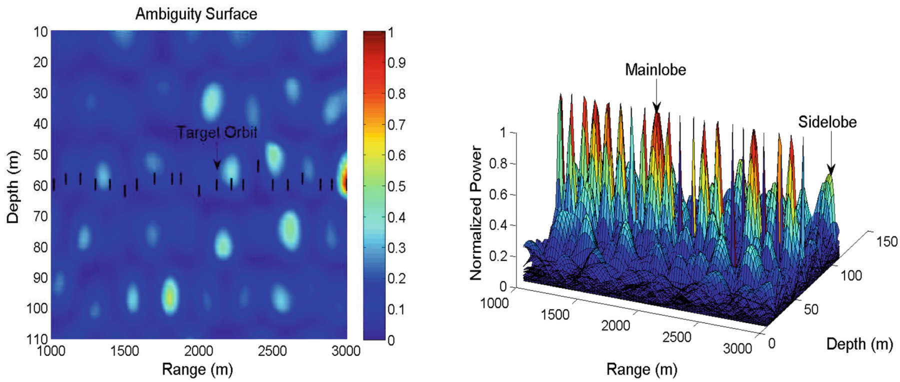

Fig. 8. The ambiguity surface for the case of moving target with 16 sensors.

5 Conclusion

The paper investigates on the influence of the sensors amount on the localization performance when applying the WNC-MFP method in a typical environmental condition. When the parameters of the environment and the criteria of the localization error varies, the requirement of the hydrophone number could be changed in order to guarantee the localization performance. The simulation results show that at least six sensors need to be deployed to ensure the accuracy of the localization performance with respect to the environmental parameters observed and positioning error criteria in this paper. With higher level of accuracy and resolution requirements, the sensors number need to be used is higher than 6 sensors to ensure localization performance. The localization performance will be improved if the sensor number increase.

References

1. Baggeroer, A.B., Kuperman, W.A., Mikhalevsky, P.N.: An overview of matched field methods in ocean acoustics. IEEE J. Oceanic Eng. **18**(4), 401–424 (1993)
2. Del Balzo, D.R., Feuillade, C., Rowe, M.M.: Effects of water-depth mismatch on matched-field localization in shallow water. J. Acoust. Soc. Am. **83**(6), 2180–2185 (1988)
3. Feuillade, C., Del Balzo, D.R., Rowe, M.M.: Environmental mismatch in shallow-water matched-field processing: geoacoustic parameter variability. J. Acoust. Soc. Am. **85**(6), 2354–2364 (1989)
4. Gebbie, J.T.: Advances in aquatic target localization with passive sonar (2014)
5. Harley, J.B., Mourn, J.M.F.: Matched field processing localization with random sensor topologies. In: 2014 IEEE International Conference on Acoustics, Speech and Signal Processing (ICASSP), pp. 1404–1408. IEEE (2014)
6. Jensen, F.B., Kuperman, W.A., Porter, M.B., Schmidt, H.: Computational Ocean Acoustics. Modern Acoustics and Signal Processing. Springer, New York (2011). https://doi.org/10.1007/978-1-4419-8678-8

7. Kolev, N.Z., Georgiev, G.D.: Reduced rank MVDR shallow water matched field processing for passive vertical sonar array source localization. In: 2007 15th International Conference on Digital Signal Processing, pp. 87–90. IEEE (2007)
8. Kolev, N.: Sonar Systems. InTech (2011)
9. Trinh, D.K., Tran, P.N., Nguyen, Q.T.: An investigation of the effects of factors on underwater localization with low source level in shallow water. Int. J. Adv. Eng. Technol. (IJAET) **9**(3), 584–591 (2016)
10. Wang, Q., Jiang, Q.: Simulation of matched field processing localization based on empirical mode decomposition and Karhunen-Loeve expansion in underwater waveguide environment. EURASIP J. Adv. Sign. Process. **2010**(1), 483–524 (2010)
11. Xiao, Z., Xu, W., Gong, X.: Robust matched field processing for source localization using convex optimization. In: Oceans 2009, Europe, pp. 1–5. IEEE (2009)
12. Zhang, K., Xu, W.: Performance of robust matched-field processing with convex optimization. In: OCEANS 2016, Shanghai, pp. 1–5. IEEE (2016)

Evaluation on UiTiOt Container-Based Emulation Testbed

Chuong Dang-Le-Bao, Nhan Ly-Trong, and Quan Le-Trung(✉)

Department of Computer Networks, University of Information Technology, Vietnam National University Ho Chi Minh City, Ho Chi Minh City, Vietnam
{chuongdlb,nhanlt,quanlt}@uit.edu.vn

Abstract. In this paper, we present a container-based emulation testbed, namely UiTiOt. The testbed integrated a well-known wireless emulation tool called QOMET to imitate the wireless network models over established wired network. Our testbed was developed based on a state-of-the-art technology called container-based virtualization. With our proposed design, we aim to provide researcher with the capability of running large-scale wireless/IoT experiments at affordable cost. Therefore, we did an insightful evaluation to ensure the feasibility and accuracy of the implementation of UiTiOt testbed. The evaluation includes several test-cases with different network topologies and routing protocols.

Keywords: Network architectures · Network evaluation
Container-based emulation · Network testbed

1 Introduction

As the trend of Internet of Things (IoT) continues to thrive in recent years, where the number of connected devices will reach 20.8 billions in 2020 [1] and leads to rapid movement in development of modern network protocols and standards. It is necessary to test the new device functionality in both hardware and software aspects before mass production. However, there has been a challenge to setup hundred-node or thousand-node in real-world scenarios because one has to consider a number of factors such as geographical position, mobility, transmit power and the budget to afford real devices. Since the simulation only solved the large-scale experiment in theoretical model where many environmental variables would be assumed or randomly set like node mobility, communication range or propagation loss, and in addition it was unable to execute in real-time like real-world testbed as illustrated in Table 1 [2].

Our work [3] has proposed a wireless/IoT Emulation Testbed based on container-based virtualization and QOMET, a wireless network emulation set of tools that made the wired-network adaptable for wireless network experiment. In our testbed system, each node in experimental scenario is represented by a container, which a simple Linux-runtime process that encapsulate user-namespace and relevant binaries and libraries to form a thinner Operating System-like environment. By implementation, we proved the proposed design's feasibility and usability, but we have yet to perform any further evaluation on its performance. Hence in this paper, **we focus on evaluating the performance of our emulation testbed, namely UiTiOt through many test-cases**

© ICST Institute for Computer Sciences, Social Informatics and Telecommunications Engineering 2018
Y. Chen and T. Q. Duong (Eds.): INISCOM 2017, LNICST 221, pp. 57–66, 2018.
https://doi.org/10.1007/978-3-319-74176-5_6

Table 1. Comparison of wireless testing techniques

	Simulation	Real world	Emulation
Real-time execution	No	Yes	Usually
Control level	High	Low	High
Condition range	Large	Small	Large
Result realism	Low	High	Medium
Experimentation cost	Low	High	Medium
Ease of use	High	Low	Medium

with different set of parameters. Instead of using OpenStack as underlying infrastructure [3], we setup small scale setup by using VMware virtual machines running on a high-performance laptop. By doing this, we possibly remove any underlying network constraints which had occurred in previous work [3], where traffic flows between containers would be routed to unwanted path despite our configuration. Our paper is organized as follows: the first section is the introduction, Sect. 2 discuss related research in emulation testbed and container-based virtualization, Sect. 3 revisits the architecture of our testbed design, Sect. 4 shows the experimental results of performance evaluation and followed by a conclusion.

2 Related Work

Testbed especially the emulation testbed systems has been playing an important role in development and evaluation of wireless protocols and application. Recent research has shown the advantages of emulation testbed, for instance EmuStack [4] which based on OpenStack and Docker showed the efforts of building a distributed emulation testbed for Delay Tolerant Network (DTN) at a reasonable cost, but no large-scale evaluation has yet been addressed. In addition, QOMB [2] which derived from a general-purpose wireless network test bench StarBED [5], which is large-scale testbed infrastructure comprised of physical computer nodes and network hardware. QOMB and related research and emulation experiments on StartBED system has proven the its efficiency and usability in the field of wireless network experiment but still required a large budget to develop and operate. In addition, recent work of [6] has proposed an emulation testbed based on OpenStack Cloud where an experiment node substituted by a virtual machine instance. On each *experiment* node of QOMET [7], the emulation process would be executed on-the-fly to mimic the wireless behavioral communication over the top of wired network setup. In recent year, container-based virtualization has embarked most aspects of software production in general. Though, many have utilized the advantages of container technology to apply in their research, most used it as an alternative for VM to deploy large-scale network experiment such as reproducing popular network experiments while others used container-based virtualization for Information-Centric Networking (ICN) [8] testbed or even in high-performance computing [9] and ubiquitous computing. Recent research [10] has shown the impressive performance of container technology in cloud context which outperform virtual machines and nearly the same as native performance.

3 Architectural Design

Our testbed system was created by integrating a well-known wireless emulator QOMET into a virtual container, also known as container-based virtualization technique [11]. In a brief, container-based virtualization is a lightweight alternative to the hypervisors, also known as Operating System (OS) Level virtualization. In container-based virtualization, physical resources of one machine are divided into multiple isolated user-space instances called containers. This can be achieved by using a feature of the Linux kernel called kernel namespaces, which allow different processes to have different view on the system, network-namespace feature can also be used to enable network virtualization. The container-based virtualization is basically a piece of software that works at the OS-level, providing abstractions directly for the guest processes. Since it works at OS-level, all virtual containers share the same Linux kernel with the host operating system, hence will have weaker isolation in comparison with hypervisor-based virtualization. However, each container behaves exactly like a stand-alone OS from the user's perspective. In our system, we used Docker [12], the state-of-art software that extended LXC [13] (Linux container – the most popular implementation of virtual container).

3.1 Qomet

QOMET [7] is short for Quality Observation and Mobility Experiment Tools, which is a set of tools used for wireless network emulation. It has been developed by researchers at JAIST since 2006. Our system used the version of QOMET (v2.1), released in June 2013 (Fig. 1).

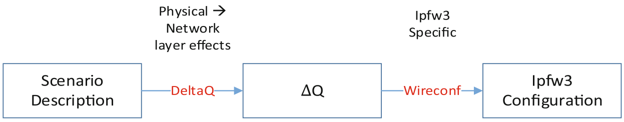

Fig. 1. QOMET model for the emulation.

The emulation mechanism of QOMET consists of two main stages. Firstly, a scenario description was defined by user to represent the wireless communication conditions and topology, that are then used to generate the experimental nodes and computing the network degradation values called *deltaQ*. Secondly, those degradation values were applied to the actual traffic by *wireconf* module (Fig. 2), which is a wrapper for a link-level emulator called DummyNet [14]. In this case, the degradation computation step is very simple, but in order to execute the degradation on real-time traffic of complex topologies was quite a challenge. Our main work focus on creating a Linux run-time environment for QOMET to be deployed and executed the artificial wireless network over wired/virtual network, and virtual container is inevitably the most ideal candidate for creating the QOMET run-time environment.

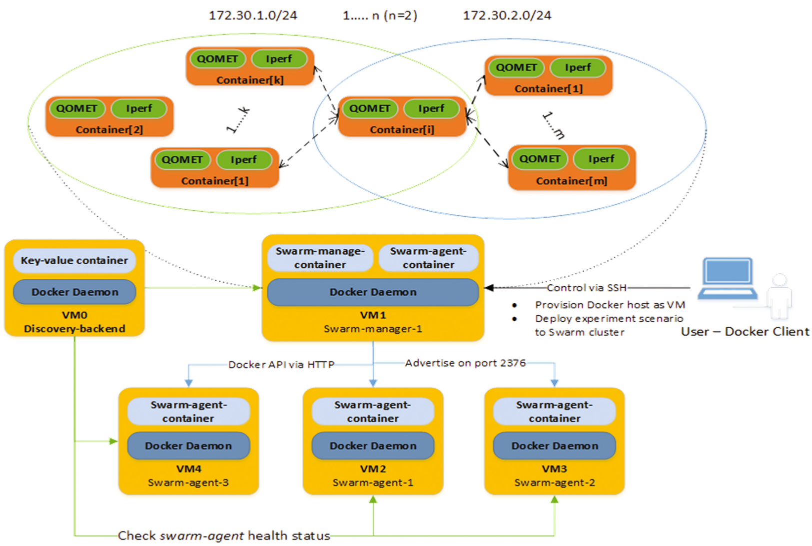

Fig. 2. Architecture of UiTiOt testbed using container-based virtualization.

3.2 UiTiOt Testbed

It is important to mention that the underlying infrastructure for the container-based virtualization is not necessarily the physical machine, a virtual machine can be used to deploy the container runtime software like LXC, Docker. As shown in Fig. 2, we used virtual machines to provide an OS-based computing instances for the upper container-based virtualization. In Fig. 2, a group of virtual machines (VMs) have been created to deploy a Docker-provided technology called Docker Swarm, which enable Docker-running VMs to share their computing resource (e.g. CPUs, memory, NIC) to form a single pool of compute resources that can be interacted transparently from the user point of view. The most notable feature of this distributed containers model is *overlay* networks, which are networks spanning on top of other networks [15]. In other words, one container from one VM will be able to communication with other containers from VMs that running Docker Swarm agents, VM0 in this model was dedicated to be a discovery backend service that stores the identities of all VMs in the Docker swarm setup, this help the VM running Swarm manager discover and check the availability of Swarm agents it manages. In our model, the overlay networks spanned on top of lower virtual networks of virtual machines, which otherwise can be physical networks if we had used physical computers to setup Docker Swarm. In this model, each *experiment node* described in QOMET scenario file is substituted by a container. At first, user had to defined the his experimental scenario in QOMET XML-file, which was then automatically parsed into Docker-compose YML-file. The file contained description about number of containers (each represent an *experiment node)*, number of overlay networks, environment variables inside each container, etc. It important to mention that QOMET executable binaries (e.g. *deltaQ, wireconf, etc.*) into the *container image*, which is a versioning image defined which software should be installed and run inside the container. In Docker engine, those container image configuration is defined a single file called *Dockerfile*. As all relevant file were put into container including a set of routing software like Quagga [16], OLSRd[1]. The *deltaQ* value was computed on-the-fly in the progress of building the image. At the end of *Dockerfile,* we defined an entry point, which points to the application will execute when the container is created and hence we setup multiple start-up applications at once using a custom script. Finally, the container image packaged with all necessary files for specific experiment was distributed across all VMs via a cloud-based container image hosting *Docker Hub*[2]. Finally, the virtual wired-network environment had been established for emulating environment, the system now creates a number of containers and overlay networks according to Docker-compose YML-based file. The container distribution was managed by the Docker Swarm manage and agent to spread the containers across VMs which currently have available resources. We can also manually define the and container distribution and container-consumed resources (CPU, memory, etc.) by specific configuration inside Docker-compose YML-based file[3]. All relevant logs of the experiment will be automatically pushed to a pre-defined central file server.

4 Experimental Results

In this section, we evaluated the performance and accuracy of our distributed container-based testbed through several test-cases. The Docker Swarm setup was hosted on VMware Fusion hyper-visor running inside a laptop, which is a MacBook Pro model 2015 equipped with Core i7 (2.2 GHz) and 16 GB of memory. The virtual machines setup was quite similar to the design, which it has four VM(s): one for discovery service was assign 1 vCPU/ 1 GB RAM, one as a Swarm manager with 2 vCPU/ 4 GB RAM, two as Swarm agents in which each has 1 vCPU/3 GB RAM.

In our experiment, we deploy 32-node scenario, in which these nodes form a tree topology network as illustration in Fig. 3. Besides, two routing schemes were used to enable multi-hop communication among *experiment nodes*, the first routing mechanism was RIP which enable by using Quagga routing suite, the second one was Optimized Link State Routing which implemented by using OLSR daemon (OLSRd). The communications environment was defined in QOMET test-cases using a list of parameters shown in the Table 2. α, σ, W respectively specify the parameters attenuation constant, shadowing parameter, wall attenuation of the log-distance path loss propagation modeltransmit power specifies the power of the power in dBm. The two main testing cases were interference and non-interference where pre-defined conditions shown in Table 2 will artificially affect the link quality between nodes, hence the wireless network communication will be emulated on top of the wired network by execution of *wireconf* module in each node. In the third test-case, the execution of *wireconf* module of QOMET was disabled to capture the normal network performance

1 *OLSRd:* http://www.olsr.org/mediawiki/index.php/Olsr_Daemon

2 *Docker Hub:* http://hub.docker.com/

3 https://docs.docker.com/compose/compose-file/

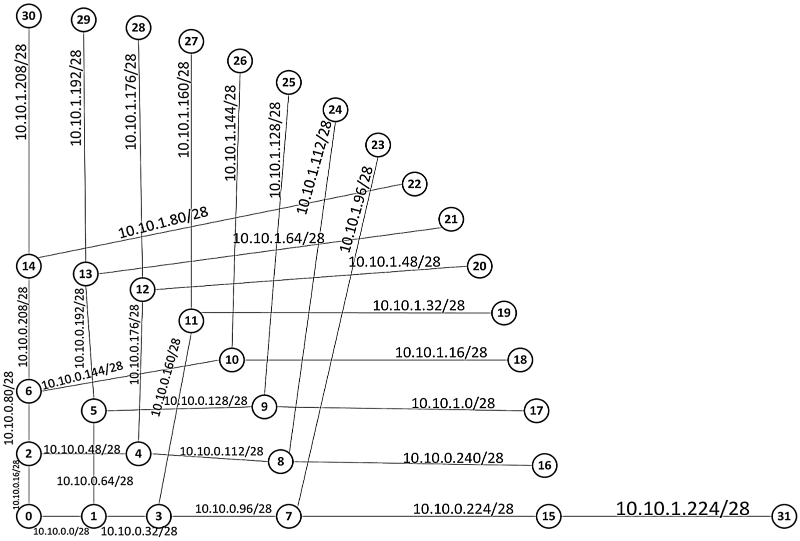

Fig. 3. Tree topology consist of 32 nodes and multiple subnets

Table 2. QOMET XML-file configuration for two main testing cases

Test-case	With interference	Without interference
Transmit power	2.5	
α	3.2	2.0
σ	0	
W	0	
Noise power	−100	0
Standard	802.11a	

without emulation. The popular network performance measurement tool Iperf [17] was used to generate network traffic and capture the bandwidth pattern as well as loss-rate. In detail, the test duration last for 200 s, but the actual duration when *iperf* client really communicate with *iperf* server is approximately 190 s.

We combined 3 mentioned test-cases with two types of routing protocol to create six different testing cases. Two intended connections were chosen to illustrate the emulation effects on **wired** network are: the first connection is from *node15* to *node31* where the transmission occurred directly between two nodes; and the second connection is from *node0* to *node31*, the multi-hop connection is be the longest branch of the tree structure. The measured bandwidth of these connections are shown respectively in following figures Figs. 4 and 5.

In Fig. 4 we continue to discuss the measured bandwidth of a direct connection from *node15* to *node31*. It is clear from the graph that the figures for 6 cases fluctuated in a small range during the period except the scenario without interference using OLSR performed a wide range fluctuation at the beginning of the period, which was till

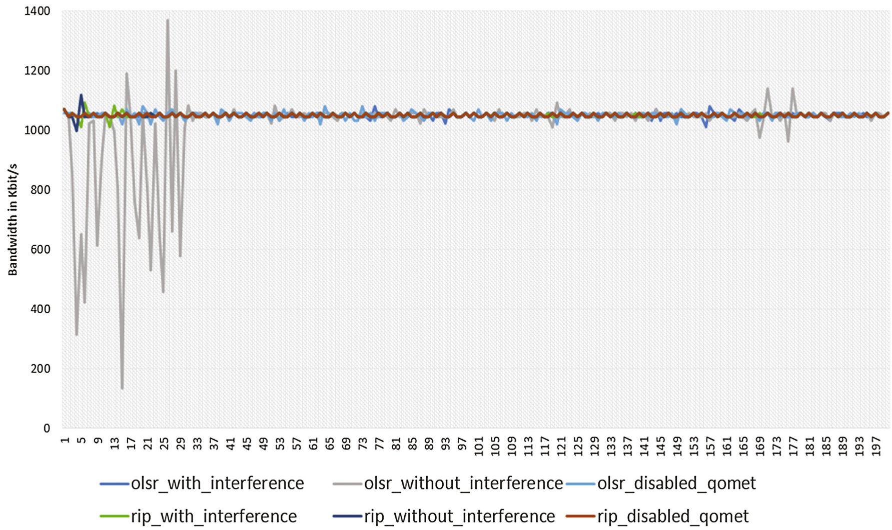

Fig. 4. Bandwidth measured of connection from *node15 to node31*

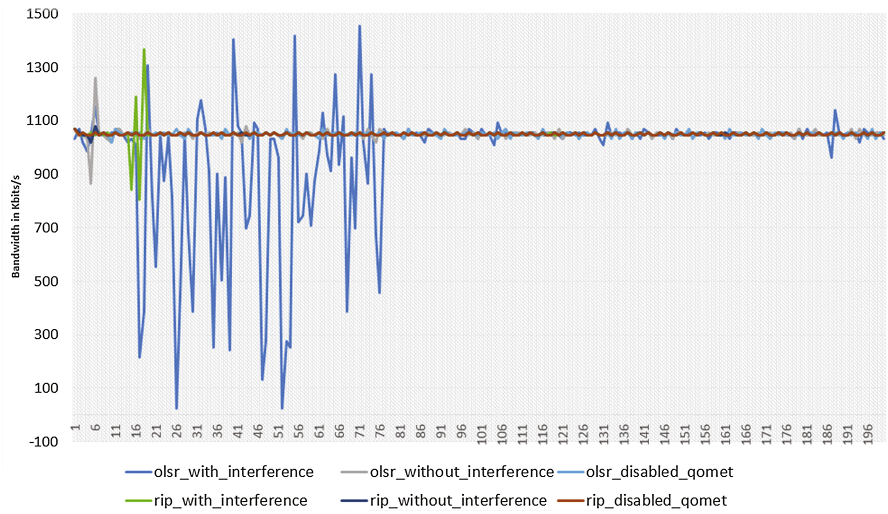

Fig. 5. Bandwidth measured in 6 test-cases from *node0 to node31*

unexplanable at the moment. The average bandwidth in the experiment without interference using OLSR was reported to approximately 1015 kbps. Meanwhile, the figures for the other ones were nearly the same as each other at just under 1050 kbps.

As is shown by the above line chart, the measured bandwidth in both 2 cases which disabled QOMET was seen to be more stable than the other ones. The figures were fluctuated in a tenuous range from around 1020 to almost 1080 kbps. Meanwhile, the 2 test-cases with interference and the one without interference using RIP performed a fluctuation in the bandwidth of the connection from node 15 to node 31 in a wider range. They were changed from under 1000 to just above 1110 kbps. In contrast, the bandwidth in the experiment without interference using OLSR fluctuated in a wide range at the beginning of the period. The minimum and maximum figures for this scenario were reported to approximately 130 and over 1300 kbps respectively.

In general, the proportions of packet loss in the experiment with interference were always at a higher level than the other ones. They were followed by the figures for the experiment without interference and the one that disabled QOME. In Figs. 6 and 7, the connection from node 15 to node 31 which was a direct connection, had the lowest percent of packet loss among 6 connections. The loss-rate for this connection in the experiment with interference was just under 8%, which was almost 3 times higher than the figure for the one without interference. Similarly, only approximately 1% packets of this connection which were unable to reach the destination in the experiment that disabled QOMET. Regarding the figures for indirect connections which were connections consisting intermediary nodes, the measured loss-rates for the scenario with interference were at least 18% and up to approximately 24% whereas the corresponding figures for the one without interference oscillated between 15 and just above 17%. In the scenario that disabled QOMET, the connections were reported with the lowest loss-rates among 3 test-cases which were from around 7.5% to 15%. Similar to Figs. 6 and 7 depicts the loss-rates of 3 test-cases but using OLSR instead of RIP. It is clear from the graph that the experiments using OLSR were reported with a considerably lower loss-rates than the ones using RIP. In most of connections, the loss-rates among 3 experiments followed a descending order from the experiment with interference then without interference to the experiment that disabled QOMET. In contrast, a different order of loss-rates among the 3 test-cases was shown in 2 connections from node 16 to

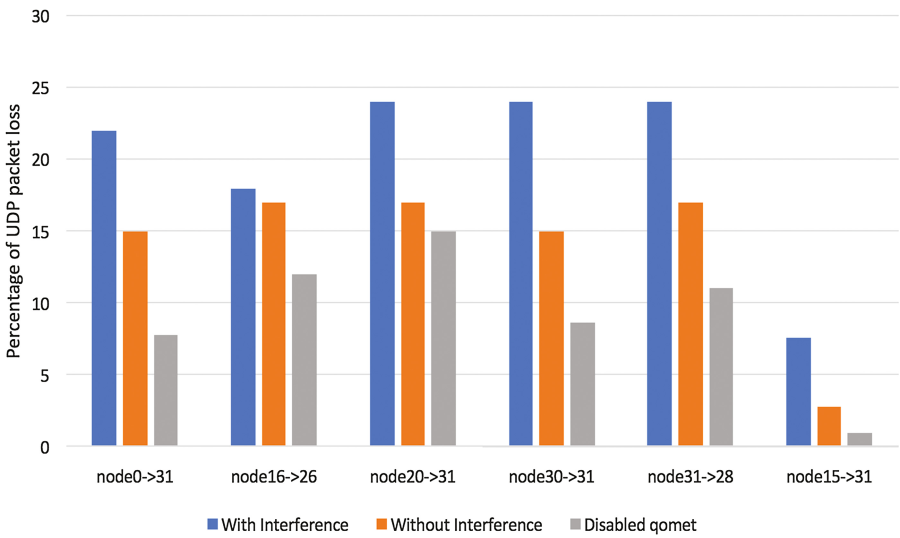

Fig. 6. Lossrates of test-cases using RIPd (Quagga)

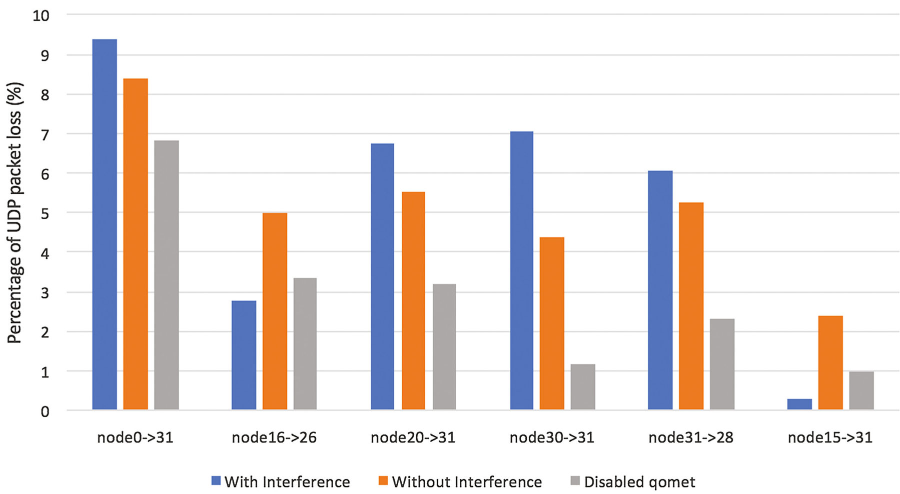

Fig. 7. Lossrates of test-cases using OLSRd

node 26 and from node 15 to node 31. The lowest figure among 3 test-cases was reported to the experiment with interference at about 0.25% for the connection from node 15 to node 31 and under 3% for the one between node 16 and node 26. At around 2.3% and exactly 5% packet sloss respectively for these 2 connections, the scenario without interference was the leader among these 3 test-cases. Meanwhile, the loss-rates for the experiment that disabled QOMET were shown at 1% for the connection between node 15 and node 31 and approximately 3.3% for the one from node 16 to node 26.

5 Conclusion

In a conclusion, we have evaluated the UiTiOt Testbed throughout six test-cases in a complex tree-based topology. The loss-rate results shown that the system work perfectly as our expectation. However, the measured bandwidths showed some abnormal patterns, in which non-interference case have a wide range of fluctuation than the interference case, and we have yet addressed any root causes of this problem. We believe our architecture design have a great potential in large-scale experiment in term of emulation accuracy, automatic deployment and reasonable cost. Though, there are still many to work need to be done to improve the testbed: deploying and extending the underlying infrastructure to more physical or virtual machines to support more *experiment nodes*, and we also aim to support more latest wireless/IoT routing protocol like ZigBee, 802.11n, etc., in the near future. Finally, we do hope that this system will potentially contribute to the development of domestic and international IoTs research and innovation.

Acknowledgement. This research is funded and supported by Department of Science & Technology Ho Chi Minh City, under the contract number: 48/2015/HĐ-SKHCN.

References

1. Gartner.com, 10 November 2015. http://www.gartner.com/newsroom/id/3165317. Accessed 13 April 2017
2. Beuran, R., Nguyen, L.T., Miyachi, T., Nakata, J., Chinen, K., Tan, Y., Shinoda, Y.: QOMB: a wireless network emulation testbed. In: Global Telecommunications Conference, GLOBECOM 2009. IEEE (2009)
3. Chuong, D.L.B., Trong, N.L., Le-Trung, Q.: UiTiOt: a container-based network emulation testbed. In: Proceedings of the 2017 International Conference on Machine Learning and Soft Computing (2017)
4. Li, H., Zhou, H., Zhang, H., Feng, B.: EmuStack: an openstack-based DTN network emulation platform. In: 2016 International Conference on Networking and Network Applications (2016)
5. Miyachi, T., Chinen, K., Shinoda, Y.: StarBED and SpringOS: large-scale general purpose network testbed and supporting software. In: Proceedings of the 1st International Conference on Performance Evaluation Methodolgies and Tools (2006)
6. Le-Trung, Q.: Towards an IoT network testbed emulated over OpenStack cloud infrastructure. In: Recent Advances in Signal Processing, Telecommunications and Computing (SigTelCom) (2017)
7. Razvan, B., Nakata, J., Okada, T., Tan, Y., Lan Tien, N., Yoichi, S.: A multi-purpose wireless network emulator: Qomet. In: 22nd International Conference on Advanced Information Networking and Applications-Workshops, AINAW 2008 (2008)
8. Asaeda, H., Li, R., Choi, N.: Container-based unified testbed for information-centric networking. IEEE Netw. **28**(6), 60–66 (2014)
9. Xavier, M.G., Neves, M.V., Rossi, F.D., Ferreto, T.C., Lange, T., De Rose, C.A.: Performance evaluation of container-based virtualization for high performance computing environments (2013)
10. Seo, K.T., Hwang, H.S., Moon, I.-Y., Kwon, O.-Y., Kim, B.-J.: Performance comparison analysis of linux container and virtual machine for building cloud. Adv. Sci. Technol. Lett. **66**, 105–111 (2014)
11. Soltesz, S., Potzl, H., Fiuczynski, M.E., Bavier, A., Peterson, L.: Container-based operating system virtualization: a scalable, high-performance alternative to hypervisors. ACM SIGOPS Oper. Syst. Rev. **41**(3), 275–287 (2007)
12. Merkel, D.: Docker: lightweight Linux containers for consistent development and deployment. Linux J. **2014**, 2 (2014)
13. Bernstein, D.: Containers and cloud: From LXC to docker to Kubernetes. IEEE Cloud Comput. **1**(3), 81–84 (2014)
14. Rizzo, L.: Dummynet: a simple approach to the evaluation of network protocols. ACM SIGCOMM Comput. Commun. Rev. **27**(1), 31–41 (1997)
15. Chowdhury, N.M.K., Boutaba, R.: A survey of network virtualization. Comput. Netw. **54**(5), 862–876 (2010)
16. Jakma, P., Lamparter, D.: Introduction to the quagga routing suite. IEEE Netw. **28**(2), 42–48 (2014)
17. Tirumala, A., Qin, F., Dugan, J., Ferguson, J., Gibbs, K.: iPerf - The ultimate speed test tool for TCP, UDP and SCTP (2005). https://iperf.fr. Accessed 25 Feb 2017

ICI Mitigation by Estimation of Double Carrier Frequency Offsets in High-Speed-Railway Communication Systems for Smart Cities

Yem Van Vu[1(✉)], Thi Huong Trinh[1,2], Nhat Minh Vu[1], Canh Minh Nguyen[2], and Duy Viet Nguyen[2]

[1] Hanoi University of Science and Technology, Hanoi, Vietnam
yem.vuvan@hust.edu.com
[2] University of Transport and Communications, Hanoi, Vietnam
trinhhuong@utc.edu.com

Abstract. OFDM is substantial against Inter-symbol-interference due to long symbol duration. However, inter-carrier interference (ICI) caused by high Doppler frequency shift has a severe impact on OFDM in case of high channel variations. In this paper, we propose an ICI mitigation method by utilizing the estimation and pre-compensation of high Doppler shifts in high-speed railway communication systems for smart cities. The estimate of the Doppler shift is based on a preamble frame of data in communication link between EnodeB and user equipment. The simulation results show that the performance of system has been improved using the proposed model.

Keywords: Doppler effect · CFO · OFDM · HSR · ICI · Smart cities

1 Introduction

In smart cities, the means of intelligent transportations need to be connected to a huge communication network to transfer the real-time properties of transportation as well as the control signals, which manages autonomous vehicles in order to reduce urban traffic congestions, to detect accidents and to avoid crashes [1–3]. In high speed railway (HSR), the demands for high-speed data connections of passengers on board as Internet, video calls, online TV are increasing. But the global system for mobile communications-railway (GSM-R) based on GSM technology does not meet the increasing requirements of broadband communications for supervising, controlling the train operation and services for passengers [4]. Currently, there are a lot of multimodal systems supplying broadband communications for HSR. One of them is the global broadband multimodal radio systems (MOWGLY) in Europe, which provides WiFi signal for passengers on board, the satellite signal for communications between train and the ground with a big delay. It is also used on Thalys and TGV East to supply broadcast internet [5]. With the speed of train is 300 kph, the maximum speed of data downlink and uplink are 4 Mbps and 2 Mbps, respectively [6]. Although current technologies temporarily meet the demands for HSR radio communications, they do

© ICST Institute for Computer Sciences, Social Informatics and Telecommunications Engineering 2018
Y. Chen and T. Q. Duong (Eds.): INISCOM 2017, LNICST 221, pp. 67–78, 2018.
https://doi.org/10.1007/978-3-319-74176-5_7

not meet the requirements for the fastest speed trains, high-speed data, real-time and reliable communications. According to recent studies, the required data rate for a train in HSR is around 37.5 Mbps and over 0.5–5 Gbps in the near future [7]. 4G long term evolution (LTE) standard has been widely investigated to satisfy the HSR communication system needs as well as for the train communication and the transmission of train control data [8].

The main core of 4G LTE standard in radio access network is orthogonal frequency division multiplexing (OFDM). OFDM provides high bandwidth efficiency and reliable signal transmission by dividing the available spectrum into group of closely spaced orthogonal sub-carriers, instead of transmitting a high data stream with a single carrier. Nevertheless, a series of difficulties caused by high movement speed such as over-frequent handover and high Doppler shift need to be solved urgently [9]. Particularly, when the OFDM based systems are considered for HSR communications, the Doppler frequency shift compensation techniques are vital due to the fact of that the OFDM systems are vulnerable to the carrier frequency offset (CFO) which may introduce the inter-carrier interference (ICI) to the system. Therefore, CFO problem plays a crucial role in OFDM systems for HSR communications. In the single input single output (SISO) or the co-located multiple input multiple output (MIMO) OFDM systems, there is only one CFO between the transceivers and a lot of researches on CFO approximation have been carried out with both data-aided approach and blind approach [10–16]. On the other side, when distributed transmitters transmit data streams at the same time, multiple CFOs will be obtained at the receiver, making the CFO approximation and compensation more perplexing. A well-known scenario is the so-called orthogonal frequency division multiple access (OFDMA), in which the subcarriers are completely occupied by the many users. Throughout the past few years, several multiuser CFO estimation techniques for OFDMA uplink have been proposed [17, 18], where different CFOs could either be estimated from an iterative methods or be detected from some subspace schemes. There are very few researches on multiple CFO estimation for multiuser OFDM transmission. Besson and Stoica made the first trial in [19] while limited their simulation only for flat fading channels. In [20], a semi-blind scheme was suggested to instantaneously approximate the multiple CFOs and channels in frequency selective fading channels. However, the technique is only effective for zero-padding (ZP) OFDM, as ZP can make the channel estimation and equalization simpler. A joint CFO and channel estimation for multiuser cyclic-prefix (CP) MIMO-OFDM systems based on the maximum likelihood (ML) criterion was introduced [21]. The high-complex multi-dimensional search is reduced from the importance sampling technique. However, the remaining complexity to create sufficient samples for importance sampling may still be large for real application implementation. A suboptimal estimation algorithm was presented in [22]. More recently, the authors of [23] introduced a semi-blind multi-CFO approximation and an independent component analysis based equalization scheme for multiuser coordinated multi-point OFDM systems. In this paper, the problem of double CFOs is investigated. The contributions of this paper is that the estimation of CFOs with only one received antenna rather than many antennas as shown in [19–23] and without the implement of training sequence as in [23]. We also show that our proposed method outperforms the conventional estimation method in [24] at high bit energy to noise ratio.

2 System Model

The HSR system that we investigate is a two-hoop network structure formed by distributed eNODE-Bs as illustrated in Fig. 1, in which d1 and d2 are distance from e-NODE-B1 and e-NODE-B2 to Mobile Station respectively, d_B is the perpendicular distance of E-NODE-B and railway, d_S is the coverage radius of one E-NODE-B and Δd is the overlap distance of two coverage area. Here we primarily examine the communication of E-NODE-B-MS links. Each E-NODE-B can be designed with one or more antennas. We make the assumption that the coverage region of each E-NODE-B forms a logic cell, and each E-NODE-B has one antenna and the MS also has one antenna. All the antennas have no correlation with each other. The Doppler frequency shifts are our main research objective, so we assume the system has been synchronized in time and oscillator frequency.

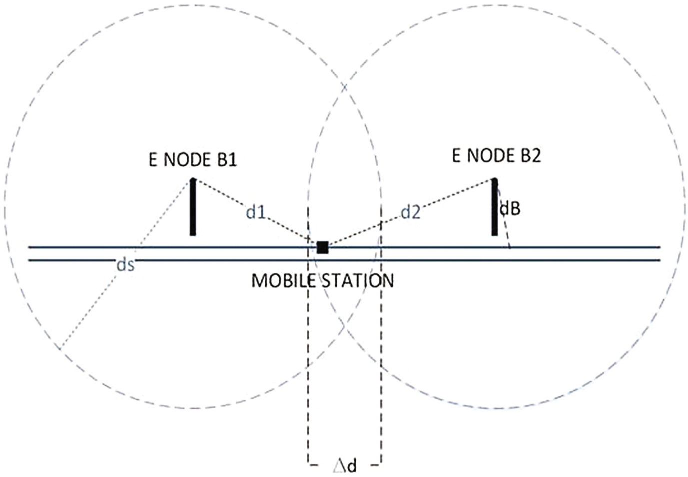

Fig. 1. Communication scenario in HSR

We assign time-frequency resource to the two adjacent E-NODE-Bs just as the two-TX scenario in downlink system in [22]. Desired signals from the two E-NODE-Bs reach the MS almost instantaneously. The two signal streams can not be detached easily because they occupy the same time-frequency slot in the OFDM communication link. Consequently, it is still problematic to compensate Doppler frequency offsets precisely at the receiver. Our proposed solution is given as in Fig. 2. The MS estimates Doppler frequency shifts based on the received data and then feeds the estimated value back to E-NODE-B. When the new data is sent, the frequency offset pre-compensation is made for the data. It is worth to note that the prediction according to variation of Doppler frequency shift is also possible to further enhance the effect of pre-compensation. We also have to point out that error would be presented because of the feedback delay produced by the fast time-varying channel.

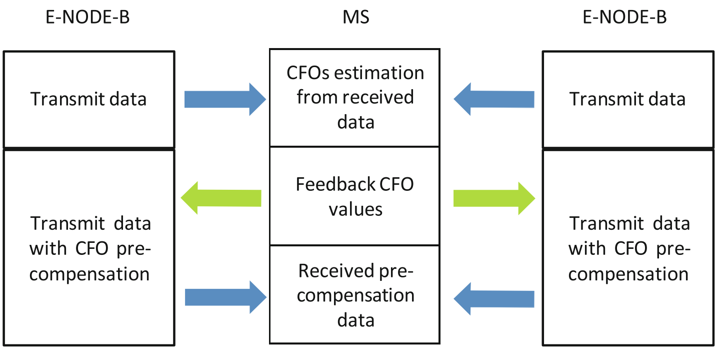

Fig. 2. Scheme for pre-compensation CFOs communication

As in Figs. 1 and 2, we can see that the received signal is the mixture of two signals from two separated E-NODE-Bs. As the MS is moving away from E-NODE-B1 and toward E-NODE-B2, the Doppler frequency shift of these two signals are undoubtedly different. In this paper, through mathematical models of channel and communication scenarios, we find out the two frequency shifts based on a preamble frame of data in communication link between E-NODE-Bs and MS.

3 Theoretical Analysis

3.1 Mathematical Model

In OFDM, multiple sinusoidal with frequency separation $1/T_s$ is used where T_s is the symbol duration.

Denote:

N: Number of subcarriers
P: Number of slots for data in N subcarriers (P < N)
s(k): the k^{th} *OFDM symbol.*

We have:

$$s(k) = [s_1(k)\, s_2(k) \ldots s_P(k)]^T \tag{1}$$

The OFDM modulation is performed by applying an inverse discrete fourier transform (IDFT) operator to the data stream. Using matrix representation, the resulting N-point time domain signal is given by:

$$x(k) = [x_1(k)\, x_2(k) \ldots x_N(k)]^T = \boldsymbol{W}_P s(k) \tag{2}$$

where $\boldsymbol{W_P}$ is a first P column of the $N \times N$ IDFT matrix $\boldsymbol{W}$:

$$\boldsymbol{W} = IDFT(N) = [w_l \ldots w_N] \tag{3}$$

$$\boldsymbol{W}_P = [w_1 \ldots w_P] \tag{4}$$

In practice, to prevent transmit filtering in OFDM system, some subcarriers are not modulated. In other words, the number of sub-channels carrying the information is generally smaller than the size of the discrete fourier transform (DFT) block. Without adjacent-channel-interference, the outputs from these virtual carriers are zero. Without loss of generality, we assume that carriers from 1 to P are used for data transmission so that we have Eq. (4). In DFT-based OFDM, a cyclic prefix (CP) is added to the multiplexed output of the IDFT before it is transmitted through a fading channel [23]. After that, the CP is detached at the receiver. Here, we do not put it into equation.

Denote:

$\boldsymbol{h}$: *Channel Impulse Response.*
$[H(1) \ldots H(N)] = FFT(\boldsymbol{h})(N - point\, FFT\, of\, \boldsymbol{h})$.

$$\boldsymbol{H} = diag[H(1) \ldots H(N)] \tag{5}$$

$$\boldsymbol{H}_P = diag[H(1) \ldots H(P)] \tag{6}$$

The receiver input for the k-th block from one E-NODE-B without noise and CFO is given by:

$$y(k) = \boldsymbol{h}\boldsymbol{W}_P s(k) = \boldsymbol{W}_P \boldsymbol{H}_{\boldsymbol{P}} s(k) \tag{7}$$

It is clear that, each subchannel, with a scalar ambiguity, can be recovered by applying a DFT to *y(k)*:

$$\boldsymbol{W}_P^H y(k) = \boldsymbol{H}_{\boldsymbol{P}} s(k) \tag{8}$$

Denote φ the normalized carrier frequency offset and Ng the guard interval duration of OFDM symbol. In the presence of a carrier offset, $e^{j\varphi}$, the receiver input *y(k)* without noise is modulated by:

$$\boldsymbol{E}(\varphi) = diag[1, e^{j\varphi}, e^{j2\varphi}, \ldots, e^{j(N-1)\varphi}] \tag{9}$$

and becomes:

$$y(k) = \boldsymbol{E}(\varphi)\boldsymbol{W}_P \boldsymbol{H}_{\boldsymbol{P}} s(k) e^{j(k-1)(N+Ng)\varphi} \tag{10}$$

Since $\boldsymbol{W}_P^H \boldsymbol{E}(\varphi)\boldsymbol{W}_P \neq \boldsymbol{I}$, the $\boldsymbol{E}(\varphi)$ matrix breaks the orthogonality among the sub-channels and, as a result, introduces ICI. To recover *s(k)*, the carrier offset, φ requires be estimating and compensating before applying the DFT.

In the situation that we investigate, the received signal is the combination of signals from two sources. From Eq. (10), we denote the received signal from one transmitter without noise is:

$$y1(k) = \boldsymbol{E}(\varphi_l)\boldsymbol{W}_P\boldsymbol{H}_{\boldsymbol{1P}}s(k)e^{j(k-1)(N+Ng)\varphi} \tag{11}$$

where φ_1 is the normalized carrier frequency shift from the first E-NODE B and $\boldsymbol{H}_{\boldsymbol{1P}}$ is the channel frequency response matrix similar to $\boldsymbol{H}_{\boldsymbol{P}}$. With K is the number of OFDM symbols in one frame, we have one frame of the received signal from one E-NODE B is:

$$\boldsymbol{y1} = \boldsymbol{E}(\varphi_l)\boldsymbol{W}_P\boldsymbol{H}_{1P}\boldsymbol{s}^{\boldsymbol{T}}\boldsymbol{B}(\varphi_l) \tag{12}$$

in which $\boldsymbol{s} = [s(1), s(2), \ldots s(K)]^T$

and $\boldsymbol{B}(\varphi) = diag[1, e^{j(N+Ng)\varphi}, e^{j2(N+Ng)\varphi}, \ldots, e^{j(K-1)(N+Ng)\varphi}]$ are the sending data in one frame and the carrier frequency offset matrix along OFDM symbols.

When there are two E-NODE-Bs, the received data frame without noise is:

$$\boldsymbol{y} = \boldsymbol{E}(\varphi_l)\boldsymbol{W}_P\boldsymbol{H}_{\boldsymbol{1P}}\boldsymbol{s}^T\boldsymbol{B}(\varphi_l) + \boldsymbol{E}(\varphi_2)\boldsymbol{W}_P\boldsymbol{W}_{\boldsymbol{2P}}\boldsymbol{s}^T\boldsymbol{B}(\varphi_2) \tag{13}$$

In order to recover $s(k)$, the carrier offsets, φ_1 and φ_2, need to be estimated and compensated before performing the DFT.

3.2 Estimation Algorithm

Since $\boldsymbol{W}_P$ contains of a subset of the columns of the IDFT matrix, $\boldsymbol{W}$, its orthogonal complement, $\boldsymbol{W}^{\perp} = [w_{P+1} \ldots w_N]$, is known. We define:

$$\boldsymbol{Z}(\omega) = diag[1, e^{j\omega}, e^{j2\omega}, \ldots, e^{j(N-1)\omega}] \tag{14}$$

It is obvious that when $\omega = \varphi, \boldsymbol{Z}(\omega) = E(\varphi)$.

Considering a preamble data frame in which $\boldsymbol{s}$ is known in prior. Let the number of symbols per frame K greater than the number of data slots P, we construct $\dot{\boldsymbol{s}}$ from $\boldsymbol{s}$. Firstly, we make singular value decomposing $\boldsymbol{s}^{\boldsymbol{T}}$ into $\boldsymbol{U}, \boldsymbol{D}, \boldsymbol{V}(\boldsymbol{s}^{\boldsymbol{T}} = \boldsymbol{UDV})$ in which $\boldsymbol{U}$ and $\boldsymbol{V}$ are $P \times P$ and $K \times K$ unitary matrix respectively. $\boldsymbol{D}$ is a rectangular diagonal matrix with non-negative real numbers on the diagonal. Then, we set $\dot{\boldsymbol{s}}$ to be the last K −P column of the $K \times K$ matrix $\boldsymbol{V} : \dot{\boldsymbol{s}} = [v_{K-P+1}, \ldots, v_K] = [\dot{s}_1, \dot{s}_2, \ldots, \dot{s}_{K-P}]$. Consequently, we have $\boldsymbol{s}^{\boldsymbol{T}}\dot{s}_k$ is a null vector.

Denote:

$$\boldsymbol{T}(\omega) = diag[1, e^{j(N+Ng)\omega}, e^{j2(N+Ng)\omega}, \ldots, e^{j(K-1)(N+Ng)\omega}] \tag{15}$$

In the absence of noise, if $\omega_l = \varphi_l$ and $\omega_2 = \varphi_2$, we have:

$$
\begin{aligned}
& w_{p+i}^{H}\boldsymbol{Z}(\omega_1)^{-\mathbf{1}}\boldsymbol{y}\boldsymbol{T}(\omega_2)^{-\mathbf{1}}\dot{s}_k \\
& = w_{p+i}^{H}\boldsymbol{Z}(\omega_1)^{-\mathbf{1}}\{\boldsymbol{E}(\varphi_1)\boldsymbol{W}_P\boldsymbol{H}_{\mathbf{1P}}\boldsymbol{s}^T\boldsymbol{B}(\varphi_1)+\boldsymbol{E}(\varphi_2)\boldsymbol{W}_P\boldsymbol{H}_{\mathbf{2P}}\boldsymbol{s}^T\boldsymbol{B}(\varphi_2)\}\boldsymbol{T}(\omega_2)^{-\mathbf{1}}\dot{s}_k \\
& = w_{p+i}^{H}\boldsymbol{Z}(\omega_1)^{-\mathbf{1}}\boldsymbol{E}(\varphi_1)\boldsymbol{W}_P\boldsymbol{H}_{\mathbf{1P}}\boldsymbol{s}^T\boldsymbol{B}(\varphi_1)\boldsymbol{T}(\omega_2)^{-\mathbf{1}}\dot{s}_k \\
& + w_{p+i}^{H}\boldsymbol{Z}(\omega_1)^{-\mathbf{1}}\boldsymbol{E}(\varphi_1)\boldsymbol{W}_P\boldsymbol{H}_{\mathbf{2P}}\boldsymbol{s}^T\boldsymbol{B}(\varphi_2)\boldsymbol{T}(\omega_2)^{-\mathbf{1}}\dot{s}_k \\
& = 0, \; (i = 1,\ldots,N-P; k = 1,\ldots,K-P).
\end{aligned} \tag{16}
$$

This observation suggests that we form a cost function given a finite number of data vectors as follows:

$$
\begin{aligned}
P(\omega_1,\omega_2) &= \sum_{k=1}^{K-P}\sum_{i=1}^{N-P}\left||w_{p+i}^{H}\boldsymbol{Z}(\omega_1)^{-\mathbf{1}}\boldsymbol{y}\,\boldsymbol{T}(\omega_2)^{-\mathbf{1}}\dot{s}_k|\right|^2 \\
&= \sum_{k=1}^{K-P}\sum_{i=1}^{N-P} w_{p+i}^{H}\boldsymbol{Z}(\omega_1)^{-\mathbf{1}}\boldsymbol{y}\,\boldsymbol{T}(\omega_2)^{-1}\dot{s}_k\dot{s}_k^{H}\boldsymbol{T}(\omega_2)\boldsymbol{y}^H\boldsymbol{Z}(\omega_1)w_{p+i}
\end{aligned} \tag{17}
$$

Clearly, $P(\omega_1,\omega_2)$ is zero when $\omega_1 = \varphi_1$ and $\omega_2 = \varphi_2$. Therefore, one can find the carrier offsets by evaluating $P(\omega_1,\omega_2)$ along the two independent unit circles. However, we can see that the cost function also has root $\omega_1 = \varphi_2$ and $\omega_2 = \varphi_1$; hence, the cost function has two minimas.

Due to the fact that the we have to solve in the form (φ_1,φ_2) and (φ_2,φ_1); we propose finding maxima of the following symmetric cost function to further enhance the performance:

$$
\boldsymbol{Q}(\omega_1,\omega_2) = P(\omega_1,\omega_2) + P(\omega_2,\omega_1) \tag{18}
$$

The proposed algorithm is summarized as follows:

(1) Constructing $\dot{\boldsymbol{s}}$ at the receiver based on the preamble data $\boldsymbol{s}$.
(2) Forming the cost function $\boldsymbol{Q}(\omega_1,\omega_2)$ as in (17) and (18) using the known receiver outputs $\boldsymbol{y}$ and the constructed $\dot{\boldsymbol{s}}$.
(3) Estimating the carrier offset as the minima of $\boldsymbol{Q}(\omega_1,\omega_2)$:

$$
(\hat{\varphi}_1,\hat{\varphi}_2) = (\omega_{0_1},\omega_{0_2}) : \boldsymbol{Q}(\omega_{0_1},\omega_{0_2}) = min\,\boldsymbol{Q}(\omega_1,\omega_1)
$$

(4) Compensating the results $(\hat{\varphi}_1,\hat{\varphi}_2)$ into the sending data for several next rounds of communication.
(5) Redoing the preamble data estimation after data transmission with another preamble data.

4 Simulation Results

We use the parameters shown in Table 1 to establish the communication scenario. In the simulation, we focus on the two communication links between E-NODE-Bs and MS. We assume that the system has already achieve the signal time synchronization at the receiver.

Table 1. Simulation parameters for double CFO estimation

Parameters	Values
Cell radius (ds)	500 m
Overlap coverage region (Δd)	400 m
Initial distance between train and E-NODE-B1 (d1)	100 m
Initial distance between train and E-NODE-B2 (d2)	400 m
Distance between railway and E-NODE-Bs (d_B)	50 m
Velocity of train (v)	360 km/h
Total number of subcarriers	128
Modulation	BPSK
Subcarrier spacing (Δf)	120 kHz
Bandwidth (BW)	10 MHz
Sampling frequency (fs)	15.36 MHz
Frequency	2.6 GHz

Figures 3 and 4 show the CFO of communication links when the MS is going far away from E-NODE-B1 and toward E-NODE-B2. Similar with Single CFO estimation, the proposed algorithm was not accurate at low E_b/N_0. However, it achieves high accuracy at higher E_b/N_0.

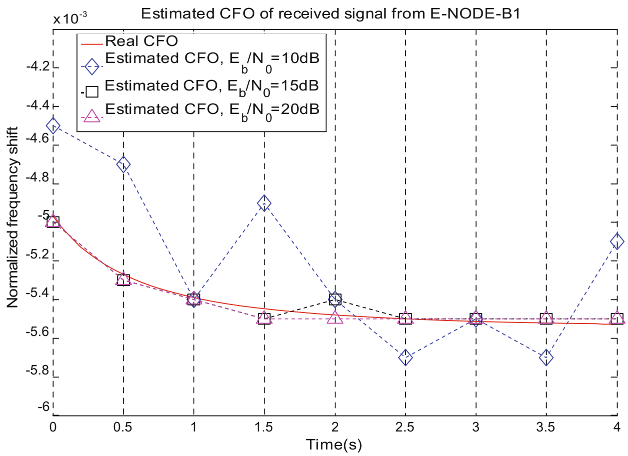

Fig. 3. The estimated CFO and the actual CFO at E-NODE-B1

The mean square error of our proposed method is described in Fig. 5. In the simulation, we compare our proposed method to the conventional solution as shown in [18]. From Fig. 5, it can be seen clearly that at higher *16 dB* E_b/N_0, our algorithm has shown its dominance.

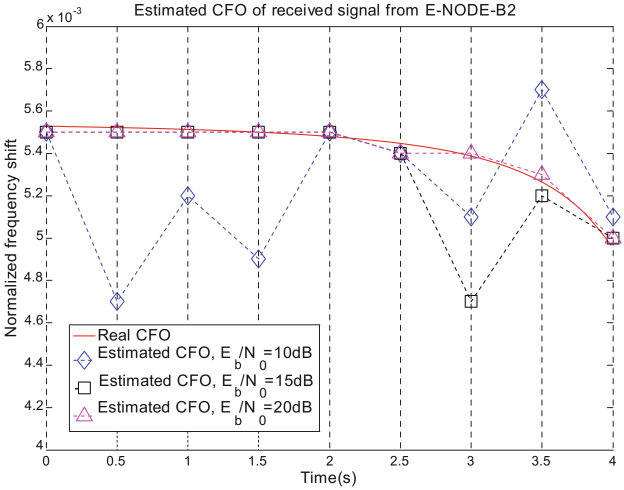

Fig. 4. The estimated CFO and the actual CFO at E-NODE-B2

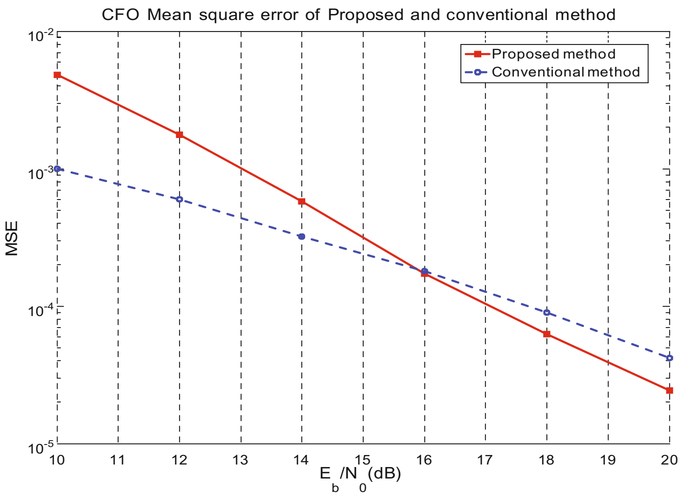

Fig. 5. MSE of the proposed algorithm and conventional method

Figure 6 is the BER of our communication scheme compare to communication link with no CFO and communication link with CFO but no CFO compensation. As E_b/N_0 got higher, our algorithm results approached the real CFO value; hence, the performance got closer to ideal case.

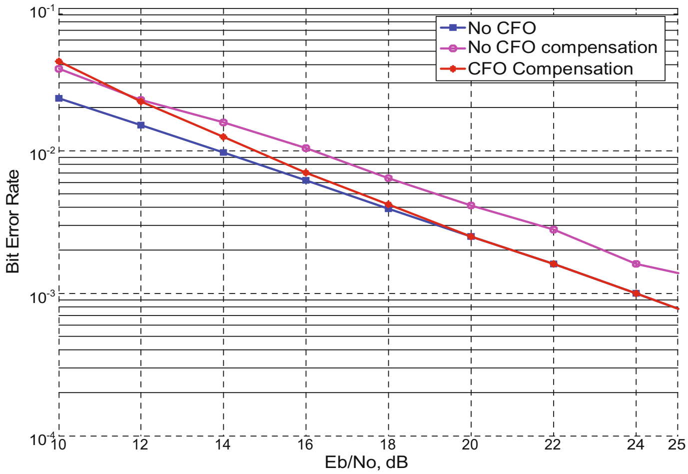

Fig. 6. BER with and without CFO compensation

5 Conclusions

We propose an inter-symbol-interference mitigation method by estimation of double carrier frequency offsets and pre-compensation of high Doppler shifts in High-Speed-Railway Communication Systems with distributed E-NODE-B. Our proposed method is based on a preamble frame of data and received signal without the implement of multiple received antennas. In our proposed solution, the MS estimates Doppler frequency shifts based on the received data and then feeds the estimated value back to E-NODE-B. When the new data is sent, the frequency offset pre-compensation is made for the data. The system is simulated and the double CFOs are estimated using the proposed algorithm. The mean square error of estimation is compared to conventional solution in order to show the performance. The proposed method gets a better accuracy and the CFOs are eliminated effectively and at high E_b/N_0. By the proposed method, the passengers's demand and transportation management networks require high-speed data services can be provided with reliable connections. This can be considered as a promising solution to solve problem of transportation infrastructures and High Speed Railway (HSR) in digital or smart cities.

Acknowledgment. This work is supported by the university of transport and communications, Vietnam, under the framework of the research project "Research on signal processing algorithms in high speed rail communications", code T2017-ĐĐT-51. The authors would like to thank the University for financial support.

References

1. Bhagat, S.S., Shah, P.S., Patel, M.J.: Smart cities in context to Urban development. Int. J. Civ. Struct. Environ. Infrastruct. Eng. Res. Dev. **4**(1), 41–48 (2014)
2. Xiong, Z., Sheng, H., Rong, W., Cooper, D.E.: Intelligent transportation systems for smart cities: a progress review. Sci. China Inf. Sci. **55**(12), 2908–2914 (2012)
3. Al-Dubai, A.Y.: Reliable intelligent transportation systems for smart cities. In: 2nd International Conference and Business Expo on Wireless & Telecommunication, Theme: Connecting People to Connecting Global, 21–22 April. The Oberoi Centre, Dubai, UAE (2016)
4. UIC GSM-R Functional Group. GSM-R functional requirement specification (FRS). UIC, Paris, France, UIC EIRENE Technology Report, UIC Code 950, version 7.3.0 (2012)
5. Barbu, G.: E-Train - Broadband communication with moving trains-Technology state of the art, Technical Report, June 2010
6. Jiang, X., Zou, F., Lin, Z., Wang, T.: A survey on the internet application on passenger trains. J. China Railway Soc. **29**, 103–110 (2007)
7. Lannoo, B., Colle, D., Pickavet, M., Demeester, P.: Radio-over-fiber-based solution to provide broadband internet access to train passengers. IEEE Commun. Mag. **45**, 56–62 (2007)
8. Guan, K., Zhong, Z.D., Ai, B.: Assessment of LTE-R using high speed railway channel model. In: Proceedings of International Conference on Communications and Mobile Computing, pp. 461–464 (2011)
9. Zhao, Y., Li, J.: Analysis of the impact of Doppler spread on OFDM-based next- generation high-speed rail broadband mobile communications. In: IET International Conference on Communication Technology and Application (ICCTA 2011), pp. 116–120 (2011)
10. Moose, P.H.: A technique for orthogonal frequency division multiplexing frequency offset correction. IEEE Trans. Commun. **42**(10), 2908–2914 (1994)
11. Yu, J.H., Su, Y.T.: Pilot-assisted maximum-likelihood frequency-offset estimation for OFDM systems. IEEE Trans. Commun. **52**(11), 1997–2008 (2004)
12. Roman, T., Koivunen, V.: Subspace method for blind CFO estimation for OFDM systems with constant modulus constellations. In: Proceedings of IEEE VTC, Stockholm, Sweden, pp. 1253–1257 (2005)
13. Yang, F., Li, K.H., Teh, K.C.: A carrier frequency offset estimation with minimum output variance for OFDM systems. IEEE Commun. Lett. **8**(11), 677–679 (2004)
14. Van Zelst, A., Schenk, T.C.W.: Implementation of a MIMO OFDM based wireless LAN system. IEEE Trans. Signal Process. **52**(2), 483–494 (2004)
15. Jiang, Y., Gao, X., You, X., Heng, W.: Training sequence assisted frequency offset estimation for MIMO OFDM. In: Proceedings of IEEE International Conference on Communications, Istanbul, Turkey, pp. 5371–5376 (2006)
16. Van de Beek, J.J., Sandell, M., Brjesson, P.O.: ML estimation of timing and frequency offset in OFDM systems. IEEE Trans. Signal Process. **45**(7), 1800–1805 (1997)
17. Sun, P., Zhang, L.: Low complexity pilot aided frequency synchronization for OFDMA uplink transmissions. IEEE Trans. Wirel. Commun. **8**(7), 3758–3769 (2009)
18. Bai, L., Yin, Q.: Frequency synchronization for the OFDMA uplink based on the tile structure of IEEE 802.16e. IEEE Trans. Veh. Technol. **61**(5), 2348–2353 (2012)
19. Besson, O., Stoica, P.: On parameter estimation of MIMO flat-fading channels with frequency offsets. IEEE Trans. Signal Process. **51**(3), 602–613 (2003)
20. Zeng, Y., Leyman, R.A., Ng, T.S.: Joint semi blind frequency offset and channel estimation for multiuser MIMO-OFDM uplink. IEEE Trans. Commun. **55**(12), 2270–2278 (2007)

21. Chen, J., Su, Y.C., Ma, S., Ng, T.S.: Joint CFO and channel estimation for multiuser MIMO-OFDM systems with optimal training sequences. IEEE Trans. Signal Process. **56**(8), 4008–4019 (2008)
22. Wu, Y., Bergmans, J.W.M., Attallah, S.: Carrier frequency offset estimation for multiuser MIMO OFDM uplink using CAZAC sequences: performance and sequence optimization. EURASIP J. Wirel. Commun. Netw. **2011** (2011). Article ID: 570680
23. Jiang, Y., Zhu, X., Lim, E., Huang, Y., Lin, H.: Low-complexity semi blind multi-CFO estimation and ICA-based equalization for CoMP OFDM systems. IEEE Trans. Veh. Technol. **63**(4), 1928–1934 (2014)
24. Xiong, J., Gui, L., Liu, H., Cheng, P.: On channel estimation and equalization in 2x1 MISO TDS-OFDM based terrestrial DTVsystems. IEEE Trans. Broadcast. **58**, 130–138 (2012)
25. 3GPP. TR 36.211 v8.6.0 Physical Channel and Modulation for Evolved UTRA (2009)
26. Sari, H., Karam, G., Jeanclaude, I.: Transmission techniques for digital terrestial TV broadcasting. IEEE Commun. Mag. **33**(2), 100–109 (1995)

Three-Way Massive MIMO Relaying with Successive Cancelation Decoding

Chung Duc Ho[1(✉)], Hien Quoc Ngo[1,2], and Michail Matthaiou[1]

[1] Institute of Electronics, Communications and Information Technology (ECIT), Queen's University Belfast, Belfast BT3 9DT, UK
{choduc01,m.matthaiou}@qub.ac.uk

[2] Department of Electrical Engineering (ISY), Linköping University, 581 83 Linköping, Sweden
hien.ngo@liu.se

Abstract. In this paper, we propose a novel transmission scheme for a three-way massive multiple-input multiple-output (MIMO) relay network where three users exchange their data with the help of a decode-and-forward relay station equipped with a very large antenna array. Our proposed scheme needs only two time-slots for the information exchange. More precisely, the three users first send their symbols to the relay. Then, the relay uses the maximum-ratio combining technique to decode all transmitted symbols and simultaneously transmits these symbols to all three users. Each user applies successive cancelation decoding to decode symbols transmitted from other users. We study the sum spectral efficiency of our proposed transmission protocol. We show that the sum spectral efficiency of our proposed scheme increases noticeably compared to the one of the conventional scheme where three time-slots are required to exchange data among the three users, without increasing the system complexity.

Keywords: Decode-and-forward · Maximum-ratio combining
Multi-way relay massive MIMO · Successive cancelation decoding

1 Introduction

Over the past decade, multi-way relaying networks have received a lot of research interest [1–3]. In multi-way relaying networks, multiple users located in different areas in the networks exchange their data with the help of a relay. The relay can be equipped with single or multiple antennas and can use different processing such as amplify-and-forward (AF) or decode-and-forward (DF). It was shown in [1] that multi-way relaying systems can boost the spectral efficiency and energy efficiency of the system, as well as, the robustness against the channel variations in different propagation environments. Furthermore, in [2,3], the authors illustrated that multi-way relaying networks offer higher communication reliability than one-way or two-way relaying systems do.

© ICST Institute for Computer Sciences, Social Informatics and Telecommunications Engineering 2018
Y. Chen and T. Q. Duong (Eds.): INISCOM 2017, LNICST 221, pp. 79–90, 2018.
https://doi.org/10.1007/978-3-319-74176-5_8

In parallel, there has also been a great deal of interest in massive MIMO [4–6] since it can serve at the same time many users with good service, and with very low power consumption. In massive MIMO, the base station (BS) is equipped with hundreds or thousands antennas using simple linear processing to serve simultaneously tens or hundreds users in the downlink and the uplink. Owing to the favorable propagation property of massive MIMO (the channel vectors between the BS and the users are (nearly) pairwisely orthogonal when the number of antennas is large), the uncorrelated noise and inter-user interference disappear with simple linear processing such as maximum-ratio and zero-forcing processing. This makes massive MIMO feasible for practical implementation [7]. More importantly, by leveraging time division duplex (TDD) mode, massive MIMO is scalable to any desired degrees of freedom with respect to the number of antennas at the BS [2]. For all above reasons, massive MIMO is a very strong candidate for the fifth-generation (5G) of wireless networks [8].

Multi-way massive MIMO relay networks—the combination of multi-way relaying and massive MIMO technologies—offer very high throughput, communication reliability, and energy efficiency, and have received increasing research interest recently [9,10]. In [9,10], the authors demonstrated that with a simple linear processing (e.g. zero-forcing and/or maximum-ratio processing) in the downlink and uplink data transmission, the system performance is nearly optimal. Furthermore, by using very large antenna arrays at the relay, the transmit power of each user and/or the relay can be scaled down proportionally to the number of relay antennas, while maintaining a desired quality-of-service [9,10].

In this paper, we consider a three-way massive MIMO relaying network which is the most simplified version of multi-way systems. Different with the aforementioned works, we focus on the aspects of transmission design for DF operation. We propose a new transmission protocol in which the broadcast phase needs only 1 time-slot to send all symbols to all users (the conventional scheme [11] requires 2 time-slots). We derive the sum spectral efficiency of our proposed scheme. Compared with the conventional scheme, our proposed scheme improves the sum spectral efficiency by a factor of 1.5.

Notation: Matrices and vectors are represented via upper- and lowercase boldface letters, respectively. The Hermitian transpose, Frobenius norm of matrix $\mathbf{Z}$, and expectation operator are denoted by $(\cdot)^H$, $\|\mathbf{Z}\|_{\mathrm{F}}$, and $\mathbb{E}\{\cdot\}$, respectively. The (m, n)-th element of matrix $\mathbf{Z}$ is denoted by z_{mn}. Finally, we use $\mathbf{z}_k$ to denote the k-th column of matrix $\mathbf{Z}$.

2 System Model

We consider a DF three-way massive MIMO relay system as shown in Fig. 1. The system includes one relay station having M antennas and 3 users, each having a single-antenna. The relay station helps the users to exchange their data under time-division duplex operation. We assume that the users have perfect channel state information (CSI) and they operate in half-duplex mode. We further assume that the direct channels from user-to-user do not exit due to large

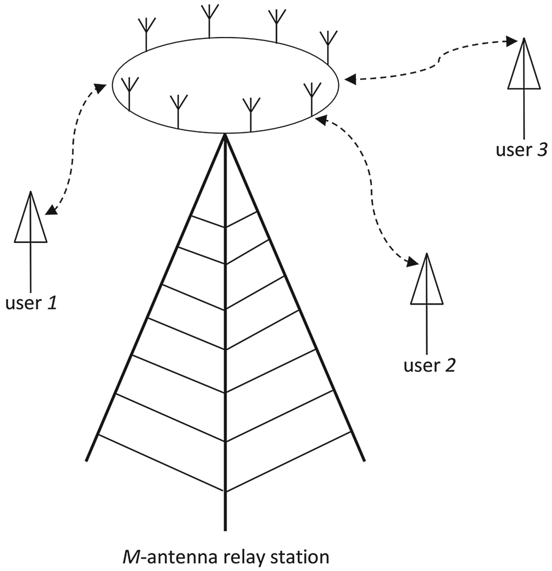

Fig. 1. Decode-and-forward three-way massive MIMO relay networks.

obstacle and/or heavy shadowing. The information exchange among three users is conducted via the relay station.

Regarding the channel model, we consider both large-scale fading (path loss and log-normal attenuation) and small-scale fading (Rayleigh fading). Let g_{mk} be the channel coefficient from the m-th antenna of the relay station and the k-th user, $m = 1, \ldots, M$, $k = 1, 2, 3$. Then g_{mk} can be represented by

$$g_{mk} = h_{mk}\sqrt{\beta_k}, \tag{1}$$

where $h_{mk} \sim \mathcal{CN}(0, 1)$ represents the small-scale fading and β_k represents the large-scale fading. We can see in (1) that the large-scale fading β_k does not depend on the antenna index m. This is reasonable since the distance between the users and the relay station is much greater than the distance between the antennas at the relay station.

Denote by $\mathbf{G} \in \mathbb{C}^{M\times 3}$ the channel matrix between the 3 users and M-antenna relay station. Then, from (1), we have

$$\mathbf{G} = \mathbf{H}\mathbf{D}^{1/2}, \tag{2}$$

where $\mathbf{H} \in \mathbb{C}^{M\times 3}$ is a $M \times 3$ small-scale matrix whose (m, k)-th element is $h_{m,k}$, and $\mathbf{D} \in \mathbb{C}$ is a 3×3 diagonal matrix of large-scale fading whose k-th diagonal element is β_k.

The transmission protocol is generally divided into two phases: multiple-access phase, and broadcast phase. In the first phase, all three users transmit their symbols to the relay station. Then, the relay station decodes all these symbols. In the second phase, the relay station sends the decoded symbols to all users. In what follows, we will introduce two different transmission protocols: conventional transmission scheme and proposed transmission scheme.

3 Multi-way Relaying with the Conventional Transmission Scheme

In this section, DF multi-way massive MIMO relaying with the conventional transmission protocol is presented. The corresponding spectral efficiency is also derived.

3.1 Multiple-Access Phase

In this phase, all 3 users transmit their bearing-data to the relay in the same time-frequency resource. The $M \times 1$ signal vector received at the relay is given by

$$\mathbf{y}_{\mathtt{R}} = \sqrt{\rho_{\mathrm{u}}}\mathbf{G}\mathbf{x} + \mathbf{n}_{\mathtt{R}}, \tag{3}$$

where ρ_{u} is the normalized transmit power at each user, $\mathbf{n}_{\mathtt{R}}$ is an AWGN vector whose elements are i.i.d. $\mathcal{CN}(0,1)$ random variables, and $\mathbf{x} \triangleq [x_1,\ x_2,\ x_3]^T$, with $\mathbb{E}\left\{|x_k|^2\right\} = 1$, is the vector of signals transmitted from 3 users to the relay.

To decode $\mathbf{x}$, the relay uses the maximum-ratio combining scheme. With maximum-ratio combining, the relay first multiply its received signal vector $\mathbf{y}_{\mathtt{R}}$ with $\mathbf{G}^H$ as

$$\begin{aligned}\mathbf{r} &= \mathbf{G}^H\mathbf{y}_{\mathtt{R}} \\ &= \sqrt{\rho_{\mathrm{u}}}\mathbf{G}^H\mathbf{G}\mathbf{x} + \mathbf{G}^H\mathbf{n}_{\mathtt{R}}.\end{aligned} \tag{4}$$

Then, it decodes each symbols x_1, x_2, and x_3 separately by considering each element of $\mathbf{r}$ as a point-to-point scalar channel. Denote by r_k the k-th component of $\mathbf{r}$. Then, from (4), we have

$$r_k = \sqrt{\rho_{\mathrm{u}}}\|\mathbf{g}_k\|^2 x_k + \sqrt{\rho_{\mathrm{u}}}\sum_{\substack{i=1\\ i\neq k}}^{K}\mathbf{g}_k^H\mathbf{g}_i x_i + \mathbf{g}_k^H\mathbf{n}_{\mathtt{R}}, \tag{5}$$

where $\mathbf{g}_k$ is the k-th column of $\mathbf{G}$. The k-th stream r_k will be used to decode x_k. Thus, the corresponding uplink spectral efficiency (measured in bit/s/Hz) is

$$\mathtt{R}^{\mathrm{ul}}_{\mathrm{cov},k} = \mathbb{E}\left\{\log_2\left(1 + \frac{\rho_{\mathrm{u}}\|\mathbf{g}_k\|^4}{\rho_{\mathrm{u}}\sum\limits_{\substack{i=1\\ i\neq k}}^{3}\left|\mathbf{g}_k^H\mathbf{g}_i\right|^2 + \|\mathbf{g}_k\|^2}\right)\right\}. \tag{6}$$

3.2 Broadcast Phase

In this phase, the symbols, which are decoded at the relay in the multiple-access phase, are broadcasted from the relay to all users in 2 time-slots.

(1) First time-slot: The relay wants to transmit symbol $x_{j(k,1)}$ to the k-th user, $k = 1, \ldots, 3$, where

$$j(k,1) \triangleq \begin{cases} (k+1) \text{ modulo } 3, & \text{if } (k+1) \neq 3 \\ 3, & \text{otherwise.} \end{cases} \tag{7}$$

Therefore, the transmitted signal vector from the relay in the first time-slot is

$$\mathbf{s}^{(1)} = \sqrt{\frac{\rho_{\mathrm{r}}}{M \sum_{i=1}^{3} \beta_i}} \sum_{i=1}^{3} \mathbf{g}_i x_{j(i,1)}, \tag{8}$$

where ρ_{r} is the normalized transmit power at the relay. Note that the constant $\sqrt{\frac{\rho_{\mathrm{r}}}{M \sum_{i=1}^{3} \beta_i}}$ in (8) is chosen to satisfy that the transmitted power at the relay is ρ_{r}, i.e., $\mathbb{E}\left\{\|\mathbf{s}^{(1)}\|^2\right\} = \rho_{\mathrm{r}}$.

With the transmitted signal vector given in (8), the received signal at the k-th user is given by

$$\begin{aligned} y_k^{(1)} &= \mathbf{g}_k^H \mathbf{s}^{(1)} + n_k^{(1)} \\ &= \sqrt{\frac{\rho_{\mathrm{r}}}{M \sum_{i=1}^{3} \beta_i}} \sum_{i=1}^{3} \mathbf{g}_k^H \mathbf{g}_i x_{j(i,1)} + n_k^{(1)}. \end{aligned} \tag{9}$$

Since the k-th user knows its transmitted symbol x_k (or $x_{j(k-1,1)}$) and has perfect CSI, it can subtract self-interference before detecting the desired symbol $x_{j(k,1)}$. From (9), the received signal after removing self-interference is

$$\begin{aligned} \tilde{y}_k^{(1)} &\triangleq y_k^{(1)} - \sqrt{\frac{\rho_{\mathrm{r}}}{M \sum_{i=1}^{3} \beta_i}} \mathbf{g}_k^H \mathbf{g}_{j(k+1,1)} x_{j(k-1,1)} \\ &= \sqrt{\frac{\rho_{\mathrm{r}}}{M \sum_{i=1}^{3} \beta_i}} \|\mathbf{g}_k\|^2 x_{j(k,1)} + \sqrt{\frac{\rho_{\mathrm{r}}}{M \sum_{i=1}^{3} \beta_i}} \sum_{\substack{i=1 \\ j(i,1) \neq j(k,1), j(k-1,1)}}^{3} \mathbf{g}_k^H \mathbf{g}_i x_{j(i,1)} + n_k^{(1)}. \end{aligned} \tag{10}$$

Thus, we obtain the corresponding downlink spectral efficiency of the system in the first time-slot as follows:

$$\mathtt{R}_{\mathrm{cov},k}^{\mathrm{dl},(1)} = \mathbb{E}\left\{ \log_2 \left(1 + \frac{\frac{\rho_{\mathrm{r}}}{M \sum_{i=1}^{3} \beta_i} \|\mathbf{g}_k\|^4}{\frac{\rho_{\mathrm{r}}}{M \sum_{i=1}^{3} \beta_i} \sum\limits_{\substack{i=1 \\ j(i,1) \neq j(k,1), j(k-1,1)}}^{3} \left|\mathbf{g}_k^H \mathbf{g}_i\right|^2 + 1} \right) \right\}. \tag{11}$$

(2) Second time-slot: The relay wants to transmit symbol $x_{j(k,2)}$ to the k-th user, where

$$j(k,2) \triangleq \begin{cases} (k+2) \text{ modulo } 3, & \text{if } \ (k+2) \neq 3 \\ 3, & \text{otherwise.} \end{cases} \tag{12}$$

Thus, the transmitted signal vector from the relay in the second time-slot is

$$\mathbf{s}^{(2)} = \sqrt{\frac{\rho_{\mathrm{r}}}{M\sum_{i=1}^{3}\beta_i}} \sum_{i=1}^{3} \mathbf{g}_i x_{j(i,2)}, \tag{13}$$

and the received signal at the k-th user is given by

$$\begin{aligned} y_k^{(2)} &= \mathbf{g}_k^H \mathbf{s}^{(2)} + n_k^{(2)} \\ &= \sqrt{\frac{\rho_{\mathrm{r}}}{M\sum_{i=1}^{3}\beta_i}} \sum_{i=1}^{3} \mathbf{g}_k^H \mathbf{g}_i x_{j(i,2)} + n_k^{(2)}. \end{aligned} \tag{14}$$

Since the k-th user knows perfect CSI and its transmitted symbol x_k (or $x_{j(k-2,2)}$), it can subtract self-interference prior to detecting the desired symbol $x_{j(k,2)}$. The received signal after removing self-interference is

$$\tilde{y}_k^{(2)} = \sqrt{\frac{\rho_{\mathrm{r}}}{M\sum_{i=1}^{3}\beta_i}} \|\mathbf{g}_k\|^2 x_{j(k,2)} + \sqrt{\frac{\rho_{\mathrm{r}}}{M\sum_{i=1}^{3}\beta_i}} \sum_{\substack{i=1 \\ j(i,2)\neq j(k,2), j(k-2,2)}}^{3} \mathbf{g}_k^H \mathbf{g}_i x_{j(i,2)} + n_k^{(2)}. \tag{15}$$

Therefore, we obtain the corresponding downlink spectral efficiency of the system in the second time-slot as

$$\mathtt{R}_{\mathrm{cov},k}^{\mathrm{dl},(2)} = \mathbb{E}\left\{ \log_2 \left(1 + \frac{\frac{\rho_{\mathrm{r}}}{M\sum_{i=1}^{3}\beta_i}\|\mathbf{g}_k\|^4}{\frac{\rho_{\mathrm{r}}}{M\sum_{i=1}^{3}\beta_i} \sum\limits_{\substack{i=1 \\ j(i,2)\neq j(k,2), j(k-2,2)}}^{3} \left|\mathbf{g}_k^H \mathbf{g}_i\right|^2 + 1} \right) \right\}. \tag{16}$$

From (6), (11), and (16), the sum spectral efficiency of the conventional scheme is given

$$\mathtt{SE}_{\mathrm{cov}} = \frac{1}{3}\sum_{k=1}^{3}\sum_{t=1}^{2} \min\left(\mathtt{R}_{\mathrm{cov},k}^{\mathrm{ul}}, \mathtt{R}_{\mathrm{cov},k}^{\mathrm{dl},(t)}\right). \tag{17}$$

The pre-log factor $1/3$ in (17) comes from the fact that we spend 3 time-slots to exchange all symbols to 3 users.

4 Proposed Scheme: Multi-way Relaying with Successive Cancelation Decoding

In this section, a novel technical transmission protocol is proposed by using successive the cancelation decoding method. With our proposed scheme, we need only one time-for the broadcast phase.

4.1 Multiple-Access Phase

Follow the same transmission protocol as in the multiple-access phase of the conventional scheme. See Sect. 3.1. Therefore, the uplink spectral efficiency is

$$\mathtt{R}^{\mathrm{ul}}_{\mathrm{new},k} = \mathbb{E}\left\{\log_2\left(1+\frac{\rho_{\mathrm{u}}\|\mathbf{g}_k\|^4}{\rho_{\mathrm{u}}\sum\limits_{\substack{i=1\\ i\neq k}}^{3}\left|\mathbf{g}_k^H\mathbf{g}_i\right|^2+\|\mathbf{g}_k\|^2}\right)\right\}. \tag{18}$$

4.2 Broadcast Phase

In section, we propose a new broadcast scheme which needs only 1 time-slot to transmit all symbols to all users. The detail of this technique is given as follows.

The transmitted signal vector from the relay is given by

$$\mathbf{s} = \sqrt{\frac{\rho_{\mathrm{r}}}{M\sum_{i=1}^{3}\beta_i}}\sum_{i=1}^{3}\mathbf{g}_i x_{j(i,1)}. \tag{19}$$

where $j(i,1)$ is defined in (7).

(1) The first user: From (19), the received signal at the first user is

$$\begin{aligned} y_1 &= \mathbf{g}_1^H\mathbf{s}+n_1 \\ &= \sqrt{\frac{\rho_{\mathrm{r}}}{M\sum_{i=1}^{3}\beta_i}}\sum_{i=1}^{3}\mathbf{g}_1^H\mathbf{g}_i x_{j(i,1)}+n_1. \end{aligned} \tag{20}$$

Again, by using self-interference cancelation scheme, the received signal at user 1 after removing self-interference is

$$\tilde{y}_1 = \sqrt{\frac{\rho_{\mathrm{r}}}{M\sum_{i=1}^{3}\beta_i}}\|\mathbf{g}_1\|^2 x_2 + \sqrt{\frac{\rho_{\mathrm{r}}}{M\sum_{i=1}^{3}\beta_i}}\mathbf{g}_1^H\mathbf{g}_2 x_3 + n_1, \tag{21}$$

and the downlink spectral efficiency for the first user to decode x_2 is

$$\mathtt{R}^{\mathrm{dl},(1)}_{\mathrm{new},1} = \mathbb{E}\left\{\log_2\left(1+\frac{\frac{\rho_{\mathrm{r}}}{M\sum_{i=1}^{3}\beta_i}\|\mathbf{g}_1\|^4}{\frac{\rho_{\mathrm{r}}}{M\sum_{i=1}^{3}\beta_i}\left|\mathbf{g}_1^H\mathbf{g}_2\right|^2+1}\right)\right\}. \tag{22}$$

After decoding x_2, user 1 knows signal transmitted from user 2, and hence, it can remove symbol x_2. Thus, the received signal at the first user after canceling x_2 is

$$\tilde{\tilde{y}}_1 = \sqrt{\frac{\rho_\mathrm{r}}{M\sum_{i=1}^{3}\beta_i}}\mathbf{g}_1^H\mathbf{g}_2 x_3 + n_1. \tag{23}$$

Therefore, the downlink spectral efficiency of the first user to decode x_3 is given by

$$\mathtt{R}_{\mathrm{new},1}^{\mathrm{dl},(2)} = \mathbb{E}\left\{\log_2\left(1 + \frac{\rho_\mathrm{r}}{M\sum_{i=1}^{3}\beta_i}\left|\mathbf{g}_1^H\mathbf{g}_2\right|^2\right)\right\}. \tag{24}$$

(2) The second user: Similarly, the received signal at the second user can be written as

$$\begin{aligned} y_2 &= \mathbf{g}_2^H\mathbf{s} + n_2 \\ &= \sqrt{\frac{\rho_\mathrm{r}}{M\sum_{i=1}^{3}\beta_i}}\sum_{i=1}^{3}\mathbf{g}_2^H\mathbf{g}_i x_{j(i,1)} + n_2. \end{aligned} \tag{25}$$

Since, user 2 knows its transmitted symbol x_2, it can subtract self-interference before detecting symbol x_3 transmitted from user 3. Therefore, the received signal at user 2 can be presented as

$$\tilde{y}_2 = \sqrt{\frac{\rho_\mathrm{r}}{M\sum_{i=1}^{3}\beta_i}}\|\mathbf{g}_2\|^2 x_3 + \sqrt{\frac{\rho_\mathrm{r}}{M\sum_{i=1}^{3}\beta_i}}\mathbf{g}_2^H\mathbf{g}_3 x_1 + n_2, \tag{26}$$

and then the downlink spectral efficiency for user 2 to decode x_3 is

$$\mathtt{R}_{\mathrm{new},2}^{\mathrm{dl},(1)} = \mathbb{E}\left\{\log_2\left(1 + \frac{\frac{\rho_\mathrm{r}}{M\sum_{i=1}^{3}\beta_i}\|\mathbf{g}_2\|^4}{\frac{\rho_\mathrm{r}}{M\sum_{i=1}^{3}\beta_i}\left|\mathbf{g}_2^H\mathbf{g}_3\right|^2 + 1}\right)\right\}. \tag{27}$$

After decoding x_3, user 2 knows the signal transmitted from user 3, and hence, it can eliminate the symbol x_3. Thus, the received signal at user 2 is

$$\tilde{\tilde{y}}_2 = \sqrt{\frac{\rho_\mathrm{r}}{M\sum_{i=1}^{3}\beta_i}}\mathbf{g}_2^H\mathbf{g}_3 x_1 + n_2, \tag{28}$$

and the corresponding downlink spectral efficiency is given by

$$\mathtt{R}_{\mathrm{new},2}^{\mathrm{dl},(2)} = \mathbb{E}\left\{\log_2\left(1 + \frac{\rho_\mathrm{r}}{M\sum_{i=1}^{3}\beta_i}\left|\mathbf{g}_2^H\mathbf{g}_3\right|^2\right)\right\}. \tag{29}$$

(3) The third user: With the same methodology, the received signal at the third user can be written as

$$\begin{aligned} y_3 &= \mathbf{g}_3^H \mathbf{s} + n_3 \\ &= \sqrt{\frac{\rho_{\mathrm{r}}}{M \sum_{i=1}^{3} \beta_i}} \sum_{i=1}^{3} \mathbf{g}_3^H \mathbf{g}_i x_{j(i,1)} + n_3. \end{aligned} \tag{30}$$

Since user three knows its transmitted signal, it can subtract self-interference before detecting x_1. The received signal at user 3 after self-interference cancelation is

$$\tilde{y}_3 = \sqrt{\frac{\rho_{\mathrm{r}}}{M \sum_{i=1}^{3} \beta_i}} \|\mathbf{g}_3\|^2 x_1 + \sqrt{\frac{\rho_{\mathrm{r}}}{M \sum_{i=1}^{3} \beta_i}} \mathbf{g}_3^H \mathbf{g}_1 x_2 + n_3, \tag{31}$$

then the downlink spectral efficiency for user 3 to decode x_1 is

$$\mathtt{R}_{\mathrm{new},3}^{\mathrm{dl},(1)} = \mathbb{E}\left\{ \log_2 \left(1 + \frac{\frac{\rho_{\mathrm{r}}}{M \sum_{i=1}^{3} \beta_i} \|\mathbf{g}_3\|^4}{\frac{\rho_{\mathrm{r}}}{M \sum_{i=1}^{3} \beta_i} \left|\mathbf{g}_3^H \mathbf{g}_1\right|^2 + 1} \right) \right\}. \tag{32}$$

After decoding x_1, user 3 can subtract x_1 to obtain

$$\tilde{\tilde{y}}_3 = \sqrt{\frac{\rho_{\mathrm{r}}}{M \sum_{i=1}^{3} \beta_i}} \mathbf{g}_3^H \mathbf{g}_1 x_2 + n_3. \tag{33}$$

Therefore, the downlink spectral efficiency for user 3 to decode x_2 is given by

$$\mathtt{R}_{\mathrm{new},3}^{\mathrm{dl},(2)} = \mathbb{E}\left\{ \log_2 \left(1 + \frac{\rho_{\mathrm{r}}}{M \sum_{i=1}^{3} \beta_i} \left|\mathbf{g}_3^H \mathbf{g}_1\right|^2 \right) \right\}. \tag{34}$$

From (18), (22), (24), (27), (29), (32), and (34), we obtain the sum spectral efficiency for our proposed scheme as

$$\mathtt{SE}_{\mathrm{new}} = \frac{1}{2} \sum_{k=1}^{3} \sum_{t=1}^{2} \min \left(\mathtt{R}_{\mathrm{new},k}^{\mathrm{ul}}, \mathtt{R}_{\mathrm{new},k}^{\mathrm{dl},(t)} \right). \tag{35}$$

The pre-log factor of (35) is 1/2. This comes from the fact that we spend 2 time-slots to exchange all symbols to 3 users. Compared with the conventional scheme (17), our proposed scheme improves the pre-log factor 1.5 times, and hence, may improve the sum spectral efficiency significantly.

5 Numerical Results

In this section, the numerical results are provided to verify the benefit of our proposed scheme. We focus on the sum spectral efficiency defined in (17) and (35).

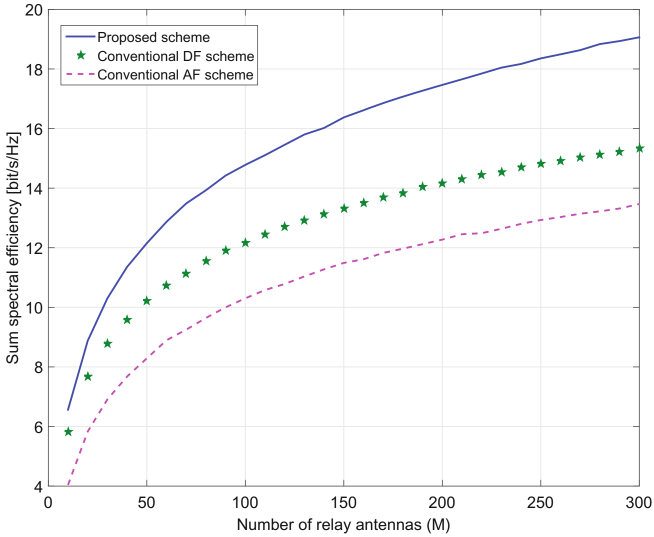

Fig. 2. The comparison of spectral efficiency of different schemes versus the number of relay antennas. We choose $\rho_{\mathrm{u}} = 0$ dB, $\rho_{\mathrm{r}} = 10$ dB, $\beta_k = 1$.

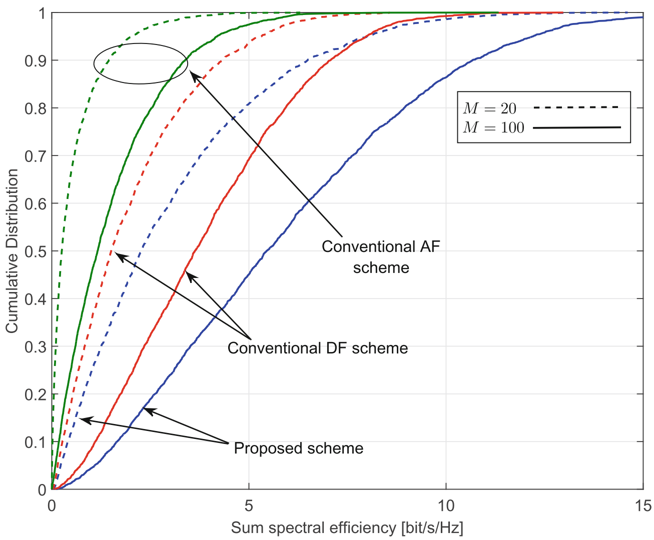

Fig. 3. The comparison of cumulative distribution for different schemes versus sum spectral efficiency. We choose $\rho_{\mathrm{u}} = 0$ dB, $\rho_{\mathrm{r}} = 10$ dB, $M = 100$.

First we consider a simple scenario where the large-scale fading is neglected, i.e. $\beta_1 = \beta_2 = \beta_3 = 1$. We compare the sum spectral efficiency of our proposed scheme with those of the conventional scheme given in Sect. 3.2 and the conventional scheme with AF mode given in [11]. Figure 2 shows the sum spectral efficiency of our proposed scheme, conventional DF scheme (see Sect. 3.2), and conventional AF scheme [11] versus the number of relay antennas, with $\rho_{\mathrm{u}} = 0$ dB and $\rho_{\mathrm{r}} = 10$ dB. Clearly, our proposed scheme is much better than other schemes. The reason is that, our proposed scheme needs only 2 time-slots to exchange the bearing-information among 3 users, while the conventional scheme needs 3 time-slots. The conventional DF scheme is better than the conventional AF scheme since with AF, the noise and interference of the multiple-access phase is amplified. Furthermore, we can see that the sum spectral efficiency increases significantly when the number of relay antennas increases.

We next investigate a more realistic scenario in which the large-scale fading β_k is modeled by path loss and lognormal shadowing. In order to generate the large-scale fading, we follow the same model presented in [10]. Figure 3 shows the comparison of three transmission schemes as in Fig. 2 via the cumulative distribution of the sum spectral efficiency. We can see that the sum spectral efficiency of our proposed scheme outperforms other schemes. The performance gap increases when the number of relay antennas increases. In particular, when $M = 100$, the 95%-likely sum spectral efficiency of our proposed scheme is around 1.5 times and 5 times higher than those of the conventional DF scheme and the conventional AF scheme, respectively.

6 Conclusion

In this paper, we investigated a DF three-way massive MIMO relay system under time-division duplex operation. A novel transmission protocol was proposed to reduce the number of time-slots for exchanging data among the users. Our proposed scheme relied on success cancelation decoding, and hence, needs only 2 time-slots, while the conventional scheme requires 3 time-slots. The sum spectral efficiency of our proposed scheme was derived. We showed that our proposed scheme offers much higher sum spectral efficiency than the conventional AF and DF schemes do.

Acknowledgment. This work was supported by project no. 3811/QD-UBND, Binh Duong government, Vietnam. The work of H. Q. Ngo was supported by the Swedish Research Council (VR) and ELLIIT.

References

1. Gündüz, D., Yener, A., Goldsmith, A., Poor, H.V.: The multiway relay channel. IEEE Trans. Inf. Theory **59**(1), 51–63 (2013)
2. Tian, Y., Yener, A.: Degrees of freedom for the MIMO multi-way relay channel. IEEE Trans. Inf. Theory **60**(5), 2495–2511 (2014)

3. Amah, A., Klein, A.: Non-regenerative multi-way relaying with linear beamforming. In: Proceedings of IEEE PIMRC, pp. 1843–1847, September 2009
4. Marzetta, T.L., Larsson, E.G., Yang, H., Ngo, H.Q.: Fundamentals of Massive MIMO. Cambridge University Press, Cambridge (2016)
5. Marzetta, T.L.: Massive MIMO: an introduction. Bell Labs Tech. J. **20**, 11–22 (2015)
6. Ngo, H.Q., Larsson, E.G.: Spectral efficiency of the multipair two-way relay channel with massive arrays. In: Asilomar Conference on Signals, Systems and Computers, pp. 275–279, November 2013
7. Ngo, H.Q., Larsson, E.G., Marzetta, E.G.: Energy and spectral efficiency of very large multiuser MIMO systems. IEEE Trans. Commun. **61**(4), 1436–1449 (2013)
8. Larsson, E.G., Edfors, O., Tufvesson, F., Marzetta, T.L.: Massive MIMO for next generation wireless systems. IEEE Commun. Mag. **52**(2), 186–195 (2014)
9. Amarasuriya, G., Poor, H.V.: Multi-way amplify-and-forward relay networks with massive MIMO. In: Proceedings of IEEE PIMRC, pp. 595–600, September 2014
10. Ho, C.D., Ngo, H.Q., Matthaiou, M., Duong, T.Q.: On the performance of zero-forcing processing in multi-way massive MIMO relay networks. IEEE Commun. Lett. (2017, to appear)
11. Ho, C., Ngo, H.Q., Matthaiou, M., Duong, T.Q.: Multi-way massive MIMO relay networks with maximum-ratio processing. In: Proceedings of IEEE SigTelCom, pp. 124–128, January 2017

Performance Analysis of Time-Switching Energy Harvesting Device-to-Device Link Underlying Small-Cell-Networks

Mohammed Nasser Altawaim(✉), Nam-Phong Nguyen, and Wiliam G. Scanlon

Queen's University Belfast, Belfast, UK
{maltawaim01,pnguyen04,w.scanlon}@qub.ac.uk

Abstract. In this paper, we propose an underlying Small-Cell-Networks (SCNs) Device-to-Device (D2D) pair with the use of time-switching Energy Harvesting (EH) techniques. More specifically, we have a D2D transmitter and receiver underlying SCNs operating in closeness to a SCNs primary user (PU). We propose two scenarios, in the first scenario we harvest energy from all of the available SCN base stations (BSs). Whereas in the second scenario we select the best BS link to harvest energy from. Moreover, the transmission is kept under a certain threshold between the D2D pair, so that it does not have any deleterious effect on the PU transmission link.

Keywords: Device-to-Device communication · Small cell networks
Energy harvesting

1 Introduction

Currently, there are more than five billion devices connected to the cellular network and it is predicted that 50 billion devices will be connected by 2020 [3]. This shows the importance of broadband cellular networks in modern life. The tremendous growth in this market has been driven by the introduction of smart phones, tablets and netbook devices and its swiftly developing and rising innovative applications, such as online gaming, mobile social networks applications and virtual and augmented reality in multimedia applications. Correspondingly, there continues to be a significant growth in the demand for data capacity. To address this, various new technologies have been proposed to improve the spectral efficiency in the traditional communication methods of cellular networks and increase its throughput. These include technologies such as, Millimetre waves (MM wave), Massive multiple input and multiple output (MIMO), Small Cell Networks (SCNs) and Device-to-Device communication (D2D) [1]. Furthermore, out of the all aforementioned technologies, D2D communication and SCN technologies arise to be promising concepts. Particularly underlying D2D communication, which is a technology that allows devices that are in close proximity to each other to use cellular resources to communicate with each other without routing the information through the base station (BS).

© ICST Institute for Computer Sciences, Social Informatics and Telecommunications Engineering 2018
Y. Chen and T. Q. Duong (Eds.): INISCOM 2017, LNICST 221, pp. 91–99, 2018.
https://doi.org/10.1007/978-3-319-74176-5_9

D2D communication was first introduced in [2] as an approach to allow multi-hop relays in cellular networks. Subsequently, the authors in [3,4] considered the possibility of using D2D communication networks as a way to enhance the spectral efficiency and diminish communication delay. The reported numerical simulation results show that the proposed D2D scheme improves the cell throughput by 40%. Moreover, different possible D2D use-cases were introduced such as machine-to-machine (M2M) communication [6], peer-to-peer communication [5] and video braodcasting [7].

Recently, Energy Harvesting (EH) in cellular networks has arose as promising concept in providing a different source of energy to power cellular devices [9]. EH allows wireless devices to scavenge an alternative source of energy that is provided by nature or man-made phenomena [12]. The authors in [13], investigated the use of EH based D2D communication and proposed a power transfer and information signal model for secure EH information transmission. In [14], a beamforming design for wireless information and power transfer was suggested to maximize the minimum user rate and minimize the maximum BS transmit power under both the BS transmit power and the user data rate constraints respectively, considering the user harvested energy constraint as well. Furthermore, maximizing the achievable user date rate was studied as well in [15] by suggesting a mutually optimal power and time fraction allocation and optimal power allocation with a fixed time fraction for EH.

Consisting of a number of low cost and power radio access nodes, SCNs introduced to deal with the coverage issues in conventional cellular networks [20]. Later on, their use was extended to replace the traditional cellular network BSs in some cases as a way of increasing the capacity and quality of service (QoS) [21]. This was due to their ability to achieve higher signal-to-interference-plus-noise ratio (SINR) and shorter transmit-receive distance. Moreover, the authors in [22] suggest that SCNs will be a key element in the next generation cellular architecture in regards to minimizing energy consumption and providing a higher end-user data rates.

The rest of this paper is organized as follows. System and channel models are discussed in Sect. 2. The outage probabilities of the proposed system in the both schemes are described in Sect. 3. In Sect. 4, numerical simulations results are presented to validate the correctness of our analyses. Finally, the paper is concluded in Sect. 5.

2 System Model

In this paper, we consider a D2D pair communication underlying SCNs. The D2D pair consists of D2D transmitter (D_{tx}) and D2D receiver (D_{rx}) operating in closeness to a SCNs primary user (PU) as shown in Fig. 1. We propose two scenarios, the first scenario, when D_{tx} harvests energy from all of the SCNs available BSs in order to communicate with D_{rx}. Whereas in the second scenario the best BS link is selected for D_{tx} to harvest energy from. The received signal (y) and harvested energy (e) at D_{tx} can be calculated as:

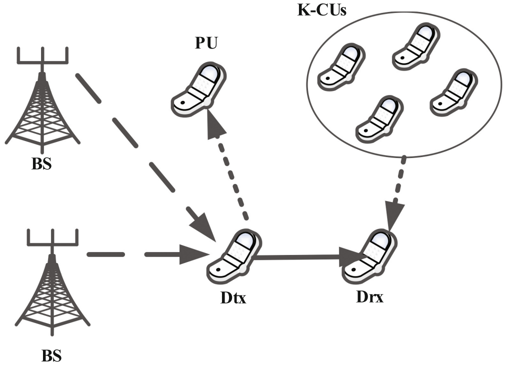

Fig. 1. D2D pair underlying a small cellular network.

$$y = P_o h_1 x + \zeta_o. \tag{1}$$

$$E = P_o |h_1|^2 \eta \alpha T, \tag{2}$$

where

$$|h_1|^2 = \begin{cases} \sum_{i=0}^{M} |h_m|^2 & \text{, EH scenario 1} \\ \max\limits_{m} |h_m|^2 & \text{, EH scenario 2} \end{cases}. \tag{3}$$

Assuming a Rayleigh fading channel, h_1 is the channel coefficient between the D_{tx} and BS, P_o denotes the transmitting power of the BS, x is the transmitted signal from the m-th BS, e$|x|^2$=1, and ζ_o is the additive white Gaussian noise (AWGN) with zero mean and variance N_o. η and α are the EH efficiency coefficient and fraction respectively, and T is the period time for the transmission symbol. K represent the number of SCNs users causing interference to D_{rx} and h_k is the channel coefficient between the D_{tx} and K users. M is the number of SCNs BSs and the channel coefficients between the D_{tx} and D_{rx} is h_2, where it is defined as h_3 between D_{tx} and PU. The transmitted power of D_{tx} is defined as:

$$PD_{tx}^{'} = \frac{E}{(1-\alpha)T} = \frac{P_o |h_1|^2 \eta \alpha}{(1-\alpha)}. \tag{4}$$

Nonetheless, the D2D pair link transmission power is kept under a certain threshold so it could not have any effect on the transmission link of PU. Therefore, D_{tx} will be constrained by a peak interference constraint (I_p) at D_{rx}. Therefore, the transmitted power of D_{tx} is redefined as:

$$PD_{tx} = \min\left(\frac{P_o |h_1|^2 \eta \alpha}{(1-\alpha)}, \frac{I_p}{|h_3|^2}\right). \tag{5}$$

Now, the SINR at D_{rx} can be calculated as:

$$\begin{aligned}\Psi &= \frac{PD_{tx}|h_2|^2}{\sum_{k=0}^{K} P_I|h_k|^2 + N_0} = \frac{\min\left(\frac{P_o|h_1|^2\eta\alpha}{(1-\alpha)}, \frac{I_p}{|h_3|^2}\right)|h_2|^2}{\sum_{k=0}^{K} P_I|h_k|^2 + N_0} \\ &= \frac{\min\left(P_o|h_1|^2\delta, \frac{I_p}{|h_3|^2}\right)|h_2|^2}{\sum_{k=0}^{K} P_I|h_k|^2 + N_0} = \frac{\min\left(\gamma_o|h_1|^2\delta, \frac{\gamma_p}{|h_3|^2}\right)|h_2|^2}{\gamma_i\sum_{k=0}^{K} |h_k|^2 + 1}. \end{aligned} \tag{6}$$

The cumulative distribution function (CDF) of h_1 is:

$$F_{h_1}(x) = [1 - \exp(-\lambda_1 x)]^M. \tag{7}$$

The probability density function (PDF) of h_1 is:

$$f_{h_1}(x) = \sum_{m=0}^{M} C_M^m(-1)^m \exp(-m\lambda_1 x). \tag{8}$$

The CDF of X is:

$$F_X(x) = \frac{1}{\Gamma(K)}\Upsilon(K, x\lambda_4) = 1 - \exp(-\lambda_4 x)\sum_{k=0}^{K-1}\frac{x^k\lambda_4^k}{k!}. \tag{9}$$

The achievable rate of the D2D link is:

$$C = (1-\alpha)\log_2\left(1 + \frac{\min\left(\gamma_o|h_1|^2\delta, \frac{\gamma_p}{|h_3|^2}\right)|h_2|^2}{\gamma_i\sum_{k=0}^{K}|h_k|^2 + 1}\right). \tag{10}$$

3 Outage Probability

The outage probability of the D2D communication link is the probability that the achievable rate of the D2D communication link falls below a certain threshold (R_{th}).

$$\begin{aligned} P_{out} &= P_r C < R_{th} = P_r\Psi < 2^{\frac{R_{th}}{(1-\alpha)}} \\ &= P_r\left(|h_2|^2 < \frac{(\gamma_i x + 1)\beta}{\min(\gamma_o|h_1|^2\delta, \frac{\gamma_p}{|h_3|^2})}\right) \\ &= 1 - \int_0^\infty \exp\left(\underbrace{\frac{\lambda_2(\gamma_i x + 1)\beta}{\min(\gamma_o|h_1|^2\delta, \frac{\gamma_p}{|h_3|^2})}}_{\mathcal{U}}\right) f_X(x)dx \\ &= 1 - \lambda_4^K \exp\left(\frac{-\lambda_2\beta}{\mathcal{U}}\right)\left(\frac{\mathcal{U}}{\lambda_4\mathcal{U} + \lambda_2\beta\gamma_I}\right)^K, \end{aligned} \tag{11}$$

where

$$\mathcal{U} = \begin{cases} \frac{\gamma_P}{|h_3|^2}, & \text{if } |h_1|^2 > \frac{\gamma_p}{\gamma_p \delta |h_3|^2} \\ \gamma_P \delta |h_3|^2, & \text{if } |h_1|^2 < \frac{\gamma_p}{\gamma_p \delta |h_3|^2} \end{cases} . \tag{12}$$

Now, (11) can be rewritten as:

$$\begin{aligned} P_{out} = 1 - &\left(\frac{\gamma_p}{\lambda_4 \gamma_p + \lambda_2 \beta \gamma_i h_3} \right)^K \\ &\times \int_{\frac{\gamma_p}{\gamma_o \delta h_1}}^{\infty} \lambda_4^K \exp\left(\frac{-\lambda_2 \beta h_3}{\gamma_p} \right) f_{h_3}(h_3) dh_3 \\ &- \left(\frac{\gamma_o \delta h_1}{\lambda_4 \gamma_o \delta h_1 + \lambda_2 \beta \gamma_i} \right)^K \\ &\times \int_0^{\frac{\gamma_p}{\gamma_o \delta h_1}} \lambda_4^K \exp\left(\frac{-\lambda_2 \beta}{\gamma_o \delta h_1} \right) f_{h_3}(h_3) dh_3, \end{aligned} \tag{13}$$

$$\begin{aligned} &= 1 - \underbrace{\int_{\frac{\gamma_p}{\gamma_o \delta h_1}}^{\infty} \lambda_4^K \exp\left(\frac{-\lambda_2 \beta h_3}{\gamma_P} \right) \mathcal{A} \lambda_3 \exp(-\lambda_3 h_3) dh_3}_{\mathcal{J}_1} \\ &- \lambda_4^K \exp\left(\frac{-\lambda_2 \beta}{\gamma_o \delta h_1} \right) \left(\frac{\gamma_o \delta h_1}{\lambda_4 \gamma_o \delta h_1 + \lambda_2 \beta \gamma_i} \right)^K \\ &\left(1 - \exp\left(-\lambda_3 \frac{\gamma_p}{\gamma_o \delta h_1} \right) \right), \end{aligned} \tag{14}$$

where $\mathcal{A} = \left(\frac{\gamma_p}{\lambda_4 \gamma_p + \lambda_2 \beta \gamma_I h_3} \right)^K$, and $\mathcal{J}_1$ are calculated as:

$$\begin{aligned} \mathcal{J}_1 = \mathcal{N}_3 \Bigg[&\left(\exp \frac{-\gamma_p}{\gamma_o \delta h_1} \mathcal{N}_1 \right) \sum_{k=1}^{K-1} \frac{(k-1)!(\mathcal{N}_1)^{K-k-1}}{(K-1)!(\frac{\gamma_p}{\gamma_o \delta h_1} + \mathcal{N}_2)^k} \\ &- \frac{-\mathcal{N}_1{}^{K-1}}{(k-1)!} \exp(\mathcal{N}_2 \cdot \mathcal{N}_1) E_i \left(-\left(\frac{\gamma_p}{\gamma_o \delta h_1} + \mathcal{N}_2 \right) \mathcal{N}_1 \right) \Bigg], \end{aligned} \tag{15}$$

where $\mathcal{N}_1 = (\frac{\lambda_2 \beta}{\gamma_p} + \lambda_3), \mathcal{N}_2 = (\frac{\lambda_4 \gamma_p}{\gamma_i \lambda_2 \beta}), \mathcal{N}_3 = ((\gamma_i \lambda_2 \beta)^K)$.

Now with the use of (13) and $\mathcal{N}_1, \mathcal{N}_2, \mathcal{N}_3$:

$$\begin{aligned} P_{out} = 1 - \mathcal{N}_3 &\sum_{k=1}^{K-1} \frac{(k-1)!(\mathcal{N}_1)^{K-k-1}}{(K-1)!} \\ &\underbrace{\int_0^{\infty} \frac{(\gamma_o \delta h_1)^k}{(\gamma_p + \gamma_o \delta h_1 \mathcal{N}_2)^k} f_{h_1}(h_1) dh_1}_{\mathcal{J}_2} \\ &+ \frac{\mathcal{N}_3 (-\mathcal{J}_1)^{K-1}}{(K-1)!} \exp(\mathcal{N}_1 \mathcal{N}_2) \end{aligned}$$

$$\int_0^\infty \underbrace{E_i(-\mathcal{N}_1[\frac{\gamma_p}{\gamma_o\delta h_1}+\mathcal{N}_2])f_{h_1}(h_1)dh_1}_{\mathcal{J}_3}$$
$$-\lambda_4^K(\lambda_o\delta)^K$$
$$\int_0^\infty \underbrace{\exp(\frac{-\lambda_2\beta}{\lambda_o\delta h_1})\frac{h_1^K}{(\lambda_4\gamma_o\delta h_1+\lambda_2\beta\gamma_i)^K}f_{h_1}(h_1)dh_1}_{\mathcal{J}_4}$$
$$+\lambda_4^K\int_0^\infty \underbrace{\exp(-\frac{1}{h_1}(\mathcal{N}_4))\mathcal{B}f_{h_1}(h_1)dh_1,}_{\mathcal{J}_5} \tag{16}$$

where $\mathcal{N}_4=\left(\frac{\lambda_1\beta}{\gamma_o\delta}+\frac{\lambda_3\gamma_p}{\gamma_o\delta}\right), \mathcal{B}=\left(\frac{(\gamma_o\delta h_1)^K}{(\lambda_4\gamma_o\delta h_1+\lambda_2\beta\gamma_i)^K}\right)$.

Furthermore, $\mathcal{J}_2, \mathcal{J}_3, \mathcal{J}_4$ and $\mathcal{J}_5$ are calculated as:

$$\mathcal{J}_2=\sum_{m=1}^{M}C_M^m(-1)^{m+1}m\lambda_1\times\int_0^\infty\frac{(h_1)^k}{\mathcal{N}_2^K(\frac{\gamma_p}{\gamma_o\delta\mathcal{N}_2}+h_1)^k}\exp(-m\lambda_1h_1)dh_1.$$
$$\mathcal{J}_3=\int_0^\infty E_i\left(-\mathcal{N}_1[\frac{\gamma_p}{\gamma_o\delta h_1}\mathcal{N}_2]\right)\times\sum_{m=1}^{M}C_M^m(-1)^{m+1}m\lambda_1\exp(-m\lambda_1h_1)dh_1.$$
$$\mathcal{J}_4=\sum_{m=1}^{M}C_M^m(-1)^{m+1}\frac{m\lambda_1}{\lambda_4\gamma_o\delta}\int_0^\infty\exp\left(\frac{-\lambda_2\beta}{\gamma_o\delta h_1}-m\lambda_4h_1\right)$$
$$\times\left(\frac{(h_1)^k}{\left(h_1+\underbrace{\frac{\lambda_2\beta\gamma_i}{\lambda_4\gamma_i\delta}}_{\mathcal{N}_5}\right)^K}\right)dh_1. \tag{17}$$

$$\mathcal{J}_5=\sum_{m=1}^{M}C_M^m(-1)^{m+1}m\lambda_1$$
$$\times\int_0^\infty\exp(\frac{-\mathcal{N}_4}{h_1}-m\lambda_1h_1)\frac{(h_1)^k}{\lambda_4^K(h_1+\mathcal{N}_5)^K}dh_1. \tag{18}$$

4 Numerical Results

Figure 2 shows the theoretical and simulation results of the outage probability of the D2D link when harvesting energy from all of the SCNs BSs, under different peak interference constraints I_p values. We set α= 0.7, η= 0.8 and the number of the SCNs users that cause interference to the D_{rx} to K= 4 with the power of P_I= 5 dB. Furthermore, we set number of SCNs BSs M to 10, $\lambda_1=\lambda_3=\lambda_4=1$, $\lambda_2=0.1$ and $R_{th}=0.4$. As we can see, the simulation results

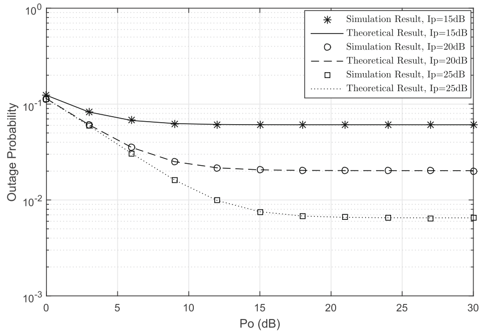

Fig. 2. Outage probability of the D2D link when harvesting energy from All BSs. $\eta = 0.8$, $\alpha = 0.7$, $M = 10$, $K = 4$, $P_I = 5\,\text{dB}$, $\lambda_1 = \lambda_3 = \lambda_4 = 1$, $\lambda_2 = 0.1$, $R_{th} = 0.4$.

are almost matched perfectly with the theoretical results. Moreover, the outage probability of the D2D link decreases and then saturates when the transmit power of the BS increases. Further, when the transmit power of the BSs is small, the D2D transmitter will also have a small transmit power, smaller than the peak interference constraint which leads the outage probability of the D2D link to improve when the BSs power is increased.

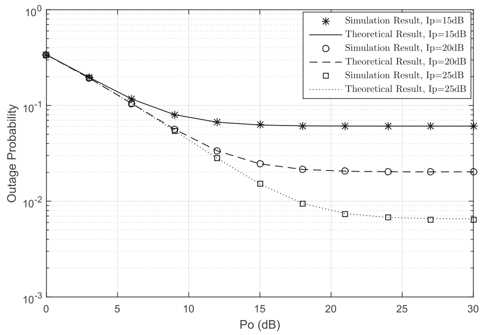

Fig. 3. Outage probability of the D2D link when harvesting energy from the best BS link. $\eta = 0.8$, $\alpha = 0.7$, $M = 10$, $K = 4$, $P_I = 5\,\text{dB}$, $\lambda_1 = \lambda_3 = \lambda_4 = 1$, $\lambda_2 = 0.1$, $R_{th} = 0.4$.

Figure 3 shows the outage probability of the D2D link when harvesting energy from the best BS link available at the time of the transmission under different I_p values. The parameters are set exactly as used in Fig. 2. We can see that the outage probability increased slightly in comparison to Fig. 2, and that is due to the fact that we are only harvesting energy from one BS link, where in Fig. 2 we harvest energy from multiple BS links. Figure 4 shows the theoretical and simulation results of the outage probability of the D2D link with the variation of α from 0 to 1 under different peak interference constraints I_p. As we can see, the outage probability of the D2D link decreases when higher peak interference is allowed.

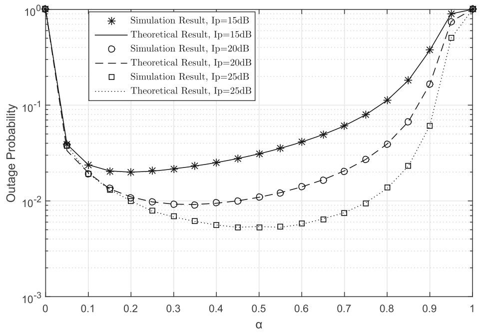

Fig. 4. Outage probability of the D2D link when α varies from 0 to 1. $\eta = 0.8$, $M = 10$, $K = 4$, $P_o = 15\,\mathrm{dB}$, $P_I = 5\,\mathrm{dB}$, $\lambda_1 = \lambda_3 = \lambda_4 = 1$, $\lambda_2 = 0.1$, $R_{th} = 0.4$.

5 Conclusion

In this paper, we investigated the performance of an underlying SCNs D2D link with the use of Time-switching EH techniques. We proposed two scenarios, in the first scenario we investigated the performance when the D2D transmitter harvests energy from all of the available BSs in the SCNs. In the second scenario, we investigated the performance of the system when the D2D transmitter harvests energy from the best available SCNs BS. From the obtained results, we can see clearly that the first scenario outperform the second scenario. We discovered that the performance of the system will decreases when increasing the number of interference links. Furthermore, the primary user peak interference constraint has a huge impact on the outage probability of the D2D link. Finally, for the best performance of the D2D link, the energy harvesting time fraction should be carefully set.

References

1. Asadi, A., Wang, Q., Mancuso, V.: A survey on device-to-device communication in cellular networks. IEEE Commun. Surv. Tutorials **16**(4), 1801–1819 (2014)
2. Lin, Y.-D., Hsu, Y.-C.: Multihop cellular: A new architecture for wireless communications. In: IEEE INFOCOM 2000, Tel Aviv, Israel, vol. 3, pp. 1273–1282, March 2000
3. Kaufman, B., Aazhang, B.: Cellular networks with an overlaid device to device network. In: 2008 42nd Asilomar Conference on Signals, Systems and Computers, Pacific Grove, CA, pp. 1537–1541, October 2008
4. Peng, T., Lu, Q., Wang, H., Xu, S., Wang, W.: Interference avoidance mechanisms in the hybrid cellular and device-to-device systems. In: IEEE PIMRC 2009, Tokyo, Japan, pp. 617–621, September 2009
5. Lei, L., Zhong, Z., Lin, C., Shen, X.: Operator controlled device-to-device communications in LTE-advanced networks. IEEE Wirel. Commun. **19**(3), 96–104 (2012)

6. Pratas, N.K., Popovski, P.: Underlay of low-rate machine-type D2D links on downlink cellular links. In: 2014 IEEE ICC Workshops, Sydney, Australia, pp. 423–428, June 2014
7. Doppler, K., Rinne, M., Wijting, C., Ribeiro, C.B., Hugl, K.: Device-to-device communication as an underlay to LTE-advanced networks. IEEE Commun. Mag. **47**(12), 42–49 (2009)
8. Wu, X., Tavildar, S., Shakkottai, S., Richardson, T., Li, J., Laroia, R., Jovicic, A.: FlashLinQ: A synchronous distributed scheduler for peer-to-peer ad hoc networks. IEEE/ACM Trans. Netw. **21**(4), 1215–1228 (2013)
9. Yuen, C., Elkashlan, M., Qian, Y., Duong, T.Q., Shu, L., Schmidt, F.: Energy harvesting communications: Part 1 [Guest Editorial]. IEEE Commun. Mag. **53**(4), 68–69 (2015)
10. Yuen, C., Elkashlan, M., Qian, Y., Duong, T.Q., Shu, L., Schmidt, F.: Energy harvesting communications: Part 2 [Guest Editorial]. IEEE Commun. Mag. **53**(6), 54–55 (2015)
11. Yuen, C., Elkashlan, M., Qian, Y., Duong, T.Q., Shu, L., Schmidt, F.: Energy harvesting communications: Part 3 [Guest Editorial]. IEEE Commun. Mag. **53**(6), 54–55 (2015)
12. Pejoski, S., Hadzi-Velkov, Z., Duong, T.Q., Zhong, C.: Wireless powered communication networks with non-ideal circuit power consumption. IEEE Commun. Lett. **21**(6), 1429–1432 (2017)
13. Liu, Y., Wang, L., Zaidi, S.A.R., Elkashlan, M., Duong, T.Q.: Secure D2D communication in large-scale cognitive cellular networks: A wireless power transfer model. IEEE Trans. Commun. **64**(1), 329–342 (2016)
14. Nasir, A.A., Tuan, H.D., Ngo, D.T., Duong, T.Q., Poor, H.V.: Beamforming design for wireless information and power transfer systems: Receive power-splitting versus transmit time-switching. IEEE Trans. Commun. **65**(2), 876–889 (2017)
15. Hadzi-Velkov, Z., Zlatanov, N., Duong, T.Q., Schober, R.: Rate maximization of decode-and-forward relaying systems with RF energy harvesting. IEEE Commun. Lett. **19**(12), 2290–2293 (2015)
16. Jiang, X., Zhong, C., Chen, X., Duong, T.Q., Tsiftsis, T.A., Zhang, Z.: Secrecy performance of wirelessly powered wiretap channels. IEEE Trans. Commun. **64**(9), 3858–3871 (2016)
17. Nguyen, N.P., Duong, T.Q., Ngo, H.Q., Hadzi-Velkov, Z., Shu, L.: Secure 5G wireless communications: A joint relay selection and wireless power transfer approach. IEEE Access **4**, 3349–3359 (2016)
18. Nasir, A.A., Tuan, H.D., Duong, T.Q., Poor, H.V.: Secrecy rate beamforming for multi-cell swipt networks. In: 2016 IEEE Globecom Workshops, Washington, DC, pp. 1–5, December 2016
19. Hoang, T.M., Duong, T.Q., Vo, N.S., Kundu, C.: Physical layer security in cooperative energy harvesting networks with a friendly jammer. IEEE Wirel. Commun. Lett. **6**(2), 174–177 (2017)
20. Muirhead, D., Imran, M.A., Arshad, K.: A survey of the challenges, opportunities and use of multiple antennas in current and future 5G small cell base stations. IEEE Access **4**, 2952–2964 (2016)
21. Chandrasekhar, V., Andrews, J.G., Gatherer, A.: Femtocell networks: A survey. IEEE Commun. Mag. **46**(9), 59–67 (2008)
22. Andrews, J.G., Buzzi, S., Choi, W., Hanly, S.V., Lozano, A., Soong, A.C.K., Zhang, J.C.: What will 5G be? IEEE J. Sel. Areas Commun. **32**(6), 1065–1082 (2014)

Secure Energy Harvesting Communications with Partial Relay Selection over Nakagami-m Fading Channels

Cheng Yin, Xiangyu He, Nam-Phong Nguyen(✉), and Emiliano Garcia-Palacios

Queen's University Belfast, Belfast, UK
{cyin01,xhe07,pnguyen04}@qub.ac.uk, e.garcia@ee.qub.ac.uk

Abstract. In this paper, a secure energy harvesting relay communication system with partial relay selection over Nakagami-m fading channels is proposed. A power beacon can provide wireless energy for the source and relay. A time-switching-based (TS) radio frequency energy harvesting technique is deployed at the power beacon. An eavesdropper is able to wiretap to the signal transmitted from the source and the relays. The exact closed-form expression of secrecy outage probability is derived. The results show that with increasing number of relays the system performs better in terms of secrecy outage probability (SOP). In addition, the energy harvesting duration has a significant effect on the secrecy outage probability. There exist an optimal energy harvesting duration that can achieve the lowest SOP and therefore this parameter should be carefully designed.

Keywords: Physical layer security · Energy harvesting
Relay networks · Nakagami-m fading

1 Introduction

Human activities are considered the main reason for climate change. A large amount of energy is consumed in wireless communication because of the increasing number of mobile devices and base stations. Therefore, a sustainable network approach has been widely studied [1–3]. Energy harvesting appeals as a promising solution. In conventional terms, renewable energy involves energy like for example solar, wind, vibration or piezoelectric. However, in recent years, RF (radio frequency) [4] energy harvesting (EH) has emerged as a new approach. Radio transmitters around the world can broadcast signals which carry wireless information and can be utilized for power transfer (SWIPT) [5]. Apart from the environmental benefits, energy harvesting is a promising way to prolong the lifetime in energy-constrained networks. There is low maintenance monitoring and no need for replacing or recharging batteries. RF signals can carry information and energy at the same time. In this way, nodes can receive energy for harvesting and also process information [6].

© ICST Institute for Computer Sciences, Social Informatics and Telecommunications Engineering 2018
Y. Chen and T. Q. Duong (Eds.): INISCOM 2017, LNICST 221, pp. 100–110, 2018.
https://doi.org/10.1007/978-3-319-74176-5_10

Wireless energy harvesting also brings significant benefits to a cooperative relaying network where the source can transmit information to the destination with the help of relays. This is because energy-constrained relays can harvest energy from a power beacon to stay active [7]. In [8], the authors consider a full-duplex energy harvesting network with time-switching (TS) protocol which allows the relays to harvest energy to forward information from the source to the destination. The authors in [4] propose a relay system where both the source and the relay are energy-constrained, and a power beacon with multi-antenna can provide energy for them.

The deployment of relays to establish longer range communications is desirable for many applications. Although increasing the transmit power can increase the range, it can also bring significant interference which is difficult to prevent. In this context, the relay network is a promising way to extend the coverage of a system. There are two protocols that can be deployed at the relays, i.e., amplify-and-forward (AF) and decode-and-forward (DF) [9]. In AF, the signal will be amplified first then transmitted to the destination, the problem is that the unwanted interference will also be amplified. In DF, the signal is decoded and then forwarded to the destination. Compared with AF, DF has lower interference but the system is complex and high-cost. In addition, relay selection schemes can also enhance relay networks. In [10], the authors investigate a cognitive radio network with best relay selection scheme. The authors in [11] propose a cognitive radio network with buffer-aided relay selection where the relay selected is the one with the highest signal-to-interference (SIR) from all relay nodes.

Another important issue to consider in future communications is security. Due to the broadcast nature of wireless communications, information is vulnerable to be wiretapped by eavesdroppers. Therefore, the security of wireless transmissions has attracted increasing interest. The traditional way to secure wireless communications is deploying upper layer cryptographic techniques. However, cryptographic protocols have been utilized at higher-layers on the unrealistic condition that there are no errors at the physical layer [12]. Other major drawbacks are that cryptographic methods are extremely complex to implement and that when used to encrypt and decrypt data they result in significant energy consumption. Therefore, in recent years, physical layer security (PLS) has emerged as an attractive way to enhance the secrecy performance of a system.

Wyner firstly proposed the classical wiretap channel model in 1975 which recently has been studied with different fading channels such as Rayleigh and Nakagami-m to evaluate the secrecy performance of a system [13]. In PLS networks, most research consider two cooperation techniques: cooperative relaying and cooperative jamming. In [14], an intermediate jammer which can transmit signals to confuse an eavesdropper is considered. Cooperative relaying has been utilized widely in the presence of eavesdroppers [15–24]. Relay selection schemes can be proposed to enhance the performance. In [23], the authors proposed three criteria to select the best relay. In [12], the authors considered outdated relay selection to enhance the performance.

In the research context discussed above energy harvesting has never been considered. However in [18], the combination of energy harvesting, cooperative relaying and PLS in a wireless network is studied over Rayleigh fading. In our research, we extend their work by considering Nakagami-m fading.

Motivated by their research, the secrecy performance of an energy harvesting network with multiple relays in the presence of an eavesdropper over Nakagami-m fading channels is investigated. The contributions of this paper are summarized as follows:

- Partial relay selection is considered to secure the network.
- The exact-closed form expressions of secrecy outage probability (SOP) is derived.
- The results have shown that increasing the number of relays significantly enhances the security performance of the considered system. In addition, the EH duration shows a huge effect on SOP of the considered system. There is optimal point of EH duration in our example which can achieve minimum SOP of the considered system.

The remainder of the paper is organized as follows. System and channel models are described in Sect. 2. Performance analysis with exact closed-form expressions is developed in Sect. 3, while numerical results based on Monte-Carlo simulations to validate the correctness of our analyses is presented in Sect. 4. Finally, the paper is concluded in Sect. 5.

2 System and Channel Models

Consider an energy harvesting network consisting of a power beacon B , an information source S, K DF relays R_k, $k = \{1, ..., K\}$, a destination D and an eavesdropper E , as shown in Fig. 1. The power beacon B, S, R_k, E, and D are equipped with single antenna.The additive white Gaussian noise (AWGN) at R_k and D has zero mean and variance N_0. Assuming all the channels are Nakagami-m fading, and the channel power gains $|h_X|^2$ are gamma distributed with mean power λ_X, and severity parameters m_X, where $X \in \{SR, SE, BS, BR, RE, RD\}$. The cumulative distribution function (CDF) and probability function (PDF) of the random variable X can be written as

$$F_X(x) = 1 - \exp\left(-\frac{x}{\theta_X}\right) \sum_{i=0}^{m_X - 1} \frac{1}{i!} \left(\frac{x}{\theta_X}\right)^i, \tag{1}$$

$$f_X(x) = \frac{x^{m_X - 1}}{\Gamma(m_X)\theta_X^{m_X}} \exp\left(-\frac{x}{\theta_X}\right). \tag{2}$$

where $\theta_X = \frac{\lambda_X}{m_X}$, and $\Gamma(\cdot, \cdot)$ is the incomplete gamma function [25, Eq. (8.352.6)].

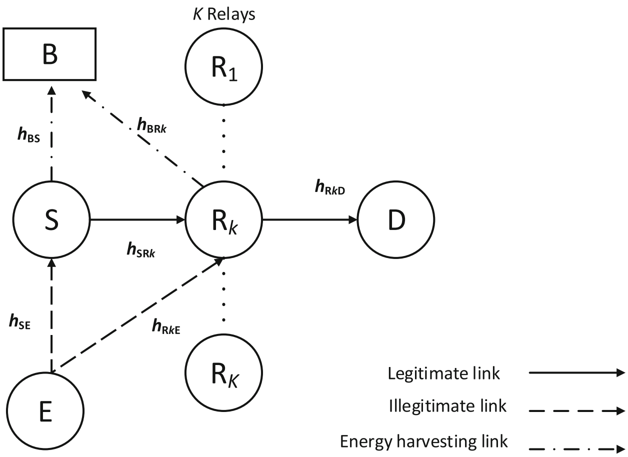

Fig. 1. System model.

2.1 Energy Harvesting Scheme

In the proposed system, S and R_k can harvest energy from B, and then transmit signals with the energy. The power beacon can provide wireless energy to S and R_{k^*}, where the R_{k^*} is the selected aiding relay to forward information. In the paper, time switching (TS) policy based energy harvesting is used, as shown in Fig. 2. In a transmission block time T, S and R_{k^*} harvest energy for αT seconds. Then both $\mathsf{S} \rightarrow \mathsf{R}_{k^*}$ and $\mathsf{R}_{k^*} \rightarrow \mathsf{D}$ transmissions spend $(1-\alpha)T/2$ equally to forward information, where α is the EH time fraction and $0 < \alpha < 1$. Therefore, the harvested energy at S and R_{k^*} are

$$E_{\mathsf{S}} = \eta \mathcal{P}_{\mathsf{B}} \alpha T |h_{\mathsf{BS}}|^2, \tag{3}$$

$$E_{\mathsf{R}} = \eta \mathcal{P}_{\mathsf{B}} \alpha T |h_{\mathsf{BR}_{k^*}}|^2, \tag{4}$$

where η is the efficiency coefficient and $0 < \eta < 1$. $\mathcal{P}_{\mathsf{B}}$ is the transmit power of power beacon B. $|h_{\mathsf{BS}}|^2$ and $|h_{\mathsf{BR}_{k^*}}|^2$ are channel links from power beacon B to source S and B to selected aiding relay R_{k^*}. Assuming the processing energy at S and R_{k^*} can be ignored. Therefore, the transmit power of S and R_{k^*} are

$$\mathcal{P}_{\mathsf{S}} = \frac{2\eta \mathcal{P}_{\mathsf{B}} |h_{\mathsf{BS}}|^2 \alpha}{(1-\alpha)}, \tag{5}$$

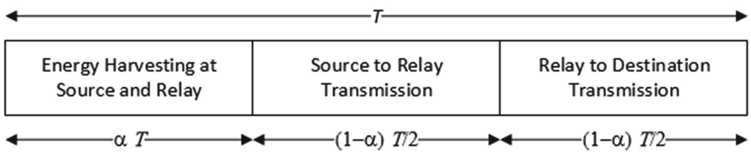

Fig. 2. Time switching based protocol

$$\mathcal{P}_{\mathsf{R}} = \frac{2\eta\mathcal{P}_{\mathsf{B}}|h_{\mathsf{BR}_{k^*}}|^2\alpha}{(1-\alpha)}. \tag{6}$$

2.2 Security Scenarios

In the considered system, E can eavesdrop information during the $\mathsf{S} \rightarrow \mathsf{R}_{k^*}$ and $\mathsf{R}_{k^*} \rightarrow \mathsf{D}$ transmissions. We assume that there is no direct link from $\mathsf{B} \rightarrow \mathsf{E}$. Therefore, the energy harvesting at S and R_{k^*} can not be disturbed in the presence of E. Decode-and-forward (DF) technique and different code books are used in order to enhance the performance of considered system. The secrecy capacity of the considered system is written as

$$C_s = \min(C_{1s}, C_{2s}), \tag{7}$$

where C_{1s} and C_{2s} are the achievable secrecy rate of the first hop and the second hop, they can be expressed as follows:

$$C_{1s} = \frac{1-\alpha}{2}\left[\log_2\left(\frac{1+\gamma_{1\mathsf{M}}}{1+\gamma_{1\mathsf{E}}}\right)\right]^+ = \epsilon\left[\log_2\left(\frac{1+\gamma_{1\mathsf{M}}}{1+\gamma_{1\mathsf{E}}}\right)\right]^+, \tag{8}$$

$$C_{2s} = \frac{1-\alpha}{2}\left[\log_2\left(\frac{1+\gamma_{2\mathsf{M}}}{1+\gamma_{2\mathsf{E}}}\right)\right]^+ = \epsilon\left[\log_2\left(\frac{1+\gamma_{2\mathsf{M}}}{1+\gamma_{2\mathsf{E}}}\right)\right]^+, \tag{9}$$

where $\epsilon = \frac{1-\alpha}{2}$ accounts for the fact that during a block time T, both the first hop and second hop spends $(1-\alpha)T/2$ equally to forward information, and $[x]^+ = \max(x, 0)$. $\gamma_{1\mathsf{M}}$ is the SNR at the first link $\mathsf{S} \rightarrow \mathsf{R}_{k^*}$, $\gamma_{2\mathsf{M}}$ is the SNR at the second link $\mathsf{R}_{k^*} \rightarrow \mathsf{D}$, $\gamma_{1\mathsf{E}}$ is the SNR at $\mathsf{S} \rightarrow \mathsf{E}$ and $\gamma_{2\mathsf{E}}$ is the SNR at $\mathsf{R}_{k^*} \rightarrow \mathsf{E}$. The SNR of the first hop $\gamma_{1\mathsf{M}}$ is given as

$$\gamma_{1\mathsf{M}} = \frac{\mathcal{P}_{\mathsf{S}}|h_{\mathsf{SR}_{k^*}}|^2}{N_0} = \frac{2\eta\alpha\mathcal{P}_{\mathsf{B}}|h_{\mathsf{BS}}|^2|h_{\mathsf{SR}_{k^*}}|^2}{N_0(1-\alpha)} = \xi\gamma_{\mathsf{M}}|h_{\mathsf{BS}}|^2|h_{\mathsf{SR}_{k^*}}|^2, \tag{10}$$

where $\gamma_{\mathsf{M}} = \frac{\mathcal{P}_{\mathsf{B}}}{N_0}$, $\xi = \frac{2\eta\alpha}{(1-\alpha)}$, and $|h_{\mathsf{SR}_{k^*}}|^2$ is the channel power gain of $\mathsf{S} \rightarrow \mathsf{R}_{k^*}$ link. Similarly, $\gamma_{2\mathsf{M}}$, $\gamma_{1\mathsf{E}}$, and $\gamma_{2\mathsf{E}}$ can be written as

$$\gamma_{2\mathsf{M}} = \gamma_{\mathsf{M}}\xi|h_{\mathsf{BR}_{k^*}}|^2|h_{\mathsf{R}_{k^*}\mathsf{D}}|^2, \tag{11}$$

$$\gamma_{1\mathsf{E}} = \gamma_{\mathsf{E}}\xi|h_{\mathsf{BS}}|^2|h_{\mathsf{SE}}|^2, \tag{12}$$

$$\gamma_{2\mathsf{E}} = \gamma_{\mathsf{E}}\xi|h_{\mathsf{BR}_k}|^2|h_{\mathsf{R}_{k^*}\mathsf{E}}|^2, \tag{13}$$

where $|h_{\mathsf{R}_{k^*}\mathsf{D}}|^2$, $|h_{\mathsf{SE}}|^2$, and $|h_{\mathsf{R}_{k^*}\mathsf{E}}|^2$ are the channel power gains of $\mathsf{R}_{k^*} \rightarrow \mathsf{D}$, $\mathsf{S} \rightarrow \mathsf{E}$, and $\mathsf{R}_{k^*} \rightarrow \mathsf{E}$ links. $\gamma_{\mathsf{E}} = \frac{\mathcal{P}_{\mathsf{B}}}{N_{\mathsf{E}}}$, and N_{E} is the variance of the AWGN at E. In some networks, it is not possible to know the full knowledge of channel state information (CSI) of all the links. Therefore, in this paper, we consider a partial relay selection (PRS) that only need to know CSI of the first hop $\mathsf{S} \rightarrow \mathsf{R}_k$. The best link is selected when the first hop has the maximum SNR, and can be expressed as

$$k^* = \arg\max_{k=1,\ldots,K}(|h_{\mathsf{SR}_k}|^2). \tag{14}$$

Therefore, according to (14), the SNR of the first hop given by (10) can be rewritten as

$$\gamma_{1\mathsf{M}} = \gamma_{\mathsf{M}}\xi|h_{\mathsf{BS}}|^2 \max_{k=1,\ldots,K}(|h_{\mathsf{SR}_{k^*}}|^2), \tag{15}$$

The achievable secrecy rates of PRS scheme in the considered system is written as

$$C_{\mathsf{PRS}} = \epsilon\left[\log_2 \min\left(\frac{1+\gamma_{\mathsf{M}}\xi|h_{\mathsf{BS}}|^2|h_{\mathsf{SR}_{k^*}}|^2}{1+\gamma_{\mathsf{E}}\xi|h_{\mathsf{BS}}|^2|h_{\mathsf{SE}}|^2}, \frac{1+\gamma_{\mathsf{M}}\xi|h_{\mathsf{BR}_{k^*}}|^2|h_{\mathsf{R}_{k^*}\mathsf{D}}|^2}{1+\gamma_{\mathsf{E}}\xi|h_{\mathsf{BR}_{k^*}}|^2|h_{\mathsf{R}_{k^*}\mathsf{E}}|^2}\right)\right]^+. \tag{16}$$

3 Secrecy Outage Probability

In this section, the closed-form expressions of secrecy outage probability (SOP) for PRS is provided to evaluate the security performance of the considered system. In a communication system, the security outage probability is defined by the probability that the instantaneous mutual information is below a rate R_{th}, and can be expressed as

$$P(C < R_{th}) = P(\gamma < \beta) = F_{\gamma_{\mathsf{PRS}}}(\beta)\,, \tag{17}$$

where $C = \log_2(1+\gamma)$, γ is the SNR of the considered system, and $\beta = 2^{\frac{R_{th}}{\epsilon}}$.

From (16) and(17), we have

$$P(C_{\mathsf{PRS}} < R_{th}) = P(\gamma_{\mathsf{PRS}} < \beta) = F_{\gamma_{\mathsf{PRS}}}(\beta)\,, \tag{18}$$

where

$$\gamma_{\mathsf{PRS}} = \min\left(\frac{1+\gamma_{\mathsf{M}}\xi|h_{\mathsf{BS}}|^2|h_{\mathsf{SR}_{k^*}}|^2}{1+\gamma_{\mathsf{E}}\xi|h_{\mathsf{BS}}|^2|h_{\mathsf{SE}}|^2}, \frac{1+\gamma_{\mathsf{M}}\xi|h_{\mathsf{BR}_{k^*}}|^2|h_{\mathsf{R}_{k^*}\mathsf{D}}|^2}{1+\gamma_{\mathsf{E}}\xi|h_{\mathsf{BR}_{k^*}}|^2|h_{\mathsf{R}_{k^*}\mathsf{E}}|^2}\right). \tag{19}$$

$F_{\gamma_{\mathsf{PRS}}}(\beta)$ is the cumulative distribution function (CDF) of γ_{PRS}. From (18), we have the following Lemma.

Lemma 1. *The SOP of the considered system in partial relay selection scheme is formulated as follows:*

$$\begin{aligned}
F_{\gamma_{\mathsf{PRS}}}(\beta) &= 1 + \sum_{k=1}^{k}\sum_{v=0}^{l}\sum_{l=0}^{k(m_{\mathsf{SR}}-1)}\sum_{i=0}^{m_{\mathsf{RD}}-1}\sum_{j=0}^{i}\binom{k}{k}\binom{l}{v}\binom{i}{j}(-1)^k(\beta-1)^{l-v+i-j}(\gamma_{\mathsf{E}}\beta)^{v+j}\\
&\times \frac{w(l,k,m_{\mathsf{SR}})}{i!\gamma_{\mathsf{M}}^{l+i}\xi^{l-v+i-j}\theta_{\mathsf{SR}}^{l}\theta_{\mathsf{RD}}^{i}\Gamma(m_{\mathsf{SE}})\theta_{\mathsf{SE}}^{m_{\mathsf{SE}}}\Gamma(m_{\mathsf{BS}})\theta_{\mathsf{BS}}^{m_{\mathsf{BS}}}\Gamma(m_{\mathsf{RE}})\theta_{\mathsf{RE}}^{m_{\mathsf{RE}}}\Gamma(m_{\mathsf{BR}})\theta_{\mathsf{BR}}^{m_{\mathsf{BR}}}}\\
&\times \Gamma(v+m_{\mathsf{SE}})\left(\frac{k\beta}{\theta_{\mathsf{SR}}}+\frac{1}{\theta_{\mathsf{SE}}}\right)^{-(v+m_{\mathsf{SE}})}\Gamma(v+m_{\mathsf{RE}})\left(\frac{\beta\gamma_{\mathsf{E}}}{\gamma_{\mathsf{M}}\theta_{\mathsf{RD}}}+\frac{1}{\theta_{\mathsf{RE}}}\right)^{-(j+m_{\mathsf{RE}})}\\
&\times 4\times\left(\frac{k\theta_{\mathsf{BS}}(\beta-1)}{\theta_{\mathsf{SR}}\gamma_{\mathsf{M}}\xi}\right)^{\frac{m_{\mathsf{BS}}-l+v}{2}}\left(\frac{\theta_{\mathsf{BR}}(\beta-1)}{\theta_{\mathsf{RD}}\gamma_{\mathsf{M}}\xi}\right)^{\frac{m_{\mathsf{BR}}-i+j}{2}}\mathbf{K}_{m_{\mathsf{BS}}-l+v}\left(2\sqrt{\frac{k(\beta-1)}{\theta_{\mathsf{SR}}\theta_{\mathsf{BS}}\gamma_{\mathsf{M}}\xi}}\right)\\
&\times \mathbf{K}_{m_{\mathsf{BR}}-i+j}\left(2\sqrt{\frac{\beta-1}{\theta_{\mathsf{RD}}\theta_{\mathsf{BR}}\gamma_{\mathsf{M}}\xi}}\right)
\end{aligned} \tag{20}$$

where $\mathbf{K}_1(\cdot)$ *defined in* [25, Eq. (3.471.9)] *is the modified Bessel function of the second kind and* $w(\cdot,\cdot,\cdot)$ *function is derived as*

$$w(l,k,m_{\mathsf{SR}}) = \begin{cases} \left(\frac{1}{l!}\right)^k, & \text{if } l=0 \\ \frac{k}{l!}, & \text{if } l=1 \\ \frac{1}{l}\sum_{q=1}^{l}(qk-l+q)\frac{1}{q!}w(l-q,k,m_{\mathsf{SR}}), & \text{if } 2\leqslant l\leqslant (m_{\mathsf{SR}}-1) \\ \frac{1}{l}\sum_{q=1}^{m_{\mathsf{SR}}-1}(qk-l+q)\frac{1}{q!}w(l-q,k,m_{\mathsf{SR}}), & \text{if } m_{\mathsf{SR}}\leqslant l< k(m_{\mathsf{SR}}-1) \end{cases} \tag{21}$$

Proof. The proof is given in Appendix A.1.

4 Numerical Results

In this section, the simulation results using Monte Carlo method are provided to validate the accuracy of the above secrecy outage probability analysis. In this section, the following parameters are fixed: γ_{E}=10 dB, $R_{th}=0.2$ bits/s/Hz, $\eta=0.8$. The parameters of channel links are fixed: $m_{\mathsf{BS}}=2$, $\theta_{\mathsf{BS}}=10$, $m_{\mathsf{BR}}=2$, $\theta_{\mathsf{BR}}=10$, $m_{\mathsf{SR}}=2$, $\theta_{\mathsf{SR}}=10$, $m_{\mathsf{RD}}=2$, $\theta_{\mathsf{RD}}=10$. The parameters of the eavesdropping links are designed: $m_{\mathsf{SE}}=2$, $\theta_{\mathsf{SE}}=2$, $m_{\mathsf{RE}}=2$, $\theta_{\mathsf{RE}}=2$.

In Fig. 3, the analysis match the simulation very well. In this setup, $\alpha=0.01$. This is because in Fig. 4, $\alpha=0.01$ seems as an optimal point that has the lowest SOP. The result shows that the number of relays has significant effect on the secrecy outage probability of PRS scheme. More specifically, when K increases, the system performs better in terms of SOP.

Figure 4 investigates the effect of energy harvesting time in a transmission block time on the secrecy outage probability. In the considered system, $k=3$,

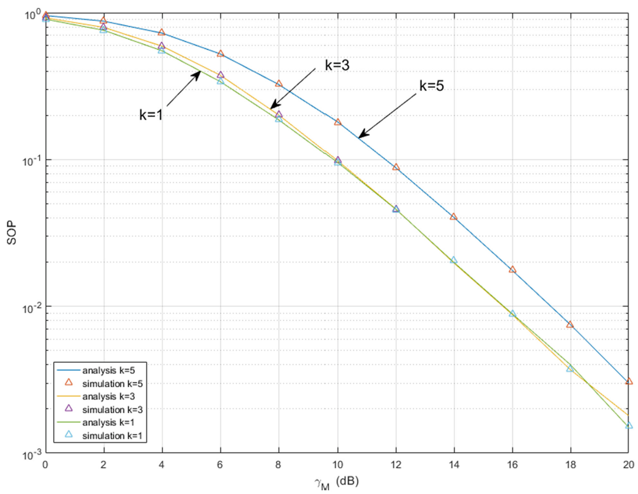

Fig. 3. SOP in PRS scheme with different number of relays

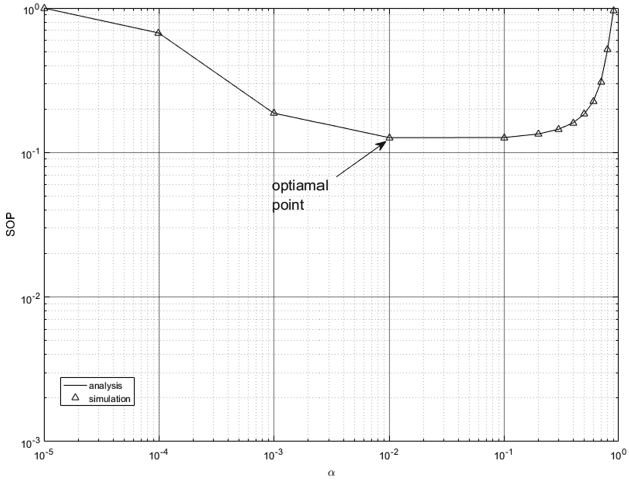

Fig. 4. SOP in PRS scheme is plotted as a function of α

$\gamma_{\mathsf{M}} = 10\,\mathrm{dB}$. The SOP is very large when α is too small or too high. This is because when the energy harvesting time is too long, S and R_{k^*} do not have sufficient time to forward information and when the transmission duration is too long, there is little time for the nodes to harvest energy. In both two cases, the SOP will be extremely large. The results also show that the SOP has an optimal point at $\alpha = 10^{-2}$ in PRS scheme. Specifically, there is very little difference of SOP when α is between 10^{-2} and 10^{-1}. In general, α has a significant effect on the performance of the considered system. Therefore, the EH duration should be mindfully determined in order to secure the communication.

5 Conclusions

In this paper, a system with multiple DF relays and a power beacon with single antenna in the presence of an eavesdropper has been investigated. Partial relay selection has been proposed in order to enhance the performance of the considered system. The exact closed-form expressions of SOP has been derived. The results show that with the increasing number of relays, the security performance can be enhanced. Finally, the EH duration has huge impact on the system performance and should be carefully designed. In our examples, there is an optimal point at α=10^{-2}.

A Appendices

A.1 Proof of Lemma 1

The SNR of first hop and second hop in PRS scheme can be written as

$$\gamma_{1\mathsf{PRS}} = \frac{1 + \gamma_{\mathsf{M}}\xi|h_{\mathsf{BS}}|^2|h_{\mathsf{SR}_{k^*}}|^2}{1 + \gamma_{\mathsf{E}}\xi|h_{\mathsf{BS}}|^2|h_{\mathsf{SE}}|^2}, \tag{A.1}$$

$$\gamma_{2\mathsf{PRS}} = \frac{1 + \gamma_{\mathsf{M}}\xi|h_{\mathsf{BR}_{k^*}}|^2|h_{\mathsf{R}_{k^*}\mathsf{D}}|^2}{1 + \gamma_{\mathsf{E}}\xi|h_{\mathsf{BR}_{k^*}}|^2|h_{\mathsf{R}_{k^*}\mathsf{E}}|^2}. \tag{A.2}$$

The CDF of $\gamma_{1\mathsf{PRS}}$ is expressed as

$$\begin{aligned}
P(\gamma_{1\mathsf{PRS}} < x) = 1 + &\sum_{k=1}^{K}\sum_{v=0}^{l}\sum_{l=0}^{k(m_{\mathsf{SR}}-1)} \binom{K}{k}\binom{v}{l}(-1)^k(x-1)^{l-v}(\xi)^{v-l}(\gamma_{\mathsf{E}}x)^v \\
&\times \frac{\Gamma(v+m_{\mathsf{SE}})}{\Gamma(m_{\mathsf{SE}})\theta_{\mathsf{SE}}^{m_{\mathsf{SE}}}}\frac{w(l,k,m_{\mathsf{SR}})}{\theta_{\mathsf{SR}}^l\gamma_{\mathsf{M}}^l}\frac{1}{\Gamma(m_{\mathsf{BS}})\theta_{\mathsf{BS}}^{m_{\mathsf{BS}}}}\left(\frac{\theta_{\mathsf{SR}}\gamma_{\mathsf{M}}\theta_{\mathsf{SE}}}{k\gamma_{\mathsf{E}}x\theta_{\mathsf{SE}}+\theta_{\mathsf{SR}}\gamma_{\mathsf{M}}}\right)^{v+m_{\mathsf{SE}}} \\
&\times \mathbf{K}_{m_{\mathsf{BS}}-l+v}\left(2\sqrt{\frac{k(x-1)}{\theta_{\mathsf{SR}}\theta_{\mathsf{BS}}\gamma_{\mathsf{M}}\xi}}\right) \times 2 \times \left(\frac{k(x-1)\theta_{\mathsf{BS}}}{\theta_{\mathsf{SR}}\gamma_{\mathsf{M}}\xi}\right)^{\frac{m_{\mathsf{BS}}-l+v}{2}}
\end{aligned} \tag{A.3}$$

The CDF of $\gamma_{2\mathsf{PRS}}$ is expressed as

$$\begin{aligned}
P(\gamma_{2\mathsf{PRS}} < x) = 1 - &\sum_{i=0}^{m_{\mathsf{RD}}-1}\sum_{j=0}^{i}\binom{i}{j}\frac{1}{i!}\frac{(x-1)^{i-j}(\gamma_{\mathsf{E}}x)^j}{\gamma_{\mathsf{M}}^i\xi^{i-j}\theta_{\mathsf{RD}}^i}\frac{\Gamma(v+m_{\mathsf{RE}})}{\Gamma(m_{\mathsf{RE}})\theta_{\mathsf{RE}}^{m_{\mathsf{RE}}}\Gamma(m_{\mathsf{BR}})\theta_{\mathsf{BR}}^{m_{\mathsf{BR}}}} \\
&\times \left(\frac{x\gamma_{\mathsf{E}}}{\gamma_{\mathsf{M}}\theta_{\mathsf{RD}}}+\frac{1}{\theta_{\mathsf{RE}}}\right)^{-(v+m_{\mathsf{RE}})}\mathbf{K}_{m_{\mathsf{BR}}-i+j}\left(2\sqrt{\frac{x-1}{\theta_{\mathsf{RD}}\theta_{\mathsf{BR}}\gamma_{\mathsf{M}}\xi}}\right) \\
&\times 2 \times \left(\frac{\theta_{\mathsf{BR}}(x-1)}{\theta_{\mathsf{RD}}\gamma_{\mathsf{M}}\xi}\right)^{\frac{m_{\mathsf{BR}}-i+j}{2}}
\end{aligned} \tag{A.4}$$

The SOP of the considered system in PRS scheme is formulated as follows:

$$F_{\gamma_{\mathsf{PRS}}}(\beta) = 1 - [(1 - F_{\gamma_{1\mathsf{PRS}}}(\beta))(1 - F_{\gamma_{2\mathsf{PRS}}}(\beta))] \tag{A.5}$$

After performing some mathematical manipulations, (20) can be achieved with the help of [25, Eq. (3.471.9)].

References

1. Yuen, C., Elkashlan, M., Qian, Y., Duong, T.Q., Shu, L., Schmidt, F.: Energy harvesting communications: Part 1 [Guest Editorial]. IEEE Commun. Mag. **53**(6), 54–55 (2015)
2. Yuen, C., Elkashlan, M., Qian, Y., Duong, T.Q., Shu, L., Schmidt, F.: Energy harvesting communications: Part 2 [Guest Editorial]. IEEE Commun. Mag. **53**(6), 54–55 (2015)
3. Yuen, C., Elkashlan, M., Qian, Y., Duong, T.Q., Shu, L., Schmidt, F.: Energy harvesting communications: Part 3 [Guest Editorial]. IEEE Commun. Mag. **53**(6), 54–55 (2015)
4. Zhong, C., Zheng, G., Zhang, Z., Karagiannidis, G.: Optimum wirelessly powered relaying. IEEE Signal Process. Lett. **22**(10), 1–1 (2015)
5. Zhou, X., Zhang, R., Ho, C.K.: Wireless information and power transfer: Architecture design and rate-energy tradeoff. IEEE Trans. Commun. **61**(11), 4754–4767 (2013)

6. Nasir, A.A., Zhou, X., Durrani, S., Kennedy, R.A.: Relaying protocols for wireless energy harvesting and information processing. IEEE Trans. Wirel. Commun. **12**(7), 3622–3636 (2013)
7. Michalopoulos, D.S., Suraweera, H.A., Schober, R.: Relay selection for simultaneous information transmission and wireless energy transfer: A tradeoff perspective. IEEE J. Sel. Areas Commun. **33**(8), 1 (2015)
8. Mohammadi, M., Chalise, B.K., Suraweera, H.A., Zhong, C., Zheng, G., Krikidis, I.: Throughput analysis and optimization of wireless-powered multiple antenna full-duplex relay systems. IEEE Trans. Commun. **64**(4), 1769–1785 (2016)
9. Rankov, B., Wittneben, A.: Spectral efficient protocols for half-duplex fading relay channels. IEEE J. Sel. Areas Commun. **25**(2), 379–389 (2007)
10. Bao, V.N.Q., Duong, T.Q., da Costa, D.B., Alexandropoulos, G.C., Nallanathan, A.: Cognitive amplify-and-forward relaying with best relay selection in non-identical Rayleigh fading. IEEE Commun. Lett. **17**(3), 475–478 (2013)
11. Chen, G., Tian, Z., Gong, Y., Chambers, J.: Decode-and-forward buffer-aided relay selection in cognitive relay networks. IEEE Trans. Veh. Technol. **63**(9), 4723–4728 (2014)
12. Yang, M., Guo, D., Huang, Y., Duong, T.Q., Zhang, B.: Secure multiuser scheduling in downlink dual-hop regenerative relay networks over Nakagami-m fading channels. IEEE Trans. Wireless Commun. **15**(12), 8009–8024 (2016)
13. Fan, L., Lei, X., Yang, N., Duong, T.Q., Karagiannidis, G.K.: Secrecy cooperative networks with outdated relay selection over correlated fading channels. IEEE Trans. Veh. Technol. **66**(8), 7599–7603 (2017)
14. Hoang, T.M., Duong, T.Q., Vo, N.S., Kundu, C.: Physical layer security in cooperative energy harvesting networks with a friendly jammer. IEEE Wirel. Commun. Lett. **6**(2), 174–177 (2017)
15. Fan, L., Lei, X., Yang, N., Duong, T.Q., Karagiannidis, G.K.: Secure multiple amplify-and-forward relaying with cochannel interference. IEEE J. Sel. Topics Signal Process. **10**(8), 1494–1505 (2016)
16. Duong, T.Q., Hoang, T.M., Kundu, C., Elkashlan, M., Nallanathan, A.: Optimal power allocation for multiuser secure communication in cooperative relaying networks. IEEE Wirel. Commun. Lett. **5**(5), 516–519 (2016)
17. Huang, Y., Wang, J., Zhong, C., Duong, T.Q., Karagiannidis, G.K.: Secure transmission in cooperative relaying networks with multiple antennas. IEEE Trans. Wireless Commun. **15**(10), 6843–6856 (2016)
18. Nguyen, N.P., Duong, T.Q., Ngo, H.Q., Hadzi-Velkov, Z., Shu, L.: Secure 5G wireless communications: A joint relay selection and wireless power transfer approach. IEEE Access **4**, 3349–3359 (2016)
19. Fan, L., Yang, N., Duong, T.Q., Elkashlan, M., Karagiannidis, G.K.: Exploiting direct links for physical layer security in multiuser multirelay networks. IEEE Trans. Wireless Commun. **15**(6), 3856–3867 (2016)
20. Hoang, T.M., Duong, T.Q., Suraweera, H.A., Tellambura, C., Poor, H.V.: Cooperative beamforming and user selection for improving the security of relay-aided systems. IEEE Trans. Wireless Commun. **63**(12), 5039–5051 (2015)
21. Rodriguez, L.J., Tran, N.H., Duong, T.Q., Le-Ngoc, T., Elkashlan, M., Shetty, S.: Physical layer security in wireless cooperative relay networks: State of the art and beyond. IEEE Commun. Mag. **53**(12), 32–39 (2015)
22. Wang, L., Kim, K.J., Duong, T.Q., Elkashlan, M., Poor, H.V.: Security enhancement of cooperative single carrier systems. IEEE Trans. Inf. Forensics Secur. **10**(1), 90–103 (2015)

23. Fan, L., Lei, X., Duong, T.Q., Elkashlan, M., Karagiannidis, G.K.: Secure multiuser communications in multiple amplify-and-forward relay networks. IEEE Trans. Commun. **62**(9), 3299–3310 (2014)
24. Wang, L., Elkashlan, M., Huang, J., Tran, N.H., Duong, T.Q.: Secure transmission with optimal power allocation in untrusted relay networks. IEEE Wirel. Commun. Lett. **3**(3), 289–292 (2014)
25. Gradshteyn, I.S., Ryzhik, I.M.: Table of Integrals, Series, and Products, 7th edn. Academic press, San Diego (2007)

Optimization of Multi-function Sensor Placement Satisfying Detection Coverage

Qingzhong Liang[1,2] and Yuanyuan Fan[1,2(✉)]

[1] School of Computer Science, China University of Geosciences, Wuhan 430074, China
{qzliang, yyfan}@cug.edu.cn
[2] Hubei Key Laboratory of Intelligent Geo-Information Processing, Wuhan 430074, China

Abstract. Wireless Sensor Networks (WSNs) have become essential parts in Industrial Internet of Things (IIoT). However, owing to the type associated with data acquisition and the large scale of monitoring, sensors are often installed at a lot of locations and a wide variety of sensors make WSN topology more complex. To address these limitations, a complementary promising solution, known as software defined wireless sensor network (SDWSN), is proposed. SDWSN acquires desired information based on users' demands from large-scale sensor networks by dynamically customizing its function. Thanks to the SDWSN, multi-type data sensing is able to enlarge the sensing scale and reduce the cost. Existing sensor placement techniques are usually focus on simple function sensor or multi-type sensor. Witness the development of SDWSN, it is ideal to explore such abilities such that the multi-type sensing functions can be conducted in a same node. Because each area covered by different multi-function sensor nodes has different detection requirements, multi-function sensor nodes placement faces many challenges. In this paper, based on multi-objective decomposition, we study the number and function redundancy of all nodes minimization problem in multi-function sensor nodes placement. Specially, we propose an improved MOEA/D-DE algorithms based on orthogonal experiment design. Simulation and evaluations validate the efficiency of our proposal.

Keywords: WSN · Placement · Multi-objective · Optimization

1 Introduction

Nowadays, wireless sensor networks (WSNs) become more and more popular for real-time monitoring. The WSN nodes can be sensors such as magnetic, vibration, sound, and so on, that are often used to monitor humidity, temperature, pressure, and other factors. Usually, in industrial applications, a variety of types of physical factors need be measured at the same time. Therefore, multi-type sensors are placed to meet different monitoring needs in a variety of detected areas. For example, multi type sensors, including CO concentration sensor, CO_2 concentration sensor, smoke concentration sensor, air temperature/relative humidity sensor, can be placed in a forest to identify smoldering and flaming combustion phases of forest fire [1]. Additionally,

© ICST Institute for Computer Sciences, Social Informatics and Telecommunications Engineering 2018
Y. Chen and T. Q. Duong (Eds.): INISCOM 2017, LNICST 221, pp. 111–120, 2018.
https://doi.org/10.1007/978-3-319-74176-5_11

multi type sensors are place for structural health monitoring of long-span suspension bridges [2, 3]. However, as a result of single-hop or multi-hop data transmission, the use of multi-type sensor will increase the scale of wireless network, and make the network topology more complex.

After decades of extensive study, Software Defined sensor wireless network (SDWSN) has experienced fast development, and has been another alternative technique that satisfies multi type data monitoring [4]. SDWSN actively acquires desired information based on users' demands from large-scale sensor networks by dynamically customizing its function by injecting roles into the reconfigurable multi-functional sensor nodes [5, 6]. Therefore, by optimizing the placement of the multi-function sensor nodes in the SDWSN, it is possible to effectively reduce the number of sensors required for multi-type data monitoring and make the network topology simpler. As shown in Fig. 1, detected areas (in shadow) are covered only by two multi-function sensors, which require two temperature sensors, two sulfur sensors and one carbon sensor before.

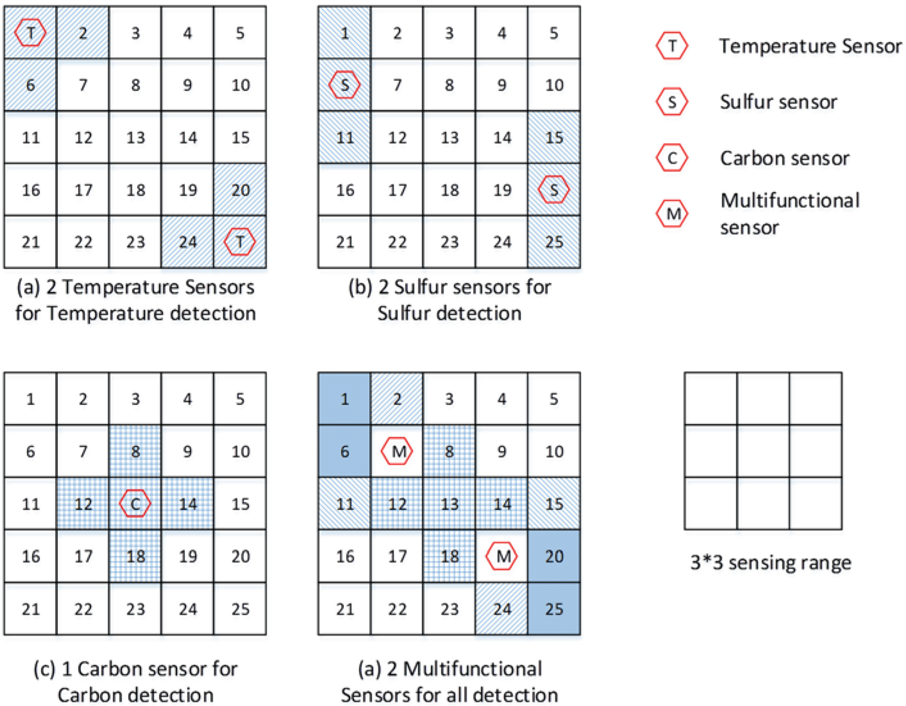

Fig. 1. Replacing multi-type sensors with multi-function sensors

Detected areas, workload capacity of each node, and number of available nodes should be considered to optimizing multi-function sensor placement. Therefore, essentially, we shall seek how to optimize multi-function sensor placement according to different monitoring requirements. The main contributions of this work exist in three folds.

Firstly, the optimizing placement problem of multi-function sensor nodes is modeled as a bipartite graph problem model in which a power set with the maximum position correlation will be found with the goal of minimizing the redundancy of the function and the number of nodes.

Secondly, because the two optimization goals proposed in the modeling are mutually exclusive, an improved MOEA/D-DE algorithm is proposed to solve this problem where the initial population generation strategy is improved by orthogonal method.

Thirdly, virtual-world trace based simulations are conducted after compared with the benchmark functions. Experiment results validate the efficiency of our proposals. The advantage of our algorithm verifies the equitable function redundancy in sensor nodes placement decisions.

2 Related Work

The problem of sensor nodes placement has been extensive studied in health monitoring [7], water distribution system [8], and so on. Moreno-Salinas et al. [9] offer a solutions to the problem of optimal acoustic sensor placement for underwater target positioning with the goal of maximizing the range-related information available for positioning. Eliades and Polycarpou [2] considers the problem of water quality sensor placement in drinking water distribution networks such that the presence of any contaminant substance in the network is detected as effectively as possible, and formulate it in a fault detection framework with which a computational solution methodology is presented based on the iterative deepening of Pareto solutions. However, most of these solutions are based on single functional sensor which can not be directly applied to the multi-functional sensors placement due to the combination relationship of functions.

Moreover, multi-type sensor WSN are playing increasing role on multi-source data sensing. Placing multi-type sensors to satisfy heterogeneous monitoring demands refers from many factors, such as cost, communication capability, number of sensors. Zeng et al. [10] consider a water quality monitoring sensor network consisting of two kinds of sensors with different prices. The cost-efficient sensor deployment problem is investigated on how to deploy these two kinds of sensors in a given water distribution system to minimize the deployment cost, without violating the quality-of-sensing requirement. Furthermore,sensor placement problem will be more complex when more types of sensors are considered. Xu et al. [11] use the updated finite element (FE) model to select the sensor types, which include fiber Bragg grating (FBG) sensors, laser displacement transducers, and accelerometers, numbers, and locations for structural health monitoring of long-span suspension bridges, while Soman et al. [3] place multi-type sensors with integer Genetic Algorithm (GA) to maximize a common metric to ensure adequate Modal Identification (MI) and Accurate Mode Shape Expansion (AMSE). Unfortunately, when all kinds of sensors are integrated in a multi-functional sensor node, these above methods will be never suitable to multi-functional sensors placement because of different functional limit. We are motivated to address this issue in this paper.

3 System Model and Constraints

3.1 System Model

In this paper, a graph model is used to describe the combinatorial optimization problem of multi-function sensor placement problem. As shown in Fig. 2, all the observed areas are regarded as an observation area set A. All the necessary detection functions are regarded as a set F. The sensor nodes are treated as a power set S representing the set F.

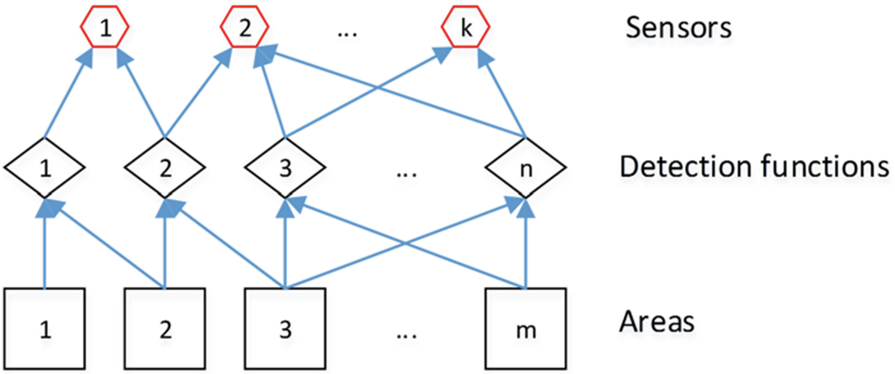

Fig. 2. Mapping relationship between functions assigned to sensors and areas

We assume the system holds the following assumptions:

The sensor node has multi software defined functions. So that, according to the observation area requirements, it can be programmed to different detection functions, such as perception of temperature, light, carbon dioxide and so on. When the detection function is not required, the sensor node can turn it off.

To satisfy the coverage of all observed areas, the sensing range of the sensor node can be increased or reduced.

The observed areas are irrelevant, so the detecting results from the different observation areas do not affect each other. Moreover, all observed areas that have a variety of detecting functional requirements must be satisfied.

All the sensor nodes do not communicate with each other, and send data to the server directly.

In order to simplify the problem model, the detection range of the sensor is represented by a matrix, such as that a sensor with range of 3 can cover the detection range is around 3 * 3 of the matrix area.

Regardless of the energy and storage capacity limit of the sensor, it is assumed that each sensor has enough energy and storage capacity to complete monitoring tasks and record all the detection data.

It can be seen that the final model of the multi-function sensor placement problem is a constraint combinatorial optimization model of a bipartite graph mapping functions of sensors to the observed areas. Therefore, in this paper, the multi-function sensor placement problem is solved to achieve the following objectives:

Under the premise of satisfying the coverage of all observed areas, the number of sensor nodes is the least to reduce the entire network construction costs.

The detection functions of all sensors have the least redundancy in detecting requirements relative to the covered observed areas to improve the utilization of the sensor.

3.2 Problem Statement

The objective of the multi-function sensor placement optimization is to minimize the number of sensors required and the function redundancy of all sensor nodes. An optimal placement scheme allows the detection functions with the same observation area to be assigned centrally on as few sensor nodes as possible. In another word, the detection functions detecting the same observation area are allocated as much as possible to a same node. The objective of minimization the sensors' number can be expressed in an integrated and weighted count Z, as following formula 1.

$$Z = (1 - \alpha) * S + \alpha * \sum_{i=0}^{n} f(x_i) \tag{1}$$

Where α *(0 < α < 1)* is the weight parameter, and n is the total number of observed areas. Function $f(x_i)$ indicates the total number of sensor nodes required for the observed area x_i, and S is the total number of sensors required in this scheme.

Another objective is minimization the function redundancy. The the function redundancy is defined as follows.

Definition 1 (Function redundancy): The function redundancy of the sensor placement is represented by the difference between the number of areas covered by all the detection functions minus the total number of detection requirements in the actual observation area. There are M observation areas, and the number of detection requirements of the i-th area is t_i. For the placement of N multi-function sensors, the number of functions of the j-th sensor is f_j, and the number of coverage areas is s_j. Then, the function redundancy can be expressed as formula 2.

$$R = \sum_{j=1}^{N} f_j * s_j - \sum_{i=1}^{M} t_i \tag{2}$$

When the number of sensor nodes is less, the detection functions required by the observation areas are more likely to be arranged on a same sensor node leading to higher function redundancy after increasing number of coverage areas of the sensor node. To reduce function redundancy, the number of sensor nodes will increase due to reduce the number of coverage areas of a single sensor. Therefore, there are two optimization objectives, such as minimizing the weighted count Z of sensor nodes required and the sensor node function redundancy R.

There are two constraints in this model. One is the maximum number of detection functions that the sensor node can run, and the other is the maximum number of sensor nodes covering a same observed area.

Although all functions can be configured on the node, the load capacity of each node is not sufficient to run more than a certain number of functions. Therefore, a strong constraint is added in the placement problem that the number of any sensor nodes in the placement scheme does not exceed the upper limit of the sensor load. This can be expressed as the formula 3.

$$\bigcap_{i=0}^{S} (Counts(S_i) \leq Up_i) = true \tag{3}$$

Where $Counts(S_i)$ represents the number of functions that the i-th sensor node S_i has, and Up_i is the upper limit of the load capacity of the sensor node S_i.

In a placement scheme, the number of sensor nodes covering a same observed area is less, the utilization of the sensor nodes is higher for the smaller detection function redundancy. According to this constraint, the maximum number of nodes covering a same area should be limited. This constraint condition can be expressed as the formula 4.

$$\bigcap_{j=1}^{n} (L_j \leq Sum(T_j) \leq U_j) = true \tag{4}$$

Where $Sum(T_j)$ represents the total number of nodes covering the j-th area T_j, and L_j and U_j denote the maximum and minimum values of the number of sensor nodes covering the T_j area, respectively.

4 An MOEA/D-DE Algorithm for Multi-function Sensor Node Placement

Because this multi-function sensor arrangement optimization is a multi-objective optimization problem, in this paper, an improved multi-objective evolutionary algorithm based on decomposition (MOEA/D) algorithm is used to solve it. The whole Pareto Frontier (PF) approximation of this problem is about to decompose into a certain number of single-objective optimization problems, and then the evolutionary algorithm is used to solve these single-objective optimization problems at the same time. The algorithm maintains a population composed of the optimal solution of each subproblem. The neighborhood relation between subproblems is defined as the distance between the weight vectors of the subproblems. The optimization process of each subproblem is carried out by the evolution between the subproblems. MOEA/D-DE uses a differential evolution method in the MOEA/D hybridization process and generates a new solution by polynomial mutation. It is better than MOEA/D to maintain the diversity of the population.

In this paper, orthogonal experiment design method is used to improve the population initialization process of the MOEA/D-DE algorithm. This method selects the most representative test combination from the complete test based on the experimental factors and the level orthogonality. Because the selected test combinations are evenly dispersed and neatly comparable, the conclusion can basically replace the conclusion of the complete testing design for improving the efficiency of the algorithm.

In the implementation process, selecting the orthogonal tests from the complete tests is completed in accordance with the orthogonal array. The orthogonal array is generated following probability statistics and certain principles, which can be regarded as $L_m(q^n)$, where m is the number of combinations of levels, n is the number of factors, and q is the number of levels. In this paper, a relatively simple special orthogonal array is used in which q is a prime number and $m = q^2$, $p = q + 1$.

The population initialization process based on the orthogonal test design is done by operations shown in algorithm 1.

Algorithm 1: orthogonal test design for population initialization

Input: $X \in R^{[a_i,b_i]}(i = 1,2,\cdots,n)$

Output: $X = \{x_1, x_2, \cdots, x_n\}$

1: Select q according to X;
2: m = q * q;
3: p = q + 1;
4: for row i from 1 to m do:
5: a[i,1] = int((i-1)/q) mod q;
6: a[i,2] = (i-1) mod q;
7: for row i from 1 to m and column t from 3 to p do:
8: a[i,t+2] = (a[i,1]*t + a[i,2]) mod q;
9: for each x_i with range $[a_i, b_i]$ in vector X do:
10: for column j from 1 to q - 1 step 2 do:
11: calculate $\{a_i + j * (b_i - a_i)/q, \cdots, b_i\}$;
12: for row k from 1 to m do:
13: $x_k = \left(a_1 + \partial_{k,1} * (b_1 - a_1)/q, \cdots a_i + \partial_{k,i} * (b_i - a_i)/q, \cdots, a_n + \partial_{k,n} * (b_n - a_n)/q\right)$

In the algorithm 1, the number of rows and columns (m, n) is calculate firstly after selecting a suitable q according the input vector X. Then, these parameters are used to construct an orthogonal array. Thirdly, the range $[a_i, b_i]$ of each dimension $x_i(i = 1, 2, \cdots, n)$ in the input vector X , $X = \{x_1, x_2, \cdots, x_n\}$, is divided into q horizontal spaces $\{a_i + j * (b_i - a_i)/q, \cdots, b_i\}(j = 0, 2, \cdots, q - 1)$, according to the horizontal number q. The value of each dimension of the individual x_k in each factor combination a_k corresponding to each row of the orthogonal array is obtained. As a result, there are a total of m uniform and neatly scattered initial individuals in the search space $R^{[a_i,b_i]}(i = 1, 2, \cdots, n)$.

5 Performance Evaluation and Analysis

5.1 Configuration of Algorithm Parameters

In the evaluation, main parameters of the improved MOEA/D-DE algorithm are shown in Table 1.

Table 1. Configuration of algorithm parameters

Parameters	Value or Range
Prime number: q	13
Population size: N	300
Neighborhood: T	30
The probability of selecting T:δ	0.5
Crossover probability: CR	0.8
Mutation probability: P_m	0.125
Maximum number of parent individuals: n_r	3
Number of generations: Gen	500
Normal distribution mean and variance of stretching Factor F	(1,0.15)
Decomposition mode	Tchebycheff Approach

5.2 Verification of Multi-function Sensor Placement

In the experimental simulation, a test set with 15 areas and a total of 50 observation function requirements is constructed. In the constraint, the upper limit of the number of sensor nodes is 20, to ensure that each region has at least one sensor node to cover. Each sensor node's load capacity is set to 50, to ensure that all the observation requirements at least can be mapped to a same node. The number of iterations of the population is set to 1000 times. The results are as follows.

As shown in the Fig. 3, The purple dot represents the optimal solution of the Pareto, and the blue dot represents the solution reached during the algorithm iteration. In the multi-function sensor node placement scheme, the fewer the number of sensor

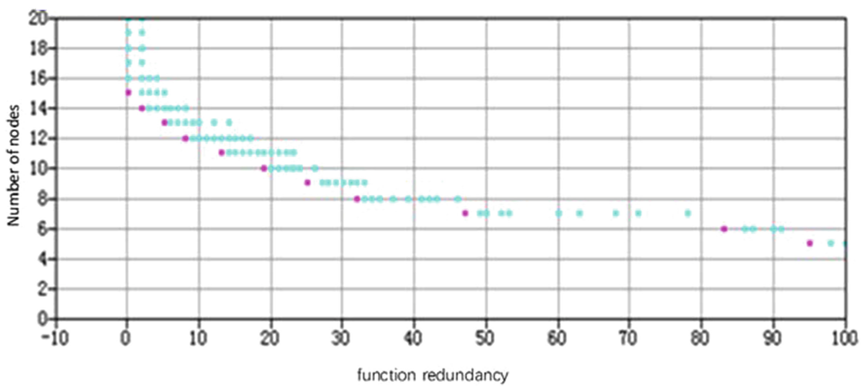

Fig. 3. Simulation of multi-function sensors placement.

nodes are used, the greater the functional redundancy is. In contrast, the more the number of sensor nodes is, the lower the functional redundancy is. This is consistent with the theoretical analysis.

6 Conclusion

In this paper, we have studied placement problem for multi-function sensor in wireless sensor networks. Our objective is to minimize the number of sensor nodes required and function redundancy of all sensor nodes. We first formally state the problem studied in this paper, with a special emphasis on the multi-function sensor node. To address the placement optimization problem, we propose an improved MOEA/D-DE algorithm. To verify the efficiency of our proposals, we conduct extensive simulations to evaluate the performance of our algorithms. The experiment results demonstrate that our algorithm has the advantages of fast convergence and strong population distribution. This validate the correctness of our algorithm design by taking the simulation of sensor application scenarios into consideration.

Acknowledgment. This research was supported by the NSF of China (Grant No. 61673354, 61672474, 61402425, 61272470, 61305087, 61440060, 61501412), the Provincial Natural Science Foundation of Hubei (Grant No. 2015CFA065). This paper has been subjected to Hubei Key Laboratory of Intelligent Geo-Information Processing, China University of Geosciences, Wuhan 430074, China. It was also supported by Open Research Project of The Hubei Key Laboratory of Intelligent Geo-Information Processing (KLIGIP201603 and KLIGIP201607).

References

1. Yan, X., Cheng, H., Zhao, Y., Yu, W., Huang, H., Zheng, X.: Real-Time identification of smoldering and flaming combustion phases in forest using a wireless sensor network-based multi-sensor system and artificial neural network. Sensors **16**(8), 1228 (2016)
2. Eliades, D.G., Polycarpou, M.M.: Multi-objective optimization of water quality sensor placement in drinking water distribution networks. In: Proceedings of European Control Conference, pp. 1626–1633 (2015)
3. Soman, R.N., Onoufrioua, T., Kyriakidesb, M.A., Votsisc, R.A., Chrysostomou, C.Z.: Multi-type, multi-sensor placement optimization for structural health monitoring of long span bridges. Smart Struct. Syst. **14**(1), 55–70 (2014)
4. Kobo, H.I., Abu-Mahfouz, A.M., Hancke, G.P.: A Survey on software-defined wireless sensor networks: challenges and design requirements. IEEE Access **5**, 1872–1899 (2017)
5. Miyazaki, T., Iwata, H., Kobayashi, K., Yamaguchi, S., Zeng, D., Guo, S., Kitamichi, J., Hayashi, T., Tsukahara, T.: DASN: demand-addressable sensor network for active information acquisition. In: Proceedings of the 8th International Conference on Ubiquitous Information Management and Communication, p. 1. ACM (2014)
6. Liang, Q., Li, H., Fan, Y., Yan, X., Hu, C., Yao, H.: SAPSN: a sensor network for signal acquisition and processing. In: IEEE 12th International Conference on Dependable, Autonomic and Secure Computing (DASC) 2014, pp. 475–478. IEEE (2014)

7. Yi, T.H., Li, H.N., Song, G., Zhang, X.D.: Optimal sensor placement for health monitoring of high-rise structure using adaptive monkey algorithm. Struct. Control Health Monit. **22**(4), 667–681 (2015)
8. Hu, C.Y., Tian, D.J., Liu, C., Yan, X.: Sensors placement in water distribution systems based on co-evolutionary optimization algorithm. In: International Conference on Industrial Networks and Intelligent Systems, pp. 7–11 (2015)
9. Moreno-Salinas, D., Pascoal, A., Aranda, J.: Optimal sensor placement for acoustic underwater target positioning with range-only measurements. IEEE J. Oceanic Eng. **41**(3), 620–643 (2016)
10. Zeng, D., Gu, L., Lian, L., Guo, S.: On cost-efficient sensor placement for contaminant detection in water distribution systems. IEEE Trans. Ind. Inf. **12**(6), 2177–2185 (2016)
11. Xu, Y.L., Zhang, X.H., Zhu, S., Zhan, S.: Multi-type sensor placement and response reconstruction for structural health monitoring of long-span suspension bridges. Sci. Bull. **61** (4), 313–329 (2016)

Toward a Real-Time Development and Deployment of IoTs Application for Smart Garden on OpenStack Cloud

Dang Huynh-Van, Khanh Tran-Quoc, and Quan Le-Trung(✉)

Department of Computer Networks, University of Information Technology, Viet Nam National University, Ho Chi Minh City, Vietnam
{13520180,13520388}@gm.uit.edu.vn, quanlt@uit.edu.vn

Abstract. While lots of Internet of Things (IoTs) applications have been designed and implemented for many areas, especially for the ambient-assisted living domain, real-time development and deployment of those IoTs applications have still been an open issue. This paper focuses on such an open issue through our developed web-based IoTs application for a smart garden, be integrated into and managed via the OpenStack Infrastructure at University of Information Technology (UiT). An intelligent model applying fuzzy logic to process measured data for the smart garden, has also developed to give useful information on keeping plants growing, monitoring, and taking care of plants more easily and effectively. Load-balance network architecture on cloud is used to deal with the scalability, availability of the deployed system.

Keywords: Wireless sensor network · Smart model · Fuzzy logic controller
Smart garden · TinyOS · Collection Tree Protocol

1 Introduction

Nowadays, Internet of Things (IoTs) is one of the newest research topics all over the world. Lots of research have been focused on such a domain to develop more creative products to enhance our life quality. IoTs applications appear in a lot of different domains [1], e.g., health care, industry, environment monitoring, weather forecast, transportation as well as agriculture. In smart agriculture field, there are lots of systems based on IoTs. These systems have been developed to solve many practical problems in the modern agriculture domain, e.g., environmental monitoring, soil parameters monitoring, automatically watering, etc. For example, in "Smart Rabbit Farm" [2], there is an IoT-based application to monitor the rabbit farm conditions with various sensors. On this system, the authors also used the cloud network infrastructure to store the collected data and after that visualizing these environmental parameters as well as useful notifications generated by basically comparing these values with the threshold. Some other system as in [3–5], environmental parameters or soil parameters were also concerned to create some useful IoTs-based applications. Most of these systems have been developed by using a single standalone server [3] or an application running on a smartphone [4] to store and visualize measured data. These solutions are only suitable for

© ICST Institute for Computer Sciences, Social Informatics and Telecommunications Engineering 2018
Y. Chen and T. Q. Duong (Eds.): INISCOM 2017, LNICST 221, pp. 121–130, 2018.
https://doi.org/10.1007/978-3-319-74176-5_12

small-scale areas or some decorated houseplants while the *scalability* and *availability* are not the primary requirements. However, with the high demands of the modern life, to deploy a smart solution in a real situation, there are many challenges [6] we must consider, such as the real-time monitoring, the scalability and the availability.

In this paper, we present a Smart Garden IoTs-based system. *This system deals with above challenges by using a load-balance network architecture on the Open Stack cloud as well as applying the fuzzy logic controller to analyze measured data.* Our system not only helpful for the gardeners on keeping their plants growing well, but also suitable to deal with high demand for real-time monitoring.

The structure of this paper is organized as follows. Section 1 introduces the research topic and break down current challenges on IoTs-based in smart agriculture domain as well as our paper's contribution. Section 2 clarifies our system implementation. This Section includes fours sub-Sections, and each sub-Section presents a part of our core system modules. Section 3 is the results of our system working in a practical situation. Section 4 shows the related work in the current IoTs-based application for smart agriculture as well as wireless sensor devices and wireless sensor network architecture. Finally, Sect. 5 ends this paper with the conclusions and future work.

2 Implementation

In this Section, we clearly explain our system architecture by stating every part of the model. Figure 1 shows the overview of our system, there are three important modules: wireless sensor nodes (IoTs end devices), servers system, and web interface.

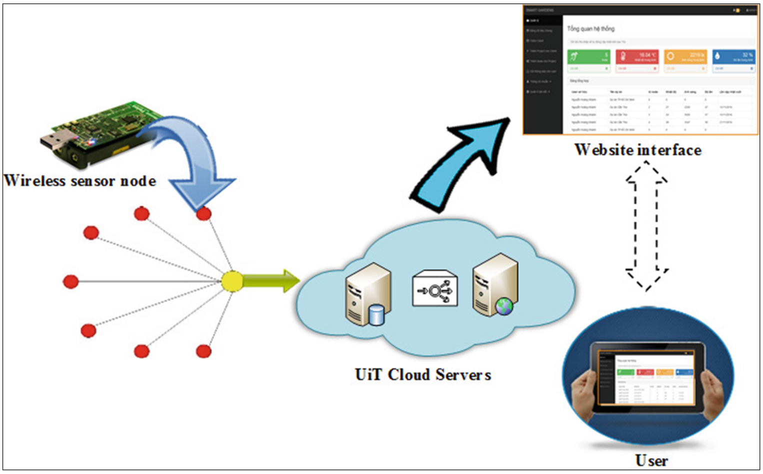

Fig. 1. Overview of IoTs application system architecture over UiT cloud servers

2.1 Programming Wireless Sensor Devices

In our system, we used Telosb Mote which was developed by UC Berkeley. It is an open source platform includes all the essentials for lab studies such as USB programming capability, an IEEE 802.15.4 radio with integrated onboard antenna, TI Micro Controller MSP430 with 10 kB. It also has optional sensor suit include: temperature, light and humidity sensor. The Telosb platform run TinyOS 1.1.10 or higher as well as Contiki – which are current most popular open source operating system for wireless sensor devices. In our implementation, we used TinyOS 2.1.2.

For the purpose of this study, we write a program in nesC – a programming language for creating TinyOS applications [7]. This program is loaded into sensor nodes to collect environment data as temperature, light, and humidity then sends these data to root node. SensorCollection program has three important files: module file (SensorCollecionC.nc), configuration file (SensorCollectionAppC.nc) and Makefile. The module file lists all interfaces that we will use in our application and define the program implementation. The configuration file is responsible for assembling other components together, connecting interfaces used by components to interfaces provided by others. The Makefile is used to compile the application.

In the SensorCollection application, we used Collection Tree Protocol (CTP) provided by *ColectionC* component in TinyOS as a collection routing protocol for data transmission. CTP is a distance vector protocol designed for sensors network and used in research, teaching and commercial products. CTP is a tree-based collection protocol. Some number of nodes in network work as a tree root. Other nodes create a set of routing tree to these roots. CTP is address-free so that it does not send a packet to a specific root; instead, it chooses a root by choosing next hop – called its parent node. CTP uses a value called expected transmission (ETX) as its routing gradient (similarly to metric value in other routing protocol). Root's ETX is 0 and other node's ETX are the ETX of its parents plus the ETX of its link to its parents. When choosing a route for transmitting data, CTP chooses the path which has lowest ETX value. An implementation of CTP is stored in tos/lib/net/ctp directory of TinyOS.

2.2 Building Server System

Our server system is developed based on OpenStack Cloud of the University of Information Technology. The model systems include two web servers, two database servers, two load balancers. All of them run Centos version 6.6. The full topology architecture is shown in Fig. 2.

By using double-quantity servers, our system guarantees if one of web server dies then all request of users will automatically redirect to another that enhance the scalability and availability of the deployed system. **Web server:** On the web server Apache is installed (Apache is as well-known open source web server). After completing installation Apache, we continue installing PHP and PHP's module as a server site language to develop our website. To make the content on the directory/var/www of two web servers automatically synchronized, we use unison solution. Unison is a file synchronization tool, which synchronizes manner Master-Slave. For example, when files on server 1 modified, it also happened in server 2. **Database server:** About the

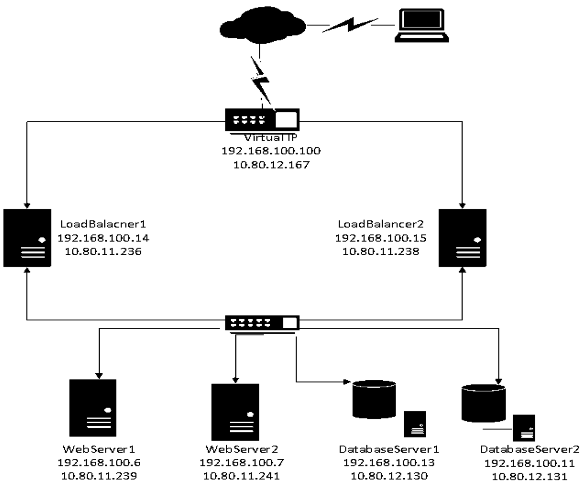

Fig. 2. The server system architecture

database, we use MySQL as an open-source relational database management system. Also for the simple management of tracking activities, we use phpMyAdmin - The open source software written in Php is used for administering the Mysql server through a web browser. Because we use two databases to ensure real-time store collected data from sensor nodes, we must configure MySQL Replication to make one of them become the master database, and other become slave database. **Load balancer:** The load balancer is a transfer and control information system, which ensure secure web server and database server. We use Keep alive to make a Virtual IP, after that, we install HAproxy - a well-known open source software for TCP/HTTP load balancer, it helps handle the incoming packets to different servers to help our server system not be overloaded.

2.3 Developing Web Application

After we set up our server system, we build a web application to analyze and visualize collected sensors data. This application is designed for two different using objects: administrators and normal users. The administrators are the garden owner, and normal users are gardeners who work in the garden and use this system for looking after their plants easily and more efficiently. We have created a database that includes four primary tables named client, project, node, and tree for storing corresponding data. *Client:* this table stores user information like user id, username, password, user role, and some contact information (phone number, address…) *Project:* storing information related to the project that will be assigned to a particular user defined in the client table. *Node:* this table stores wireless sensor node information, including node id, project id, tree id, time update new data and sensors data (temperature, light, humidity). *Tree:* designed for storing information of the plants in our garden. These data will be used as standard data in fuzzy logic controller; we will clearly explain in next section. After we complete the database, we implement our visualization system by creating and website for two usage purpose as we said above: administrators and normal users. The administrators have full privileges to manage their gardens. They can visualize the garden overview status as well as control all devices, gardeners and their post on the website. While normal users – the gardeners have limited features, the only can view the garden that administrator assigned them. This user also can manage the sensors nodes used for their areas and read the posts created by administrators to get useful information related to their plants.

2.4 Applying Fuzzy Logic Controller for Data Processing

One of the most important part in our web-based application is data processing mechanism. In order to provide helpful information to gardeners, the system must analyze collected raw sensors data before it displays alerts or reports on web interface. Figure 3 shows the data flow processing:

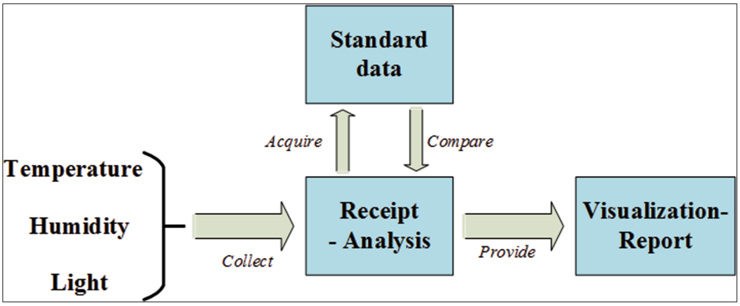

Fig. 3. Collected data processing flow.

As we show in this figure, raw data from sensor nodes are sent to server system for storing and then analyzed by the reasoning engine to create helpful information displayed on website. In *Receipt and Analysis* block, our system handles these data in different controller engine depend on their types. In particular, temperature data will be considered in temperature fuzzy logic controller as we show below.

Temperature fuzzy logic controller: To analyze temperature collected data value, we propose a simple fuzzy logic model as explained below (Fig. 4):

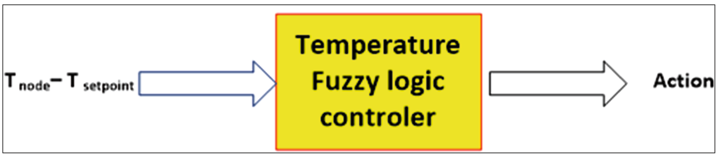

Fig. 4. Temperature fuzzy logic controller model

Input: $T_{node} - T_{setpoint}$ is the difference between the collected data from sensor node the standard value set before (the best suitable temperature recommended for the development of specific plant which we are taking care of). In this model, we defined five input level named: *NB* (negative big), *NM* (negative medium), *Z* (Zero), *PM* (positive medium) and *PB* (positive big). *Output*: Action is the necessary activities that gardener should follow to keep their plants growing well. To create the make sense output, we called five output value as *HeatHi* (gardener should doing something to increase temperature with a "high" level), similarly other values is *HeatLo* (heating with lower level), *Nothing* (doing nothing), *VenLo* (ventilating or slowing down temperature with low level) and the last in *VenHi* (we should slow down temperature steadily).

- *Membership functions:* The membership function associated with the input and output control variables are shown in the following figures (Figs. 5 and 6):

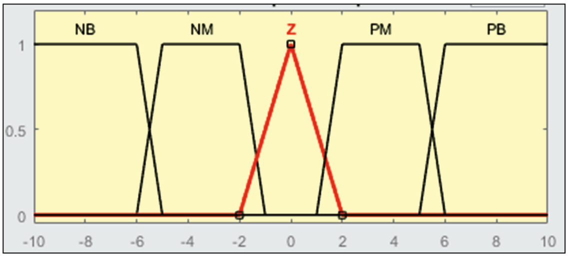

Fig. 5. The membership function of the input variables ($T_{node} - T_{setpoint}$)

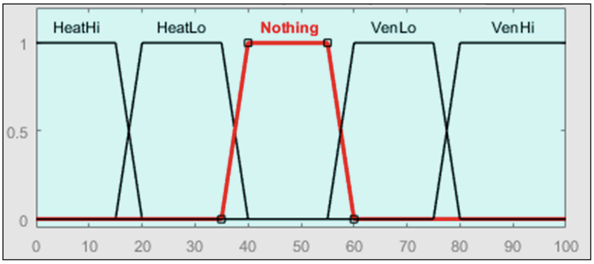

Fig. 6. The membership function for output control variables - Action

- *Inference rules:* The inference rules is shown on Table 1 based on Mandani rules composition: **IF** $(T_{node} - T_{setpoint})$ **is** (NB, NM, Z, PM, PB) **THEN** *Action* **is** (HeatHi, HeatLo, Nothing, VenLo, VenHi).

The Humidity and Light Controller are also similar with the Temperature Controler.

Table 1. The inference rules of temperature fuzzy logic controller

Rule	IF	$T_{node} - T_{setpoint}$	THEN	Action
1	IF	Negative big (NB)	THEN	Heating (High)
2	IF	Negative medium (NM)	THEN	Heating (Low)
3	IF	Zero (Z)	THEN	Nothing
4	IF	Positive medium (PM)	THEN	Ventilation (Low)
5	IF	Positive big (PB)	THEN	Ventilation (High)

3 Result and Evaluation

Using Mathlab to simulate those fuzzy reasoning model, we get result as shown in following figures (Fig. 7):

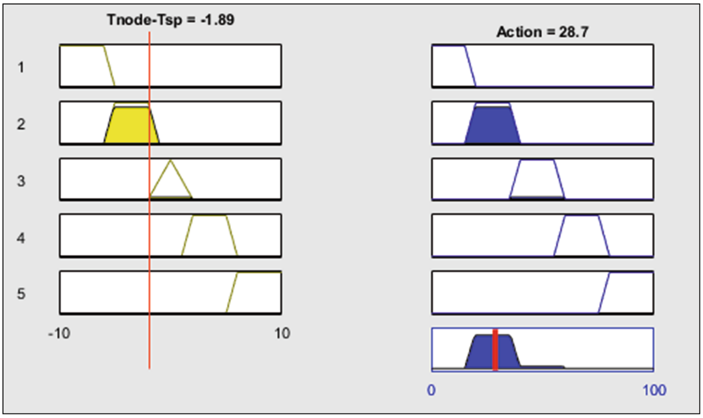

Fig. 7. An example of temperature fuzzy rule implementation.

This figure demonstrates the temperature fuzzy controller with a specific input value and the corresponding output action values by applying the interference rules that we defined in above section. As the figure shows, when the collected temperature value is smaller than the set point (–2 units) we have the output which towards to the second partition (should reduce the garden temperature slightly).

By using a PHP-based fuzzy logic library, we have embedded this reasoning engine to our web-based system. We also present the signal level from the *action* output as human-readable alerts so that the gardeners can easily know what they should do next for their plants growing well. Some sample alerts from our system is shown in Fig. 8.

As the figure shows, we define three levels for alert displaying, they are red, yellow and green. The green color means collected data is in a safe zone, which is the proper condition for plants growing. The yellow color informs received data is slightly higher than our expected value while the red color is dangerous, we must focus on this area because of the extremely difference between values from the sensor node and our standard values (Fig. 8).

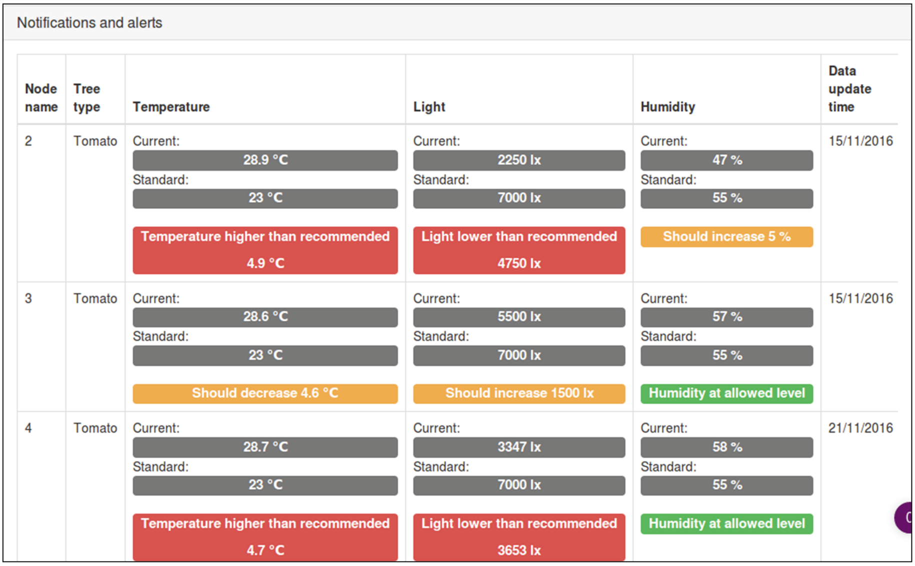

Fig. 8. A screen shot of our web-app visualization when operating in a practical experience. (Color figure online)

To verify if our reasoning model is working well, we have run the fuzzy logic controller with some sample input value on Matlab as well as on our web application. Table 2 shows the result of our experiment with the temperature controller:

Table 2. The experiment result from the temperature controller with some different input value

Input values	MatLab output	Web-app output	Web's notification
−8	8.56	8.33	*Red:* Temperature lower than recommended 7°C
−4	27.5	27.65	*Yellow:* Should increase 3°C
1	47.5	47.61	*Green:* Temperature at allowed level
4	67.5	67.65	*Yellow:* Should decrease 3°C
8	89	89.6	*Red:* Temperature higher than recommended 7°C

As the table shows, the output value from simulation on Matlab is similar with our fuzzy controller implemented on the web-app.

4 Related Work

IoT-based application. In the environmental monitoring field, applied for smart agriculture, there are many systems based on Internet of Things [2, 4]. In [3], a private cloud was developed for the use in precision agriculture and ecological monitoring.

In that system, the authors used many open source tools: Linux, LAMP stack, PHP programming language and Laravel framework as well as lots of sensor nodes based on Arduino, Raspberry Pi and Libelium Plug and Sense. The system has just developed and tested using a single-core stand-alone server so that not guarantee for availability of the deployed system. Another real monitoring system based on IoT [5], which used some wireless sensor devices as Raspberri Pi, soil moisture sensor, temperature and water level sensor as well as AWS IoT technology for implementing an automatically take care of houseplants. In generally, the IoT-based system for smart agriculture is a new research topic and still attracting many researchers and investors to develop more intelligent systems for solving the practical problems and enhance our life quality. These systems must deal with some challenges as scalability, availability as well as security. In that trends, cloud computing is an emerging technology necessary for considering and applying on future IoT-based systems [6]. **Wireless sensor node.** Depend on the using purposes, there are many types of wireless sensor nodes. Each node consists of many optimized modules for saving energy, low-power transceiver by using modern wireless standard as Zigbee, Bluetooth, 6LowPan and sensor array for monitoring environmental parameters. The sensor array includes pH sensor, temperature sensor, humidity sensor, electromagnetic wave detector, photo-detector, gas sensor and other sensor for some factors from the air as CO2, SO2… Telosb, Micaz, Mica2, Arduino, RassberryPi are some of the most popular integrated wireless sensors node, which used widely in research and development IoT application. **Network topology**. A wireless sensor network is a collection of many nodes organized for working in a cooperative network. This network is well designed for lower-power consumption and resource friendly operation. To archive that challenges, many kinds of traditional network topologies were optimized for wireless sensor network as Bus, Tree, Start, Mesh, Ring, Cellular, and Grid [8]. Each of these types has different characteristics and compatible for using in a particular situation. For example, bus topology is easy to install but network congestion and single path transmission. In the start topology, there is a central node works as a sink node, other nodes in the network communicate to each other by using the route through the central node. If the central node has a problem, it will affect for all the network. This topology is compatible for application work as server – client model. In our system, we use tree topology to implement our sensor network.

5 Conclusion and Future Work

Our system is a simple model which implements an IoTs-based application for Smart Garden. By using wireless sensor network under the Collection Tree Protocol, the wireless devices collect basic environmental parameters (temperature, light, humidity) for analyzing through the fuzzy logic controller to give helpful information to the gardeners. Our system also deals with real-time monitoring, scalability and availability by implementing on Open Stack cloud computing. In the future, to improve our system more practically and efficiently we should continue to develop the reasoning engine to be more intelligent as well as upgrade the website more useful by adding some convenient features. We also should research and learn more about the automatic technology system so that we can combine our system with a modern actuator system in order to generate a full stack “Smart Garden” architecture as a smart solution for the modern agriculture.

Acknowledgement. This research is funded by Vietnam National University HoChiMinh City (VNU-HCM) under grant number C2016-26-01/HĐ-KHCN.

References

1. Gubbi, J., Buyya, R., Marusic, S., Palaniswami, M.: Internet of Things (IoT): a vision, architectural elements, and future directions. Future Gener. Comput. Syst. **29**(7), 1645–1660 (2013)
2. Yang, J., Guo, B., Wang, Z.: A study on the rabbit farm environmental monitoring system based on Internet of Things. Adv. Sci. Technol. Lett. **121**, 178–182 (2016)
3. Bajceta, M., Sekulic, P., Krstajic, B., Djukanovic, S., Popovic, T.: A private IoT cloud platform for precision agriculture and ecological monitoring. In: International Conference on Electrical, Electronic and Computing Engineering (2016)
4. Na, A., Isaac, W., Varshney, S., Khan, E.: An IoT based system for remote monitoring of soil characteristics In: 2016 International Conference on Information Technology (InCITe) - The Next Generation IT Summit on the Theme - Internet of Things: Connect Your Worlds, pp. 316–320 (2016)
5. Kuruva, H., Sravani, B.: Remote plant watering and monitoring system based on IOT. Int. J. Technol. Res. Eng. **4**, 668–671 (2016)
6. Mehta, A., Patel, S.: IOT based smart agriculture research opportunities and challenges. Int. J. Technol. Res. Eng. **4**, 541–543 (2016)
7. Gay, D., Levis, P., Behren, R.V., Welsh, M., Brewer, E., Culler, D.: The nesC language: a holistic approach to networked embedded systems. In: Proceedings of the ACM SIGPLAN 2003 Conference on Programming Language Design and Implementation, vol. 38, pp. 1–11 (2003)
8. Sharma, D., Verma, S., Sharma, K.: Network topologies in wireless sensor networks: a review. IJECT **4**, 93–97 (2013)

An Energy-Aware Approach for Event-Driven Multimedia Data Acquisition in WMSNs

Phan Van Vinh[1(✉)] and Hoon Oh[2]

[1] School of Engineering, Eastern International University (EIU), Binh Duong City, Vietnam
vinh.phan@eiu.edu.vn

[2] Ubicom Lab, School of Computer Engineering and Information Technology, University of Ulsan, P.O. Box 18, Ulsan 680-749, Korea
hoonoh@ulsan.ac.kr

Abstract. In context-aware monitoring and control applications, multimedia data generated by multimedia sensors at a critical moment have to be delivered to a server reliably with tight time constraint. However, it is challengeable to process those data using a wireless multimedia sensor network with limited resources in terms of energy, bandwidth and processing power. Therefore, in this paper, we propose an energy-aware approach to deliver those event-driven bursty data in a reliable and timely manner by exploiting the advantage of slot scheduling technique and channel allocation. Our approach enables the concurrent transmission of a burst of multimedia data in order to shorten the multimedia data acquisition time and reduce the energy consumption. The simulation results show that the proposed approach can satisfy the requirements of multimedia applications in terms of data acquisition time and energy consumption compared with other approaches.

Keywords: WMSNs · Multimedia data · Slot scheduling

1 Introduction

A wireless multimedia sensor network (WMSN) for a context-aware monitoring and control application usually consists of several scalar sensors that report the readings from environment to a server periodically and multiple multimedia sensors that generate and transmit a burst of multimedia data (or bursty data) such as still image or video on demand only when a critical event occurs. Due to the limited bandwidth and energy of a sensor node, it is challengeable to design a protocol that can satisfy the tight time constraint and the reliability of multimedia data transmission in such a critical moment.

Various TDMA-based media access control (MAC) protocols such as TreeMAC [1], I-MAC [2], RRMAC [3] have been proposed for reliable and real-time data transmission in WMSNs. However, these protocols were basically designed for periodic data acquisition, they may not be suitable for transmitting bursty data with the time constraint reliably. In addition, for an efficient bursty data transmission with the traditional MAC protocols, the complex slot scheduling algorithm may be required and/or the wasted energy consumption of the sensor nodes is inevitable since sensor nodes may still remain active or idle listening state during the duration of bursty data transmission.

© ICST Institute for Computer Sciences, Social Informatics and Telecommunications Engineering 2018
Y. Chen and T. Q. Duong (Eds.): INISCOM 2017, LNICST 221, pp. 131–141, 2018.
https://doi.org/10.1007/978-3-319-74176-5_13

Recently, some approaches have been proposed to support the transmission of bursty data in WMSNs. Multimode Hybrid Medium Access Control (MMH-MAC) [4] can support bursty traffic in dynamic networks with the use of slot reuse technique. BurstMAC [5] which relies on the TDMA and multi-channel mechanism is proposed to enhance the network performance and prolong the network lifetime. Advertisement-based Time-division Multiple Access (ATMA) [6] reserves transmission slots by using the CSMA technique and manages the reservation of nodes in an energy-efficient way by making the use of the nature of bursty traffic to reduce the energy consumption of nodes. However, it may not be suitable for dealing with multi-hop bursty traffic and may also suffer from the funneling effect problem when applying in a tree-based network. iQueue-MAC [7] is proposed to deal with bursty traffic by using a hybrid mechanism: CSMA/CA is used in light traffic load while TDMA is used in case of bursty traffic to provide better throughput with support of the multi-channel technique. An optimized low energy adaptive clustering hierarchy (Op-LEACH) [8] allows the nodes with bursty data to get more transmission slots which are released by the nodes without having data during the bursty data transmission. However, this passive way of acquiring slots cannot guarantee the delivery of bursty data in a timely manner. An approach in [9] tries to reduce transmission collision and thus transmits bursty data efficiently by allocating the different channels to the nodes in underwater sensor networks. This approach is complicated by dealing with channel allocation problem, multi-channel hidden terminal problem and missing receiver problem.

The aforementioned MAC protocols mostly deal with the periodic scalar data in general, while they try to transmit bursty data using slot scheduling when necessary. Accordingly, they have difficulty in predicting the amount of time to transmit bursty data since they do not take the time constraint of bursty data into account in designing a slot scheduling and transmission method. In order to solve such kind of problems, the approach in [10] reserves a particular path from an active multimedia node to the sink and then assigns dedicated slots for the nodes along the path for the bursty data transmission. However, without using the slot reuse technique may cause more latency under high traffic load conditions. Therefore, to reduce the bursty data collection time, the approach in [11] uses a channel-slot allocation scheme where the vertically two-hop away nodes along the reserved path are allowed to transmit data simultaneously either if they are located outside of their transmission range or the transmissions of those nodes are performed on different channels. However, this approach requires very tight time synchronization and it only achieves high performance in a long treesize network.

Taking into consideration the requirements of multimedia data applications and the above problems discussed so far, we propose an energy-aware approach with the aim of delivering bursty data in a reliable and timely manner. In this approach, the optimal path from active multimedia nodes to the server is set up with the consideration of bandwidth requirement for multimedia data transmission. Only the nodes along the optimal path will involve transmitting multimedia data, the other nodes get into a sleep state during multimedia data acquisition for conserving energy. Moreover, to shorten the bursty data transmission time, we exploit an efficient scheme that collects the bandwidth demand of the network and then assigns a number of dedicated slots to corresponding nodes based on their demands in an optimal way. Hence, the bursty data are delivered safely to the server in a contention-free manner while satisfying the tight time constraint of multimedia applications. The evaluation results indicate that the proposed approach improves the application performance significantly.

In what follows, the system model is described in Sect. 2. We present the principle design of the proposed approach in Sect. 3. Section 4 covers the performance evaluation. Finally, we make concluding remarks in Sect. 5.

2 System Model

In this paper, we consider a typical model for the safety monitoring and control (SMOCS) system which consists of one server and multiple sinks for collecting data readings from sensors in the network. Typically, there are two types of sensor nodes: *Ordinary sensor* (e.g. gas, heat, light, and humidity) and *multimedia sensor* (equipped with a camera module for taking a still image or video of a monitored object). An ordinary node (*ON*) senses data from environment and sends it to the server periodically. The server collects and then analyzes the data to judge whether a critical event has occurred or not. In case that a critical event is detected in a particular area, the server and/or sink sends a command to request the multimedia node (*MN*) in that spot to send a still image or video stream of the monitored object to confirm the critical situation. In that case, an *MN* with active camera module is called an active multimedia node (*AMN*).

Figure 1 illustrates a typical network model for WMSNs. There are multiple trees where each tree originates at a sink and then connects to other nodes via wireless link to form a tree-topology network. A wireless link can be disrupted due to node failure, battery depletion, or the effect of hard industrial environment. If a node belongs to a specific tree, it is called as a tree-node and the corresponding link is called a tree-link.

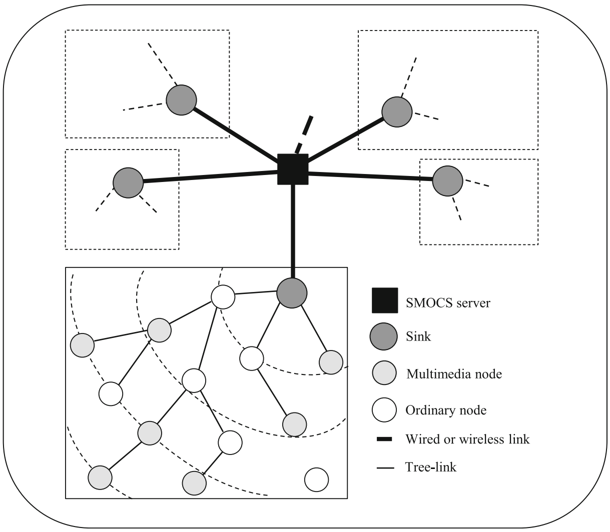

Fig. 1. An example of SMOCS system model

3 Principle Design of the Proposed Approach

3.1 Protocol Operation

The proposed protocol begins with the initial contention period (*ICP*), followed by the MAC Operation period and the multimedia data acquisition period (*MDAP*), as illustrated in Fig. 2.

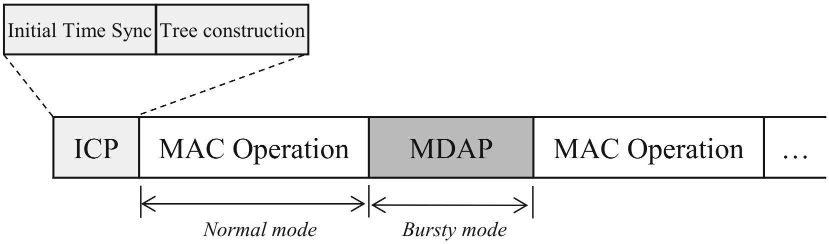

Fig. 2. The structure of the proposed approach operation

In the ICP, a tree is initially constructed and then time synchronization is performed. In this approach, every sensor node works in either of two modes: *normal mode* or *bursty mode*. A node operates in a normal mode in the MAC operation period which follows the ICP. In this mode, sensor nodes can report data readings to the sink periodically by using one of existing MAC protocols. When an abnormal situation is perceived, the sink starts the MDAP by sending a request of multimedia data to a specified multimedia sensor. Then, every node switches to bursty mode for sending or forwarding bursty data. In this paper, we do not explain the protocol operation in the normal mode and limit our discussion to the acquisition of event-driven multimedia data in the bursty mode.

For more convenience, the following notations are used in the rest of the paper as shown in Table 1.

Table 1. Some notations used in the paper

Notation	Definition
$D(i)$	A set of descendant list of node i
$T(i)$	T(i) = D(i) ∪ {i}
$C(i)$	A set of children of node i
$mIDs(i) = \{x \mid x \in T(i) \wedge x = MN\}$	A set of multimedia nodes in the subtree of node i
$mIDs^A(i) = \{x \mid x \in T(i) \wedge x = AMN\}$	A set of multimedia nodes in the subtree of node i
η_i	The number of packets generated by node i
S_i	A sending bandwidth demand of node i
R_i	A receiving bandwidth demand of node i
B_i	Total bandwidth demand of node i

3.2 Tree Construction

At the initialization, all nodes cooperate to build a tree which is rooted at the sink (as shown in Fig. 1). A link (i, j) is said to be *reliable* if node i can transmit a packet to node j successfully when there is no interference. Then, we can construct a robust tree such that every tree-link is bi-directionally reliable (*B-reliable*) [2].

Tree construction is initiated by an *advertisement* (*ADV*) message issued by the sink which is the only tree member at the initialization stage. Upon receiving the *ADV* message, an orphan that has a *reliable link* joins the sink by sending a *join request (JREQ)* message. A sending node attaches a set of its neighbors with a reliable link in the *ADV* message or the *JREQ* message so that the receiver can determine whether it has a *B-reliable* link to the sender or not. Upon receiving *JREQ*, the member sends a *join response* (*JRES*) message and takes the orphan as its child if the corresponding link between them is *B-reliable*. When the orphan receives *JRES*, it takes the member as its parent. Another orphan who has overheard *JREQ* can take the same procedure to become a member if its corresponding link is *B-reliable*. If an orphan overhears *JREQs* from multiple members with *B-reliable* links, it pairs with a member that has the shortest distance to the sink. During the operation time, if a certain node detects the failure of the link to its parent, it tries to find one neighbor that can provide the *B-reliable* link and shortest distance to the sink and then joins that node by sending *JREQ*.

3.3 Data Transmission Model and Our Motivation

In the previous work [12], a sharable slot is allocated to each level of a tree, starting from the nodes at the highest level down to those at the lowest one, and then data transmission is performed progressively in the level-order fashion (as shown in Fig. 1). Accordingly, interference or contention is narrowed down to the nodes located at the same level. However, within a sharable slot, those nodes also have to compete against other sibling nodes for data transmission, thereby increasing latency and network overhead when traffic load goes high. To overcome this problem, in our approach, instead of using a big sharable slot, a small fixed slot is assigned to each node dedicatedly. The proposed approach is twofold. *First*, for the nodes belonging different sibling groups, a dedicated channel is allocated to each parent node to receive data from its children (which is done by the distributed channel allocation scheme presented in [9]). *Second*, for the nodes within the same sibling group, each node is assigned a number of dedicated slots proportional to its bandwidth demand.

Figure 3 illustrates the operation of the proposed approach. Two different sibling groups belonging to two different parent nodes (e.g. x and y) work on different channels (channel X and channel Y, respectively), therefore channel contention can be narrowed down to a group of sibling nodes having the same parent. It is obvious that the fewer sibling nodes in the level of the tree, the less competition in channel access.

Suppose that a node x has m children, thus it has a sibling group, represented as $S(x) = \{x_1, x_2, \ldots, x_m\}$. By using a scheduling algorithm, each node in $S(x)$ is assigned a number of distinct slots for data transmission based on their bandwidth requirements. Note that, since two sibling groups work on different channels, their scheduled slot time can be overlapped each other, thereby contributing to reducing latency significantly.

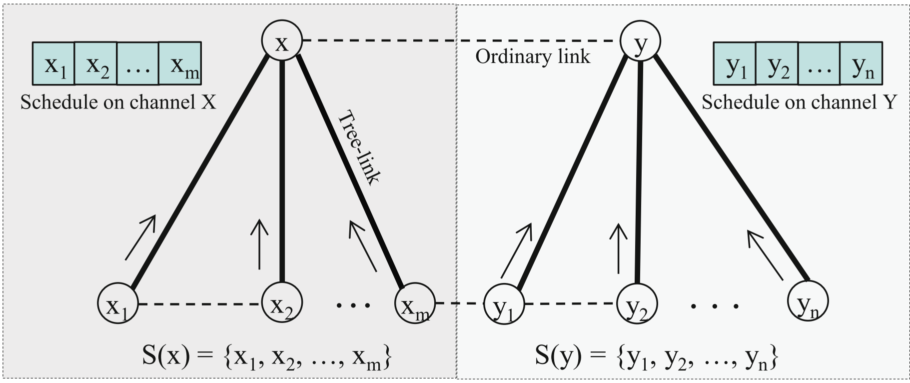

Fig. 3. Data transmission model.

3.4 Event-Driven Multimedia Data Acquisition

In this section, we describe the operation of the proposed approach for the acquisition of multimedia data in the bursty mode.

Initially, upon detecting an abnormal event in the monitoring field, the sink *S* starts the multimedia path setup phase by sending a special message, called a multimedia data request message (*MREQ*), to the specified multimedia node(s) in that area. When receiving *MREQ*, an intermediate node, if it found that the target multimedia node locates in its subtree, will forward *MREQ* toward the target *MN* node; otherwise, *MREQ* will be discarded. Then the process is continued until *MREG* reaches the target *MN* nodes. Upon receiving MREQ, an *MN* becomes active (called *AMN*) and then sends resource reservation request message (*RRREQ*) to the sink with the information of its bandwidth demand. The intermediate node located on the path from the *AMN* to the sink becomes the forwarding node and then forwards *RRREQ* to the upstream node until it reaches the sink. Upon receiving *RRREQ*, the sink responds to the resource request by broadcasting a resource reservation response (*RRRES*) message. Every node, except for the leaf nodes, needs to rebroadcast *RRRES*.

Note that *RRRES* contains the information of the slot schedule for every node locating on the multimedia transmission path. Therefore, upon receiving *RRRES* from the sink, the *AMN* starts sending its bursty data within the duration of the MDAP according to the assigned schedule. The intermediate nodes located on the path from the *AMN* to the sink need to forward those bursty data, whereas the others get into a sleep state to conserve bandwidth and energy. The structure of some messages used in the path setup phase is shown in Table 2.

Table 2. Multimedia path setup message structure

Path setup message	Description
$MREQ = (mIDs(s))$	*Multimedia data request message*
$RRREQ(i) = (\eta_i, S_i, R_i)$	*Resource reservation request message*
$RRRES(i) = (mIDs^A(i), MDAP)$	*Resource reservation response message*

During the multimedia path setup phase, based on each node's bandwidth demand, the sink produces a slot scheduling which defines the time that a node is allowed to work on. As shown in Eq. (1), bandwidth demand B_i of a node i consists of two parts: (i) *sending-bandwidth demand* S_i which corresponds to the number of necessary slots for sending all data packets in its subtree $T(i)$, and (ii) *receiving-bandwidth demand* R_i which corresponds to the number of required slots for collecting data from its children. Therefore, the bandwidth demand B_i can be presented as follows:

$$B_i = S_i + R_i \tag{1}$$

where S_i and R_i are determined by:

$$S_i = \sum\nolimits_{k \in T(i)} \eta_i \tag{2}$$

$$R_i = \begin{cases} \left(\sum\nolimits_{x \in C(i)} S_x\right) + max\{R_x \mid x \in C(i)\} & \text{where } C(i) \neq \emptyset \\ 0 & \text{otherwise} \end{cases} \tag{3}$$

As discussed in Sect. 3.3, data transmission is performed according to the parent-children relationship in the tree. In fact, if two nodes have the same parent, they cannot send data at the same time because of the physical characteristic of a wireless transceiver. However, two distinct nodes can receive data from their children in parallel if no interference between two pairs of data transmissions. Therefore the receiving bandwidth demand of a node is determined as the sum of the sending-bandwidth demands of its children and the maximum of the receiving-bandwidth demand of its children as shown in Eq. (3).

Figure 4 shows an example of the multimedia path setup phase. The network topology consists of one sink S, five multimedia nodes (*nodes 1, 3, 4, 6* and *7*) and three ordinary nodes. Suppose that in this example, the sink S only needs to get multimedia data from *nodes 4, 6* and *7*.

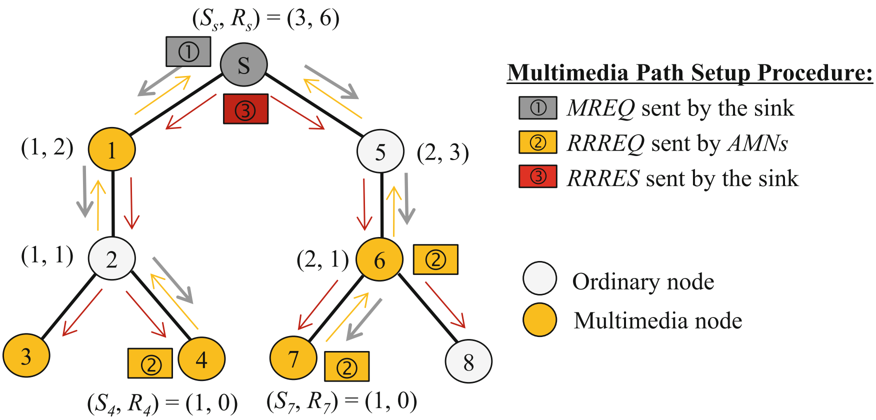

Fig. 4. An example of path setup procedure

Initially, the sink sends *MREQ* = {4, 6, 7} to notify that it wants to get data from nodes 4, 6, and 7. The intermediate nodes (1 and 5) forward *MREQ* toward its children until it reaches the destination. Upon receiving *MREQ*, nodes 4, 6 and 7 respond with *RRREQ* including the bandwidth demand for sending multimedia data. In this example, each *AMN* sends only one packet in each round.

In Fig. 4, node 7 sends *RRREQ* with $(S_7, R_7) = (1, 0)$ since it needs 01 slot for sending one data packet in each round, and no need slot for receiving since it has no children. Similarly, node 6 sends *RRREQ* with $(S_6, R_6) = (2, 1)$ since it needs to send two data packets (one is its own and the other is from its child) and receive one packet from its child (node 7). Finally, the sink needs totally 6 slots for receiving data from the network in each round of data collection.

4 Performance Evaluation

4.1 Simulation Setup

For performance evaluation, the proposed approach is compared with the slot demand-based path reservation (SDPR) approach [7], which has shown the good performance for bursty data transmission in WMSNs, by using the QualNet network simulator [13].

In the simulations, sensor nodes are static and randomly distributed in a square terrain of 100 × 100 (m^2). Since we consider the performance of bursty data acquisition, the performance metrics are evaluated based on that activity only. In each critical event, a burst of data has 100 data packets (each of 127 bytes) that are generated at a multimedia source node. A critical event is generated randomly in the network. Some key simulation parameters and values in the simulations are shown in Table 3.

Table 3. Simulation parameters

Parameter	Value
Default transmission power	−25 dBm (power level 3)
Sensor energy model	MicaZ
Path loss model	2-ray
Noise factor	10 dB
Slot size	6 ms
Dimensions	100 × 100 (m^2)
Simulation time	600 s
Number of nodes	1 sink; 25 sensor nodes
Data packet length	127 bytes
Bursty data load (each event)	100 packets

4.2 Simulation Results and Discussions

(1) Data Acquisition Time

In WMSNs, data readings from the monitored environment have to be reported to the sink or server within a specified time (*application deadline*). It means that the received data can be useless, even though it is received at the sink successfully. Therefore, in this paper, to evaluate whether a protocol can satisfy the requirement of the multimedia application, we use *data acquisition time* which is defined as the duration to send a burst of data packets from the multimedia source nodes to the sink.

Figure 5 compares the data acquisition time of the two protocols according to the variation of the number of AMNs which are requested to send multimedia data to the sink. We can see that two approaches have linearly increasing curves when increasing the number of AMNs. However, our proposed approach can achieve the better performance in term of data acquisition time and it can reduce the data acquisition time more than 30% compared with SDPR. Since the slot reuse technique is not used in SDPR, the transmission delay increases largely under the high traffic loads. However, our proposed approach allows two pairs of nodes to send data in parallel if they do not interfere with each other. Therefore, the data acquisition time is significantly reduced, thereby satisfying the tighter time constraint of multimedia applications.

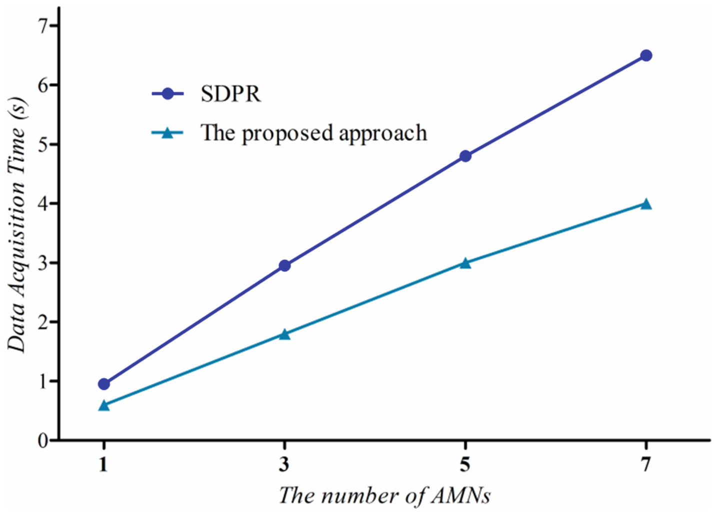

Fig. 5. Data acquisition time

(2) Energy Consumption

Energy is one of major concerns in WMSNs because of the difficulty in battery replacement, and therefore minimizing energy consumption of a sensor node is a main issue that needs to be considered [2]. A wireless transceiver of a node (e.g., CC2420 transceiver module in TelosB or Kmotes) usually consumes much more energy than the other components. Therefore, the operation of wireless transceiver should be controlled in an effective way to extend the network lifetime. For example, the radio should be in active state when processing data, and go to sleep state to conserve energy when having no data.

In this paper, we use *energy consumption* to evaluate how effectively a protocol spends energy in data transmission. Energy consumption can be calculated by measuring total energy consumed by all sensor nodes (except for the sink) and then dividing it by the total number of packets received at the sink.

Figure 6 shows the results of the two approaches in terms of energy consumption. We can see that the energy consumption in our proposed approach is much lower than the one in SDPR. Actually, to support for bursty data transmission, both approaches also reserve a path from the source of multimedia data to the sink. The other nodes which are outside of this path get into a sleep state to conserve energy. However, our approach can reduce the time to acquire multimedia data by allowing the concurrent data transmissions. As a result, the time of a node in active state is also reduced, thereby lowering the energy consumption significantly.

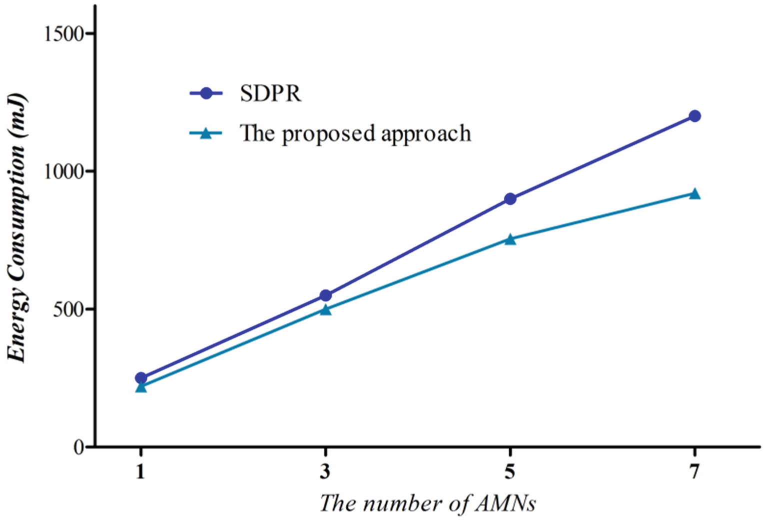

Fig. 6. Energy consumption per successfully received packet at the sink.

5 Concluding Remarks

In this paper, we propose an efficient approach for event-driven multimedia data acquisition in WMSNs that not only delivers bursty data reliably from the multimedia node to the sink, but also reduces bursty data acquisition time significantly by allowing the concurrent data transmission. Moreover, the network operation is fully controlled by the sink. The source node and the corresponding upstream nodes are assigned a number of slots enough for bursty data transmission while the others get into sleep state for saving energy. In this way, the source node can deliver bursty data packets to the sink successfully in a contention-free manner while satisfying the tighter time constraint of bursty data acquisition.

References

1. Wen-Zhan, S., Renjie, H., Shirazi, B., LaHusen, R.: TreeMAC: localized TDMA MAC protocol for real-time high-data-rate sensor networks. In: 2009 IEEE International Conference on Pervasive Computing and Communications (PerCom 2009), pp. 1–10 (2009)
2. Oh, H., Van Vinh, P.: Design and implementation of a MAC protocol for timely and reliable delivery of command and data in dynamic wireless sensor networks. Sensors **13**, 13228–13257 (2013)
3. Jungsook, K., Jaehan, L., Pelczar, C., Byungtae, J.: RRMAC: a sensor network MAC for real time and reliable packet transmission. In: IEEE International Symposium on Consumer Electronics (ISCE), pp. 1–4 (2008)
4. Bernardo, L., Agua, H., Pereira, M., Oliveira, R., Dinis, R., Pinto, P.: A MAC protocol for mobile wireless sensor networks with bursty traffic. In: IEEE Wireless Communications and Networking Conference (WCNC), pp. 1–6 (2010)
5. Ringwald, M., Romer, K.: BurstMAC - an efficient MAC protocol for correlated traffic bursts. In: 2009 Sixth International Conference on Networked Sensing Systems (INSS), pp. 1–9 (2009)
6. Ray, S., Demirkol, I., Heinzelman, W.: ATMA: advertisement-based TDMA protocol for bursty traffic in wireless sensor networks. In: IEEE Global Telecommunications Conference (GLOBECOM 2010), pp. 1–5 (2010)
7. Zhuo, S., Wang, Z., Song, Y.Q., Wang, Z., Almeida, L.: iQueue-MAC: a traffic adaptive duty- cycled MAC protocol with dynamic slot allocation. In: 10th Annual IEEE Communications Society Conference on Sensor, Mesh and Ad Hoc Communications and Networks (SECON), pp. 95–103 (2013)
8. Gambhir, S., Fatima, N.: Op-LEACH: an optimized LEACH method for busty traffic in WSNs. In: 2014 Fourth International Conference on Advanced Computing & Communication Technologies (ACCT), pp. 222–229 (2014)
9. Chao, C.M., Lu, M.W., Lin, Y.C.: Energy-efficient multichannel MAC protocol design for bursty data traffic in underwater sensor networks. IEEE J. Oceanic Eng. **40**(2), 1–8 (2014)
10. Van Vinh, P., Oh, H.: A slot demand-based path reservation approach for the timely and reliable delivery of bursty traffic in WMSNs. Concurrency Comput. Pract. Experience **27** (10), 2569–2587 (2015)
11. Van Vinh, P., Oh, H.: An optimized approach for time-constrained and reliable bursty data acquisition in WMSNs. Int. J. Distrib. Sens. Netw. **11**(6), 826937 (2015)
12. Van Vinh, P., Oh, H.: Optimized sharable-slot allocation using multiple channels to reduce data- gathering delay in wireless sensor networks. Sensors **16**, 505 (2016)
13. QualNet simulator. http://web.scalable-networks.com/content/qualnet

Program Popularity Prediction Approach for Internet TV Based on Trend Detecting

Chengang Zhu[1,2], Guang Cheng[1,2](✉), and Kun Wang[3]

[1] School of Computer Science and Engineering, Southeast University, Dhaka, Bangladesh
{cgzhu, gcheng}@njnet.edu.cn

[2] Key Laboratory of Computer Network and Information Integration, Ministry of Education, Southeast University, Dhaka, Bangladesh

[3] School of Internet of Things, Nanjing University of Posts and Telecommunications, Nanjing, China
kwang@njupt.edu.cn

Abstract. Predicting program popularity precisely and timely is of great value for content providers, advertisers, as well as Internet TV operators. Existing prediction methods usually need large quantity of samples and long training time, while the prediction accuracy is poor for the programs that experience a high peak or sharp decrease in popularity. This paper presents our improved prediction approach based on trend detecting. First, we apply a dynamic time warping (DTW) distance based k-medoids algorithm to group programs popularity evolution into 4 trends. Then, 4 trend-specific prediction models are built separately using random forests (RF) regression. According to the features extracted from electronic program guide (EPG) and early view records, newly published programs are classified into the 4 trends by a gradient boosting decision tree. Finally, combining forecasting values from the trend-specific models and classification probability, our proposed approach achieves better prediction results. The experimental results show that, compared to the existing prediction models, the prediction accuracy can increase more than 20%, and the forecasting period can be effectively shortened.

Keywords: Internet TV · Popularity prediction · Dynamic time warping
Random forests regression · Gradient boosting decision tree

1 Introduction

With the maturity and popularity of high-definition (HD) and 3D technology, IP video traffic will be a major part of all consumer Internet traffic. According to data published by Cisco Visual Networking Index at July 2016 [1], Internet video to TV will continue to grow at a rapid pace, which will be 26% of consumer Internet video traffic by 2020. Nevertheless, users' attention is not uniformly distributed among all programs. Only a few of programs can attract massive user's attention, and the rest will be left without anybody to care for it. Take Tencent video for example [2], the cumulative requests for the top 50 programs is 45 billion, which is more than 80% of the total requests.

© ICST Institute for Computer Sciences, Social Informatics and Telecommunications Engineering 2018
Y. Chen and T. Q. Duong (Eds.): INISCOM 2017, LNICST 221, pp. 142–154, 2018.
https://doi.org/10.1007/978-3-319-74176-5_14

In this context, it is of great importance to predict the popularity of Internet TV programs. First, using the program popularity prediction results, audience will save much time to find more valuable TV programs from mass video resource. Secondly, based on program popularity forecasting data, commercial company is able to maximize advertising effect by choosing the TV programs with highest potential. Finally, with the help of popularity prediction model, the Internet TV operator can optimize configuration of network in advance by deploying enough transmission and storage resource to distribution hot programs.

However, accurately predicting the popularity of Internet TV programs is a quite challenging task. First of all, there are a lot factors to influence TV program popularity which is hard to measure, such as the quality of the program and the interests of audience. Then the relationship between hot events in real world and TV programs cannot be easily introduced in the prediction model. Last but not least, there is a massive gap between the popularity evolution of different programs, which should be considered when designing the prediction model. In this paper, cooperating with an Internet TV operator, we analyze massive user behavior data and present our improved method to predict the popularity for Internet TV programs. The main contribution of our work is as follows:

1. We apply a dynamic time warping (DTW) distance based k-medoids algorithm to group programs with similar popularity into 4 evolution trends, which has the ability to capture the inherent heterogeneity of program popularity. It's computationally more efficient than previous methods used to delineate popularity evolution trends, such as K-Spectral Clustering (KSC) models [3]. Computation in these models is always extensive due to model training and the transformation of features in semantic spaces. By contrast, the DTW distance based k-medoids algorithm is directly driven by raw data. Our method can be implemented without much human intervention, and has a much lower computational cost.
2. We build trend-specific prediction models using random forests (RF) regression, which have an overall higher predictive performance than a single model trained from the entire data set. The popularity prediction model trained separately from different popularity trends data sets can focus on particular types of programs, reduce the effects of noise. To our knowledge, we are the first to tackle the inherent challenges of predicting Internet TV program popularity combining forecasting values from the trend-specific models and classification probability.

The proposed method is evaluated with the data collected from Jiangsu Cloud-media TV, one of the largest Internet TV platforms in China. The rest of this paper is organized as follows. Section 2 discusses related work, whereas Sect. 3 formally presents our new Internet TV program popularity prediction model. Our evaluation methodology and main results are discussed in Sect. 4. Section 5 concludes this paper.

2 Related Works

Due to the rich variety and strong timeliness, semantic understanding of Internet TV programs is more difficult than that of news, microblogging and other web content. An ideal prediction model for Internet TV programs not only needs high prediction accuracy, but also needs good calculation performance, which means prediction result should be given before audience interest fades. At present, there is little research on program popularity prediction of Internet TV. The existing popularity prediction methods are for other media forms, but can be used as a reference. Commonly used web content popularity prediction methods include cumulative growth, temporal analysis and evolution trends.

Cumulative growth. Some researchers studied the cumulative growth of attention, such as the amount of attention that one item received from the moment it was published until the prediction moment. Kaltenbrunner et al. [4] proposed that depending on the time of the publication, news stories followed a constant growth. A log-linear model was proposed by Szabo and Huberman [5], outperformed the constant growth models in terms of mean squared error (MSE). A different approach was proposed by Lee et al. [6]. They used survival analysis model to detect the threads that would receive more than 100 comments in MySpace with 80% accuracy. Tatar et al. [7] used a simple linear regression based on the early number of comments to predict the final number of comments for news articles. Kim et al. [8] used a linear model on a logarithmic scale to predict popularity ranges for political blog posts. Predicting the popularity of web content, based on the aggregate user behavior, has also been addressed as a classification problem. Jamali and Rangwala [9] trained different classification methods to predict the popularity class of a Digg story with an accuracy of 80%. Wang et al. [10] proposed a local data processing architecture to solve the problem of rapid analysis and processing of massive data.

Temporal analysis. Some researchers performed a temporal analysis of how content popularity evolved over time until the prediction moment. Pinto et al. [11] relied on a multivariate linear regression model to predict the popularity of YouTube videos. Maass et al. [12] built a large recurrent neural network that could consider more complex interactions between early and late popularity values. Gürsun et al. [13] observed that the daily number of views could be modeled through a time series prediction model using Autoregressive Moving Average (ARMA). Wang et al. [14] presented a novel model for enhancing classification precision and reducing network overload

Evolution trends. Other researchers used clustering methods to find web items with similar popularity evolution trends. Crane and Sornette [15] observed that a Poisson process could describe the attention around the majority of videos and the remaining ones followed three popularity evolution trends. Ahmed et al. [16] proposed a model that used a more granular description of the temporal evolution of content popularity, which showed a significant improvement over the log-linear model. Wang et al. [17] proposed a context-aware system architecture to realize accurate detection of the leak points in large-scale petrochemical plants.

Most of the previous studies focus on building a general model to predict popularity of certain content in some media, but neglect the fact that there is massive gap between contents popularity evolution progresses. That leads those methods are generally ineffective for programs popularity prediction of Internet TV, especially when predicting programs with early peaks and later bursts of accesses. To our knowledge no other work has studied the predictive power of features extracted from electronic program guide. In summary, we are first to detect different popularity evolution trend of Internet TV automatically, and develop an integrated predicting model combining forecasting values from the trend-specific models and classification probability.

3 Methodology

3.1 Problem Statement

The program popularity prediction problem can be defined as follows. Let $c \in C$ be an individual program from a set of programs C observed during a period T. We use $t \in T$ to describe the age of a program (i.e., duration since the time it was published) and mark two important moments: indication time t_i, representing the time we perform the prediction and reference time t_r, the moment of time when we want to predict program popularity. Let $N_c(t_i)$ be the popularity of c from the time it was published until t_i and $N_c(t_r)$ be the value that we want to predict, i.e., the popularity at a later time $N_c(t_r)$. We define $\hat{N}_c(t_i, t_r)$ at the prediction outcome: the predicted popularity of program c at time t_r using the information available until t_i. Thus, the better the prediction, the closer $\hat{N}_c(t_i, t_r)$ is to $N_c(t_r)$.

3.2 Method Overview

Our method follows 3 steps. The first step is to detect popularity evolution trends. We calculate the DTW distances between historical-record time series and try to cluster popularity evolution into optimal trends. 11 static features extracted from EPG are introduced to strengthen the result of clustering. A few trials are performed to determine an appropriate value for the number of popularity trends (k) in our case study (Fig. 1).

The second step is to build trend-specific prediction model using RF regression. We spilt the view records into 4 groups according to the above trends, and feed them to the RF regression model together with static features.

The third step is to use gradient boosting decision tree (GBDT) to classify newly published programs popularity into the trends, and get the final prediction results based on the prediction values of 4 models and the probability of classification.

A pictorial representation is shown in Fig. 3. Compared to existing methods, our approach incorporates multiple trend-specific forecasting models, combines the predicting results with probability of each program belonging to each tend, and leads to better results.

3.3 Popularity Trend Detecting

In this section, we describe the details of our method for k-medoids [18] clustering of program popularity time series with DTW [19] distance. DTW distance is an accurate similarity measurement which is generally used for time series data. An optimal

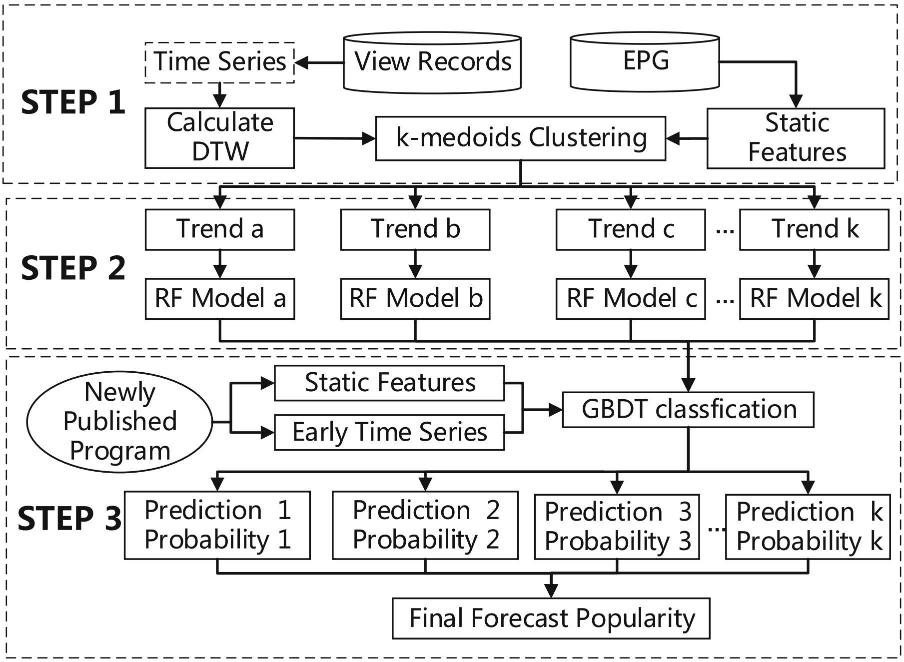

Fig. 1. Overview of Internet TV program popularity prediction method

alignment and distance between two sequences $P = (p_1, p_2 \ldots p_n)$ and $Q = (q_1, q_2 \ldots q_m)$ can be determined as follows:

$$DTW(P, Q) = \sqrt{dist(p_n, q_m)} \tag{1}$$

$$dist(p_i, q_j) = (p_i - q_j)^2 + \min \begin{cases} dist(p_{i-1}, q_j) \\ dist(p_i, q_{j-1}) \\ dist(p_{i-1}, q_{j-1}) \end{cases} \tag{2}$$

DTW distance is calculated through dynamic programming to discover the minimum cumulative distance of each element in $n \times m$ matrix. In addition, the warping path between two sequences can be found by tracing back from the last cell. Wang et al. [20] proposed an interests-based reduced variable neighborhood search queue architecture to process large amounts of data. In this work, DTW distance is used to measure the similarity between each program popularity time series data and cluster centers to give more accurate results.

The k-medoids algorithm is similar to the well-known k-means for performing clustering analysis. However, these two methods differ in how they update the center location for a certain cluster. In the k-means approach, the center of a cluster is indeed virtual, because it denotes the mean position of the members that are currently within the cluster. However, the k-medoids method treats the center as the median of the cluster, which thus coincides with one of the actual members. Owing to this difference, k-medoids is more robust in responding to the outliers in the dataset.

The k-medoids based on DTW algorithm is described briefly as in Algorithm 1. First, we arbitrarily choose k programs in D as the initial medoids, and assign each remaining program to the cluster with the nearest medoids. Then we randomly select a non-medoid program to compute a new DTW distance of the trends. If the new DTW distance is less than the previous one after the swapping, we swap to form a new set of k medoids. Above steps are repeated until there is no change of programs in each trend.

Algorithm KMDTW(D,C)

D: the data set containing program popularity time series
C: the number of trends
K: the set of trend centers
M: the set of popularity sequences in each trend
initialize C as trend centers of K
do
    for i = 1:size(D)
        for k = 1:K
            $Dist_{Di,Ck}$ = DTW(D_i,C_k)
        end for
        if($Dist_{Di,Ck}$ is min)
            assign D_i into M_k
        end if
    end for
while(the cluster membership changes)
return K,M

3.4 Trend-Specific Prediction Models

In this section, we describe the details of training trend-specific prediction models using RF regression [21]. RF is an extension of bagging and a competitor to boosting. It uses either categorical (i.e., classification) or continuous (i.e., regression) response variables, and either categorical or continuous predictor variables. In RF modelling, the training parameters that needed specification were: (i) the number of trees to grow in the forest (n tree), the number of randomly selected predictor variables at each node (m try), and the minimal number of observations at the terminal nodes of the trees (node size). In our study, those were set to 1000, 12, and 5, respectively. The default of n tree was 500, but it has been observed that more stable results for estimating variable importance are achieved with a higher number. The training data that were left out of the bootstrap (i.e., Out-Of-Bag, OOB) samples were used to estimate prediction error and variable importance. In error estimation, the OOB samples were predicted by the respective trees and by aggregating the predictions, the mean square error of OOB was calculated by (3).

$$MSE_{OOB} = \frac{1}{N}\sum_{i=1}^{N}(y_i - \hat{y}_{i_{OOB}})^2 \tag{3}$$

Where $\hat{y}_{i_{OOB}}$ is the OOB prediction for observation y_i. Regarding variable importance, the values of a specific predictor variable were randomly permutated in the OOB data of a tree while the values of other predictors remain fixed. The modified OOB data were predicted, and the differences between the MSEs obtained from the permutated and original OOB data gave a measure of variable importance. In our dataset, we will use the attributes of the Internet TV programs, the first-7-day view records and some derivation as the predictor, and the 30th day records as y. For each cluster, we train a unique model to fit the dataset.

3.5 Classification of Newly Published Programs Popularity

Gradient Boosting Decision Trees (GBDT) [22] is an additive regression model consisting of an ensemble of decision trees. A single decision tree has the problem of over-fitting, however the GBDT algorithm can overcome this by combining hundreds of weak decision trees consisting of a few leaf nodes. GBDT owns a few advantages, including the ability to find non-linear transformations, the ability to handle skewed variables without requiring transformations, computational robustness and high scalability.

In this paper, we build decision trees to classify newly published programs into 4 popularity evolution trends. 11 attributes of program are extracted from electronic program guide, which are described in Table 1.

Table 1. Description of attributes extracted from EPG

Attribute	Description
Time	The time when the program is firstly published
Name	The formal name or nickname of the program
Duration	Time length of the program
Actors	The names of main actors and actresses
Director	The names of directors for the program
Language	The language for dialogue and subtitle
Area	The country where the program is filmed
Category	The type of the program, such as news, cartoon
Rating	The scores given by douban.com
Publisher	The program production company name
Summary	Brief introduction of the program

Those attributes and first-7-day view records are predictors and the 4 trends are the targets of classification. With the help of GBDT and RF prediction model, for each program, we get its probabilities P_{cj} of belonging to each trend k and the temporary popularity value $\hat{N}_{ck}(t_i, t_r)$ predicted by corresponding model. To maximize the information gain, we use Eq. 4 to calculate the final predicted popularity of program c at time t_r using the information available until t_i.

$$\hat{N}_c(t_i, t_r) = \sum_{k=1}^{4} P_{ck}\hat{N}_{ck}(t_i, t_r) \tag{4}$$

4 Experiments

4.1 Datasets

The experiment data originates from Jiangsu Cloud-media TV, one of the largest Internet TV platforms in China. The data set is summarized in Table 2. It contains Internet TV requests over 213 days between January 1st and July 31st 2016. During this period 423254 programs were requested. The data set includes more 1.3 million clients making more than 2 billion requests.

Table 2. The data sets in figures

	Requests	Programs	Clients
Daily max	2300747	20447	407133
Daily min	1066706	17552	225290
Daily median	1678506	19098	318052
Total	201420717	423254	1309381

By cleaning the RTSP (Real Time Streaming Protocol) packets from video server and the analysis of the EPG information, we obtained programs popularity time series and 11 static features for 110 thousand program. The static features include the directors' name, writers' name and actors/actresses' name, country, language, categories, duration, premiere channel, premiere time and content description. These experiment results were computed using 10-fold cross. We split the dataset into 10 folds, where 9 are used as training set and one as test set and rotate the folds such that each fold is used for testing once.

4.2 Performance Metrics

A comprehensive and reasonable error analysis can effectively evaluate the performance of the prediction model. Commonly used metrics are divided into the absolute ones, i.e., MSE, RMSE (Root of MSE) Eq. (5) and MAE (Mean Absolute Error), and the relative ones, i.e., MRE (Mean Relative Error) and MRSE (Mean Relative Squared Error). When using the absolute metrics, researchers have to make a clear understanding of the numerical range of the prediction values. Relative metrics are useful to compare the efficiency of prediction algorithm across studies, except for actual values is zero. The quality of a numerical prediction can also be reported using the correlation coefficient or the coefficient of determination (R^2) Eq. (6). In order to compare the performance between existing methods to ours and avoid the zero-inflated problem, we choose RMSE and R^2 as performance metrics.

$$\mathrm{RMSE} = \sqrt{\frac{1}{|C|}\sum_{c \in C}\left(\hat{N}_c(t_i, t) - N_c(t_r)\right)^2} \tag{5}$$

$$\mathrm{R}^2 = 1 - \frac{\sum_{c \in C}\left(N_c(t_r) - \hat{N}_c(t_i, t)\right)^2}{\sum_{c \in C}\left(N_c(t_r) - \bar{N}_c(t_r)\right)^2} \tag{6}$$

4.3 Prediction Results

We use the scikit-learn [23], a Python machine learning package, to implement the required clustering and regression algorithms in this study. A few trials are performed to determine an appropriate value for the number of popularity trends (k) in our case study. This is achieved by running the DTW distance based k-medoids method with different values of k (ranging from 2 to 10). Figure 2 shows that as the value of k increases, the DTW distance value between different trends decreases significantly, reaching 8.3 at k = 4. However, the speed of DTW distance value decreasing is much slower when k is within [5, 10]. That means clustering program popularity into more trends than 4 will not improve the accuracy of the predicting model, but degrade the performance. Therefore, we decide to cluster the popularity evolution of Internet TV program into 4 categories.

Figure 3 shows the popularity trends discovered in our dataset. Each graph shows the number of views as function of time. We note that the 4 categories of trends produced by k-medoids based on DTW distance algorithm, are consist with similar shapes identified in other research [3, 11]. Although the 4 trends cannot match popularity evolution progress of all programs, the most prevalent trends are detected which can greatly improve the accuracy of our prediction models.

We measured the RMSE and R^2 to evaluate the prediction performance, and compared our prediction method with three other existing method: Szabo-Huberman (S-H) [5], Multivariate Linear [7] and MRBF model [11]. Table 3 shows the MRSE results produced by all 4 models, considering $t_i = 7$ and $t_r = 30$. Result for other values of t_i and t_r are quite similar. The overall MRSE reductions achieved with our model over the others, across all trends, are 20% for the datasets. The grains are especially large for trend c which popularity reaches a high peak and then declines sharply.

Figure 4 shows the coefficient of determination (R^2) values produced with different indication time by all 4 models. As the history data accumulates, R^2 values are close to 100%. The sooner reliable prediction results are made, the more profitable Internet TV service is. To get 95% R^2, other 3 models at least need collect popularity data of 12 days while our model needs only 9 days, which means our model can give a reliable result much earlier.

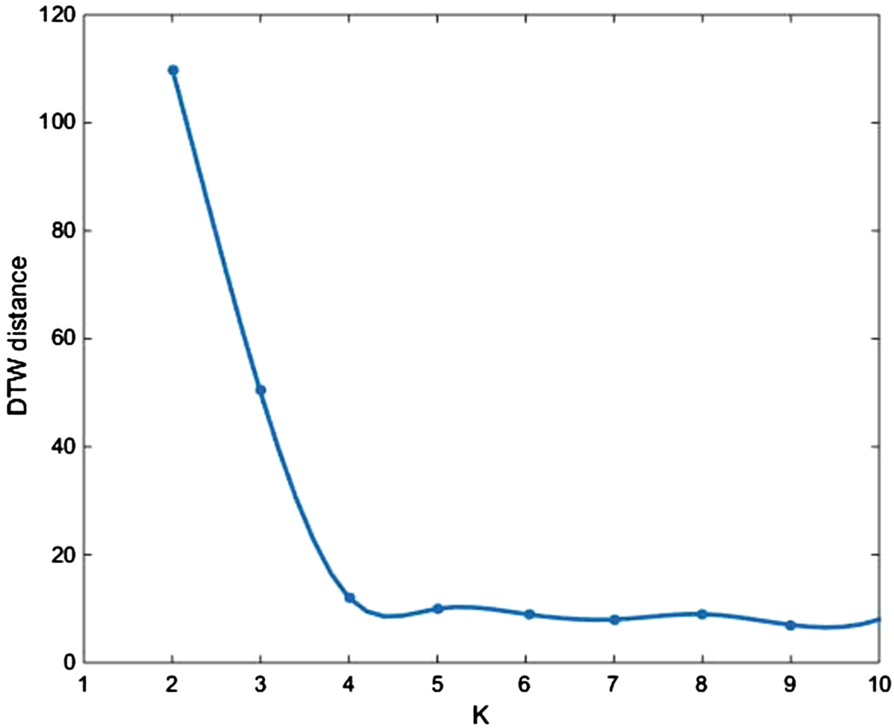

Fig. 2. The DTW distance between trends with different values of k

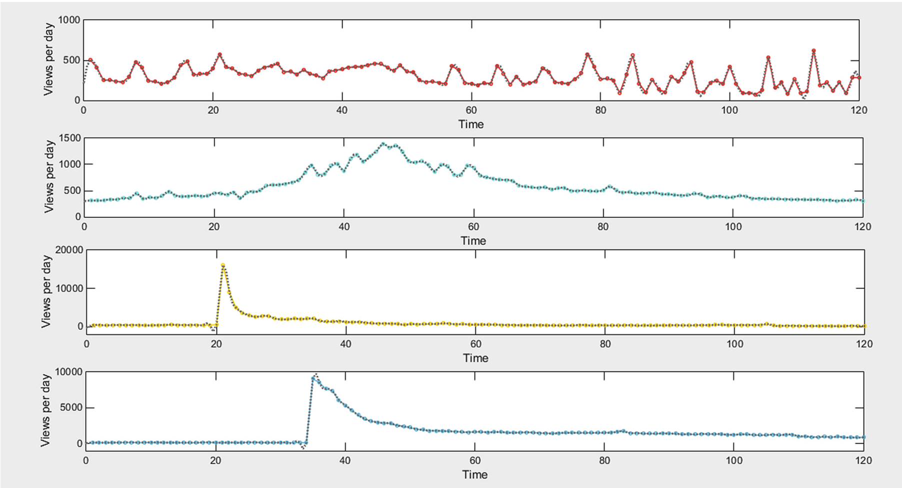

Fig. 3. Prevalent popularity trends of Internet TV programs

Table 3. Prediction RMSE for S-H, ML, MRBF and our models for programs with different popularity trends.

Popularity trend	Numbers of programs	S-H	ML	MRBF	Our model
Trend a	1554	0.4588 ± 0.0283	0.1402 ± 0.0274	0.1268 ± 0.0319	0.1039 ± 0.0263
Trend b	80528	0.2086 ± 0.0040	0.1788 ± 0.0041	0.1713 ± 0.0040	0.1576 ± 0.0040
Trend c	6636	0.1921 ± 0.0124	0.1707 ± 0.0283	0.1490 ± 0.0199	0.1302 ± 0.0172
Trend d	24143	0.3351 ± 0.0099	0.2929 ± 0.0120	0.2641 ± 0.0111	0.2223 ± 0.0104
Overall	112861	0.2382 ± 0.0038	0.2022 ± 0.0043	0.1892 ± 0.0032	0.1677 ± 0.0028

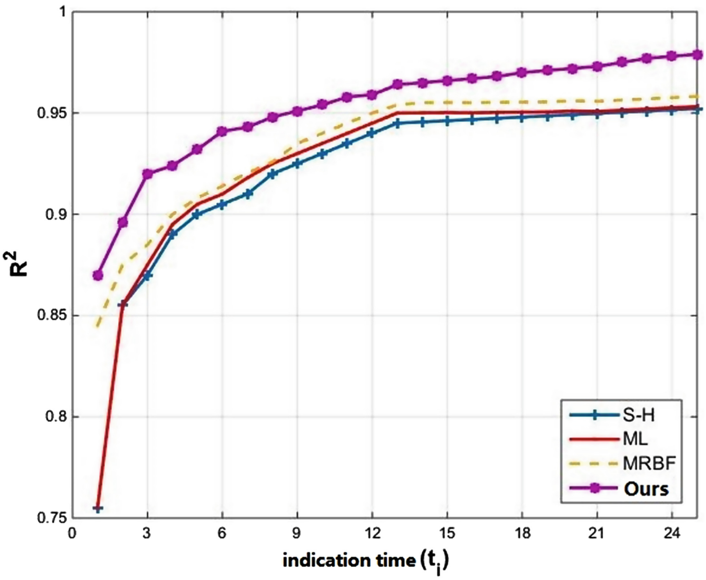

Fig. 4. Comparison of coefficient of determination as function of indication time

5 Conclusions

In this paper, we have analyzed massive user behavior data and presented our improved method to predict the popularity for Internet TV programs. To the extent of our knowledge, we are first work to tackle the problem of prediction of programs popularity in Internet TV platform. We applied a dynamic time warping (DTW) distance based k-medoids algorithm to group programs with similar popularity into 4 evolution trends, which has the ability to capture the inherent heterogeneity of program popularity. Moreover, we built trend-specific prediction models using random forests regression, which have an overall higher predictive performance than a single model trained from the entire data set.

We performed an extensive experimental evaluation of our method, comparing it with 3 representative methods. Our method outperforms with gain in accuracy of at least 20%, and can give reliable prediction result much faster.

In future, we plan to apply our method to the infrastructure of Internet TV platform, and try to build cache replacement strategy which can proactively adapt to evolution of programs popularity.

References

1. Cisco Visual Networking Index: Forecast and Methodology. http://www.cisco.com/c/en/us/solutions/collateral/service-provider/visual-networking-index-vni/complete-white-paper-c11-481360.htm
2. Tencent Video. http://v.qq.com/rank/detail/2_-1_-1_-1_1_1.html
3. Figueiredo, F., Almeida, J.M., Gonçalves, M.A., Benevenuto, F.: TrendLearner: early prediction of popularity trends of user generated content. Inf. Sci. **349–350**, 172–187 (2016)
4. Kaltenbrunner, A., Gómez, V., López, V.: Description and prediction of slashdot activity. In: 2007 Latin American Web Conference (LA-WEB 2007), pp. 57–66 (2007)
5. Szabo, G., Huberman, B.A.: Predicting the popularity of online content. Commun. ACM **53**, 80–88 (2010)
6. Lee, J.G., Moon, S., Salamatian, K.: Modeling and predicting the popularity of online contents with Cox proportional hazard regression model. Neurocomputing **76**, 134–145 (2012)
7. Tatar, A., Leguay, J., Antoniadis, P., Limbourg, A., Amorim, M.D., Fdida, S.: Predicting the popularity of online articles based on user comments. In: Proceedings of the International Conference on Web Intelligence, Mining and Semantics, pp. 1–8. ACM, Sogndal (2011)
8. Kim, S.D., Kim, S.H., Cho, H.G.: Predicting the virtual temperature of web-blog articles as a measurement tool for online popularity. In: 2011 IEEE 11th International Conference on Computer and Information Technology, pp. 449–454 (2011)
9. Jamali, S., Rangwala, H.: Digging digg: comment mining, popularity prediction, and social network analysis. In: 2009 International Conference on Web Information Systems and Mining, pp. 32–38 (2009)
10. Wang, K., Shao, Y., Shu, L., Zhu, C., Zhang, Y.: Mobile big data fault-tolerant processing for ehealth networks. IEEE Netw. **30**, 36–42 (2016)
11. Pinto, H., Almeida, J.M., Gon, M.A.: Using early view patterns to predict the popularity of youtube videos. In: Proceedings of the Sixth ACM International Conference on Web Search and Data Mining, pp. 365–374. ACM, Rome (2013)
12. Maass, W., Natschläger, T., Markram, H.: Real-time computing without stable states: a new framework for neural computation based on perturbations. Neural Comput. **14**, 2531–2560 (2002)
13. Gürsun, G., Crovella, M., Matta, I.: Describing and forecasting video access patterns. In: 2011 Proceedings IEEE INFOCOM, pp. 16–20 (2011)
14. Wang, K., Shao, Y., Shu, L., Han, G., Zhu, C.: LDPA: a local data processing architecture in ambient assisted living communications. IEEE Commun. Mag. **53**, 56–63 (2015)
15. Crane, R., Sornette, D.: Robust dynamic classes revealed by measuring the response function of a social system. Proc. Nat. Acad. Sci. **105**, 15649–15653 (2008)
16. Ahmed, M., Spagna, S., Huici, F., Niccolini, S.: A peek into the future: predicting the evolution of popularity in user generated content. In: Proceedings of the Sixth ACM International Conference on Web Search and Data Mining, pp. 607–616. ACM, Rome (2013)

17. Wang, K., Lu, H., Shu, L., Rodrigues, J.J.P.C.: A context-aware system architecture for leak point detection in the large-scale petrochemical industry. IEEE Commun. Mag. **52**, 62–69 (2014)
18. Sun, W., Xiang, L., Liu, X., Zhao, D.: An improved k-medoids clustering algorithm based on a grid cell graph realized by the P system. In: Zu, Q., Hu, B. (eds.) HCC 2016. LNCS, vol. 9567, pp. 365–374. Springer, Cham (2016). https://doi.org/10.1007/978-3-319-31854-7_33
19. Mueen, A., Keogh, E.: Extracting optimal performance from dynamic time warping. In: Proceedings of the 22nd ACM SIGKDD International Conference on Knowledge Discovery and Data Mining, pp. 2129–2130. ACM, San Francisco (2016)
20. Wang, K., Mi, J., Xu, C., Zhu, Q., Shu, L., Deng, D.J.: Real-time load reduction in multimedia big data for mobile internet. ACM Trans. Multimedia Comput. Commun. Appl. **12**, 1–20 (2016)
21. Hannan, M.A., Ali, J.A., Mohamed, A., Uddin, M.N.: A random forests regression based space vector PWM inverter controller for the induction motor drive. IEEE Trans. Ind. Electron. **64**, 2689–2699 (2017)
22. Wang, Y., Feng, D., Li, D., Chen, X., Zhao, Y., Niu, X.: A mobile recommendation system based on logistic regression and Gradient Boosting Decision Trees. In: 2016 International Joint Conference on Neural Networks (IJCNN), pp. 1896–1902 (2016)
23. Varoquaux, G., Buitinck, L., Louppe, G., Grisel, O., Pedregosa, F., Mueller, A.: Scikit-learn: machine learning without learning the machinery. GetMobile Mob. Comput. Commun. **19**, 29–33 (2015)

Exact Outage Probability of Two-Way Decode-and-Forward Scheme with Energy Harvesting from Intermediate Relaying Station

Tan-Phuoc Huynh[1(✉)], Pham Ngoc Son[2], and Miroslav Voznak[3]

[1] Eastern International University (EIU), Thu Dau Mot, Vietnam
phuoc.huynh@eiu.edu.vn
[2] Ho Chi Minh City University of Technology and Education, Ho Chi Minh City, Vietnam
sonpndtvt@hcmute.edu.vn
[3] VSB Technical University of Ostrava, Ostrava, Czech Republic
miroslav.voznak@vsb.cz

Abstract. In this paper, we propose a two-way energy-harvesting scheme (called a TWEH protocol) in which an intermediate full-power relay provides energy for two source nodes and implements digital network coding to compress received data from these source nodes. In the proposed TWEH protocol, two source nodes do not have enough energy to exchange data with each other, they have to collect energy from the intermediate relay through wireless signals before transmitting their data. We analyze and evaluate the system performance in terms of exact closed-form outage probabilities over Rayleigh fading channels. For comparison purposes, a conventional two-way scheme without using digital network coding and energy harvesting (called a TWNEH protocol) is also obtained. Results show that the proposed TWEH protocol outperforms the TWNEH protocol. In addition, the theoretical analyses are verified by performing Monte Carlo simulation.

Keywords: Energy harvesting · Two-way scheme · Cooperative communication Decode-and-forward · Digital network coding · Outage probability

1 Introduction

Cooperative relaying is very essential to increase diversity capacity and thus to improve range of wireless communication. The aim of the cooperative relaying is to help wireless source nodes to transmit their data to destinations. During the first (broadcast) phase, the source nodes broadcast their data to relays while in the second (cooperation) phase, the relays help the sources to forward the received data to the destinations. In other to transfer data from the sources to the destinations through the relays, cooperative solutions are considered as: Amplify-and-Forward (AF) and Decode-and-Forward (DF) techniques [1–6].

There are many studied cases in cooperative networks about energy harvesting [7–11]. The researchers in [7] studied about the throughput maximization based on the assumptions of both causal and non-causal knowledge of the harvested energy in the

© ICST Institute for Computer Sciences, Social Informatics and Telecommunications Engineering 2018
Y. Chen and T. Q. Duong (Eds.): INISCOM 2017, LNICST 221, pp. 155–166, 2018.
https://doi.org/10.1007/978-3-319-74176-5_15

energy harvesting two-hop AF relaying network. In addition, the authors assumed that the channel state information was well recognized before the data were transmitted to the destination by the collaboration of the single relay node and the transmitter.

In [12], the author studied about power transmission policies for the energy harvesting two-way relay which maximize the sum throughput. The energy harvesting relay can perform AF, DF, compress-and-forward, or compute-and-forward relaying.

Most of the above researchers, the authors have considered the situation that the source nodes have enough power in the initial phase of the transmission processes. Exceptionally, in [13], the source nodes do not have enough energy which operate in the one-way scheme. None of the researchers considers two-way relaying networks with limited energies at the source and the destination nodes.

Inspired by the above ideas, in this paper, we propose a two-way energy-harvesting scheme (called a TWEH protocol) in which an intermediate relay supports power to two source nodes and apply digital network coding to compress received data from the source nodes. There are two main considerations as folows. Firstly, we suppose that both sources have insufficiently energy to transmit as well as to receive the data. Hence, each source has to collect energy from the RF signals of the relay. For example in real wireless systems, source nodes sometimes do not have enough energy to transmit and get signals from other sources and relays while original stations have fully energy. In other to set up these systems, we assume that the source nodes get energy from the RF signals of the nodes with full energy (original stations) to charge their battery so that these source nodes have sufficiently energy. The second consideration is the analysis and comparison of the proposed TWEH protocol with a conventional two-way DF scheme without using digital network coding and energy harvesting (called a TWNEH protocol).

This paper is organized as follows: Sect. 2 describes a two-way system model with the energy harvesting architecture and operation principles of the proposed TWEH protocol; Sect. 3 analyzes and calculates the exact outage probabilities of the source nodes, and infers the sum outage probabilities of the protocols TWEH and TWNEH; the simulation results are presented in Sect. 4 and Sect. 5 summarizes our conclusions.

2 System Model

As illustrated in Fig. 1, in this paper, we investigate a system model of a DF two-way energy-harvesting scheme with a relay R and two source nodes S_1 and S_2 in which S_1 and S_2 are energy harvesting source nodes. In this figure, we assume that two sources S_1 and S_2 have not enough energy in the transmitting-receiving process of the pilot messages in the set-up phase,and each source harvests energy from the RF signals of the relay R. After the sources harvest energy from the relay, the packets of two source nodes S_1 and S_2 are carried to the intermediate relay node R.

There are some assumptions as follows. Firstly, each node has a private antenna. Secondly, variances of Zero-mean White Gaussian Noises (AWGNs) are equal, denoted similarly as N_0. Thirdly, all channels are designated to flat and block Rayleigh fading. Finally, Channel State-Information (CSI) are recognized at the source nodes S_1 and S_2 [14].

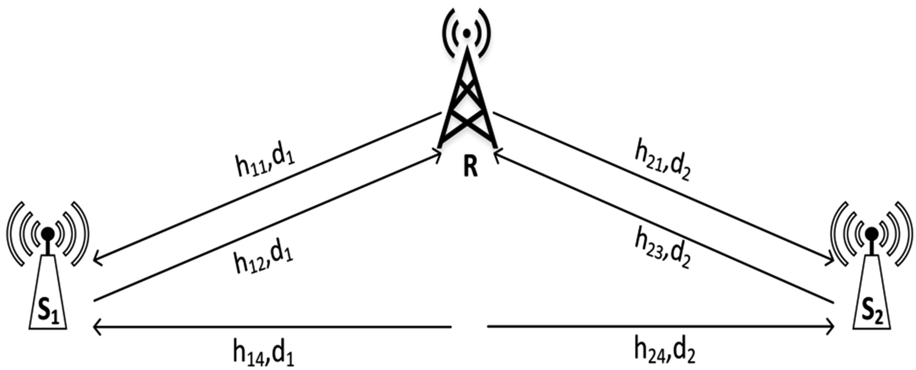

Fig. 1. System model of a DF two-way energy-harvesting scheme

In Fig. 1, (h_{1i}, d_1) and (h_{2i}, d_2) are Rayleigh fading channel coefficients and the link distances of R-S_1, R-S_2, respectively, where $i \in \{1,2,3,4\}$, where the first subscript of the Rayleigh fading channel coefficients denotes the hop index whereas the remaining second subscript presents the time slot index. Hence, the random variables $g_{1i} = |h_{1i}|^2$ and $g_{2i} = |h_{2i}|^2$ have exponential distributions with the parameters $\lambda_1 = d_1^{\beta}$ and $\lambda_2 = d_2^{\beta}$, respectively, where β is a path-loss exponent. The respectively distances d_1 and d_2 from the source S_1 and S_2 to the relay R have considered in [14].

The Cumulative Distribution Function (CDF) and probability density function (pdf) of random variables g_{ji} are expressed as $F_{g_{ji}}(x) = 1 - e^{-\lambda_i x}$ and $f_{g_{ji}}(x) = \lambda_i e^{-\lambda_i x}$, respectively, where $j \in \{1,2\}$.

As above assumptions, the fading channel h_{ji} do not change during a block time T, and are independent and identically distributed between two consecutive block times, $j \in \{1,2\}$.

Based on a time division channel model and each source harvests energy from the RF signals of the relay, the operation principle of the DF two-way energy-harvesting scheme (called the TWEH protocol) is split into four time slots as follows. In the initial time slot, an energy-provided packet of the relay is transmitted to all of the sources. In the next time slot, after harvesting energy from the relay, S_1 sends an information-carrying packet x_1 to the relay. Similar to S_1, S_2 also dispatches an information-carrying packet x_2 to the relay R in the third time slot. Finally, in the last time slot, a coded packet is based on digital network coding by an XOR operation ($x = x_1 \oplus x_2$) is broadcasted to the source nodes S_1 and S_2.

The mathematical expressions and outage probability analyses of the TWEH and TWNEH protocols will be discussed in the next section.

3 Outage Probability Analysis

To analyze the outage probability of the DF two-way schemes (the TWEH and TWNEH protocols), we assume that a node successfully decodes the received packet if its achievable data rate is larger than a target data rate R_t.

3.1 The TWEH Protocol

Because the system model in Fig. 1 is symmetric, the outage probability of the source node S_2 is calculated in the same way as that of the source node S_1. Hence, we only present the outage probability of the source node S_1, and then we will infer the outage probability of the source node S_2.

At the first time slot point of the block time T, the relay R broadcasts energy signals e to the source nodes S_1 and S_2 with a transmitting power P, where $E\{|e|^2\} = 1$($E\{x\}$ is notated for the expectation process of x). The energy-carried signals received at the source nodes S_j are given, respectively, as

$$y_{S_j}^{(1)} = \sqrt{P}h_{j1}e + n_{S_j} \tag{1}$$

where n_{S_j} denote the AWGNs at receiving antennas of the source nodes S_j, respectively, with the same variance N_0, $j \in \{1, 2\}$. The harvested energies at the source nodes S_j over a time interval T are obtained from (1), as

$$E_{S_j} = P|h_{j1}|^2 T\eta_j \tag{2}$$

where η_i are energy conversion efficiencies at the source nodes S_j, $0 < \eta_j \leq 1$. Assuming that the source nodes S_j has the same constructions, then the energy conversion efficiencies η_j are constant, denoted as $\eta_j = \eta$.

In the second time slot, the signal received at the relay R from the source node S_1 is given by

$$y_R^{(2)} = \sqrt{P_{S_1}}h_{12}x_1 + n_R \tag{3}$$

The power P_{S_1} in (3) can be achieved from the harvested energy E_{S_1} as in (2) for sending the signal x_1 to the cooperative relay R over a time interval T as follows

$$P_{S_1} = \frac{E_{S_1}}{T} \tag{4}$$

Substituting the harvested energy E_{S_1} from (2) into (4), we obtain the following result:

$$P_{S_1} = P|h_{11}|^2\eta \tag{5}$$

With the same way, at the third time slot, the signal received at the relay R from the source node S_2 is given by

$$y_R^{(3)} = \sqrt{P_{S_2}} h_{23} x_2 + n_R \tag{6}$$

Similarly as from (3), over a time interval T, the power P_{S_2} can be obtained from the harvested energy E_{S_2} as in (4) for transmitting the signal x_2 from the source S_2 to the cooperative relay R as follows

$$P_{S_2} = P|h_{21}|^2 \eta \tag{7}$$

The received Signal-to-Noise Ratio (SNR) SNR_{S_2R} at the relay R for decoding the information signal x_2 is obtained as follows

$$SNR_{S_2R} = \frac{P_{S_2}|h_{23}|^2}{N_0} = \frac{P\eta|h_{21}|^2|h_{23}|^2}{N_0} = \gamma\eta g_{21} g_{23} \tag{8}$$

where γ is defined as a transmit SNR, $\gamma = \frac{P}{N_0}$.

The achievable data rate at the relay R to decode the information signal x_2 of the source S_2 is given as:

$$R_{S_2R} = \frac{1}{4}\log_2(1 + SNR_{S_2R}) \tag{9a}$$

where a ratio ¼ denotes that the TWEH protocol operates in four time slots.

Substituting the received SNR_{S_2R} from (8) into (9a), R_{S_2R} is expressed as:

$$R_{S_2R} = \frac{1}{4}\log_2(1 + \gamma\eta g_{21} g_{23}) \tag{9b}$$

Decoding operation of the information signal x_1 of the source node S_1 was performed at the relay R in the second time slot. After receiving the packets x_1 and x_2, the relay R codes these packets using the digital network coding as $x = x_1 \oplus x_2$. Then, in the fourth time slot, the relay broadcasts the coded packet x, thus the received signals at the source nodes S_j is expressed, respectively, as

$$y_{S_j}^{(4)} = \sqrt{P} h_{j4} x + n_{S_j} \tag{10}$$

The received SNR_{RS_1} at the source S_1 for decoding the information signal x is obtained from (10) as follows

$$SNR_{RS_1} = \frac{P|h_{14}|^2}{N_0} = \gamma g_{14} \tag{11}$$

We have SNR_{RS_1} in hand, the achievable data rate at the source node S_1 from the transmission x of the relay R is given as:

$$R_{RS_1} = \frac{1}{4}\log_2(1 + SNR_{RS_1}) \tag{12a}$$

Substituting the SNR_{RS_1} from (11) into (12a), we obtain the following result:

$$R_{RS_1} = \frac{1}{4}\log_2(1 + \gamma g_{14}) \tag{12b}$$

The outage probability of the source node S_1 in the TWEH protocol in which the source node S_1 does not receive signal from the source node $S_{2,}$ is obtained by a math expression as follows

$$P_{TWEH}^{out\_S_1} = \underbrace{\Pr[R_{S_2R} < R_t]}_{\Pr 1} + \underbrace{\Pr[R_{S_2R} \geq R_t, R_{RS_1} < R_t]}_{\Pr 2} \tag{13}$$

Pr1 is calculated by substituting (9b) into the expression of Pr1 in (13), we obtain the following result:

$$\Pr 1 = \Pr\left[\frac{1}{4}\log_2(1 + \gamma\eta g_{21}g_{23}) < R_t\right] = \int_0^\infty f_{g_{21}}(x)F_{g_{23}}(a/x)dx \tag{14a}$$

where a = $\frac{2^{4R_t}-1}{\gamma\eta}$.

Applying the pdf of the random variable g_{21} and the CDF of the random variable g_{23} into (14a), Pr1 is solved in a closed form expression as

$$\Pr 1 = \int_0^\infty \lambda_2 e^{-\lambda_2 x}\left(1 - e^{-\lambda_2(a/x)}\right)dx = 1 - u_1 \times K_1(1, u_1) \tag{14b}$$

where $u_1 = 2\lambda_2\sqrt{a}$ and $K_1(.)$ is the modified Bessel function [15, Eq. (8.432.6)].

Similarly as Pr1, Pr2 is manipulated by substituting (9b) and (12b) into the formula of Pr2 in (13), Pr2 is rewritten as

$$\begin{aligned}\Pr 2 &= \Pr\left[\frac{1}{4}\log_2(1 + \gamma\eta g_{21}g_{23}) \geq R_t, \frac{1}{4}\log_2(1 + \gamma g_{14}) < R_t\right] \\ &= \underbrace{\Pr\left[\frac{1}{4}\log_2(1 + \gamma\eta g_{21}g_{23}) \geq R_t\right]}_{\Pr 2.1} \times \underbrace{\Pr\left[\frac{1}{4}\log_2(1 + \gamma g_{14}) < R_t\right]}_{\Pr 2.2}\end{aligned} \tag{15}$$

The probability Pr2.1 is calculated as

$$\Pr 2.1 = 1 - \Pr\left[\frac{1}{4}\log_2(1 + \gamma\eta g_{21}g_{23}) < R_t\right] = 1 - \Pr 1 = u_1 \times K_1(1, u_1) \tag{16}$$

The probability Pr2.2 is solved as follows:

$$\Pr 2.2 = \Pr\left[g_{14} < \frac{2^{4R_t} - 1}{\gamma}\right] = \Pr[g_{14} < a\eta] = F_{g_{14}}(a\eta) = 1 - e^{-\lambda_1 a\eta} \tag{17}$$

From (16) and (17), Pr2 is obtained as follows:

$$\Pr 2 = \Pr 2.1 \times \Pr 2.2 = u_1 \times K_1(1, u_1) \times \left(1 - e^{-\lambda_1 a\eta}\right) \tag{18}$$

Finally, owing Pr1 in (14b) and Pr2 in (18) in hand, the outage probability of the source node S_1 in the TWEH protocol $P_{TWEH}^{out\_S_1}$ is obtained in the closed-form expression as

$$\begin{aligned} P_{TWEH}^{out\_S_1} &= \Pr 1 + \Pr 2 \\ &= 1 - u_1 \times e^{-\lambda_1 a\eta} \times K_1(1, u_1) \end{aligned} \tag{19}$$

Similarly, the outage probability of the source node S_2 in the TWEH protocol $P_{TWEH}^{out\_S_2}$ is inferred by changing λ_2 to λ_1 and vice versa as

$$P_{TWEH}^{out\_S_2} = 1 - u_2 \times e^{-\lambda_2 a\eta} \times K_1(1, u_2) \tag{20}$$

where $u_2 = 2\lambda_1\sqrt{a}$

From (19) and (20), the sum outage probability $P_{TWEH}^{out\_sum}$ in the TWEH protocol is obtained to evaluate the asymmetric two-way energy-harvesting scheme as

$$\begin{aligned} P_{TWEH}^{out\_sum} &= P_{TWEH}^{out\_S_1} + P_{TWEH}^{out\_S_2} \\ &= 2 - u_1 \times e^{-\lambda_1 a\eta} \times K_1(1, u_1) - u_2 \times e^{-\lambda_2 a\eta} \times K_1(1, u_2) \end{aligned} \tag{21}$$

3.2 The TWNEH Protocol

In the TWNEH protocol, the two source nodes S_1 and S_2 have enough power. At first, the packet x_1 of source node S_1 is transmitted to the relay R. This packet is decoded and then is transferred to the source node S_2 through the relay R in the next time slot. After receiving the packet from the relay, the source node S_2 transmits its own packet x_2 to the relay R. In the fourth time slot, the relay also decodes and forwards the packet x_2 to the source node S_1.

The outage probability of the source node S_1 in the TWNEH is expressed as

$$P_{TWNEH}^{out\_S_1} = \underbrace{\Pr[R_{S_2R}^{NEH} < R_t]}_{\Pr 3} + \underbrace{\Pr[R_{S_2R}^{NEH} \geq R_t, R_{RS_1}^{NEH} < R_t]}_{\Pr 4} \tag{22}$$

where $R_{S_2R}^{NEH}$ and $R_{RS_1}^{NEH}$ are achievable data rates at the relay R and the source node S_1, respectively.

In the TWNEH protocol, the sum energy equals to $4 \times T \times P_{NEH}$, where P_{NEH} is the same power of the nodes S_1, S_2 and R, whereas the sum energy in the TWEH is $2 \times T \times P$. With fair comparison purpose about used energy, we set as $4 \times T \times P_{NEH} = 2 \times T \times P$, then $P_{NEH} = P/2$.

The achievable data rates at the relay R and the source node S_1 to decode the information signal x_2 of the source node S_2 are given, respectively, as:

$$R_{S_2R}^{NEH} = \frac{1}{4}\log_2\left(1 + SNR_{S_2R}^{NEH}\right) = \frac{1}{4}\log_2\left(1 + \frac{\gamma g_{23}}{2}\right) \tag{23}$$

$$R_{RS_1}^{NEH} = \frac{1}{4}\log_2\left(1 + SNR_{RS_1}^{NEH}\right) = \frac{1}{4}\log_2\left(1 + \frac{\gamma g_{14}}{2}\right) \tag{24}$$

By substituting $R_{S_2R}^{NEH}$ from (23) into the formula of Pr3 in (22), Pr3 is solved as follows

$$\begin{aligned} \Pr 3 &= \Pr\left[\frac{1}{4}\log_2\left(1 + \frac{\gamma g_{23}}{2}\right) < R_t\right] = \Pr\left[g_{23} < 2\frac{2^{4R_t} - 1}{\gamma}\right] \\ &= \Pr[g_{23} < 2a\eta] = F_{g_{23}}(2a\eta) = 1 - e^{-2\lambda_2 a\eta} \end{aligned} \tag{25}$$

Similarly as Pr3, Pr4 are obtained by substituting $R_{S_2R}^{NEH}$ from (23) and $R_{RS_1}^{NEH}$ from (24) into the formula of Pr4 in (22) as

$$\begin{aligned} \Pr 4 &= \left[1 - \Pr\left(g_{23} < 2\frac{2^{4R_t} - 1}{\gamma}\right), \Pr\left(g_{14} < 2\frac{2^{4R_t} - 1}{\gamma}\right)\right] \\ &= e^{-2\lambda_2 a\eta} \times \left(1 - e^{-2\lambda_1 a\eta}\right) \end{aligned} \tag{26}$$

From (25) and (26), the outage probability of the source node S_1 in the TWNEH protocol $P_{TWNEH}^{out\_S_1}$ is also obtained in the closed-form expression as

$$P_{TWNEH}^{out\_S_1} = \Pr 3 + \Pr 4 = 1 - e^{-(\lambda_1 + \lambda_2)2a\eta} \tag{27}$$

Because of identical effects of the relay R on the transmission between the source node S_1 and S_2 in the TWNEH protocol, the outage probability $P_{TWNEH}^{out\_S_2}$ of the source node S_2 is equal to $P_{TWNEH}^{out\_S_1}$ and the sum outage probability $P_{TWNEH}^{out\_sum}$ in the TWNEH protocol is $2 \times P_{TWNEH}^{out\_S_1}$.

4 Simulation Results

In this section, the system performance of two protocols TWEH and TWNEH is analyzed and evaluated using the exact theoretical analyses and the Monte Carlo simulations of the (sum) outage probabilities. In the two-dimensional plane, the coordinates of S_1, S_2, and R are S_1 (0, 0), S_2 (1, 0) and R (x, y), respectively, satisfying

0 < x < 1. Therefore, $d_1 = \sqrt{x^2 + y^2}$ and $d_2 = \sqrt{(1-x)^2 + y^2}$. We assume that the path-loss exponent β is set to 3, and the SNR on the x-axis is defined as SNR = P/N_0.

Figure 2 presents the outage probabilities of the source nodes S_1 and S_2 in the protocols TWEH and TWNEH versus the SNR (dB) when the symmetric network model is considered with $x = 0.5$, y = 0, $R_t = 1$ (bit/s/Hz) and $\eta = 0.9$. Due to the symmetric network model, the outage probabilities of the source nodes S_1 and S_2 are identical. As shown in Fig. 2, the outage probabilities of the source nodes S_1 and S_2 in both protocols decrease when the SNRs increase because the harvested energies as in formulas (21) and (27), the decoding capacities at the nodes S_1, S_2 and R are larger at the higher SNRs. In addition, the performance of the proposed TWEH protocol outperforms the conventional TWNEH protocol because the proposed TWEH protocol applies the digital network coding to compensate the loss of the bandwidth for the energy harvesting phase (the first time slot). Lastly, we can see that the simulation results fit well to the theoretical results. Hence, we can conclude that the derived formulas during analyzing are accurate.

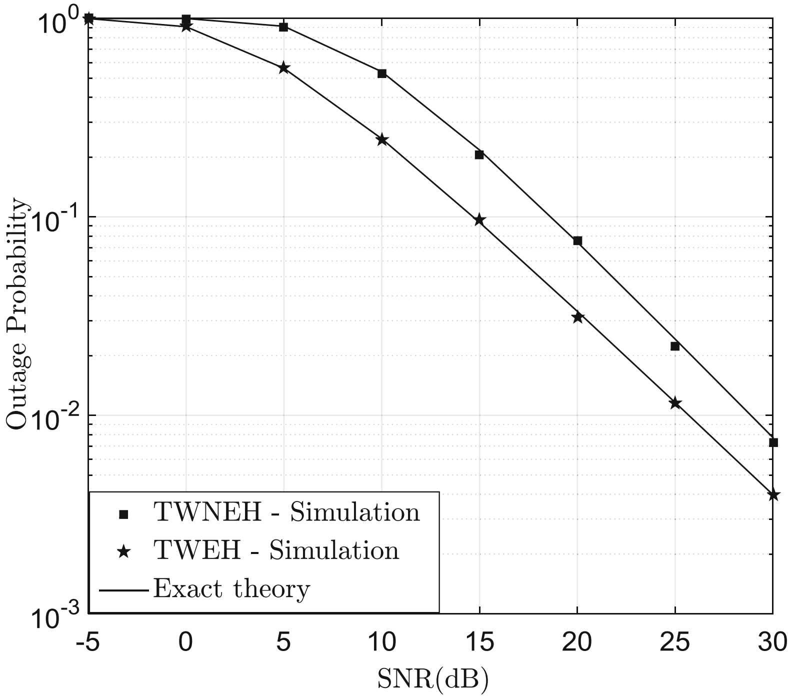

Fig. 2. The outage probabilities of the source nodes S_1 and S_2 in the protocols TWEH and TWNEH versus SNR (dB) when x = 0.5, R_t = 1 (bit/s/Hz), η = 0.9.

Figure 3 presents the sum outage probabilities versus η in the asymmetric network scheme of the protocols TWEH and TWNEH with $R_t = 1$(bit/s/Hz), $x = 0.5$, y = 0, η is changed from 0.1 to 1, and the SNR values are set to 10 and 20 (dB). In Fig. 3, the TWEH protocol has the smaller sum outage probability in comparison with TWNEH protocol at SNR = 10 dB. At SNR = 20 dB, the sum outage probability values of the TWEH protocol are greater than those of the TWNEH protocol when $\eta < 0.2$ (small energy conversion efficiency). Nevertheless, when the energy conversion efficiency increases from 0.2 to 1, the sum outage probability of the TWEH protocol also goes down and lower than the sum outage probability of the TWNEH protocol. We note that the protocol TWNEH does not apply the energy harvesting so that the sum outage probability does not depend on η and is constant versus η.

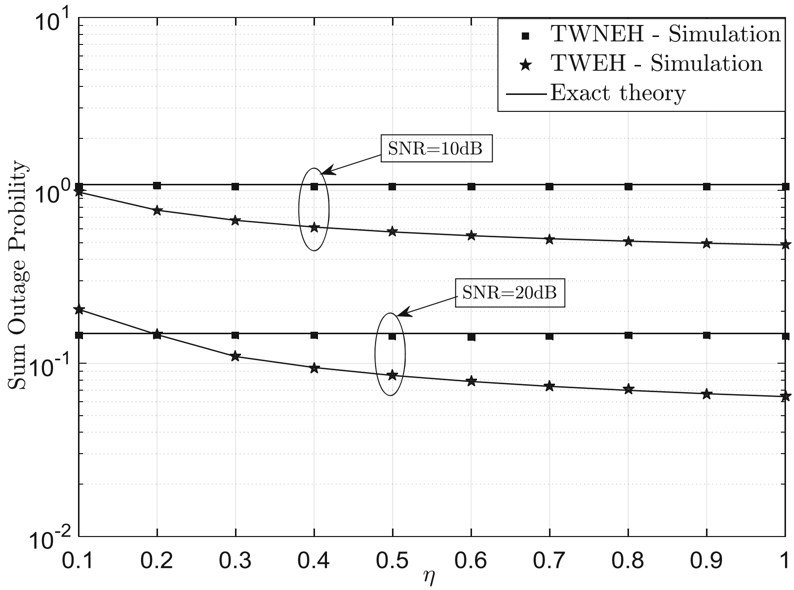

Fig. 3. The sum outage probabilities of the scheme in the TWEH and TWNEH protocols versus η when x = 0.5, y = 0, $R_t = 1$ (bit/s/Hz) and SNR is considered at 10 and 20 (dB).

Figure 4 illustrates the sum outage probability of the protocols TWEH and TWNEH in the asymmetric network scheme as a function of R_t when x = 0.5, y = 0, SNR values are set to 10 (dB) and 20 (dB). It can be seen that when target data rate R_t goes up, the system performance of the protocols TWEH and TWNEH decreases and then moves to the worst regions (about $R_t > 2.5$).

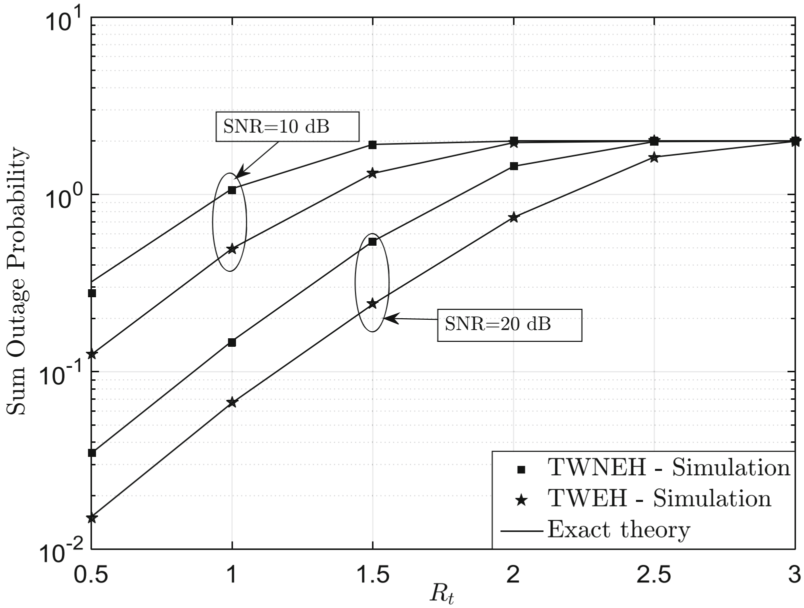

Fig. 4. The sum outage probabilities of the scheme in the TWEH and TWNEH protocols versus R_t when x = 0.5, y = 0, and SNR is considered at 10 and 20 (dB).

5 Conclusions

In this paper, we propose the two-way energy-harvesting scheme (called the TWEH protocol) in which the intermediate relay provides power to two source nodes and applies the digital network coding to compress received data from the source nodes. In the proposed TWEH protocol, during the first time slot, each source has to collect energy from the RF signals of the relay to have sufficiently energy to transmit as well as to receive the data in the next three time slots. The exact closed-form outage probability expressions are used to evaluate the system performance of the proposed protocol and are verified by the Monte Carlo simulation method. The results show that the proposed TWEH protocol achieves higher performance when comparing with the conventional two-way DF scheme without using digital network coding and energy harvesting (called the TWNEH protocol), and both protocols reach the smallest sum outage probabilities when the relay is located at the midpoint of the two sources. In addition, the closed-form theory expressions of the (sum) outage probabilities match well with the Monte Carlo simulation results.

References

1. Bletsas, A., Shin, H., Win, M.Z.: Outage optimality of opportunistic amplify-and-forward relaying. IEEE Commun. Lett. **11**(3), 261–263 (2007)
2. Li, D.: Amplify-and-Forward relay sharing for both primary and cognitive users. IEEE Trans. Veh. Technol. **65**(4), 2796–2801 (2016)
3. Wyne, S., Alvi, S.: On amplify-and-forward relaying over Hyper-Rayleigh fading channels. Radioengineering **23**(4), 1226–1233 (2014)
4. Zhou, Q.F., Mow, W.H., Zhang, S., Toumpakaris, D.: Two-Way decode-and-forward for low-complexity wireless relaying: selective forwarding versus one-bit soft forwarding. IEEE Trans. Wirel. Commun. **15**(3), 1866–1880 (2016)
5. Nguyen, N.-P., Duong, T.Q., Ngo, H.Q., Hadzi-Velkov, Z., Shu, L.: Secure 5G wireless communications: a joint relay selection and wireless power transfer approach. IEEE Access **4**, 3349–3359 (2016)
6. Liu, Y., Wang, L., Elkashlan, M., Duong, T.Q., Nallanathan, A.: Two-Way Relay Networks with Wireless Power Transfer: Design and Performance Analysis. IET Commun. **10**(14), 1810–1819 (2016)
7. Minasian, A., Shahbazpanahi, S., Adve, R.S.: Energy harvesting cooperative communication systems. IEEE Trans. Wirel. Commun. **13**(11), 6118–6131 (2014)
8. Ding, Z., et al.: Power allocation strategies in energy harvesting wireless cooperative networks. IEEE Trans. Wirel. Commun. **13**(2), 846–860 (2014)
9. Mekikis, P.-V., et al.: Wireless energy harvesting in two-way network coded cooperative communications: a stochastic approach for large scale networks. IEEE commun. Lett. **18**(6), 1011–1014 (2014)
10. Li, T., Fan, P., Letaief, K.B.: Outage probability of energy harvesting relay-aided cooperative networks over Rayleigh fading channel. IEEE Trans. Veh. Technol. **65**(2), 972–978 (2016)
11. Zhai, C., Liu, J.: Cooperative wireless energy harvesting and information transfer in stochastic networks. EURASIP J. Wirel. Commun. Netw. **2015**(1), 44 (2015)
12. Tutuncuoglu, K., Varan, B., Yener, A.: Throughput maximization for two-way relay channels with energy harvesting nodes: The impact of relaying strategies. IEEE Trans. Commun. **63**(6), 2081–2093 (2015)
13. Hadzi-Velkov, Z., Zlatanov, N., Duong, T.Q., Schober, R.: Rate maximization of decode-and-forward relaying systems with RF energy harvesting. IEEE Commun. Lett. **19** (12), 2290–2293 (2015)
14. Son, P.N., Kong, H.Y.: Exact outage analysis of energy harvesting underlay cooperative cognitive networks. IEICE Trans. Commun. **98**(4), 661–672 (2015)
15. Jeffrey, A., Zwillinger, D.: Table of Integrals, Series, and Products. Academic Press, Burlington (2007)

Enhancing Performance of Asynchronous Cooperative Relay Network with Partial Feedback

The-Nghiep Tran(✉)

Faculty of Radio-Electronics, Le Quy Don Technical University, Hanoi, Vietnam
nghiepsqtt@gmail.com
http://www.lqdtu.edu.vn

Abstract. Distributed close-loop extended orthogonal space-time block code (DCL EO-STBC) was demonstrated to achieve a significant improvement of performance for closed-loop cooperative relay network systems with limited feedback channel. This paper proposes a decode-and-forward (DF) cooperative strategy with using partial feedback in stead of DCL EO-STBC to obtain a distributed cooperative diversity gain. Based on the partial phase feedback technique, the new scheme has only previous inter-symbol interference (ISI) components in the received signals and obtains an enhancing system performance in term of signal-noise power ratio (SNR) at the destination node. Theoretical analysis and Monte-Carlo simulations confirm that the using near-optimum detection (NOD) at the destination can completely remove interference components before detection process. In comparison to previous DCL EO-STBC scheme, this work not only has simpler signal processing due to not using DCL EO-STBC endcoder and decoder, but also outperforms sytem performance without decrease transmission rate.

Keywords: Partial feedback · Near-optimum detection
Inter-symbol interference · Distributed space-time code
Asynchronous cooperative network

1 Introduction

Distributed space-time code (DSTC) is used in distributed relay networks, such as ad-hoc or wireless sensor networks, to achieve spatial diversity gain [1–3]. However, due to the different location of cooperative relay nodes and their distinct local oscillators, the received signals at the destination are not the same time in the symbol level. This imperfect synchronization results in inter-symbol interference (ISI) between the received symbols at the destination node, which damages the orthogonally of the DSTC and degrades the total system performance. Thus, the solutions of interference cancellation have attracted considerably attentions from the scientists in a few years ago [4–11].

In [2], the distributed close loop quasi-orthogonal space-time code (DCL QO-STBC) and sub-optimum detection (SOD) (called as DCL QO-STBC scheme)

© ICST Institute for Computer Sciences, Social Informatics and Telecommunications Engineering 2018
Y. Chen and T. Q. Duong (Eds.): INISCOM 2017, LNICST 221, pp. 167–179, 2018.
https://doi.org/10.1007/978-3-319-74176-5_16

are proposed for the DF asynchronous cooperative networks. Although this scheme based on sub-optimum detection proves to be very effective to eliminate the ISI components with reducing detection complexity at the destination it relies mainly on the existence of a direct transmission (DT) link between the source node and the destination node. In [1], the DCL EO-STBC and near-optimum detection (NOD) (called as DCL EO-STBC scheme) is proposed for the same configuration network as Ref. [2] without the DT link between the source node and the destination node. The DCL EO-STBC scheme not only obtains a significant improving performance by canceling the interference components in the received signals, but also performs without the requirement of the DT link. However, both DCL EO-STBC scheme and DCL QO-STBC scheme are only the solution of interference cancellation at the destination node.

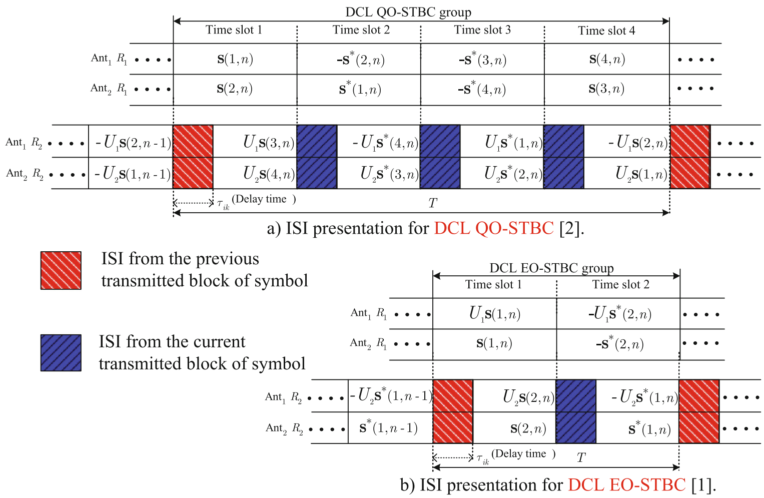

Fig. 1. The ISI representations in the DCL EO-STBC scheme [1] and DCL QO-STBC scheme [2].

The ISI components of the DCL EO-STBC and DCL QO-STBC schemes can be classified into two categories, one of them is due to the current transmitted symbol and the other is from the previous transmitted block of symbols as shown in Fig. 1 [3]. The SOD [2] and NOD [1] are proved that they can completely remove the previous ISI components if the detection process has been initialized properly. Whereas the current ISI components still exist in the received symbol vector after using either the SOD or NOD. Moreover, the number of current ISI components depends on the durations of between the second time slot and the last time slot in each DCL-STBC group. Hence, it is noticeable from the Fig. 1 that there are two and six current interference components at the received signals in DCL EO-STBC and DCL QO-STBC schemes respectively while their configuration networks are similar. Therefore, the using SOD or NOD does not work well in these schemes.

In this paper, we propose a new DF asynchronous cooperative relay network with partial feedback where there are only previous ISI components in received signals at the destination node. Although the proposed scheme is the similar configuration network in DCL EO-STBC scheme [1] and DCL QO-STBC scheme [2] it differs from those in the following points. Firstly, our proposed scheme uses the partial feedback technique [12] to ensure that there are only previous ISI components in the received symbols, and then near-optimum detection is utilized to remove completely them. Whereas, the solutions of interference cancellation in both DCL-QO STBC and DCL-EO STBC schemes are solved only at the destination node. Secondly, the previous works use the DCL-STBC encoding and decoding to achieve the distributed cooperative diversity, but the using partial feedback in new scheme is a better alternative in the term of received signal to noise ratio (SNR). Thirdly, the application NOD in this paper does not depend on the detection result of DT link while the performing sub-optimum detection [2] bases on the existence of that.

The rest of this paper is organized as follows: The DF asynchronous cooperative relay network with partial feedback is described in the Sect. 2. Near-optimum detection and feedback bit selection are presented in the Sect. 3. Simulation results and performance comparisons are provided in the Sect. 4. Finally, the Sect. 5 givens the conclusions of the paper.

In the remaining part of this paper, $[.]^T$, $[.]^*$ and $\|.\|^2$ denote transpose, complex conjugate, and Frobenius operation, respectively; $\Re$ and $\Im$ present to take the real and imaginary part of the complex variable, respectively; $\mathbb{E}[.]$ represents an expectational operation; and $\mathcal{A}$ indicates the signal constellation.

2 The Proposed Asynchronous Cooperative Relay Network with Partial Feedback

The proposed partial feedback scheme is depicted in Fig. 2 with the source node and destination node have a single antenna, relay nodes have two antennas. The DT link from the source node to the destination node is unavailable due to the effect of path loss and the limited transmitted power. All relay nodes operate in half-duplex mode and DF strategy. Let f_{ik} denotes the channel coefficient from the source node to the $i\,th$ antenna of the $k\,th$ relay node and g_{ik} is the channel coefficient from the $i\,th$ antenna of the $k\,th$ relay node to the destination node. We also assume that all channel coefficients f_{ik} and g_{ik} (for $i,\, k = \overline{1, 2}$) are kept constant during two symbol intervals and varied randomly in the next two symbol intervals (i.e. a quasi-static fading). The noise terms of both the relay and destination node are assumed AWGN with distribution $\mathcal{CN}(0, 1)$. If the total transmission power in the whole scheme is fixed as P (dB). The optimal power allocation is represented as follows [13]:

$$P_1 = \frac{P}{2},\ P_2 = \frac{P}{4}, \tag{1}$$

where, $P_1,\ P_2$ are the transmit power at the source and the each relay node, respectively.

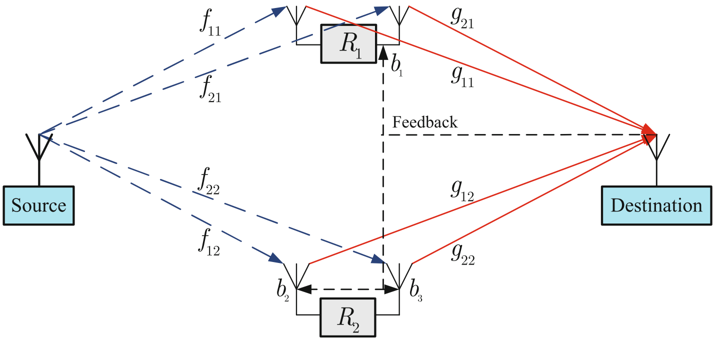

Fig. 2. The asynchronous cooperative relay network with partial feedback.

The transmission between the source node and the destination node comprises two phases. In the first phase, the source node broadcasts information symbol $s(n)$ to the relay node during the first symbol period. As the similar previous works [1] and [2], the DF protocol is used by the relay nodes and the detection of relay node is supported a cyclic redundancy code (CRC) at the source. To limit focus of paper on the imperfect synchronization issue, the relaying nodes are assumed to detect the symbols correctly received signal from the source.

In the second phase, relay nodes cooperate together to transmit symbol to destination node by using partial feedback technique [12] before transmission, information symbols at the second antenna of the first relay, the first and second antenna of the second relay are multiplied by b_1, b_2, and b_3 respectively and which show in the Fig. 3. Thus, the transmitted symbol vector at the relay nodes is presented as follows:

$$E_B = \left[\, s(n)\ b_1 s(n)\ b_2 s(n)\ b_3 s(n) \,\right], \tag{2}$$

where b_i $(i = 1,\ 2,\ 3)$ gets value 1 or -1 depending on the feedback information from the destination node.

In this paper, the transmitted symbol from the relay nodes will undergo an asynchronous issue due to the different distances between the each delay node and the destination node. As the propagation delay of the distinct links is different which results in a inter-symbol interference at the destination node.

Without loss of generality, it is assumed that the received signals at the destination from both antenna of the first relay (denotes R_1) are fully synchronized (i.e. $\tau_1 = \tau_{11} = \tau_{12} = 0$). We also suppose that both antenna of the second relay node (denotes R_2) is not synchronized to the destination (i.e. $\tau_2 = \tau_{21} = \tau_{22} \neq 0$) [1]. Following that, the received symbol at the destination can be expressed as:

$$r(n) = \sqrt{\frac{P_2}{2}} h s(n) + I_{\text{int}}(n) + z(n), \tag{3}$$

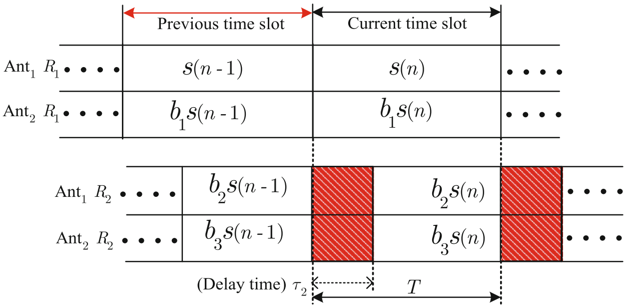

Fig. 3. The ISI presentations in the proposed asynchronous cooperative relay network.

where $h = g_{11} + b_1 g_{21} + b_2 g_{12} + b_3 g_{22}$ is the equivalent channel gain, $z(n)$ is the noise term at the destination node, and $I_{\text{int}}(n)$ is the ISI components:

$$I_{\text{int}}(n) = \sqrt{\frac{P_2}{2}} \left\{ b_2 g_{12}(-1) + b_3 g_{22}(-1) \right\} s(n-1). \tag{4}$$

The coefficients $g_{i2}(-1), (i = 1, 2)$ in Eq. (4) represent the complex channel gains from both antennas of the second relay to the destination due to the effect of asynchronous issue. In this paper, the value of $g_{i2}(-1)$ can be expressed as a ratio as [1]:

$$\beta = |g_{i2}(-1)|^2 / |g_{i2}|^2; \quad i = 1, 2 \tag{5}$$

Normally, $\beta = 0$ for $\tau = 0$ and $\beta = 1$ (i.e. 0 dB) for $\tau = 0.5T$ [1]. Note that, the coefficients $g_{i2}(-1), l = -2, -3...$ are ignored because they are small. The factor $\sqrt{P_2/2}$ in the Eq. (3) ensures that the total transmitted power of the each relay node is P_2. Figure 3 and Eq. (4) show that there are only two previous ISI components in the received symbols at the destination node. It is clear that the number of ISI components of the proposed scheme is reduced as compared with the DCL EO-STBC [1] and DCL QO-STBC scheme [2].

3 Near-Optimum Detection and Feedback Bit Selection

3.1 Feedback Bits

From Eq. (3), the signal-to-noise ratio (SNR) of received signal $r(n)$ is

$$\gamma = \frac{P_2 \lambda}{2} \tag{6}$$

where $\lambda = h^* h = \alpha_B + \beta_B$ is the total performance gain. α_B and β_B are given as:

$$\alpha_B = |g_{11}|^2 + |g_{21}|^2 + |g_{12}|^2 + |g_{22}|^2; \tag{7}$$

$$\beta_B = 2b_1\Re\left(g_{11}g_{21}^*\right) + 2b_2\Re\left(g_{11}g_{12}^* + b_1g_{21}g_{12}^*\right) + 2b_3\Re\left(g_{11}g_{22}^* + b_1g_{21}g_{22}^* + b_2g_{12}g_{22}^*\right). \quad (8)$$

The total gain of the proposed scheme includes the conventional diversity gain α_B, that is always a positive value and the addition array performance gain β_B, which is depended on the value of three feedback bits. In order to enhance the system performance, an exhaustive search algorithm can be used to select feedback bits as following:

$$b_1, b_2, b_3 = \arg \max_{b_1,b_2,b_3 \in \{-1,1\}} \beta_B \quad (9)$$

As an alternative approach, the 3 bits for feedback may be selected according to the inductive algorithm follows to ensure a positive α_B value:

Step 1: $b_1 = \begin{cases} 1 & \text{if} \quad \Re\left(g_{11}g_{21}^*\right) \geq 0 \\ -1 & \text{if} \quad \Re\left(g_{11}g_{21}^*\right) < 0 \end{cases}$

Step 2: $b_2 = \begin{cases} 1 & \text{if} \quad \Re\left(g_{11}g_{12}^* + b_1g_{21}g_{12}^*\right) \geq 0 \\ -1 & \text{if} \quad \Re\left(g_{11}g_{12}^* + b_1g_{21}g_{12}^*\right) < 0 \end{cases}$

Step 3: $b_3 = \begin{cases} 1 & \text{if} \quad \Re\left(g_{11}g_{22}^* + b_1g_{21}g_{22}^* + b_2g_{12}g_{22}^*\right) \geq 0 \\ -1 & \text{if} \quad \Re\left(g_{11}g_{22}^* + b_1g_{21}g_{22}^* + b_2g_{12}g_{22}^*\right) < 0 \end{cases}$

The exhaustive search will provide the larger array gain but at additional computational complexity than the inductive search. It is clear that the addition array performance gain of the proposed scheme β_B is better than conventional array performance gain λ_a as compared with previous DCL EO-STBC scheme (see λ_a in Eq. (13) [1]). Therefore, the system performance of the new scheme is enhanced in the term of the received SNR to compare with former one.

3.2 Near-Optimum Detection

It is evident from the Eq. (4) that the number of ISI components of the new scheme is less than amount of those in the previous works [1,2]. However, the existence of interference components in the received signals can still degrade the system performance in the asynchronous channel assumptions. This subsection presents a detector which can completely remove ISI components and improve the total system performance in this case. Fortunately, there are only two previous interference components in the received signals of the proposed scheme. Therefore, the application of NOD scheme at the destination node can completely remove the ISI components $I_{\text{int}}(n)$ in (3) before the information detection process. In fact, $s(n-1)$ is already known if the detection process has been initialized properly (e.g. through the use of pilot symbols at the start of the packet). Hence, the interference components $I_{\text{int}}(n) = \sqrt{P_2/2}\left\{b_2g_{12}(-1) + b_3g_{22}(-1)\right\}s(n-1)$ in the Eq. (3) can completely removed as the following steps:

Step 1: Remove the ISI component $I_{\text{int}}(n)$ in the Eq. (3):

$$r'(n) = r(n) - I_{\text{int}}(n) = \sqrt{\frac{P_2}{2}}hs(n) + z(n). \quad (10)$$

Step 2: Apply the Least Square (LS) at the destination:

$$\tilde{s}(n) = \arg\min_{s_m \in \mathcal{A}} \left| r'(n) - \sqrt{\frac{P_2}{2}} h s_m \right|^2, \tag{11}$$

where $\mathcal{A}$ denotes the signal constellation.

Its clear that, the received symbol $r'(n)$ in (10) will has no ISI component if the initialized signals have no decision feedback error. More details about the effect of initialized signals are illustrated clearly by Monte-Carlo method in the following section. Since the received symbol $r'(n)$ has no interference component, the LS detection in (11) has been improved.

4 Performance Comparisons and Time Delay Experimental Results

4.1 Comparison Results

This subsection provides some comparisons between the BER performance of the proposed partial feedback scheme and the DCL EO-STBC scheme [1] under the channel conditions such as perfect synchronous or imperfect synchronous. The QPSK modulation is used in all simulations. The BER system performances are shown as function of total transmit power in the whole network.

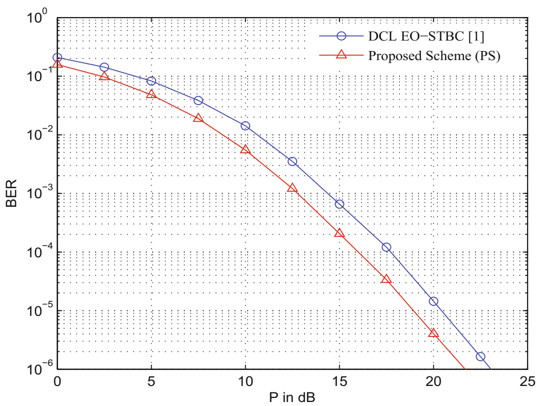

Fig. 4. BER performance comparisons between the proposed scheme and DCL EO-STBC scheme [1] under perfect synchronization condition.

Figures 4 and 5 represents simulation results are corresponding to synchronous and asynchronous channel conditions. From these simulation results, we can have several observations. Firstly, in the perfect synchronous channels, the proposed partial feedback scheme can obtain a SNR gain of 2.3 dB at BER of 10^{-3} in comparison to the DCL EO-STBC scheme [1]. Secondly, the degradation of BER performance of the proposed scheme under asynchronous channels is very small when compared with perfect synchronous channel, i.e., it is robust against asynchronous channels. Thirdly, by decreasing the β factor (i.e., more loss of synchronization), the proposed scheme becomes superior to the DCL EO-STBC scheme (for example, an improvement of 2.5 dB, 5.0 dB and 8.2 dB at BER of 10^{-3} correspond to β factors of -6 dB, -3 dB and 0 dB).

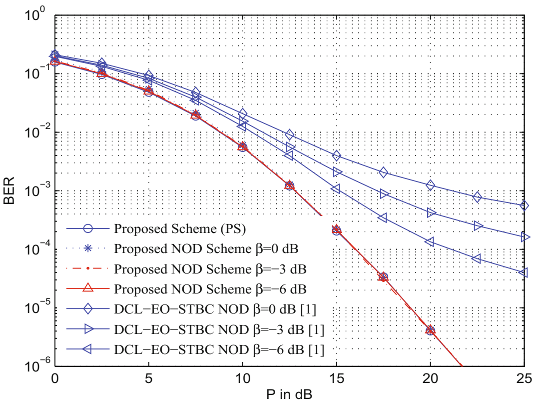

Fig. 5. The comparison of BER performance proposed scheme.

As previous discussion in Sect. 3, the interference cancellation is dependent on the initialized signal $\tilde{s}(n-1)$. It could be detected either correctly or incorrectly. To determine the effect of error propagation to system performance, we perform simulation for two cases, one has error propagation (EP), i.e., $\tilde{s}(n-1)$ hence gets the value of previous detection and can different from information symbol $s(n-1)$, the other has no EP, i.e., $\tilde{s}(n-1)$ gets the value of true information symbol $s(n-1)$. The simulation results in Fig. 6 demonstrate that the effect of error propagation in the proposed scheme is very small and acceptable.

4.2 Time Delay Experimental Results

This subsection presents the performance analysis of time delay based on both impact of imperfect synchronization and decoding complexity. As previous mention, the communication between the source and destination node is performed over two phase. The relays are assumed to detect the correctly received signals from the source. Hence, time delay is depended on the process at relay nodes, multipath channel coefficients and decoding time [14]. Time delay between transmission from the antennas on the relays to destination was presented by factor value reflecting of imperfect synchronous β. The process complexity of the relays and destination was shown in the number of operation requirement.

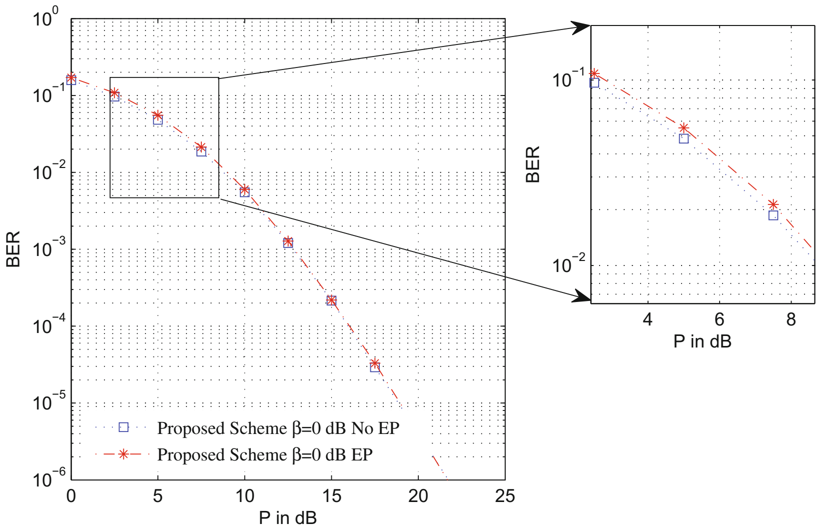

Fig. 6. The impact of error propagation (EP) on the BER performance.

This paper utilizes and adopts all notation and definition as representation in [15]. We denote the complexity of the proposed scheme by C_{New} and $C_{DCLEO-STBC}$ for DCL EO-STBC scheme [1], respectively. The complexity formula was split into two parts in order to represent C_M, that is a real multiplication and C_A, which means a real addition operation independently. The total decoding complexity of the proposed scheme can be written as (see the Appendix A for more details):

$$C_{New} = 36C_M + 20C_A + (90C_M + 74C_A)\,M. \tag{12}$$

Similarly, the DCL EO-STBC scheme has the total processes as follows (see the Appendix B for more details):

$$C_{DCL\,EO-STBC} = 102C_M + 56C_A + (170C_M + 134C_A)\,M. \tag{13}$$

From Eqs. (12) and (13), it could be noticeable that process time requirement of DCL EO-STBC scheme is higher than its proposed scheme. In order to make it more clearly, we provide the experimental results of the performance by using Monte-Carlo method to get the average transmission time delays between the relays and destination, which are as function of size constellation M (4, 8, 16, 32, 64, 128 and 256-QAM constellations) with $\beta = -3$ dB. In the simulation, the delay time (second) of one symbol includes required time of feedback process, encoding process and decoding operation. Figure 7 shows simulation results by using the computer with CPU dual-core i5 3230M, clock rate of 2.60 GHz and

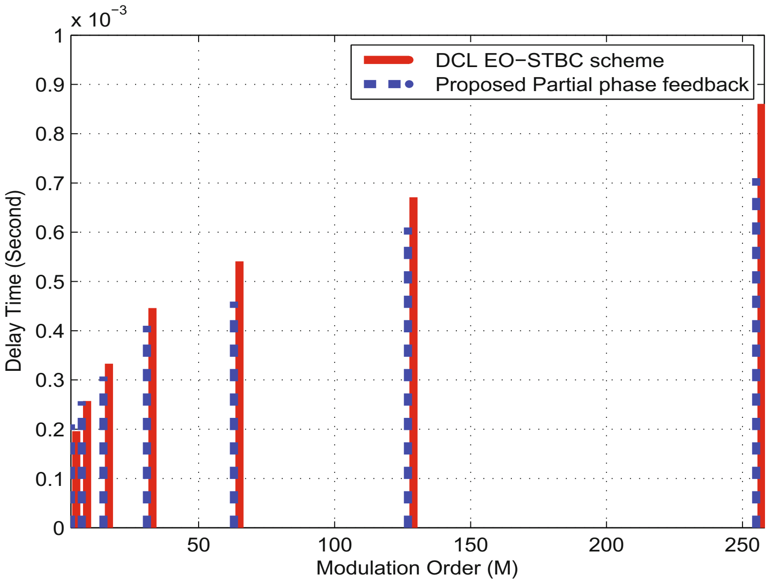

Fig. 7. Comparison time delay between the proposed scheme and DCL EO-STBC [1].

4 Gb random-access memory. These experimental results confirm that our proposed scheme is more efficient than the DCL EO-STBC in terms of time delay.

5 Conclusion

In this paper, a partial feedback scheme for asynchronous cooperative DF relay networks is considered. The proposed partial feedback technique allows to obtain more additional received SNR gain than the DCL EO-STBC scheme and has only previous ISI components at the received symbols. Different from the DCL EO-STBC scheme [1], the proposed scheme does not use DSTC encoding at relay nodes and DSTC decoding at destination node, so it is simpler than the DCL EO-STBC scheme in practical signal processing. The analysis and simulation results demonstrated that the proposed scheme improves the performance of cooperative relay network in both the perfect synchronous and asynchronous channel conditions as compared with existing DCL-STBC works. Moreover, the partial feedback technique is able to extended general cooperative relay network where each relay node has larger than two antennas without an extra study. With these advantages, we believe the proposed scheme can become a prospective candidate for practical cooperative relay networks.

Appendix

A The Processional Requirement of the Proposed Scheme

Firstly, from the step 1 to step 3 at the Subsect. 3.2 in Sect. 3 we can calculate the number of operation for choosing three feedback bits as follows:

$$C_{new\_feedback} = 30C_M + 20C_A. \tag{14}$$

Then, transmitted symbols at the relays are multiplied by these three feedback bits as shown in the Eq. (2) which require the processional complexity as follows:

$$C_{new\_relay} = 6C_M. \tag{15}$$

The decoding complexity of the proposed NOD scheme depends on both the Eqs. (10) and (11) as following:

$$\begin{aligned} C_{new\_NOD} &= C_{new\_eq10} + C_{new\_eq11} \\ &= (32C_M + 22C_A)\,M + (58C_M + 52C_A)\,M \\ &= (90C_M + 74C_A)\,M \end{aligned} \tag{16}$$

where, M is the size of constellation $\mathcal{A}$ (e.g. M-QAM or M-PSK). Therefore, the total processional requirement of the proposed scheme can be written as:

$$\begin{aligned} C_{New} &= C_{new\_feedback} + C_{new\_relay} + C_{new\_NOD} \\ &= 30C_M + 20C_A + 6C_M + (90C_M + 74C_A)\,M \\ &= 36C_M + 20C_A + (90C_M + 74C_A)\,M. \end{aligned} \tag{17}$$

B The Processional Requirement of the DCL EO-STBC Scheme

From the Eqs. (15) and (16) in [1], the requirement of feedback process can be written as:

$$C_{DCL\,EO-STBC\_feedback} = 96C_M + 48C_A. \tag{18}$$

The process of the relays is used to encode the DCL EO-STBC as shown in Eq. (5) [1] and requires the number of operations as follow:

$$C_{DCL\,EO-STBC\_relay} = 16C_M + 8C_A. \tag{19}$$

The complexity of DCL EO-STBC detection is the number of operations from the Eqs. (20) to (24) in [1] and can be written as following:

$$C_{DCL\,EO-STBC\_detection} = (170C_M + 134C_A)\,M. \tag{20}$$

Then, the total processional requirement of the DCL EO-STBC scheme is written as:

$$\begin{aligned} C_{DCL\,EO-STBC} &= C_{DCL\,EO-STBC\_feedback} + C_{DCL\,EO-STBC\_relay} \\ &+ C_{DCL\,EO-STBC\_detection} \\ &= 96C_M + 48C_A + 16C_M + 8C_A + (170C_M + 134C_A)\,M \\ &= 102C_M + 56C_A + (170C_M + 134C_A)\,M. \end{aligned} \tag{21}$$

References

1. Qaja, W.M., Elazreg, A.M., Chambers, J.A.: Near-optimum detection scheme with relay selection technique for asynchronous cooperative relay networks. IET Commun. **8**(8), 1347–1354 (2014)
2. Elazreg, A., Kharaz, A.: Sub-Optimum detection scheme for distributed closed-loop quasi orthogonal space time block coding in asynchronous cooperative two dual-antenna relay networks. In: Mumtaz, S., Rodriguez, J., Katz, M., Wang, C., Nascimento, A. (eds.) WICON 2014. LNICST, vol. 146, pp. 217–228. Springer, Cham (2015). https://doi.org/10.1007/978-3-319-18802-7_30
3. Astal, M.T.O.E., Olivier, J.C.: Distributed closed-loop extended orthogonal STBC: improved performance in imperfect synchronization. In: Proceedings of the Personal Indoor and Mobile Radio Communications (PIMRC), England, pp. 1941–1945 (2013)
4. Elazreg, A.M., Abdurahman, F.M., Chambers, J.A.: Distributed closed-loop quasi-orthogonal space time block coding with four relay nodes: overcoming imperfect synchronization. In: Proceedings of the IEEE International Conference on Wireless and Mobile Computing, Networking and Communication, WIMOB, pp. 320–325 (2009)
5. Desouky, A., El-Mahdy, A.: Asynchronous down-link cooperative communication scheme in Rayleigh fading wireless environment. In: Proceedings of the Signal Processing: Algorithms, Architectures, Arrangements, and Applications, pp. 142–146 (2016)
6. Elazreg, A., Chambers, J.: Closed-loop extended orthogonal space time block coding for four relay nodes under imperfect synchronization. In: Proceedings of the Workshop on Statistical Signal Processing, pp. 545–548 (2009)
7. Zheng, F.-C., Burr, A.G., Olafsson, S.: Signal detection for distributed space-time block coding: 4 relay nodes under quasi-synchronisation. IEEE Trans. Commun. **57**(5), 1250–1255 (2009)
8. Elazreg, A.M., Chambers, J.A.: Sub-optimum detection scheme for asynchronous cooperative relay networks. IET Commun. **5**(15), 2250–2255 (2011)
9. Guangxiang, L., Zhuo, W.: Signal detection for cooperative cellular systems with 4 relay nodes under imperfect synchronization. In: Proceedings of the Signal Processing, Communication and Computing (ICSPCC), KunMing, China, pp. 1–6 (2013)
10. Zheng, F.C., Burr, A.G., Olafsson, S.: Near-optimum detection for distributed space-time block coding under imperfect synchronization. IEEE Trans. Commun. **56**(11), 1795–1799 (2008)
11. Astal, M.-T.E., Abu-Hudrouss, A.M., Olivier, J.C.: Improved signal detection of wireless relaying networks employing space-time block codes under imperfect synchronization. Wireless Pers. Commun. **82**(1), 533–550 (2015)

12. Van Bien, P., Son, P.T., Thap, P.H.: Enhancing performance of four transmit antennas and one receive antenna system with partial feedback. In: Proceedings of the International Conference on Advanced Technologies for Communications, pp. 259–262 (2012)
13. Jing, Y.: Combination of MRC and distributed space-time coding in networks with multiple-antenna relays. IEEE Trans. Wireless Commun. **9**, 2550–2559 (2010)
14. Celik, G., Celebi, H.: G-CRLB analysis of time delay based localization for decode-and-forward cooperative relay networks in multipath environments. In: Proceedings of the International Wireless Communications and Mobile Computing, pp. 454–459 (2015)
15. Pham, V.-B.: Spacetime block code design for LTE-advanced systems. Trans. Emerg. Telecommun. Technol. **26**(5), 918–928 (2013)

Outage Probability for Cognitive Heterogeneous Networks with Unreliable Backhaul Connections

Huy T. Nguyen[1], Dac-Binh Ha[2], Sang Quang Nguyen[2], and Won-Joo Hwang[1](✉)

[1] Department of Information and Communication System, Inje University, 197, Gimhae, Gyeongnam, Korea
huynguyencse@gmail.com, ichwang@inje.ac.kr
[2] Duy Tan University, Da Nang, Vietnam
hadacbinh@duytan.edu.vn, sangnqdv05@gmail.com

Abstract. To enhance the spectrum scarcity of cooperative heterogeneous networks (HetNets) with unreliable backhaul connections, we examine the impact of cognitive spectrum sharing over multiple small-cell transmitters in Nakagami-m fading channels. In this system, the secondary transmitters are connected to macro-cell via wireless backhaul links and communicate with the secondary receiver by sharing the same spectrum with the primary user. Integrating cognitive radio (CR), we address the combined power constraints: (1) the peak interference power and (2) the maximal transmit power. In addition, to exclude the signaling overhead for exchanging channel-state-information (CSI) at the transmitters, the selection combining (SC) protocol is assumed to employ at the receivers. The closed-form statistics of the end-to-end signal-to-noise (SNR) ratio are derived to attain the exact formulas of outage probability and its asymptotic performance to reveal further insights into the effective unreliable backhaul links.

Keywords: Cognitive Radio · Cooperative system
Wireless backhaul · Outage probability · Nakagami-m fading

1 Introduction

Wireless broadband services have driven high transport capacity requirements among cellular networks. As a result, the deployment of wireless infrastructure will get more dense and heterogeneous in the near future [1]. To achieve such higher data rate systems, backhaul links is becoming an emerging technology in heterogeneous networks (HetNets). Wired backhaul has high reliability but would lead to an ineffective increase in the costs of maintenance. For this reason, wireless backhaul is considered as an alternative solution since it offers cost-efficiency and flexibility. However, wireless backhaul is not completely reliable compared to wired backhaul due to the existence of non-line-of-sight (n-LOS) propagation and fading of transmission signals [2].

© ICST Institute for Computer Sciences, Social Informatics and Telecommunications Engineering 2018
Y. Chen and T. Q. Duong (Eds.): INISCOM 2017, LNICST 221, pp. 180–193, 2018.
https://doi.org/10.1007/978-3-319-74176-5_17

There are several existing studies that investigated unreliable wireless backhaul links. For example, in [3], the impact of unreliable backhaul connections on Coordinated Multi-Point (CoMP) systems has been analyzed in the cooperative downlink system. Taking into account the limited resources such as the number of transmitters, interferers and backhaul reliability, the performance of a cooperative wireless network has been examined in [4,5]. For most of research works, backhaul reliability is shown as one of the key parameters that have significant impact on the system performance.

Cooperative systems in dense networks aim to extend the coverage or enhance the system capacity [6]. Hence, the diversity gain can be improved by taking advantage of the multiple receptions at various transmitters and transmission paths. For relay selection over Rayleigh fading channels, the authors in [7] investigated the secrecy performance of three different diversity combining schemes, namely maximum ratio combining (MRC), selection combining (SC), switch-and-stay combining (SSC). For a cyclic-prefix single carrier (CP-SC) system, the best relay selection scheme has been employed to analyze the performance in cognitive radio (CR) sharing spectrum [8].

As the demand for additional bandwidth continues to grow exponentially [9], many experts have sought solutions to efficiently deploy the available licensed spectrum. In recent years, the investigation on CR technologies has attracted the research community as a key factor to improve the spectrum scarcity in HetNets [10,11]. Under Nakagama-m fading, the authors in [12] analyzed the performance impacts of amplify-and-forward (AF) protocol subject to the transmit power constraints at the source and relay node. In [13], the authors investigated the transmit antenna selection with receive generalized selection combining (TAS/GSC) in CR networks.

Since the spectrum in primary networks has not been well utilized, it is important to integrate the CR technologies in the dense communication networks. To the best of the authors' knowledge, most of previous works only considered CR by neglecting the impact of unreliable backhaul [14,15]. Considering the cognitive HetNets, we take into account the scarcity of the spectrum utilization together with the wireless backhaul links reliability. Excluding the signaling overhead, we employ the SC protocol at the transmitters [16]. Moreover, the Nakagami-m fading is used to model the communication and interference channels since it provides various empirical scenarios for simulation [17]. Based on the derived statistics of the end-to-end SNR of the proposed systems, we derive the closed-form expression of the outage probability along with the asymptotic expressions in high-SNR regime. Thus, the analytical results are validated using Monte Carlo simulation.

Notation: $\mathcal{CN}(\mu, \sigma_n^2)$ denotes the complex Gaussian distribution with mean μ and variance σ_n^2; $F_\lambda(\gamma)$ and $f_\lambda(\gamma)$ denote the cumulative distribution (CDF) and probability density function (PDF) of the random variable (RV) λ, respectively; $\mathbb{E}_\lambda\{f(\gamma)\}$ denotes the expectation of $f(\gamma)$ with regard to the RV λ. In addition, $\binom{\tau_1}{\tau_2} = \dfrac{\tau_1!}{\tau_2!(\tau_1-\tau_2)!}$ denotes the binomial coefficient.

2 System and Channel Models

As illustrated in Fig. 1, we consider a cognitive network in a cooperative spectrum sharing system consisting of a macro base station (macro-BS) which is connected to the backbone network, K small-cells $\{\mathrm{SC}_1, ..., \mathrm{SC}_k, ..., \mathrm{SC}_K\}$ as the secondary network transmitters (SU-T_k) are connected to the macro-BS via unreliable wireless backhaul links, one secondary receiver (SU-D) and one primary user (PU-P). The K transmitters communicate with the secondary receiver SU-D by sharing the same spectrum with the primary user PU-P. All nodes are assumed to be equipped with a single antenna and operate in half-duplex mode.

In the practical systems, the transmit powers at each transmitter SU-T_k are constrained due to the interference of the secondary network and must not exceed the peak interference power $\mathcal{I}_p$ at the receiver PU-P. In addition, each transmitter is allowed to transmit up to their maximum power $\mathcal{P}_T$ [12,13]. Under the combined power constraints, the transmit power at the transmitter SU-T_k can be mathematically written as

$$\tilde{P}_k = \min\left(\mathcal{P}_T, \frac{\mathcal{I}_p}{|h_k^p|^2}\right). \tag{1}$$

where $h_k^p, k \in \{1, 2, ..., K\}$ denotes the channel coefficients of the interference links SU-$\mathrm{T}_k \rightarrow$ PU-P. Recall that $\mathcal{I}_p$ denotes the peak interference power at the receiver PU-P [18]. Let define S-SNR as the end-to-end SNR at the receiver SU-D. Without considering the backhaul reliability, the S-SNR over the channel from the transmitter SU-T_k to the receiver SU-D is given as

$$\gamma_k^s = \min\left(\bar{\gamma}_{\mathcal{P}}|h_k^s|^2, \frac{\bar{\gamma}_{\mathcal{I}}}{|h_k^p|^2}|h_k^s|^2\right), \tag{2}$$

where $h_k^s, k \in \{1, 2, ..., K\}$ denotes the channel coefficients of the communication links SU-$\mathrm{T}_k \rightarrow$ SU-D. The average SNR of the primary and secondary network is given as $\bar{\gamma}_{\mathcal{I}} = \mathcal{I}_p/\sigma_n^2$ and $\bar{\gamma}_{\mathcal{P}} = \mathcal{P}_T/\sigma_n^2$, respectively, with σ_n^2 representing the noise variance.

Due to the unreliable nature backhaul links, the signal received at the receiver SU-D via the transmitter SU-T_k is given by

$$r^{k,s} = \sqrt{\tilde{P}_k}(h_k^s)(\mathbb{I}_k)x + n^{k,s}, \tag{3}$$

where $\tilde{P}_k$ recalls the combined constraints transmit power at the transmitter SU-T_k and $n^{k,s} \sim \mathcal{CN}(0, \sigma_n^2)$. Since the message is transmitted from the core network to the receiver, it must go through the backhaul links and perform the success/failure transmission due to the characteristic of wireless links. Thus, the backhaul reliability $\mathbb{I}_k$ of the transmitter SU-T_k is modeled as Bernoulli process [19] with successful probability $\{\Lambda_k, \forall k\}$, i.e., the SU-T_k will successfully receive the message from macro-BS and forward to the receiver SU-D. Otherwise, the transmitter SU-T_k does not send anything with failure probability being $(1-\Lambda_k)$.

We denote x as the desired symbol transmitted by the small-cell transmitters and assume that $\mathbb{E}\{x\} = 0$ and $\mathbb{E}\{|x|^2\} = 1$.

Herein, we assume the SC protocol at the receiver SU-D[1] by selecting the small-cell station which has the best SNR over the received signals from K transmitters. Upon applying the SC protocol, it can be defined as

$$k^* = \max \arg_{[k \in K]}(\gamma_k^s \mathbb{I}_k), \tag{4}$$

is the selected transmitter SU-T$_k$ index. Consequently, the instantaneous S-SNR at the receiver SU-D can be obtained as

$$\gamma_S = \min\left(\bar{\gamma}_{\mathcal{P}} |h_{k^*}^s|^2, \frac{\bar{\gamma}_{\mathcal{I}}}{|h_{k^*}^p|^2} |h_{k^*}^s|^2\right) \mathbb{I}_{k^*}. \tag{5}$$

As can be seen from (5), the end-to-end SNR is decided by the unreliable backhaul of the considered HetNets, i.e., the Bernoulli RV $\mathbb{I}_k$. In addition, we assume all channels undergo Nakagami-m fading, i.e., a set of channel coefficients $\{h_k^s, \forall k\}$ of the links SU-T$_k$ $\rightarrow$ SU-D and a set of channels $\{h_k^p, \forall k\}$ of the links SU-T$_k$ $\rightarrow$ PU-P are distributed according to the gamma distribution, which is denoted by $|h_k^s|^2 \sim \text{Ga}(\mu_k^s, \eta_k^s)$ and $|h_k^p|^2 \sim \text{Ga}(\mu_k^p, \eta_k^p)$, respectively. Hence, The PDF and CDF of the RV $\chi \sim \text{Ga}(\mu_\chi, \eta_\chi)$, where $\chi \in \{h_k^s, h_k^p\}$ are given, respectively, as

$$\begin{aligned} f_\chi(x) &= \frac{1}{(\mu_\chi - 1)!(\eta_\chi)^{\mu_\chi}} x^{\mu_\chi - 1} e^{(-x/\eta_\chi)}, \\ F_\chi(x) &= \left(1 - e^{(-x/\eta_\chi)} \sum_{i=0}^{\mu_\chi - 1} \frac{1}{i!} \left(x/\eta_\chi\right)^i\right), \end{aligned} \tag{6}$$

where $\mu_\chi \in \{\mu_k^s, \mu_k^p\}$ represents the positive fading severity parameter [5,22,23], with channel powers $\{\Omega_k^s, \Omega_k^p\}$, and $\eta_\chi \in \{\eta_k^s = \Omega_k^s/\mu_k^s, \eta_k^p = \Omega_k^p/\mu_k^p\}$ indicates the scale factor on the corresponding channel.

3 Closed-Form Statistics of S-SNR in Cognitive Heterogeneous Systems

In this section, our challenges are how to derive the statistical properties of the S-SNR with respect to the backhaul reliability and the combined power constraints at SU-T$_k$. Without loss of generality, we assume that all channels follow the independent and identically distributed (i.i.d.) Nakagami-m fading, i.e., $\mu_s = \mu_k^s, \eta_s = \eta_k^s, \Lambda = \Lambda_k, \mathbb{I} = \mathbb{I}_k, \forall k \in K$ for transmission signals respect to the receiver SU-D and $\mu_p = \mu_k^p, \eta_p = \eta_k^p, \forall k \in K$ for the interference signals at the receiver PU-P, respectively. We first obtain the CDF of S-SNR for the signal between the particular SU-T$_k$ and SU-D, which is given in the following lemma.

[1] In the literature in unreliable backhaul [4,5], the perfect knowledge of CSI is not required at the transmitters, which is different from maximum ratio transmission (MRT) protocol [20,21].

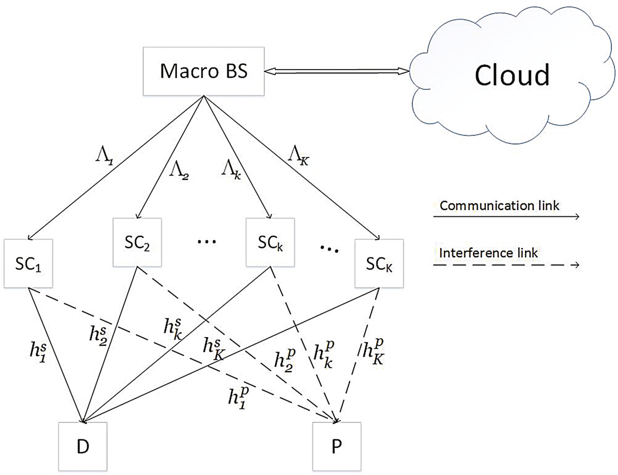

Fig. 1. A cognitive HetNet with unreliable backhaul links.

Lemma 1. *For a cognitive HetNet with unreliable backhaul links, where transmitter SU-T_k utilizes the sharing spectrum with the primary user PU-P, the CDF of the S-SNR for particular transmitter, γ_k^s, is given as*

$$F_{\gamma_k^s \mathbb{I}_k}(x) = 1 - \Lambda(\Theta_1(x) + \Theta_2(x)), \tag{7}$$

where $\Phi = \dfrac{\Upsilon\left(\mu_p, \bar{\gamma}_{\mathcal{I}}/\bar{\gamma}_{\mathcal{P}}\eta_p\right)}{\Gamma(\mu_p)}$, $\epsilon = \dfrac{\bar{\gamma}_{\mathcal{I}}\eta_s}{\eta_p}$ *and*

$$\Theta_1(x) = \Phi e^{-(x/\bar{\gamma}_{\mathcal{P}}\eta_s)} \sum_{i=0}^{\mu_s-1} \frac{1}{i!} \left(x/\bar{\gamma}_{\mathcal{P}}\eta_s\right)^i,$$

$$\Theta_2(x) = \sum_{j=0}^{\mu_s-1} \sum_{g=0}^{\mu_p+j-1} \binom{\mu_p+j-1}{\mu_p-1} \frac{1}{g!(\bar{\gamma}_{\mathcal{P}}\eta_s)^g} \epsilon^{\mu_p} e^{-(\bar{\gamma}_{\mathcal{I}}/\bar{\gamma}_{\mathcal{P}}\eta_p)} \frac{x^j e^{-(x/\bar{\gamma}_{\mathcal{P}}\eta_s)} (x+\epsilon)^g}{(x+\epsilon)^{\mu_p+j}}. \tag{8}$$

Proof. The proof is given in Appendix A.

In (7), $\Gamma(.)$ and $\Upsilon(.,.)$ are the Gamma function [24, Eq. (8.310.1)] and the lower incomplete Gamma function [24, Eq. (8.350.1)], respectively. Next, the corresponding CDF and PDF for the received S-SNR at the receiver SU-D will be derived in the following theorem.

Theorem 1. *For the i.i.d. Nakagami-m fading channels between K cooperative transmitters and the secondary receiver SU-D in the cognitive spectrum sharing with the primary user PU-P, the CDF of the RV $\gamma_S \triangleq \max(\gamma_1^s \mathbb{I}_1, ..., \gamma_K^s \mathbb{I}_K)$ with* *respect to SC protocol and unreliable backhaul links is given by* (9) *in the top of next page.*

$$F_{\gamma_S}(x) = 1 + \sum_{k=1}^{K} \binom{K}{k} (-1)^k \widehat{\sum_{k,\mu_s,\mu_p,\Lambda,\Phi}} \frac{x^{\widetilde{\varphi_1}} e^{-\beta x}}{(x+\epsilon)^{\widetilde{\varphi_2}}}, \tag{9}$$

where $\widetilde{L_{a_n}}$ *is defined as* $\widetilde{L_{a_n}} \triangleq \sum_{b_n=0}^{\mu_p+n-2} b_n a_{b_n+1}$, $\beta \triangleq k/\bar{\gamma}_{\mathcal{P}}\eta_s, \widetilde{\varphi_1} \triangleq \sum_{\vartheta=0}^{\mu_s-1} \vartheta u_{\vartheta+1} + \sum_{t=0}^{\mu_s-1} t w_{t+1} + c_1 + c_2 + ... + c_{\mu_s}$, $\widetilde{\varphi_2} \triangleq \sum_{t=0}^{\mu_s-1} (\mu_p + t) w_{t+1}$ *and* $\widehat{\sum_{k,\mu_s,\mu_p,\Lambda,\Phi}}$ *is a shorthand notation of*

$$\widehat{\sum_{k,\mu_s,\mu_p,\Lambda,\Phi}} \triangleq \sum_{l=0}^{k} \binom{k}{l} \sum_{u_1 \dots u_{\mu_s}}^{k-l} \sum_{w_1 \dots w_{\mu_s}}^{l} \sum_{a_{1,1} \dots a_{1,\mu_p}}^{w_1} \sum_{a_{2,1} \dots a_{2,\mu_p+1}}^{w_2} \dots \sum_{a_{\mu_s,1} \dots a_{\mu_s,\mu_p+\mu_s-1}}^{w_{\mu_s}}$$
$$\frac{(k-l)!}{u_1! \dots u_{\mu_s}!} \frac{l!}{w_1! \dots w_{\mu_s}!} \frac{w_1!}{a_{1,1}! \dots a_{1,\mu_p}!} \frac{w_2!}{a_{2,1}! \dots a_{2,\mu_p+1}!} \dots \frac{w_{\mu_s}!}{a_{\mu_s,1}! \dots a_{\mu_s,\mu_p+\mu_s-1}!}$$
$$\prod_{t=0}^{\mu_s-1} \binom{\mu_p+t-1}{\mu_p-1}^{w_{t+1}} \frac{1}{\prod_{\vartheta=0}^{\mu_s-1} \left(\vartheta! (\bar{\gamma}_{\mathcal{P}}\eta_s)^{\vartheta}\right)^{u_{\vartheta+1}}} \frac{1}{\prod_{b_1=0}^{\mu_p-1} \left(b_1! (\bar{\gamma}_{\mathcal{P}}\eta_s)^{b_1}\right)^{a_{1,b_1+1}}}$$
$$\frac{1}{\prod_{b_2=0}^{\mu_p} \left(b_2! (\bar{\gamma}_{\mathcal{P}}\eta_s)^{b_2}\right)^{a_{2,b_2+1}}} \dots \frac{1}{\prod_{b_{\mu_s}=0}^{\mu_p+\mu_s-2} \left(b_{\mu_s}! (\bar{\gamma}_{\mathcal{P}}\eta_s)^{b_{\mu_s}}\right)^{a_{\mu_s,b_{\mu_s}+1}}} \sum_{c_1=0}^{\widetilde{L_{a_1}}} \sum_{c_2=0}^{\widetilde{L_{a_2}}} \dots \sum_{c_{\mu_s}=0}^{\widetilde{L_{a_{\mu_s}}}}$$
$$\binom{\widetilde{L_{a_1}}}{c_1} \binom{\widetilde{L_{a_2}}}{c_2} \dots \binom{\widetilde{L_{a_{\mu_s}}}}{c_{\mu_s}} \Lambda^k \Phi^{k-l} e^{-(\bar{\gamma}_{\mathcal{I}} l / \bar{\gamma}_{\mathcal{P}} \eta_p)} \epsilon^{\left(\widetilde{L_{a_1}} + \widetilde{L_{a_2}} + \dots + \widetilde{L_{a_{\mu_s}}} + \mu_p l - (c_1 + c_2 + \dots + c_{\mu_s})\right)}. \tag{10}$$

Proof. The proof is given in Appendix B.

Hence, the PDF of the received S-SNR can be derived as follows

$$f_{\gamma_S}(x) = \sum_{k=1}^{K} \binom{K}{k} (-1)^k \widehat{\sum_{k,\mu_s,\mu_p,\Lambda,\Phi}} \frac{e^{-\beta x}}{(x+\epsilon)^{\widetilde{\varphi_2}+1}}$$
$$\left((\widetilde{\varphi_1} - \widetilde{\varphi_2} - \epsilon\beta) x^{\widetilde{\varphi_1}} + \widetilde{\varphi_1} \epsilon x^{\widetilde{\varphi_1}-1} - \beta x^{\widetilde{\varphi_1}+1} \right). \tag{11}$$

4 Outage Probability Analysis

To investigate the performance of the proposed cognitive HetNets with unreliable backhaul connections over i.i.d. Nakagami-m fading channels, we focus on the outage probability, where the exact formula of the outage probability are presented based on the statistics derived in Sect. 3.

Given a certain SNR threshold γ_{th}, the outage probability of the S-SNR is defined as the probability that the S-SNR is below the threshold γ_{th}, which can be written as

$$\mathcal{P}_{out}(\gamma_{\text{th}}) \triangleq \Pr(\gamma_S \le \gamma_{\text{th}}) = F_{\gamma_S}(\gamma_{\text{th}}). \tag{12}$$

In other words, the outage probability can be expressed as the CDF of the S-SNR at the given γ_{th}. By substituting (9) into (12), the outage probability is derived in the following theorem.

Theorem 2. *The outage probability closed-form expression for the proposed cognitive HetNets with respect to the unreliable backhaul links is derived as*

$$\mathcal{P}_{out}(\gamma_{th}) = 1 + \sum_{k=1}^{K} \binom{K}{k} (-1)^k \widehat{\sum_{k,\mu_s,\mu_p,\Lambda,\Phi}} \frac{{\gamma_{th}}^{\widetilde{\varphi_1}} e^{-\beta\gamma_{th}}}{(\gamma_{th} + \epsilon)^{\widetilde{\varphi_2}}}. \tag{13}$$

To provide insight into how the fading parameters and backhaul reliability impact the network performance, we next derive the asymptotic outage probability in the high-SNR regime of the considered system. In this case, we assume the peak interference threshold $\bar{\gamma}_{\mathcal{I}}$ is proportional to the maximum transmit power $\bar{\gamma}_{\mathcal{P}}$. The asymptotic outage probability is given in the following theorem as

Theorem 3. *At the high-SNR regime with respect to $\bar{\gamma}_{\mathcal{P}}$ as $\bar{\gamma}_{\mathcal{P}} \rightarrow \infty$ in the cognitive sharing system with K cooperative transmitters and unreliable backhaul links, the asymptotic outage probability is given by*

$$\mathcal{P}_{out}^{Asy}(\gamma_{th}) \overset{\bar{\gamma}_{\mathcal{P}} \rightarrow \infty}{=} (1 - \Lambda)^K = \Xi. \tag{14}$$

Proof. The proof is given in Appendix C.

5 Numerical Results and Discussions

In this section, we present the numerical results of the outage probability to verify the analysis under the impact of unreliable backhaul links. The "Sim" curves indicate the link-level Monte Carlo simulation results, while the "Ana" and "Asy" curves represent the analytical results and asymptotic performance at high-SNR regime, respectively. We fix the S-SNR threshold $\gamma_{\text{th}} = 3$ dB. Without loss of generality, we assume that the secondary user SU-D and the primary user PU-P are located at point $[0, 0]$ and $[0.5, 0.5]$, respectively. Those small-cell transmitters SU-T$_k$ are located at $[0, 0.5]$. Hence, the channel mean powers are calculated by $\Omega_k^s = \Omega_k^p = \left(\sqrt{(x_k - x_u)^2 + (y_k - y_u)^2}\right)^{\zeta}$, where $u \in \{D, P\}$ and $\zeta = 4$ as the path-loss exponent. In this setting, we obtain the mean power of all links is equal to 16. We also assume the ratio of the interference power $\bar{\gamma}_{\mathcal{I}}$ and the maximum transmit power $\bar{\gamma}_{\mathcal{P}}$ is constant for all numerical results. We define the average SNR as $\bar{\gamma} = \bar{\gamma}_{\mathcal{P}}$.

5.1 Outage Probability Analysis

Figures 2, 3 and 4 show the outage probability for various scenarios. In Fig. 2, we verify the accurate of the derived analytical outage probability versus the average SNR with the simulation. Assuming ($\Lambda_1 = 0.98, \Lambda_2 = 0.98, \Lambda_3 = 0.98$) for $K = 1$, $K = 2$, $K = 3$, respectively. The fading severity parameters are initialized as $\mu_\chi = \{\mu_k^s = 1, \mu_k^p = 1, \forall k\}$. From this figure, it can be observed that all curves converge to the asymptotic limitation as $\bar{\gamma}$ increases. Furthermore, the outage probability values get lower when more transmitters cooperate due to the correlation of multiple signals at the receiver SU-D.

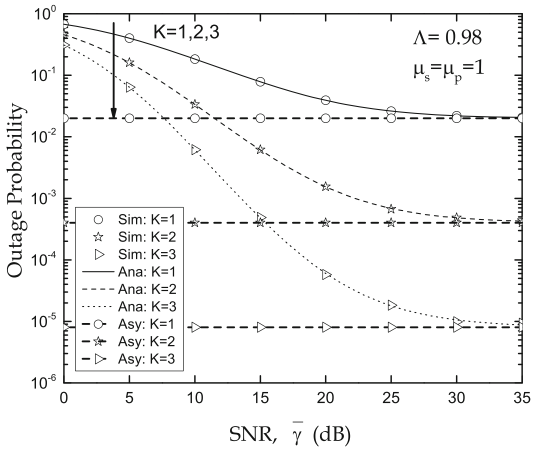

Fig. 2. Outage probability for various level of the degree of transmitter cooperation with fixed unreliable backhaul links.

To investigate the outage probability behavior at the same asymptotic threshold when the degree of transmitter cooperation is changed, we show it in Fig. 3. Assuming $\Xi = 6.4\text{E}{-5}$, we set ($\Lambda_1 = 0.999936$), ($\Lambda_1 = 0.992, \Lambda_2 = 0.992$), and ($\Lambda_1 = 0.96, \Lambda_2 = 0.96, \Lambda_3 = 0.96$) for case $K = 1$, $K = 2$, $K = 3$, respectively. The fading severity parameters are similar as in Fig. 2. We can observe that at the same outage probability asymptotic limitation, the higher degrees of transmitter cooperation converge faster than the others. Moreover, at the same degrees of transmitter cooperation ($K = 1$ or $K = 3$), the outage probability performance gets worst if the backhaul links is more unreliable, otherwise, the receiver SU-D performs the good performance.

Figure 4 plots the outage probability with various Nakagami-m fading severity scenarios at the fixed value ($K = 2, \Lambda = 0.988$). From these curves, it can be seen that the outage probability is strongly affected by the fading severity of the secondary network μ_s rather than the primary network fading severity μ_p. Specifically, the performance at the receiver SU-D tends to be better with the increase of μ_s while the outage probability values seem unchanged with the alternation of μ_p.

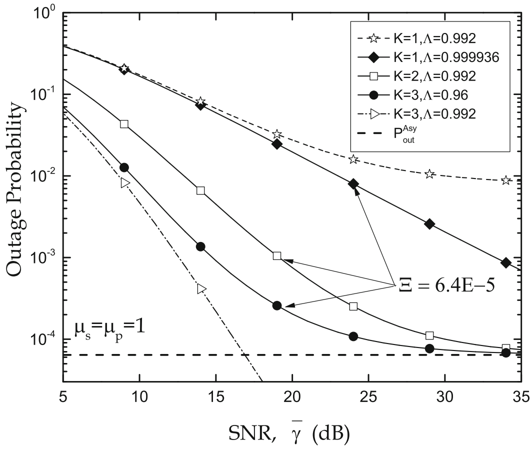

Fig. 3. Outage probability for various level of backhaul unreliability with fixed asymptotic limitation.

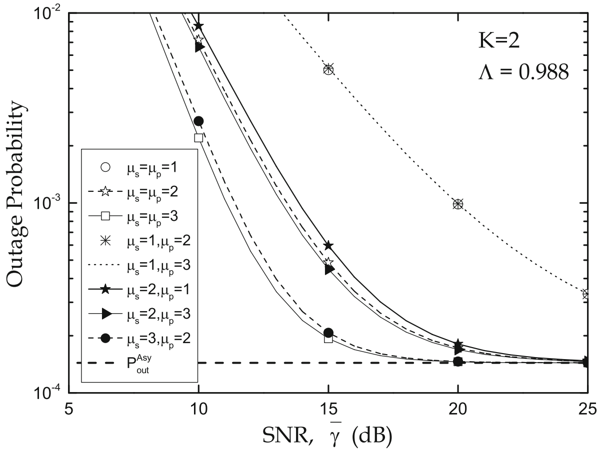

Fig. 4. Outage probability for various Nakagami-m fading severity with $\Xi = 1.44\text{E}{-}4$.

6 Conclusions

In this paper, we have taken into account the cognitive HetNets with unreliable backhaul links over i.i.d. Nakagami-m fading. The constrained transmit power of transmitters have been practically considered, i.e., the peak interference power $\mathcal{I}_p$ and the maximal transmit power $\mathcal{P}_T$. We have derived the closed-form expressions of the outage probability as well as asymptotic performance to obtain study insights. It has been shown that the asymptotic performance is only determined by the unreliable backhaul links in the high-SNR regime. The performance of the proposed system is highly improved proportionally to the degree of cooperation and the fading severity of secondary network. Our analyzed results provide suitable framework for network designers to clearly understand the effects of unreliable backhaul links and decide whether enabling the CR networks for those cooperative transmitters in order to efficiently utilize the spectrum.

Acknowledgement. This work was supported by the Ministry of Science, ICT and Future Planning, South Korea, through the Grand Information Technology Research Center Program under Grant IITP-2017-2016-0-00318

A Appendix A: Proof of Lemma 1

According to the definition of RV γ_k^s at particular SU-T$_k$, which was given as $\gamma_k^s = \min\left(\bar{\gamma}_{\mathcal{P}}|h_k^s|^2, \frac{\bar{\gamma}_{\mathcal{I}}}{|h_k^p|^2}|h_k^s|^2\right)$, results the CDF as

$$\begin{aligned} F_{\gamma_k^s}(x) &= \Pr\left\{\min\left(\bar{\gamma}_{\mathcal{P}}|h_k^s|^2, \frac{\bar{\gamma}_{\mathcal{I}}}{|h_k^p|^2}|h_k^s|^2\right) \le x\right\} \\ &= \underbrace{\Pr\left\{|h_k^s|^2 \le \frac{x}{\bar{\gamma}_{\mathcal{P}}}; \frac{\bar{\gamma}_{\mathcal{I}}}{|h_k^p|^2} \ge \bar{\gamma}_{\mathcal{P}}\right\}}_{\mathcal{J}_1} \\ &\qquad + \underbrace{\Pr\left\{\frac{|h_k^s|^2}{|h_k^p|^2} \le \frac{x}{\bar{\gamma}_{\mathcal{I}}}; \frac{\bar{\gamma}_{\mathcal{I}}}{|h_k^p|^2} \le \bar{\gamma}_{\mathcal{P}}\right\}}_{\mathcal{J}_2}. \end{aligned} \tag{A.1}$$

where

$$\mathcal{J}_1 = F_{|h_k^s|^2}\left(\frac{x}{\bar{\gamma}_{\mathcal{P}}}\right) F_{|h_k^p|^2}\left(\frac{\bar{\gamma}_{\mathcal{I}}}{\bar{\gamma}_{\mathcal{P}}}\right), \text{ and} \tag{A.2}$$

$$\mathcal{J}_2 = \int_{\frac{\bar{\gamma}_{\mathcal{I}}}{\bar{\gamma}_{\mathcal{P}}}}^{\infty} f_{|h_k^p|^2}(y) F_{|h_k^s|^2}\left(\frac{xy}{\bar{\gamma}_{\mathcal{I}}}\right) dy. \tag{A.3}$$

After some manipulations, we obtain the CDF of γ_k^s as follows.

$$\begin{aligned} F_{\gamma_k^s}(x) &= 1 - \Phi e^{-\left(\frac{x}{\bar{\gamma}_{\mathcal{P}}\eta_s}\right)} \sum_{i=0}^{\mu_s-1} \frac{1}{i!}\left(\frac{x}{\bar{\gamma}_{\mathcal{P}}\eta_s}\right)^i \\ &- \sum_{j=0}^{\mu_s-1} \binom{\mu_p+j-1}{\mu_p-1} \epsilon^{\mu_p} e^{-\left(\frac{\bar{\gamma}_{\mathcal{I}}}{\bar{\gamma}_{\mathcal{P}}\eta_p}\right)} \\ &\frac{x^j e^{-\left(\frac{x}{\bar{\gamma}_{\mathcal{P}}\eta_s}\right)} \sum_{g=0}^{\mu_p+j-1} \frac{1}{g!(\bar{\gamma}_{\mathcal{P}}\eta_s)^g}(x+\epsilon)^g}{(x+\epsilon)^{\mu_p+j}}, \end{aligned} \tag{A.4}$$

with the help of [24, Eq. (8.352.4)]. The PDF of a particular RV $\gamma_k^s \mathbb{I}_k$ is modeled by the mixed distribution as

$$f_{\gamma_k^s \mathbb{I}_k}(x) = (1 - \Lambda)\delta(x) + \Lambda \frac{\partial F_{\gamma_k^s}(x)}{\partial x}, \tag{A.5}$$

where $\delta(x)$ indicates the Dirac delta function. Hence, the CDF of the RV $\gamma_k^s \mathbb{I}_k$ can be written as follows

$$F_{\gamma_k^s \mathbb{I}_k}(x) = \int_0^\infty f_{\gamma_k^s \mathbb{I}_k}(x)dx = 1 - \Lambda(\Theta_1(x) + \Theta_2(x)). \tag{A.6}$$

B Appendix B: Proof of Theorem 1

From the definition of S-SNR γ_S in (5), which is given by

$$\gamma_S = \max_{k \in K} \left(\gamma_1^s \mathbb{I}_1, \gamma_2^s \mathbb{I}_2, ..., \gamma_k^s \mathbb{I}_k, ..., \gamma_K^s \mathbb{I}_K\right). \tag{B.1}$$

Since all RVs $\gamma_k^s \mathbb{I}_k$ are independent and identically distributed with each other, the CDF of SNR γ_S can be written as

$$\begin{aligned} F_{\gamma_S}(x) &= F^K_{\gamma_k^s \mathbb{I}_k}(x) \\ &= 1 + \sum_{k=1}^{K} \binom{K}{k} (-1)^k \Lambda^k (\Theta_1(x) + \Theta_2(x))^k \\ &= 1 + \sum_{k=1}^{K} \binom{K}{k} (-1)^k \Lambda^k \sum_{l=0}^{k} \binom{k}{l} \Theta_1(x)^{k-l} \Theta_2(x)^l. \end{aligned} \tag{B.2}$$

Applying multinomial theorem provides the following expression

$$\begin{aligned} \Theta_1(x)^{k-l} &= \left(\Phi e^{-\left(\frac{x}{\bar{\gamma}_{\mathcal{P}} \eta_s}\right)} \sum_{i=0}^{\mu_s - 1} \frac{1}{i!} \left(\frac{x}{\bar{\gamma}_{\mathcal{P}} \eta_s}\right)^i \right)^{k-l} \\ &= \sum_{u_1 \dots u_{\mu_s}}^{k-l} \frac{(k-l)!}{u_1! \dots u_{\mu_s}!} \frac{\Phi^{k-l} e^{-((k-l)/\bar{\gamma}_{\mathcal{P}} \eta_s) x} x^{\sum_{\vartheta=0}^{\mu_s-1} \vartheta u_{\vartheta+1}}}{\prod_{\vartheta=0}^{\mu_s-1} \left(\vartheta! (\bar{\gamma}_{\mathcal{P}} \eta_s)^{\vartheta}\right)^{u_{\vartheta+1}}}. \end{aligned} \tag{B.3}$$

Again multinomial and binomial theorem give the following expression for $\Theta_2(x)^l$ as

$$\Theta_2(x)^l = \sum_{w_1 \ldots w_{\mu_s}}^{l} \frac{l!}{w_1! \ldots w_{\mu_s}!} \prod_{t=0}^{\mu_s-1} \binom{\mu_p + t - 1}{\mu_p - 1}^{w_{t+1}}$$
$$e^{-(\bar{\gamma}_{\mathcal{I}} l / \bar{\gamma}_{\mathcal{P}} \eta_p)} \epsilon^{\mu_p l} e^{-(l/\bar{\gamma}_{\mathcal{P}} \eta_s) x} x^{\sum_{t=0}^{\mu_s-1} t w_{t+1}}$$
$$\underbrace{\prod_{t=0}^{\mu_s-1} \left(\sum_{g=0}^{\mu_p+t-1} \frac{1}{g! (\bar{\gamma}_{\mathcal{P}} \eta_s)^g} (x+\epsilon)^g \right)^{w_{t+1}}}_{\mathcal{J}_3} \left(\underbrace{\prod_{t=0}^{\mu_s-1} \left((x+\epsilon)^{\mu_p+t} \right)^{w_{t+1}}}_{\mathcal{J}_4} \right)^{-1}. \tag{B.4}$$

Let denotes $\widetilde{L_{a_n}} = \sum_{b_n=0}^{\mu_p+n-2} b_n a_{b_n+1}$. By expanding $\mathcal{J}_3$ and $\mathcal{J}_4$, together with (B.2), (B.3), (B.4), yields (9).

Appendix C: Proof of Theorem 3

From (7), we can rewrite it as the Gamma form as

$$F_{\gamma_k^s \mathbb{I}_k}(x) = 1 - \Lambda \Phi \frac{\Upsilon\left(\mu_s, \frac{x}{\bar{\gamma}_{\mathcal{P}} \eta_s}\right)}{\Gamma(\mu_s)} - \Lambda \sum_{j=0}^{\mu_s-1} \frac{\epsilon^{\mu_p} x^j \Gamma\left(\mu_p + j, \frac{x+\epsilon}{\bar{\gamma}_{\mathcal{P}} \eta_s}\right)}{j! \Gamma(\mu_p) (x+\epsilon)^{\mu_p+j}}. \tag{C.1}$$

It can be easily seen that as y goes to infinity,

$$\lim_{y \to \infty} \frac{\Upsilon(\mu_\chi, x/y)}{\Gamma(\mu_\chi)} \approx 0 \text{ and}$$
$$\lim_{y \to \infty} \frac{\Gamma(\mu_\chi, x/y)}{\Gamma(\mu_\chi)} \approx 1. \tag{C.2}$$

Substituting (C.2) into (C.1) with the given outage threshold γ_{th}, we can obtain

$$\mathcal{P}_{out}^{Asy}(\gamma_{\text{th}}) \overset{\bar{\gamma}_{\mathcal{P}} \to \infty}{=} \prod_{k=1}^{K} \left(1 - \Lambda \frac{1}{\left(1 + \frac{x}{\epsilon}\right)^{\mu_p}} \right)$$
$$\overset{\bar{\gamma}_{\mathcal{P}} \to \infty}{=} \prod_{k=1}^{K} (1 - \Lambda), \tag{C.3}$$

where $\sum_{j=0}^{\mu_s-1}(.)$ is dominated by $j = 0$ as $\bar{\gamma}_{\mathcal{P}} \to \infty$.

References

1. Andrews, J.G.: Seven ways that HetNets are a cellular paradigm shift. IEEE Commun. Mag. **51**(3), 136–144 (2013)
2. Coldrey, M., Koorapaty, H., Berg, J.-E., Ghebretensae, Z., Hansryd, J., Derneryd, A., Falahati, S.: Small-cell wireless backhauling: a non-line-of-sight approach for point-to-point microwave links. In: Proceedings of IEEE Vehicular Technology Conference, Quebec City, Canada, pp. 1–5 (2012)
3. Mayer, Z., Li, J., Papadogiannis, A., Svensson, T.: On the impact of backhaul channel reliability on cooperative wireless networks. In: Proceedings of IEEE International Conference on Communications, Budapest, Hungary, pp. 5284–5289 (2013)
4. Kim, K.J., Orlik, P.V., Khan, T.A.: Performance analysis of finite-sized cooperative systems with unreliable backhauls. IEEE Trans. Wirel. Commun. **15**(7), 5001–5015 (2016)
5. Kim, K.J., Khan, T., Orlik, P.: Performance analysis of cooperative systems with unreliable backhauls and selection combining. IEEE Trans. Veh. Technol. **66**, 2448–2461 (2016)
6. Peng, M., Liu, Y., Wei, D., Wang, W., Chen, H.-H.: Hierarchical cooperative relay based heterogeneous networks. IEEE Wirel. Commun. **18**(3), 48–56 (2011)
7. Al-Qahtani, F.S., Zhong, C., Alnuweiri, H.M.: Opportunistic relay selection for secrecy enhancement in cooperative networks. IEEE Trans. Commun. **63**(5), 1756–1770 (2015)
8. Kim, K.J., Duong, T.Q., Tran, X.-N.: Performance analysis of cognitive spectrum-sharing single-carrier systems with relay selection. IEEE Trans. Signal Process. **60**(12), 6435–6449 (2012)
9. Andrews, J.G., Buzzi, S., Choi, W., Hanly, S.V., Lozano, A., Soong, A.C., Zhang, J.C.: What will 5G be? IEEE J. Sel. Areas Commun. **32**(6), 1065–1082 (2014)
10. Zhang, R., Liang, Y.-C.: Exploiting multi-antennas for opportunistic spectrum sharing in cognitive radio networks. IEEE J. Sel. Top. Signal Process. **2**(1), 88–102 (2008)
11. Niyato, D., Hossain, E.: Competitive pricing for spectrum sharing in cognitive radio networks: dynamic game, inefficiency of nash equilibrium, and collusion. IEEE J. Sel. Areas Commun. **26**(1), 192–202 (2008)
12. Duong, T.Q., da Costa, D.B., Elkashlan, M., Bao, V.N.Q.: Cognitive amplify-and-forward relay networks over Nakagami-m fading. IEEE Trans. Veh. Technol. **61**(5), 2368–2374 (2012)
13. Deng, Y., Wang, L., Elkashlan, M., Kim, K.J., Duong, T.Q.: Generalized selection combining for cognitive relay networks over Nakagami-m fading. IEEE Trans. Signal Process. **63**(8), 1993–2006 (2015)
14. Duong, T.Q., Bao, V.N.Q., Alexandropoulos, G.C., Zepernick, H.-J.: Cooperative spectrum sharing networks with AF relay and selection diversity. IET Electron. Lett. **47**(20), 1149–1151 (2011)
15. Duong, T.Q., Bao, V.N.Q., Zepernick, H.-J.: Exact outage probability of cognitive AF relaying with underlay spectrum sharing. IET Electron. Lett. **47**(17), 1001–1002 (2011)
16. Guimaraes, F.R.V., da Costa, D.B., Tsiftsis, T.A., Cavalcante, C.C., Karagiannidis, G.K.: Multiuser and multirelay cognitive radio networks under spectrum-sharing constraints. IEEE Trans. Veh. Technol. **63**(1), 433–439 (2014)
17. Lodhi, A., Said, F., Dohler, M., Aghvami, A.H.: Closed-form symbol error probabilities of STBC and CDD MC-CDMA with frequency correlated subcarriers over Nakagami-m fading channels. IEEE Trans. Veh. Technol. **57**(2), 962–973 (2008)

18. Duong, T.Q., Yeoh, P.L., Bao, V.N.Q., Elkashlan, M., Yang, N.: Cognitive relay networks with multiple primary transceivers under spectrum-sharing. IEEE Signal Process. Lett. **19**(11), 741–744 (2012)
19. Khan, T.A., Orlik, P., Kim, K.J., Heath, R.W.: Performance analysis of cooperative wireless networks with unreliable backhaul links. IEEE Commun. Lett. **19**(8), 1386–1389 (2015)
20. Tsiftsis, T.A., Karagiannidis, G.K., Sagias, N.C., Kotsopoulos, S.A.: Performance of MRC diversity receivers over correlated Nakagami-m fading channels. In: Proceedings of Communication Systems, Networks and Digital Signal Processing, Patras, Greece, pp. 84–88 (2006)
21. Cavers, J.K.: Single-user and multiuser adaptive maximal ratio transmission for Rayleigh channels. IEEE Trans. Veh. Technol. **49**(6), 2043–2050 (2000)
22. Duong, T.Q., da Costa, D.B., Tsiftsis, T.A., Zhong, C., Nallanathan, A.: Outage and diversity of cognitive relaying systems under spectrum sharing environments in Nakagami-m fading. IEEE Commun. Lett. **16**(12), 2075–2078 (2012)
23. Duong, T.Q., Alexandropoulos, G.C., Zepernick, H.-J., Tsiftsis, T.A.: Orthogonal space-time block codes with CSI-assisted amplify-and forward relaying in correlated Nakagami-m fading channels. IEEE Trans. Veh. Technol. **60**(3), 882–889 (2011)
24. Gradshteyn, I.S., Ryzhik, I.M.: Table of Integrals, Series, and Products. Academic Press, New York (2007)

Computer Science

Coupling Statistical and Agent-Based Models in the Optimization of Traffic Signal Control

Dang-Truong Thinh[1], Hoang-Van Dong[1], Nguyen-Ngoc Doanh[2,3], and Nguyen-Thi-Ngoc Anh[1,3](✉)

[1] Hanoi University of Science and Technology, Hanoi, Vietnam
truongthinh074@gmail.com, donghv.mi@gmail.com, anh.nguyenthingoc@hust.edu.vn

[2] Thuy Loi University, Hanoi, Vietnam
doanh.nguyenngoc@edu.tl

[3] IRD, Sorbonne Universités, UPMC Univ Paris 06 UMMISCO, 32 Avenue Henri Varagnat, 93143 Bondy Cedex, France

Abstract. There have been two directions to target to the problem of Traffic Signal Control (TSC): macroscopic and microscopic. On one hand, macroscopic help to find the optimal solution with an assumption of homogenization (both for vehicles and environment). On the other hand, microscopic one can take into account heterogeneity in vehicles as well as in environment. Therefore, it is very important to couple the two directions in the study of TSC. In this paper, we proposed to couple statistical and agent-based models for TSC problem in one intersection. The experiment results indicated that the proposed model is sufficient good in comparison with some others TSC strategies.

1 Introduction

Recently, Traffic Signal Control (TSC) is an important problem that has attracted the attention of many researchers [1,12–19]. There are many different approaches to study TSC such as Markov state transition model [19], Mixed-integer programming [16], Kinematic wave model [12], fundamental diagram [13], Agent-based model [17,18]. These approaches can be divided into two groups: macroscopic model and microscopic one. The strengths of the macroscopic models are able to find the optimal solution, but these approaches only consider the homogeneous vehicles as well as the homogeneous environment. In contrast, the strengths of microscopic model are taking into account many different behaviors of vehicles and heterogeneous environment. However, the weakness of the simulation model is hardly finding the optimal solution. Therefore, the combination of statistical and agent-based models uses advantage of each model.

In this paper, we focus on optimizing multiple performance indices (i.e., multi-objective traffic signal control) at each intersection. In the fact that traffic signal control can be viewed as a multi-objective optimization problem in two levels. First, the system level optimizes the routing on the whole transportation network. Second, the local level optimizes the routing at an intersection.

© ICST Institute for Computer Sciences, Social Informatics and Telecommunications Engineering 2018
Y. Chen and T. Q. Duong (Eds.): INISCOM 2017, LNICST 221, pp. 197–211, 2018.
https://doi.org/10.1007/978-3-319-74176-5_18

The multi-objective function can have a global objective for the entire road network or there may be different objectives for the different parts of the road network different times of the day for the same part of the road network [1].

Dynamic Traffic Signal Control modeling is the formulation of rigorous mathematical models and Agent-based model that represent the various dynamics of the traffic system. This includes drivers's behavior in acceleration, deceleration, lane changing, phenomena such as rubbernecking, and behavior change under different weather conditions. Dynamic Traffic Signal Control simulators are used for experimentation and validation of the underlying traffic models and traffic control mechanisms [1,5].

On the other hand, there are several researchers who are currently exploring full Bayes modeling [9,10] for evaluating parameters. There are a number of attractive characteristics of the full Bayes approach. In the fact that, Bayesian statistics offers an ideal framework for analyzing uncertainties conditions to identify parameters. However, the exact Bayesian formulation usually require the posterior distributions of modal parameters [9]. This paper, the advantage of Bayes modelling is use to evaluate parameters of signal traffic lights.

In this paper, we investigate the research problem about optimizing traffic signal control by using new hybrid-based model that integrating statistical model and agent-based model. In the fact that two flows of vehicles meet together at an intersection are considered. Traffic signal lights are assumed to use to control these vehicle flows at the intersection. The research problem is finding the time of green lights at intersection to minimize the waiting time of vehicles. To modelling this problem, the other researchers often using mathematical models such as LWR models, cellular automata models, social force model, statistical analysis model [6,7]. However, mathematical models can not take into account the complex environment and heterogeneous behaviours of vehicles so Agent-based models being used [8]. The disadvantage of agent-based models are computing cost and very difficult to optimize this problem. Thus, we propose a hybrid-based model integrating statistical model and Agent-based model by using advantage of each model that see Fig. 1.

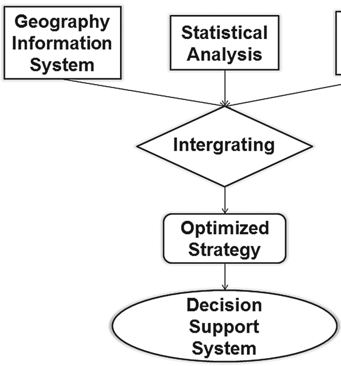

Fig. 1. Hybrid-based model compound by GIS, statistical model and agent-based model.

This paper is divided into four sections: Introduction that represents the important role of artificial Intelligent and research objects in dynamic traffic signal control and related works are concerned. The second section, methodology of optimization traffic signal control is investigated. Concretely, integrating two approaches to enhance effective optimization dynamic traffic signal control is represented in this section. The third section, implementation and applications for particular cases in Hanoi, Vietnam at an intersection are established; The last subsection is conclusion and discussion.

2 Methodology

The research problem consider two flows of vehicles meet together at an intersection are considered. At the intersection, traffic signal lights are assumed to use to control these vehicle flows. Finding the time of green lights at intersection to minimize the waiting time of vehicles is solved by integrating two methods.

2.1 Initial Assumption

Assumption. We will list assumptions used in this paper as follows:

– An intersection is a cross-point between two one-way roads with the same length. It has only two traffic lights for controlling the flow of transportation.
– Time interval in green state of traffic lights at A and B are integers belonged in the interval $[30, 60]$.
– Time interval in green state of a traffic light on road A (B) is a random variable followed exponential distribution.
– When a traffic light on a road stays in green or yellow state, the other must stay in red state.
– Number of vehicles that arrives to the intersection between road A and B in one second is a random variable followed Poisson distribution.
– The pattern for switching states process of traffic lights is: red $\rightarrow$ green $\rightarrow$ yellow $\rightarrow$ red.
– Time period in a yellow state constantly equals ye seconds.
– A traffic light's period is defined as a time interval that starts at the beginning of a green state and stops at the end of next red state.
– There is no one that has to wait more than a traffic light's period (condition for no traffic jam) (Fig. 2).

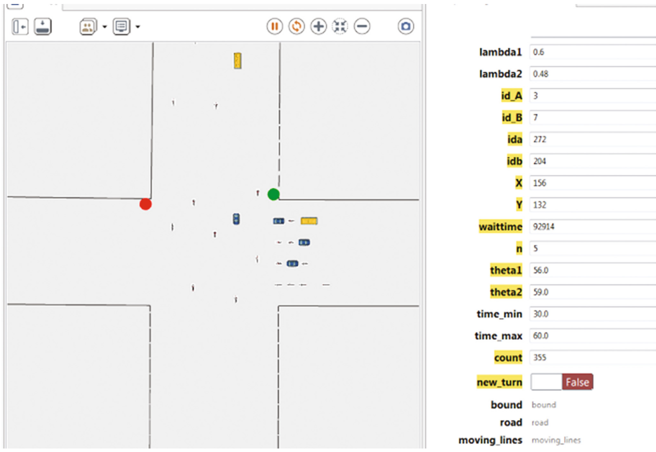

Fig. 2. Intersection is a cross-point between two one-way roads. Two traffic lights for controlling the flow of transportation. (Color figure online)

Variables Are Used in This Paper. Some notations of parameters and variables that will be used in Bayes estimation are described in the table as follows:

Variable	Description
A, B	The roads cross at intersection
Fl^A, Fl^B	Random variables that describe the number of vehicles entering the intersection from road A, B
X, Y	Random variables that describe the number of waiting vehicles on roads A, B during a traffic light's period
λ_1, λ_2	Average number of traffic capacity that are counted on the number of vehicles entering the intersection from roads A, B during 1 s
θ_1, θ_2	Random variables that describe the time interval in green state of traffic lights
$W_{vehicle}$	The number of vehicles waiting for traffic light on intersection in the interval $[0, T]$
W_{time}	The total of waiting time of all vehicles that have to wait at the intersection in the interval $[0, T]$
$\overline{\theta_1}, \overline{\theta_2}$	Mean value of random sample of θ_1, θ_2

Constant Parameter is Used in This Paper. The constant parameters being used in this method are listed in the table as follows:

Constant	Description
ye	Time interval in yellow state of traffic lights
a	Minimum interval time of green light
b	Maximum interval time of green light
T	The maximum time is considered in our model
N	The number of traffic light's period in the interval $[0, T]$

2.2 Statistical Models

Purpose of this subsection is estimate the expected number of vehicles entering the intersection and the time interval in green state of traffic lights which optimize this problem with the number of waiting vehicles.

Estimate the Expected Number of Vehicles Entering the Intersection. Estimate λ_1, λ_2 Let Fl^A, Fl^B be random variables represent the number of vehicles on the road A, B in one second. Many researchers assume that the flow of vehicles is Poisson process. Thus, the same the other researcher we assume that Fl^A, Fl^B are Poisson random variables with rate λ_1, λ_2 in one second [11]. We need to estimate two parameters λ_1, λ_2.

We assume that we have observation data of road A, B are $(Fl_1^A, Fl_2^A, \cdots, Fl_{N_A}^A)$, $(Fl_1^B, Fl_2^B, \cdots, Fl_{N_B}^B)$ respectively. To estimate two parameters λ_1, λ_2, the maximum likelihood estimation method is used. Concretely, $\hat{\lambda_1}$ is estimated as follows:

$$
\begin{aligned}
\hat{\lambda_1} &= \arg\max_{\lambda_1} \left(p(Fl^A, \lambda_1) \right) = \arg\max_{\lambda_1} \left(\prod_{i=1}^{N} p(Fl_i^A | \lambda_1) \right) \\
&= \arg\max_{\lambda_1} \left(\prod_{i=1}^{N} \frac{\lambda_1^{Fl_i^A} e^{-\lambda_1}}{Fl_i^A!} \right) = \arg\max_{\lambda_1} \left(ln \left(\prod_{i=1}^{N} \lambda_1^{Fl_i^A} e^{-\lambda_1} \right) \right) \\
&= \arg\max_{\lambda_1} \left(ln(\lambda_1) \left(\sum_{i=1}^{N} Fl_i^A \right) - N\lambda_1 \right) \qquad (1)
\end{aligned}
$$

We consider λ_1 as a variable then take derivate the Eq. 1 then take it equal 0 then we have:

$$
\begin{aligned}
&\frac{\sum_{i=1}^{N} Fl_i^A}{\lambda_1} - N = 0 \\
&\Leftrightarrow \lambda_1 = \frac{\sum_{i=1}^{N} Fl_i^A}{N} \qquad (2)
\end{aligned}
$$

By the maximum likelihood estimation method, (2) is unbias estimation of λ_1. Same as λ_1, we have an unbias estimation of λ_2 is $\frac{\sum_{i=1}^{N} Fl_i^B}{N}$ $((Fl_1^B, Fl_2^B, \ldots, Fl_N^B)$ is a random sample of $Fl^B)$.

Bayes Estimation Model. Bayesian estimation is used to estimation parameters of stochastic processes. Bayesian estimation is investigated to find out the unknown parameters duration green light time. In our approach, the current and previous duration green light time become the prior for the next time step. This estimation is considered more stable and more adaptable to the changing environment dynamics. That is if a change occurs in the network dynamics such as rush hours the controller using this probability estimation can handle the traffic efficiently by the way that optimizes the various performance indices (e.g., waiting time, queue lengths, etc.) in the congested periods.

Concretely, let X be a stochastic random variable, S_X be the sample space of X. We assume that X follow the distribution that depends on parameter θ on the sample space Θ. We collect an observer sample space $(X_1, X_2, ..., X_n)$ of the random experiment generated form the random variable X.

Let θ be random variable has prior probability density function $h(\theta)$, $\theta \in \Theta$.

First, we define *likelihood* function:

$$p(X|\theta) = \prod_{i=1}^{n} p(X = X_i|\theta)$$

Using Bayes' theorem, the posterior density function $p(\theta|X)$ is defined:

$$p(\theta|X) = \frac{p(X|\theta).h(\theta)}{p(X)} = \frac{likelihood.prior}{p(X)}$$

New Statistical Model. Considering a traffic light's period on road A. We will calculate the number of waiting vehicles $\overline{X}$ based on $\overline{\theta_1}, \overline{\theta_2}$.

We conduct some remarks as follows:

- All vehicles that arrive the intersection during the time interval from 0 to second $(\overline{\theta_1})$ can go through the intersection.
- All vehicles that arrive the intersection during time interval from second $(\overline{\theta_1})$ to $(\overline{\theta_1} + \overline{\theta_2} + ye)$ must wait in front of stop boarder (wA with vehicles on road A and wB with road B).
- Vehicles that arrive the intersection after second $(\overline{\theta_1} + \overline{\theta_2} + ye)$ can pass the intersection in green state of the next traffic light's period.

First, we consider a traffic light's period on road A. Our goal is to calculate the number of waiting vehicles X based on θ_1, θ_2. We will use notation ye as the yellow state duration ($ye = const$) for further inferences.

From initial conditions, we infer the following remarks:

- Vehicles that arrive the intersection during the time interval from 0 to second θ_1 can go through the intersection.
- All vehicles that arrive the intersection during time interval from second θ_1 to $(\theta_1 + \theta_2 + ye)$ must wait in red state of traffic light.
- Vehicles that arrive the intersection after second $\theta_1 + \theta_2 + ye$ can pass the intersection in green state of the next traffic light's period.

We imply from remarks above that the number of waiting vehicles in a traffic light's period equals the number of arriving vehicles during time interval from second (θ_1) to ($\theta_1+\theta_2+ye$) in the same period. Since the assumptions that number of vehicles arriving the intersection from road A follows Poisson distribution with average number per second λ_1, we can imply the following formula:

$$\begin{aligned} p(X|\theta_1,\theta_2) &= poisson(X,(\theta_2+\theta_1+ye-ye-\theta_1+ye)\lambda_1) \\ &= poisson(X,(\theta_2+ye)\lambda_1) \end{aligned}$$

So we imply that:

$$\begin{aligned} p(X|\theta_1,\theta_2) &= poisson(X,(\theta_2+ye)\lambda_1) \\ &= \frac{((\theta_2+ye)\lambda_1)^X e^{(\theta_2+ye)\lambda_1}}{X!} \end{aligned} \tag{3}$$

In the same manner we can see that:

$$p(Y|\theta_1,\theta_2) = \frac{((\theta_1+ye)\lambda_2)^Y e^{(\theta_1+ye)\lambda_2}}{Y!} \tag{4}$$

According to (3) and (4), we have

$$E(X|\theta_1,\theta_2) = \lambda_1(\theta_2+ye) \tag{5}$$

$$E(Y|\theta_1,\theta_2) = \lambda_2(\theta_1+ye) \tag{6}$$

We next consider time interval T that quite greater than the traffic light's period. Define $W_{vehicle}$ as the number of waiting vehicles in this duration. From these assumptions, we can estimate the average number of waiting vehicles during T based on (5), (6):

$$W_{vehicle} = \sum_{i=1}^{N} (\lambda_1(\theta_2(i)+ye) + \lambda_2(\theta_1(i)+ye)) + G \tag{7}$$

Define N as the total number of light's periods during T, G is the number of waiting vehicles in the last light's period (when time interval T equals N times of light's period, $G=0$). We can assume $\lambda_1 \geq \lambda_2$ that without losing the generality of our inferences:

We assign:

$$\overline{\theta_1} = \frac{\sum_{j=1}^{N}\theta_1(j)}{N}$$

$$\overline{\theta_2} = \frac{\sum_{k=1}^{N}\theta_2(k)}{N}$$

Because G can be estimated by $\lambda_1\theta_2^{'}+\lambda_2\theta_1^{'}$ with $\theta_1^{'}$, $\theta_2^{'}$ are red state durations on road A, B ($\theta_1^{'}$ and $\theta_2^{'}$ can be equal to 0), respectively, we can transform formula (7) into:

$$\begin{aligned} W_{vehicle} &= \sum_{i=1}^{N}(\lambda_1-\lambda_2)\theta_2(i) + N\lambda_1 ye + \sum_{i=1}^{N}\lambda_2(\theta_1(i)+\theta_2(i)+ye) + \lambda_1\theta_2^{'} + \lambda_2\theta_1^{'} \\ &= N((\lambda_1-\lambda_2)\overline{\theta_2} + \lambda_1 ye) + (\lambda_1-\lambda_2)\theta_2^{'} + \lambda_2 T \end{aligned} \tag{8}$$

From the condition that A is quite greater than a traffic light's period, we can use approximate estimation without any significant changes in the result:

$$N((\lambda_1 - \lambda_2)\overline{\theta_2} + \lambda_1 ye) + (\lambda_1 - \lambda_2)\theta_2^{'} \approx \frac{T((\lambda_1 - \lambda_2)\overline{\theta_2} + \lambda_1 ye)}{\overline{\theta_1} + \overline{\theta_2} + ye}$$

Therefore, the problem of finding $\{\theta_1(i)\}_{i \leq N}$ and $\{\theta_2(i)\}_{i \leq N}$ to get the smallest W_T can be recognized as the following problem:

$$\min_{\{\overline{\theta_1}, \overline{\theta_2}\}} \left(\frac{T((\lambda_1 - \lambda_2)\overline{\theta_2} + \lambda_1 ye)}{\overline{\theta_1} + \overline{\theta_2} + ye} \right) \tag{9}$$

Where there conditions must be satisfied:

(i) $\theta_1, \theta_2 \in [a, b]$
(ii) $T \gg b$
(iii) $a \gg ye$

Solving problem (9) relates to the problem of optimizing a two-variable rational function. It can be solved easily in specific cases. After solving (9), we can select two satisfied constant sets $\{\theta_1(i)\}_{i \leq N}$ and $\{\theta_2(i)\}_{i \leq N}$ with corresponding values $\overline{\theta_1}$, $\overline{\theta_2}$.

2.3 Agent-Based Model

Modellers using Agent-based models can take into account different behaviours of vehicles depended on city and complex environment such as geometric information system (GIS).

- Each passenger has a motorcycle, a car, a truck, a bus, etc. is an agent has different behaviours such as its own size that occupies space of road, velocity, accelerate, target, etc.
- $\hat{\theta_1}, \hat{\theta_2}$ in this model could be consider with a range replace the average value of statistical model.

Geometric Agents. We built geometric agents based on the real data of an intersection from GIS database. These agents contain the data of roads, start - waiting - end points, and traffic lanes, and thus have all geometric properties (i.e.: position, length, etc.) and do not possess any behaviors.

Vehicle Agents. Vehicle agents represent active vehicles on an intersection. They are the main factors of our model as always be in any traffic models. Vehicle agents have following properties: lanes, current speed. In addition, each mean of transportation has different limitations in speed, size, and minimal distance to others, etc. Vehicle agents' behaviors are described below (Fig. 3):

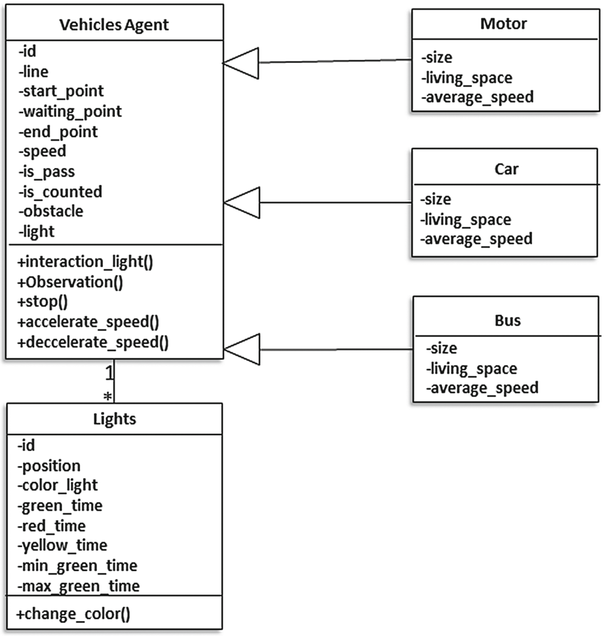

Fig. 3. Interaction between vehicles with control traffic lights

– Moving: Current position changes of the agent follow a given direction.
– Waiting: Vehicles stop in front of a wait-boarder of the road when the traffic light is red state or there is no free space to move (this condition is equivalent to ahead vehicle has an obstacle).

Behavior performing steps are illustrated in the following diagram (in Fig. 4).

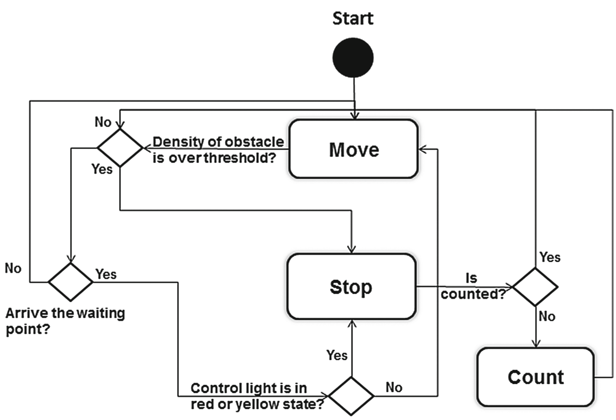

Fig. 4. Behavior of vehicles

Light Agents. Light agents control the traffic flows on an intersection. Their properties includes: color of current state, time intervals of red and yellow state, maximum and minimum time intervals of green state. Light agents' behaviors are shown below:

– As a time counter: Counting time interval of the light agent's current state.
– Color changing: When time counter meets a predetermined threshold, the light agent changes its state as following: green → yellow, yellow → red, red → green.

The relation between light agents' behaviors are illustrated in the diagram below (in Fig. 5):

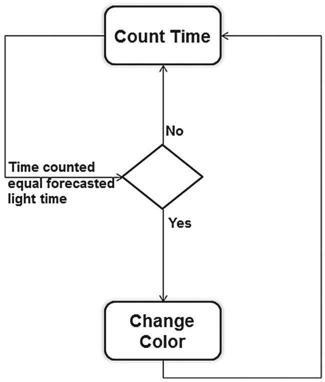

Fig. 5. Behavior of light agents

2.4 Algorithms of the Hybrid Method Integrating Statistical Model and Agent-Based Model

See Fig. 6.

Algorithm 1: Estimated light time by statistical estimation.

Input: Random samples $\left(Fl_1^A, Fl_2^A, \ldots, Fl_{M_A}^A\right)$, $\left(Fl_1^B, Fl_2^B, \ldots, Fl_{M_B}^B\right)$ $(X_1, X_2, \ldots, X_N)$ and $(Y_1, Y_2, \ldots, Y_N)$
T, ye

Output: $\hat{\theta_1}, \hat{\theta_2}$ **and** λ_1**,** λ_2

Estimate λ_1 and λ_2 using (2)
Estimate $\hat{\theta_1}$ and $\hat{\theta_2}$ using (9)

Algorithm 2: Simulation transportation by using Agent-Based Model

Input:	GIS data Ratio of car/bus/motor $\hat{\theta_1}, \hat{\theta_2}, \lambda_1, \lambda_2, T, ye$
Output:	$(X_1^{new}, X_2^{new}, \ldots, X_N^{new})$ and $(Y_1^{new}, Y_2^{new}, \ldots, Y_N^{new})$
	Generate the vehicles cars, bus, motors entering the road A, B having different behaviors Counting the number of waiting vehicles Change θ_1, θ_2 follow different scenarios return $(X_1^{new}, X_2^{new}, \ldots, X_N^{new})$ and $(Y_1^{new}, Y_2^{new}, \ldots, Y_N^{new})$

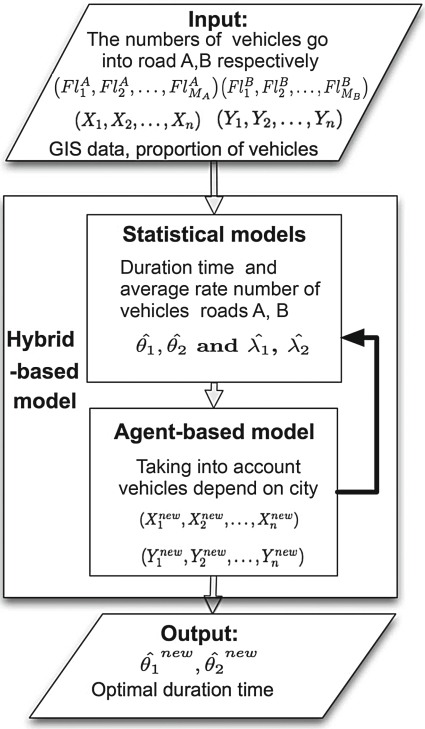

Fig. 6. Hybrid-based model compound by statistical model and agent-based model.

Algorithm 3: Hybrid Based Algorithm

Input: Random samples $(X_1, X_2, \ldots, X_N)$ and $(Y_1, Y_2, \ldots, Y_N)$ λ_1, λ_2, ρ_1, ρ_2

Output: $\{\theta_1(i)\}$ and $\{\theta_2(i)\}$ that make $W_{vehicle}$ minimum

Repeat
Estimate $\hat{\theta_1}, \hat{\theta_2}$ using Algorithm 1.
Using Algorithm 2.
Replace $(X_1, X_2, \ldots, X_n)$ and $(Y_1, Y_2, \ldots, Y_n)$ with $(X_1^{new}, X_2^{new}, \ldots, X_n^{new})$ and $(Y_1^{new}, Y_2^{new}, \ldots, Y_n^{new})$
Estimate $\hat{\theta_1}^{new}, \hat{\theta_2}^{new}$ using Algorithm 1.
until $||\hat{\theta_1}^{new} - \hat{\theta_1}|| + ||\hat{\theta_2}^{new} - \hat{\theta_2}|| < \epsilon$
return $hat\theta_1{}^{new}, hat\theta_2{}^{new}$

3 Experiments and Results

We set up and designed four scenarios which are given in the first table. The result about the total number of waiting vehicles are shown in the second table and are also represented in Fig. 7.

	Description
Scenario 1	θ_1, θ_2 are constants
Scenario 2	θ_1, θ_2 are random variables following truncated Gaussian distribution with mean is mean of t_{min}, t_{max}
Scenario 3	θ_1, θ_2 following truncated Gaussian distribution and estimated by Bayes estimation
Scenario 4	θ_1, θ_2 are constants and obtained by optimal calculation

	θ_1	θ_2	ye	T	λ_1	λ_2	W_{time}	$W_{vehicle}$
Scenario 1	50	40	5	4000	0.6	0.48	72579.4	2598.1
Scenario 2	45	45	5	4000	0.6	0.48	72158.9	2653.5
Scenario 3	59	58	5	4000	0.6	0.48	84772.4	2590.6
Scenario 4	60	30	5	4000	0.6	0.48	76402.4	2529.2

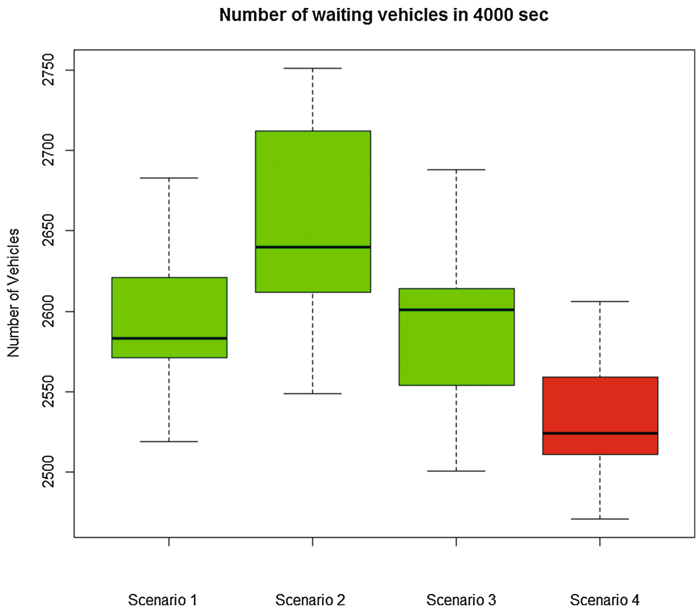

Fig. 7. Results of 4 scenarios that the proposed models is better than the other models.

4 Conclusion and Discussion

This paper opens a protocol for coupling statistical and agent-based models for optimizing TSC. There are three principal messages in the paper. The first is that, based on statistical model from actual and empirical data. The second message is a caution against the homogeneous of behaviour of vehicles and environment so Agent-based model is used. Combining statistical model and ABM to create a new hybrid method. To this end, a number of issues that are critical to the proper conduct of ABM evaluations were raised and illustrated based on recent experience.

Mathematical method using statistical model, agent-based model, hybrid-based model support different and complementary views of the traffic system. Then, we illustrate the agreement between these models. Thus, we show that our proposal model integrating statistical model and Agent-based model by using advantage of each model. Conclusively, the results of this paper are obtained:

- Integrating three models (GIS analysis, statistical estimation model, and Agent-based model) are feasible.
- Integrating model is more effective than GIS analysis approach by considering the dynamic context.
- Integrating model is less timing simulation cost than that of ABM.
- Integrating simulation allows to visualize the vehicles and lights at intersection traffic.

Finally, in future research activity, we need to extend to the case of large-scale environment. In this paper, we just focus on the number of waiting vehicle. In the future, we need to focus on the waiting time and total waiting time.

References

1. Khamis, M.A., Gomaa, W.: Adaptive multi-objective reinforcement learning with hybrid exploration for traffic signal control based on cooperative multi-agent framework. Eng. Appl. Artif. Intell. **29**, 134–151 (2014)
2. Favorskaya, M., Kazmiruk, E., Popov, A.: Distributed system for crossroads traffic surveillance with prediction of incidents. Procedia Comput. Sci. **35**, 851–860 (2014)
3. Antoniou, C., Koutsopoulos, H.N., Yannis, G.: Dynamic data-driven local traffic state estimation and prediction. Transp. Res. Part Emerg. Technol. **34**, 89–107 (2013)
4. Cipriano, F.R.A.: Agent-based model predictive control for the holding problem in a metro system. IFAC Proc. Vol. **46**(9), 1666–1671 (2013). ISSN 1474-6670
5. Nguyen, M.H., Ho, T.V., Nguyen, T.H.: On the dynamic optimization of traffic lights. In: Asian Simulation and Modeling, pp. 35–43. Mahidol University (2013)
6. Nguyen, T.N.A., Chevaleyre, Y., Zucker, J.D.: Optimizing the placement of evacuation signs on road network with time and casualties in case of a Tsunami, enabling technologies. In: 2012 IEEE 21st International Workshop on Infrastructure for Collaborative Enterprises (WETICE), pp. 394–396. IEEE (2012)
7. Anh, N.T.N., Daniel, Z.J., Du, N.H., Drogoul, A., An, V.D.: A hybrid macro-micro pedestrians evacuation model to speed up simulation in road networks. In: Dechesne, F., Hattori, H., ter Mors, A., Such, J.M., Weyns, D., Dignum, F. (eds.) AAMAS 2011. LNCS (LNAI), vol. 7068, pp. 371–383. Springer, Heidelberg (2012). https://doi.org/10.1007/978-3-642-27216-5_28
8. Drogoul, A., Amouroux, E., Caillou, P., Gaudou, B., Grignard, A., Marilleau, N., Taillandier, P., Vavasseur, M., Vo, D.-A., Zucker, J.-D.: Gama: multi-level and complex environment for agent-based models and simulations. In: Proceedings of the 2013 International Conference on Autonomous Agents and Multi-Agent Systems, pp. 1361–1362. International Foundation for Autonomous Agents and Multiagent Systems (2013)
9. Li, B., Der Kiureghian, A.: Operational modal identification using variational Bayes. Mech. Syst. Signal Process. **88**, 377–398 (2017). https://doi.org/10.1016/j.ymssp.2016.11.007. ISSN 0888-3270
10. Park, J., Abdel-Aty, M., Lee, J.: Use of empirical and full Bayes beforeafter approaches to estimate the safety effects of roadside barriers with different crash conditions. J. Saf. Res. **58**, 31–40 (2016). https://doi.org/10.1016/j.jsr.2016.06.002. ISSN 0022-4375
11. Zhang, T., De Grande, R.E., Boukerche, A.: Design and analysis of stochastic traffic flow models for vehicular clouds. Ad Hoc Netw. **52**, 39–49 (2016). ISSN 1570-8705
12. Chow, A.H.F., Li, S., Zhong, R.: Multi-objective optimal control formulations for bus service reliability with traffic signals. Transp. Res. Part B Methodol. **103**, 248–268 (2017). Available online 15 March 2017
13. Yan, F., Tian, F., Shi, Z.: An extended signal control strategy for urban network traffic flow. Phys. A Stat. Mech. Appl. **445**, 117–127 (2016)

14. He, Z., Hua, Y., Wang, L.: Steady-state traffic signal control with variable phase combinations and sequences. IFAC-PapersOnLine **49**(3), 11–18 (2016)
15. Smith, M.: Traffic signal control and route choice: a new assignment and control model which designs signal timings. Transp. Res. Part C Emerg. Technol. **58**, 451–473 (2015)
16. He, Q., Kamineni, R., Zhang, Z.: Traffic signal control with partial grade separation for oversaturated conditions. Transp. Res. Part C Emerg. Technol. **71**, 267–283 (2016)
17. Fang, F.C., Xu, W.L., Lin, K.C., Alam, F., Potgieter, J.: Matsuoka neuronal oscillator for traffic signal control using agent-based simulation. Procedia Comput. Sci. **19**, 389–395 (2013)
18. Stroeve, S.H., Everdij, M.H.C.: Agent-based modelling and mental simulation for resilience engineering in air transport. Saf. Sci. **93**, 29–49 (2017)
19. Xu, Y., Xi, Y., Li, D., Zhou, Z.: Traffic signal control based on Markov decision process. IFAC-PapersOnLine **49**(3), 67–72 (2016)

Optimizing Vehicle Routing with Path and Carbon Dioxide Emission for Municipal Solid Waste Collection in Ha Giang, Vietnam

Anh Dao-Tuan[1], Anh Nguyen-Thi-Ngoc[1,4(✉)], Khanh Nguyen-Trong[2,4], Anh Bui-Tuan[1], and Van Dinh-Thi-Hai[3]

[1] Hanoi University of Science and Technology, Hanoi, Vietnam
anh.nguyenthingoc@hust.edu.vn
[2] Posts and Telecommunications Institute of Technology, Hanoi, Vietnam
[3] Department of Environmental Management, Vietnam National University of Agriculture, Hanoi, Vietnam
[4] IRD, Sorbonne Universités, UPMC Univ Paris 06 Unité Mixte Internationale de Modélisation Mathématique et Informatiques des Systèmes Complexes (UMMISCO), 32 Avenue Henri Varagnat, 93143 Bondy Cedex, France

Abstract. Municipal solid waste (MSW) management issues emerged in many countries due to the steadily increasing population over the last decade, followed by the rising amount of solid waste generated. In most of the urban areas, current waste collection are already overloaded arising from the lack of facilities and insufficient resources. Mathematical optimization models are known to propose useful solutions that get multi-objectives and save cost for decision-makers. In this paper, Geographic Information System (GIS) analysis, integer linear programming (ILP) and mixed integer linear programming (MILP) for optimizing vehicle routing and carbon dioxide emission of municipal solid waste collection will be proposed. Firstly, GIS analysis for the real urban data is handled. Then vehicle routing optimization models considering path and carbon dioxide emission using ILP, MILP are developed. Finally, the results of proposal optimized models have been implemented in a case study in Ha Giang City, Vietnam. Concretely, the total cost the MSW collection using the ILP proposal model is reduced by from 7% to 13.7%, and MILP proposal model is reduced by from 15.1% to 21.5%.

Keywords: Municipal solid waste
Mixed Integer linear programming · Optimization · Simulation
GIS · Waste management

1 Introduction

Daily activities at homes, hospitals, schools, businesses, industries and so on are primarily sources, that generated municipal solid waste (MSW). Multiple components such as population, waste generation rates, technology, resident behavior,

© ICST Institute for Computer Sciences, Social Informatics and Telecommunications Engineering 2018
Y. Chen and T. Q. Duong (Eds.): INISCOM 2017, LNICST 221, pp. 212–227, 2018.
https://doi.org/10.1007/978-3-319-74176-5_19

the state of the economy relate to the municipal solid waste management [16]. In many municipalities of cities in developing countries, the transportation cost of the waste to different facilities such as transfer stations, temporary storage sites, landfills and also the fixed costs and operational of these facilities are the total cost of the solid waste management [10].

Thus, many problems about route optimization of waste collection were asserted in order to achieve effective waste management system. Reduction of operational expenses and optimization of vehicle fleet size need to be researched. The aim of optimizing waste collection vehicle routing is to minimize on fuel consumption rather than finding shortest distances. This can be explained that in many city areas, some of the shorter distances may be inconvenient for driving leading to more fuel consumption, pollution, and/or congestion [10].

Routing involves the use of extensive spatial data making it possible to use new technologies such as Geographic Information System (GIS). GIS is able to provide effective handling, display and manipulation of both geographic and spatial information. GIS also plays a potential role for solving various types of engineering and management problems in siting waste disposal sites. GIS supports development of a multi objective model, especially in collection vehicle routing and scheduling for solid waste management systems such as reduction of travel time, cost of site selection and provides a data bank for future monitoring [10].

Researchers highlighted that mathematical optimization models can propose useful solutions that obtain multi-objectives and save cost for decision-makers. Integer linear programing (ILP) and mixed-integer linear programing (MILP) empowered many researches in optimizing vehicle routing (see [4,10,12,16]). Concretely, Archetti *et al.* [2] proposed an integer programming formulation to solve the orienteering vehicle routing problem. They maximized the total collected profit while satisfying a maximum time duration of the route where ILP solutions are obtained by branch-and-cut algorithm [3]. Moreover, according to Lee *et al.* [11] if a user only has some preliminary data which are restricted only to integers, ILP is appropriate to use. If other specific data are available, which includes both integers and non-integers, the user can use mixed integer programming approach that is expected to give a more accurate solution. Decision makers can choose different approaches based on their preferences and actual situations.

1.1 Case Study: Ha Giang Province, Vietnam

Ha Giang is located in the northernmost region of Vietnam, with mountainous and rocky topography. It shares a common international border of 270 Km with China. Ha Giang has an area of nearly 8000 km^2 and a population of 806,702 (2015). It includes one city, ten districts, five wards, 13 towns, and 177 communes.

Ha Giang city is located in the centre of Ha Giang province with the total area is 133,5 km^2 are habitat of 54,240 people. It is also the economic, cultural and politic center of the province. Tourism is especially developed in recent years. The sharp development in the number of tourists, followed by economic growth and uncontrolled urbanization, has greatly magnified Ha Giang with many problems regarding the exponential amounts of solid waste generation.

The current waste collection and transportation is already overtaxed due to the lack of physical facilities and insufficient human and technical resources as can be evidenced by low collection rates and inefficiency waste transportation. How to deal with its solid waste in Ha Giang city will only become more and more critical.

Hagiang city is currently facing challenges of solid waste management. On an average, about from 1500 to 2500 metric tons of waste is generated in the City per day. The city has a single recognized landfill A. The majority of the remaining waste is indiscriminately disposed of in drainage channels or open land spaces, where it is later burned. Only a small proportion of the waste comprising of plastics and metals is re-used or recycled (Fig. 1).

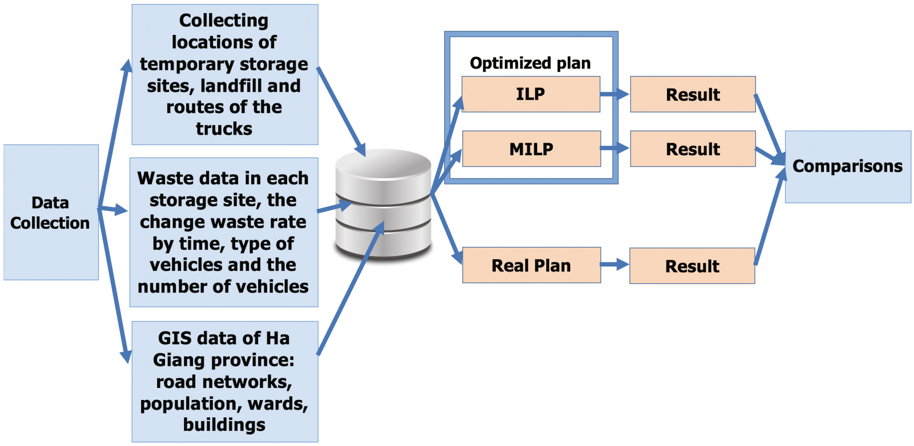

Fig. 1. Methodology structure to find the routes for waste collection in municipal waste management.

This paper is divided into four sections: the introduction represents the important role of MSW and research objects in municipal waste management with related works being investigated; Sect. 2 describes the problem from mathematical view. Two models are built for finding the optimal solution for waste collection problem: MILP and ILP models; we show some computational experiments applying proposed approach for particular cases in Ha Giang, Vietnam; the last subsection is conclusion and discussion.

2 Optimization Formulation for Municipal Solid Waste Collection Problem

2.1 Research Problem of Vehicle Collection Routing

Two main processes of municipal solid waste (MSW) collection are described in Fig. 2. Firstly, the waste are collected from different sources (such as offices, schools, hospitals, ...) and gathered to the nearest collection centre. Each collection centre temporarily stores a huge amount of waste from its nearby sources. Twice per day, there are trucks starting from a depot, traveling through these collection centres on an assigned schedule to collect all waste in its route and finishing the route by returning to the depot.

We are interested in the latter part of the process when municipal solid waste is collected by the trucks to the depot. Because, as proposed by [6], in contemporary MSW management systems, the total management cost is mainly used for waste collection and transportation, namely 80–90% in low-income countries, and 50–80% in middle-income countries.

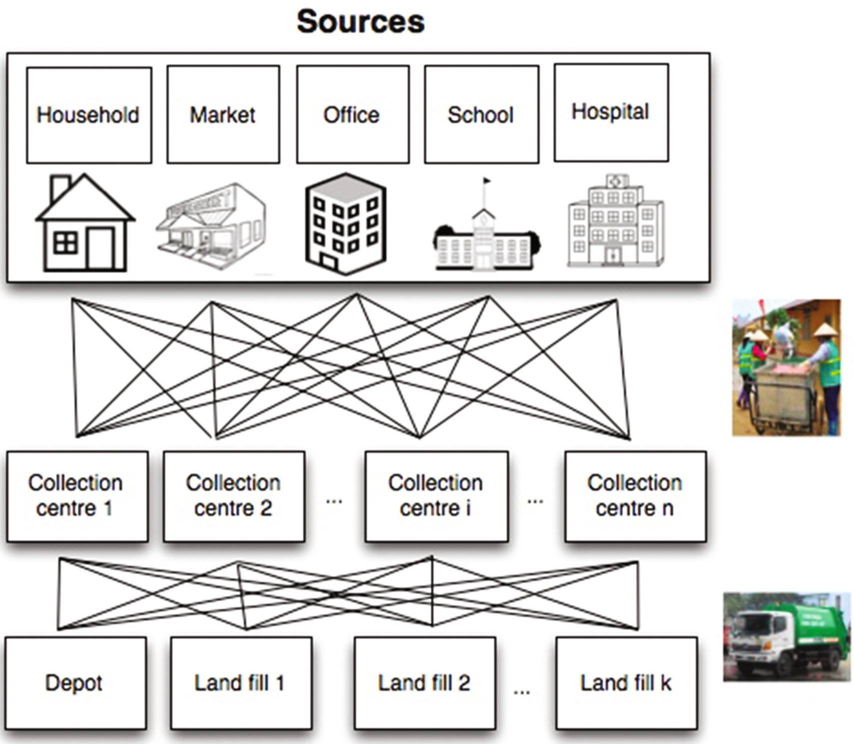

Fig. 2. Architecture of municipal solid waste collection and transportation.

In this paper, we assume these following statements:

- There exists feasible collecting tours of which total volume of waste is less than or equal to the capacity of a truck. By this assumption, our problem is also considered as a Vehicle Routing Problem (VRP). For the VRPs which violate this rule, we can separate the problem into many classic VRPs;
- The landfill is also the depot;
- The distance between any two nodes is well-defined;
- The demand of each waste collection centre is known.

In this section, we consider two equation-based models to identify the optimized plan. The first model is an integer linear programming problem, and the second is a mixed integer programming problem. Let $G = (V, A)$ be the directed graph that indicates the route of a vehicle, where V is a set of collection centres, i.e. $V = \{v_0, \ldots, v_n\}$, and A is a set of arcs representing path connecting vertices, i.e. $A = \{(v_i, v_j) \mid v_i, v_j \in V, i \neq j\}$.

Let v_0 be the depot (also the landfill). $V^{'} = V \setminus \{v_0\}$ is the subset of V that includes n collection centres. Let S be a subset of $V^{'}$ containing all routes that satisfy all constraints of our objectives. Let C be the matrix of non-negative travel costs, where c_{ij} denotes the cost of traveling from v_i to v_j. Let m be the number of vehicles available. Each vehicle has a capacity of q. All vehicles stop at the landfill.

We define some relevant variables as follows:

- Let $A(S) = \{(v_i, v_j) \in V^{'} \mid v_i \in S, v_j \in S\}$ be the set of edges joining all pairs of collection centers in S;
- Let x_{ij} be the number of times that edge (v_i, v_j) is traveled. X is a matrix of x_{ij}, $X = [x_{ij}]_{i,j=\overline{0,n}}$;
- Let a positive q_i be the weight of solid waste in collection centre i, $i = 1, \ldots, n$.

2.2 The Objective Function

We consider two factors for the objective function. The first factor is transportation cost, which is given by

$$F_c = \sum_{i,j=0}^{n} c_{ij} x_{ij}. \tag{1}$$

The second one is the emission factor as proposed by [12], which is given by

$$F_e = \sum_{k=1}^{m} W_k D_k \frac{ER_k}{CR_k \times LF_k}, \tag{2}$$

where W_k is the total weight of waste transported by truck k, ER_k is the carbon dioxide emission rate of fuel ($\mathrm{kgCO_2/l}$), CR_k stands for the fuel consumption rate (km/l), LF_k is the load factor for truck k, representing the average weight of waste for each truck. D_k is the total transport distance of truck i (km). Let $A_k \subseteq A$ be the set arcs traveled by truck k. Since the cost matrix C is relatively calculated on the distances between collection centres, D_k can be expressed as

$$D_k = \frac{1}{\mu} \sum_{(v_i,v_j)\in A_k} c_{ij}x_{ij}, \tag{3}$$

where μ is the travel cost per kilometer of a truck (dollar/km).

The final objective function for optimal path calculation is formulated to minimize the cost for the municipal solid waste collection system with an effort to minimize the impact of carbon dioxide emission. In general, we cannot form an objective function by adding the two objective factors because they do not have the same dimensions, namely dollar per hour and ton per hour, respectively. To deal with this problem we use an approach of the weighted sum method [20], where each factor is assigned a weight to determine its importance. The combined objective function (4) also includes a penalty coefficient

$$\sigma = \frac{\max(F_c)}{\max(F_e)}(\text{km/dollar})$$

that is necessary to normalize the dimension and value range of each factor. Due to the characteristics of the constraints in our following sections, both $\max(F_c)$ and $\max(F_e)$ can be easily calculated using any optimization method to minimize an affine function over a polyhedral convex set. The objective function is defined as

$$F_w = wF_c + (1-w)\sigma F_e, \tag{4}$$

where w is a user-specified weight, which can be any number between 0 and 1. In this paper, we consider the case that two factors are treated equally by setting w equal to 0.5. Equation 4 is rewritten as follows:

$$F = F_c + \sigma F_e. \tag{5}$$

2.3 Integer Linear Programming Model

In Eq. 2, considering the case same type of truck is used, we assume $ER_i = ER$, $CR_i = CR$, $LF_i = LF$, $W_i = q$, $i = 1, \ldots, m$.

We consider the following integer linear programming model, of which objective function is derived from (5):

$$\min F = \left(\sum_{(v_i,v_j)\in A} c_{ij}x_{ij} \right) \left(1 + \sigma\mu q \frac{ER}{CR \times LF} \right) \tag{6}$$

subject to:

$$\sum_{j=0,j\neq i}^{n} x_{ji} = \sum_{j=0,j\neq i}^{n} x_{ij},\ i = 1,\ldots,n; \tag{7}$$

$$\sum_{i=0,i\neq j}^{n} x_{ij} \geq 1,\ j = 1,\ldots,n; \tag{8}$$

$$\sum_{j=0,j\neq i}^{n} x_{ij} \geq 1,\ i = 1,\ldots,n; \tag{9}$$

$$\sum_{i=0}^{n} x_{i0} = m; \tag{10}$$

$$\sum_{j=0}^{n} x_{0j} = m; \tag{11}$$

$$\sum_{v_i \notin S} \sum_{v_j \in S} x_{ij} \geq \sum_{v_k \in S} \frac{q_k}{q},\ \ \forall S \subseteq V^{'}, S \neq \emptyset; \tag{12}$$

$$x_{ij} \in \{0,1\}, \forall i,j \in \{0,\ldots,n\}. \tag{13}$$

The classical assessment restrictions (7)–(9) ensure that each collection centre is visited at least one time. Constraints (10) and (11) indicate the number of trucks in our model and make sure that all the trucks finish their routes at the landfill. Constraints (12) are the capacity cut constraints, which impose that the routes must be connected and that the demand on each route must not exceed the vehicle capacity. These are known to include an exponential number of constraints. Some suggestions are proposed such as to consider a smaller subset of these constraints, or limit to the ones which have a polynomial cardinality (MTZ constraints, see [4,14]). Constraints (13) represent an usual assignment decision logic.

2.4 Mixed Integer Linear Programming Model

Apart from variables and definitions in Sect. 2.1, we add some variables as follows:

- Let y_{ij} present the total remaining load of all vehicles when crossing arc $(v_i, v_j) \in A$. Y is a matrix of y_{ij}, $Y = [y_{ij}]_{i,j=\overline{1,n}}$;
- Let z_i be the number of times that collection centre i is visited by vehicles.

The problem is formulated with the same objective function of (6) and constraints replaced with (14)–(23).

$$\sum_{j|(v_i,v_j)\in A} x_{ij} = \sum_{j|(v_i,v_j)\in A} x_{ji} = z_i,\ \forall i = 1,\ldots,n; \tag{14}$$

$$\sum_{j|(v_i,v_j)\in A} y_{ij} - \sum_{j|(v_i,v_j)\in A} y_{ji} = \begin{cases} -q_i & \text{if } i \neq 0 \\ \sum_{i\in V'} q_i & \text{if } i = 0 \end{cases}; \tag{15}$$

$$y_{ij} \leqslant q x_{ij} \qquad \forall (v_i, v_j) \in A; \tag{16}$$

$$\sum_{v_i \in V'} z_i \leqslant n + m - 1; \tag{17}$$

$$0 \leqslant x_{ij} \leqslant m, x_{ij} \in \mathbb{N}, \qquad \forall (v_i, v_j) \in A(V) \setminus A(V^{'}); \tag{18}$$

$$x_{ij} \in \{0, 1\} \qquad \forall (v_i, v_j) \in A(V^{'}); \tag{19}$$

$$\sum_{v_i \in V'} \frac{q_i}{q} \leqslant z_0 \leqslant m, z_0 \in \mathbb{N}; \tag{20}$$

$$1 \leqslant z_i \leqslant m, \qquad \forall i = 1, \ldots, n; \tag{21}$$

$$y_{ij} \geqslant 0, \qquad \forall (v_i, v_j) \in A; \tag{22}$$

$$y_{0i} = q, \qquad \forall i \neq 0. \tag{23}$$

Constraints (14), (18)–(22) are obvious, followed by the way we define variables. Constraints (15) ensure the load balance. Constraints (16) prevent the vehicles from overloading. Constraints (17) limit the number of times a collection center is visited [2]. The final constraints (23) ensure the vehicles to leave the depot with empty load.

2.5 Algorithm for Finding Routes

We use an algorithm to obtain a feasible solution of the MSW problem, if exists, from a solution after solving the given ILP or MILP. We have this done by matching each pair of an incoming arc and an outgoing arc so that they satisfy the flow constraints.

Considering the solution obtained from the ILP/MILP, it can be seen that y variables only exist in MILP model. However, whether or not, the idea is quite the same. We now provide a pseudo code of procedure FindRoutes, followed by a detailed explanation. The statements in square brackets are only applied for solutions obtained from MILP model and excluded when being used for ILP model.

At the beginning of the algorithm, we sort arcs in $\mathrm{Out}(i)$ in order of non-increasing value of y variables, while $\mathrm{In}(i)$ in order of non-decreasing value of y variables instead. We sequentially consider each arc in $\mathrm{Out}(i)$ and assign it to the first unassigned arc in $\mathrm{In}(i)$. When the assigned incoming arc is arc $(0, i)$, if $x_{0i} > 1$, the current load of $(0, i)$ is set equal to the load of outgoing arc, y_{0i} is decreased by the same amount, and x_{0i} is decreased by one. Otherwise, we assign the current load of arc $(0, i)$ to be equal to y_{0i}.

Algorithm 1. Route finding algorithm

procedure FINDROUTES
    for $i = 1, \ldots, n$ **do**
        [Determine $\mathrm{Out}(i)$ the set of non-increasing positive $y_{ij}, j = 1, \ldots, n$]
        [Determine $\mathrm{In}(i)$ the set of non-decreasing positive $y_{ti}, t = 1, \ldots, n$]
        for each arc $(i, j) \in \mathrm{Out}(i)$ **do**
            Match arc (i, j) to the first arc (t, i) in $\mathrm{In}(i)$ [such that $y_{ti} \geqslant y_{ij}$]
            if there is no such arc **then**
                the Procedure terminates, no route feasible
            end if
            Set $L_{ij} = (t, i)$
            if $t \neq 0$ **then**
                [Set $y_{L_{ij}} = y_{ti}$]
                Remove (t, i) from $\mathrm{In}(i)$
            else
                if $x_{0i} > 1$ **then**
                    Set [$y_{L_{ij}} = y_{ij}, y_{0i} = y_{0i} - y_{ij},$]$x_{0i} = x_{0i} - 1$
                    Insert arc $(0, i)$ in the sorted set $\mathrm{In}(i)$
                    [according to the new value of y_{0i}]
                else
                    [Set $y_{L_{ij}} = y_{0i}$]
                    Remove $(0; i)$ from $\mathrm{In}(i)$
                end if
            end if
        end for
    end for
end procedure

3 Implementation and Application for Case Study in Ha Giang, Vietnam

Hagiang has 33 collection centres as shown in Fig. 3 (the yellow circles denote the collection centres, while the bigger blue circle indicates the location of depot). The waste generation rate is 181.4 tones or 365.4 m^3. Hagiang has two types of trucks (35 m^3 and 50 m^3) that are responsible for the collection and transportation at two regions. Each vehicle collects twice a day (in the morning and in the afternoon).

We present some computational experiments on eight scenarios described in Table 1. In the first four scenarios, we apply two proposed models with the bigger type of trucks. While the rest is for the smaller one. The optimized plans found are described in Table 2.

The comparison of the results obtained for the real plan and the optimized plans of each model are presented in Table 3 and Fig. 4. In Fig. 4, the blue columns indicate the results on current plan, while the white columns and the red columns indicate the results after being optimized when using ILP Model and MILP Model, respectively.

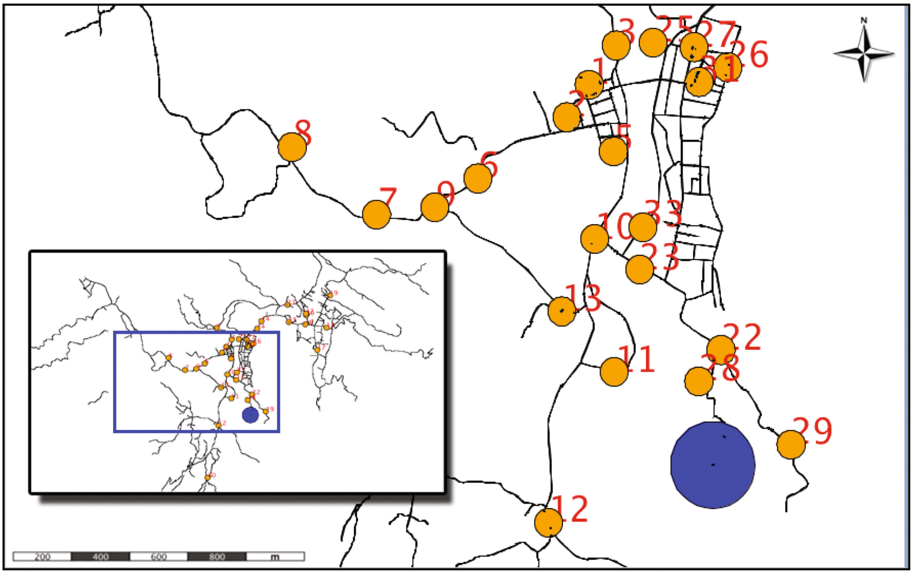

Fig. 3. GIS map of solid waste collection centres and depot in Ha Giang, Vietnam. The smaller map inside describes the locations of overall investigated region; the bigger map is a zoomed view of a smaller part; the yellow circles denote the collection centres, while the bigger blue circle indicates the location of depot. (Color figure online)

Table 1. Scenarios

	Number of trucks	Type of trucks	Collection time	Methodology
Scenario 1	4	50 m^3	Morning	ILP
Scenario 2	4	50 m^3	Morning	MILP
Scenario 3	4	50 m^3	Afternoon	ILP
Scenario 4	4	50 m^3	Afternoon	MILP
Scenario 5	5	35 m^3	Morning	ILP
Scenario 6	5	35 m^3	Morning	MILP
Scenario 7	5	35 m^3	Afternoon	ILP
Scenario 8	5	35 m^3	Afternoon	MILP

Substantial differences can be observed in the values obtained both from the optimization of routes for distance and CO_2 based on MILP model, when compared to the ones estimated for the actual plan, and also ILP. In this case, the optimized solution finding by MILP is better than the solution finding by ILP.

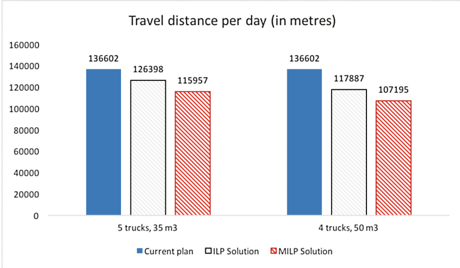

(a) The total travel distance of trucks (metres) per day.

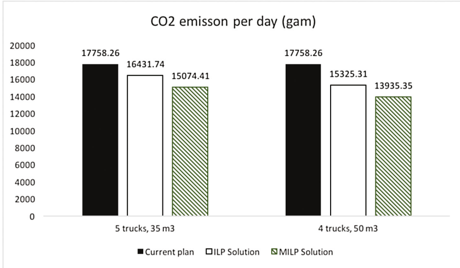

(b) Total weights of CO_2 emission (gams) per day.

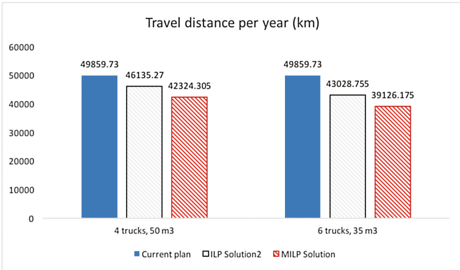

(c) The total travel distance of trucks (km) per year.

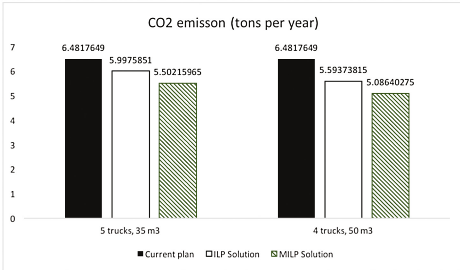

(d) Total weights of CO_2 emission (ton) per year.

Fig. 4. The results are compared among scenarios by different methodologies. The blue columns indicate the results on current plan, while the white columns and the red columns indicate the results after being optimized when using ILP model and MILP model, respectively. (Color figure online)

Table 2. Computational results

Scenario	Schedule	Travel distance (metre)	CO_2 emission (gam)	Objective value
Real plan (morning)	Route 1: 1 → 32 → 27 → 28 → 24 → 1	76674	9967.62	153348
	Route 2: 1 → 22 → 21 → 33 → 18 → 19 → 20 → 17 → 16 → 25 → 28 → 34 → 24 → 1			
	Route 3: 1 → 29 → 30 → 23 → 6 → 2 → 1			
	Route 4: 1 → 4 → 5 → 3 → 7 → 8 → 9 → 10 → 14 → 1			
	Route 5: 1 → 24 → 31 → 13 → 12 → 11 → 6 → 2 → 24 → 1			
Real plan (afternoon)	Route 1: 1 → 27 → 28 → 34 → 24 → 1	59928	7790.64	119856
	Route 2: 1 → 25 → 15 → 16 → 17 → 18 → 19 → 20 → 21 → 22 → 26 → 1			
	Route 3: 1 → 29 → 23 → 6 → 5 → 4 → 2 → 1			
	Route 4: 1 → 3 → 7 → 8 → 9 → 10 → 14 → 13 → 12 → 11 → 1			
	Route 5: 1 → 24 → 1			
Scenario 1	Route 1: 1 → 19 → 20 → 18 → 17 → 16 → 22 → 33 → 21 → 5 → 2 → 4 → 9 → 8 → 10 → 1	62820	8166.60	125640
	Route 2: 1 → 24 → 1			
	Route 3: 1 → 32 → 27 → 25 → 28 → 23 → 30 → 29 → 1			
	Route 4: 1 → 34 → 12 → 13 → 31 → 11 → 14 → 7 → 3 → 6 → 1			
Scenario 2	Route 1: 1 → 24 → 12 → 13 → 31 → 14 → 9 → 8 → 10 → 7 → 3 → 24 → 23 → 1	57941	7532.33	115882
	Route 2: 1 → 27 → 25 → 11 → 34 → 28 → 32 → 23 → 30 → 1			
	Route 3: 1 → 28 → 25 → 16 → 21 → 17 → 19 → 18 → 20 → 21 → 33 → 22 → 5 → 4 → 2 → 3 → 6 → 1			
	Route 4: 1 → 29 → 1			
Scenario 3	Route 1: 1 → 5 → 4 → 6 → 11 → 16 → 19 → 18 → 20 → 21 → 22 → 17 → 15 → 1	55067	7158.71	110134
	Route 2: 1 → 25 → 26 → 28 → 27 → 1			
	Route 3: 1 → 29 → 23 → 24 → 1			
	Route 4: 1 → 34 → 14 → 13 → 12 → 8 → 9 → 10 → 7 → 3 → 2 → 1			

(*continued*)

Table 2. (*continued*)

Scenario	Schedule	Travel distance (metre)	CO_2 emission (gam)	Objective value
Scenario 4	Route 1: 1 → 24 → 6 → 7 → 8 → 9 → 10 → 14 → 12 → 13 → 11 → 23 → 1	49254	6403.02	198508
	Route 2: 1 → 27 → 28 → 15 → 16 → 20 → 19 → 17 → 18 → 21 → 22 → 5 → 4 → 2 → 3 → 6 → 1			
	Route 3: 1 → 28 → 25 → 26 → 34 → 29 → 1			
	Route 4: 1 → 29 → 24 → 1			
Scenario 5	Route 1: 1 → 8 → 7 → 10 → 9 → 13 → 31 → 12 → 14 → 1	67765	8809.45	135530
	Route 2: 1 → 11 → 6 → 4 → 5 → 2 → 3 → 24 → 1			
	Route 3: 1 → 24 → 1			
	Route 4: 1 → 28 → 25 → 27 → 32 → 1			
	Route 5: 1 → 30 → 16 → 19 → 20 → 18 → 21 → 33 → 22 → 17 → 34 → 29 → 23 → 1			
Scenario 6	Route 1: 1 → 6 → 4 → 5 → 22 → 33 → 21 → 20 → 19 → 18 → 17 → 16 → 25 → 28 → 27 → 1	59978	7797.14	119956
	Route 2: 1 → 23 → 30 → 11 → 13 → 31 → 12 → 24 → 1			
	Route 3: 1 → 24 → 29 → 1			
	Route 4: 1 → 29 → 14 → 9 → 8 → 10 → 7 → 3 → 2 → 6 → 1			
	Route 5: 1 → 34 → 28 → 32 → 1			
Scenario 7	Route 1: 1 → 15 → 28 → 27 → 29 → 1	58633	7622.29	117266
	Route 2: 1 → 21 → 22 → 20 → 19 → 18 → 17 → 16 → 25 → 26 → 1			
	Route 3: 1 → 23 → 7 → 9 → 8 → 10 → 14 → 12 → 13 → 11 → 34 → 1			
	Route 4: 1 → 24 → 1			
	Route 5: 1 → 24 → 6 → 3 → 2 → 4 → 5 → 1			
Scenario 8	Route 1: 1 → 9 → 8 → 10 → 7 → 3 → 2 → 4 → 6 → 34 → 1	55979	7277.27	111958
	Route 2: 1 → 24 → 14 → 12 → 13 → 11 → 23 → 1			
	Route 3: 1 → 27 → 28 → 15 → 16 → 19 → 18 → 17 → 20 → 21 → 22 → 5 → 4 → 1			
	Route 4: 1 → 28 → 25 → 26 → 1			
	Route 5: 1 → 29 → 24 → 1			

Table 3. Result comparison table. The table below compares the computational results among current plan, ILP and MILP optimized plan.

Methodology	Type of truck	Travel cost	Emission cost	Total cost	Percentage saved
Current plan	$35\,m^3$ & $50\,m^3$	49859.73	6.4817549	99719.46	0%
ILP	$35\,m^3$	46135.27	5.9975851	92270.54	7.5%
	$50\,m^3$	43028.755	5.59373815	86057.51	13.7%
MILP	$35\,m^3$	42324.305	5.50215965	84648.61	15.1%
	$50\,m^3$	39126.175	5.08640275	78252.35	21.5%

4 Conclusion and Discussion

This paper proposes two models to optimize the collection and transportation of municipal solid waste, in term of costs and carbon dioxide emissions. These models compose of two steps: (i) firstly, the real and GIS data of municipal solid waste collection and transportation are collected and analyzed; (ii) secondly, the GIS data are integrated with vehicle routing problem in order to find optimized solutions. In the first model, we use an integer linear programming (ILP) approach, while it is the mixed integer linear programming (MILP) approach for the second one. The result of each model is then applied with an algorithm to determine the collection plan.

We presented some experiments in a case study of Hagiang, Vietnam. The results show that the optimized solution finding by MILP is better than the solution finding by ILP. Concretely, the total cost the MSW collection using the ILP proposed model is reduced by from 7% to 13.7%, and MILP proposed model is reduced by from 15.1% to 21.5%.

The achieved results of this paper are as follows:

- Proposing new models for optimizing municipal solid waste collection;
- Integrating two models (GIS analysis, ILP or MILP) are feasible;
- Giving the algorithm for finding route;
- Analysing and comparing path cost, carbon dioxide emission and total cost of eight scenarios to find the best strategy for the decision maker.

Last but not least, in the future works, we will consider multiple types of vehicles in the model and other pollutants (such as NO, PM and so on). Moreover, the objective function of this paper is linear, it is difficult to cover models with complicated factors such as the velocity of vehicles. Therefore, the objective function will be in non-linear form that is a challenge for researchers.

Acknowledgment. This work is funded by the AI Programme with the Vietnam National University of Agriculture (VNUA) (2014–2019).

References

1. Antmann, E.D., Shi, X., Celik, N., Dai, Y.: Continuous-discrete simulation-based decision making framework for solid waste management and recycling programs. Comput. Ind. Eng. **65**(3), 438–454 (2013)
2. Archetti, C., Speranza, M.G., Savelsbergh, M.W.: An optimization-based heuristic for the split delivery vehicle routing problem. Transp. Sci. **42**(1), 22–31 (2008)
3. Archetti, C., Bianchessi, N., Speranza, M.G.: Branch-and-cut algorithms for the split delivery vehicle routing problem. Eur. J. Oper. Res. **238**(3), 685–698 (2014)
4. Christofides, N., Mingozzi, A., Toth, P.: The Vehicle Routing Problem, pp. 315–338. Wiley, Chichester (1979)
5. Chou, I.H., Fan, C.F.: An agent-based national radioactive waste management framework design. Prog. Nucl. Energy **52**(5), 470–480 (2010)
6. Das, S., Bhattacharyya, B.K.: Optimization of municipal solid waste collection and transportation routes. Waste Manag. **43**, 9–18 (2015)
7. Fernández, C., Manyà, F., Mateu, C., Sole-Mauri, F.: Approximate dynamic programming for automated vacuum waste collection systems. Environ. Model. Softw. **67**, 128–137 (2015)
8. Guo, P., Huang, G.H., He, L.: ISMISIP: an inexact stochastic mixed integer linear semi-infinite programming approach for solid waste management and planning under uncertainty. Stoch. Environ. Res. Risk Assess. **22**(6), 759–775 (2008)
9. Nguyen-Trong, K., Nguyen-Thi-Ngoc, A., Nguyen-Ngoc, D., Dinh-Thi-Hai, V.: Optimization of municipal solid waste transportation by integrating GIS analysis, equation-based, and agent-based model. Waste Manag. **59**, 14–22 (2017)
10. Kinobe, J.R., Bosona, T., Gebresenbet, G., Niwagaba, C.B., Vinnerås, B.: Optimization of waste collection and disposal in Kampala city. Habitat Int. **49**, 126–137 (2015)
11. Lee, C.K.M., Yeung, C.L., Xiong, Z.R., Chung, S.H.: A mathematical model for municipal solid waste management - a case study in Hong Kong. Waste Manag. **58**, 430–441 (2016)
12. Lin, T.P.: Carbon dioxide emissions from transport in Taiwan's national parks. Tour. Manag. **31**(2), 285–290 (2010)
13. Malakahmad, A., Bakri, P.M., Mokhtar, M.R.M., Khalil, N.: Solid waste collection routes optimization via GIS techniques in Ipoh city, Malaysia. Procedia Eng. **77**, 20–27 (2014)
14. Miller, C.E., Tucker, A.W., Zemlin, R.A.: Integer programming formulation of traveling salesman problems. J. ACM (JACM) **7**(4), 326–329 (1960)
15. Minoglou, M., Komilis, D.: Optimizing the treatment and disposal of municipal solid wastes using mathematical programming - a case study in a Greek region. Resour. Conserv. Recycl. **80**, 46–57 (2013)
16. Maimoun, M.A., Reinhart, D.R., Gammoh, F.T., Bush, P.M.: Emissions from US waste collection vehicles. Waste Manag. **33**(5), 1079–1089 (2013)
17. Sauvageau, G., Frayret, J.M.: Waste paper procurement optimization: an agent-based simulation approach. Eur. J. Oper. Res. **242**(3), 987–998 (2015)
18. Simic, V.: Fuzzy risk explicit interval linear programming model for end-of-life vehicle recycling planning in the EU. Waste Manag. **35**, 265–282 (2015)
19. Simic, V.: Interval-parameter chance-constraint programming model for end-of-life vehicles management under rigorous environmental regulations. Waste Manag. **52**, 180–192 (2016)

20. Stanzani, A.L., Balbo, A.R., Nepomuceno, L., Baptista, E.C.: Solving the multiobjective environmental/economic dispatch problem using weighted sum and ε-constraint strategies and a predictor-corrector primal-dual interior point method. J. Control Autom. Electr. Syst. **4**(25), 503–515 (2014)
21. Tascione, V., Mosca, R., Raggi, A.: Optimizing the environmental performance of integrated waste management scenarios by means of linear programming: a case study. J. Clean. Prod. **112**, 3086–3096 (2016)

Model-Based Sensitivity of a Disaster Tolerant Active-Active GENESIS Cloud System

Tuan Anh Nguyen[1], Xuhua Rui[1], Damsub Lim[1], Jun Oh[1], Dugki Min[1(✉)], Eunmi Choi[2], Tran Duc Thang[3], and Nguyen Nhu Son[3]

[1] School of Computer Science and Engineering, Konkuk University, Seoul, South Korea
{anhnt2407,abealasd,miaow89,ohkakaru,dkmin}@konkuk.ac.kr

[2] School of Management Information Systems, Kookmin University, Seoul, South Korea
emchoi@kookmin.ac.kr

[3] Institute of Information Technology, Vietnam Academy of Science and Technology, Hanoi, Vietnam
{thang,nnson}@ioit.ac.vn

Abstract. Modern cloud computing systems are prone to disasters. And the true cost due to service outages is reportedly huge. Some of previous works presented the use of hierarchical models: fault tree (FT), reliability block diagram (RBD) along with state-space models: continuous time Markov chain (CTMC) or stochastic petri nets (SPN) to assess the reliability/availability of cloud systems, but with much simplification. In this paper, we attempt to propose a combinatorial monolithic model using reliability graph (RG) for a real-world cloud system called general purpose integrated cloud system (GENESIS). The system is designed in active-active high availability configuration with two geographically distributed cloud sites for the sake of disaster tolerance (DT). We then present the model-based comprehensive analysis of system reliability/availability and their sensitivity. The results pinpoint different findings in which the architecture of active-active and geographically dispersed sites with appropriate interconnections of the cloud apparently enhance the system reliability/availability and assure disaster tolerance for the cloud.

Keywords: Disaster tolerance · High availability · GENESIS
Reliability graph

1 Introduction

Disaster tolerance for cloud computing system is of paramount importance for business continuity in many of internet enterprises nowadays. The physical computing system may suffer different failures leading a long period of outage because of component malfunction, man-made faults or even in more severe manner, system cascading failures and natural-cause disasters [1]. According to

© ICST Institute for Computer Sciences, Social Informatics and Telecommunications Engineering 2018
Y. Chen and T. Q. Duong (Eds.): INISCOM 2017, LNICST 221, pp. 228–241, 2018.
https://doi.org/10.1007/978-3-319-74176-5_20

a research report [2], a data center suffers in average a rising of downtime cost to $740,357 from $500,000 (increased 38%). In addition, within the clusters of 1800 servers used as the building block of Google's IT infrastructure, about 1000 failures of individual machines happen in the first year of each cluster; also thousands of hard drives fails and it takes almost $300 to repair each of these failures [3]. In a statistics in 2013 of 13 major cloud providers [4], the cloud service of these enterprises suffered 7.5 h outage per year in the period 2007–2012 with a huge amount of downtime cost at about 70 millions USDs estimated under hourly costs accepted in industry. Individually, Amazon as one of the largest cloud providers suffered 49 min downtime for its electronic commerce online shopping website (at https://www.amazon.com/) on Jan. 31, 2013 and the cost amounted more than $4 million in lost sales [5]. Recently, Facebook, a completely online-service company, has annouced its revenue of first-quarter 2017 at about $8,032 millions [6], which roughly implies that for every hour of online-service outage, the Facebook is incurred almost $3 millions in sales. Thus, understanding the true cost of cloud outages is crucial for online-service enterprises. In this concern, designing cloud system for continuous and disaster tolerance (DT) is one of critical business strategies to reform their information infrastructure. Comprehending the reliability/availability of a cloud system is thus, essential for internet enterprises to either not overestimate/underestimate the cost of service downtimes and to determine correctly the amount of investment to be made in cloud services in order to create effective Service Level Agreement (SLA) with cloud providers. The ICT enterprises are demanding to perform comprehensive studies on modeling and evaluation of different scales and architectures of cloud systems.

Since 2012, a general purpose integrated cloud system (GENESIS) has been developed in a cooperative project between Konkuk University, Seoul, South Korea and Busan University, Busan, South Korea. The aim of GENESIS cloud is to build up a distributed/parallel platform for streaming big data processing for logistics and transportation applications. For the sake of constant big-data processing, the cloud system architecture needs DT to eliminate various types of severe failures (including man-made, system-originated or natural ones) and thus to enhance the system's reliability/availability. The cloud is architected based on active-active high availability (HA) configuration [7] associated with disaster tolerant design, in which the cloud architecture comprises of two geographically dispersed and identical sites. The cloud is furthermore, designed to be capable of provisioning and scheduling the cloud resources in response to the amount of users' requests coming over time. In this paper, we take GENESIS as a typical active-active cloud system for DT in modeling and analysis to evaluate the system's reliability/availability.

Many of previous work demonstrated the evaluation of system reliability/availability using stochastic models. A variety of previous works [8–12] typically present comprehensive studies on availability modeling and analysis of virtualized server systems (as basic computing blocks) in cloud/data centers with detailed incorporation of failure modes and different recovery strategies.

Trivedi *et al.* [13] shows various availability assessment using stochastic models of real-world systems such as from Cisco, Sun Microsystem. Most of the above-mentioned works demonstrate the use of state-space models like continuous time Markov chain (CTMC) or stochastic reward net (SRN) to capture detailed system behaviors and operational processes. Some other works attempt to compose hierarchical models using combinatorial models and state-space models to resolve the state-space explosion problem in modeling of complex systems. Smith *et al.* [14] presented a thorough study using hierarchical modeling of fault tree (FT) and CTMC for reliability evaluation of blade server systems in data centers. Maciel *et al.* in [15–19] proposed various hierarchical models using reliability block diagram (RBD) and CTMC or stochastic petri net (SPN) for the evaluation of different measures of interest including reliability, availability, survivability and performability of simplified cloud computing systems. Nguyen *et al.* [20] used reliability graph (RG) and SRN to model and evaluate the availability of a typical software defined network (SDN). Preliminary solutions and architecture designs to achieve HA and DT were presented and discussed in a number of works [1,7,21–25]. But very few previous works attempted to model cloud system for DT. Nguyen *et al.* [1] proposed a monolithic SRN for a comprehensive availability assessment of data center for DT. Silva *et al.* [26,27] also used SRN to evaluate the dependability and performability of IaaS designed for disaster tolerant cloud systems. Andrade *et al.* [28] recently presented a detailed modeling of a disaster-recovery-as-a-service solution using the combination of RBD and SRN models. We find a demanding and stimulating fact to conduct a comprehensive study to model a real-world cloud system for DT using RG. The RG is much capable of capturing the overall architecture and networking inside a complex cloud system. Therefore, in this work we attemp to propose a monolithic RG model for the thorough reliability/availability assessment of a real-world disaster tolerant cloud system.

The main contributions of this paper are summarized as follows:

- Propose a stochastic model for the reliability/availability evaluation of a typical cloud system in practice using RG
- Assess thoroughly the active-active cloud for DT with regards to important measures of interest including reliability, Steady State Availability (SSA) and sensitivity of SSA
- Elaborate several findings to help guide the design and development of disaster tolerant cloud systems in practice

The rest of this paper is organized as follows. Section 1 presents a preliminary introduction of cloud-based system for DT. Section 2 introduces a typical architecture of the GENESIS cloud system in consideration. Section 3 presents the modeling of the system. Section 4 presents the numerical results and system assessment. We discuss limitations and feasible directions for the extension of this work in Sect. 5. Section 6 concludes this paper.

2 A Disaster Tolerant Active-Active Cloud System

Figure 1 presents the overall architecture design of the disaster tolerant active-active GENESIS cloud system. The physical system consists of two identical computing sites which are both connected to distant customers. In order to perform DT for the system, the two sides are geographically distributed in distant areas which are far enough to avoid any type of disasters on both sides simultaneously. In addition to fault/disaster tolerance of the both sites, the system is designed in active-active HA configuration in which both sites operate and serve customers independently in order to proactively respond to the varying load of the changing number of users connected to the cloud, and also to probably enhance the system's availability/reliability for cloud users.

The architecture design and operations of both sites are identical. The cloud system in a site consists of four composite divisions including (i) cloud security, (ii) cloud management system, (iii) cloud computing system, and (iv) cloud storage system. When customers access to GENESIS cloud, the requests are delivered to a cloud gateway. A traffic monitor (server) is attached to the gateway to examine and control the user traffics coming into the cloud. The user requests could be directed to the remaining cloud site through the backbone network if the current cloud site undergoes a downtime period or the cloud site does not respond properly to the user requests. After passing the security examination through the firewall, the user requests come to the cloud frontend server. At this time, the user requests have passed the cloud security part and thus the customers can interact with the cloud. The customers now can define their own configuration of the computing system in demand through the cloud management system. Based on the cloud configurations and the number of requests coming to the cloud frontend server, a virtual cloud (VC) manager communicates with the servers of VC provisioning system and VC scheduling system in order to provision/schedule Virtual Machine (VM)s running on a provisioned physical server system. All the requests then are delivered to a cloud management system. This server manages the cloud computing system which comprises of GENESIS cloud system (a cluster of physical computing nodes) and GENESIS cloud database system (a cluster of database nodes). This farm of cloud servers connect to the cloud management server via a central switch with very HA. A load balancer is attached to the cloud farm in order to balance the processing load among the servers. Every computing nodes and database nodes are also interconnected to each other via the central switch in order to process computing jobs with high performance. The system is designed so that an application either for computing or To assure and enhance HA for the GENESIS cloud system, an automated cloud computing node creator is provided to create new computing node (physical server) and install all pre-defined software and environment as initial. There is also an automated cloud storage creator with the same purposes attached to the GENESIS cloud database system. With these automatic creators, we expect to enhance the cloud system's availability and readiness. At the border of the cloud system architecture, the cloud storage system is designed for HA consisting of a storage area network (SAN) and a storage system. For the sake of DT for physical cloud system, two specific networking connections between the two sites are established, one connects the two cloud computing systems via the two central switches and the other connects the two storage systems via the two SANs. The two connections use different technologies, (i) overlay transport virtualization (OTV) [29] for business resiliency to deploy multiple geographically disparate cloud systems; and (ii) switched virtual circuit (SVC) for temporary data transmission between the two storage systems to get the data most updated and synchronized. We will use the above-described cloud system architecture for the modeling and analysis using RG model. For the ease of stochastic modeling in this paper, we assume to limit the number of computing servers and database servers in the cloud computing system at a small number. The detailed description of the system components is summarized in Table 1. In the following sections, we present the overall model of the whole cloud system.

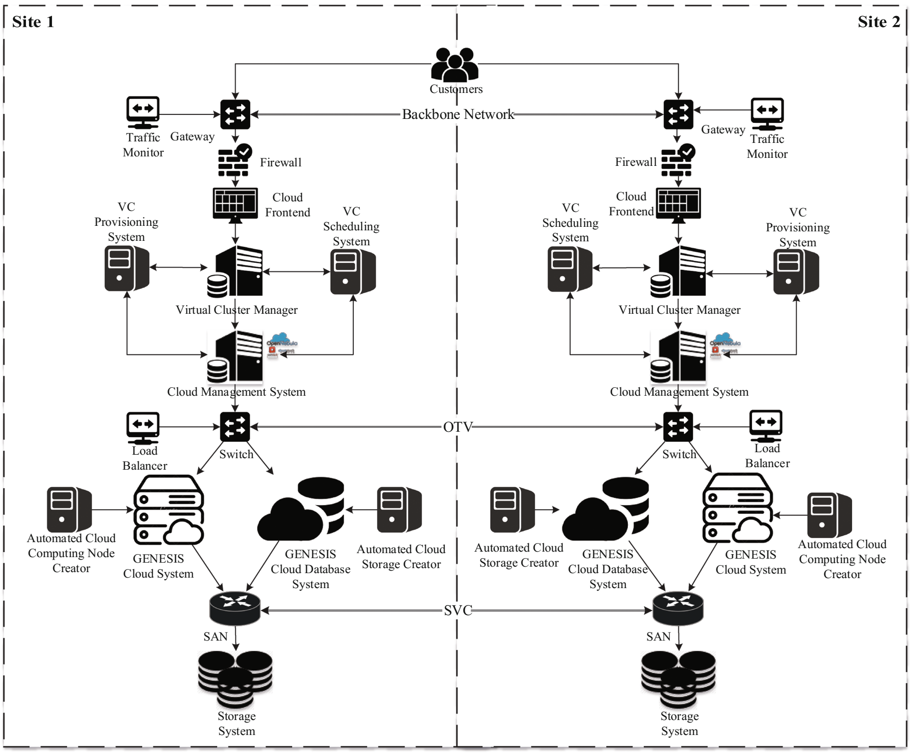

Fig. 1. A disaster tolerant active-active cloud system

3 Reliability Graph Models

Figure 2 illustrates the RG model of the overall two-sites disaster tolerant active-active GENESIS cloud system. The RG model basically consists of two types of elements which are nodes and edges connecting the two different nodes. A node can have a certain number of input/output edges but only two special nodes are different which are sink node (S) with no input edges and destination node (D) with no output edges. An edge in the RG model represents for a certain component of the system. A failure/recovery of a certain component in the system corresponds to the breakage/continuity of the respective edge in the RG model. The information of the system component such as mean time to failure (MTTF) and mean time to repair (MTTR) thus, can be attached to the edges in order to compute the measures of interest like reliability/availability. The whole cloud system is considered reliable/available if the user requests can be dilivered from the customers to the cloud computing division which in turn frequently accesses the storage systems. In term of modeling, the there exists at least one uninterrepted path connecting the sink node and the destination node throughout the edges and normal nodes.

The RG model is constructed strictly based on the overall system architecture. Thus, as shown in Fig. 2, the model also comprises of two branches from sink node to destination node. The connections between the sink node (S) and the nodes (1) and (2) as well as the connection between the destination nodes (D) and the nodes (19) and (48) represent for the connections of users to the two sites which are supposed to be always available. The notation on each edge in RG (summarized in Table 1) depicts the corresponding component of the system residing either in site 1 or site 2. In the cloud system, we assume that there are n_{cS} number of cloud servers hosting n_{App} number of cloud applications in overall. Also correspondingly, there are n_{DB} number of database applications running on respective n_{cDB} cloud database servers. We assume that a certain app can run with multiple instances on different servers. Thus there is no dependences between the edges in the RG models. It is noted to consider the notations in the RG model. The edges with their notations as follows, cS_{ij}, App_{ik}, DB_{ig} and cDB_{il} (where, $i = 1, 2$; $j = 1, n_{cS}$; $k = 1, n_{App}$; $g = 1, n_{DB}$ and $l = 1, n_{cDB}$) respectively represent for the cloud server j, cloud application k, database application g and cloud database server l in the corresponding cloud site i. As shown in the RG model, the model is symmetrical because the two cloud sites are identical. Thus the upper part of the RG model represents for the modeling of the cloud site 1 and the lower part of the RG model is for the cloud site 2.

4 Numerical Results

In this section, we present the evaluation results of the cloud system. The RG model in Fig. 2 is implemented and analyzed using Symbolic Hierarchical Automated Reliability and Performance Evaluator (SHARPE) [30,31] developed by DUKE University, USA. The default values of input parameters for the model

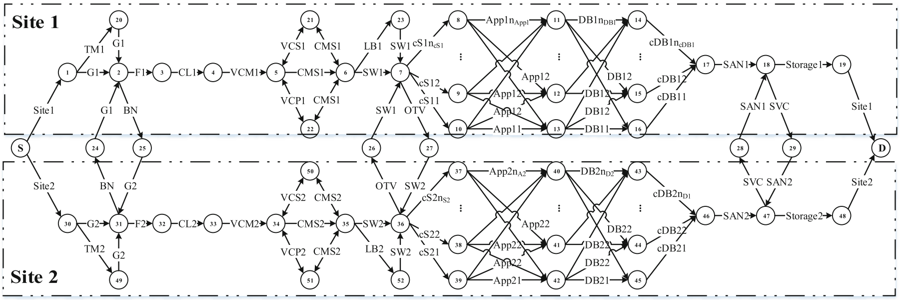

Fig. 2. Reliability Graph Model of the cloud system

are given in Table 2. To realize the pros and cons of the proposed cloud architecture for DT, in this paper, we attempt to evaluate the two cloud systems as follows:

– *Case I*: the cloud system has only one cloud site with no other redundant sites. This system is modeled by either the upper/lower part of the RG model in Fig. 2.
– *Case II*: the cloud system comprises of two redundant cloud sites as proposed in Fig. 1. This system is modeled exactly by the overall RG model in Fig. 2.

Our measures of interest are:

– Reliability of the two cases over time, as shown in Fig. 3
– SSA of the two cases under default values of input parameters, as shown in Table 3
– Sensitivity of SSA with respect to major impacting parameters including λ_{cS} and λ_{cDB}, as shown in Fig. 4a; and λ_{BN}, λ_{OTV} and λ_{SVC}, as shown in Fig. 4b.

Relaibility Analysis: Fig. 3 depicts the reliability analysis results of the cloud system in two cases (i) 1 site and (ii) 2 sites. The gap between the two graphs clearly shows that the system with two redundant sites is much higher reliable over time in comparision with the cloud with only one site. Particularly, the reliability of the system with one site exposes a much faster decaying rate in accordance with the high slope of the respective reliability graph (which is not desired in reliability engineering).

Steady State Analaysis: Under the default parameters, we perform SSA analysis for the cloud systems in the two cases as shown in Table 3. Apparently, the cloud with two sites gains much higher availability (four nines after decimal point) than the one with only one site does (only two nines after decimal point). As we compute downtime minutes for the cloud systems, the two-sites cloud undergoes only about 38 min in a year whereas the another one suffers from 5129 min of outage per year.

Sensitivity analysis of SSA: Fig. 4a shows the variation of the cloud's SSA with respect to major impacting factors in consideration. Figure 4a illustrates the

Table 1. Description of system components and abbreviation in RG system model

Abbreviation	Name	Description
G1, G2	Gateway (switch)	A configured switch specifically receives requests from outer customers
TM1, TM2	Traffic monitor	A server is in charge of monitoring and controlling the amount of traffics flowing into the cloud
BN	Backbone network	A specific network connection between the two sites of the cloud system in order to abstract the physical cloud system with respect to the users
F1, F2	Firewall	A firewall mechanism to examine the coming user requests for security
CL1, CL2	Cloud frontend	A server runs a GUI for user interactions in demanding desired cloud configuration
VCM1, VCM2	Virtual cluster management system	A server runs a cloud management software to configure and request for cluster formation of physical servers
VCS1, VCS2	Virtual cluster scheduling system	A server runs a software to schedule the realistic cluster of servers based on statistic prediction to match with the users' varying load
VCP1, VCP2	Virtual cluster provisioning system	A server runs a prediction software to provision physical server farm to fit with the varying coming requests of customers at a time based on statistic user data
CMS1, CMS2	Cloud management system	A server runs a management software to control and monitor the whole cloud computing system and cloud database system
SW1, SW2	Switch	Cloud central switches connect the two divisions: cloud management system with cloud computing system and also to interconnect the cloud server farm and the cloud database servers
LB1, LB2	Load balancer	A server to balance the processing loads among the computing nodes
OTV	Overlay transport virtualization	A network connection with OTV technology for DT between the two cloud physical infrastructure
cS	Cloud physical server	A server in the cloud farm in charge of processing the user requests
App	Cloud application	A requested application running on a cloud server
DB	Database application	A corresponding database application running along with a certain cloud application
cDB	Cloud database server	A server in the cloud database farm in charge of hosting database applications
SAN1, SAN2	Storage area network	A high-speed network for block-level access to storage system
SVC	Switched virtual circuit	A network connection between the two networks of SANs for data synchronization of storage systems between the two sites
Storage1, storage2	Storage system	A redundant storage system with HA configurations

dependence of the SSA on the MTTFs of cloud servers and cloud database servers (λ_{cS} and λ_{cDB}). As shown in the figure, the two-sites cloud gains clearly higher SSA over time than the one-site cloud does. The distant differences of the graphs are particularly huge in the early range of small values and reduce quickly as the values of the parameters increase. This implies that even for the farm of normal physical servers with low values of MTTF (which may suffer downtime periods more frequently), the architecture of two-sites cloud apparently boosts the system availability compared to the one of one-site cloud. Figure 4b depicts the SSA variation on the MTTFs of the network connection BN, OTV and SVC (λ_{BN}, λ_{OTV} and λ_{SVC}). We observed that, as long as any of the network connection for DT stay available (MTTFs increase), the overall availability of the two-sites cloud is accordingly enhanced. Furthermore, the OTV connection which inter-connects the two central switches of the cloud computing server farm and cloud database server farm is more sensitive than the remaining connections in which a small change of its MTTF (especially in the early period) can cause an apparent variation of the SSA. In comparison, a failure of the BN connection does not pull down the SSA as much as a failure of SVC or OTV connection does. Thus, we realize that the failure of OTV connection causes the most severe consequence to the system's availability. When we compare the two figures Fig. 4a and b, we find that even though the effects of the MTTFs on the system's SSA are similar, but the values of the SSA are much different. In particular, a small change of MTTFs of cloud server and cloud database servers (λ_{cS} and λ_{cDB}) leads to a big difference of the SSA. Whereas an increase or decrease of the MTTFs of the network connection BN, OTV or SVC causes a small change in value of the SSA, in comparison with the previously-mentioned case.

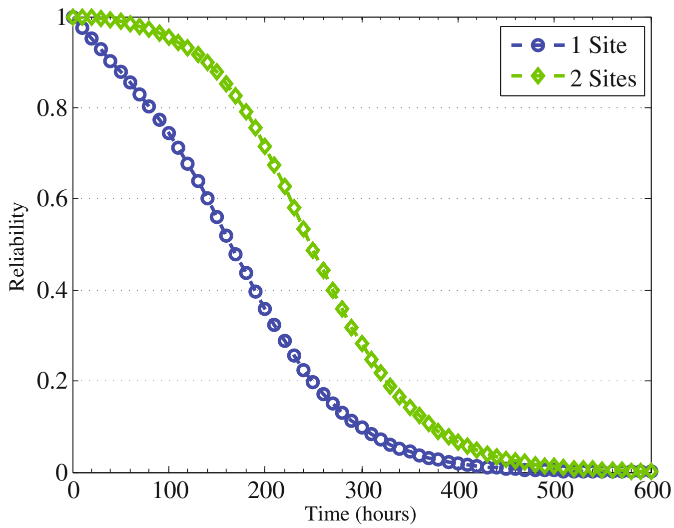

Fig. 3. Reliability analysis

Table 2. Default input parameters

Notation	Description	Value
$1/\lambda_{App}$	Mean time to failure of an application on a server	5 days
$1/\lambda_{BN}$	Mean time to failure of backbone network	3 months
$1/\lambda_{CL}$	Mean time to failure of a cloud frontend server	1.5 months
$1/\lambda_{CMS}$	Mean time to failure of a server of cloud management system	3 weeks
$1/\lambda_{DB}$	Mean time to failure of a database software	3 days
$1/\lambda_{F}$	Mean time to failure of a firewall component	3 months
$1/\lambda_{G}$	Mean time to failure of a gateway component	8 months
$1/\lambda_{LB}$	Mean time to failure of a load-balancer	2 weeks
$1/\lambda_{OTV}$	Mean time to failure of overlay transport virtualization (OTV) connection	5 months
$1/\lambda_{SAN}$	Mean time to failure of a SAN	9 months
$1/\lambda_{SW}$	Mean time to failure of a switch	1 year
$1/\lambda_{Storage}$	Mean time to failure of a storage system	6 months
$1/\lambda_{SVC}$	Mean time to failure of switched virtual circuit (SVC) connection	4 months
$1/\lambda_{TM}$	Mean time to failure of a traffic monitor server	2 weeks
$1/\lambda_{VCM}$	Mean time to failure of a virtual cluster manager server	2 months
$1/\lambda_{VCP}$	Mean time to failure of a virtual cluster provisioning server	3 weeks
$1/\lambda_{VCS}$	Mean time to failure of a virtual cluster scheduling server	3 weeks
$1/\lambda_{cDB}$	Mean time to failure of a cloud database server	2 months
$1/\lambda_{cS}$	Mean time to failure of a cloud server	2 months
$1/\lambda_{DB}$	Mean time to recovery of an application on a server	10 min
$1/\mu_{BN}$	Mean time to recovery of backbone network	5 h
$1/\mu_{CL}$	Mean time to recovery of a cloud frontend server	2 h
$1/\mu_{CMS}$	Mean time to recovery of a server of cloud management system	3 h
$1/\mu_{DB}$	Mean time to recovery of a database software	30 min
$1/\mu_{F}$	Mean time to recovery of a firewall system	2 h
$1/\mu_{G}$	Mean time to recovery of a gateway component	2 h
$1/\mu_{LB}$	Mean time to recovery of a load-balancer	8 h
$1/\mu_{OTV}$	Mean time to recovery of overlay transport virtualization (OTV) connection	7 h
$1/\mu_{SAN}$	Mean time to recovery of a SAN	5 h
$1/\mu_{SW}$	Mean time to recovery of a switch	8 h
$1/\mu_{Storage}$	Mean time to recovery of a storage system	3 h
$1/\mu_{SVC}$	Mean time to recovery of switched virtual circuit (SVC) connection	3 h
$1/\mu_{TM}$	Mean time to recovery of a traffic monitor server	1 h
$1/\mu_{VCM}$	Mean time to recovery of a virtual cluster manager server	8 h
$1/\mu_{VCP}$	Mean time to recovery of a virtual cluster provisioning server	6 h
$1/\mu_{VCS}$	Mean time to recovery of a virtual cluster scheduling server	6 h
$1/\mu_{cDB}$	Mean time to recovery of a cloud database server	8 h
$1/\mu_{cS}$	Mean time to recovery of a cloud server	8 h
n_{cS}, n_{App}, n_{DB}, n_{cDB}	Respectively, numbers of cloud servers, cloud applications, cloud database applications and cloud database servers in each site of the system	3

Table 3. Steady state analysis

Case	Description	SSA	Downtime (minutes/year)
I	Cloud system with 1 site	0.990240932	5129
II	Cloud system with 2 sites	0.999927727	38

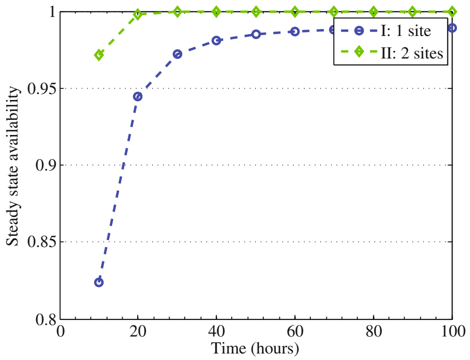

(a) λ_{cS} and λ_{cDB}

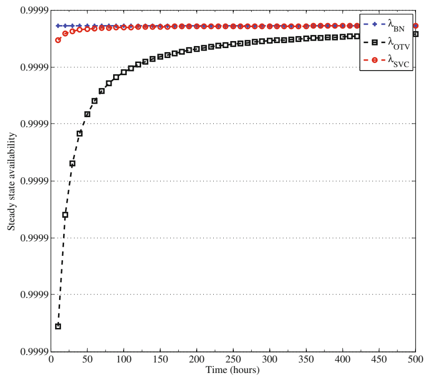

(b) λ_{BN}, λ_{OTV}, and λ_{SVC}

Fig. 4. Sensitivity analysis of SSA wrt. some major impacting parameters

5 Limitations and Extentions

We find an open future research avenue for the reliability/availability of disaster tolerant cloud based systems. The extensions of this work can go in several directions.
Scalability: This work takes into consideration only a small scale system for cloud-based DT. The number of physical nodes in server farm is limited for the sake of modeling and analysis. Nevertheless as the rapid advancement of the real-world data centers and cloud computing systems, it is required to consider the system with a large number of servers or even a multiple number of redundant sites in the cloud system.

Hierarchical modeling: The RG model in this work captures the general architecture and configuration of the cloud system. Nevertheless, we also need to capture the operational states of every components and processes. This direction usually encounters with the largeness problem in modeling in which the hierarchical modeling is an efficient approach for the future extension of this work.

Security: Security for cloud currently is of paramount importance. Although the cloud architecture in this work takes into account security elements in design, but the modeling and analysis for security along with availability/reliability needs an appropriate extension.

6 Conclusion

This paper presented a reliability/availability modeling and analysis of an active-active cloud system for DT. The typical cloud physical system consists of two sites which are geographically dispered and interconnected for the sake of DT. The modeling using RG is the main approach to capture the overall system architecture. We carried out a comprehensive evaluation of system reliability, SSA and the sensitivity of SSA with respect to MTTFs of physical servers and interconnecting network connections between the two cloud sites. The results showed that the proposed architecture of active-active two-sites cloud can assure DT and enhance overall reliability/availability. Furthermore, the analysis also figured out the importances of network connection between the two sites. This work is also planned to extend in different manners including scalability of the system, hierarchical modeling for the whole physical system and security modeling and analysis for the cloud in future work.

Acknowledgment. – This research was supported by the Vietnam-Korea cooperation project: VAST.HTQT.HANQUOC.01/17-18 managed by Vietnam Academy of Science and Technology.

– This work was supported under the framework of international cooperation program managed by the National Research Foundation of Korea (project number, FY2016K2A9A1A06925440).

References

1. Nguyen, T.A., Kim, D.S., Park, J.S.: Availability modeling and analysis of a data center for disaster tolerance. Future Gener. Comput. Syst. (2015). http://www.sciencedirect.com/science/article/pii/S0167739X15002824
2. Ponemon Institute: Calculating the Cost of Data Center Outages (Report). Technical report (2013)
3. Miller, R.: Failure rates in google data centers (Report). Technical report, Data Center Knowledge (2008)
4. Gagnaire, M., Diaz, F., Coti, C., Cérin, C., Shiozaki, K., Xu, Y., Delort, P., Smets, J.-P., Lous, J.L., Lubiarz, S., Leclerc, P.: Downtime statistics of current cloud solutions. Technical report, The International Working Group on Cloud Computing Resiliency (2013)
5. Linthicum, D.: Calculating the true cost of cloud outages (2013). http://www.infoworld.com/article/2613537/cloud-computing/calculating-the-true-cost-of-cloud-outages.html
6. Facebook: Facebook Reports First Quarter 2017 Results (2017). https://investor.fb.com/investor-news/press-release-details/2017/Facebook-Reports-First-Quarter-2017-Results/default.aspx
7. Loveland, S., Dow, E.M., LeFevre, F., Beyer, D., Chan, P.F.: Leveraging virtualization to optimize high-availability system configurations. IBM Syst. J. **47**(4), 591–604 (2008). http://ieeexplore.ieee.org/lpdocs/epic03/wrapper.htm?arnumber=5386515

8. Kim, D.S., Machida, F., Trivedi, K.S.: Availability modeling and analysis of a virtualized system. In: 2009 15th IEEE Pacific Rim International Symposium on Dependable Computing, vol. 1, pp. 365–371. IEEE, November 2009. http://ieeexplore.ieee.org/lpdocs/epic03/wrapper.htm?arnumber=5368189
9. Nguyen, T.A., Kim, D.S., Park, J.S.: Availability modeling and analysis of a virtualized servers system (2014). https://doi.org/10.1155/2014/165316
10. Nguyen, T.A., Min, D., Park, J.S.: A comprehensive sensitivity analysis of a data center network with server virtualization for business continuity. Math. Probl. Eng. **2015**, 1–20 (2015). http://www.hindawi.com/journals/mpe/aa/521289/ http://www.hindawi.com/journals/mpe/2015/521289/
11. Kim, D.S., Hong, J.B., Nguyen, T.A., Machida, F., Trivedi, K.S.: Availability modeling and analysis of a virtualized system using stochastic reward nets. In: Proceedings of 16th IEEE International Conference on Computer and Information Technology (IEEE CIT 2016). IEEE, Fiji (2016)
12. Machida, F., Kim, D.S., Trivedi, K.S.: Modeling and analysis of software rejuvenation in a server virtualized system with live VM migration. Perform. Eval. **70**(3), 212–230 (2013)
13. Trivedi, K.S., Kim, D.S., Ghosh, R.: System availability assessment using stochastic models. Appl. Stoch. Models Bus. Ind. **29**(2), 94–109 (2013). http://doi.wiley.com/10.1002/asmb.951
14. Smith, W.E., Trivedi, K.S., Tomek, L.A., Ackaret, J.: Availability analysis of blade server systems. IBM Syst. J. **47**(4), 621–640 (2008). http://ieeexplore.ieee.org/lpdocs/epic03/wrapper.htm?arnumber=5386524
15. Costa, I., Araujo, J., Dantas, J., Campos, E., Silva, F.A., Maciel, P.: Availability evaluation and sensitivity analysis of a mobile backend-as-a-service platform. Qual. Reliab. Eng. Int. (2015). http://doi.wiley.com/10.1002/qre.1927
16. Matos, R., Dantas, J., Araujo, J., Trivedi, K.S., Maciel, P.: Redundant eucalyptus private clouds: availability modeling and sensitivity analysis. J. Grid Comput. 1–22 (2016). http://link.springer.com/10.1007/s10723-016-9381-z
17. Melo, M., Maciel, P., Araujo, J., Matos, R., Araujo, C.: Availability study on cloud computing environments: live migration as a rejuvenation mechanism. In: 2013 43rd Annual IEEE/IFIP International Conference on Dependable Systems and Networks (DSN), pp. 1–6. IEEE, June 2013. http://ieeexplore.ieee.org/lpdocs/epic03/wrapper.htm?arnumber=6575322
18. Sousa, E., Silva, E., Lins, F., Tavares, E., Maciel, P.: Dependability evaluation of cloud infrastructures. In: 2014 IEEE International Conference on Systems, Man, and Cybernetics (SMC), pp. 1282–1287. IEEE (2014). http://ieeexplore.ieee.org/lpdocs/epic03/wrapper.htm?arnumber=6974091
19. Silva, B., Maciel, P.R.M., Zimmermann, A., Brilhante, J.: Survivability evaluation of disaster tolerant cloud computing systems. In: Proceedings of Probabilistic Safety Assessment and Management (PSAM12), p. 453, Hawaii, USA (2014). http://psam12.org/proceedings/paper/paper_453_1.pdf
20. Nguyen, T.A., Eom, T., An, S., Park, J.S., Hong, J.B., Kim, D.S.: Availability modeling and analysis for software defined networks. In: 2015 IEEE 21st Pacific Rim International Symposium on Dependable Computing (PRDC), April, pp. 159–168. IEEE, November 2015. http://ieeexplore.ieee.org/document/7371859/ieeexplore.ieee.org/lpdocs/epic03/wrapper.htm?arnumber=7371859
21. Radhakrishnan, R., Mark, K., Powell, B.: IT service management for high availability. IBM Syst. J. **47**(4), 549–561 (2008). http://ieeexplore.ieee.org/lpdocs/epic03/wrapper.htm?arnumber=5386521

22. Morrill, H., Beard, M., Clitherow, D.: Achieving continuous availability of IBM systems infrastructures. IBM Syst. J. **47**(4), 493–503 (2008). http://ieeexplore.ieee.org/lpdocs/epic03/wrapper.htm?arnumber=5386519
23. Lumpp, T., Schneider, J., Holtz, J., Mueller, M., Lenz, N., Biazetti, A., Petersen, D.: From high availability and disaster recovery to business continuity solutions. IBM Syst. J. **47**(4), 605–619 (2008)
24. Clitherow, D., Brookbanks, M., Clayton, N., Spear, G.: Combining high availability and disaster recovery solutions for critical IT environments. IBM Syst. J. **47**(4), 563–575 (2008). http://ieeexplore.ieee.org/lpdocs/epic03/wrapper.htm?arnumber=5386509
25. Adeshiyan, T., Attanasio, C.R., Farr, E.M., Harper, R.E., Pelleg, D., Schulz, C., Spainhower, L.F., Ta-Shma, P., Tomek, L.A.: Using virtualization for high availability and disaster recovery. IBM J. Res. Dev. **53**(4), 8:1–8:11 (2009). http://ieeexplore.ieee.org/lpdocs/epic03/wrapper.htm?arnumber=5429062
26. Silva, B., Maciel, P., Zimmermann, A.: Performability models for designing disaster tolerant Infrastructure-as-a-Service cloud computing systems. In: 8th International Conference for Internet Technology and Secured Transactions (ICITST-2013), pp. 647–652. Infonomics Society, December 2013. http://ieeexplore.ieee.org/articleDetails.jsp?arnumber=6750283
27. Silva, B., Maciel, P., Tavares, E., Zimmermann, A.: Dependability models for designing disaster tolerant cloud computing systems. In: 2013 43rd Annual IEEE/IFIP International Conference on Dependable Systems and Networks (DSN), pp. 1–6. IEEE, June 2013. http://ieeexplore.ieee.org/xpl/articleDetails.jsp?arnumber=6575323
28. Andrade, E., Nogueira, B., Matos, R., Callou, G., Maciel, P.: Availability modeling and analysis of a disaster-recovery-as-a-service solution. Computing **99**, 1–26 (2017). http://link.springer.com/10.1007/s00607-017-0539-8
29. Santana, G.A.A.: Data Center Virtualization Fundamentals: Understanding Techniques and Designs for Highly Efficient Data Centers with Cisco Nexus, UCS, MDS, and Beyond. Cisco Press, Indianapolis (2013)
30. Trivedi, K.S.: SHARPE 2002: symbolic hierarchical automated reliability and performance evaluator. In: Proceedings of the 2002 International Conference on Dependable Systems and Networks, p. 544. IEEE Computer Society (2002). http://ieeexplore.ieee.org/lpdocs/epic03/wrapper.htm?arnumber=1028975
31. Trivedi, K.S., Sahner, R.: SHARPE at the age of twenty two. ACM SIGMETRICS Perform. Eval. Rev. **36**(4), 52 (2009). http://dl.acm.org/citation.cfm?id=1530873.1530884

Integrated Sentiment and Emotion into Estimating the Similarity Among Entries on Social Network

Thi Hoi Nguyen[1], Dinh Que Tran[2], Gia Manh Dam[1], and Manh Hung Nguyen[2,3](✉)

[1] Vietnam Commercial University, Hanoi, Vietnam
hoint2002@gmail.com, damgiamanh@gmail.com
[2] Posts and Telecommunications Institute of Technology (PTIT), Hanoi, Vietnam
tdque@yahoo.com, nmh.nguyenmanhhung@gmail.com
[3] UMI UMMISCO 209 (IRD/UPMC), Hanoi, Vietnam

Abstract. Similar measures play an important role in information processing and have been widely investigated in computer science. With the exploration of social media such as Youtube, Wikipedia, Facebook etc., a huge number of entries have been posted on these portals. They are often described by means of short text or sets of words. Discovering similar entries based on such texts has become challenges in constructing information searching or filtering engines and attracted several research interests. In this paper, we firstly introduce a model of entries posted on media or entertainment portals, which is based on their features composed of title, category, tags, and content. Then, we present a novel similar measure among entries that incorporates their features. The experimental results show the superiority of our incorporation similarity measure compared with the other ones.

Keywords: Similar measure · Social network · Text · Entry
Social media

1 Introduction

Recently, the exploration of social networks attracts not only the user to participle, but also many of researchers to mining and benefit the huge amount of data posted in these social networks. The entries posted are often included short text or sets of words to describe viewpoints, comments and so on. Discovering similar entries based on such texts has become challenges in constructing information searching or filtering engines and attracted several research interests.

The problem of how to detect the similarity between two objects, in general, has been investigated for decades (Lin [1], Sayal and Kumar [2], Reddy and Krishnaiah [3], Nguyen and Nguyen [4]). However, these models are too general to be applied into estimating the similarity among entries posted in social networks.

© ICST Institute for Computer Sciences, Social Informatics and Telecommunications Engineering 2018
Y. Chen and T. Q. Duong (Eds.): INISCOM 2017, LNICST 221, pp. 242–253, 2018.
https://doi.org/10.1007/978-3-319-74176-5_21

A closer approach to the problem is to use models to detect the similarity among texts, including the models based on semantic such as Buscaldi et al. [5], or Han et al. [6], Lee et al. [7], Marsi et al. [8], Oliva et al. [9], Agirre et al. [10], Nguyen and Tran [11,12], Novelli and Oliveira [13]; or based on statistic method such as Bollegala et al. [14], Buscaldi et al. [15], Croce et al. [16], Finkel et al. [17], Lintean and Rus [18], Proisl et al. [19], Saric et al. [20], Severyn et al. [21], Sultan et al. [22], Xu and Lu [23]. However, most of these models consider only the text body to estimate their similarity. They lack of investigating additional information such as the tags, category, title, keywords, sentiment, and emotion which may contribute greatly to estimate the similarity of entities.

On the line with our previous work (Nguyen et al. [24]) which considered three features of entries (*content*, *category*, *tags*), this paper integrates two more features to distinguish entries: *sentiment* and *emotion* implicitly presented in the entries. Experiments will be performed to validate and evaluate the performance of our model compared with other ones.

In order to see the role of *sentiment* and *emotion* in distinguishing entries, let's consider three following entries (which are extracted from Twitter - www.twitter.com):

- A: *Gone for a run beautiful morning man do I love iOS 5 @apple #iPhone*
- B: *I hate my apple computer. Thats 3500 dollars down the drain.*
- C: *Thank you @apple for Find My Mac - just located and wiped my stolen Air.*

If there ware only three features of *content*, *category*, and *tags* considered, it could be difficult to conclude whether the entry B or the entry C is more similar to the entry A than the other because all three entries say about the same category (*technology*), the same tags (*apple, iPhone, Mac, iOS*). However, if we take into account the features of *sentiment* and *emotion*, it is more easily than before to conclude that the entry C is more similar to the entry A than the entry B is: the entry A and C have the same *sentiment* (positive), meanwhile the entry B has a negative value of *sentiment*. And, at the level of *emotion*, the entry A may have *love, joy*, that more or less close to the *gratitude* emotion from the entry C, and that is contrary the *disgust* emotion from the entry B.

Someone could argues why do we need to consider both *sentiment* and *emotion* of entries while the sentiment could be inferred from emotion such as: positive emotion brings positive sentiment, and vice versa. However, in reality, the answer is yes, we do. The *sentiment* is the opinion of the user about the topic in the entry. Meanwhile the *emotion* is the emotional status of the user in the entry. Consequently, in many cases, *sentiment* is independent from the *emotion* in an entry. Let's consider these following entries (which are also extracted from Twitter):

- D: *@Mayati I think @Apple did not do such a thorough job with the step x steps for upgrade and move to iCloud.*
- E: *just like a coin has 2 sides, everyone has 2 faces...?*

– F: *@azee1v1 @apple @umber AppStore is well done so is iTunes on the mobile devices. I was talking about desktop app.*

It is easy to see that the entry D has negative *sentiment*, but no *emotion*. The entry E has neutral value of *sentiment*, but has confused in *emotion*. The entry F has positive *sentiment* but has no *emotion*. These examples indicate that the *sentiment* and *emotion* of an entry sometimes could be independent from each other. That's why we need to consider both these features in distinguishing the entries. The empirical results in our experiment also indicate the importance of both these two features.

The paper is organized as follows. Section 2 presents the model of entries and their similarity measure based on similarities of features. Section 3 describes experiments to evaluate the proposed model. Section 4 is the conclusion and perspectives.

2 A Similarity Measure Model for Social Network Entries

The general model takes the two entries as input data and the output is the estimated similarity between the two entered entries. Inside the model, there are four main steps:

– Step 1: Modeling entries.
– Step 2: Extracting the value for *implicit attribute* of entries.
– Step 3: Estimating the similarity on each entry attribute.
– Step 4: Aggregating the similarity between entries from their similarities on attributes.

These steps will be described in detail in the next sections.

2.1 Modeling Entries

Without loss of generality, we assume that:

– An entry on a social network could be: a text, an image, an audio stream, a video stream, or a combination of these medias. In this model, we consider only the textual part in an entry. Therefore, an entry could be considered as a text.
– An entry could be originally posted by an user, or shared (referred) from another user or another online source. This model consider an entry is the whole text, including the directly posted text, and the text referred from other source.
– An entry could have several attributes, including *explicit* attributes such as the *content*, and the *implicit* attributes such as: category, sentiment, emotion. As the *implicit* attributes could not directly extracted from an entry, the model needs a step to extract these attributes before estimating the similarity on them. This model consider five attributes of an entry:

- *Content* of entry i, noted as f^i_{con}: is the whole text part in the entry itself. This is an *explicit* attribute.
- *Tags* of entry i, noted as f^i_{tag}: An entry could be tagged to a set of tags. Each tag is an independent word or expression. In some case, tags could be directly tagged by the user (explicit). In some other case, it is not explicitly tagged by the user (implicit).
- *Category* of entry i, noted as f^i_{cat}: An entry could be assigned to a category. Each category is represented by an independent word or expression.
- *Sentiment* of entry i, noted as f^i_{sen}: An entry could have a sentiment of the user. A sentiment be in agree (positive), disagree (negative), or neutral opinion.
- *Emotion* of entry i, noted as f^i_{emo}: An entry could also have some emotion of the user. Each emotion is represented by an independent word or expression.

As an entry is considered as a set of attributes and only their textual values are considered. And then the problem of estimating the similarity among entries becomes the computation of the similarity among texts or among sets of expressions.

2.2 Auto Extract Value for Implicit Attribute of Entry

Let's consider an example of a status on Twitter: "*Thank you @apple for Find My Mac - just located and wiped my stolen Air*". When we see this status, only the *content* is explicitly presented, that is the whole text of the status. However, we could quickly identify some other attributes of this status, such as *category* could be (*technology*), *tags* could be (*apple, Mac*), *sentiment* could be (*neutral* - neither agree nor disagree), and *emotion* could be (*gratitude, joy*). The attributes whose value is not explicitly presented in the entry but it could be extracted from the inside of the entry are called *implicit attributes*. Our objective in this step is to extract the value of *implicit attributes* of an entry.

In order to do this, we could apply any existed supervised machine learning method. In this model, we apply a method to extract value of each of four implicit attributes as follow:

- Step 1: Construct a set of labeled samples (texts), called *training set*. In which, each text is assigned to a set of labels. The union of all labels of all texts called the set of labels L.
- Step 2: For each label $l_i \in L$, create two sets of text sample:
  - T_{l_i} is the set of all texts which are labeled with the label l_i.
  - $T_{\neg l_i}$ is the set of all texts which are not labeled with the label l_i.
- Step 3: For each text $t_k \in T_{l_i}$ $(T_{\neg l_i})$, calculate the label oriented features as follow:
  - Split t_i into a set of n-gram or term (stop words could be removed).
  - Take the union of all terms in all texts in the set T_{l_i} and $T_{\neg l_i}$

  - Calculate the *label oriented term score* of each term in the corresponding set for each label l_i:

$$s_{LOT}(x, l_i) = \frac{N^x_{l_i}}{N_{l_i}} * log\left(\frac{N_{\neg l_i}}{N^x_{\neg l_i}}\right) - \frac{N^x_{\neg l_i}}{N_{\neg l_i}} * log\left(\frac{N_{l_i}}{N^x_{l_i}}\right) \quad (1)$$

    where, $N_l, N_{\neg l}$ are the number of text in the set T_l, $T_{\neg l}$, respectively. $N^x_l, N^x_{\neg l}$ are the number of text in the set T_l, $T_{\neg l}$, respectively, which contains the term x.
- Step 4: For a new text t, the choice of label to assign to the text is follow:
  - Split t into a set of n-grams or terms $X = (x_1, x_2, ...x_n)$.
  - Calculate the *term frequency* for each term x_i in the text t: $tf(x_i, t)$.
  - For each label $l_i \in L$, calculate the *label oriented document score*:

$$s_{LOD}(t, l_i) = \frac{1}{n_t} * \sum_{x \in t} s_{LOT}(x, l_i) * tf(x, t) \quad (2)$$

  - If $s_{LOD}(t, l_i) > 0$:
    - In the multi-label problem where a text could be assigned to several labels, the text t will be labeled with the label l_i.
    - In the single label problem where a text could be assigned to only one label, it is needed to calculate all the final label oriented (disoriented) scores of the text t for the all labels $l_i \in L$. And the label whose *label oriented document score* is the highest score will be assigned to the text t.

2.3 Similarity on Each Attribute

As only textual value of feature is considered, we distinguish two kinds of textual value of feature:

- First, the feature value is already in form of a set of expressions, such as the value of feature *tag*, *category*, *sentiment*, and *emotion*. Their similarity is resulted to considered among sets of expressions.
- Second, the feature value is in form of a general text, such as the value of feature *content*. Their similarity is considered among texts.

Attribute Whose Value is a Set of Expressions. Since the attribute value is in the form of a set of textual expressions, their similarity is defined as follows:

Suppose that $A_1 = (a^1_1, a^2_1, ...a^m_1)$, $A_2 = (a^1_2, a^2_2, ...a^n_2)$ are two sets of expressions or strings, where m, n are the sizes of the set A_1 and A_2, respectively. Let v be the size of the intersection of A_1 and A_2. The similarity between A_1 and A_2 is defined by the formula:

$$s_{exp}(A_1, A_2) = \frac{2* \mid A_1 \cap A_2 \mid}{\mid A_1 \mid + \mid A_2 \mid} = \frac{2 * v}{m + n} \quad (3)$$

It is clear that all possible values of $s_{exp}(A_1, A_2)$ are lied in the interval $[0, 1]$. This formula could be applied to the attributes whose value is a set of expressions.

Suppose that $i = (f_1^i, f_2^i, ..f_n^i)$, $j = (f_1^j, f_2^j, ..f_n^j)$ are two entries represented by their attributes. Let consider the attribute k whose value is a set of expressions. The similarity between entries i and j on the attribute k is defined by the formula:

$$s_k(i, j) = s_{exp}(f_k^i, f_k^j) \tag{4}$$

where f_k^i, f_k^j are the expression values of the attribute k of the two entries i and j. For examples, the similarity on attribute *category*, *tags*, *sentiment*, and *emotion* of two entries are given as follows:

$$s_{cat}(i, j) = s_{exp}(f_{cat}^i, f_{cat}^j) \tag{5}$$

$$s_{tag}(i, j) = s_{exp}(f_{tag}^i, f_{tag}^j) \tag{6}$$

$$s_{sen}(i, j) = s_{exp}(f_{sen}^i, f_{sen}^j) \tag{7}$$

$$s_{emo}(i, j) = s_{exp}(f_{emo}^i, f_{emo}^j) \tag{8}$$

Attribute Whose Value is a Text. In this case, the problem becomes the estimation the similarity between two texts. We could apply the technique TF-IDF (Term Frequency - Inverse Document Frequency) [25] to characterize the texts, which are used in many statistic-based models such as Buscaldi et al. [15], Finkel et al. [17]. In our work, TF-IDF is also used to estimate the similarity between two features of text value as follows:

- Extract the attribute value (a text) into a set of n-gram $t^1 = (g_1^1, g_2^1, ...g_n^1)$ and $t^2 = (g_1^2, g_2^2, ...g_m^2)$
- Calculate the TF-IDF of each n-gram in the text. Then represent the attribute value by a vector whose each element is a pair $<$ *n-gram, td-idf* $>$: $v^1 = (< g_1^1, v_1^1 >, < g_2^1, v_2^1 >, ... < g_n^1, v_n^1 >)$ and $v^2 = (< g_1^2, v_1^2 >, < g_2^2, v_1^2 >, ... < g_m^2, v_m^2 >)$
- Calculate the distance between the two vectors:

$$D(v^1, v^2) = \frac{1}{N} \sum_1^N d_k \tag{9}$$

  where N is the number of different n-grams considered in both $t^1 \cup t^2$, d_k is the distance on each element $< g_i^1, v_i^1 >$ of v^1 (or element $< g_j^2, v_j^2 >$ of v^2, respectively):
  - If there is an element $< g_l^2, v_l^2 >$ of v^2 (or element $< g_l^1, v_l^1 >$ of v^l, respectively) such that $g_l^2 = g_i^1$, then:

$$d_k = \frac{| v_i^1 - v_l^2 |}{max(v_i^1, v_l^2)} \tag{10}$$

  - Otherwise, $d_k = 1$.

– It is clear that the value of $D(v^1, v^2)$ is in the interval $[0, 1]$. Similarity between the two features is then:

$$s_{txt}(t^1, t^2) = 1 - D(v^1, v^2) \tag{11}$$

For example, similarity between the attribute *content* of two entries i and j is as follows:

$$s_{con}(i, j) = s_{txt}(f^i_{con}, f^j_{con}) \tag{12}$$

2.4 Similarity Between Two Entries

Once the similarities between two entries on each attribute are estimated, the similarity between two entries is then computed by a weighted average aggregation of the similarity on all considered attributes as follows.

Suppose that $i = (f^i_1, f^i_2, ..f^i_n)$, $j = (f^j_1, f^j_2, ..f^j_n)$ are two entries represented by their attributes. The similarity between entries i and j on all considered attributes is defined by the formula:

$$s_{entry}(i, j) = \sum_{k=1}^{n} w_k * s_k(i, j) \tag{13}$$

where $s_k(i, j)$ is the similarity on attribute k of entries i and j; w_k is the weight of the feature k such that:

$$\sum_{k=1}^{n} w_k = 1 \tag{14}$$

The more this similarity is closed to 1, the more the two entries are similar. And vice versa, the more this similarity is closed to 0, the less the two entries are similar.

3 Experimental Evaluation

This section first describes the construction of sample set and then presents the experiments and evaluation results.

3.1 Construction of Sample Set

In order to have entries which have sentiment and emotions, we collected more than 1000 statuses posted on Twitter (twitter.com). Samples are then constructed from these Twitter statuses. Each sample contains:

– The *id* of the sample.
– The *value* of the sample. It could be 1 or 2.

- Each sample contains three entries collected from Twitter. These entries are called as entry A, B, and C. And the *value* of the sample is determined as follow:
  - If the entry A is more similar to the entry B than C, then the *value* of this sample is 1.
  - In the contrary, if the entry A is more similar to the entry C than B, then the *value* of this sample is 2.

In this experiment, we constructed and use 500 samples. For instance, a sample is presented in Table 1. In this sample, the entry A is similar to the entry C than the entry B, so the *value* of the sample is 2.

Table 1. An example of a sample constructed from Twitter entries

ID	354
Value	2
A	Gone for a run beautiful morning man do I love iOS 5 @apple #iPhone
B	@AsimRang @apple @umber the desktop app is wack though
C	Thank you @apple for Find My Mac - just located and wiped my stolen Air

3.2 Method of Experiment and Evaluation

In order to compare the results of our model to other related works, we choose and implement these following models:

- *Model 1*: It is the model of Buscaldi et al. [15] which takes into account only the *content* attribute of entries.
- *Model 2*: It is the model of Nguyen et al. [24] which takes into account three attributes of entries: *content*, *category*, and *tags*.
- *Model 3*: It is our model which takes into account five attributes of entries: *content*, *category*, *tags*, *sentiment*, and *emotion*. In this model, we use 3 values of *sentiment*, and 16 values of *emotion* as indicated in Table 2. These emotions are detected based on the cognitive definition of emotion proposed by Ortony et al. [26], Frijda [27], and Reisenzei [28].

The experiment is performed as follows on each model:

- For each sample, we use model proposed in this paper to estimate the similarity between the entry B and A, and that between entry C and A.
- If A is more similar to B than C is, then the *result* of this sample is 1. In the contrary, If A is more similar to C than B is, then the *result* of this sample is 2.

Table 2. Values of *sentiment* and *emotion* used in the Model 3

Attribute	Values
Sentiment	Positive
	Negative
	Neutral
Emotion	Joy
	Sad
	Happyfor
	Sorry
	Hope
	Fear
	Regret
	Disappointed
	Love
	Disgust
	Confused
	Pride
	Anger
	Gratitude
	Admiration
	No emotion

– We then compare the *result* and the *value* of each sample. If they are identical, we increase the variable *number of correct sample* by 1.

In order to evaluate the results, we make use of the correct ratio (CR) of the model over the given sample set which is calculated as follows:

$$CR = \frac{\text{number of correct sample}}{\text{total of sample}} * 100\% \tag{15}$$

The more the CR value is closed to 100%, the more the model is correct. We expect that the obtained value of CR is high as much as possible.

3.3 Results

The results are presented in the Table 3. They indicate that our model, which reaches the correct ratio of 86.20%, is significantly better than the model of Buscaldi et al. [15] (with $CR = 69.00\%$) and Nguyen et al. [24] (with $CR = 79.40\%$), regarding the given sample set.

The results also determined the best combination of attribute weights for each model. Meanwhile the model of Buscaldi et al. [15] concentrate 100% on the *content* so there is no option to choose the best. The model of Nguyen et al. [24] considered only three attributes *content*, *category*, and *tag*, so the best combination of weights is 0.65 : 0.20 : 0.15, respectively. The best combination of

Table 3. Results of considered models

Model	CR (%)	Best weight combination				
		w_1	w_2	w_3	w_4	w_5
Buscaldi et al. [15]	69.00	1				
Nguyen et al. [24]	79.40	0.65	0.20	0.15		
Our model	86.20	0.30	0.30	0.05	0.05	0.30

five weights corresponding five attributes *content*, *category*, *tag*, *sentiment*, and *emotion* in our model is 0.30 : 0.30 : 0.05 : 0.05 : 0.30, respectively. This results also indicate the role of *sentiment* and *emotion* in differentiating the entries in Twitter.

4 Conclusions

This paper presented the integration of two new attributes, *sentiment* and *emotion*, into the considered attribute set to estimate the similarity among entries in social networks. The model is then validated with empirical data collected from Twitter. The experimental results indicate that the proposed model could reach a higher value in accuracy than some recent related models.

Currently, we are considering how to take the semantic of text into account to compare expressions. These research results will be presented in our future work.

References

1. Lin, D.: An information-theoretic definition of similarity. In: Proceedings of the 15th International Conference on Machine Learning, pp. 296–304. Morgan Kaufmann, San Francisco (1998)
2. Sayal, R., Kumar, V.V.: A novel similarity measure for clustering categorical data sets. Int. J. Comput. Appl. **17**(1), 25–30 (2011). Published by Foundation of Computer Science
3. Reddy, G.S., Krishnaiah, R.V.: A novel similarity measure for clustering categorical data sets. IOSR J. Comput. Eng. (IOSRJCE) **4**(6), 37–42 (2012)
4. Nguyen, M.H., Nguyen, T.H.: A general model for similarity measurement between objects. Int. J. Adv. Comput. Sci. Appl. (IJACSA) **6**(2), 235–239 (2015)
5. Buscaldi, D., Roux, J.L., Flores, J.J.G., Popescu, A.: Lipn-core: Semantic text similarity using n-grams, wordnet, syntactic analysis, esa and information retrieval based features (2013)
6. Han, L., Kashyap, A.L., Finin, T., Mayfield, J., Weese, J.: Semantic textual similarity systems. In: Second Joint Conference on Lexical and Computational Semantics (*SEM), Volume 1: Proceedings of the Main Conference and the Shared Task: Semantic Textual Similarity, pp. 44–52. Association for Computational Linguistics, Atlanta, June 2013

7. Lee, M.C., Chang, J.W., Hsieh, T.C.: A grammar-based semantic similarity algorithm for natural language sentences. Sci. World J. **2014**, 17 (2014)
8. Marsi, E., Moen, H., Bungum, L., Sizov, G., Gambäck, B., Lynum, A.: Combining strong features for semantic similarity. In: Second Joint Conference on Lexical and Computational Semantics (*SEM), Volume 1: Proceedings of the Main Conference and the Shared Task: Semantic Textual Similarity, pp. 66–73. Association for Computational Linguistics, Atlanta, June 2013
9. Oliva, J., Serrano, J.I., del Castillo, M.D., Iglesias, Á.: Symss: a syntax-based measure for short-text semantic similarity. Data Knowl. Eng. **70**(4), 390–405 (2011)
10. Agirre, E., Cer, D., Diab, M., Gonzalez-Agirre, A., Guo, W.: Semantic textual similarity. In: Second Joint Conference on Lexical and Computational Semantics (*SEM), Volume 1: Proceedings of the Main Conference and the Shared Task: Semantic Textual Similarity, pp. 32–43. Association for Computational Linguistics, Atlanta, June 2013
11. Nguyen, M.H., Tran, D.Q.: A semantic similarity measure between sentences. South-East Asian J. Sci. **3**(1), 63–75 (2014)
12. Tran, D.Q., Nguyen, M.H.: A mathematical model for semantic similarity measures. South-East Asian J. Sci. **1**(1), 32–45 (2012)
13. Novelli, A.D.P., Oliveira, J.M.P.D.: Article: a method for measuring semantic similarity of documents. Int. J. Comput. Appl. **60**(7), 17–22 (2012)
14. Bollegala, D., Matsuo, Y., Ishizuka, M.: A web search engine-based approach to measure semantic similarity between words. IEEE Trans. Knowl. Data Eng. **23**(7), 977–990 (2011)
15. Buscaldi, D., Rosso, P., Gomez-Soriano, J.M., Sanchis, E.: Answering questions with an n-gram based passage retrieval engine. J. Intell. Inf. Syst. **34**(2), 113–134 (2010)
16. Croce, D., Storch, V., Basili, R.: Combining text similarity and semantic filters through sv regression. In: Second Joint Conference on Lexical and Computational Semantics (*SEM), Volume 1: Proceedings of the Main Conference and the Shared Task: Semantic Textual Similarity, pp. 59–65. Association for Computational Linguistics, Atlanta, June 2013
17. Finkel, J.R., Grenager, T., Manning, C.: Incorporating non-local information into information extraction systems by gibbs sampling. In: Proceedings of the 43rd Annual Meeting on Association for Computational Linguistics, ACL 2005, pp. 363–370. Association for Computational Linguistics, Stroudsburg (2005)
18. Lintean, M.C., Rus, V.: Measuring semantic similarity in short texts through greedy pairing and word semantics. In: Youngblood, G.M., McCarthy, P.M. (eds.) Proceedings of the Twenty-Fifth International Florida Artificial Intelligence Research Society Conference, Marco Island, Florida, 23–25 May 2012. AAAI Press (2012)
19. Proisl, T., Evert, T., Greiner, P., Kabashi, B.: Robust semantic similarity at multiple levels using maximum weight matching. In: Proceedings of the 8th International Workshop on Semantic Evaluation (SemEval 2014), pp. 532–540. Association for Computational Linguistics and Dublin City University, Dublin, August 2014
20. Šarić, F., Glavaš, G., Karan, M., Šnajder, J., Bašić, B.D.: Takelab: systems for measuring semantic text similarity. In: Proceedings of the First Joint Conference on Lexical and Computational Semantics - Volume 1: Proceedings of the Main Conference and the Shared Task, and Volume 2: Proceedings of the Sixth International Workshop on Semantic Evaluation, SemEval 2012, pp. 441–448. Association for Computational Linguistics, Stroudsburg (2012)

21. Severyn, A., Nicosia, M., Moschitti, A.: Tree kernel learning for textual similarity. In: Second Joint Conference on Lexical and Computational Semantics (*SEM), Volume 1: Proceedings of the Main Conference and the Shared Task: Semantic Textual Similarity, pp. 53–58. Association for Computational Linguistics, Atlanta, June 2013
22. Sultan, M.A., Bethard, S., Sumner, T.: Sentence similarity from word alignment. In: Proceedings of the 8th International Workshop on Semantic Evaluation (SemEval 2014), pp. 241–246. Association for Computational Linguistics and Dublin City University, Dublin, August 2014
23. Xu, J., Lu, Q.: Computing semantic textual similarity using overlapped senses. In: Second Joint Conference on Lexical and Computational Semantics (*SEM), Volume 1: Proceedings of the Main Conference and the Shared Task: Semantic Textual Similarity, pp. 90–95. Association for Computational Linguistics, Atlanta, June 2013
24. Nguyen, T.H., Tran, D.Q., Dam, G.M., Nguyen, M.H.: Multi-feature based similarity among entries on media portals. In: Akagi, M., Nguyen, T.-T., Vu, D.-T., Phung, T.-N., Huynh, V.-N. (eds.) ICTA 2016. AISC, vol. 538, pp. 373–382. Springer, Cham (2017). https://doi.org/10.1007/978-3-319-49073-1_41
25. Salton, G., McGill, M.J.: Introduction to Modern Information Retrieval. McGraw-Hill Inc., New York (1986)
26. Ortony, A., Clore, G.L., Collins, A.: The Congnitive Structure of Emotions. The Cambridge University Press, Cambridge (1988)
27. Frijda, N.H.: The Emotions: Studies in Emotion & Social Interaction. Edition de la Maison des Sciences de l'Homme, ser edn. Cambridge University Press, Paris (1986)
28. Reisenzein, R.: Emotions as metarepresentational states of mind: Naturalizing the belief-desire theory of emotion. Cognit. Syst. Res. **10**(1), 6–20 (2009)

A Functional Optimization Method for Continuous Domains

Viet-Hung Dang[1], Ngo Anh Vien[2(✉)], Pham Le-Tuyen[3], and Taechoong Chung[3]

[1] Research and Development Center, Duy Tan University, Da Nang, Vietnam
[2] Machine Learning and Robotics Lab, University of Stuttgart, Stuttgart, Germany
vien.ngo@gmail.com
[3] Department of Computer Engineering, Kyung Hee University, Seoul, Korea

Abstract. Smart city solutions are often formulated as adaptive optimization problems in which a cost objective function w.r.t certain constraints is optimized using off-the-shelf optimization libraries. Covariance Matrix Adaptation Evolution Strategy (CMA-ES) is an efficient derivative-free optimization algorithm where a black-box objective function is defined on a parameter space. This modeling makes its performance strongly depends on the quality of chosen features. This paper considers modeling the input space for optimization problems in reproducing kernel Hilbert spaces (RKHS). This modeling amounts to functional optimization whose domain is a function space that enables us to optimize in a very rich function class. Our CMA-ES-RKHS framework performs black-box functional optimization in the RKHS. Adaptive representation of the function and covariance operator is achieved with sparsification techniques. We evaluate CMA-ES-RKHS on simple functional optimization problems which are motivated from many problems of smart cities.

Keywords: Functional optimization · Smart city · Cross-entropy
Covariance matrix adaptation evolution strategy

1 Introduction

The smart city initiative uses information and communication technology (ICT) and Internet of things (IoT) solutions to manage a city's assets, e.g. transportation systems, grid networks, schools, hospitals, etc. The goal is to build a smart city that improves the quality of life and the efficiency of services. These goals are often realized as a cost objective function of energy, price, consumption, user's comfort, and so on [3]. Optimizing such an objective can be handled via various optimization libraries depending on different situations. The covariance matrix adaptation evolutionary strategy (CMA-ES) is a derivative-free method [12] that is a practical optimizer for continuous optimization problems. It is a general optimization framework that possesses many appealing characteristics, e.g. derivative-free, covariant, off-the-shelf, scalable etc. It is especially

© ICST Institute for Computer Sciences, Social Informatics and Telecommunications Engineering 2018
Y. Chen and T. Q. Duong (Eds.): INISCOM 2017, LNICST 221, pp. 254–265, 2018.
https://doi.org/10.1007/978-3-319-74176-5_22

useful on problems that are non-convex, non-separable, ill-conditioned, multi-modal, and with noisy evaluations. Applying CMA-ES requires explicitly a finite-dimensional search space on which solution candidates live. CMA-ES has been used to solve problems in power prediction for smart grid [15], driver assistance [6], smart transportation (which used evolutionary algorithm as a special form of CMA-ES) [2,24], metro regenerative energy [7], etc. In the context of robotics, CMA-ES has been widely used in many tasks: biped locomotion [31], whole-body locomotion optimization [8,9], swimming [26], skill learning via reinforcement learning [13,14,25], inverse reinforcement learning [5,21], etc.

Applying CMA-ES requires explicitly a finite-dimensional search space on which solution candidates live. In many domains, e.g. robotics, an optimization objective is often defined as a function of another parametric function. For instance, it might be an overall cost function depending on a robot controller, e.g. robot skill learning [25], policy search [14], or a loss function in the contexts of inverse optimal control [5,21], etc.

In this work, we propose CMA-ES-RKHS that enables functional optimization over a non-parametric solution space. Specifically, we assume that the solution space is a reproducing kernel Hilbert space (RKHS). Each candidate is a function in RKHS. Modeling the solution space this way, CMA-ES-RKHS can not only inherit full characteristics from CMA-ES, but also enjoy other appealing properties. *Firstly*, CMA-ES-RKHS is able to optimize a functional objective whose domain is a RKHS. That means the solution space does not need to depend on any manual parametrization. *Secondly*, by modeling the solution space in RKHS, all updates step in CMA-ES-RKHS are handled analytically. We show that updated mean functionals, other intermediate terms, evolution path functionals or conjugate evolution path functionals are functions in the underlying RKHS. Moreover, the updated covariance is also an operator on the underlying RKHS. *Thirdly*, via sparsification in RKHS, a very complex search space can be represented compactly, however we can still achieve a solution of guaranteed quality.

2 Covariance Matrix Adaptation - Evolution Strategy

The Covariance Matrix Adaptation - Evolution Strategy (CMA-ES) is a global optimization method introduced by [12]. It works by forming a parametric distribution over the solution space, e.g. the space of policy parameter in policy search, or the space of parameters of the loss function in inverse optimal control, etc. It iteratively samples a population of solution candidates from a parametrized search distribution. These candidates are then evaluated by a black-box function. Tuples of candidate-evaluation make up a dataset in order for CMA-ES to update the search distribution, i.e. its mean and its covariance matrix. Specifically, a cost function $f(\theta)$ is parametrized by a parameter space $\theta \in \Re^n$, $f : \Re^n \mapsto \Re$. It is common that a CMA-ES algorithm maintains a multi-variate Gaussian distribution over the solution space as $\theta \sim \mathcal{N}(\theta; \mathbf{m}, \mathbf{C})$. At each iteration k, it generates the kth population of λ candidates from the kth distribution as

Algorithm 1. The CMA-ES algorithm

1: Initialize $\mathbf{m} \in \Re^n$, $\sigma \in \Re^+$, λ, μ
2: Initialize $\mathbf{C} = \mathbf{I}, \mathbf{p}_c = \mathbf{0}, \mathbf{p}_\sigma = \mathbf{0}$
3: **while** (not terminate) **do**
4: Sampling: $\theta_i = \mathbf{m} + \sigma \mathbf{y}_i$, $\mathbf{y}_i \sim \mathcal{N}(\mathbf{0}, \mathbf{C}), i = 1, \ldots, \lambda$
5: Evaluating: $f(\theta_i), i = 1, \ldots, \lambda$
6: *// mean update*
7: $\mathbf{m} \leftarrow \mathbf{m} + \sigma \bar{\mathbf{y}}$, where $\bar{\mathbf{y}} = \sum_1^\mu w_i \mathbf{y}_{i:\lambda}$
8: *// step-size control update*
9: $\mathbf{p}_\sigma \leftarrow (1 - c_\sigma)\mathbf{p}_\sigma + \sqrt{c_\sigma(2 - c_\sigma)\mu_w} \mathbf{C}^{-\frac{1}{2}} \bar{\mathbf{y}}$
10: $\sigma \leftarrow \sigma \exp\left(\frac{c_\sigma}{d_\sigma}\left(\frac{\|\mathbf{p}_\sigma\|}{\mathbb{E}\|\mathcal{N}(\mathbf{0},\mathbf{I})\|} - 1\right)\right)$
11: *// covariance matrix update*
12: $\mathbf{p}_c \leftarrow (1 - c_c)\mathbf{p}_c + \sqrt{c_c(2 - c_c)\mu_w} \bar{\mathbf{y}}$
13: $\mathbf{C} \leftarrow (1 - c_1 - c_\mu)\mathbf{C} + c_1 \mathbf{p}_c \mathbf{p}_c^\top + c_\mu \sum_1^\mu w_i \mathbf{y}_{i:\lambda} \mathbf{y}_{i:\lambda}^\top$
14: **end while**

$\theta_i \sim \mathcal{N}(\theta; \mathbf{m}_k, \mathbf{C}_k)$, $i = 1, \cdots, \lambda$. Then, the candidates are sorted ascendingly according to their evaluations $f(\theta_i)$. Only the first μ best candidates are selected for use in updates of $\mathbf{m}_k$ and $\mathbf{C}_k$. Another parameter is the global step-size $\sigma \in \Re$ that controls the convergence rate of the covariance matrix update. The parameter σ is defined as a global standard deviation. Hence, a full set of parameters in CMA-ES is $\{\mathbf{m}, \mathbf{C}, \sigma\}$.

In Algorithm 1, we give a full summary of the CMA-ES algorithm. The updated mean is a weighted sum of the best μ candidates as in step 7, in which the weights w_i are set to $1/\mu$ or to a better values $\log(\mu/2) - \log(i)$. The notation $\mathbf{y}_{i:\lambda}$ means the best candidate out of $\mathbf{y}_i, \ldots, \mathbf{y}_\lambda$. The covariance matrix update in step 13 consists of three parts: old information, rank-1 update which computes the change of the mean over time as encoded in the *evolution path* $\mathbf{p}_c$, and rank-μ update which takes into account the *good* variations in the last population. This step-size control update constraints the expected changes of the distribution. Thus, this update in step 10 is based on the *conjugate evolution path* $\mathbf{p}_\sigma$. It targets to accelerate convergence to an optimum, and meanwhile prevents premature convergence. The other parameters: μ_w is the variance effective selection mass, c_1, c_c, c_σ are learning rates, and d_σ is a damping factor for σ. The setting of these parameters is well studied and discussed in-depth in [10].

The updates of CMA-ES can alternatively be derived using the information-geometric concept of a natural gradient as shown in [11], which shares the same insight with the *natural evolution strategies* (NES) [32].

There are less efficient techniques that can also adapt the covariance matrix: *estimation of distribution algorithms* (EDA) and *the cross-entropy method* (CEM). The major difference from CMA-ES is at the choice of the reference mean value. EDA and CEM estimate the variance within the current population, $\mathbf{y}_{1:\lambda}$, instead of exploiting old information as encoded in previous $\mathbf{C}$ and $\mathbf{p}_c$. Specifically, for the Gaussian search distribution, analytic updates at iteration k for EDA and CEM [19,20] change steps 9 and 13 in Algorithm 2 to

$$\mathbf{m}^{(k)} = \frac{1}{\mu}\sum_{i=1}^{\mu}\theta_i$$
$$\mathbf{C}_{\text{EDA}}^{(k)} = \frac{1}{\mu}\sum_{i=1}^{\mu}\left(\theta_i - \mathbf{m}^{(k)}\right)\left(\theta_i - \mathbf{m}^{(k)}\right)^\top$$
$$\mathbf{C}_{\text{CEM}}^{(k)} = \frac{\mu}{\mu-1}\mathbf{C}_{\text{EDA}}^{(k)}$$

The difference between EDA and CEM is: EDA updates the empirical covariance matrix, meanwhile CEM updates the *unbiased* empirical covariance matrix.

3 CMA-ES in Reproducing Kernel Hilbert Space

3.1 Problem Statement

We consider a functional optimization problem [28] that finds the maximum of an unknown functional $f : \mathcal{H} \mapsto \Re$, where $\mathcal{H} = \{h : \mathcal{X} \mapsto \Re\}$ is a separable Hilbert space of input real-valued functions with a domain $\mathcal{X}$. Assuming that $\mathcal{H}$ is specifically a square-integrable function space $\mathcal{L}^2(\mathcal{X}, \mu)$ w.r.t a probability measure μ. For each queried function $h \in \mathcal{H}$, an evaluation $y = f(h)$ is returned.

3.2 CMA-ES in RKHS

We propose a new general-purposed CMA-ES-RKHS framework that solves the above problem. We explicitly assume the function space $\mathcal{H}$ is a reproducing kernel Hilbert space (RKHS) associated with a kernel K. Each $h \in \mathcal{H}$ is defined as a mapping from an arbitrary space $\mathcal{X}$ to $\mathcal{Y}$, $h : \mathcal{X} \mapsto \mathcal{Y}$. The function space $\mathcal{H}$ may be a vector-valued RKHS, denoted as $\mathcal{H}_K$, [17] with the kernel $K : \mathcal{X} \times \mathcal{X} \mapsto \mathcal{L}(\mathcal{Y})$, where $\mathcal{L}(\mathcal{Y})$ is the space of linear operators on $\mathcal{Y}$. For example, when $\mathcal{X} = \Re^n$ the simplest choice of K might be $K(x, x') = \kappa(x, x')\mathrm{I}_n$, where I_n is an $n \times n$ identity matrix, and κ is a scalar-valued kernel [22]. Each function $h \in \mathcal{H}$ is then represented as a linear span of finite elements $\{x_i, y_i\}$ as

$$h(\cdot) = \sum_i K(x_i, \cdot)y_i \tag{1}$$

Now we define a search distribution over $\mathcal{H}$. A direct extension of parametric CMA-ES is to use a Gaussian process over the solution function h, $h \sim \mathcal{GP}(m, \sigma^2 C)$, where m is a mean function, C is a covariance operator, and σ is a scalar global step-size. We discuss now how to update the functionals $\{m, C\}$ and the parameter σ in our CMA-ES-RKHS framework, which is also summarized in Algorithm 2.

Algorithm 2. The CMA-ES-RKHS algorithm

1: Initialize $m \in \mathcal{H}_K$, $\sigma \in \Re^+$, λ, μ
2: Initialize $C = \delta(\cdot,\cdot), p_c \in \mathcal{H}_K, p_\sigma \in \mathcal{H}_K$
3: **while** (not terminate) **do**
4: *Sampling*: $\tilde{g}_i \sim \mathcal{GP}(0, C), i = 1, \ldots, \lambda$
5: Via kernel regression: for each $\tilde{g}_i$, fit a function $g_i \in \mathcal{H}_K$
6: Set samples: $h_i = m + \sigma^{(t)} g_i$
7: *Evaluating*: $f_i = f(h_i), i = 1, \ldots, \lambda$
8: // *mean update*
9: $m \leftarrow m + \sigma \bar{g}$, where $\bar{g} = \sum_1^\mu w_i g_{i:\lambda}$
10: // *step-size control update*
11: $p_\sigma \leftarrow (1 - c_\sigma) p_\sigma + \sqrt{c_\sigma (2 - c_\sigma) \mu_w} C^{-\frac{1}{2}} \bar{g}$
12: $\sigma \leftarrow \sigma \exp\left(\frac{c_\sigma}{d_\sigma}\left(\frac{\|p_\sigma\|}{\mathbb{E}\|\mathcal{GP}(0,\delta(\cdot,\cdot))\|} - 1\right)\right)$
13: // *covariance matrix update*
14: $p_c \leftarrow (1 - c_c) p_c + \sqrt{c_c (2 - c_c) \mu_w} \bar{g}$
15: $C \leftarrow (1 - c_1 - c_\mu) C + c_1 p_c \otimes p_c + c_\mu \sum_1^\mu w_i g_{i:\lambda} \otimes g_{i:\lambda}$
16: Sparsify m, C and derive $C^{-\frac{1}{2}}$
17: **end while**

Mean Function Update in RKHS. Assuming that at iteration k, we can sample a set of λ functions $\tilde{g}_i \sim \mathbb{GP}(0, C)$ (Step 4), many sampling techniques are basically described in [18]. Our following derivation is not restricted to which kernel, vector-valued or scalar-valued, is used. A sample from a Gaussian process is not in $\mathcal{H}_K$ with probability of 1, as discussed in detail by [1]. For any sampling techniques of a Gaussian process, we receive $\tilde{g}_i$ in a form of data tuples $(x^{(i)}, y^{(i)})$ from which we can use kernel ridge regression with the covariance operator $C(\cdot,\cdot)$ (Step 5). Hence, in our framework each function $\tilde{g}_i$ is approximated by a function $g_i \in \mathcal{H}_K$. As a result, a new function candidate sampled from the function distribution is $h_i = m + \sigma g_i$. The new mean function is updated as (Step 9),

$$m = m + \sigma \sum_{i=1}^{\mu} w_i g_{1:\lambda} \in \mathcal{H}_K \tag{2}$$

where the weights w_i satisfy

$$\sum_{i=1}^{\mu} w_i = 1, \quad w_1 \geq w_2 \geq \cdots \geq w_\mu > 0$$

As a result, after the update the new functional mean is an element in $\mathcal{H}_K$. We denote $\bar{g}$ as

$$\bar{g} = \sum_{i=1}^{\mu} w_i g_{1:\lambda}$$

There are a number of settings for w, which might inherit from CMA-ES, such as: $w_i = 1/\mu$, $w_i \propto \mu - i + 1$; or $w_i = \log(\mu + \frac{1}{2}) - \log(i)$. In our experiment, we implement the last choice.

Covariance Operator Update. The covariance operator update is based on the best selected candidate functions, based on their evaluations $f(h_i)$. Hence an empirical estimate of the covariance operator C on $\mathcal{H}_K$, called *rank-μ update*, is

$$C = (1 - c_\mu)C + c_\mu \sum_{i=1}^{\mu} w_i g_{i:\lambda} \otimes g_{i:\lambda}$$

Similar to parametric CMA-ES, we also consider the change of the mean function over time by estimating a functional evolution path p_c as (Step 14),

$$p_c = (1 - c_c)p_c + \sqrt{c_c(2 - c_c)\mu_w}\bar{g} \in \mathcal{H}_K \tag{3}$$

This is low-pass filtered of chosen steps $\bar{g}$, hence p_c is also an element in RKHS $\mathcal{H}_K$. As a result, a complete update of the covariance operator that combines both rank-1 and rank-μ is computed as (Step 15),

$$C = (1 - c_\mu - c_1)C + c_1 p_c p_c^\top + c_\mu \sum_{i=1}^{\mu} w_i g_{i:\lambda} \otimes g_{i:\lambda} \tag{4}$$

where c_c is the backward time horizon for the functional evolution path p_c, c_1, c_μ are learning rates of rank-1 and rank-μ respectively, and μ_w is a variance-effectiveness constant. This reduces to a rank-1 update if $c_1 = 1, c_\mu = 0$. Similarly, the update becomes a rank-μ update when $c_1 = 0, c_\mu = 1$.

Step-Size Update. The global step-size σ is adapted through the computation of a functional conjugate evolution path as (Step 11),

$$p_\sigma = (1 - c_\sigma)p_\sigma + \sqrt{c_\sigma(2 - c_\sigma)\mu_{\text{eff}}}\mathrm{C}^{-\frac{1}{2}}\bar{g} \tag{5}$$

where c_σ is a backward time horizon for the conjugate evolution path p_σ. According to the bounded inverse theorem in functional analysis [4], C as computed in Eq. 4 is a linear operator in the RKHS $\mathcal{H}_K$, hence it has a bounded inverse C^{-1}. Therefore, p_c is updated in a way that renders it an element in $\mathcal{H}_K$. The volume and the correlation of the selected steps are compared to the expected value of the standard Gaussian process with a Dirac kernel. The fact that the former is larger than the latter makes σ increased, otherwise decreased. The update formula of σ (Step 12) is

$$\sigma = \sigma \exp\left(\frac{c_\sigma}{d_\sigma}\left(\frac{\|p_\sigma\|}{\mathbb{E}\|\mathcal{GP}(0, \delta(\cdot,\cdot))\|} - 1\right)\right) \tag{6}$$

The term $\mathbb{E}\|\mathcal{GP}(0, \delta_x)\|$ can be computed in advance using Monte-Carlo simulations

$$\mathbb{E}\|\mathcal{GP}(0, \delta(\cdot,\cdot))\|_{\mathcal{H}_K} \approx \frac{1}{N}\sum_{i=1}^{N}\langle g_i(\cdot), g_i(\cdot)\rangle_{\mathcal{H}_K}$$

where $g_i(\cdot)$ is a function in $\mathcal{H}_K$ approximated (via kernel ridge regression) from a sample $\tilde{g}_i$ drawn from $\mathcal{GP}(0, \delta(\cdot,\cdot))$.

Sparsification and Adaptive Representation. We now discuss implementation concerns of the CMA-ES-RKHS algorithm. The first and most critical one is the representation issue of mean functions m and covariance operators C. Then, it follows with discussions of parameter setting in CMA-ES-RKHS. Then we discuss how to deal with the update rule in Eq. 5 that involves to find the inverse operator $C^{-\frac{1}{2}}$.

In general, we can use the kernel matching pursuit algorithm [30] to sparsify C. However, we aim to look for a method that will both sparsify C and together compute the inverse square root operator $C^{-\frac{1}{2}}$. Therefore, we propose to use the *kernel PCA* method (kPCA) from [23] for achieving efficiently and fast both a sparse and compact covariance operator and its inverse square root operator.

4 Experiments

We evaluate the advantages and general applications of CMA-ES-RKHS on two optimization problems: a synthetic functional optimization, and a power prediction scenario. We compare the behavior of CMA-ES-RKHS with other three base-line methods: the standard CMA-ES, the adaptive CMA-ES version (CMA-ES-A), and the functional gradient techniques. In all experiments, we use the RBF kernel where the bandwidths are set using *median-trick*. These experiments aim to evaluate the proposed CMA-ES-RKHS for: (i) the quality of the returned compact solution function, (ii) the flexibility and the power of our proposed method in capturing a complex solution function which can not be found easily by existing methods, and (iii) the applicability in practice.

4.1 Synthetic Domains

We design an unknown 2-dimensional functions f^*. This function is a mixture of two (multi-variate) Gaussians. All optimizers are tasked to find a function $h : \mathcal{X} \mapsto \Re$, where $h \in \mathcal{H}_K$ that minimizes the objective function as a square distance

$$J(h) = \int_{x_0}^{x_T} \big(f^*(x) - h(x)\big)^2 dx \tag{7}$$

where $x \in \Re^2$. This task is a simplified version of many similar problems in machine learning and robotics, e.g. regularized risk functional [22], trajectory optimization [27,29], trajectory optimization in RKHS [16], loss minimization inverse optimal control [5], etc. However, these work must rely on discretization and parametric modeling.

Functional Gradient: Using functional gradient requires to know J and have access to the ground-truth function f^* (CMA-ES-RKHS only accesses to evaluations $J(h)$) from which we are able use discretization to approximate J as

$$J(h) \approx \sum_{k=0}^{T} \big(f^*(x_k) - h(x_k)\big)^2$$

The functional gradient can be computed as

$$\nabla_h J(h) = \sum_{k=0}^{T} 2\big(h(x_k) - f^*(x_k)\big) K(t_k, \cdot)$$

Thus, a functional gradient update is

$$h \leftarrow h + \alpha \nabla_h J(h)$$

A sparsification technique [30] can be used to achieve a compact representation of h which renders the functional gradient approach an adaptive method too. That means the representation of h will be adaptively adapted to best approximate f^*. Hence, discretization is required to be fine enough (T is large enough, we used $T \gg N$) to guarantee accurate approximation.

CMA-ES: We assume that a parametric representation of h as a linear expansion of N features

$$h(x) = \sum_{k=1}^{N} w_k \phi_k(x) = \mathbf{w}^\top \phi(x)$$

We use RBF features $\phi_k(x) = \exp(-\|x - x_t\|^2/\sigma^2)$ in which N centers x_t are regular intervals in the domain of x. Hence we apply CMA-ES to optimize J in a parameter space $\mathbf{w} \in \Re^N$. CMA-ES-A would optimize over a search space of $\{\mathbf{w}, \{x_t\}_{t=1}^N\}$.

Results: For all optimizers, we use the same number N of features in CMA-ES and CMA-ES-A, and centres after sparsification in CMA-ES-RKHS and functional gradient methods, $N = 100$. We use a standard way of CMA-ES to initialize other parameters, N is the effective dimensionality in CMA-ES-RKHS. The results are reported w.r.t the number of evaluations, i.e. queries to the objective function.

We report the squared error J and the solution function in Figs. 2 and 3. We create two versions for CMA-ES-A, one with good initialization (initial values of x_t are centres for CMA-ES) and one with random initialization, called CMA-ES-A-R. CMA-ES-A performs much worse than our method. This is explained by the way our method approaches from a principled way, i.e. kernel methods, for the scaling of parameters. The functional gradient method performs very well which re-confirms that it can be very competitive when gradient information is known (in this case the form of $J(h)$ is known). Figure 2 shows very interesting results where other methods like CMA-ES and CMA-ES-A are still struggling around the optimal regions.

4.2 Power Prediction Scenarios

In this section, we apply CMA-ES-RKHS for prediction of power demand by designing a simulated scenario in which one nation's electricity consumption

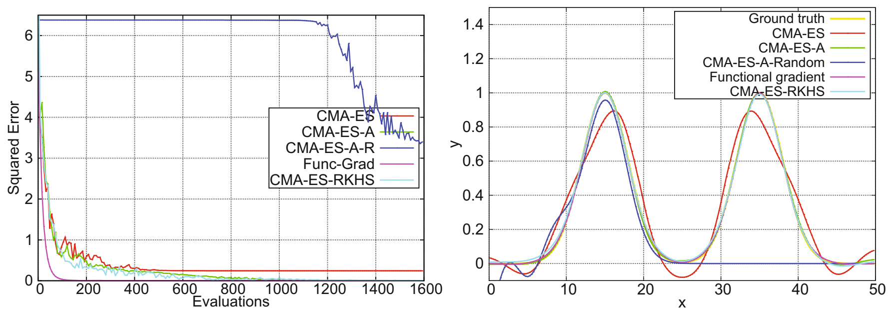

Fig. 1. Power Prediction Scenarios: (left) squared error, (right) solution functions (x-axis: time; y-axis: scaled consumption in mega-watt)

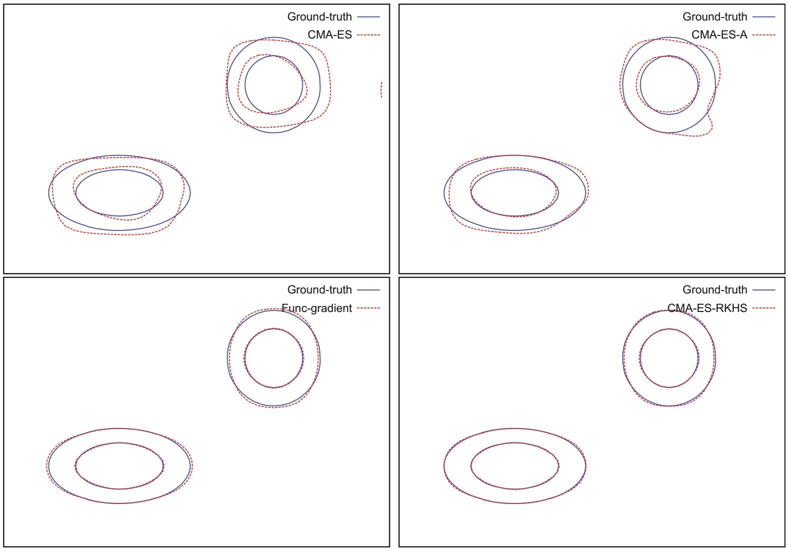

Fig. 2. Solution functions: contours of levels equivalent to the first and second deviations

is given by an unknown function $f^* : \Re \mapsto \Re$ where it maps a moment in continuous time to a real value of mega-watt (MW). The goal is to use a black-box optimization method to estimate that unknown function. For this task, we will also look for an estimate function h that minimizes the least square term J as introduced in Eq. 7. This objective is similar to the work in [15] in which they fit a parametric function over a statistical data.

We also design the unknown consumption function f^* as a mixture of two univariate Gaussians, called the ground-truth function. We use $N = 10$ for this task. We report the squared error J and the solution function in Fig. 1. The performance of CMA-ES-A-R is very bad in terms of error. As demonstrated on the

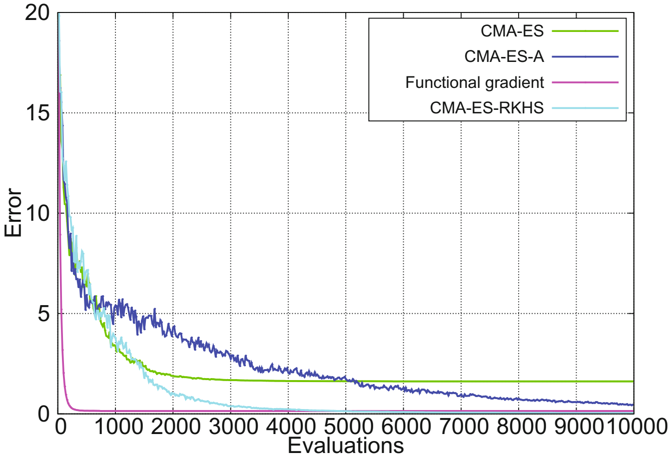

Fig. 3. Results for the 2D synthetic domain

right picture, it can detect only one mode of the optimal function. One remarkable note is that CMA-ES initialization does not consists of two correct modes in its set of centres, hence it gives poor approximation error. With adaptive ability, CMA-ES-A and CMA-ES-RKHS are able to estimate the true modes correctly.

5 Conclusion

This paper proposes a CMA-ES-RKHS framework that enables functional optimization where the search is handled over a function space. The fact that the function space is modeled in reproducing kernel Hilbert space results in analytic update rules for CMA-ES-RKHS. On the other hand, the solution function attains compactness and flexibility characteristics. Our experiments show that CMA-ES-RKHS is able to represent a complex solution function compactly and adaptively. The result shows many interesting aspects and results of CMA-ES-RKHS: (i) explicitly handling functional optimization in principle; (ii) overcoming the issue of hand-designed feature functions in many practical applications of CMA-ES.

Acknowledgement. This research is funded by Vietnam National Foundation for Science and Technology Development (NAFOSTED) under grant number 102.05-2016.18. Tuyen and Chung are funded through the Basic Science Research Program through the National Research Foundation of Korea (NRF) funded by the Ministry of Education, Science, and Technology (2014R1A1A2057735).

References

1. Adler, R.J.: The Geometry of Random Fields. Wiley, Chichester (1981)
2. Armas, R., Aguirre, H., Zapotecas-Martínez, S., Tanaka, K.: Traffic signal optimization: minimizing travel time and fuel consumption. In: Bonnevay, S., Legrand, P., Monmarché, N., Lutton, E., Schoenauer, M. (eds.) EA 2015. LNCS, vol. 9554, pp. 29–43. Springer, Cham (2016). https://doi.org/10.1007/978-3-319-31471-6_3
3. Chourabi, H., et al.: Understanding smart cities: an integrative framework. In: 2012 45th Hawaii International Conference on System Science (HICSS), pp. 2289–2297. IEEE (2012)
4. Conway, J.B.: A Course in Functional Analysis, vol. 96. Springer, New York (2013)
5. Doerr, A., Ratliff, N.D., Bohg, J., Toussaint, M., Schaal, S.: Direct loss minimization inverse optimal control. In: Robotics: Science and Systems XI (2015)
6. Edelbrunner, H., Handmann, U., Igel, C., Leefken, I., von Seelen, W.: Application and optimization of neural field dynamics for driver assistance. In: 2001 IEEE Proceedings of the Intelligent Transportation Systems, pp. 309–314. IEEE (2001)
7. Fournier, D., Fages, F., Mulard, D.: A greedy heuristic for optimizing metro regenerative energy usage. In: Railways 2014 (2014)
8. Ha, S., Liu, C.K.: Iterative training of dynamic skills inspired by human coaching techniques. ACM Trans. Graph. **34**(1), 1:1–1:11 (2014)
9. Ha, S., Liu, C.K.: Evolutionary optimization for parameterized whole-body dynamic motor skills. In: ICRA, pp. 1390–1397 (2016)
10. Hansen, N.: The CMA Evolution Strategy: A Tutorial. CoRR, abs/1604.00772 (2016)
11. Hansen, N., Auger, A.: Principled design of continuous stochastic search: from theory to practice. In: Borenstein, Y., Moraglio, A. (eds.) Theory and Principled Methods for the Design of Metaheuristics. NCS, pp. 145–180. Springer, Heidelberg (2014). https://doi.org/10.1007/978-3-642-33206-7_8
12. Hansen, N., Müller, S.D., Koumoutsakos, P.: Reducing the time complexity of the derandomized evolution strategy with covariance matrix adaptation (CMA-ES). Evol. Comput. **11**(1), 1–18 (2003)
13. Heidrich-Meisner, V., Igel, C.: Hoeffding and Bernstein races for selecting policies in evolutionary direct policy search. In: ICML, pp. 401–408 (2009)
14. Heidrich-Meisner, V., Igel, C.: Neuroevolution strategies for episodic reinforcement learning. J. Algorithms **64**(4), 152–168 (2009)
15. Kramer, O., Satzger, B., Lässig, J.: Power prediction in smart grids with evolutionary local kernel regression. In: Graña Romay, M., Corchado, E., Garcia Sebastian, M.T. (eds.) HAIS 2010. LNCS (LNAI), vol. 6076, pp. 262–269. Springer, Heidelberg (2010). https://doi.org/10.1007/978-3-642-13769-3_32
16. Marinho, Z., Boots, B., Dragan, A., Byravan, A., Gordon, G.J., Srinivasa, S.: Functional gradient motion planning in reproducing kernel Hilbert spaces. In: RSS (2016)
17. Micchelli, C.A., Pontil, M.: On learning vector-valued functions. Neural Comput. **17**(1), 177–204 (2005)
18. Rasmussen, C.E., Williams, C.K.I.: Gaussian Processes for Machine Learning. The MIT Press, Cambridge (2006)
19. Rubinstein, R.: The cross-entropy method for combinatorial and continuous optimization. Methodol. Comput. Appl. Probab. **1**(2), 127–190 (1999)
20. Rubinstein, R.Y., Kroese, D.P.: The cross-entropy method: a unified approach to combinatorial optimization. Monte-Carlo Simulation And Machine Learning. Springer, New York (2013)

21. Rückert, E.A., Neumann, G., Toussaint, M., Maass, W.: Learned graphical models for probabilistic planning provide a new class of movement primitives. Front. Comput. Neurosci. **6**(97), 1–20 (2013)
22. Schölkopf, B., Smola, A.J.: Learning with kernels support vector machines, regularization, optimization, and beyond. Adaptive Computation and Machine Learning series. MIT Press, Cambridge (2002)
23. Schölkopf, B., Smola, A., Müller, K.-R.: Kernel principal component analysis. In: Gerstner, W., Germond, A., Hasler, M., Nicoud, J.-D. (eds.) ICANN 1997. LNCS, vol. 1327, pp. 583–588. Springer, Heidelberg (1997). https://doi.org/10.1007/BFb0020217
24. Stolfi, D.H., Alba. E.: Eco-friendly reduction of travel times in European smart cities. In: Proceedings of the 2014 Annual Conference on Genetic and Evolutionary Computation, pp. 1207–1214. ACM (2014)
25. Stulp, F., Sigaud, O.: Path integral policy improvement with covariance matrix adaptation. In: ICML (2012)
26. Tan, J., Gu, Y., Turk, G., Liu, C.K.: Articulated swimming creatures. ACM Trans. Graph. (TOG) **30**(4), 58 (2011)
27. Toussaint, M.: Newton Methods for K-order Markov Constrained Motion Problems. CoRR, abs/1407.0414 (2014)
28. Ulbrich, M.: Optimization with PDE Constraints. Optimization methods in Banach spaces, pp. 97–156. Springer, Dordrecht (2009)
29. Vien, N.A., Toussaint, M.: POMDP manipulation via trajectory optimization. In: 2015 IEEE/RSJ International Conference on Intelligent Robots and Systems, IROS 2015, September 28 - October 2, Hamburg, pp. 242–249 (2015)
30. Vincent, P., Bengio, Y.: Kernel matching pursuit. Mach. Learn. **48**(1–3), 165–187 (2002)
31. Wang, J.M., Hamner, S.R., Delp, S.L., Koltun, V.: Optimizing locomotion controllers using biologically-based actuators and objectives. ACM Trans. Graph **31**(4), 25:1–25:11 (2012)
32. Wierstra, D., Schaul, T., Glasmachers, T., Sun, Y., Peters, J., Schmidhuber, J.: Natural evolution strategies. J. Mach. Learn. Res. **15**(1), 949–980 (2014)

Data Mining Approaches for IP Address Clustering

Madeleine Victoria Kongshavn, Anis Yazidi(✉), Hårek Haugerud, and Hugo Hammer

Department of Computer Science,
Oslo and Akershus University College of Applied Sciences, Oslo, Norway
Anis.Yazidi@hioa.no

Abstract. Distributed Denial of Service (DDoS) attacks have for the last two decades been among the greatest threats facing the internet infrastructure. Mitigating DDoS attacks is a particularly challenging task as an attacker masks the attack traffic among legitimate users. Mitigation approaches within DDoS has therefore often been investigated within the field of anomaly intrusion detection. This means that even a successful mitigation approach will risk a high disregard of legitimate users. This article proposes to use data mining and machine learning approaches to find unique hidden data structures which keep a high degree of accepted legitimate traffic, while still being able to remove illegitimate and irrelevant data traffic which don't follow the hidden structure. In this perspective, we devise and evaluate two novel IP Address clustering algorithms for DDoS mitigation, namely, Geographical Clustering (GC) and Reduced Geographical Clustering (RGC).

1 Introduction

A Denial of Service (DoS) attack is an explicit attempt to render a server incapable of providing normal service to its users. This can be accomplished through a variety of methods, however, the common pattern is that a DoS attack will try to exploit some limited system or network resources to accomplish this goal. We can differentiate between DoS attacks and DDoS attacks; A DoS is where one attacker, with one network connection, executes an attack, while a DDoS attack adds a many-to-one dimension problem to the equation. Instead of using one connection, a DDoS attack often uses thousands of compromised hosts to execute an attack. This amplifies both the available resources of an attacker and the complexity of the DoS problem. DDoS attacks have over the last decade become an immense threat to the Internet infrastructure where attacks have become commonplace with a wide range of global victims in everything from commercial websites and educational institutions to public chat servers and government organizations [1]. Akamai, which is a leading network services provider for media and software delivery as well as for delivering cloud security solutions, reported a 125% increase in total DDoS attacks from 2015 to 2016 [2].

© ICST Institute for Computer Sciences, Social Informatics and Telecommunications Engineering 2018
Y. Chen and T. Q. Duong (Eds.): INISCOM 2017, LNICST 221, pp. 266–275, 2018.
https://doi.org/10.1007/978-3-319-74176-5_23

In a general sense, it is preferable to mitigate DDoS attacks as close to the source as possible, in order to reduce as much of the collateral damage as possible. However, this is generally difficult for a number of reasons; it's generally hard to identify attack traffic close to the source, as the attack traffic is highly distributed and comes from multiple sources. Moreover, the Internet is built around an authorization-free nature which makes it difficult to implement any scheme to a high degree. It is therefore a strong need to mitigate DDoS attacks near the target victim, as this seems to be the only solution for the current Internet infrastructure [3]. This article proposes two clustering algorithms to mitigate DDoS attack. The algorithms are tested on an anonymous dataset gathered from a web-server in Oslo and Akershus University College of Applied sciences. The dataset is henceforth denoted by D10C and consists of a training phase and a testing phase. The training phase consists of 1 million unique requests and the testing set consists of 500 thousands unique requests. The proposed algorithms build on the following research question that we shall explore in this article:

How can we use data mining to find pattern correlations on data history to build efficient filtering rules that are able to mitigate DDoS attacks near the targeted server?

2 Related Research

In this section, some prominent closely related research is reviewed which deals directly or indirectly with filtering DDoS attacks based on elements from data mining.

Peng et al. suggested to use a database of previously seen legitimate IP addresses to counter DDoS attacks. This method bases itself on the common assumption that normal network traffic differentiates itself from network traffic under an attack [4]. This mechanism, known as History-based IP filtering(HIF), uses an IP address database (IAD) containing previously seen IP addresses over a certain time period. Under an attack, only IP addresses from the IAD are allowed to access the network or service.

Goldstein et al. [5] suggested taking advantage of IP neighborhood relations, by using density estimation, to counter DDoS attacks. The idea is that IP addresses that are close or similar to each other, share similar characteristics. To evaluate the distances between the different objects, $Xor+$ and Euclidean distance is used on the IP address. To avoid that distances within the given network mask are always constant, regardless of variation within the subnet, Euclidean distances are added to the distance calculation. The approach used a modified K-means clustering algorithm to compute the clustering centers. Once the clustering centers were computed, an area was defined around the clusters, which would be the IP addresses the model expected to see in the future [5].

3 Proposed IP Address Clustering Algorithms

Previous clustering techniques, as seen in the last section, focus on clustering data based on existing data features in the traffic pattern. These features include packet attributes as source addresses, time to live (TTL), flags and protocols [5–12]. Clustering based on IP address has not been well investigated in the literature and is shown to be a very promising step towards mitigating DDoS. At this juncture, we shall present two novel IP address clustering algorithms; Geographical Clustering (GC) and Reduced Geographical Clustering (RGC). Instead of focusing the initial clustering approach on the distance between existing features, the clustering approaches try to expand clusters based on the distance between geographical points where traffic are located. GC tries to expand a cluster based on frequent geographical points. Since GC relays on a packets location repeating, this can amplify the amount of data that can be covered as GC can identify new networks which has not necessarily been seen under the training phase. RGC further expands on this idea, by limiting the amount of accepted location points. This limitation is done by employing different constraints on the cluster expansion by only accepting the most legitimate points in RGC. The amount of accepted networks can be limited without affecting the amount of accepted data from the testing phase.

3.1 GC

The first proposed density-based clustering algorithm, *GC*, tries to estimate a data pattern based on geographical location and builds on the hypothesis: *If network x from location y reaches the server under the training phase, there is a higher chance for network z from location y + 1 to reach the server, than network q that doesn't belong to a location close to network x.*

The clustering algorithm, *GC*, which is based on *DBSCAN* [13], tries to expand a cluster as long as there are points close to the cluster. *GC* begins by defining core points from where a cluster can continue to expand. Defining start points is a computationally hard task, as the definition of the start points will essentially define how and where the cluster will expand and how well the clustering algorithm will be able to represent new and unknown data. We can make the assumption that frequent networks often in some form reoccur in the data pattern. Since frequent networks represent a huge portion of the incoming traffic, it is reasonable to assume that every frequent network, or in this case location, is automatically assumed as a start point or core point. The core points will then look in their close proximity based on distance x to see if there are more points that can belong to this cluster. If a core point finds a point y that is within distance x, it will include the point to its own cluster. Point y will then look in its close proximity to find any new points that can be included in the cluster. If any points that are part of a cluster are within the given distance to other points that are part of a different cluster, the two clusters will merge and become one cluster. The pseudo code for density-based clustering can be seen in Algorithm 1 below. The algorithm takes three arguments: the dataset containing a list of latitude/longitude locations with the frequency of packets from that locations, D which is the maximum distance from a point to a cluster for this point to still be considered a part of that cluster and T which is the frequency threshold for a point to be considered a core point. According to this algorithm,

Algorithm 1. Pseudo code for the GC.

```
function DENSITY_CLUSTERING(dataset, D, T)
    all_clusters ← (dataset.points ≥ T)
    for cluster in all_cluster do
        cluster ← (dataset.points ≤ cluster.D)
        while cluster ≠ converged do
            points ← (dataset.points ≤ cluster.D)
            if points in all_cluster.points then
                cluster.merge(points in all_cluster.points)
            end if
        end while
    end for
    return all_cluster
end function
```

two essential parameters, core-point threshold and maximum distance, need to be pre-defined. The definition of these attributes varies greatly between different datasets and consequently the data pattern that these clusters cover, will have different strengths and weaknesses based on the chosen attributes.

Deciding Core-Point Threshold

As aforementioned, the definition of frequent locations, or core points, is just the definition of an initial cluster, which is just a single start point for a cluster to continue to expand. This threshold would vary greatly between different datasets and with a new and unknown dataset, it could be beneficial to decide these location points based on an upper percentile of all points which have the highest frequency of seen traffic. The definition of the threshold for a core-point is beyond the scope of this paper. However, as seen in Fig. 1 more initial clusters will exist with a low threshold and this is not necessarily preferable as this will lead to clusters where there are seen considerable little data traffic. Moreover, as it is the location points we are talking about, considering if we are able to identify new locations correctly, we might risk to cover a substantial location pattern, and therefore start accepting traffic which is not necessarily representative for the known data pattern. Therefore, when choosing the initial cluster points, the amount of covered training data should be seen in correspondence with the amount of initial clusters. Since we want clusters to expand based on the initial clusters, we don't need to cover most of the training pattern from the beginning, as we assume, most of the relevant data pattern, will still be covered, when the cluster expand to points nearby. Therefore, we should preferably choose a high core-point threshold which will cover the most relevant locations. These location points will have a higher possibility of repeating later, and we should be able to make the assumption that areas near these points will also have a high chance of repeating, although little traffic might be seen in the area during the training phase.

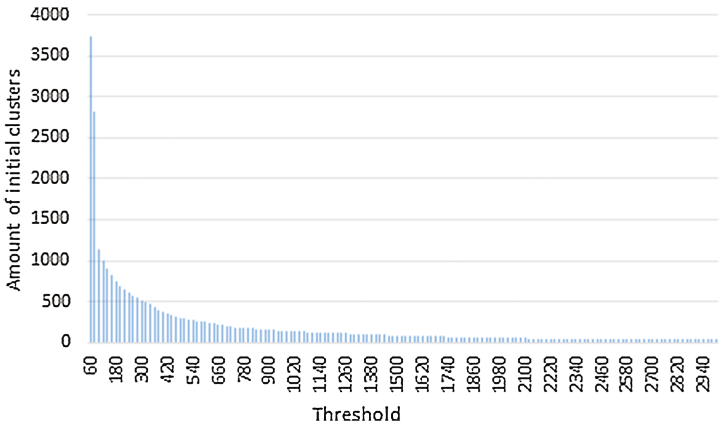

Fig. 1. The amount of initial clusters for D10C with different thresholds.

Deciding Maximum Distance

As we are assuming, from the hypothesis, a lot of lower networks or locations with less frequent packets will still be covered as they exist in the surrounding area of the defined core points. This leads to the question; what is the maximum distance from point x to point y, for point x to still be a part of point y*'s* cluster? We have previously stated that every core point is automatically assumed to be cluster, the question now is; What is the maximum distance for one or more cluster points to any new point, for the point to be a part of the given cluster? The answer to this question would vary widely based on the training data. However, we should try to minimize the maximum distances, so we don't end up with clusters where data have little to none similarities with other data in the same cluster. Based on our hypothesis, we can assume that data points exist close to our cluster in all directions of the initial core points. Therefore, we can based on this, get a certain view of the necessary distance, by measuring how much training pattern is covered with different maximum distances.

Figure 2 shows the amount of data for *D10C*, which is covered with different thresholds and maximum distances. A lower threshold will cover more of the training data, regardless of the maximum distance and at most, with a threshold of 700, *81.56%* of D10C training data is covered with a maximum allowed distances of *50* km. It would be preferable to cover most of the training as this will result in a higher coverage for the test data. However, the coverage of new points should, to a large degree, be proportional to the higher maximum distance. In other words, we should be able to assume that a cluster does not expand forever.

Figure 3 gives a clearer view of the difference in increased percentage points for each threshold. Most points have a good increase in the amount of covered data until around 20–25 km. At this point, the different calculated clusters have managed to increase around 10% points. At the remaining calculated distances of 30–50 km, clusters have a high variance, with no particular pattern for the

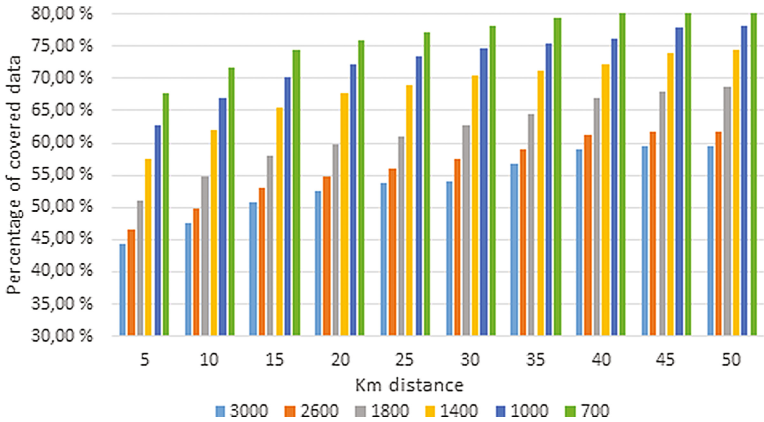

Fig. 2. The amount of data, for D10C, which is covered with various initial cluster sizes and with different maximum distances.

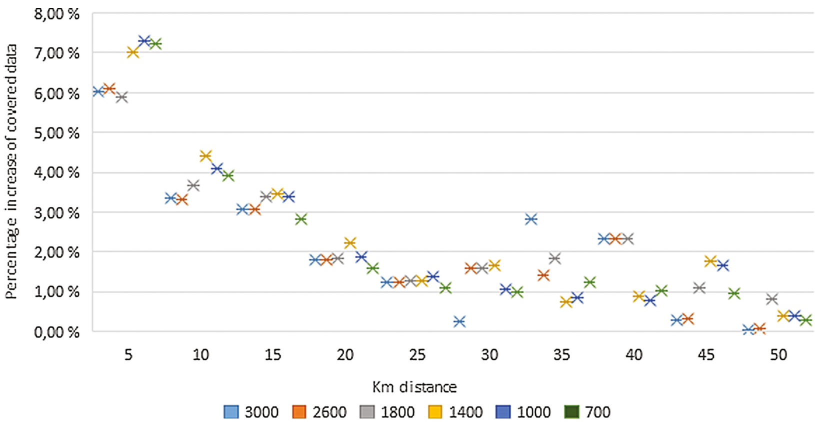

Fig. 3. The increase in % points that is covered with different km threshold and core points threshold, for D10C.

remaining increased percentage points. It would therefore, for most clusters, be beneficial to have a maximum km distance between 20–25 km.

GC Result

To find the optimal result for geographical clusters, data or source IP addresses, which has not necessarily been seen in the training phase, but is part of a cluster based on the geographical locations should be counted as well. We should therefore, not only count the direct points that have appeared in the training phase, but also count points that fit inside a cluster, but which has not necessarily been seen in the training phase. *GC* manages with an optimal result, as seen in Fig. 4 where a packet location can be identified, to achieve from 40% to 77%.

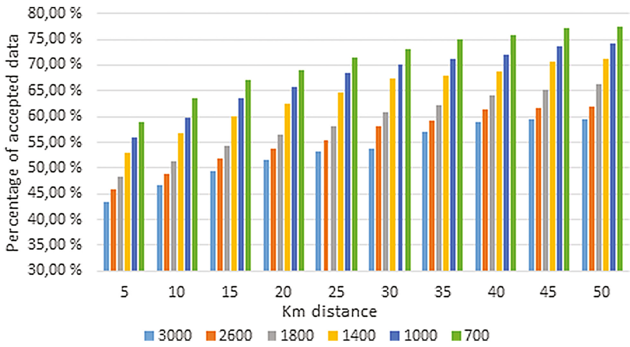

Fig. 4. The optimal result of accepted packets for the D10C testing set.

For D10C, when only 24-bit networks which have previously been seen in the training phase and are a part of a cluster are accepted, the amount of accepted data result diminishes radically, compared to an optimal result where a packets location can be identified. At the minimum, when new data can not be identified, 7.50% points less are accepted in the testing phase for D10C. At the highest point, with a cluster computation of 50 km and a threshold of 700, 27.02% points less are accepted in the testing phase.

3.2 RGC

Although, *GC* has a potential of acquiring an unique pattern and performing well under unknown traffic, the algorithm does not define any consideration when defining a pattern. The previous algorithm, which states that if a point x is near one or more points that are a part of cluster y, point x should also be stated as a part of *y's* cluster, is not necessarily ideal, as multiple issues are raised in regards to the algorithm's ability to sustain a pattern without accepting too much illegitimate traffic.

To create a stronger algorithm, several steps can be taken. First, to prevent the pattern composition in clusters from deteriorating when clusters are merged, merging of clusters can be overlooked. Instead, clusters can be forced to expand and converge separately. Assume that $x_1, x_2, ..., x_{n-1}, x_n$ is a set of data points in a two dimensional space and $c_1, c_2, ..., c_{n-1}, c_n$ is a set of core-points which contains at least the amount y of seen requests. Let $d(x_m, c_z)$ be the geographical distance between the point x_m and the core point c_z. Potentially x_m could be part of any of the clusters with core point c_n. The algorithm decides that x_m will be a part of cluster c_z if $d(x_m, c_z) < d(x_m, c_1), ..., d(x_m, c_{n-1}), d(x_m, c_n)$ for all core points. Moreover, clusters should only expand to points that are more likely to occur later. We can build on the hypothesis and make the assumption that a request is more likely to occur in a point x if it has at least y points in its near area. Only points that satisfy this criterion, are allowed to be a part of a cluster. Finally, to prevent big cities, which have a natural ability to easier create core points, from being able to create a cluster if there are not other points nearby, clusters that are not able to expand over a certain amount of points should be dismantled. The dismantled points, including the core point, should then be re-positioned to clusters nearby. As seen in Fig. 5, different minimum applied lengths, in a D10C cluster, radically and rapidly diminishes the amount of accepted data. Both the amount of covered data in the training and testing phase decrease fast with higher minimum cluster length. However, the amount of covered data in the training phase decreases faster than the amount of covered data in the testing phase. At a minimum length of 10, the amount of covered data in D10C training set decreases below the amount of covered data in the testing set.

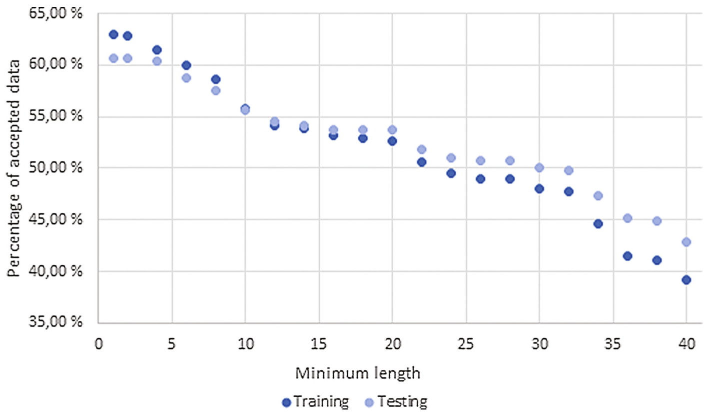

Fig. 5. The amount of covered data in the training and testing phase with different minimum lengths constraints set for a cluster.

RGC Result

When clusters are computed with a minimum length of 10, minimum points of 3, different km distances and different core-point thresholds, the clusters will (for D10C) in most instances cover 40% to 50%. This calculation can be seen in Fig. 6. These calculations give a lower acceptance rate than for GC. However, while GC manages to have a zero percentage differences between the accepted data in the training and testing phase, RGC manages to accept upwards of 30% points more in the testing phase than in the training phase. This implies that RGC is to a higher degree able to identify the most relevant points that have a high likelihood of occurring later.

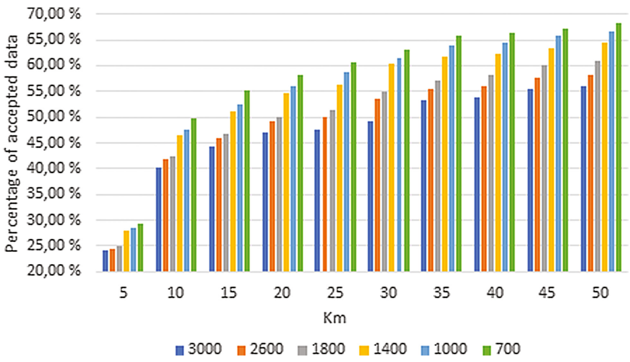

Fig. 6. The optimal amount of accepted D10C testing data that was seen in a cluster.

4 Conclusion

Previous clustering techniques focused on clustering data based on existing data features in the traffic pattern. These features included packet attributes as source addresses, TTL, flags and protocols. Clustering on IP address has not been well investigated in the literature and is in this paper shown to be a very promising step towards mitigating DDoS. Clustering IP addresses based on distances between bits gives a limited clustering ability when addresses are close geographically, but not necessarily close in the address range. Two novel IP address clustering algorithms were devised and evaluated. GC expanded a cluster based on frequent geographical points. This gave GC clustering an advantage over previous clustering approaches. As *GC* relayed on a packets locations repeating, the amount of accepted legitimate traffic was amplified. GC was shown to be able to identify new networks which had not necessarily been seen under the training phase. RGC further expanded on this hypothesis, by limiting the amount of accepted location points.

References

1. Moore, D., Shannon, C., Brown, D.J., Voelker, G.M., Savage, S.: Inferring internet denial-of-service activity. ACM Trans. Comput. Syst. (TOCS) **24**(2), 115–139 (2006)
2. Akamai: Akamai's state of the internet report q1 2016 (2016)
3. Goldstein, M., Lampert, C., Reif, M., Stahl, A., Breuel, T.: Bayes optimal ddos mitigation by adaptive history-based IP filtering. In: Seventh International Conference on Networking (ICN 2008), pp. 174–179. IEEE (2008)
4. Peng, T., Leckie, C., Ramamohanarao, K.: Protection from distributed denial of service attacks using history-based IP filtering. In: IEEE International Conference on Communications (ICC 2003), vol. 1, pp. 482–486. IEEE (2003)
5. Goldstein, M., Reif, M., Stahl, A., Breuel, T.: Server-side prediction of source IP addresses using density estimation. In: International Conference on Availability, Reliability and Security, 2009 (ARES 2009), pp. 82–89. IEEE (2009)

6. Qin, X., Xu, T., Wang, C.: DDoS attack detection using flow entropy and clustering technique. In: 2015 11th International Conference on Computational Intelligence and Security (CIS), pp. 412–415. IEEE (2015)
7. Yu, J., Li, Z., Chen, H., Chen, X.: A detection and offense mechanism to defend against application layer DDoS attacks. In: Third International Conference on Networking and Services (ICNS), p. 54. IEEE (2007)
8. Li, Z., Li, Y., Xu, L.: Anomaly intrusion detection method based on k-means clustering algorithm with particle swarm optimization. In: 2011 International Conference on Information Technology, Computer Engineering and Management Sciences (ICM), vol. 2, pp. 157–161. IEEE (2011)
9. Mingqiang, Z., Hui, H., Qian, W.: A graph-based clustering algorithm for anomaly intrusion detection. In: 2012 7th International Conference on Computer Science & Education (ICCSE), pp. 1311–1314. IEEE (2012)
10. Ranjan, R., Sahoo, G.: A new clustering approach for anomaly intrusion detection, arXiv preprint arXiv:1404.2772 (2014)
11. Guan, Y., Ghorbani, A.A., Belacel, N.: Y-means: a clustering method for intrusion detection. In: Canadian Conference on Electrical and Computer Engineering (CCECE), vol. 2, pp. 1083–1086. IEEE (2003)
12. Xue-Yong, L., Guo-hong, G., Jia-xia, S.: A new intrusion detection method based on improved DBSCAN. In: 2010 WASE International Conference on Information Engineering (ICIE), vol. 2, pp. 117–120. IEEE (2010)
13. Ester, M., Kriegel, H.-P., Sander, J., Xu, X., et al.: A density-based algorithm for discovering clusters in large spatial databases with noise. In: *Kdd*, vol. 96, no. 34, pp. 226–231 (1996)

Intelligent Systems, Industrial Networks, and Applications

A Short Survey on Fault Diagnosis of Rotating Machinery Using Entropy Techniques

Zhiqiang Huo[1,2(✉)], Yu Zhang[1], and Lei Shu[1,2]

[1] School of Engineering, University of Lincoln, Lincoln, UK
{zhuo,yzhang,lshu}@lincoln.ac.uk
[2] Guangdong Provincial Key Laboratory on Petrochemical Equipment Fault Diagnosis, Guangdong University of Petrochemical Technology, Maoming, China

Abstract. Fault diagnosis is significant for identifying latent abnormalities, and implementing fault-tolerant operations for minimizing performance degradation caused by failures in industrial systems, such as rotating machinery. The emergence of entropy theory contributes to precisely measure irregularity and complexity in a time series, which can be used for discriminating prominent fault information in rotating machinery. In this short paper, the utilization of entropy techniques for fault diagnosis of rotating machinery is summarized. Finally, open research trends and conclusions are discussed and presented respectively.

Keywords: Fault diagnosis · Rotating machinery · Entropy

1 Introduction

In recent decades, the world has witnessed a tremendous growth in the theory and practice of fault diagnostic approaches, which have been widely and successfully applied in fault diagnosis of rotating machinery, such as failure detection in rotors, rolling bearings and shafts. As a result, signal-based fault diagnosis has been a prominent technique to analyze non-linear and non-stationary signals. In this kind of diagnostic methods, feature extraction is one of the significant steps for characterizing fault information of interest in fault detection and identification. The traditional time-frequency domain parameters include peak value, mean value, root mean square (RMS), power spectrum, and RMS of the spectrum difference, etc. Apart from that, in the recent decade, entropy-based features have been applied extensively in the field of fault diagnosis by means of evaluating the irregularity and complexity in signals with different conditions.

2 Fault Diagnosis Based on Entropy Methods

Entropy techniques can be considered as a powerful measurement tool that is capable of quantifying the irregularity in a time series. The occurrence of defects in rotating components usually produces subcritical frequencies and

© ICST Institute for Computer Sciences, Social Informatics and Telecommunications Engineering 2018
Y. Chen and T. Q. Duong (Eds.): INISCOM 2017, LNICST 221, pp. 279–284, 2018.
https://doi.org/10.1007/978-3-319-74176-5_24

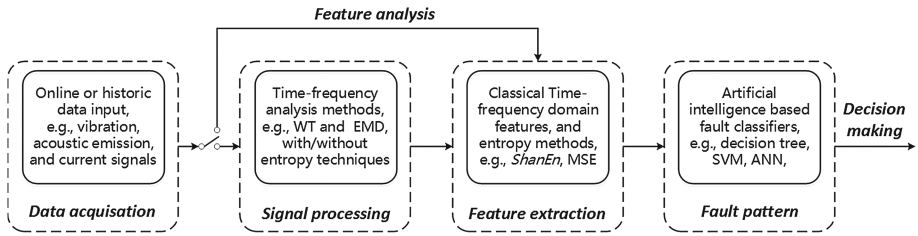

Fig. 1. Data flow of fault diagnosis of rotating machinery based entropy methods.

finally increases the amplitude of impulses in signals obtained from rotating machines, such as vibration and acoustic signals. According to literatures, the steps in fault diagnosis using entropy methods can be categorized into two main classes: (1) selection of multi-scale decomposed vectors obtained from multi-resolution analysis (MRA), such as wavelet transform (WT); (2) feature extraction of desired decomposed vectors or original signals. The traditional procedure of signal-based fault diagnosis using entropy methods is illustrated in Fig. 1. The most commonly used entropy features include power spectrum energy ($PowerEn$), Shannon entropy ($ShanEn$), approximate entropy ($ApEn$), sample entropy ($SampEn$), fuzzy entropy ($FuzzyEn$), permutation entropy ($PerEn$), and their corresponding multiple scale entropies.

2.1 Single-Scale Entropy Approaches

$PowerEn$ is one of useful tools that is adopted to describe how the energy of a signal or a time series is distributed within time domain [1], which can be defined as the absolute-value squared of the time series. $ShanEn$, named after Claude Shannon, was developed to solve the measurement problem of system's disorder in microscopic particle in information theory. Generally, $PowerEn$ is applied together jointly with $ShanEn$ to determine decomposed vectors obtained from MRA, such as wavelet coefficients and intrinsic mode functions (IMFs) obtained from WT and empirical mode decomposition (EMD) methods respectively. Later in 1990s, $ApEn$ was proposed by Pincus to determine changing complexity from data. Subsequently, $SampEn$ and $FuzzyEn$, as a modification of $ApEn$ were later developed to overcome the drawbacks that $ApEn$ subjected to, such as problems of small value obtained from short length of data and lack of relative consistency. To compare the effectiveness of $ApEn$, $SampEn$ and $FuzzyEn$, comparative study was conducted in [2], where it was found that $FuzzyEn$ yields more satisfying results when characterizing signals with different complexity. Similarly, $PerEn$ [3] was also developed and applied as a measure of complexity.

Table 1. A summary of recent methods for fault diagnosis of rotating machinery using entropy techniques.

Author	Year	Object	Signal monitored	Signal processing	EEA method		Classifier used
					Type	Role	
Bin [7]	2012	Motor	Vibration	WPT and EMD	*Power Energy*	Vector selection	ANN
Tabrizi [8]	2015	Bearing	Vibration	WPT and EEMD	*Power Energy*	Vector selection	SVM
Kankar [9]	2011	Bearing	Vibration	CWT	Entropy ratio	Parameter selection	SOM, SVM, ANN
Gu [10]	2012	Shaft	AE	DWT	*ShanEn*	Feature extraction	N/A
Camarena [11]	2016	Motor	Vibration	N/A	*ShanEn*	Feature extraction	k-Means
He [12]	2012	Bearing	AE	N/A	*ApEn*	Feature extraction	N/A
Sampaio [13]	2016	Shaft	Vibration	N/A	*ApEn*	Feature extraction	N/A
Lin [14]	2017	Gear and bearing	Vibration	SLA and WSM	*ApEn* and *SampEn*	Feature extraction	N/A
Liang [15]	2015	Gearbox	AE	WT-EMD	*SampEn*	Vector selection	SVM
Wu [16]	2016	Bearing	Vibration	EMD	MSE	Vector selection	Decision tree
Pan [17]	2016	Motor	Vibration	N/A	MSE	Feature extraction	SVM
Verma [18]	2016	Motor	Vibration, Current	N/A	MSE	Feature extraction	ANN
Aouabdi [19]	2017	Gearbox	Current	DWT	PCA-MSE	Feature extraction	N/A
Chen [20]	2016	Gearbox	Vibration	LMD	*FuzzyEn*	Vector selection	ANFIS
Metha [21]	2016	Bearing	Vibration	N/A	MFE	Feature extraction	VPMCD
Zhao [22]	2016	Bearing	Vibration	EEMD	MFE	Feature extraction	SVM
Zheng [23]	2017	Bearing	Vibration	N/A	Composite MFE	Feature extraction	Ensemble SVM
Wu [24]	2012	Bearing	Vibration	N/A	MPE	Feature extraction	SVM
Vakharia [25]	2015	Bearing	Vibration	CWT	MPE	Parameter selection	ANN, SVM
Zhang [26]	2015	Bearing	Vibration	EEMD	*PerEn*	Vector selection	SVM
Yi [27]	2017	Bearing	Vibration	TSSA	*PerEn*	Vector selection	N/A

2.2 Multiple-Scale Entropy Approaches (MEA)

The concept of analyzing and measuring a time series from multiple scales was proposed by Costa, who proposed that the single-scale entropy algorithm yielded contradictory results when applied to real-world data sets obtained in health and disease states. On this basis, a variety of MEA methods have been proposed and widely applied in the field of fault diagnosis, such as multiscale entropy (MSE) [4], multiscale fuzzy entropy (MFE) [5], multiscale permutation entropy (MPE) [6]. The key ideas behind the concept of MEA methods can be simply concluded as two major steps as described: (1) obtain multiple-scale time series from the original time series through a coarse-grained procedure at a scale factor of τ (τ is the length of non-overlapping windows); (2) apply corresponding single scale entropy method to estimate complexity in each coarse-grained time series.

Recently, entropy-based approaches have been successfully applied in not only selection of dominant decomposed vectors but also fault feature extraction in applications of fault diagnosis of rotating components, such as shafts, bearings, gearboxes, and rotors. In this short paper, the utilization of entropy-based methods for fault diagnosis of rotating machinery in the recent decade is summarized, as presented in Table 1. It presents a comprehensive view of entropy-based applications and functionalities regarding to fault diagnosis of rotating machinery. In addition, it concludes a variety of entropy-based techniques that can be adaptively chosen by researchers to be applied in the field of fault diagnosis for rotating machinery.

3 Open Research Trends

It should be pointed that feature extraction has significant effects on the efficiency and accuracy of fault detection and identification in rotating machinery. In addition, due to the fact that industrial systems are becoming more and more complex in recent decades, continuing effects are still essential to be continuously put into improving the confidence of reliability and safety of industrial process. Some challenges are therefore needed to be focused, which are listed as following:

1. Robustness of the entropy methods under various operating conditions
2. Consistency in values of similarity and parameters selected
3. Removal of the magnitude influence of the data sets
4. Enrichment and modification of the entropy techniques
5. Able to deal with non-linear and non-stationary signals
6. Capable of identifying defects with increasing severity.

4 Conclusions

In this short paper, most commonly used entropy techniques are briefly introduced. After that, the utilization of entropy-based methods for fault diagnosis of rotating machinery is summarized. In addition, future trends are proposed to improve the effectiveness of entropy-based diagnostic methods. However, with increasing efforts been put into the entropy methods applied in characterizing fault information, it is believed that entropy-based techniques would be constituently applied as promising techniques in fault diagnosis of rotating machinery.

Acknowledgement. This work is partially supported by International and Hong Kong, Macao & Taiwan collaborative innovation platform and major international cooperation projects of colleges in Guangdong Province (No. 2015KGJHZ026), The Natural Science Foundation of Guangdong Province (No. 2016A030307029), and Maoming Engineering Research Center on Industrial Internet of Things (No. 517018).

References

1. CusidÓCusido, J., Romeral, L., Ortega, J.A., Rosero, J.A., Espinosa, A.G.: Fault detection in induction machines using power spectral density in wavelet decomposition. IEEE Trans. Industr. Electron. **55**(2), 633–643 (2008)
2. Xiong, G., Zhang, L., Liu, H., Zou, H., Guo, W.: A comparative study on ApEn, SampEn and their fuzzy counterparts in a multiscale framework for feature extraction. J. Zhejiang Univ. SCIENCE A **11**(4), 270–279 (2010)
3. Bandt, C., Pompe, B.: Permutation entropy: a natural complexity measure for time series. Phys. Rev. Lett. **88**(17), 174102 (2002)
4. Costa, M., Goldberger, A.L., Peng, C.-K.: Multiscale entropy analysis of biological signals. Phys. Rev. E **71**(2), 021906 (2005)
5. Zheng, J., Cheng, J., Yang, Y., Luo, S.: A rolling bearing fault diagnosis method based on multi-scale fuzzy entropy and variable predictive model-based class discrimination. Mech. Mach. Theor. **78**, 187–200 (2014)
6. Aziz, W., Arif, M.: Multiscale permutation entropy of physiological time series. In: IEEE 2005 9th International Multitopic Conference, INMIC 2005, pp. 1–6. IEEE (2005)
7. Bin, G., Gao, J., Li, X., Dhillon, B.: Early fault diagnosis of rotating machinery based on wavelet packets-empirical mode decomposition feature extraction and neural network. Mech. Syst. Sign. Process. **27**, 696–711 (2012)
8. Tabrizi, A., Garibaldi, L., Fasana, A., Marchesiello, S.: Early damage detection of roller bearings using wavelet packet decomposition, ensemble empirical mode decomposition and support vector machine. Meccanica **50**(3), 865–874 (2015)
9. Kankar, P.K., Sharma, S.C., Harsha, S.P.: Fault diagnosis of ball bearings using continuous wavelet transform. Appl. Soft Comput. **11**(2), 2300–2312 (2011)
10. Gu, D., Kim, J., Kelimu, T., Huh, S.-C., Choi, B.-K.: Evaluation of the use of envelope analysis and DWT on AE signals generated from degrading shafts. Mater. Sci. Eng., B **177**(19), 1683–1690 (2012)
11. Camarena-Martinez, D., Valtierra-Rodriguez, M., Amezquita-Sanchez, J.P., Granados-Lieberman, D., Romero-Troncoso, R.J., Garcia-Perez, A.: Shannon entropy and k-means method for automatic diagnosis of broken rotor bars in induction motors using vibration signals. Shock Vibr. **2016**, 10 (2016)
12. He, Y., Zhang, X.: Approximate entropy analysis of the acoustic emission from defects in rolling element bearings. J. Vibr. Acoust. **134**(6), 061012 (2012)
13. Sampaio, D.L., Nicoletti, R.: Detection of cracks in shafts with the approximated entropy algorithm. Mech. Syst. Sign. Process. **72**, 286–302 (2016)

14. Lin, J., Dou, C.: A novel method for condition monitoring of rotating machinery based on statistical linguistic analysis and weighted similarity measures. J. Sound Vibr. **390**, 272–288 (2017)
15. Liang, J., Yang, Z.: A novel wavelet transform – empirical mode decomposition based sample entropy and SVD approach for acoustic signal fault diagnosis. In: Tan, Y., Shi, Y., Buarque, F., Gelbukh, A., Das, S., Engelbrecht, A. (eds.) ICSI 2015. LNCS, vol. 9142, pp. 232–241. Springer, Cham (2015). https://doi.org/10.1007/978-3-319-20469-7_26
16. Wu, T.-Y., Yu, C.-L., Liu, D.-C.: On multi-scale entropy analysis of order-tracking measurement for bearing fault diagnosis under variable speed. Entropy **18**(8), 292 (2016)
17. Pan, S., Han, T., Tan, A.C., Lin, T.R.: Fault diagnosis system of induction motors based on multiscale entropy and support vector machine with mutual information algorithm. Shock Vibr. **2016**, 12 (2016)
18. Verma, A.K., Sarangi, S., Kolekar, M.: Misalignment faults detection in an induction motor based on multi-scale entropy and artificial neural network. Electr. Power Compon. Syst. **44**(8), 916–927 (2016)
19. Aouabdi, S., Taibi, M., Bouras, S., Boutasseta, N.: Using multi-scale entropy and principal component analysis to monitor gears degradation via the motor current signature analysis. Mech. Syst. Signal Process. **90**, 298–316 (2017)
20. Chen, X., Cheng, G., Li, H., Zhang, M.: Diagnosing planetary gear faults using the fuzzy entropy of LMD and ANFIS. J. Mech. Sci. Technol. **30**(6), 2453–2462 (2016)
21. Mehta, P., Gaikwad, J.A., Kulkarni, J.V.: Application of multi-scale fuzzy entropy for roller bearing fault detection and fault classification based on VPMCD. In: IEEE International Conference on Recent Trends in Electronics, Information & Communication Technology (RTEICT), pp. 256–261. IEEE (2016)
22. Zhao, H., Sun, M., Deng, W., Yang, X.: A new feature extraction method based on EEMD and multi-scale fuzzy entropy for motor bearing. Entropy **19**(1), 14 (2016)
23. Zheng, J., Pan, H., Cheng, J.: Rolling bearing fault detection and diagnosis based on composite multiscale fuzzy entropy and ensemble support vector machines. Mech. Syst. Signal Process. **85**, 746–759 (2017)
24. Wu, S.-D., Wu, P.-H., Wu, C.-W., Ding, J.-J., Wang, C.-C.: Bearing fault diagnosis based on multiscale permutation entropy and support vector machine. Entropy **14**(8), 1343–1356 (2012)
25. Vakharia, V., Gupta, V., Kankar, P.: A multiscale permutation entropy based approach to select wavelet for fault diagnosis of ball bearings. J. Vibr. Control **21**(16), 3123–3131 (2015)
26. Zhang, X., Liang, Y., Zhou, J., et al.: A novel bearing fault diagnosis model integrated permutation entropy, ensemble empirical mode decomposition and optimized SVM. Measurement **69**, 164–179 (2015)
27. Yi, C., Lv, Y., Ge, M., Xiao, H., Yu, X.: Tensor singular spectrum decomposition algorithm based on permutation entropy for rolling bearing fault diagnosis. Entropy **19**(4), 139 (2017)

An Intrusion Detection System Based on Machine Learning for CAN-Bus

Daxin Tian[1,3,4], Yuzhou Li[1,3,4], Yunpeng Wang[1,3,4(✉)], Xuting Duan[3], Congyu Wang[3], Wenyang Wang[2], Rong Hui[2], and Peng Guo[2]

[1] Beijing Advanced Innovation Center for Big Data and Brain Computing, Beihang University, XueYuan Road No. 37, Beijing 100191, China
ypwang@buaa.edu.cn

[2] China Automotive Technology and Research Center, Automotive Engineering Research Institute, East Xianfeng Road No. 68, Tianjin 300300, China

[3] Beijing Key Laboratory for Cooperative Vehicle Infrastructure Systems and Safety Control, School of Transportation Science and Engineering, Beihang University, XueYuan Road No. 37, Beijing 100191, China

[4] Jiangsu Province Collaborative Innovation Center of Modern Urban Traffic Technologies, Si Pai Lou. 2, Nanjing 210096, China

Abstract. The CAN-Bus is currently the most widely used vehicle bus network technology, but it is designed for needs of vehicle control system, having massive data and lacking of information security mechanisms and means. The Intrusion Detection System (IDS) based on machine learning is an efficient active information security defense method and suitable for massive data processing. We use a machine learning algorithm—Gradient Boosting Decision Tree (GBDT) in IDS for CAN-Bus and propose a new feature based on entropy as the feature construction of GBDT algorithm. In detection performance, the IDS based on GBDT has a high True Positive (TP) rate and a low False Positive (FP) rate.

Keywords: CAN-Bus · Information security · IDS · Machine learning GBDT · Entropy · Detection performance

1 Introduction

CAN-Bus (Controller Area Network Bus) [1, 2] is a kind of field bus and the most widely used vehicle bus network technology. Now, the vehicle is equipped with a large number of electronic equipment, in addition to the basic electronic control, media systems, as well as intelligent advanced auxiliary driving system, even that mobile phones and other intelligent devices connect to the infotainment system, these systems and devices will be from the car CAN-Bus to obtain data [3]. With the rapid progress of the automotive industry and the Internet, in the near future, Internet technology will be applied to every car and the electronic devices, intelligent information systems are likely to become hackers inbound vehicle network system approach [4]. Vehicle information security [5] is not only related to data confidentiality authenticity and integrity, but also related to traffic safety, which is directly related to human life and

© ICST Institute for Computer Sciences, Social Informatics and Telecommunications Engineering 2018
Y. Chen and T. Q. Duong (Eds.): INISCOM 2017, LNICST 221, pp. 285–294, 2018.
https://doi.org/10.1007/978-3-319-74176-5_25

property safety. Therefore, the well-designed security system is a very significant and urgent to every modern car especially the IoV (Intelligent Connected Vehicle).

In the field of information security protection, there are passive security measures and active security measures. Passive security includes data encryption [6, 7], security authentication [8], firewall [9] and others. Active security is mainly based on Intrusion Detection System (IDS) [10] which is the essence of greatly much data, behavior analysis and detection in network, so as to find abnormal network behavior process. There are much data which contains ECUs' conditions, latencies, and behaviors in CAN-Bus, IDS is very suitable for a real-time security protection of CAN-Bus.

Vehicle information security is closely relate to the life and property safety of drivers and passengers. There are several researches to do works on IDS for vehicle CAN-Bus. Paper [11, 12] proposes a rate-based algorithm to detect the anomaly network behaviors, but it is too simple for complex CAN-Bus data, and the period selection of the algorithm is a difficult problem. Paper [13, 14] use entropy based message ID and frequency to be as the algorithm of IDS, but it can not detect the contents of the CAN-Bus message which is full of control commands, sensor information and other vehicle system key information. Paper [15] proposes a protocol-level security specifications for IDS in CAN-Bus, but the CAN-Bus protocol is the top secret of automobile enterprise and is almost impossible to get the protocol from every automobile enterprise of the industry. Therefore, the protocol-level is not versatility and unpractical.

In this paper, we propose an IDS based on a machine learning algorithm—Gradient Boosting Decision Tree (GBDT) [16] for CAN-Bus. GBDT is suitable for data detection which has great volume and few features. In feature engineering, we create a new entropy-based feature based on characteristics of CAN-Bus data to reflect the stability of the entire data, and that could be more robust. We get a very high True Positive (TP) rate and a quite low False Positive (FP) rate [17] in detection performance with a short time, and that means it has a great performance for detection and efficiency.

In this paper, we proposed the IDS based on GBDT for CAN-Bus in Sect. 2; detection performance based on real car CAN-Bus data and analysis is in Sect. 3; conclusion and outlook are in Sect. 4.

2 Gradient Boosting Decision Tree (GBDT) Algorithm in Intrusion Detection System (IDS) for CAN-Bus

Intrusion detection method is to design the network behavior classifier to distinguish the data set, simulation or network of normal and abnormal data, in order to achieve the alarm function of attract behaviors in CAN-Bus data. Machine learning can learn the existing intrusion or normal mode, the characteristics of the network packet probability deduction or fuzzy matching, so that unknown intrusion, in order to improve the intrusion detection of adaptive.

2.1 Regression Decision Tree (DT)

Decision tree [18] is a supervised learning model, which expresses the logical relationship between attributes and results in a tree diagram, mainly used to solve the problem of classification and regression. In this paper, we use regression decision tree to be as the base algorithm.

In a given dataset $D = \{(x_1, y_1), (x_2, y_2), \ldots, (x_n, y_n)\}$, we assume that the input space is divided into M regions $R_1, R_2, \ldots R_J$, each unit has a fixed output value c_m, and the regression decision tree model is:

$$y = f(x) = \sum_{j=1}^{J} c_j I(x \in R_j) \tag{1}$$

The prediction error of the training data set is:

$$\sum_{x_i \in R_j} (y - f(x_i))^2 \tag{2}$$

Here R_m is the region, if x_i is belong to R_m, the value is c_m, $I()$ is an indicator function that returns 1 when the formula inside parentheses is right, otherwise it returns 0. i and j are count constants.

2.2 Boosting Decision Tree

The boosting algorithm [19] is a method of integrating several classifiers into a classifier, it can be expressed as:

$$f(X) = w_0 + \sum_{j=1}^{J} w_j \Phi_j(X) \tag{3}$$

Here w is weight, Φ is the set of weak classifier (regression classification), in fact, is an additive model (the linear combination of primary functions). j is count constant.

The boosting decision tree is an iterative multiple regression tree to make a common decision. When the squared error loss function is used, each tree of regression tree learns the conclusion and residuals of all previous trees and fits to get a current residual regression tree. The meaning of residuals is as follows:

$$r = y - f \tag{4}$$

Here r is residual, y is true value and f is prediction value.

Thus, given the current model $f_{m-1}(x)$, it is only necessary to simply fit the residuals of the current model. Now boosting algorithm for decision tree is described as follows:

Boosting Decision Tree Algorithm:

Input: the regression decision tree $f(x)$.
Output: boosting decision tree $f_M(x)$.
Step1 initialize the decision model $f_0(x) = 0$;
Step2 for $m : 1$ to M do begin

Step3 calculate the residuals:

$$r_{im} = y_y - f_{m-1}(x_i), i = 1, 2, \ldots N(1);$$

Step4 fit r_{mi} to get a regression decision tree $T(x; \varnothing m)$;
Step5 update boosting decision tree:

$$f_m(x) = f_{m-1}(x) + T(x; \varnothing m) \tag{5}$$

Step6 get boosting decision tree:

$$f_M(x) = \sum_{m=1}^{M} T(x; \varnothing m) \tag{6}$$

Step7 end;

Here r_{im} is the residuals of m.th regression decision tree. $T(x; \varnothing m)$ is a regression decision tree about r_{mi}. i and m are count constants.

2.3 Gradient Boosting Decision Tree (GBDT)

The boosting decision tree uses the additive model and the forward stepwise algorithm to realize the optimization process of learning. When the loss function is a square loss or an exponential loss, the optimization of each step is very simple, such as the square loss function in residual regression tree (Table 1).

Table 1. Gradients for commonly used loss funictions.

Setting	Loss function	Gradient
Regression	$\frac{1}{2}[y_i - f(x_i)]^2$	$y_i - f(x_i)$
Regression	$\lvert y_i - f(x_i)\rvert$	$sign[y_i - f(x_i)]$
Regression	Huber	$y_i - f(x_i)$ for $\lvert y_i - f(x_i)\rvert \leq \delta_m$ $\delta_m sign[y_i - f(x_i)]$ for $\lvert y_i - f(x_i)\rvert > \delta_m$ where $\delta_m = a\text{th} - \text{quantile}\{\lvert y_i - f(x_i)\rvert\}$
Classification	Deviance	kth component: $I(y_i = \varsigma_k) - p_k(x_i)$

But for the general loss function, often each step is not so easy to optimize, as in the table above the absolute value loss function and Huber loss function. In response to this problem, Freidman [16] proposed a gradient boosting algorithm: using the declining method of the steepest descent, that is, using the negative gradient of the loss function of the current model as an approximation of the residuals of the lifting tree algorithm in the regression problem, fitting a regression tree (Table 1).

The GBDT algorithm as follow:

Gradient Boosting Decision Tree Algorithm:

Input: the model $f(x)$.
Output: GBDT $\hat{f}(x)$.
Step1 initialize $f_0(x)$

$$f_0(x) = \arg\min_{y} \sum_{i=1}^{N} L(y_i, \gamma) \tag{7}$$

Step2 for $m : 1$ to M:

(a) for $i = 1, 2, \ldots, N$ compute

$$r_{im} = -[\frac{\partial L(y_i, f(x_i))}{\partial f(x_i)}]_{f=f_{m-1}} \tag{8}$$

(b) fit a regression tree to the targets r_{im} giving terminal regions $R_{jm}, j = 1, 2, \ldots J_m$;
(c) for $j = 1, 2, \ldots J_m$ compute

$$\gamma_{jm} = \arg\min_{\gamma} \sum_{x_i \in R_{jm}} L(y_i, f_{m-1}(x_i) + \gamma) \tag{9}$$

(d) update $f_m(x)$

$$f_m(x) = f_{m-1}(x) + \sum\nolimits_{j=1}^{J_m} \gamma_{jm} I(x \in R_{jm}) \tag{10}$$

Step3 output $\hat{f}(x) = f_M(x)$;
Step4 end;

Here r_{im} is the residuals of m.th regression decision tree. $L()$ is loss function, R_{jm} is the region m of tree j and γ_{jm} is the value of R_{jm}. i, m and j are count constants.

GBDT is one of the most popular machine learning algorithms that can handle various types of data flexibly and efficiently, and is suitable for almost any classification and regression problem. We use GBDT as the classification for IDS for its great efficiency, robustness and characteristics of CAN-Bus data in this paper.

2.4 Feature Engineering for CAN-Bus Data

There is a significant characteristic in CAN-Bus data and few features (about 8) in data. Obviously, too few features can not show the complexity of the data, will affect the IDS detection performance [20]. In this paper, we artificially construct an entropy-based [21] feature based on the ID and time of the data, it reflects the stability of the entire CAN-Bus data and conducive to the detection of abnormal behavior.

We let the random variable X, the all possible results of X are: $x_1, x_2, \ldots x_n$, the probability of each result is $p_1, p_2, \ldots p_n$, the entropy is:

$$\begin{gathered} H(X) = -\sum_{i=1}^{n} p_i \log_b p_i \\ 0 \leq H(X) \leq \log |X| \end{gathered} \tag{11}$$

In this paper, ID and time of CAN-Bus data reflects the whore stability, and we select period $T_i = 0.5s$, $i = 1, 2\ldots, n$ for the entropy-based algorithm:

$$H_{T_i}(can\_ID\_j) = p_j \ln(p_j) \Big/ \sum_{j=1}^{N} p_j \ln(p_j) \tag{12}$$

Here N is the number of different ID in period T_i, p_i is proportion of one CAN_ID in all CAN-IDs in period T_i. t is a constant.

Since we get the new feature $H_{T_i}(can\_ID)$ in feature construction for CAN-Bus data and it will get better performance for IDS.

2.5 The Processes of the Novel IDS Based on GBDT for CAN-Bus

The core of IDS is the classification, and we use GBDT algorithm to classify the CAN-Bus data. The classification contains different tress for every ID and the general processes as follows (Fig. 1):

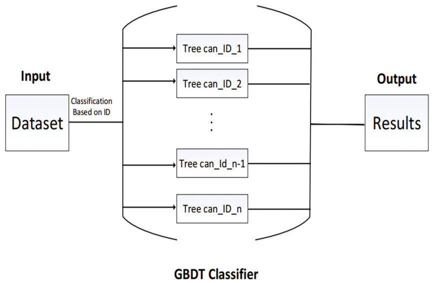

Fig. 1. The process of general GBDT classifier has many decision trees based on can_ID and we use dataset to be an input and we get the classification results.

We divide the IDS into two processes: in the train process, we construct new entropy-based feature and give every message a label for distinguishing between the normal and the abnormal, and get the known CAN-Bus behavior data and marked data. And then Preprocesses: discretization, feature extraction. Finally, we use the train set for GBDT training; in the test process, the Test Set includes unmarked CAN-Bus behavior data, and then discretization, and finally we use GBDT classifier to get behavior classification results. The processes of the IDS for CAN-Bus as follows (Fig. 2):

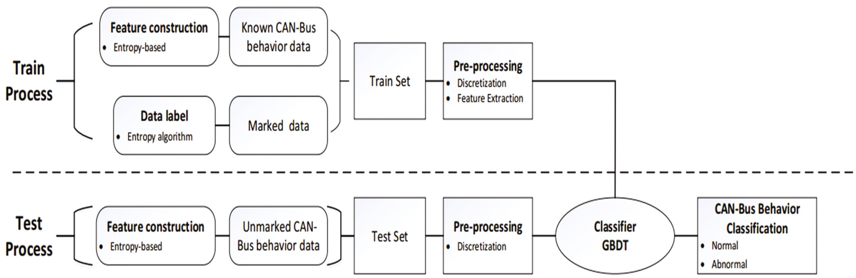

Fig. 2. The whole process: Train Process and Test process, the feature construction is in both train and test process, and data label is only in train process for marking data.

3 Detection Performance and Analysis

3.1 Dataset for Detection

In this paper, the dataset of detection is from a real domestic car—Alsvin CHANA. It contains 750,000 messages and the CAN-Bus speed is 250 kbits/s. When we collected data, the car was in a low speed and normal conditions for driving safety. Because the data is from real car and it may involve information security privacy and related legal issues, we make mosaics on some sensitive information in as follows (Fig. 3):

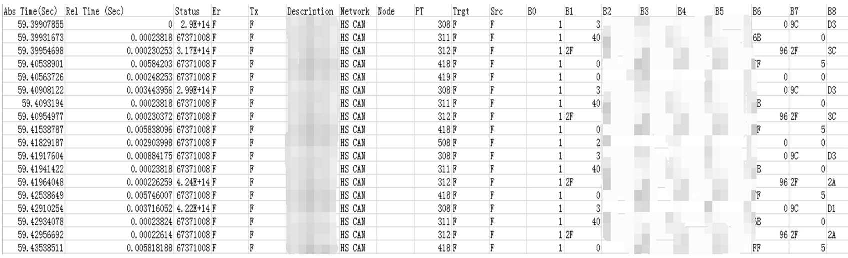

Abs Time(Sec)	Rel Time (Sec)	Status	Er	Tx	Description	Network	Node	PT	Trgt	Src	B0	B1	B2	B3	B4	B5	B6	B7	B8
59.39907855	0	2.9E+14	F	F	[illegible]	HS CAN		308	F	F	1	3	[illegible]	[illegible]	[illegible]	[illegible]	0	9C	D3
59.39931673	0.00023818	67371008	F	F	[illegible]	HS CAN		311	F	F	1	40	[illegible]	[illegible]	[illegible]	[illegible]	6B	0	
59.39954698	0.000230253	3.17E+14	F	F	[illegible]	HS CAN		312	F	F	1	2F	[illegible]	[illegible]	[illegible]	[illegible]	96	2F	3C
59.40538901	0.00584203	67371008	F	F	[illegible]	HS CAN		418	F	F	1	0	[illegible]	[illegible]	[illegible]	[illegible]	F	5	
59.40563726	0.000248253	67371008	F	F	[illegible]	HS CAN		419	F	F	1	0	[illegible]	[illegible]	[illegible]	[illegible]	0	0	
59.40908122	0.003443956	2.99E+14	F	F	[illegible]	HS CAN		308	F	F	1	3	[illegible]	[illegible]	[illegible]	[illegible]	0	9C	D3
59.4093194	0.00023818	67371008	F	F	[illegible]	HS CAN		311	F	F	1	40	[illegible]	[illegible]	[illegible]	[illegible]	B	0	
59.40954977	0.000230372	67371008	F	F	[illegible]	HS CAN		312	F	F	1	2F	[illegible]	[illegible]	[illegible]	[illegible]	96	2F	3C
59.41538787	0.005838096	67371008	F	F	[illegible]	HS CAN		418	F	F	1	0	[illegible]	[illegible]	[illegible]	[illegible]	F	5	
59.41829187	0.002903998	67371008	F	F	[illegible]	HS CAN		508	F	F	1	2	[illegible]	[illegible]	[illegible]	[illegible]	0	0	
59.41917604	0.000884175	67371008	F	F	[illegible]	HS CAN		308	F	F	1	3	[illegible]	[illegible]	[illegible]	[illegible]	0	9C	D3
59.41941422	0.00023818	67371008	F	F	[illegible]	HS CAN		311	F	F	1	40	[illegible]	[illegible]	[illegible]	[illegible]	B	0	
59.41964048	0.000226259	4.24E+14	F	F	[illegible]	HS CAN		312	F	F	1	2F	[illegible]	[illegible]	[illegible]	[illegible]	96	2F	2A
59.42538649	0.005746007	67371008	F	F	[illegible]	HS CAN		418	F	F	1	0	[illegible]	[illegible]	[illegible]	[illegible]	F	5	
59.42910254	0.003716052	4.22E+14	F	F	[illegible]	HS CAN		308	F	F	1	3	[illegible]	[illegible]	[illegible]	[illegible]	0	9C	D1
59.42934078	0.00023824	67371008	F	F	[illegible]	HS CAN		311	F	F	1	40	[illegible]	[illegible]	[illegible]	[illegible]	B	0	
59.42956692	0.00022614	67371008	F	F	[illegible]	HS CAN		312	F	F	1	2F	[illegible]	[illegible]	[illegible]	[illegible]	96	2F	2A
59.43538511	0.005818188	67371008	F	F	[illegible]	HS CAN		418	F	F	1	0	[illegible]	[illegible]	[illegible]	[illegible]	FF	5	

Fig. 3. The fig shows that there are 8 main features, ID, Abs Time and etc.

3.2 Feature Construction and Abnormal Samples

From Sect. 3.1, we find that every message has 8 main features (B1, B2, …, B8) and we artificially construct 2 new features: B0 and B9. B0 is to show that whether the message is normal or abnormal. B9 is an entropy-based feature which we describe in Sect. 2.4.

As we collect data when the real car is in a normal condition, we assume that the messages are all normal and the value of B0 should be 1. Usually, hacker will modify some features' value for tentative attacks, so we change the features' value randomly in the range of 0–255 to get abnormal messages and the value of B0 is 0 (Fig. 4).

We select 562,500 messages as the train set and number the ratio of normal messages and abnormal is 1:1, it means that there are 281,250 normal messages and

number	PT	Trgt	Src	B0	B1	B2	B3	B4	B5	B6	B7	B8	B9
1	308	F	F	1	3					0	9C	D3	0.19432
2	311	F	F	1	40					6B	0	0	0.167816
3	312	F	F	1	2F					96	2F	3C	0.186962
4	418	F	F	1	0					FF	5	44	0.205324
5	419	F	F	1	0					0	0	0	0.104288
6	308	F	F	1	3					0	9C	D3	0.19432
7	311	F	F	1	40					6B	0	0	0.167816
8	312	F	F	1	2F					96	2F	3C	0.186962
9	418	F	F	1	0					FF	5	44	0.205324
10	508	F	F	1	2					0	0	0	0.141291
11	308	F	F	1	3					0	9C	D3	0.19432
12	311	F	F	1	40					6B	0	0	0.167816
13	312	F	F	1	2F					96	2F	2A	0.186962
14	418	F	F	1	0					FF	5	44	0.104288
15	308	F	F	1	3					0	9C	D1	0.19432
16	311	F	F	1	40					6B	0	0	0.167816
17	312	F	F	1	2F					96	2F	2A	0.186962
18	418	F	F	1	0					FF	5	44	0.205324
19	508	F	F	1	2					0	0	0	0.141291
20	308	F	F	1	3					0	9C	D1	0.19432
21	311	F	F	1	40					6B	0	0	0.167816
22	312	F	F	1	2F					E	2F	2A	0.186962
23	418	F	F	1	0					F	5	44	0.205324

Fig. 4. 2 new features in data and are shown in red boxes (Color figure online)

281.250 abnormal messages. In test set, we select 187,500 messages and the ratio of normal message and abnormal ones is 1:1, is similar to train set. So there are 93,750 normal messages and 93,750 abnormal ones.

3.3 Performance Analysis

In detection performance, the experimental platform environment is: Operation System: Windows 7 ultimate, CPU 3.00 GHz, RAM 8 GB, Hard Disk 500G; Programming tools: Spyder (Python 2.7), Dataset: Real vehicle CAN-Bus data (75% Train Set and 25% Test Set), the detection performance results as follows:

FP and TP are base index of an IDS and we could find that all FPs in Fig. 5 are higher than 95%. In fact, we use the weighted average to calculate the FP value and the accurate value of TP is 97.67% and the FP is 1.20%, that means the IDS based on GBDT has a great performance and could protect information security of CAN-Bus.

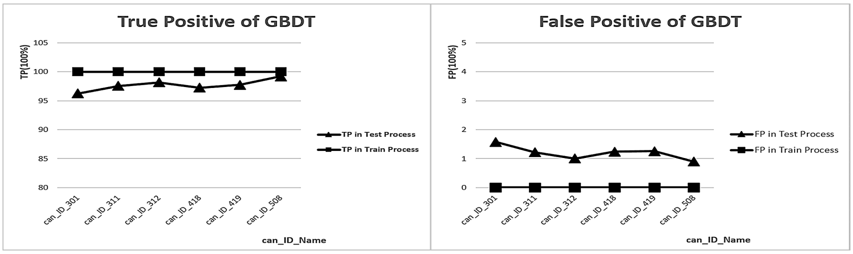

Fig. 5. The True Positive TP (TP) and False Positive (FP) of GBDT in IDS detection performance for CAN-Bus. We could find that the TPs are almost higher than 95% and FPs are lower than 1.5%.

4 Conclusion and Outlook

For the information security of CAN-Bus and traffic safety, we use IDS based on GBDT for CAN-Bus. With the popularity of intelligence connected vehicle, more and more devices and systems will connect CAN-Bus and get data from it. It is very reasonable to develop effective IDS to detect the attacks of hacker to ensure the security. In this paper, the IDS we propose could detect the abnormal behaviors in massive CAN-Bus data and has a high True Positive and quite low False Positive in detection performance, that means the IDS based on GBDT has a great performance and could protect information security of CAN-Bus, even the life and property of drivers and pedestrians.

In this IDS, we have a lot of improvement in the performance of classification, in the future work, how to find more new useful and artificial features, and improve relationship of features between features, and other machine learning algorithm, which can further enhance the classifier's ability in detection performance for complex Internet of Vehicle (IoV).

Acknowledgments. This research was supported by the National Key Research and Development Program of China (2016YFB0100902).

References

1. Senn, S.: Analysis and application for CAN-bus controller integrated in AVR MCU, pp. 2661–2674 (1996)
2. Ricci, C.P.: Controller area network bus (2013)
3. Taha, A.E.M., Nasser, N.: Utilizing CAN-Bus and smartphones to enforce safe and responsible driving, pp. 111–115 (2015)
4. Guerrero-Ibanez, J.A., Zeadally, S., Contreras-Castillo, J.: Integration challenges of intelligent transportation systems with connected vehicle, cloud computing, and internet of things technologies. IEEE Wirel. Commun. **22**, 122–128 (2015)
5. Huang, C.H., Chen, H.Y., Huang, T.F., Tzeng, Y.Y., Li, P.Y., Wu, P.S.: A self-adaptive system for vehicle information security applications. In: IEEE/IFIP International Conference on Embedded and Ubiquitous Computing, pp. 188–192 (2015)
6. Matsui, M.: The first experimental cryptanalysis of the data encryption standard. In: Desmedt, Y.G. (ed.) CRYPTO 1994. LNCS, vol. 839, pp. 1–11. Springer, Heidelberg (1994). https://doi.org/10.1007/3-540-48658-5_1
7. Biryukov, A., Cannière, C.D.: Data encryption standard (DES) (2005)
8. Lowe, G.: An attack on the Needham-Schroeder public-key authentication protocol. Inf. Process. Lett. **56**(3), 131–133 (1995)
9. Manner, J., Karagiannis, G., Mcdonald, A.: NSIS Signaling Layer Protocol (NSLP) for quality-of-service signaling. IETF **31**(2), 152–160 (2010)
10. Huang, M.Y., Jasper, R.J., Wicks, T.M.: A large scale distributed intrusion detection framework based on attack strategy analysis. Comput. Netw. **31**(23–24), 2465–2475 (1998)
11. Hoppe, T., Kiltz, S., Dittmann, J.: Security Threats to Automotive CAN networks – practical examples and selected short-term countermeasures. In: Harrison, Michael D., Sujan, M.-A. (eds.) SAFECOMP 2008. LNCS, vol. 5219, pp. 235–248. Springer, Heidelberg (2008). https://doi.org/10.1007/978-3-540-87698-4_21
12. Cheng, K., Zhang, C.: Feature-based weighted Naive Bayesian classifier. Comput. Simul. **23** (10), 92–94 (2006)
13. Müter, M., Asaj, N.: Entropy-based anomaly detection for in-vehicle networks. In: Intelligent Vehicles Symposium, pp. 1110–1115 (2011)
14. Robnikšikonja, M., Kononenko, I.: Theoretical and empirical analysis of ReliefF and RReliefF. Mach. Learn. **53**(1), 23–69 (2003)

15. Larson, U.E., Nilsson, D.K., Jonsson, E.: An approach to specification-based attack detection for in-vehicle networks. In: Intelligent Vehicles Symposium, pp. 220–225 (2008)
16. Friedman, J.H.: Greedy function approximation: a gradient boosting machine. Annal. Stat. **29**, 1189–1232 (2001)
17. Hamid, Y., Sugumaran, M., Journaux, L.: Machine learning techniques for intrusion detection: a comparative analysis. In: International Conference on Informatics and Analytics (2016)
18. Xu, M., Watanachaturaporn, P., Varshney, P.K., Arora, M.K.: Decision tree regression for soft classification of remote sensing data. Remote Sens. Environ. **97**, 322–336 (2005)
19. Takimoto, E., Maruoka, A.: Top-down decision tree learning as information based boosting. Theor. Comput. Sci. **292**, 447–464 (2003)
20. Iqbal, M.R.A., Rahman, S., Nabil, S.I., Chowdhury, I.U.A.: Knowledge based decision tree construction with feature importance domain knowledge. In: International Conference on Electrical & Computer Engineering, pp. 659–662 (2012)
21. Liang, J., Shi, Z., Li, D., Wierman, M.J.: Information entropy, rough entropy and knowledge granulation in incomplete information systems. Int. J. Gen. Syst. **35**(6), 641–654 (2006)

A Buck-Boost Multilevel Inverter for PV Systems in Smart Cities

Anh-Vu Ho[1(✉)] and Tae-Won Chun[2]

[1] School of Engineering, Eastern International University, Thu Dau Mot, Binh Duong, Vietnam
vu.ho@eiu.edu.vn

[2] School of Electrical and Electronic Engineering, University of Ulsan, Ulsan, Korea
twchun@mail.ulsan.ac.kr

Abstract. This paper proposes a new buck-boost multilevel inverter topology, which is named as a hybrid quasi-Z-source network multilevel inverter, for photovoltaic systems in smart cities. This topology employs an impedance source network and a high frequency three-level switching unit connected to the low frequency single phase inverter. In comparison with other quasi-Z-source network multilevel inverter topologies, the proposed topology uses a lower number of circuit components and more reliable operation. In addition, an effective modulation technique based on phase-shifted disposition scheme is introduced to control the shoot-through state for both boost and buck states of the output voltage. The operating principle of the proposed topology is analyzed in detail. Both simulation and experimental results are carried out to validate the performance of the proposed topology.

Keywords: Multilevel inverters · Quasi-Z-source inverter
Boost control method · Pulse width modulation (PWM)

1 Introduction

Smart city is a combination of diverse technologies to decrease their environmental influences and create citizens better lives. Increasing energy efficiency of building installation and using of renewable energy resources cover remaining energy needs [1, 2]. In photovoltaic (PV) systems, the output voltage of a PV cell widely varies with irradiation and temperature. Therefore, the conventional voltage source inverter (VSI) cannot deal with this change because the VSI is a buck inverter. Normally, a dc-dc boost converter is required to obtain the desired AC output voltage. However, the additional boost converter increases the cost and decreases the efficiency of the overall system. To overcome limitations in the VSI, the Z-source inverters (ZSI) and quasi-Z-source inverter (qZSI) proposed in [3, 4]. The qZSI topologies have advantages over the ZSI topologies such as lower voltage stress on the capacitors and continuous input current. Because of these benefits, it is more attractive to industrial applications such as electric vehicle or PV systems [5, 6].

© ICST Institute for Computer Sciences, Social Informatics and Telecommunications Engineering 2018
Y. Chen and T. Q. Duong (Eds.): INISCOM 2017, LNICST 221, pp. 295–306, 2018.
https://doi.org/10.1007/978-3-319-74176-5_26

Recently, multilevel inverters have been selected as a very attractive solution for medium-voltage high-power applications. They allow to generate a better output voltage with low distortion AC waveform by increasing the number of voltage levels and share the total dc voltage between cascaded switching devices [7, 8]. A two-stage conversion configuration with buck-boost ability will make more complex system and higher cost and trends to decrease the system reliability and efficiency.

In order to obtain the buck-boost function with a single-stage power conversion, the combination of advantages of both the impedance source networks and various multilevel inverters have been introduced in [9–12]. Three-level Z-source neutral point clamped (NPC) topology using two Z-source networks (ZSNs) are proposed in [9] and five-level Z-source NPC with two ZSNs is presented in [10]. These Z-source NPC topologies can decrease the system cost due to the lower number of impedance networks and dc voltage sources. The cascaded ZSN using two switching devices and one H-bridge unit proposed in [11]. In this topology, the number of switching devices can be reduced with respect to the conventional topology. However, two separate ZSNs and two separate dc sources are required in order to generate the output voltage with three voltage levels.

An integration of the quasi-Z-source network (qZSN) and the cascaded multilevel inverter is studied in [12]. One dc source and one qZSN are used for each H-bridge unit, therefore, many passive components are required in the qZSN. A single phase three-level NPC qZSN inverter is proposed in [13, 14]. It uses two symmetrical qZSNs fed from one dc source with a single phase three-level NPC inverter. Many diodes and switching devices are used that will increase the cost and size and reduce the reliability. In addition, if a higher number of level is required, the control method and balancing of capacitor voltage become more complex.

In this paper, the buck-boost three-level inverter is presented. The inverter is a combination of two qZSNs and a high frequency (HF) three-level switching unit connected to the low frequency (LF) single phase inverter. In this combination, the number of circuit components is reduced, the reliable operation is improved, and continuous input current is obtained. Moreover, an effective modulation technique based on a phase-shifted disposition (PSD) scheme is introduced to control the shoot-through states. The modified modulation method can be easily inserted the upper-shoot-through (UST) and lower-shoot-through states (LST) into the traditional sine modulation technique, therefore, offering a simple implementation. The performances of the proposed topology are verified by both in simulation and through experimental results.

2 Operating Principle of the Proposed Three-Level Inverters

2.1 The Proposed Topology

The power circuit of the proposed inverter is described in the Fig. 1. This inverter uses an impedance network to connect a three-level pulse width modulation (PWM) switching unit and an H-bridge unit with low switching frequency. The impedance source network consists of two identical qZSNs with a common point between two capacitors C_1 and C_2 to provide a neutral point of the topology [14]. The high frequency switches S_1 to S_4 are used as a PWM switch in order to provide the desired output voltage and the low frequency switching unit S_5 to S_8 are controlled to generate the polarity of the output voltages [15]. The qZSN is used for boosting the dc input voltage V_{in} to the higher dc-link voltage v_i. Due to the symmetrical qZSN, we can obtain $L_1 = L_4$, $L_2 = L_3$, $C_1 = C_2$ and $C_3 = C_4$. As a result, the corresponding voltages are $v_{L1} = v_{L4}$, $v_{L2} = v_{L3}$, $V_{C1} = V_{C2}$ and $V_{C3} = V_{C4}$.

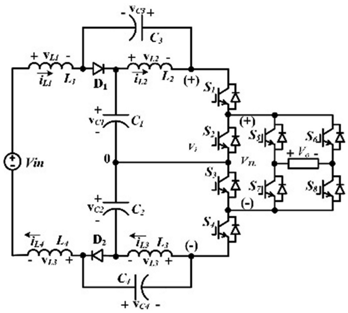

Fig. 1. Single phase three-level qZSN inverter

The operating states of the proposed inverter can be simplified into shoot-through state and non-shoot-through state. The operating principle of the proposed inverter is only discussed when the positive half of the output voltage, in which two switches (S_5, S_8) are turned on. The negative half-cycle of the output voltage with two on switches (S_6, S_7) can be similarly derived based on the previous analysis.

2.2 Shoot-Through State

The proposed inverter uses two shoot-through state types to boost the input voltage to a higher voltage value. Figure 2 describes these shoot-through states, at which the upper shoot- through state shows in Fig. 2(a) and lower shoot-through state shows in Fig. 2(b).

In the UST state for T_{UST} interval of total shoot-through time T_{SH}, three switches (S_1, S_2, and S_4) are turned on, diode D_1 is also connected, and D_2 is disconnected. The L_2 inductor stores the energy from capacitor C_1 through S_1 and S_2. In the LST state for T_{LST} interval of total short-through time T_{SH}, three switches (S_1, S_3, and S_4) are turned on, diode D_1 is disconnected, and D_2 is connected. The L_3 inductors store the energy from capacitor C_2 through S_3 and S_4. The positive half-cycle of the output voltage is provided by two switches (S_5, S_8).

The relative voltage equations in the UST can be represented as

$$v_{L1} = v_{L4} = \frac{1}{2}(V_{C3} - V_{C2} + V_{in}) \tag{1}$$

$$v_{L2} = V_{C1} \tag{2}$$

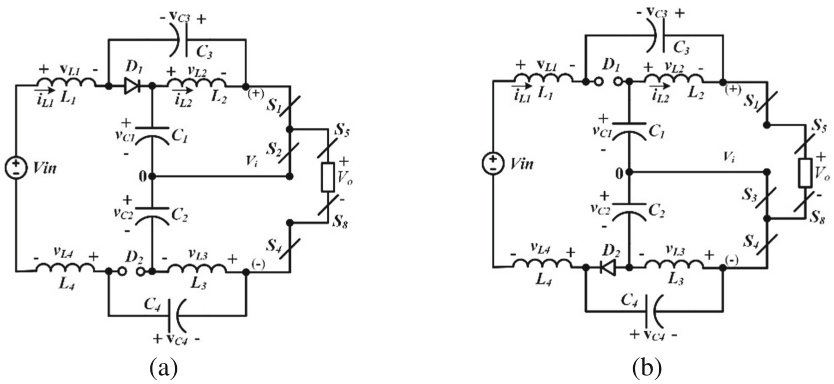

Fig. 2. Equivalent circuits of the shoot-through states: (a) upper shoot-through state, (b) lower shoot through state.

$$v_{L3} = V_{C4} \tag{3}$$

$$v_i = -(V_{C2} + V_{C4}) \tag{4}$$

The corresponding voltage equations of the LST state can be given as

$$v_{L1} = v_{L4} = \frac{1}{2}(V_{C4} - V_{C1} + V_{in}) \tag{5}$$

$$v_{L2} = V_{C3} \tag{6}$$

$$v_{L3} = V_{C2} \tag{7}$$

$$v_i = (V_{C3} + V_{C1}) \tag{8}$$

2.3 Non-Shoot-Through State

In the non-shoot-through state for the interval of Ta, the proposed inverter operates under the same operation principle of the inverter proposed in [15]. During the non-shoot-through state, both diodes D_1 and D_2 are on. The non-shoot-through state is classified by active state 1 (A-1), active state 2 (A-2), active state 3 (A-3), and null state (NS). The equivalent circuits of three active states and a null state are shown in Fig. 3. In the active state 1, as shown in Fig. 3(a), S_1 and S_4 are turned on. In this state, the peak dc-link voltage $\hat{v}_i$ can be obtained by adding the input voltage and four inductive voltages. In the active states 2 and 3, as shown in Fig. 3(b) and (c), a pair of switches (S_1, S_4) and (S_2, S_3) are turned on, respectively. Both these active states have the same dc-link voltage with the shoot-through states but they are a half of the peak dc-link voltage. The load terminal has a zero voltage in the null state.

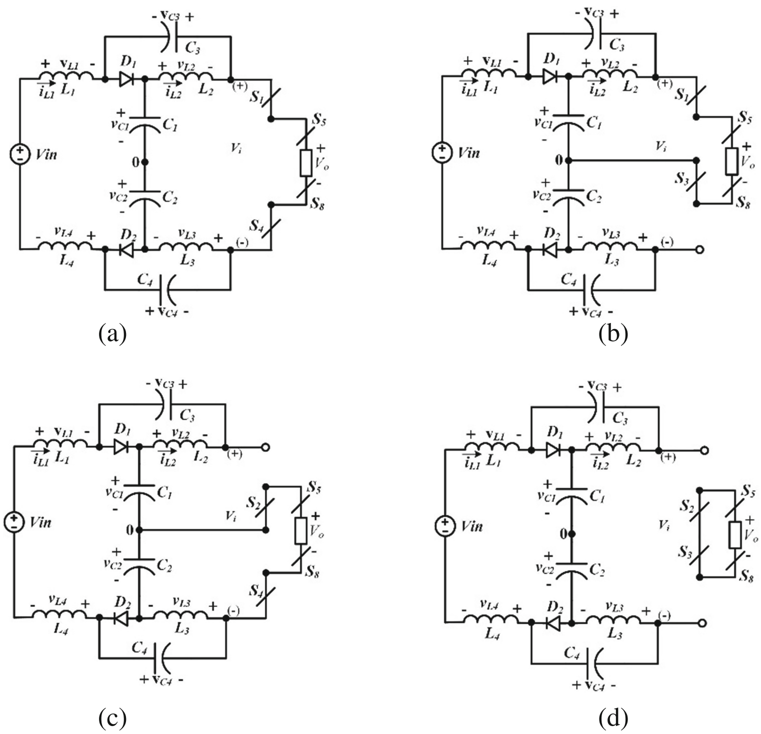

Fig. 3. Equivalent circuits of the non-shoot-through states: (a) active state 1, (b) active state 2, (c) active state 3, (d) null state.

The inductive voltage and dc-link voltage in the non-shoot through states are given as follows

$$v_{L1} = v_{L4} = \frac{1}{2}(V_{in} - 2V_{C1}) \tag{9}$$

$$v_{L2} = -V_{C3} \tag{10}$$

$$v_{L3} = -V_{C4} \tag{11}$$

$$v_i = V_{C1} + V_{C2} + V_{C3} + V_{C4} \tag{12}$$

2.4 Boost Capability

Applying the volt-second balance principle on the inductor L_2, we have

$$V_{C3} = \frac{D}{2-D}V_{C1} = \frac{D}{2-D}V_{C2} \tag{13}$$

Where $D = T_{ST}/T_s$ is the shoot-through duty cycle, and TST is the shoot-through time during switching period T_s.

Similarly, applying the volt-second balance principle on the inductor L_1, we get

$$V_{C1} = V_{C2} = \frac{D}{2 - D} V_{in} \tag{14}$$

Substituting (14) to (13), the capacitor voltage of C_3 and C_4 can be derived as follows

$$V_{C3} = V_{C4} = \frac{D}{4 - 4D} V_{in} \tag{15}$$

The peak dc-link voltage across the main inverter expressed in (8) and can be expressed as follows

$$\hat{v}_i = \frac{1}{1 - D} V_{in} \tag{16}$$

A boost factor, which is expressed as a ratio of the peak dc-link voltage and the input voltage, can be calculated as

$$B = \frac{\hat{v}_i}{V_{in}} = \frac{1}{1 - D} \tag{17}$$

Figure 4 illustrates the plot of the boost factor of the inverter with a variation of duty cycle.

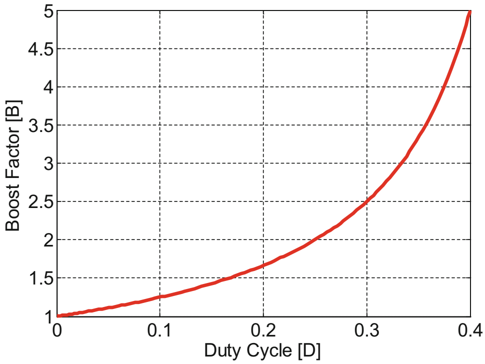

Fig. 4. Boost factor for different duty cycle.

3 Comparison of Proposed Topology with Other qZSN Topologies

The number of circuit components is used for the proposed topology is compared with different qZSN topologies. Table 2 illustrates a comparison between the proposed topology with different three-level topologies.

4 Boost Modulation Techniques

Several boost modulation techniques for the Z-source NPC [16–18] and the qZSN multilevel inverter [19], are introduced to improve the output performance such as harmonic distortion or reduced switching losses. In the paper, a proper boost control strategy for the proposed inverter is presented in Fig. 5. It is a modified modulation technique based on PSD method [20].

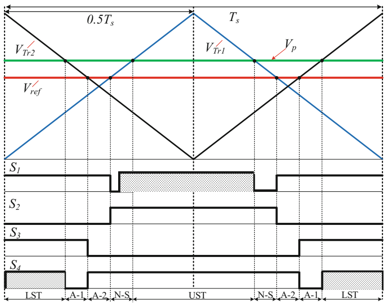

Fig. 5. Switching patterns in one switching period

The proposed technique uses two triangular carriers, where each carrier is phase shifted by 180 from its adjacent carrier. These carriers are compared with the sinusoidal reference signal V_{ref} and the straight line signal V_p, in order to generate the desired switching patterns for four switches S_1, S_2, S_3, S_4. Two switches (S_5, S_8) are turned on during the reference signal V_{ref} is positive and two switches (S_6, S_7) are turned on during the reference signal V_{ref} is negative. An output voltage is five voltage levels when the modulation index M is higher than 0.5. One switching pattern for one switching period is shown in Fig. 5. The upper and lower shoot-through states can be achieved by comparing the straight line signal V_p with the two carrier signals V_{tr1} and V_{tr2}, respectively. During one switching period, two shoot-through states and non-shoot-through states are symmetrically generated.

Table 1 summarizes the operating states, output voltage levels, and capacitor voltages. From the table, the UST and A-2 states are received energy from the capacitor voltage on V_{C1}. While the capacitor voltage V_{C2} is used for the LST and A-3 states. The two series capacitor voltage V_{C1} and V_{C2} are used for the A-1 mode. During one fundamental period, the capacitor voltage on C_2 and C_2 makes the different voltage

Table 1. Comparison of the number of circuit components

Topologies	HF switches	LF switches	Diodes	DC sources	Inductors	Capacitors
Cascaded qZSN	8	0	2	2	4	4
qZSN NPC topology	8	0	6	1	4	4
Proposed topology	4	4	2	1	4	4

Table 2. Switching patterns and output voltage

Operating modes	S_1	S_2	S_3	S_4	S_5	S_6	S_7	S_8	V_o	Capacitor voltages
A-1	1	0	0	1	1	0	0	1	$+\hat{v}_i$	$V_{C1} + V_{C2}$
UST	1	1	0	1	1	0	0	1	$+\hat{v}_i/2$	V_{C1}
LST	1	0	1	1	1	0	0	1	$+\hat{v}_i/2$	V_{C2}
A-2	1	0	1	0	1	0	0	1	$+\hat{v}_i/2$	V_{C1}
A-3	0	1	0	1	1	0	0	1	$+\hat{v}_i/2$	V_{C2}
NS	0	1	1	0	1	0	0	0	0	–
NS	0	1	1	0	0	1	1	0	0	–
A-3	1	0	1	0	0	1	1	0	$-\hat{v}_i/2$	V_{C2}
A-2	0	1	0	1	0	1	1	0	$-\hat{v}_i/2$	V_{C1}
LST	1	0	1	1	0	1	1	0	$-\hat{v}_i/2$	V_{C2}
UST	1	1	0	1	0	1	1	0	$-\hat{v}_i/2$	V_{C1}
A-1	1	0	0	1	0	1	1	0	$-\hat{v}_i$	$V_{C1} + V_{C2}$

levels of the output voltage. Due to the symmetrical characteristic of the operating states of the modified PSD technique, the capacitor voltages V_{C1} and V_{C2} can be automatically balanced during one switching period.

5 Simulation and Experimental Results

5.1 Simulation Results

In order to verify the theoretical results of the proposed topology, PSIM simulation studies are performed. The DC input is V_{in} = 80 V, and the switching frequency is f_s = 5 kHz. The simulation parameters are selected as follows:

(1) Impedance network: $L_1 = L_2 = L_3 = L_4$ = 1 mH, $C_1 = C_2 = C_3 = C_4$ = 1 mF
(2) LC output filter: L_f = 0.6 mH, C_f = 100 μF
(3) Resistive load: R_L = 30 Ω

Figure 6 shows the simulation results of the proposed topology when M = 0.65 and D = 0.35. In the Fig. 6(a), the peak dc-link voltage V_i is boosted from V_{in} = 80 V to 266 V. The capacitor voltage V_{C1} and V_{C3} are 86 V and 46 V, respectively. The AC output voltage before filter has three voltage levels, and the peak AC output voltage after filtering is V_{of} = 123 V. From the Fig. 6(b), the inductor current i_{L1} increases in the shoot-through state and decreases in the non-shoot-through state. The inductor

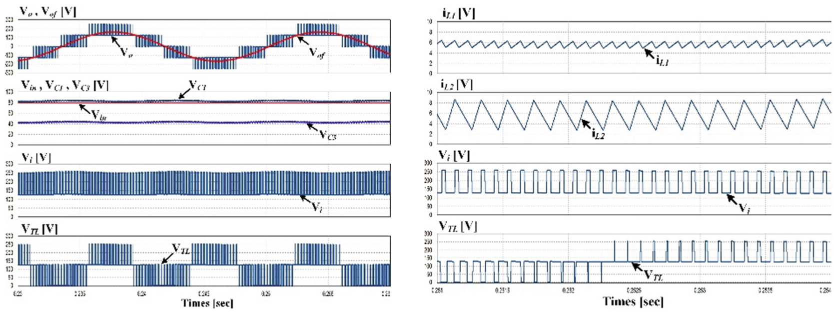

(a) (b)

Fig. 6. Simulation waveforms of the proposed inverter when M = 0.65 and D = 0.35.

current i_{L2} has a higher ripple than the i_{L1} current. The output voltage of the three-level PWM switching unit V_{TL} is a dc voltage with three voltage levels.

For illustrating the boosting capability in the transient condition, Fig. 7 shows the dc-side response where the shoot-through time is increased from 0.2 to 0.35. From top to bottom, the AC output voltage before filtering and after filtering, DC-link voltage V_i, the capacitor voltage V_{C1} and V_{C2}, and the input voltage V_{in}. At 0.2 s the D has step change and the peak DC-link voltage would change from V_i = 130 V to 265 V, capacitor voltages V_{C1} = 53 V to 87 V, and V_{C3} = 13 V to 47 V, finishing the step response at the steady state. The RMS output voltage value increases from V_{of} = 75 V to 87 V.

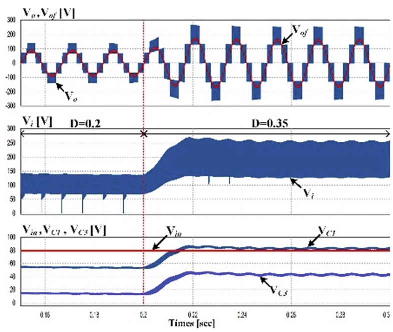

Fig. 7. Transient simulation of the proposed inverter when duty cycle changes from D = 0.2 to D = 0.35 and M = 0.65.

5.2 Experimental Results

In order to validate the analysis, a single phase three-level inverter prototype with a high performance DSP TMS320F28335 has been built in the laboratory for verifying the theoretical analysis and the simulation results. The experimental parameters are used the same as the simulation parameters.

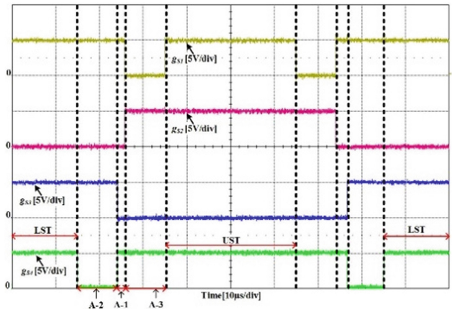

Fig. 8. Gating signal waveforms of S_1, S_2, S_3, and S_4

Figure 8 shows the gating control signals of switching devices S_1 – S_4 for one switching period. As the mentioned analysis, two shoot-through states and three active states are distributed symmetrically in one switching period.

For illustrating the boost capability, Fig. 9 shows the experimental results when M = 0.65 and D = 0.35. In the Fig. 9(a), the RMS value of the output voltage is V_{of} = 86 V and the capacitor voltage of C_1 is V_{C1} = 86 V. In Fig. 9(b), the waveforms from top to bottom are the inductive currents i_{L1} and i_{L3}, dc-link voltage V_i, and the output voltage of three-level switching unit V_{TL}. The i_{L1} current is smoother than the i_{L3} current and the V_{TL} voltage has three voltage levels. The peak value of DC-voltage is V_i = 255 V, which is lower than that of the simulation results because of the effects of the parasitic components and the average inductor currents i_{L1} = 6 A and i_{L2} = 4 A.

The measure efficiency curve varied with the duty cycle D of the proposed topology is shown in Fig. 10. It can be clearly seen that the efficiency of the proposed inverter will go down when increasing the duty cycle. From this result, it illustrates that the power losses are proportional to the boost capability of the inverter because the stronger boost factor corresponding to the higher current through the inductors and semiconductor devices. A higher efficient design can be made by optimal impedance network and switching devices.

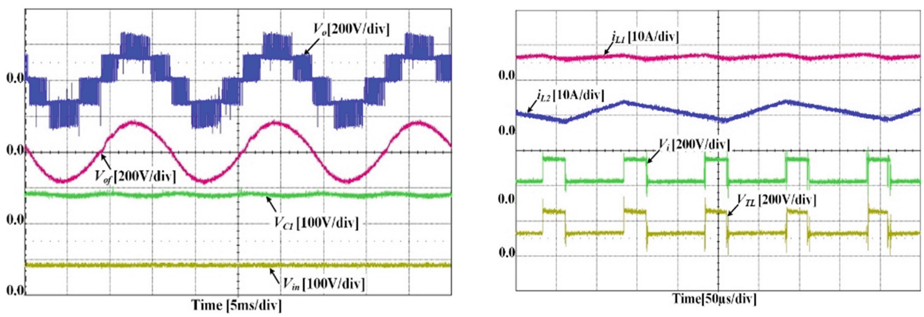

(a) (b)

Fig. 9. Experimental waveforms of the proposed topology when M = 0.65 and D = 0.35

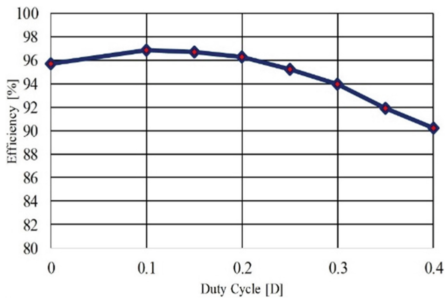

Fig. 10. Measured efficiency against duty cycle for the proposed topology

6 Conclusions

A buck-boost three-level inverter for the renewable energy systems in the smart cities has been proposed. The proposed inverter uses the qZSN to couple with the three-level switching unit. The polarity of the output voltage is produced by the LF single phase inverters. The main advantages of the proposed topology consist of continuous input current, lower circuit components, and higher operating reliability. In addition, a modified boost control technique is also presented to effectively control the shoot-through state. The operating principle and steady-state analysis are carefully performed. The simulation results show a good agreement with the theoretical analysis validating the exact operation of the proposed topology. The experimental results and the measured efficiency are obtained from the experimental prototype in the laboratory. Based on the benefits of the proposed inverter that will make it a competitive solution for renewable energy systems such as PV and fuel-cell.

References

1. Atasoy, T., Akınç, H.E., Ö, E.: An analysis on smart grid applications and grid integration of renewable energy systems in smart cities. In: 2015 International Conference on Renewable Energy Research and Applications (ICRERA), pp. 547–550 (2015)
2. Brenna, M., Falvo, M.C., Foiadelli, F., Martirano, L., Massaro, F., Poli, D., Vaccaro, A.: Challenges in energy systems for the smart-cities of the future. In: 2012 IEEE International Energy Conference and Exhibition (ENERGYCON), pp. 755–762 (2012)
3. Fang Zheng, P.: Z-source inverter. IEEE Trans. Ind. Appl. **39**, 504–510 (2003)
4. Anderson, J., Peng, F.Z.: A class of quasi-Z-source inverters. In: 2008 IEEE Industry Applications Society Annual Meeting, pp. 1–7 (2008)
5. Guo, F., Fu, L., Lin, C.H., Li, C., Choi, W., Wang, J.: Development of an 85-kW bidirectional quasi-Z-source inverter With DC-Link feed-forward compensation for electric vehicle applications. IEEE Trans. Power Electron. **28**, 5477–5488 (2013)
6. Zhou, Y., Liu, L., Li, H.: A high-performance photovoltaic Module-Integrated Converter (MIC) based on cascaded Quasi-Z-Source Inverters (qZSI) using eGaN FETs. IEEE Trans. Power Electron. **28**, 2727–2738 (2013)

7. Jih-Sheng, L., Fang Zheng, P.: Multilevel Converters-A new breed of power converters. IEEE Trans. Ind. Appl. **32**, 509–517 (1996)
8. Abu-Rub, H., Holtz, J., Rodriguez, J., Baoming, G.: Medium-voltage multilevel converters-state of the art, challenges, and requirements in industrial applications. IEEE Trans. Industr. Electron. **57**, 2581–2596 (2010)
9. Loh, P.C., Blaabjerg, F., Wong, C.P.: Comparative evaluation of pulsewidth modulation strategies for Z-source neutral-point-clamped inverter. IEEE Trans. Power Electron. **22**, 1005–1013 (2007)
10. Gao, F., Loh, P.C., Blaabjerg, F., Teodorescu, R., Vilathgamuwa, D.M.: Five-level Z-source diode-clamped inverter. IET Power Electron. **3**, 500–510 (2010)
11. Banaei, M.R., Dehghanzadeh, A.R., Salary, E., Khounjahan, H., Alizadeh, R.: Z-source-based multilevel inverter with reduction of switches. IET Power Electron. **5**, 385–392 (2012)
12. Liu, Y., Ge, B., Abu-Rub, H., Peng, F.Z.: An effective control method for three-phase quasi-Z-source cascaded multilevel inverter based grid-tie photovoltaic power system. IEEE Trans. Industr. Electron. **61**, 6794–6802 (2014)
13. Husev, O., Stepenko, S., Roncero-Clemente, C., Romero-Cadaval, E., Vinnikov, D.: Single phase three-level quasi-Z-source inverter with a new boost modulation technique. In: IECON 2012 - 38th Annual Conference on IEEE Industrial Electronics Society, pp. 5852–5857 (2012)
14. Husev, O., Roncero-Clemente, C., Romero-Cadaval, E., Vinnikov, D., Stepenko, S.: Single phase three-level neutral-point-clamped quasi-Z-source inverter. IET Power Electron. **8**, 1–10 (2015)
15. Ruiz-Caballero, D.A., Ramos-Astudillo, R.M., Mussa, S.A., Heldwein, M.L.: Symmetrical hybrid multilevel DC-AC converters with reduced number of insulated DC supplies. IEEE Trans. Industr. Electron. **57**, 2307–2314 (2010)
16. Ho, A.V., Hyun, J.S., Chun, T.W.: Analysis and control of single-phase Z-source multilevel inverter. In: 2015 18th International Conference on Electrical Machines and Systems (ICEMS), pp. 2134–2139 (2015)
17. Loh, P.C., Gao, F., Blaabjerg, F., Feng, S.Y.C., Soon, K.N.J.: Pulsewidth-modulated Z-source neutral-point-clamped inverter. IEEE Trans. Ind. Appl. **43**, 1295–1308 (2007)
18. Effah, F.B., Wheeler, P., Clare, J., Watson, A.: Space-vector-modulated three-level inverters with a single Z-source network. IEEE Trans. Power Electron. **28**, 2806–2815 (2013)
19. Banaei, M.R., Oskouei, A.B., Dehghanzadeh, A.: Extended switching algorithms based space vector control for five-level quasi-Z-source inverter with coupled inductors. IET Power Electron. **7**, 1509–1518 (2014)
20. Holmes, D.G., Thomas, A.L.: CarrierBased PWM of multilevel inverters. pulse width modulation for power converters: principles and practice, pp. 453–530. Wiley-IEEE Press (2003)

A New High Step-Up DC-DC Converter for Renewable Energy Applications

Anh-Vu Ho[1(✉)], Thanh-Son Nguyen[1], Duc-Linh Tran[2], and Hoai-Nghia Duong[1]

[1] School of Engineering, Eastern International University, Thủ Dầu Một, Binh Duong, Vietnam
{vu.ho, son.nguyen, nghia.duong}@eiu.edu.vn
[2] School of Engineering, RMIT University, Melbourne, Australia
s3358328@student.rmit.edu.au

Abstract. This paper presents a new non-isolated boost converter with high boost ability and low voltage stress on the main switch. The proposed converter uses a hybrid switched-inductor (SL)/switched-capacitor (SC) technique to couple with an active switched network. The proposed converter is very suitable for many industrial applications such as photovoltaic (PV) and fuel-cell. A multicell hybrid SL/SC structure of the proposed converter is also derived in order to get a higher boost ratio. The operation principle, parameter design, and comparison with other converters are given. A laboratory prototype with the closed-loop control is designed for test, and both simulation and experimental results are given to demonstrate the effectiveness of the proposed converter.

Keywords: DC/DC converter · High step-up voltage ratio · Switched-capacitor Switched-inductor

1 Introduction

Nowadays, renewable energy resources such as fuel-cell, wind, photovoltaic (PV) systems have been significantly increased due to the impact of energy crisis and environmental pollution. In the renewable energy generation systems, a conventional boost converter is normally used for boosting voltage [1–3]. Theoretically, the boost converter can generate an infinite voltage gain when the duty ratio will tend to 1. However, the voltage gain of the boost inverter can maximally operate in 5–6 times of the input voltage in practical applications because the effects of on diodes, switches, and parasitic components of capacitors and inductors [4–6].

In order to increase the boost ability and the conversion efficiency, many high boost converter topologies have been introduced. The cascade boost converter can reach the requirements of the renewable energy resources applications [7, 8]. Although these converters have relatively high efficiency, but the complex combination and high components will be the major drawbacks of them. Recently, the switched-capacitor (SC), switched-inductor (SL), hybrid SC/SL techniques are used to achieve high step-up voltage gain [9, 10]. A non-isolated boost converter with multi-cell SC is proposed in [11]. Its advantages are transformer-less high conversion gain and modular

© ICST Institute for Computer Sciences, Social Informatics and Telecommunications Engineering 2018
Y. Chen and T. Q. Duong (Eds.): INISCOM 2017, LNICST 221, pp. 307–318, 2018.
https://doi.org/10.1007/978-3-319-74176-5_27

structure. However, the use of SC technique will cause a high surge current. Based on the coupled inductor technique, several boost converters in [12–14] can improve boost capability and reduce the sizes. Their conversion efficiency is, however, reduced because the losses associated with leakage inductors. In addition, these topologies sustain a high voltage rated switch and suffer from electromagnetic interference (EMC). Single switch isolated boost converters using magnetic coupling such as fly-back converter or single-ended primary inductance converter (SEPIC) are proposed in [15, 16]. In fact, these converters can easily reach a high boost gain by increasing the turn ratio of the transformer. However, the leakage inductance of the transformer and voltage spike are inevitable and the voltage stress on the main switch will be increased. In [17], a 3-Z-network boost converter including three active Z-networks is presented to achieve high voltage gain. But its voltage gain may be still not enough for many applications that needs a stronger voltage gain. Additionally, a large number of diodes are used for the Z-network, they will reduce the conversion efficiency with an extremely high duty cycle. Some voltage lift techniques are proposed in [18, 19]. A high boost factor can be obtained by the transferred energy from the intermediate capacitor, but both capacitor voltage stress and current stress are significantly increased. A combination of SL/SC technique in [9] and active network [20] is proposed in [21, 22]. These converters not only extend the voltage gain but also reduce the voltage stress on the switching device. However, these converters contain high voltage stress on the main switching and high conduction loss.

In this paper, a new non-isolated boost converter with high boost ability and low voltage stress on the main switch is proposed. The proposed converter uses a hybrid SC/SL technique to couple with an active switched network. In this topology, a symmetrical impedance structure is employed and two switches control the same gating signal. The proposed converter is very suitable in applying to low input voltage of PV or fuel-cells. The operation principle, steady state analysis, and comparison with different ASN boost converters are given. A 100 W laboratory prototype is designed for test. Both simulation and experimental results are given to demonstrate the effectiveness of the proposed converter.

Main applications of the proposed converter will be in the renewable energy systems such as the PV or Fuel-cell applications. A typical application of the proposed converter in the PV distributed system is presented in Fig. 1. In this system, the output voltage of solar panels is often low dc voltage and uncontrollability due to the influences of environment, so the dc output voltage must be boosted and regulated via a step-up stage. Then, a desired output voltage is obtained and connected to a dc load or utility grid connected inverter.

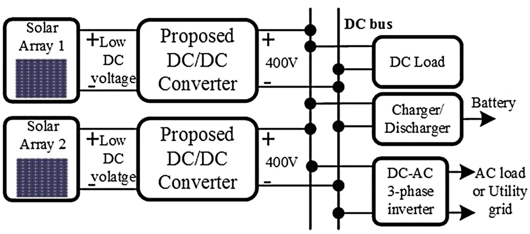

Fig. 1. Typical application of the proposed converter in PV distributed system

2 Review of Active-Switched Network Boost Converters

In this study, the existed active-switched network ASN boost converters topologies are reviewed and analyzed. Figure 2 shows the basic ASN boost converter [20] and SC-ASN boost converter [21].

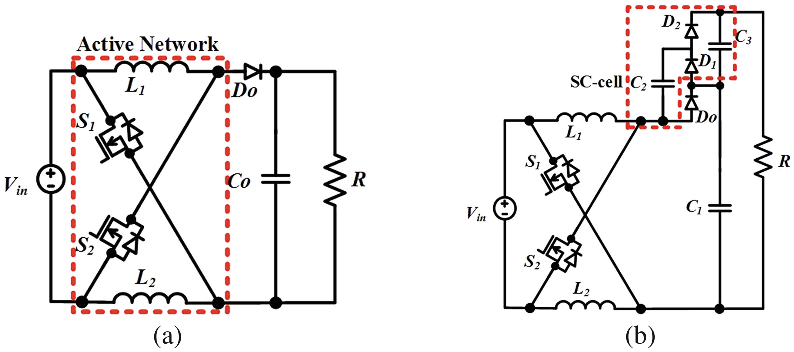

Fig. 2. Active-switched network converter: (a) ASN boost converter, (b) SC-ASN converter

The ASN boost converter concludes two inductors (L_1, L_2) with the same inductance value and two active switches (S_1, S_2) with the same gating signal as shown in Fig. 2(a). During the on-state of the switches, two inductors are charged by the input source and during the off-state, two inductors are delivered energy to the load.

The boost factor of the ASN boost converter is defined as follows

$$B = \frac{1 + D}{1 - D} \tag{1}$$

The SC-ASN boost converter is shown in Fig. 2(b) with a high boost factor. In this converter, the C_2 capacitor is charged while C_1 and C_3 are discharged during the switches are turned on. During the off-state, C_1 and C_3 are charged whereas C_3 is discharged. The boost factor of the SC-ASN converter is be calculated as

$$B = \frac{3 + D}{1 - D} \tag{2}$$

Figure 3 shows two kinds of the improved ASN boost converter. The Fig. 3(a) proposes the SL-ASN boost converter with a symmetrical structure [21, 22]. In this topology, four inductors are charged by the input source during the on-state of the switches and discharged to the load during the off-state of the switches. In the SL-cell, two inductor is in series during the on-state of switches and in parallel during the off-state of switches. The boost factor of the SL-ASN converter can be calculated as follows

$$B = \frac{1 + 3D}{1 - D} \tag{3}$$

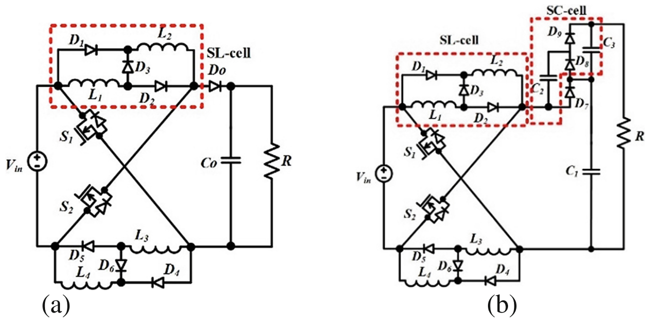

Fig. 3. Improved ASN boost converters: (a) SL-ASN converter and (b) SC/SL-ASN converter

The SC/SL-ASN converter is shown in the Fig. 3(b). The higher boost factor can be achieved with both SL and SC technique. The boost factor of the SL/SC ASN boost converter can be expressed as

$$B = \frac{3 + 5D}{1 - D} \tag{4}$$

3 Operating Principle of the Proposed Converter

In the Fig. 4, the proposed hybrid SC/SL-ASN converter based on the ASN converter is proposed. It is a combination between the active switched network and two hybrid SC/SL-cells. The switching action of the switches will be changed the connection of the hybrid SC/SL-cells.

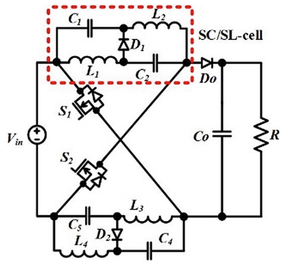

Fig. 4. SC/SL-ASN boost converter

The operating principles in continuous-conduction mode (CCM) of the proposed converter will be discussed in this section. Figure 5 illustrates the operating modes during one switching period and the theoretical waveforms for one switching cycle are given in Fig. 6. For simplicity the analysis of the operating principles, the following assumptions are considered: (1) the capacitors of the proposed converter is large enough so that the voltage on them are assumed to be constant. (2) the switches and diodes are ideal components.

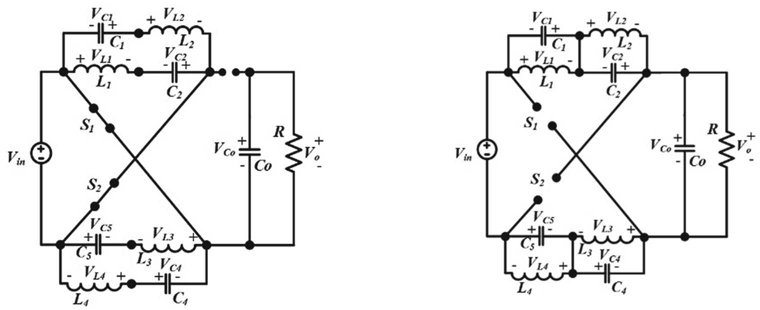

(a) (b)

Fig. 5. Operating states of the proposed SC/SL-ASN boost converter in CCM. (a) Mode 1 ($t_0 - t_1$). (b) Mode 2 ($t_1 - t_2$).

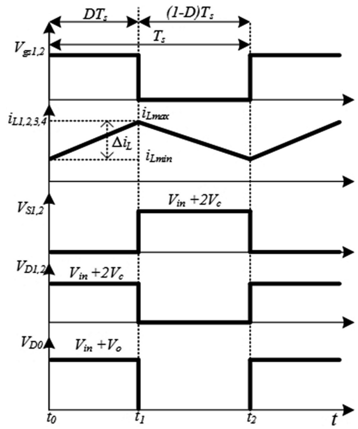

Fig. 6. Theoretical waveforms of the proposed SC/SL-ASN boost converter in CCM

(1) In mode 1 [$t_0 - t_1$]. During this interval, two switches S_1 and S_2 are turned on, while diodes D_1, D_2, and D_0 are reverse biased. The equivalent circuit is shown in Fig. 5(a). Four inductors L_1, L_2, L_3 and L_4 are charged by C_1, C_2, C_3 and C_4, respectively. The capacitor C_0 is delivered to the load.

Because the symmetrical characteristic of this converter ($C_1 = C_2 = C_3 = C_4$ and $L_1 = L_2 = L_3 = L_4$). The following equations can be given as

$$v_{L1} = v_{L2} = v_{L3} = v_{L4} \text{ and } V_{C1} = V_{C2} = V_{C3} = V_{C4} \tag{5}$$

Based on the KVL, we have

$$v_{L1} = V_{C2} + V_{in} \tag{6}$$

(2) In mode 2 [$t_1 - t_2$]. During this interval, two switches S_1 and S_2 are turned off, while diodes D_1, D_2, and D_0 are forward biased. The equivalent circuit is shown in

Fig. 5(b). Four inductors L_1, L_2, L_3 and L_4 are released the energy to the capacitor C_0 and the load.

Based on the KVL, the following equations can be derived as

$$v_{L1} = -V_{C1} = \frac{V_{in} - V_o}{4} \tag{7}$$

$$V_o = V_{in} + V_{C1} + V_{C2} + V_{C3} + V_{C4} \tag{8}$$

By applying the voltage-second balance principle to the inductor L_1, the following relationships can be obtained.

$$V_{C1} = V_{C2} = V_{C3} = V_{C4} = \frac{1}{1 - 2D} V_{in} \tag{9}$$

$$V_o = \frac{1 + 2D}{1 - 2D} V_{in} \tag{10}$$

From (10), the voltage gain B of the proposed converter is given as

$$B = \frac{V_o}{V_{in}} = \frac{1 + 2D}{1 - 2D} \tag{11}$$

4 Performance Comparisons with Different ASN Converters

In this section, the performances of the proposed converter and the existing boost converter topologies are compared. We assume that all converters are operated with the same condition.

Comparison of the number of components used in the proposed converter and different ASN boost converters are presented in Table 1. From this table, all the converters used two active switches. In compared with the SC/SL-ASN converter, the proposed converter used lower six diodes and more two capacitors. But, the voltage gain is stronger than that of the SC/SL ASN converter.

Table 1. Performance comparison with different ASN converters

Converters	Proposed	SC/SL-ASN	SC-ASN	SL-ASN
Inductor	4	4	2	4
Capacitors	5	3	3	1
Diodes	3	9	3	7
Switches	2	2	2	2
Voltage gain	$\frac{1+2D}{1-2D}$	$\frac{3+5D}{1-D}$	$\frac{3+D}{1-D}$	$\frac{1+3D}{1-D}$
Voltage stress	$\frac{2(B+1)}{B+3}$	$\frac{5+B}{8}$	$\frac{B+1}{4}$	$\frac{B+3}{4}$

As shown in Fig. 8, it is seen that the voltage gain of the proposed converter is higher than that of the other converters when the duty cycle is higher than 0.4. In an example, a fifteen times voltage gain of the proposed converter can be obtained at D = 0.43 while the voltage gain of the SC/SL-ASN converter is only nine times. Thus, the proposed converter can significantly reduce the current ripple and volume of the converters (Fig. 7).

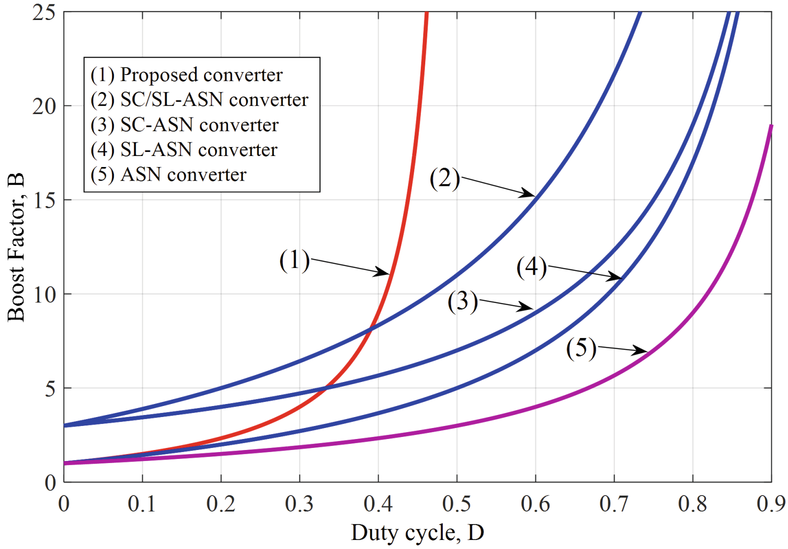

Fig. 7. Comparison of boost capability between different converters

The relationship between the normalized voltage stresses across the main switches of the proposed converter shows in Fig. 9. According to this figure, the voltage stress on the main switch of the proposed converter is lower than that of the other ASN boost converters. It means that a lower rating of the main switches can be used, which will reduce the cost and improve the efficient of the converters.

5 Simulation and Experimental Results

5.1 Simulation Results

In order to verify the performances of the proposed converter, the simulations in PSIM program based on the open loop control are presented. The circuit parameters used for the simulation is shown in Table 2.

The simulation results of the proposed converter are presented in Fig. 10. From this figure, it can be seen that the converter operates in CCM. Figure 9(a) shows the output voltage is boosted to 60 V when the duty cycle D = 0.3 and the input voltage V_{in} = 15 V. The current inductors linearly increased during the switches are turned on and linearly

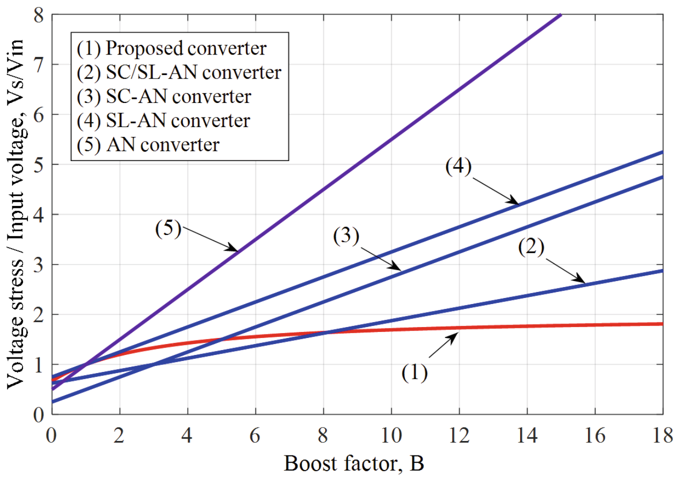

Fig. 8. Comparison of voltage stress between different converters

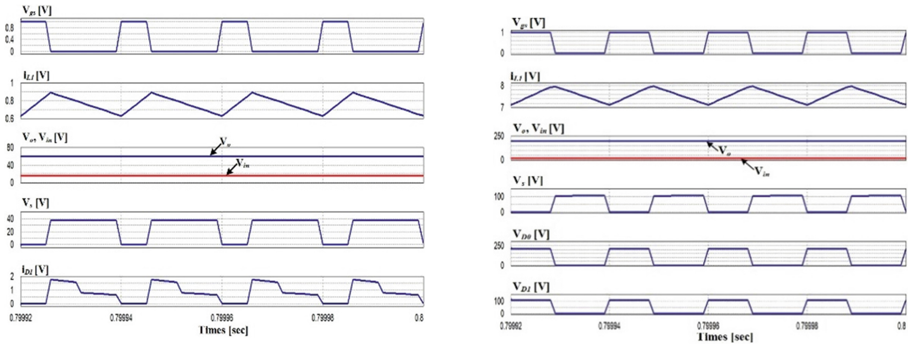

(a) (b)

Fig. 9. Simulation results when V_{in} = 15 V: (a) D = 0.3, (b) D = 0.42

Table 2. Parameters used in simulation and experiment

Parameter	Symbol	Value
Input voltage	V_{in}	15 V
Output voltage	V_o	200 V
Maximum output voltage	P_o	100 W
Switching frequency	f_s	50 kHz
Inductors	L_1, L_2, L_3, L_4	0.6 mH
Capacitors	C_1, C_2, C_3, C_4	100 µF/50 V
Output capacitor	C_o	500 µF/250 V

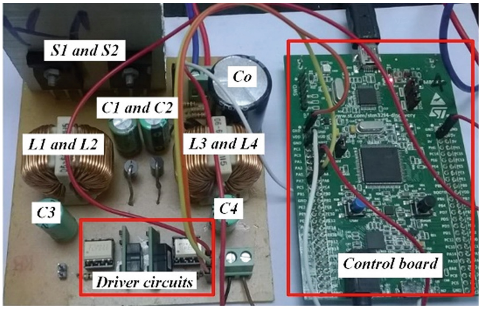

Fig. 10. Photograph of the experimental prototype.

decrease during the switches are turned off. When the duty cycle is increased to 0.42, the output voltage is boosted to 200 V. These simulation results are similar to the theoretical calculations.

5.2 Experimental Results

A 100 W experimental prototype of the proposed converter, as shown in Fig. 10, has been built in the laboratory to verify the theoretical analysis and to validate the simulation results. The experimental parameters are used the same as the circuit parameters in Table 1. The control board is based on the 32-bit STM32F407VGT6 microcontroller.

Figure 11 shows the experimental results of the proposed converter under different conditions. In the Fig. 10(a), the experimental waveforms of the proposed converter under the condition V_{in} = 15 V and D = 0.2, the measured value of the output voltage is 37.4 V. Figure 10(b) shows the experimental result when the duty cycle is increased to 0.3, the measured value of the output voltage is 55 V, which is lower than the theoretical value is 60 V.

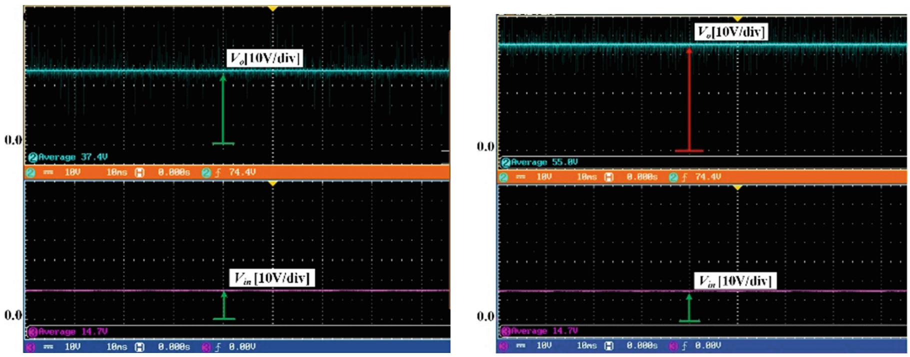

(a) (b)

Fig. 11. Experimental results when V_{in} = 15 V: (a) D = 0.2 and (b) D = 0.3

The performance of the proposed converter is investigated to confirm the transient response of the output voltage under the condition of duty cycle changes from 0.2 to 0.3. It can be observed in the Fig. 12 that the variation in the output voltage is jumped from 37 V to 55 V while the input voltage is kept at 15 V.

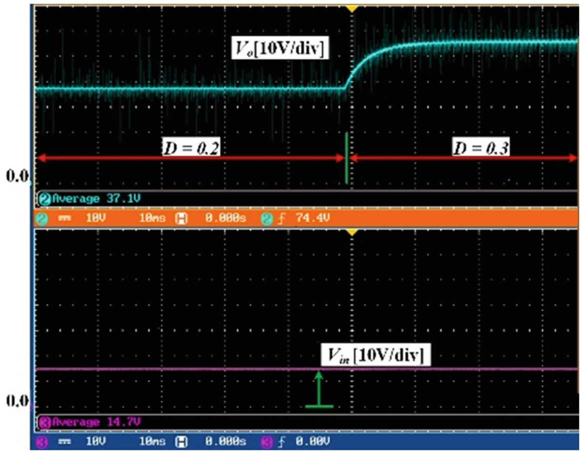

Fig. 12. Experimental results in transient response when duty cycle changes from 0.2 to 0.3

Figure 13 represents a comparison of the experimental and theoretical boost factor of the proposed converter when V_{in} = 15 V and f_s = 50 kHz. It is clearly seen that the experimental values are agreement with the theoretical values when taking into account the effectivity of the parasitic components on the inductors and capacitors as well as the forward voltage drop of the diodes. The differences between the calculated values and the experimental values are an increasing trend as the use of a higher duty cycle.

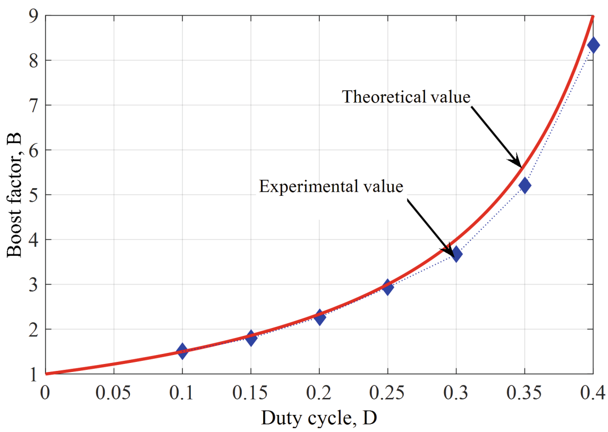

Fig. 13. DC voltage gain of the proposed converter

6 Conclusions

In this paper, a high boost capability converter is introduced to the renewable energy systems such as PV systems. The proposed converter uses two active switches and a symmetrical structure with two hybrid switched-capacitor/switched-inductor cells. The proposed converter can obtain a high voltage gain, with transformerless conversion, and also sustain low voltage stress across all main switches. Operation principles and its features have been discussed in the paper. Comparisons between the proposed converter and the existing active switches boost converters, the proposed converter has a higher voltage gain for D $\geq$ 0.4 as well as a lower voltage stress across the active switches, which requires a lower-voltage-rated MOSFET switch with a smaller drain-to-source resistance and can use Schottky diodes to reduce the reverse-recovery current problem. Thus, the proposed converter can be a competitive alternative for real applications where a high voltage capability is required. Finally, both simulations and experimental results are carried out to verify the functionality and the theoretical analysis.

References

1. Blaabjerg, F., Yang, Y., Ma, K.: Power electronics - key technology for renewable energy systems - status and future. In: 2013 3rd International Conference on Electric Power and Energy Conversion Systems, pp. 1–6 (2013)
2. Samavatian, V., Radan, A.: A high efficiency input/output magnetically coupled interleaved buck-boost converter with low internal oscillation for fuel-cell applications: CCM steady-state analysis. IEEE Trans. Industr. Electron. **62**, 5560–5568 (2015)
3. Zhu, H., Zhang, D., Athab, H.S., Wu, B., Gu, Y.: PV isolated three-port converter and energy-balancing control method for PV-Battery power supply applications. IEEE Trans. Industr. Electron. **62**, 3595–3606 (2015)
4. Ismail, E.H., Al-Saffar, M.A., Sabzali, A.J., Fardoun, A.A.: A family of single-switch PWM converters with high step-up conversion ratio. IEEE Trans. Circuits Syst. I Regul. Pap. **55**, 1159–1171 (2008)
5. Choi, H., Ciobotaru, M., Jang, M., Agelidis, V.G.: Performance of medium-voltage DC-Bus PV system architecture utilizing high-gain DC-DC converter. IEEE Trans. Sustain. Energ. **6**, 464–473 (2015)
6. Tsai, J.C., Chen, C.L., Lee, Y.H., Yang, H.Y., Hsu, M.S., Chen, K.H.: Modified hysteretic current control (MHCC) for improving transient response of boost converter. IEEE Trans. Circuits Syst. I Regul. Pap. **58**, 1967–1979 (2011)
7. Matsuo, H., Harada, K.: The cascade connection of switching regulators. IEEE Trans. Ind. Appl. **IA-12**, 192–198 (1976)
8. Xiong, S., Tan, S.C.: Cascaded high-voltage-gain bidirectional switched-capacitor DC-DC converters for distributed energy resources applications. IEEE Trans. Power Electron. **32**, 1220–1231 (2017)
9. Axelrod, B., Berkovich, Y., Ioinovici, A.: Switched-capacitor/switched-inductor structures for getting transformerless hybrid DC-DC PWM converters. IEEE Trans. Circuits Syst. I Regul. Pap. **55**, 687–696 (2008)

10. Tan, S.C., Nur, M., Kiratipongvoot, S., Bronstein, S., Lai, Y.M., Tse, C.K., Ioinovici, A.: Switched-capacitor converter configuration with low EMI emission obtained by interleaving and its large-signal modeling. In: 2009 IEEE International Symposium on Circuits and Systems, pp. 1081–1084 (2009)
11. Ganesan, R.G., Prabhakar, M.: Non-isolated high gain boost converter for photovoltaic applications. In: 2013 International Conference on Power, Energy and Control (ICPEC), pp. 277–280 (2013)
12. Hsieh, Y.P., Chen, J.F., Yang, L.S., Wu, C.Y., Liu, W.S.: High-conversion-ratio bidirectional DC-DC converter with coupled inductor. IEEE Trans. Industr. Electron. **61**, 210–222 (2014)
13. Freitas, A.A.A., Tofoli, F.L., Júnior, E.M.S., Daher, S., Antunes, F.L.M.: High-voltage gain DC-DC boost converter with coupled inductors for photovoltaic systems. IET Power Electron. **8**, 1885–1892 (2015)
14. Tang, Y., Fu, D., Wang, T., Xu, Z.: Analysis of active-network converter with coupled inductors. IEEE Trans. Power Electron. **30**, 4874–4882 (2015)
15. Kwok-Wai, M., Yim-Shu, L.: An integrated flyback converter for DC uninterruptible power supply. IEEE Trans. Power Electron. **11**, 318–327 (1996)
16. Gules, R., Santos, W.M.D., Reis, F.A.D., Romaneli, E.F.R., Badin, A.A.: A modified SEPIC converter with high static gain for renewable applications. IEEE Trans. Power Electron. **29**, 5860–5871 (2014)
17. Zhang, G., Zhang, B., Li, Z., Qiu, D., Yang, L., Halang, W.A.: A 3-Z-Network boost converter. IEEE Trans. Industr. Electron. **62**, 278–288 (2015)
18. Luo, F.L.: Positive output Luo converters: voltage lift technique. IEE Proc. Electr. Power Appl. **146**, 415–432 (1999)
19. Jiao, Y., Luo, F.L., Zhu, M.: Voltage-lift-type switched-inductor cells for enhancing DC-DC boost ability: principles and integrations in Luo converter. IET Power Electron. **4**, 131–142 (2011)
20. Yang, L.S., Liang, T.J., Chen, J.F.: Transformerless DC-DC converters with high step-up voltage gain. IEEE Trans. Industr. Electron. **56**, 3144–3152 (2009)
21. Tang, Y., Wang, T., Fu, D.: Multicell switched-inductor/switched-capacitor combined active-network converters. IEEE Trans. Power Electron. **30**, 2063–2072 (2015)
22. Tang, Y., Fu, D., Wang, T., Xu, Z.: Hybrid switched-inductor converters for high step-up conversion. IEEE Trans. Industr. Electron. **62**, 1480–1490 (2015)

Security and Privacy and Hardware and Software Design

Method for Pseudo-probabilistic Block Encryption

Moldovyan Nikolay Andreevich[1],
Moldovyan Alexander Andreevich[1], Tam Nguyen Duc[2],
Hai Nguyen Nam[2], and Minh Nguyen Hieu[2(✉)]

[1] St. Petersburg Institute for Informatics and Automation
of Russian Academy of Sciences, St. Petersburg 199178, Russia
{nmold, ma}@mail.ru
[2] Academy of Cryptography Techniques, Hanoi, Vietnam
nguenductamkma@gmail.com, nnhaivn61@gmail.com,
hieuminhmta@gmail.com

Abstract. There is considered implementation of the plan-ahead share-key deniable encryption algorithms that produce the cryptogram that satisfy criterion of the computational indistinguishability from probabilistic encryption of the fake message. This paper introduces a general design of the pseudoprobabilistic block ciphers. The proposed method includes encryption of the secret message block and the fake message block followed by a transformation procedure mapping the pair of intermediate ciphertext blocks into a single block of the output ciphertext. The transformation procedure represents solving the system of two linear congruencies.

Keywords: Block cipher · Plan-ahead Shared-key
Pseudo-probabilistic cipher · Symmetric Deniable Encryption

1 Introduction

The notions of *public-key deniable encryption* and of *shared-key deniable encryption* were introduced by Canetti et al. in 1997 [1]. These important cryptographic primitives are applied in cryptographic protocols to resist coercive attacks. In the concept of deniable encryption there are considered sender-deniable, receiver-deniable, and sender-and-receiver-deniable (bi-deniable) schemes in which coercive adversary attacks the party sending message, the party receiving message, and the both parties, correspondingly. In the model of the coercive attack it is supposed that coercive adversary has power to force a party or the both parties simultaneously to open the cryptogram (ciphertext) after it has been sent.

Paper [1] initiated a lot of investigations on developing secure and efficient methods for public-key deniable encryption [2] in which no pre-shared information is used. Some of papers propose public-key deniable encryption combined with sharing secrete key (the sender and the receiver initially share a common secret key) and plan-ahead encryption (the fake message is selected at the stage of encryption) [3, 9, 10]. Detailed attention of the researchers to this direction in the area of deniable encryption is explained by the

© ICST Institute for Computer Sciences, Social Informatics and Telecommunications Engineering 2018
Y. Chen and T. Q. Duong (Eds.): INISCOM 2017, LNICST 221, pp. 321–331, 2018.
https://doi.org/10.1007/978-3-319-74176-5_28

applicability of the public key deniable encryption to prevent vote buying in the internet-voting systems [4] and to provide secure multiparty computations [5].

Practical applications of the plan-ahead shared-key deniable encryption can be attributed to the case of the information protection against unauthorized access in computer and communication systems in the case of coercive attacks. As it is set in [1] for some models of such attacks "plan-ahead shared-key deniability is trivially solved: use different keys, and construct the ciphertext as concatenation of encryption of all messages, where the *i*th message is encrypted using the *i*th key".

The present paper considers the coercive-attack model against which this trivial construction is not applicable. To resist the proposed coercive attack, the paper proposes the plan-ahead shared-key deniable encryption methods producing cryptogram that is computationally indistinguishable from the ciphertext produced by some probabilistic cipher. The paper introduces design of pseudo-probabilistic block ciphers that satisfy the last criterion.

The organization of the paper is as follows. Section 2 describes the model of the coercive attack and criteria used for designing pseudo-probabilistic block ciphers. Section 3 proposes a simple method for pseudo-probabilistic block encryption. Section 4 introduces pseudo-probabilistic encryption algorithms satisfying an additional criterion of using the same decryption algorithm for disclosing both the secret and the fake message. The probabilistic encryption algorithms associated with the pseudo-probabilistic ones are presented in Sect. 5 followed by concluding Sect. 6.

2 Model of Adversary and Design Criteria

It is assumed that after ciphertext has been sent the adversary has possibility to force both the sender and the receiver to open the following:

– The plaintext corresponding to the ciphertext;
– Encryption and decryption algorithms;
– The encryption key with which encryption of the opened message yields all bits of the ciphertext.

Thus, in the considered model of the coercive attack the sender and the receiver are coerced to open parameters and algorithm of the ciphering procedure with which each bit of the sent ciphertext has been produced depending on the opened message (plaintext).

Security against the described attack can be provided using the symmetric deniable encryption (SDE) algorithm that produces the ciphertext like cryptogram produced as result of probabilistic encryption of the fake message with fake key. The ciphers satisfying the last criterion are called pseudo-probabilistic ciphers (PPC). Construction of the symmetric PPC can be implemented using the following design criteria:

– Symmetric deniable encryption should be performed as simultaneous encryption of two messages, secret one and fake one, using secret and fake keys (which are shared by sender and receiver);
– A probabilistic encryption algorithm should be associated with the SDE algorithm;

- The associated probabilistic encryption algorithm should transform the fake message with the fake key into the same ciphertext that is produced by the SDE algorithm;
- Using the fixed-size shared keys should provide performing secure SDE of messages having arbitrary length.

The parties of secure communication protocol can chart plausible that they used the probabilistic encryption to get higher resistance to potential attacks. Indeed, mixing the encrypted data with random data makes cryptanalysis more difficult. Next section describes a method for implementing pseudo-probabilistic block ciphering on the base of deterministic block encryption functions.

3 Simple Method for Pseudo-probabilistic Block Encryption

3.1 Method for Probabilistic Block Encryption

Suppose E be a b-bit encryption function, T be a π-bit block of plaintext, and R be a u-bit random block, where $u = b - \pi$. The b-bit input data block B can be formed as follows $B = R\|T$, where the sign $\|$ denotes the concatenation operation of two binary vectors, R and P:

$$P \to B = R||T \to C = E_K(B).$$

where K is the encryption key. Since the size of the plaintext block T is smaller than the ciphertext block, the last formula maps the given block of the plaintext block T on a large set of ciphertext blocks $\{C_1, C_2, \ldots, C_n\}$, where $n = 2^u$.

The general scheme of a probabilistic block cipher with such simple mechanism of concatenating a random bit string to plaintext block is illustrated in Fig. 1. The random number generator (RNG), like the encryption algorithm implementing the encryption function E, represents an internal part of the encryption device. It is assumed that the RNG is located in a protected part of the encryption device, and that a potential adversary cannot replace it. Thus, it is supposed that adversary has no possibility to manipulate the R value. Such assumption is acceptable, since encryption devices are designed so as to provide protection against encryption algorithm substitution, as well as against reading and copying the key. When decrypting a ciphertext block, the valid user (who knows the secret key) computes the data block $B = R\|T$ block and then the R value is discarded and the data block T of the original message is obtained.

When choosing different values of the b/π ratio, one can control performance and security of the such probabilistic encryption. Roughly speaking, the greater this ratio, the greater the security level. If the function E provides encryption rate s_0, then the speed of the probabilistic encryption is $s = s_0(b - r)/b$. Using such probabilistic encryption mechanism it is possible to provide resistance to potential future attacks based on unforeseen weaknesses of the encryption function E. Besides, such probabilistic mechanism can be also used to protect against possible attacks using trapdoors in block ciphers. However the probabilistic encryption procedure outputs ciphertext blocks that have size larger than the size of input data blocks. To compensate for the expansion effect, one can compress the source message before performing encryption.

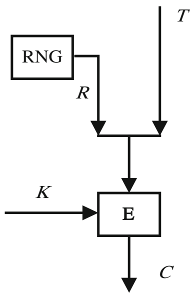

Fig. 1. The basic scheme of probabilistic block encryption.

One can also note that the compression of data before performing data encryption increases additionally resistance against ciphertext attacks.

3.2 Probabilistic Mixing Data Bits with Random Bits

The described above simple probabilistic encryption mechanism, based on generating a ciphered data block by combining random and data bits, can be used to increase encryption security when using many of the known block cryptoalgorithms. In regard to many types of attacks and well known block ciphers it is sufficient to define a relatively small ratio of random bits to data bits. However, for ciphers vulnerable to differential and linear cryptanalysis, strengthening on the basis of this probabilistic encryption method can require a significant increase the portion of random bits, which will result in noticeable reducing the data encryption performance, and significant increase of the ciphertext size.

Let us consider some variants of making the probabilistic encryption method more effective for a small portion of random bits when using encryption procedures with good diffusion properties, but possibly, with unexpected vulnerabilities to differential and linear analysis.

The probabilistic block encryption scheme shown in Fig. 1 can be complemented with a non-deterministic mix of random and data bits. To implement this idea, a random binary vector is divided into two parts with a pre-specified length: $R = R_1||R_2$. Then, prior to carrying out encryption transformations over the $R_2||T$ binary vector, a bit permutation is done, which depends on the R_1 random value that specifies randomly mixing the bits of the message T and those of the R_2 random value. For bit mixing, it is possible to use controlled operational permutation boxes **P**, used earlier as a basic cryptographic primitive to design secure fast ciphers [8]. The permutation performed by a **P** box depends on the value of the control vector V that is generated depending on R_1. The sequence of transformations in a variant with a random combination of data and random bits (see Fig. 2) is as follows:

$$T \to R_2||T \to \mathbf{P}_V(R_2||T) \to R_1||\mathbf{P}_V(R_2||T) \to \mathbf{E}_K(R_1||\mathbf{P}_V(R_2||T)).$$

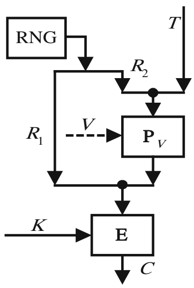

Fig. 2. A scheme with a probabilistic mixing random and data bits.

In typical **P** boxes, the length v of the V control vector is at least twice the length of the $R_2||T$ ($r_2 + t$) vector being transformed. In this case, it is assumed that the $r_1 < r_2 + t < v$ condition is true, so the control vector can be created, for example, by repeatedly replicating the R_1 vector ($V = R_1||\ldots||R_1||R_1$), or by alternating R_1 and the K_1 fragment of the private key ($V = R_1||K_1||R_1||K_1$). In the latter case, mixing the bits of R_2 and T is done probabilistically, depending on the private key. Increasing the security against differential and liner cryptanalysis is connected with the probabilistic distribution of the data bits over the bit positions of the data block being encrypted. For example, when performing a chosen-plaintext differential analysis, the probability of getting two data blocks with a given difference is significantly small for r_1, $r_2 = 8$. When $b = 64$ and 128, this corresponds to a rather small portion of random bits (25% and 12%, respectively).

The second way of making a simple probabilistic encryption scheme more secure is related to the idea of pre-encrypting an original text T using a randomly generated value R as a one-time pre-encryption key (see Fig. 3). The transformation sequence is the following:

$$T \to E'_R(T) \to E''_K(R||E'_R(T)).$$

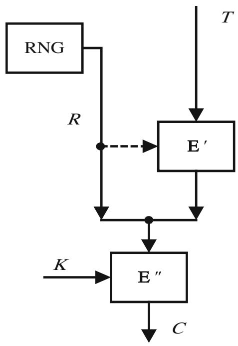

Fig. 3. Probabilistic block encryption scheme including pre-encryption of the source data block.

Strengthening is done using additional transformations with some single-use key whose repetition probability is about 2^{-r} during attacks based on the chosen values T and C (due to sufficiently good diffusion properties of E'' encryption procedures). When doing the pre-encryption, the basic scheme of probabilistic encryption can be used, which will lead to the following transformation sequence (see Fig. 4):

$$T \to R_2||T \to E'_{R1}(R_2||T) \to E''_K(R_1||E'_{R1}(R_2||T)).$$

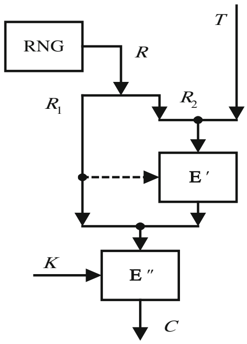

Fig. 4. Two-stage probabilistic encryption.

This case relates to the third variant of increasing security, and it is a generalization of the first variant, in which mixing up random and data bits can be considered a special case of encrypting transformation.

For a hardware implementation, the first variant is the most cost-effective,whilethe second and third variants are the most cost-effective for a software implementation. From the standpoint of increasing security, the third variant is best. In general, the increase in security in the variants discussed is related to the fact that the ratios that connect the T and C pairs of values also include a random (pseudo-random) value R during chosen-plaintext T attacks (chosen-plaintext C attacks).

These probabilistic encryption methods seem to be quite effective for insuring against unexpected weaknesses of the encryption algorithm used, and against built-in trapdoors. Expanding the ciphertext block puts significant limitations on using probabilistic ciphers in computer systems. To compensate for the expansion effect, it is possible to compress the original message beforehand. In some cases, this method makes it possible to design probabilistic ciphers in which the ciphertext length is equal to the length of the original message. Besides which, compressing data before they are encrypted significantly increases the security of the encryption. For many applications in telecommunication systems, this variant of probabilistic encryption can be used without significant limitations.

3.3 A Simple Method for Pseudo-probabilistic Block Encryption

The described variants of implementing the probabilistic block encryption can be easily transformed into methods for pseudo-probabilistic block encryption. Indeed, one can replace the PRNG by the block encryption algorithm E^* performing encryption of the secret message T^* with the key K^*. If the algorithm E^* provides sufficiently high security then the output ciphertext blocks can be used as random bit string R in the probabilistic encryption schemes shown in Figs. 1, 2, 3 and 4. At such modification the data blocks are considered as blocks of some fake message that is encrypted simultaneously with the secret message blocks T^*.

At time of the coercive attack the sender and the receiver of the secret message have possibility to cheat plausible they used probabilistic block encryption algorithm. They will open the fake message and the encryption key K with which the fake message was encrypted. The coercer can decrypt the intercepted ciphertext with key K and obtain the fake message. He is also able to get pseudo-random bit strings R^*, but for him is computationally infeasible to distinguish the pseudo-random values R^* from random ones and to demonstrate that the ciphertext contains one message more.

In the next section we consider pseudo-probabilistic block encryption methods that satisfy an important additional requirement to deniable encryption schemes, which provides security to coercive attacks with measuring the decryption time. The additional requirement is formulated as performing decryption of both the secret message and the fake message with the same decryption algorithm.

4 Method for Pseudo-probabilistic Block Encryption

It is proposed to implement pseudo-probabilistic encryption as simultaneous ciphering two messages Mess1 (fake) and Text2 (secret) the equal size using the shared keys (K_1, m_1) and (K_2, m_2), where K_1 and K_2 are keys of some block cipher E with v-bit input; m_1 and m_2 are two mutually prime numbers. The messages are divided into v-bit data blocks: Mess1 = (M_1, M_1, …, M_z) and Text2 = (T_1, T_1, …, T_z) and then pairs of the respective blocks M_i and T_i are consecutively encrypted as follows:

1. Using the block cipher E and key K_1, it is encrypted the block M of the first message: $C_M = E_{K1}(M)$.
2. Using the block cipher E and key K_2, it is encrypted the block T of the second message: $C_T = E_{K2}(T)$.
3. Using additional secret values m_1 and m_2 compute the block C of output ciphertext as solution of the following system if two congruencies

$$\begin{cases} C \equiv C_M \bmod m_1 \\ C \equiv C_T \bmod m_2 \end{cases}, \tag{1}$$

where blocks C_T and C_M of the intermediate ciphertexts are interpreted as binary numbers; m_1 and m_2 are mutually prime numbers having size v + 1 bits. The size of the output ciphertext block C is equal to $2v$ + 2 bits (i.e. the size of the block C is two bits larger than the sum of sizes of the blocks C_T and C_M). Solution of the system (1) is described as follows:

$$C = \left[C_M m_2 \left(m_2^{-1} \bmod m_1\right) + C_T m_1 \left(m_1^{-1} \bmod m_2\right)\right] \bmod m_1 m_2.$$

The values $m_2(m_2^{-1} \bmod m_1)$ and $m_1(m_1^{-1} \bmod m_2)$ can be pre-computed at moment of generating the secret keys, therefore the main contribution in computational difficulty of calculating the value C is defined by the operation of dividing the value in square brackets by the modulus $m_1 m_2$.

From practical point of view it is preferable to use the pseudo-probabilistic block encryption method that outputs the ciphertext block that have size equal exactly to $2v$ bits. This requirement can be met using the procedure of combining two blocks C_T and C_M into one block C which consists in solving the following system of two congruences defined over binary polynomials:

$$\begin{cases} C \equiv E_{K_1}(M) \bmod \mu(x) \\ C \equiv E_{K_2}(T) \bmod \lambda(x) \end{cases}, \tag{2}$$

where $\mu(x)$ and $\lambda(x)$ are mutually irreducible binary polynomials of the degree v (these two polynomials are secret elements); the v-bit blocks C_T and C_M of the intermediate ciphertexts are interpreted as binary polynomials of the degree $v - 1$. Solution of system (2) represents the binary polynomial of the degree $2v$ which is given by the following formula:

$$C = \left[E_{K1}(M)\lambda(x)\left(\lambda^{-1}(x) \bmod \mu(x)\right) + E_{K2}(T)\mu(x)\left(\mu^{-1}(x) \bmod \lambda(x)\right)\right] \\ \bmod \mu(x)\lambda(x).$$

Like in the first block encryption method, the polynomials $\lambda^{-1}(x) \bmod \mu(x)$ and $\mu^{-1}(x) \bmod \lambda(x)$ can be pre-computed to increase the encryption rate.

The related decryption algorithms are evident for the described two variants of the proposed pseudo-probabilistic block encryption method.

Decryption algorithms connected with the pseudo-probabilistic encryption algorithms described in this section coincide with the decryption algorithms connected with the associated probabilistic encryption algorithms (see Sect. 5).

5 Associated Probabilistic Block Encryption Algorithms

Let us show that the block encryption method described in Sect. 3 met criterion of computational indistinguishability from probabilistic block encryption. For this purpose one should propose a probabilistic block encryption algorithm such that, when being applied to encrypt the fake message, it can potentially produce the ciphertext coinciding with the ciphertext produced by the pseudo-probabilistic block encryption algorithm.

Probabilistic block encryption algorithm associated with the PPC including procedure of solving the system of congruences (1) is described as follows. The fake key represents the pair of secret values (K_1, m_1). To encrypt the fake message data block M the following steps are performed:

1. The data block M is encrypted with the block cipher algorithm E: $C_M = E_{K1}(M)$.
2. It is generated a random value $R < 2^v$ and a random prime number r such that $2^v < r < 2^{v+1}$.
3. It is computed the output ciphertext block C as solution of the following system of congruences

$$\begin{cases} C \equiv C_M \bmod m_1 \\ C \equiv R \bmod r \end{cases}, \tag{3}$$

It is easy to see that the arbitrary value C^* such that $C^* \equiv C_M \bmod m_1$ can be obtained as solution of system (3) at different pairs of the values $R < 2^v$ and $r < 2^{v+1}$. Indeed, let us select a random number r^* such that $2^v < r^* < 2^{v+1}$. The respective value R^* is computed as $R^* \equiv C^* \bmod r$.

Decryption of the ciphertext block is performed as follows.

Algorithm for disclosing the fake message.

1. Compute the intermediate ciphertext block C_M:$C_M = C \bmod m_1$.
2. Compute the data block M:$M = E_{K1}^{-1}(C_M)$.

Algorithm for disclosing the secret message.

1. Compute the intermediate ciphertext block C_T:$C_T = C \bmod m_2$.
2. Compute the data block T:$T = E_{K1}^{-1}(C_T)$.

Probabilistic block encryption algorithm associated with the PPC including procedure of solving the system of congruences (2) is described as follows. The fake key represents the pair of secret values (K_1, $\mu(x)$). Encryption of the data block M of the fake message is performed as follows:

1. The data block M is encrypted with the block cipher algorithm E:$C_M = E_{K1}(M)$.
2. It is generated a random binary polynomials $\lambda(x)$ (of the degree equal to v or less) and $\rho(x)$ (of the degree $v + 1$).
3. It is computed the output ciphertext block C as solution of the following system of congruences (the ciphertext block C_M is considered as binary polynomial):

$$\begin{cases} C \equiv C_M \bmod \mu(x) \\ C \equiv \lambda(x) \bmod \rho(x) \end{cases}, \tag{4}$$

Evidently, a bit string C^* such that $C^* = C_M \bmod \mu(x)$ can be obtained as solution of system (4) at different pairs of the polynomials $\lambda(x)$ and $\rho(x)$. Indeed, for arbitrary polynomial $\rho(x)$ of the degree $v + 1$ the related polynomial is $\lambda(x) = C^* \bmod \mu(x)$.

Decryption of the ciphertext block is performed as follows.

Algorithm for disclosing the fake message.

1. Compute the intermediate ciphertext block C_M:$C_M = C \bmod \mu(x)$.
2. Compute the data block M:$M = E_{K1}^{-1}(C_M)$.

Algorithm for disclosing the secret message.

1. Compute the intermediate ciphertext block C_T:$C_T = C \bmod \lambda(x)$.
2. Compute the data block T: $T = E_{K2}^{-1}(C_T)$.

6 Conclusion

It has been proposed to construct the block deniable encryption as process of pseudo-probabilistic block encryption of secret and fake messages. At time of the coercive attack the sender or/and receiver open the fake message and fake encryption key and declare their using the probabilistic block encryption of the opened message. The coercer is computationally unable to distinguish the intercepted ciphertext from ciphertext produced by probabilistic encryption. The proposed deniable encryption method is fast and provides bi-deniability (resistance to simultaneous attack on both the sender and the receiver of the message).

The main result of the paper is its contribution to the class of pseudo-probabilistic ciphers to which one can attribute the proposed block crypto schemes and introduced earlier pseudo-probabilistic stream ciphers [6, 7].

References

1. Canetti, R., Dwork, C., Naor, M., Ostrovsky, R.: Deniable encryption. In: Kaliski, B.S. (ed.) CRYPTO 1997. LNCS, vol. 1294, pp. 90–104. Springer, Heidelberg (1997). https://doi.org/10.1007/BFb0052229
2. O'Neill, A., Peikert, C., Waters, B.: Bi-deniable public-key encryption. In: Rogaway, P. (ed.) CRYPTO 2011. LNCS, vol. 6841, pp. 525–542. Springer, Heidelberg (2011). https://doi.org/10.1007/978-3-642-22792-9_30
3. Moldovyan, N.A., Shcherbacov, A.V., Eremeev, M.A.: Deniable-encryption protocols based on commutative ciphers. Quasigroups Relat. Syst. 95–108 (2017)
4. Meng, B.: A secure internet voting protocol based on non-interactive deniable authentication protocol and proof protocol that two ciphertexts are encryption of the same plaintext. J. Netw. **4**, 370–377 (2009)
5. Ishai, Y., Kushilevitz, E., Ostrovsky, R., Prabhakaran, M., Sahai, A.: Efficient non-interactive secure computation. In: Paterson, K.G. (ed.) EUROCRYPT 2011. LNCS, vol. 6632, pp. 406–425. Springer, Heidelberg (2011). https://doi.org/10.1007/978-3-642-20465-4_23
6. Moldovyan, A.A., Moldovyan, D.N., Shcherbacov, V.A.: Stream deniable-encryption algorithm satisfying criterion of the computational indistinguishability from probabilistic ciphering. In: Workshop on Foundations of Informatics, Chisinau, pp. 318–330 (2015)

7. Moldovyan, N.A., Moldovyan, A.A., Moldovyan, D.N., Shcherbacov, V.A.: Stream deniable-encryption algorithms. Comput. Sci. J. Mold. **24**, 68–82 (2016)
8. Moldovyan, N.A., Moldovyan, A.A.: Data-driven Block Ciphers for Fast Telecommunication Systems, 1st edn. Auerbach Publications, Boston (2007)
9. Dürmuth, M., Freeman, D.M.: Deniable encryption with negligible detection probability: an interactive construction. In: Paterson, K.G. (ed.) EUROCRYPT 2011. LNCS, vol. 6632, pp. 610–626. Springer, Heidelberg (2011). https://doi.org/10.1007/978-3-642-20465-4_33
10. Barakat, T.M.: A new sender-side public-key deniable encryption scheme with fast decryption. KSII Trans. Internet Inf. Syst. (TIIS) **8**, 3231–3249 (2014)

Crack Detection in Rotating Shafts Using Wavelet Analysis, Shannon Entropy and Multi-class SVM

Zhiqiang Huo[1,2(✉)], Yu Zhang[1], Zhangbing Zhou[3], and Jianfeng Huang[2]

[1] School of Engineering, University of Lincoln, Lincoln, UK
{zhuo,yzhang}@lincoln.ac.uk
[2] Guangdong University of Petrochemical Technology, Maoming, China
jianfeng.huang@outlook.com
[3] China University of Geosciences, Beijing, China
zbzhou@cugb.edu.cn

Abstract. Incipient fault diagnosis is essential to detect potential abnormalities and failures in industrial processes which contributes to the implementation of fault-tolerant operations for minimizing performance degradation. In this paper, an innovative method named Self-adaptive Entropy Wavelet (SEW) is proposed to detect incipient transverse crack faults on rotating shafts. Continuous Wavelet Transform (CWT) is applied to obtain optimized wavelet function using impulse modelling and decompose a signal into multi-scale wavelet coefficients. Dominant features are then extracted from those vectors using Shannon entropy, which can be used to discriminate fault information in different conditions of shafts. Support Vector Machine (SVM) is carried out to classify fault categories which identifies the severity of crack faults. After that, the effectiveness of this proposed approach is investigated in testing phrase by checking the consistency between testing samples with obtained model, the result of which has proved that this proposed approach can be effectively adopted for fault diagnosis of the occurrence of incipient crack failures on shafts in rotating machinery.

Keywords: Fault diagnosis · Shaft · Continuous Wavelet Transform
Shannon entropy · Multi-class SVM

1 Introduction

Fault diagnosis of rotating machinery has been drawn a great deal of attentions for meeting the increasing demands on reliability and safety of industrial systems subjected to latent process and component failures due to complex working conditions (e.g., increasing speed, power and load). As a result, significant development in operating stress can lead to premature shaft failures in rotating machinery which may cause performance degradation and even dangerous situations [1]. Hence, it is paramount to continuously monitor and diagnose conditions

© ICST Institute for Computer Sciences, Social Informatics and Telecommunications Engineering 2018
Y. Chen and T. Q. Duong (Eds.): INISCOM 2017, LNICST 221, pp. 332–346, 2018.
https://doi.org/10.1007/978-3-319-74176-5_29

of rotating shafts and finally enhance the confidence of industrial system reliability and safety. In recent decades, vibration monitoring has been widely applied in the field of fault diagnosis in rotating machinery [2]. Continuing efforts has been dedicated to reducing magnitude and redundant information in original signals by means of using advanced techniques of signal processing [3]. Fast Fourier transform and short time Fourier transform are two classical approaches for signal decomposition; however their performances are limited by the finite window size which is not suitable to analyze non-stationary and non-linear vibration signals. To solve this problem, the advent of Wavelet Transform (WT) provides a powerful technique for characterizing a variety of conditions from both time and frequency domains. To be more specific, WT enjoys good time and poor frequency resolutions at high frequencies, and good frequency and poor time resolutions at low frequencies. Therefore, WT has been successfully applied for fault detection and diagnosis of rotating machinery [4,5]. Among wavelet analysis, Continuous Wavelet Transform (CWT), Discrete Wavelet Transform (DWT), Wavelet Packets Transform (WPT) are widely used for decomposing signals into specific frequency spectrum ranges of interest. For analyzing crack faults on shafts, CWT coefficients were applied in [6,7] by analyzing sub-critical peaks and phase angles. Crack depth and growth were analyzed and identified using envelop analysis and DWT based on acoustic emission in [8]. Apart from CWT and DWT, WPT was also adopted with time-frequency features for crack detection in [9–11], which benefits from appropriately decomposing frequency spectrum into the same bands with detail and approximate coefficients.

Generally, in signal-based fault diagnostic approaches, features of monitored signals are extracted to reduce redundant information and analyze corresponding patterns, which can be in time and/or frequency domains, and nonlinear features [12]. Among those, entropy analysis is an appropriate and widely used indicator that enjoys advantages in discriminating changes in different conditions of shafts by quantifying the uncertainty in times series. One of the mostly encountered feature is Shannon Entropy ($ShanEn$) [13], which is a quantitative measure of unpredictability and irregularity in a system. It only takes into account that the probability of observing a specific event, in fault diagnosis, which is the underlying signal probability distribution used for representing fault characteristics generated from the change of different conditions of shafts.

In this paper, a Self-adaptive Entropy Wavelet (SEW) approach is proposed for fault diagnosis of rotating shafts with breathing cracks by using CWT, $ShanEn$ and multi-class support vector machine (SVM). An optimized wavelet kernel, based on impulse modelling, is applied for decomposing signals into multiscale coefficients vectors, which can be obtained using Particle Swarm Optimization (PSO) and quasi-Newton minimization algorithms in training step for achieving highest fault classification accuracy. After that, $ShanEn$ features are extracted from coefficient vectors, and then fed into SVM for training diagnostic pattern, which is carried out for fault identification and classification. The main contributions in this paper are concluded as follows:

– An optimized wavelet model named SEW was presented for crack fault detection and fault diagnosis of rotating shafts by means of applying techniques of CWT, *ShanEn*, and SVM. The experimental results have shown that 99.3% fault classification accuracy can be achieved by using this proposed approach.
– The effectiveness of feature vectors obtained from coefficient vectors having different scales on classification accuracy is evaluated and analyzed. In addition, the classification performance of SVM with four kinds of kernel functions based the proposed method are also investigated.

The rest of this paper is organized as follows: Sect. 2 briefly summarizes related work on shaft fault diagnosis based on wavelet analysis. Section 3 presents the proposed approach for crack fault detection and identification on rotating shafts. Experimental validation and results are given in Sect. 4. Finally, conclusions are drawn in Sect. 5.

2 Related Work

Advances in wavelet have paved the way for the emergence of plentiful techniques to be applied in the field of fault diagnosis. In recent decades, great efforts have been devoted to fault diagnosis of rotating shafts in industrial machinery. A detection method based on CWT was proposed by Babu et al. [6], in which the amplitudes of sub-critical and critical peaks of the CWT coefficients are considered as the crack indicators which were then fed as input to Artificial Neural Network (ANN) for crack identification. Nagaraju et al. [7] presented a shaft diagnosis method based on 3D wavelet, which considers both time and frequency features of the crack faults. To be more specific, this method considers both phase angles of different frequency components and sub-critical peaks in a CWT plot, the experiment of which showed that this method performs better than when only sub-critical is considered in the case. In addition, apart from been directly applied in signal decomposition, DWT and WPT are also adopted as preprocess techniques in signal analysis, such as band-pass filters and wavelet denoising tools. DWT was applied in purpose of detecting crack growth on a shaft in [8], in collaboration with envelope analysis and acoustic emission monitoring. In addition, a method combining WPT and Empirical Mode Decomposition (EMD) was proposed by Bin et al. [9] to precisely characteristic features of crack defects in specific frequency bands. Similarly, features related to WPT have been applied in [10,11]. By using WPT, it is great convenient to decompose a signal into approximation and detail information having the same frequency resolution. On the other hand, WPT can be applied for de-noising signals by means of either reconstructing coefficient vectors or thresholding methods. Table 1 summarizes the related work on fault diagnosis of shafts using wavelet analysis in rotating machinery.

To sum up, wavelet analysis is one of the most powerful methods of signal processing to be used for effectively detecting and identifying crack faults in rotating shafts. In practice, the selection of wavelet kernels, decomposition levels, feature vectors, and classification methods has great influences on the performance of fault identification and classification. Hence, there is still strong need to provide innovative approaches to optimize diagnostic procedures and improve the reliability of fault diagnostic approaches on the basis of wavelet analysis. For this purpose, in this study, a new diagnostic method is proposed and investigated by combining optimized wavelet function, Shannon entropy and SVM for identifying incipient breathing crack failures on rotating shafts.

Table 1. Comparison of related work for crack fault diagnosis rotating shafts using wavelet techniques.

	Nagaraju et al. [7]	Gu et al. [8]	Bin et al. [9]	Gómez et al. [10]	Gómez et al. [11]
Year	2009	2012	2012	2016	2016
Objects considered	Crack depth and position	Crack depth and growth	10 types of rotor failures	Crack depth and growth	Crack depth
Wavelet methods used	CWT	DWT and HHT	WPD and EMD	WPD	WPD
Parameters applied	Morlet, scale 30	Daubechies 8, level 1 to 5	Daubechies 8, node(4,3)	Daubechies 8, level 9	Daubechies8, level 2 to 9
Features selected	Phase angles difference between transverse vibrations	Peak, mean, RMS, entropy estimation	Bandwidth energy of vibration signal spectrum	Mean, RMS	Power energy
Classification methods	ANN	N/A	ANN	N/A	ANN
Signals monitored	Vibration	Acoustic emission	Vibration	Vibration	Vibration

3 Proposed Method

Aiming at fault diagnosis of rotating shafts with crack defects, in this study, a new data-driven model was proposed named SEW approach by combining optimized wavelet function using impulse modelling based CWT, *ShanEn* and SVM techniques. A supervisor model is used for training and testing SEW model, which are applied respectively for optimizing SEW model and checking the consistency between testing samples and obtained pattern. In the former step, PSO and quasi-Newton minimization algorithms are applied to obtain optimized wavelet kernel function. Figure 1 presents the procedure for crack fault detection and identification using the proposed approach.

3.1 Self-adaptive Entropy Wavelet (SEW)

Wavelet analysis is one of the most powerful signal processing techniques which enjoys high resolutions in both time and frequency domains [4], which enjoys the ease of interpretation at the cost of saving space using groups of non-orthogonal

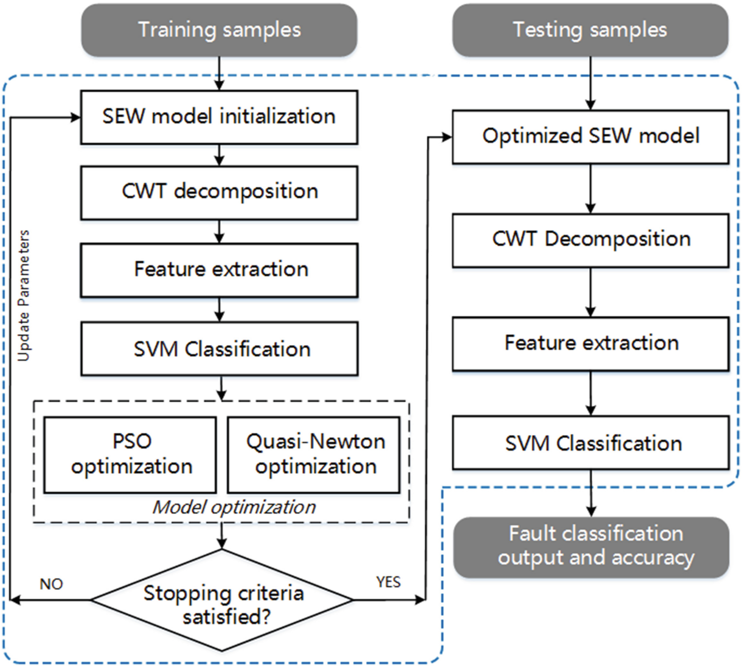

Fig. 1. Flow chart of proposed diagnostic approach.

wavelet frames to generate general symptoms. The CWT wavelet transform is defined as follows:

$$CWT_x^{\psi}(\gamma, s) = \Psi_x^{\psi}(\gamma, s) = \frac{1}{\sqrt{s}} \int x(t) \Psi \left(\frac{t-\gamma}{s} \right) dt. \quad (1)$$

where $x(t)$ is the signal, s is the scale factor, γ is the translation parameter, $\Psi(t)$ is the wavelet kernel function, and it is also called the mother wavelet.

In practice, when the rotating shaft with cracked defects is operating, the resonance or harmonic frequency components corresponding to base frequency are most likely to appear, which show the correlation with the severity of crack defect to some extent. Therefore, these kinds of changes in harmonic frequency can be captured with the help of analyzing impulse models in which differences corresponding to the change of frequency in waveform can be detected. To illustrate the effectiveness of this change case that can be effectively used for breathing crack defects in shaft, SEW is proposed in this study. The response of the system to the instant δ-impulse in vibrodiagnostics can be represented using a pattern depicted as a response of the single-degree-of-freedom-system, which can be formulated as follows [14]:

$$f(x) = \alpha e^{-\beta x} cos(wx + \varphi) \quad (2)$$

where $f(x)$ is the displacement, α is the premier amplitude, w is the resonance frequency, which is the frequency of the system fluctuation without resistance. Taking assumption that at the impulsive start the system was at rest into consideration, Eq. (2) can be applied as a mother wavelet in CWT, which can be expressed as follows:

$$\Psi(x) = sin(\alpha x + \beta)e^{-\gamma|x|} \tag{3}$$

For keeping minimum parameters in the mother wavelet, α, β, and γ are kept to represent a system's working state based on the theory of impulse modelling; therefore, in this study, Eq. (2) is selected as a wavelet kernel for helping to detect and diagnose the changes bringing in vibration signals by the occurrence of harmonic frequency. By using CWT, a signal can be respectively decomposed into numbers of coefficient vectors with different scales. Then the power energy of each vector, denoted as E_i, can be obtained from following form:

$$E_i = \int_{-\infty}^{+\infty} |c_i(t)|^2 dt \tag{4}$$

where c_i(t) is the coefficient values of a signal with the *i-th* scale obtained from a vibration signal. Hence the total energy, $E = \{E_1, E_2, \cdots, E_m\}$ (m represents the total number of vectors, namely the first m vectors), which generates energy distribution in different frequency domains of rotating shafts. Then the corresponding Shannon entropy can be defined as:

$$H_i = -\sum_{i=1}^{m} p_i \log p_i \tag{5}$$

where H_i is the $ShanEn$ value of i-th coefficient vector in total m vectors with different scales obtained from CWT method, $\{p_i = E_i/E, i = 1, 2, \cdots, m\}$ is the percent of the power energy in the total energy E. Therefore, feature vector, denoted as F, can be constructed with the first m $ShanEn$ features, $\{H_i(i = 1, 2, \cdots, m)\}$. After that, F can be then fed into SVM for fault classification. During this step, fitness function can be formed to optimize the proposed wavelet model by locating best solutions that can achieve the best accuracy. In this study, desired classification accuracy can be achieved when the values of fitness approach to minimized solutions by means of defining the fitness function as a negative number of resulting accuracy obtained from fault classification using SVM classifier.

3.2 SEW Model Optimization

In the step of parameter optimization in proposed SEW model, PSO and quasi-Newton minimization algorithms are used to locate desired parameters that can achieve the best classification accuracy. The former is first applied to locate the global best solutions and the later is applied to locate local solutions on the basis of parameters obtained from the former. PSO, proposed by Kennedy and

Eberhart [15], performs by iteratively using a population (called a swarm) of candidate solutions (called particles) in the search-space. The swarm consists of m numbers of particles, each of which has own velocity $v_{i,j}(t)$, current position $x_{i,j}(t)$, and local best known position $pbest_j(t)$ $(i = 1, 2, \cdots, m; j = 1, 2, \cdots, n)$. Each particle moves towards own best previous position and the best known positions found by other particles $gbest_j(t)$ in the search-space, which is expected to move the swarm toward the best solutions. The standard PSO can be performed according to the following equations:

$$\begin{aligned} v_{i,j}(t+1) = w \times v_{i,j}(t) + c_1 \times r1() \times (pbest_j(t) - x_{i,j}(t)) \\ + c_2 \times r2() \times (gbest_j(t) - x_{i,j}(t)) \end{aligned} \tag{6}$$

$$x_{i,j}(t+1) = x_{i,j}(t) + v_{i,j}(t+1) \tag{7}$$

where j is the $n-$th dimension of a particle $(1 \leq j \leq n)$, the velocity is restricted to the $[-v_{max}, v_{max}]$ range, $r1()$ and $r2()$ are random numbers in the range of [0,1], $c1$ and $c2$ are positive constants corresponding to personal and social learning factors, and w is the inertia weight. In this study, the initialize parameters with respect to the size of swarm, inertia weight, maximum number of iterations are selected as follows: swarm size $p = 20$, $c1 = 2$, $c2 = 2$, max stall iterations $t_{max} = 6$. The search range of α, β, γ is from [0, 0, 0] to [200, 200, 200].

After global optimization, quasi-Newton minimization algorithm [16,17] is used to locate minimum solutions around the parameters obtained from PSO, which applies curvature information at each iteration to formulate a quadratic model problem, which has the following form:

$$\min_{x \in R^n} f(x) = \frac{1}{2} x^T H x + b^T x + c \tag{8}$$

where H, the Hessian matrix, is a positive definite symmetric matrix, b is a constant vector, and c is a constant. In this study, Broyden-Fletcher-Goldfarb-Shanno (BFGS) method is applied to efficiently update an approximation to H, which aims to reduce calculation so that a mount of computing time consumption can be saved. For Hessian updating, the BFGS is generally considered as an effective method that can be used for iteratively optimizing the search direction. In BFGS, the formula for generating an approximation to H is described below:

$$H_{k+1} = H_k + \frac{q_k q_k^T}{q_k^T s_k} - \frac{H_k s_k s_k^T H_k^T}{s_k^T H_k s_k} \tag{9}$$

At each major iteration, k, a line search is performed to locate the best solution in the direction:

$$d_k = -H_k^{-1} \cdot \bigtriangledown f(x_k) \tag{10}$$

This method has optimal solutions when the partial derivatives of x approach to zero. In this paper, BFGS based quasi-Newton unconstrained minimization serves to locate local optimized parameters after global optimization. The max number of iterations, t_{max}, is set to 80, and max number of function evaluations is 300.

3.3 Fault Classification

Multi-class SVM is adopted for fault classification in this study. A supervisor mode is used for data training and testing using LIBSVM Matlab Toolbox [18,19]. A grid search method is applied to search best parameters, namely the cost parameter c and the width parameter g in the training phrase. Here, c and g are respectively set between 2^{-10} to 2^{10}. In addition, after the data training, a 5-fold cross-validation method is used for the validation of the proposed rotating shaft fault diagnostic approach. In a k-fold cross-validation method, the data sets are divided into k subsets, and the holdout method is repeated k times. After that, the average error for all k trials can be obtained to guarantee the efficiency of fault classification.

On the basis of above mentioned techniques, the process of the proposed approach is briefly described as follows:

Step 1: collect vibration signals from different conditions of rotating shafts and separate data into training data sets and testing data sets respectively.
Step 2: signals are normalized to make the signals comparable regardless of differences in magnitude using the following equation:

$$X_i = \frac{x - \bar{x}}{\sigma} \tag{11}$$

where x is the $i-$th element of the signal, $\bar{x}$ and σ are the mean and standard deviation of elements in the given signal respectively.
Step 3: initialize three parameters (α, β and γ), and then decompose vibration signals using this proposed SEW model.
Step 4: extract entropy features using SE from the first m coefficient vectors corresponding to a given signal and construct a feature vector F with the energy as element according to Eq. (5):

$$F = [H_1, H_2, H_3, \cdots, H_m] \tag{12}$$

Step 5: carry out the training and testing procedure of SVM. After that, the testing accuracy of fault classification using current SEW model and SVM can be obtained, the negative value of which can be formed as fitness function. If this is not the best solution, then take next round of optimization. Otherwise, stop optimization and output SEW and SVM models.
Step 6: perform PSO optimization by iterating steps 3–5 and updating the global best solutions having the minimum fitness value, which means high classification accuracy.
Step 7: update SEW model with global best solutions obtained from PSO optimization, and then quasi-Newton minimization algorithm is used to find local minimums of fitness function and obtain local desired solutions by repeatedly perform steps 3–5. After PSO and quasi-Newton optimization, SWE model with optimized α, β and γ can be adopted as wavelet kernel with SVM model obtained for fault diagnosis of rotating shafts using the proposed approach.

4 Experimental Study

In this section, the experimental test rig is first introduced, and the results and effectiveness of the proposed approach are then presented and discussed.

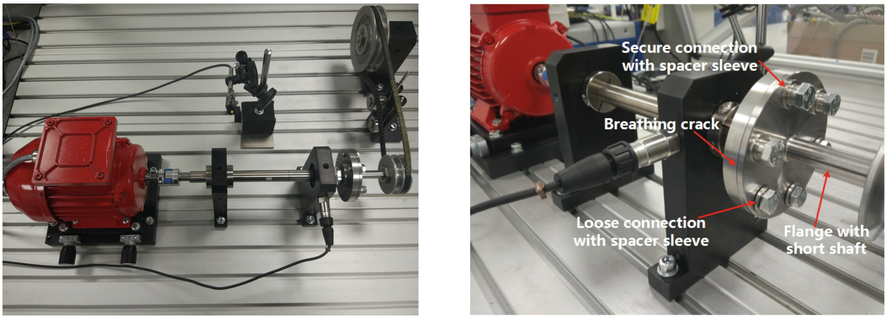

(a) PT 500 test rig [20] (b) Simulating kit for crack fault

Fig. 2. PT 500 experimental test rig and corresponding crack detection in rotating shaft kit.

4.1 Experimental Setup

In this study, PT 500 machinery diagnostic system [20] is used to collect vibration signals generated from healthy and cracked shafts respectively, as shown in Fig. 2. The fault kit applied is composed of motor assembly, motor control unit, shaft, flange, belt drive kit, and computerised vibration analyser. The control unit is used to collect speed and horsepower data. The piezo-electric sensor and measurement amplifier are used for acceleration measurement. Besides, computerised vibration analyser is used to measure the horizontal vibration signals. This test rig allows to simulate the characteristic behaviour of a shaft with a crack using asymmetrical flange connection. Tightening the flange connection with spacer sleeves gives a connection that is either loose or secure, which can very closely resembles the behaviour of a breathing crack in the shaft.

In this experiment there are in total five conditions of shaft were considered (denoted as H, C1, C2, C3 and C4) for evaluating and recognizing the health conditions of rotating shafts with breathing crack defects. To be more specific, 0, 1, 2, 3, 4 numbers of loose screws were used respectively to form loose connection and finally closely simulate the breathing cracks in the rotating shafts. For each condition, 300 data sets were used; therefore the total number of data sets includes 1500 data sets, each of which is a section of vibration signal containing 2000 sampling points. Hence, the entire data set was split into two data sets, namely 750 data sets for training and 750 data sets for testing respectively. Vibration data was captured at a sampling frequency of 8 kHz at 1850 r.p.m. In this experiment, the basic frequency is 30 Hz.

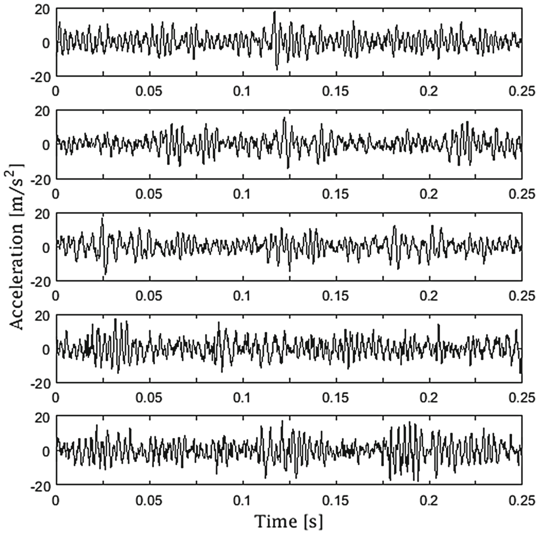

Fig. 3. Typical original vibration signals with five conditions.

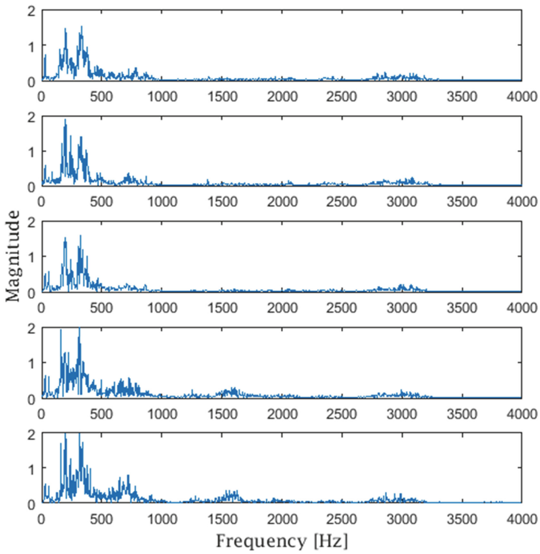

Fig. 4. Frequency spectrums obtained from vibration signals using FFT

4.2 Results and Analysis

Typical vibration signals with five conditions (i.e., H and C1–C4) generated from the rotating shaft are presented respectively in Fig. 3, the corresponding frequency spectrum of which using FFT are shown in Fig. 4. As can be seen, resonance frequencies gradually appear with the increasing depth of breathing cracks. For instance, the magnitude of 60 Hz in crack conditions are apparently greater than that in H condition.

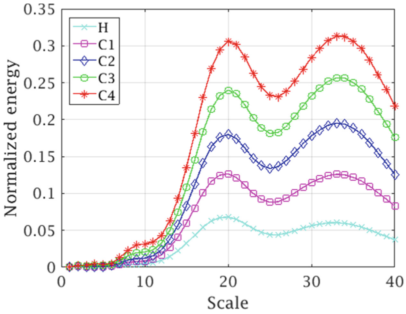

(a) Mean values using Morlet

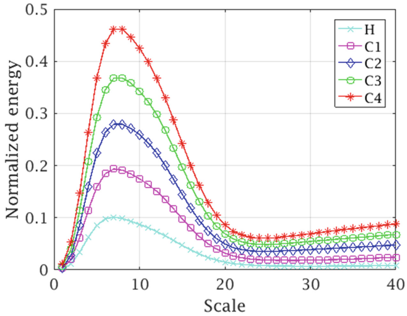

(b) Mean values using Mexican hat

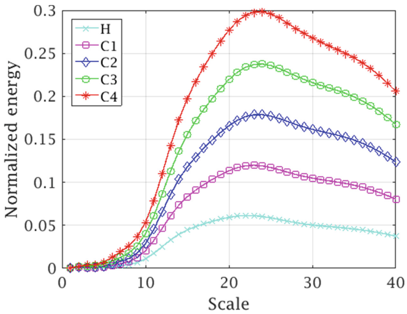

(c) Mean values using Daubechies8

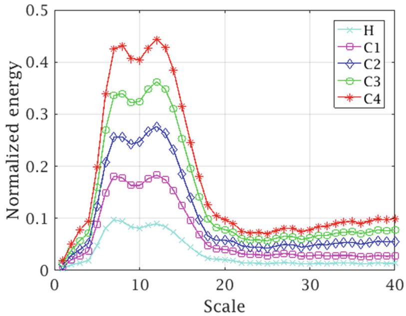

(d) Mean values using SEW

Fig. 5. Mean energy values of coefficients with the first 40 scales using four wavelets.

After vibration data acquisition, the proposed methodology, described in Sect. 2, was implemented to investigate the performance of wavelet kernel and feature extraction using different scale numbers. For this purpose, the prediction accuracy using six wavelet kernels on the shelf (e.g., Morlet, Mexican hat, and Daubechies) and proposed SEW wavelet kernel were evaluated and compared in ability of discriminating fault information among various conditions of shafts. Besides, taking optimization time consumption into consideration, the coefficient vectors with the first 40 scales were applied to evaluate the influence of scale numbers on classification accuracy. Firstly, after CWT decomposition, the performance of feature extraction using three existing functions and the proposed SEW function is compared and presented in Fig. 5. It can be seen that mean values of features representing five conditions can be clearly recognized and distinguished by using Shannon entropy. Interestingly, in the right two figures, the mean values of features sharply rise to the submit around 10 scale number, and then gradually decrease and finally keep steady. After 20, the normalized energy of each condition is no more than 0.1 value. In addition, the analysis of time-frequency domains of vibration signals generated from five conditions of rotating shafts using CWT is presented in Fig. 6. From this figure, it can be clearly found that resonance and high frequencies are increasingly apparent, the possible reason of which is that growing depths of crack on the shaft lead to more vibrations that are mainly generated by rotating belt, which is closely connected to the rotating shaft.

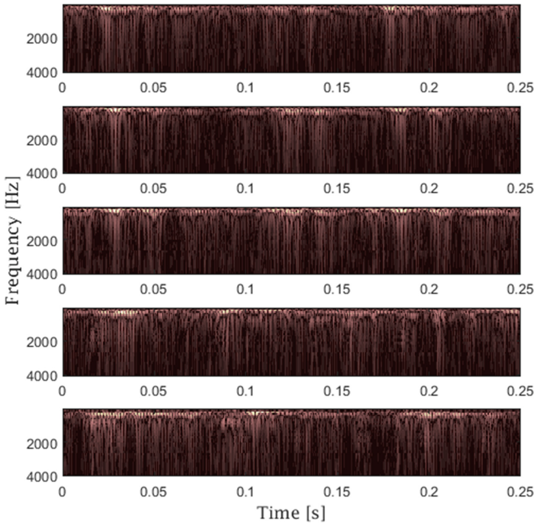

Fig. 6. Time-frequency spectrums of five conditions of rotating shaft using optimized SEW transformation.

Finally, as can be seen in Fig. 7, in comparison with other wavelets, the proposed SEW (represented by red color) is capable of achieving greater accuracy, the average classification accuracy of which is 96.82%. Interestingly, Morlet and Mexican hat enable to obtain more than 90% classification accuracy when 20 and greater number of scales are applied. However, the Daubechies wavelet types achieve minimum accuracies, the best of which is no more than 82% in this study.

To investigate the performance of SVM model used in proposed approach on prediction accuracy, in this study, four different kernel functions (i.e., liner, polynomial, Radial Basis Function (RBF) and sigmod functions) are applied respectively for obtaining optimized parameters in the training phrase for fault classification, the results of which are presented in Fig. 8. As can be seen, the SVM classifier enables to identify crack defects with greater than 90% accuracy when at least 10 scales are applied for fault diagnosis of shaft using the proposed approach. Moreover, it can be notice that the accuracies of fault classification by using four kernel functions gradually ascend following with increasing scale numbers. Interestingly, four lines representing accuracies intersect at 20 that

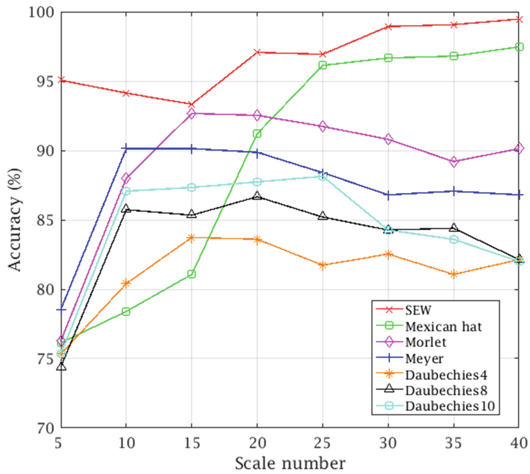

Fig. 7. Comparative prediction accuracies using four kernel functions in SVM for fault classification (Color figure online)

means those four models basically can achieve similar performance when the scale number is 20.

To sum up, through experimental validation, it has proved that the proposed diagnostic approach can be effectively used for incipient crack fault diagnosis of rotating shafts, the best accuracy of which can achieve 99.3%. Moreover, the effectiveness of feature extraction using Shannon entropy was investigated, the result of which presented it can be used for discriminating changes in time and frequency domains. Apart from that, four kernel functions were also evaluated which have showed that RBF function performed better in fault classification than the rest (Table 2).

Table 2. Classification accuracy using four kernels when 40 decomposition scales are applied using SEW model.

No.	Name	Kernel function	Testing data sets	Misclassified data sets	Testing accuracy (%)
1	Linear	$K(x,y) = x^T y + c$	150	3	98.0%
2	Polynomial	$K(x,y) = (ax^T y + c)^d$	150	3	98.0%
3	Radial basis function	$K(x_i,x_j) = exp(-\gamma \|x-y\|^2)$	150	1	99.3%
4	Sigmode	$K(x,y) = tanh(ax^T + c)$	150	2	98.7%

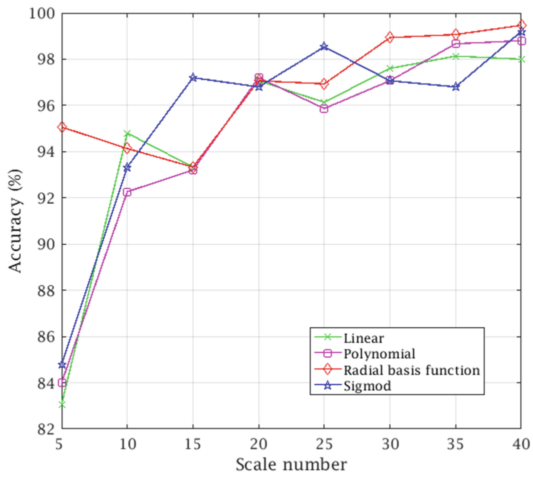

Fig. 8. SVM classification accuracy using different functions

5 Conclusion

In this study, an innovative approach named Self-adaptive Entropy Wavelet (SEW) is proposed to detect incipient transverse crack faults on a rotating shaft based on Continuous Wavelet Transform (CWT), Shannon entropy and SVM classifier. The effectiveness of the proposed approach was investigated by using a test rig, the results of which has proved that the proposed method can be used for crack detection and identification on rotating shafts. The 99.3% classification accuracy can be achieved by using RBF-based SVM. Hence, in the future the proposed method would be further extended to study the fault diagnosis performance of other rotating components in industrial rotating machinery.

Acknowledgement. This work is partially supported by International and Hong Kong, Macao & Taiwan collaborative innovation platform and major international cooperation projects of colleges in Guangdong Province (No. 2015KGJHZ026), The Natural Science Foundation of Guangdong Province (No. 2016A030307029), and Maoming Engineering Research Center on Industrial Internet of Things (No. 517018).

References

1. Yin, S., Ding, S.X., Xie, X., Luo, H.: A review on basic data-driven approaches for industrial process monitoring. IEEE Trans. Industr. Electron. **61**(11), 6418–6428 (2014)
2. Tavner, P.: Review of condition monitoring of rotating electrical machines. IET Electric Power Appl. **2**(4), 215–247 (2008)
3. Rai, A., Upadhyay, S.: A review on signal processing techniques utilized in the fault diagnosis of rolling element bearings. Tribol. Int. **96**, 289–306 (2016)

4. Yan, R., Gao, R.X., Chen, X.: Wavelets for fault diagnosis of rotary machines: a review with applications. Sig. Process. **96**, 1–15 (2014)
5. Huo, Z., Zhang, Y., Francq, P., Shu, L., Huang, J.: Incipient fault diagnosis of roller bearing using optimized wavelet transform based multi-speed vibration signatures. IEEE Access (2017)
6. Babu, T.R., Sekhar, A.: Shaft crack identification using artificial neural networks and wavelet transform data of a transient rotor. Adv. Vib. Eng **9**, 207–214 (2010)
7. Nagaraju, C., Rao, K.N., Raoo, K.M.: Application of 3D wavelet transforms for crack detection in rotor systems. Sadhana **34**(3), 407–419 (2009)
8. Gu, D., Kim, J., Kelimu, T., Huh, S.-C., Choi, B.-K.: Evaluation of the use of envelope analysis and DWT on AE signals generated from degrading shafts. Mater. Sci. Eng. B **177**(19), 1683–1690 (2012)
9. Bin, G., Gao, J., Li, X., Dhillon, B.: Early fault diagnosis of rotating machinery based on wavelet packets-Empirical mode decomposition feature extraction and neural network. Mech. Syst. Signal Process. **27**, 696–711 (2012)
10. Gómez, M., Castejón, C., Corral, E., García-Prada, J.: Analysis of the influence of crack location for diagnosis in rotating shafts based on 3 x energy. Mech. Mach. Theory **103**, 167–173 (2016)
11. Gómez, M.J., Castejón, C., García-Prada, J.C.: Automatic condition monitoring system for crack detection in rotating machinery. Reliab. Eng. Syst. Saf. **152**, 239–247 (2016)
12. Tang, J., Alelyani, S., Liu, H.: Feature selection for classification: a review. In: Data Classification: Algorithms and Applications, p. 37 (2014)
13. Coifman, R.R., Wickerhauser, M.V.: Entropy-based algorithms for best basis selection. IEEE Trans. Inf. Theory **38**(2), 713–718 (1992)
14. Schukin, E., Zamaraev, R., Schukin, L.: The optimisation of wavelet transform for the impulse analysis in vibration signals. Mech. Syst. Sig. Process. **18**(6), 1315–1333 (2004)
15. Kennedy, J.: Particle swarm optimization. In: Sammut, C., Webb, G.I. (eds.) Encyclopedia of Machine Learning, pp. 760–766. Springer, Boston (2011)
16. Shanno, D.F.: Conditioning of quasi-Newton methods for function minimization. Math. Comput. **24**(111), 647–656 (1970)
17. Battiti, R., Masulli, F.: BFGS optimization for faster and automated supervised learning. In: International Neural Network Conference, pp. 757–760. Springer, Dordrecht (1990). https://doi.org/10.1007/978-94-009-0643-3_68
18. Suykens, J.A., Vandewalle, J.: Least squares support vector machine classifiers. Neural Process. Lett. **9**(3), 293–300 (1999)
19. LIBSVM Matlab Toolbox. https://www.csie.ntu.edu.tw/~cjlin/libsvm/. Accessed 10 June 2017
20. PT 500 Machinery Diagnostic System. www.gunt.de/static/s3680_1.php. Accessed 10 June 2017

A New Resampling Parameter Algorithm for Kullback-Leibler Distance with Adjusted Variance and Gradient Data Based on Particle Filter

Nga Ly-Tu[1,2,3](✉), Thuong Le-Tien[2,3], and Linh Mai[4]

[1] School of Computer Science and Engineering, International University-VNUHCM, Ho Chi Minh City, Vietnam
ltnga@hcmiu.edu.vn

[2] Department of Electrical and Electronics Engineering, University of Technology, VNU, Hanoi, Vietnam
thuongle@hcmut.edu.vn

[3] VNUHCM, Ho Chi Minh City, Vietnam

[4] School of Electrical and Engineering, International University-VNUHCM, Ho Chi Minh City, Vietnam
mlinh@hcmiu.edu.vn

Abstract. In this paper, we propose a new resampling method of particle filter (PF) to monitor target position. The target location is to improve enhancing the effect of the received signal strength (RSS) variations. The key issue of our technique is to determine a new resampling parameter that finding the optimal bound error and lower bound variance values for Kullback-Leibler distance (KLD)-resampling adjusted variance and gradient data based on PF to ameliorate the effect of the RSS variations by generating a sample set near the high-likelihood region. To find these values, these optimal algorithms are proposed based on the maximum mean number of particles used of our proposal and other KLD-resampling methods. Our experiments show that the new technique does not only enhance the estimation accuracy but also improves the efficient number of particles compared to the traditional methods.

Keywords: SIR · Bound error · KLD-resampling · RSS

1 Introduction

The core challenge in wireless sensor network (WSN) is the estimation of target location in space, for instance, moving velocity of client and other physical parameter in [1]. These parameters of target tracking are estimated by many different techniques. The recent technique is a recursive Bayesian filter that uses a set of particles with assigned primary weights serves as the basic idea of a particle filter (PF) in [2]. A set of weighted particles is theoretically qualified to represent any filtering distribution. Therefore, each particle conforms to the dynamic model and explains the observations, and then using this assessment to update set online for evaluating filter. As a result, Bayesian posterior estimate is formed.

© ICST Institute for Computer Sciences, Social Informatics and Telecommunications Engineering 2018
Y. Chen and T. Q. Duong (Eds.): INISCOM 2017, LNICST 221, pp. 347–358, 2018.
https://doi.org/10.1007/978-3-319-74176-5_30

Over the past decade, most research in WSN has emphasized the use of PFs in [3–5] for solving many problems. Almost all of them are based on three operations. The first operation, called particle propagation, is to update the state of particles via the state transition process. The second one, namely weight computation, is the process that updates the weight of particles. The last one, called resampling, is to sample a new set of particles from the original particle population for better particle representation of the filtering distribution. Thanks the parallel processing to reduce the complexity of the former two processes and easily implement if parallel hardware is available. While the resampling step is a critical procedure for PF to avoid a degenerate set of particles (sample impoverishment) leading to the estimation inaccuracy. There are many methods are introduced such as initially employed to combat degeneracy in [6], generally replicating high-weighted particles to replace low-weighted particles in [4] for reducing the probability that the filter loses tracking.

A recent year, a number of authors have considered the effects of choosing metric and weight functional approach on PFs in [3, 8, 10]. The first approach, the PF based on Kullback-Leibler Distance (KLD)-sampling, determines the minimum number of particles needed to maintain the approximation quality in the sampling process. Meanwhile, adjusting standard deviation and then using gradient data for KLD-sampling in [10] is proposed to further improve the operation time and sample set size for target tracking thanks to the given upper bound error with fixed probability. In the KLD-sampling, the predictive belief state is used as the estimate of the underlying posterior in [8]. In contrast to KLD-sampling algorithms, KLD-resampling algorithms in [3] also determines the number of particles to resample so that the KLD between the distribution of particles before resampling and after resampling does not exceed a pre-specified error bound.

Our recent work in [9, 14] introduced an enhanced PF based on the finding lower bound variance for KLD-resampling adjusted variance and gradient data algorithm to improve the estimation error of target for WSN because of the variation of RSS measurement value is the diminished. Meanwhile, our research in [12, 15] also introduced another enhanced PF based on the finding upper bound error for KLD-resampling to further improve the estimation error of target for WSN in [12], especial in [15] show the enhancing estimation error in various power levels in localization and ubiquitous monitoring of patients system in [11].

In this paper, we more extend and apply the finding bound error algorithm for our method in [9, 14]. Our technique is to propose the finding bound error method in [12, 15], called adjusted bound error, and the finding lower bound variance algorithm in [9, 14], called adjusted lower bound variance, to further reduce the estimation error of target and maintain the proper KLD-resampling in [7]. By combining the adjusted bound error in [12, 15] and adjusted lower bound variance in [9, 14] for KLD-resampling adjusted variance and gradient data, our experiments show that the new technique not only enhances the estimation accuracy but also improves the efficient number of particles used when compared traditional methods for WSN based on RSS measurement.

The paper is organized as follows. Introduction to system is given in Sect. 2. All related schemes, namely, SIR, KLD-resampling, KLD-resampling adjusted variance and gradient data are presented in Sect. 3. Our proposal is introduced in Sect. 4.

All experimental results based on MATLAB for tracking are shown in Sect. 5. Finally, we conclude the paper in Sect. 6.

2 System Model

We consider the robot carrying the sensor node (e.g. mobile node) and the node at some position as static node or node. We assume that the mobile robot moves along the determined path and a velocity in the long and thin region. The mobile robot can send the data to anchors, and then it can receive the data from the anchors. Its position can be computed by PF algorithm. We also assume all sensor nodes that have own equal physical parameters; the movement velocity of mobile node remains the same at time; the random velocity follows normal uniform distribution and the anchors are deployed at a determined pattern and the position can not be changed. This system model is divided into three parts, including mobility, RSS statistical and system state models.

2.1 Mobility Model

When the robot moves along the direction at the constant value, the time is divided into equal time segment. The velocity of the robot has some random noise which conforms to normal distribution ($\mu = 0$, $\sigma = 1$). So the random velocity and the determined velocity can be expressed as Fig. 1. Let us denote v″ (the solid line) to be the determined velocity and v′ (the dot dash line) to be the random velocity. Then, the dash line is the last velocity of the robot. The random velocity v′ is a random variable which conforms to normal distribution.

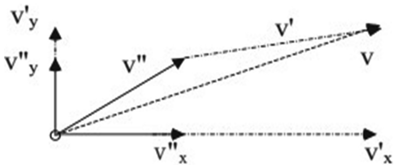

Fig. 1. Vector decomposition of determined and random velocity [16]

2.2 RSS Statistical Model

The RSS statistical model indicates the relation between the RSS and distance between nodes. The common mathematical model of WSN can be expressed as follows

$$\mathrm{P(d)} = \mathrm{P(d_0)} - 10\mathrm{n}\,log\left(\frac{\mathrm{d}}{\mathrm{d_0}}\right) + \mathrm{v}_\sigma, \tag{1}$$

where P(d) is the RSS at position d between transmitter and receiver, $\mathrm{P(d_0)}$ is the RSS at reference position (typically $\mathrm{d_0}$ = 1 m); n is the path loss parameter related to the specific application environment; and v_σ is a Gauss stochastic variable.

2.3 System State Model

The system state model for the mobile wireless sensor in [13, 16] is defined as follows

$$x_k = x_{k-1} + V_{\mathrm{k}}\Delta \mathrm{t} \;+\; w_{\mathrm{k}}, \tag{2}$$

$$z_k = Pref + Klog(x_k) + \mathrm{R}v_{\mathrm{k}}, \tag{3}$$

where x_k is the position of a mobile node from the anchor, Δt is the time segment, z_k is the RSS measurement; V_{k} is the current velocity which consists of determined velocity and random velocity in (1); the w_k and v_{k} denote the system state noise and measurement noises which obey Gauss distributions whose mean are 0 and variances are Q and R, respectively; *Pref* is reference value of RSS, and *K* is the factor in path loss.

To evaluate the required number of particles, the system state model in (2) and in (3) can be rewriten as follows

$$x_k = \begin{bmatrix} 1 & 1 & 0 & 0 \\ 0 & 1 & 0 & 0 \\ 0 & 0 & 1 & 1 \\ 0 & 0 & 0 & 1 \end{bmatrix} (x_{k-1} + V_{\mathrm{k}}\Delta \mathrm{t}) \;+\; \begin{bmatrix} 0.5 & 0 \\ 1 & 0 \\ 0 & 0.5 \\ 0 & 1 \end{bmatrix} \mathrm{Q} \begin{bmatrix} w_{1,k} \\ w_{2,k} \end{bmatrix}. \tag{4}$$

$$z_k = Pref + Klog\big(arctan(x_{1,k}, x_{3,k})\big) + \mathrm{R}v_k. \tag{5}$$

3 Particle Filters

In this section, we review all related PFs based on SIR algorithm in [5], KLD-resampling algorithm in [7], and KLD-resampling adjusted variance and gradient data algorithm in [9].

3.1 SIR PF

The concept of the SIR PF introduced in [5] is the simplest of all PFs for tracking which known as the bootstrap filter, condensation algorithm, interacting particle approximations and survival of the fittest. The core problem represents the required posterior density function by a set of random samples (particles) with associated weights, and computes the estimates by these samples and weights. When the number of samples increases very large, the Monte Carlo characterization becomes an equivalent representation of the posterior probability function.

The so-called sequential important sampling (SIS) algorithm for the PF in [5] which includes a resampling step at each instant, as described in detail in references. The SIS algorithm serves as an important density (or a proposed density to represent another one that cannot be exactly computed), that is, the sought posterior density in the present case. Then, samples are drawn from the important density instead of the actual density. A common problem with the SIS PF is the degeneracy phenomenon, where after a few states all but one particle will have negligible weight in [4]. This degeneracy implies that a large computational effort is devoted to updating particles whose contribution to the approximation of the posterior density function is almost zero. By increasing the number of particles (or more efficiently by approximately selecting the important density), this problem can be overcome. In addition, the use of resampling technique in [5] is recommended to avoid the degeneracy phenomenon (Table 1).

Table 1. SIR PF

1:	**procedure** SIR $\left(\left\{x_{k-1}^{i}, w_{k-1}^{i}\right\}_{i=1}^{N}, z_k\right)$	
2:	**for** *i=1:N* **do**	
3:	$x_k^i \sim p\left(x_k \mid x_{k-1}^i\right)$	▷ draw the signal
4:	$w_k^i = p\left(z_k \mid x_k^i\right)$	▷ the weights
5:	**end for**	
6:	$t = SUM\left[\left\{w_k^i\right\}_{i=1}^{N}\right]$	▷ total weights
7:	**for** *i=1:N* **do**	
8:	$w_k^i = t^{-1} w_k^i$	▷ normalised weights
9:	**end for**	
10:	**end procedure**	

3.2 KLD-resampling

In the sampling process, as these individuals in the population are sorted by non-domination, the use of fast KLD-sampling technique in [8], called an adaptive PF at each iteration of the PF, determine the number of samples such that, with probability $1 - \delta$, the error between the true posterior and the sample-based approximation is less than ε. KLD is used to show how to determine the number of samples so that the distance between the sample-based maximum likelihood estimate and the true posterior does not exceed a pre-specified threshold.

The KLD between the proposal (q) and (p) distributions can be defined in discrete form as follows

$$\begin{aligned} d_{KL}(p \| q) &\triangleq \sum_{x} p(x) \log\left(\frac{p(x)}{q(x)}\right) \\ &= \sum_{x} W(x) q(x) \log W(x), \end{aligned} \tag{6}$$

with $W(x) = p(x) / q(x)$. The required number N_r of samples can be determined as follows

$$N_r = \frac{1}{2\varepsilon}\chi^2_{k-1,1-\delta}, \tag{7}$$

where k is the number of bins with support, the quantizes of Chi-square distribution can be computed as follows

$$P\left(\chi^2_{k-1} \leq \chi^2_{k-1,1-\delta}\right) = 1 - \delta. \tag{8}$$

Based on Wilson-Hilferty transformation to compute the approximation of $\chi^2_{k-1,1-\delta}$ in (7) can be expressed as follows

$$N_r = \frac{k-1}{2\varepsilon}\left(1 - \frac{2}{9(k-1)} + \sqrt{\frac{2}{9(k-1)}}z_{1-\delta}\right)^3, \tag{9}$$

where $z_{1-\delta}$ is the upper quartile of the standard normal distribution.

According to the number of particles needed in (9), an upper bound ε plays important role in statistical bounds of the approximation quality of samples that are actually drawn from the proposal rather than the true posterior distributions. To avoid the mismatch between the true and the proposal distributions, the result in (9) can be applied in the resampling process to determine the total number of particles to resample. The authors in [7] proposed the method which divides the particles of the posterior distribution into bins and count the number k of bins which at least one particle is resampled to determine the total number of particles to resample as follows

$$N_{r,re} = min(N_{max}, ceil(N_r)), \tag{10}$$

where N_r is defined in (9).

4 Proposal Techniques

In this section, we propose the adjusted resampling algorithm, including the finding bound error and lower bound variance values, for KLD-resampling adjusted variance and gradient data can be presented in Table 3.

4.1 KLD-resampling with Adjusted Resampling Parameter

With successful KLD-resampling via the help of adjusted variance and gradient data [14, 17] is to enhance the operation time and Root Mean Square Error (RMSE) criteria. This thanks to adjusting the variance size by increasing variance inversely proportional to the likelihood and creating new samples near the true distribution or the high likelihood region. By the similarity to this method, our propose is to incorporate the KLD-resampling with adjusted variance and gradient data as the following.

First, the adjusted variance can be computed by using the relationship between the maximum number of samples and the number of required samples as follows

$$\sigma_{\mathrm{ad}} = \sigma_{\mathrm{ld}} + \varepsilon \frac{N_{r,re}}{N_{max}}, \tag{11}$$

where σ_{ad} and σ_{lb} are the adjusted and lower bound variances, respectively; Next, the new samples should be drawn as follows

$$x_{\mathrm{k}}^{i+N_{\mathrm{r,re}}} = \begin{cases} x_{\mathrm{k}}^{i} + \sigma_{\mathrm{ad}} \cdot randn, & \text{if}(\exists i) \left.\frac{\partial p(h(x))}{\partial x}\right|_{x=x_{\mathrm{k}}^{i}} > 0 \\ x_{\mathrm{k}}^{i} - \sigma_{\mathrm{ad}} \cdot randn, & \text{otherwise} \end{cases}, \tag{12}$$

where $\left.\frac{\partial p(h(x))}{\partial x}\right|_{x=x_k^i} = \frac{\partial}{\partial x}\left[\frac{1}{\sigma\sqrt{2\pi}} exp\left\{-\frac{(\mathrm{Z_k}-h(x))^2}{2\sigma^2}\right\}\right]\Big|_{x=x_k^i}$ is the variance of a Gaussian probability distribution function.

Final, the new samples $x_{\mathrm{k}}^{i+N_{\mathrm{r,re}}}$ in (12) is used to update the weight. This leads to generate new samples with high likelihood region. As a result, operation time reduces and the accurate of tracking objects is high due to small sample set size. To sum up, our algorithm can be shown in Table 2.

Table 2. Pseudo-code of proposal

procedure Pro $(\varepsilon, \delta, \mathrm{N}_{max}, \sigma)$
  Assign R, Q
  ε ▷ based on line 19 of ***Table 3***
  σ_{lb} ▷ based on ***Algorithm 6*** in [9]
  Assign δ, bin size, N_{max}
  Assign *k=0, i=0*; $\mathrm{N}_{r,re}=0$, all bins are zero-resampled: *b*
  while ($i \le \mathrm{N}_{\mathrm{r,re}}$ and $i \le \mathrm{N}_{max}$) **do**
    Randomly select one particle from the underlying particle set according to the weight, *i=i+1*
    if (new resampled particle comes from bin *b*) **then**
      Calculate σ_{ad} in (11)
      Draw $x_{\mathrm{k}}^{i+N_{\mathrm{r,re}}}$ ▷ draw the samples in (12)
      Update *k=k+1* ▷ the number of resampled bin
      Resampled
      Update $N_{\mathrm{r,re}}$ ▷ the required number in (10)
    end if
  end while
end procedure

4.2 Resampling Parameter Bound Error (Proposal)

The key issue of KLD-resampling with adjusted variance and gradient data is to determine the bound error in (7) and the lower bound variance in (11) to evaluate the number of particles used-based resampling process. Our works provided the finding lower bound variance algorithm with fixed bound error (0.65) in [9] through the available value in [7]. Meanwhile, our current works in [12] also provided the bound error algorithm for KLD-resampling adjusted variance and gradient data, we extend and apply this algorithm to determine the bound error for KLD-resampling with adjusted variance and gradient data in [9] as shown in Table 3.

Table 3. Finding the bound error

procedure $\varepsilon_{\text{opt}}(min, max, \Delta\varepsilon)$

  Assign R=Q

  δ ▷ fixed probability

  $i=1,\ \varepsilon_1 = min,\quad \varepsilon_{i*} = \Delta N = \{\varnothing\}$ ▷ initialized

  $\Delta\text{RMSE}^{\text{KLD-adj}}_{Pro} = \Delta\text{RMSE}^{\text{SIR}}_{Pro} = 0$

  while ($\varepsilon_i \le max$) **do**

    $\varepsilon_i = \varepsilon_i + \Delta\varepsilon$ ▷ update bound error

    $RMSE^{Pro}_{\varepsilon_i}$ ▷ RMSE of proposal

    $RMSE^{\text{KLD-adj}}$ ▷ RMSE of KLD-resampling adjusted variance and gradient data at $\varepsilon = 0.65$

    $RMSE^{\text{SIR}}$ ▷ RMSE of SIR

    $N^{\text{KLD-adj}}_{\text{r,re}}$ ▷ the number of used particles KLD-resampling adjusted variance and gradient data at $\varepsilon = 0.65$ in [9]

    $(N_{\text{r},re})^{Pro}_{\varepsilon_i}$ ▷ Proposal used particles at ε_i

    if ($\Delta\text{RMSE}^{\text{SIR}}_{Pro} > 0$ && $\Delta\text{RMSE}^{\text{KLD-adj}}_{Pro} > 0$) **then**

      $\varepsilon_{i*} = \varepsilon_{i*} \cup \{\varepsilon_i\}$ ▷ update bound error

      $\Delta N = \Delta N \cup \{\Delta N_{\varepsilon_{i*}}\}$ ▷ update the gap particles used between proposal and method in [9]

    end if

    $i=i+1$

  end while

  $\varepsilon_{\text{opt}} = max(\Delta N)$ ▷ find ε_{opt}

end procedure

Let us denote ε_i the bound error of ith, $RMSE^{Pro}_{\varepsilon_i}$ which is the RMSE value of proposal at ε_i; $RMSE^{\mathrm{KLD-adj}}$ and $RMSE^{\mathrm{SIR}}$ are respectively the RMSE values of KLD-resampling adjusted variance and gradient data (fixed bound error 0.65) in [9] and SIR in [5]. Let us denote $\Delta \mathrm{RMSE}^{\mathrm{SIR}}_{Pro}$ and $\Delta \mathrm{RMSE}^{\mathrm{KLD-adj}}_{Pro}$ are the gap of RMSE values between SIR in [5] and proposal; between KLD-resampling adjusted variance and gradient data in [9] and proposal, respectively.

Let us define $N^{\mathrm{KLD-adj}}_{\mathrm{r,re}}$ and $\left(N_{\mathrm{r,re}}\right)^{Pro}_{\varepsilon_{i*}}$ as the mean numbers of particles used of KLD-resampling with adjusted variance and gradient data (fixed bound error) [9] and proposal, respectively; and ε_{i*} (line 14) is the sets of the bound error that fulfills the condition of *Remark* 1 (line 13).

Remark 1: if $\Delta \mathrm{RMSE}^{\mathrm{SIR}}_{Pro}$ and $\Delta \mathrm{RMSE}^{\mathrm{KLD-adj}}_{Pro}$ are greater than zero (line 13), then a bound error value $\varepsilon_{\mathrm{opt}}$ (line 19) exits to maximize the function ΔN.

5 Simulation Results

We conduct a series of simulations to determine the bound error in (9) based on Table 3. Next, the performance of RMSE, mean number of particles used, and the comparison of the number of particles used between our proposal and for KLD-resampling adjusted variance and gradient data in [9] are considered.

5.1 Finding Resampling Parameter Bound Error

Setting up the range of bound error value is [0.8, 0.95] with $\Delta\varepsilon = 0.05$ as shown in Table 4 to satisfy the RMSE criteria between SIR, KLD-resampling adjusted variance and gradient data (fixed bound error $\varepsilon = 0.65$) in [9], and our algorithm under the same conditions. The parameters of system are assumed and simulated as follows [9] $\delta = 0.01$; bin size as the smaller of the standard deviations of the dynamic and the measurement ($\mathrm{R} = \mathrm{Q} = 0.5$), $\mathrm{N} = 300$, $\mathrm{N}_{\max} = \mathrm{N}$; $V_{\max} = 5$; $V_{\min} = 1$; $V_{\mathrm{init}} = 5$; $Pref = -23$; $K = -45$; and length time is 40 for sample size variation in 20 trials with various bound error values ε from 0.8 to 0.95 in Table 4. Based on Remark 1, the value $\varepsilon_{\mathrm{opt}} = 0.95$ is the optimal bound error because the function ΔN is to maximize at value *9.7* (*the italic row*, Table 4). Thus, we set up this value for our proposed method in the next section, and simulations are conducted to compare the RMSE criterion and the number of particles used for all approaches as shown in Figs. 2 and 3, respectively.

Table 4. Mean RMSE vs. Mean Number of particles used

ε	σ_{lb} (Algorithm 6 in [9])	Mean RMSE					$\Delta N^{KLD-adj}_{Pro}$	$\Delta RMSE^{SIR}_{Pro}$	$\Delta RMSE^{KLD-adj}_{Pro}$
		SIR	KLD-resampling [7]	KLD-resampling adjusted bound error [12]	KLD-resampling adjusted variance and gradient data [9]	Proposal			
0.8	0.8	0.0530	0.0812	0.0287	0.0607	0.0181	8.7	0.0349	0.0426
0.85	1.05	0.0992	0.0906	0.0413	0.0638	0.0207	9.2	0.0785	0.0431
0.9	1.4	0.1226	0.0986	0.0651	0.0918	0.0705	9.4	0.0521	0.0213
0.95	*1.3*	*0.0267*	*0.0245*	*0.0194*	*0.0191*	*0.0109*	*9.7*	*0.0158*	*0.0082*

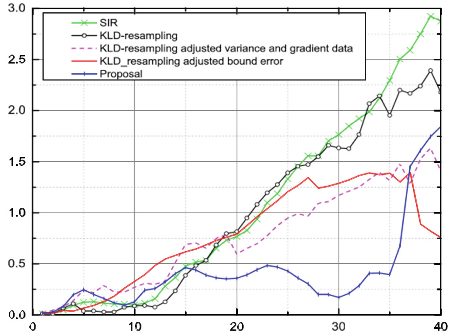

Fig. 2. RMSE of system for all approaches

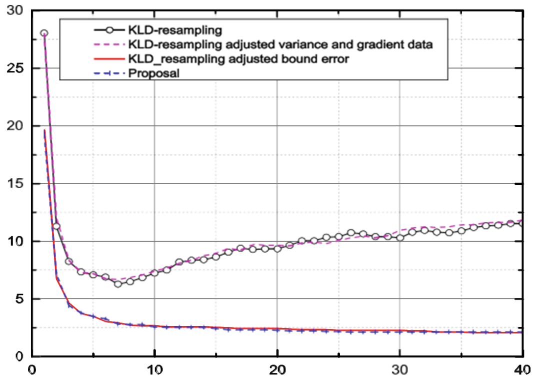

Fig. 3. Mean number of particles used for sample size variation in 20 trials

Table 5. Bound error and lower bound variance values vs. various Q

N_{max}	(ε based on Table 3; σ_{lb} based on Algorithm 6 in [9])		
	R = 0.5, Q = 0.1	R = 0.5, Q = 0.3	R = 0.5, Q = 0.7
100	(0.95; 0.3)	(0.95; 0.15)	(0.95; 0.05)
400	(0.95; 0.5)	(0.95; 0.8)	(0.95; 1.2)
800	(0.95; 1.4)	(0.95; 0.2)	(0.85; 0.3)

5.2 Performance for SIR, KLD-resampling, Proposal

Figure 2 shows the comparison of RMSE for SIR in [5], KLD-resampling ($\varepsilon = 0.65$) in [7], KLD-resampling adjusted variance and gradient data in [9] ($\sigma_{lb} = 1.3$, fixed bound error $\varepsilon = 0.65$), KLD-resampling adjusted bound error ($\varepsilon = 0.95$) in [12] and our proposal with length time 40, sample size in 20 trials. Clearly, the RMSE value of our proposal is lower than that of the others. For example, from 8 to 36 s, the gap between the proposed approach and KLD-resampling adjusted variance and gradient data in [9] regularly increases from about 0.05 to around 0.62, respectively, due to the adjusted lower variance algorithm (see Algorithm 6 in [9]). Furthermore, our method also improves the accuracy of target when compared KLD-resampling adjusted bound error.

The comparison of the mean number of particles used of KLD-resampling, KLD-resampling-based adjusted variance and gradient data in [9], KLD-resampling adjusted bound error in [12], and our proposal is shown in Fig. 3. It verifies that the curves of mean number of particles used with adjusted bound error are lower than that of without adjusted bound error. For instance, the curves of these methods maintain from 7 to 40 s. Otherwise, the number of particles used for our method is around 19 and sharply decreases after the next seconds it reaches about 4 particles used. Finally, our method slightly improves the number of particles used when compared KLD-resampling adjusted bound error in [12].

Similar to Sect. 5.1, the bound error and lower bound variance values can be found in Table 5 in case of changing various Q (0.1; 0.3; 0.7) and different number of samples. The gap of mean number particles used for KLD-resampling adjusted variance between with and without adjusted bound error under various Q can be evaluated and shown in Fig. 4. When increasing the number samples from 100 to 800, the mean number of particles used of our method is less than that of KLD-resampling adjusted variance and gradient data about 9 particles with different Q.

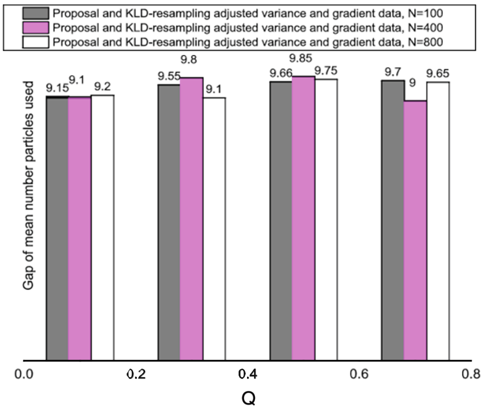

Fig. 4. Gap of mean number particles used vs. various Q and sample size variation in 20 trials

6 Conclusion

This paper, we propose a new resampling parameter for KLD-resampling adjusted variance and gradient data based on PF to estimate the location of target in WSN for reducing the fluctuations of RSS samples. In addition, in using the finding bound error and lower bound variance algorithms, this approach reduces the number of particles used when compared traditional methods.

Acknowledgments. This research is funded by Vietnam National University Ho Chi Minh City (VNU-HCM) under grant number T2016-02-IT.

References

1. Seppänen, A., et al.: State estimation in process tomography—three-dimensional impedance imaging of moving fluids. Int. J. Numer. Meth. Eng. **73**(11), 1651–1670 (2008)
2. Schön, T.B.: Solving Nonlinear State Estimation Problems Using Particle Filters-An Engineering Perspective. Department of Automatic Control, Linköping University, Linköping (2010)
3. Li, T., Bolic, M., Djuric, P.: Resampling methods for particle filtering. IEEE Sig. Process. Mag. **32**(3), 70–86 (2015)
4. Li, T., Sattar, T.P., Sun, S.: Deterministic resampling: unbiased sampling to avoid sample impoverishment in particle filters. Sig. Process. **92**(7), 1637–1645 (2012)
5. Arulampalam, M.S., et al.: A tutorial on particle filters for online nonlinear/non-Gaussian Bayesian tracking. IEEE Trans. Sig. Process. **50**(2), 174–188 (2002)
6. Gordon, N.J., Salmond, D.J., Smith, A.F.: Novel approach to nonlinear/non-Gaussian Bayesian state estimation. In: IEE Proceedings F-Radar and Signal Processing. IET (1993)
7. Li, T., Sun, S., Sattar, T.P.: Adapting sample size in particle filters through KLD-resampling. Electron. Lett. **49**(12), 740–742 (2013)
8. Fox, D.: Adapting the sample size in particle filters through KLD-sampling. Int. J. Robot. Res. **22**(12), 985–1003 (2003)
9. Ly-Tu, N., et al.: Performance of sampling/resampling-based particle filters applied to non-linear problems. REV J. Electron. Commun. **4**(3–4) (2014)
10. Park, S.-H., et al.: Improved adaptive particle filter using adjusted variance and gradient data. In: IEEE International Conference on Multisensor Fusion and Integration for Intelligent Systems, MFI 2008. IEEE (2008)
11. Redondi, A., et al.: An integrated system based on wireless sensor networks for patient monitoring, localization and tracking. Ad Hoc Netw. **11**(1), 39–53 (2013)
12. Ly-Tu, N., Le-Tien, T., Mai, L.: A modified particle filter through Kullback-Leibler distance based on received signal strength. In: 2016 3rd National Foundation for Science and Technology Development Conference on Information and Computer Science (NICS). IEEE (2016)
13. Wang, Z., Zhao, X., Qian, X.: Unscented particle filter with systematic resampling localization algorithm based on RSS for mobile wireless sensor networks. In: 2012 Eighth International Conference on Mobile Ad-hoc and Sensor Networks (MSN). IEEE (2012)
14. Ly-Tu, N., Mai, L., Le-Tien, T.: KLD-resampling with adjusted variance and gradient data-based particle filter applied to wireless sensor networks. In: 2015 2nd National Foundation for Science and Technology Development Conference on Information and Computer Science (NICS). IEEE (2015)
15. Ly-Tu, N., Le-Tien, T., Mai, L.: A study on particle filter based on KLD-resampling for wireless patient tracking. Int. J. Industr. Eng. Manage. Syst. 92–102 (2017). ISSN 1598-7248 (Print). ISSN 2234-6473 (Online). Publisher: The Korean Institute of Industrial Engineers
16. Wang, Z., Zhao, X., Qian, X.: The analysis of localization algorithm of unscented particle filter based on RSS for linear wireless sensor networks. In: 2013 32nd Chinese Control Conference (CCC). IEEE (2013)
17. Ly-Tu, N., Le-Tien, T., Vo-Thi-Luu, P., Mai, L.: Particle filter through Kullback-Leibler distance resampling with adjusted variance and gradient data for wireless biomedical sensor networks. In: Proceedings on International Conference on Ubiquitous Information Management and Communication (IMCOM 2015), Bali, Indonesia, 8–10 January 2015. ISBN 978-1-4503-3377-1. http://dx.doi.org/10.1145/2701126.2701221

Image Clustering Using Improved Particle Swarm Optimization

Thuy Xuan Pham(✉), Patrick Siarry, and Hamouche Oulhadj

Laboratory Images, Signals, and Intelligent Systems, University Paris-Est Creteil, 94400 Vitry sur Seine, France
thuy.phxuan@gmail.com, {siarry,oulhadj}@u-pec.fr

Abstract. In this paper, we propose an improvement method for image segmentation problem using particle swarm optimization (PSO) with a new objective function based on kernelization of improved fuzzy entropy clustering algorithm with spatial local information, called PSO-KFECS. The main objective of our proposed algorithm is to segment accurately images by utilizing the state-of-the-art development of PSO in optimization with a novel fitness function. The proposed PSO-KFECS was evaluated on several benchmark test images including synthetic images (http://pages.upf.pf/Sebastien.Chabrier/ressources.php), and simulated brain MRI images from the McConnell Brain Imaging Center (BrainWeb (http://brainweb.bic.mni.mcgill.ca/brainweb/)). Experimental results show that our proposed PSO-KFECS algorithm can perform better than the competing algorithms.

Keywords: Image segmentation · Particle swarm optimization
Entropy based fuzzy clustering · Fitness function

1 Introduction

Image segmentation is one of the most important and challenging problems in image analysis. Image segmentation is defined as the partitioning of an image into non-overlapped consistent regions or objects that satisfy pre-defined conditions. The level of details depends on the problem being solved or criteria being reached [1]. Image segmentation can be widely applied in many fields, such as medical imaging [2], data mining [3], pattern recognition [4], computer vision [5], etc. Due to the complexity of image content and the variety of image sizes, characteristics and other properties, there is no global solution today able to solve completely the image segmentation problem. Up to now, various methods for image segmentation have been proposed [6–9]. They can be divided into four groups: region based image segmentation [10], clustering based image segmentation [11], thresholding based image segmentation [12], and edge based image segmentation [13]. In this work, we are focused on the clustering based approach, using the state-of-the-art particle swarm algorithm equipped with a novel objective function.

Clustering is considered as the process of dividing data points into homogeneous classes or clusters, so the samples are similar within each group. Many clustering methods have been proposed in the literature [14, 15]. Among these clustering

© ICST Institute for Computer Sciences, Social Informatics and Telecommunications Engineering 2018
Y. Chen and T. Q. Duong (Eds.): INISCOM 2017, LNICST 221, pp. 359–373, 2018.
https://doi.org/10.1007/978-3-319-74176-5_31

approaches, fuzzy entropy clustering (FEC) algorithm proposed by Tran and Wagner [16] and fuzzy C-means (FCM) algorithm proposed by Bezdek et al. [17], which are based on minimization of an objective function, are widely used in data clustering and image segmentation for their simplicity and applicability. However, the major drawbacks of both methods are: (i) they are very sensitive to noise and imaging artifacts, since no local spatial information in the image is considered; (ii) the results provided depend not only on the choice of the initial clustering centroids but also on the high vulnerability of the algorithms to be trapped at the local minima. Many approaches have been proposed by researchers to overcome these drawbacks.

To overcome the first problem, many enhanced versions have been proposed by introducing local spatial information to their objective functions. It can be done by adding penalty terms, modifying elements used weighted concepts, using kernel metric, or combining with other methods. For instance, Cheng and Zhang [18] have proposed two algorithms, called KFCM_S1 and KFCM_S2, in which a neighborhood term and the kernel-induced distance replaced the Euclidean distance have been incorporated into the objective function. Krinidis and Chatzis [19] proposed a fuzzy local information c-means (FLICM) algorithm that added a penalty term using both spatial and gray-level local information with free of parameter tuning. Verma et al. [20] proposed an improved fuzzy entropy clustering (IFEC) algorithm. In the IFEC algorithm, the Euclidean distance is weighted by a new fuzzy factor, which determines both local gray-level and spatial information.

To address the second problem, many researchers proposed to use metaheuristic algorithms to perform clustering and image segmentation so as to achieve optimized performance. For example, Maulik [21], Ouadfel and Batouche [22], Hassanzadeh et al. [23], Nandy et al. [24], Omran et al. [11] proposed methods based on genetic algorithm (GA), ant colony optimization (ACO), firefly algorithm (FA), cuckoo search (CS), and particle swarm optimization (PSO), respectively, for image segmentation problem. PSO has become one of the most popular metaheuristics and has been used for clustering problems widely [25] due to simplicity and versatility. Using PSO for image segmentation problem can be in standalone form [11] or combination with other methods, such as FCM [26]. However, in PSO-based clustering, to provide good quality of image clustering, one needs both to tune a range of parameters and to design of good fitness function. Concerning these problems, Filho et al. [27] proposed a method that utilized the state-of-the-art PSO algorithm proposed by Zhang et al. [28] to improve the results of clustering data. Orman et al. [11], Wong et al. [29] proposed new fitness functions for image segmentation. Experimental results showed that their proposed methods can provide better performance when compared to classical methods.

In this work, we introduce a new method for image segmentation problem. The method uses low-discrepancy sequence initialized particle swarm optimization with high-order nonlinear time-varying inertia weight (LHNPSO) algorithm proposed by Yang et al. [30] with a new fitness function. The reason for choosing LHNPSO lies in the ability of this variant to outperform the other variants of PSO with two main advantages, namely, (i) the method can converge faster and give a much more accurate final solution [31], (ii) it is very easy to be implemented. The new fitness function takes advantages from kernelized fuzzy clustering approach; in addition, it also takes into account the spatial local information. Thus, the proposed method may tackle simultaneously the two main problems mentioned above. Experiments using synthetic images, simulated Magnetic Resonance Imaging (MRI) images are reported and the results are compared with recent fuzzy clustering and PSO-based image clustering methods.

The rest of the paper is organized as follows. Section 2 presents the related algorithms on which this work is based. Section 3 introduces the proposed method: LHNPSO algorithm with a new fitness function based on fuzzy entropy clustering for image clustering. The performance of the proposed method is evaluated and the comparison with a set of algorithms from the literature is reported in Sect. 4. Finally, in Sect. 5, we make conclusions.

2 Related Works

The algorithms on which this work is based are described in this section. They are divided in two groups: fuzzy entropy clustering algorithms and particle swarm optimization.

2.1 Fuzzy Entropy Clustering

The FEC algorithm proposed by Tran and Wagner [16] is an alternative generalization of hard c-means (HCM) clustering algorithm, which takes the advantage of fuzzy entropy. For a set of N data patterns $\mathbf{X} = \{x_1, x_2, \ldots, x_N\}$, the algorithm allows partitioning the data space, by minimizing an objective function J_{FEC} with respect to the membership matrix $\mathbf{U} = \{u_{ij}\}$ and the set C of cluster prototypes $\mathbf{C} = \{c_i\}$:

$$J_{FEC}(\mathbf{C}, \mathbf{X}, \mathbf{U}) = \sum_{i=1}^{C} \sum_{j=1}^{N} u_{ij} d^2(x_j, c_i) + n \sum_{i=1}^{C} \sum_{j=1}^{N} u_{ij} \log u_{ij} \tag{1}$$

Subject to:

$$\begin{array}{ll} 0 \le u_{ij} \le 1 & i = 1, \ldots, C \quad j = 1, \ldots, N \\ \sum_{i=1}^{C} u_{ij} = 1 \quad \forall j & 0 < \sum_{j=1}^{N} u_{ij} < N \quad \forall i \end{array} \tag{2}$$

Where x_j, a data pattern, is j^{th} pixel in the image, which can be intensity value or gray value; $d^2(x_j, c_i)$ is the Euclidean distance between the pixel x_j and centroid c_i; and n is the degree of fuzzy entropy.

The FEC objective function, J_{FEC}, can be minimized by iteratively using the following update equations:

$$u_{ij} = \left\{ \sum_{r=1}^{C} \left[\exp\left(d^2(x_j, c_i) - d^2(x_j, c_r)\right) \right]^{1/n} \right\}^{-1} \tag{3}$$

$$c_i = \frac{\sum_{j=1}^{N} u_{ij} \cdot x_j}{\sum_{j=1}^{N} u_{ij}} \tag{4}$$

The FEC algorithm can uniformly be summarized in the following steps:

Algorithm 1. FEC

Input: Fix the number C of centroids; randomly initialize $\mathbf{U} = \{u_{ij}\}$ satisfying (2); set terminate criterion ε and compute the centers $\mathbf{C} = \{c_i\}$ using **U** and equation (4)
Repeat
  Update the partition matrix using (3)
  Update the centroids using (4)
Until $\max\{||\mathbf{U}_{new} - \mathbf{U}_{old}||\} < \varepsilon$
Return the cluster centroids **C** and partition matrix **U**

After FEC clustering, each pixel will be associated with a membership value for each cluster. To get the image segmentation, the simplest way is assigning pixels to the clusters with the maximum membership values.

From Eq. (1), it is clear that the objective function of FEC does not take into account any local spatial information. Also, the metric is the Euclidean distance, $d^2(x_j, c_i)$, which measures the similarity between the pixel intensity and the cluster centroids. This metric assumes that each feature of data points is equally important and independent from others. This assumption may not be always satisfied in real applications [26]. We make the necessary corrections to this problem as explained in Sect. 2.2.

2.2 Kernelized Fuzzy Entropy Clustering with Spatial Information

2.2.1 Kernel Representation

Recently, 'kernel method' was proposed and was proved successful for various applications, such as in pattern recognition and function approximation. The idea of the method of kernel functions (called kernel trick) uses a 'nonlinear' transformation $\Phi : X^p \to H$, where X^p is input data space with low dimension and H is a high dimensional feature space. The structure of input data points may be inadequate for the analysis in the original space, but they are capable of analysis in space H [32]. In H, the Euclidean distance $||x_j - c_i||^2$ is substituted by $||\Phi(x_j) - \Phi(c_i)||^2$, which is defined by using kernel function K as

$$\left\|\Phi(x_j) - \Phi(c_i)\right\| = K(x_j, x_j) + K(c_i, c_i) - 2K(x_j, c_i) \tag{5}$$

Where $K(x_j, c_i)$ is a kernel function, which calculates the inner product. In this paper, Gaussian kernel is adopted as

$$K(x_j, c_i) = \langle \Phi(x_j), \Phi(c_i) \rangle = \exp\left(-\left\|x_j - c_i\right\|^2 / \sigma^2\right) \tag{6}$$

It is clear that the parameter σ of Gaussian kernel can greatly affect the result of kernel methods. For instance, when σ tends to zero, $K(x_j, c_i)$ turns into an impulse function with the value of 1 only at $x_j = c_i$ and 0 elsewhere. In this case, any two points in the feature space have a common value close to 1, in other words, it will be very hard to cluster. On the other hand, when σ towards to infinity, any two points in the feature space toward to zero, which makes them difficult to separate. In this work, the estimation of σ^2 is based on Yang's work [33]. It is defined as:

$$\sigma^2 = \lambda \sum_{j=1}^{N} \left\| x_j - \bar{x} \right\|^2 / N,\ \bar{x} = \sum_{j=1}^{N} x_j \tag{7}$$

λ is a constant defined by experiments.

2.2.2 Kernel Fuzzy Entropy Clustering with Spatial Information Algorithm

In this section, a new objective function based on fuzzy entropy clustering algorithm and kernel method is proposed. The objective function is given as follows:

$$\begin{aligned} J_{KFEC\_S}(\mathbf{C},\mathbf{U},\mathbf{X}) = \sum_{i=1}^{C}\sum_{j=1}^{N} u_{ij}\left(1 - K\left(x_j, c_i\right)\right) + n\sum_{i=1}^{C}\sum_{j=1}^{N} u_{ij}\log u_{ij} \\ + \eta\sum_{i=1}^{C}\sum_{j=1}^{N} u_{ij}\left(1 - K\left(\bar{x}_j, c_i\right)\right) \end{aligned} \tag{8}$$

Where the constraints in Eq. (2) must be satisfied. The third term is the spatial constraint term, in which the parameter η controls the penalty effect of the spatial constraint. The median of the neighbors within a window around the pixel x_j is used to represent $\bar{x}_j$.

By using the Lagrange multiplier method, the necessary conditions for the minimization of the objective function in Eq. (8), with the constraints in Eq. (2), can be found. Specifically, taking the first derivatives of J_{KFEC_S} with respect to u_{ij} and c_i, and zeroing them, respectively, two necessary but not sufficient conditions for J_{KFEC_S} to be at its local optimal solution will be obtained as follows:

$$u_{ij}^{-1} = \sum_{r=1}^{C} \frac{\exp\left(n^{-1}\cdot\left(\left(1 - K\left(x_j, c_i\right)\right) + \eta\cdot\left(1 - K\left(\bar{x}_j, c_i\right)\right)\right)\right)}{\exp\left(n^{-1}\cdot\left(\left(1 - K\left(x_j, c_r\right)\right) + \eta\cdot\left(1 - K\left(\bar{x}_j, c_r\right)\right)\right)\right)} \tag{9}$$

$$c_i = \frac{\sum_{j=1}^{N} u_{ij}\cdot\left(K\left(x_j, c_i\right)\cdot x_j + \eta\cdot K\left(\bar{x}_j, c_i\right)\cdot \bar{x}_j\right)}{\sum_{j=1}^{N} u_{ij}\cdot\left(K\left(x_j, c_i\right) + \eta\cdot K\left(\bar{x}_j, c_i\right)\right)} \tag{10}$$

The proposed kernelized fuzzy entropy clustering with spatial local information (KFEC_S) is described in Algorithm 2.

Algorithm 2. KFEC_S

Input: Fix the number C of centroids; randomly initialize $\mathbf{U} = \{u_{ij}\}$ satisfying (2); set terminate criterion ε, the maximum number of iterations T, the iterative index k to 1, and the parameters: n, λ, η; compute the centers $C = \{c_i\}$ using U and equation (10)
Repeat
  Update the partition matrix using (9)
  Update the centroids using (10)
  k = k + 1
Until $\max\{||\mathbf{U}_{new} - \mathbf{U}_{old}||\} < \varepsilon$ or $k > T$
Return the cluster centroids **C** and partition matrix **U**

As stated above, the Eqs. (9) and (10) are only necessary conditions for minimizing the objective function J_{KFEC_S}; as a result, obtained clustering solutions may be local optima. This is also the drawback of fuzzy clustering and its variants when solving image segmentation problem. To overcome this drawback, we use a metaheuristic optimization-based approach, as explained in the Sect. 2.3.

2.3 Particle Swarm Optimization

PSO is a population based stochastic optimization technique and is regarded as global search strategy, which was originally introduced by Kennedy and Eberhart [34]. In PSO, each individual of the population called a particle represents a potential solution to the optimization problem; and the population of individuals (P) or swarm is evolved through successive iterations. The quality of a candidate solution is evaluated by the fitness value, associated to each particle. Each particle, denoted i, has a position vector ($\mathbf{X}_i = \{x_{ir}\}$), a velocity vector ($\mathbf{V}_i = \{v_{ir}\}$), its own best position (P_{best}) found so far, and interacts with neighboring particles through the best position (G_{best}) discovered in the neighborhood so far. At each iteration k, each particle is moved according to Eq. 11 [35]:

$$V_i(k+1) = wV_i(k) + c_1r_1(P_{best}(k) - X_i(k)) + c_2r_2(G_{best}(k) - X_i(k)) \tag{11}$$

$$X_i(k+1) = X_i(k) + V_i(k+1) \tag{12}$$

Where, c_1 and c_2 are acceleration coefficients that scale the influence of the 'cognitive' and 'social' components; r_1 and r_2 are two random values, uniformly distributed in [0, 1]; w is inertia weight. The higher the w is, the higher the ability of searching in the global solution space is, and the smaller w is, the higher the ability of searching for the local solutions.

There are two basic criteria for assessing the performance of PSO algorithm, namely, convergence speed and ability to find global optima. To achieve these goals, the balance between global exploration and local exploitation is crucial. From Eqs. (11) and (12), it is clear that the performance is not only dependent on the controlling parameters (w, c_1, c_2), but also dependent on the size and the structure of neighborhood. In this work, initializing the population and tuning parameters (w, c_1, c_2) are adopted from Yang et al. [30], who designed LHNPSO algorithm. In LHNPSO, the initial population of particles is generated by using the Halton sequence to cover the search space efficiently, (c_1, c_2) are set to constants, equal to 2, and inertia weight is updated as follows:

$$w(k+1) = w_{\max} - (w_{\max} - w_{\min})\left(\frac{k}{k_{\max}}\right)^{1/\pi^2} \tag{13}$$

Where (w_{min}, w_{max}) is the range of inertia weight, with $w_{min} = 0.4$ and $w_{max} = 0.9$, k and k_{max} are the iteration number starting from iteration one and the maximum number of allowable iterations, respectively. This law of variation of w increases the exploration of the search space in the first iterations of the algorithm, and the exploitation of the best solutions found so far towards the end of the algorithm. This constitutes a very good balance between the phases of exploration of the search space and the phases of exploitation of the solutions.

The procedures of LHNPSO algorithm can be summarized as:

Algorithm 3. LHNPSO

Input: Set $k = 1$; initialize particles using the Halton sequence; set 'cognitive' and 'social' coefficients and the range of inertia weight
Repeat
    Calculate fitness value
    Determine the personal best (P_{best}) and the global best (G_{best})
    Update the inertia weight according to (13)
    Calculate the velocity and position according to (11) and (12)
Until the stopping criteria are met or the number of iterations is $k > k_{max}$
Return the optimal solution (G_{best})

The performance of LHNPSO is only tested with the unconstrained optimization problems. For more complex problems, the need of further development is still required.

3 The Proposed Algorithm, Kernelized Fuzzy Entropy Clustering with Spatial Information Using LHNPSO

As discussed in Sect. 2, the kernelized fuzzy entropy clustering with spatial information model is a complex nonlinear model. The KFEC_S algorithm can be trapped into local minima because local search method (gradient method) is used to solve the model. By contrast, the algorithm has the advantage of converging quickly. On the other hand, LHNPSO is a global optimization method, which can provide global optimum solution, but with a relatively longer convergence time. So, we use LHNPSO with minor improvements to optimize KFEC_S, trying to get the global optimum solution by escaping the trap of local optimums, and we use at the same time KFEC_S to guide the LHNPSO research process in order to converge more quickly and anticipate more accurate solution. Thus, a new image clustering algorithm based on KFEC_S and LHNPSO, named PSO-KFECS, is proposed. The details of this algorithm are given in the next section.

3.1 Particle Representations

When LHNPSO is applied to optimize the kernelized fuzzy entropy clustering with spatial information objective function J_{KFEC_S}, cluster prototypes **C** = $\{c_i\}_C$ are chosen to be optimization variables and encoded as positions of particles. For P particles or solutions, there are in total C * P optimization variables needing to be encoded. The position of i^{th} particle can be described as: $\mathbf{X}_i = [x_{i1}, x_{i2}, \ldots, x_{iC}]$. Here, x_{ij} represents the j^{th} cluster centroid among C centroids of the i^{th} solution. In this way, cluster centroids are encoded in position vector $\mathbf{X}_i$ and **C** can be obtained by decoding $\mathbf{X}_i$.

3.2 Fitness Function

After decoding $\mathbf{X}_i$ to get cluster centroids **C** and calculating fuzzy partition matrix **U** according to Eq. (9), the value of the fitness function can be calculated by evaluating J_{KFEC_S} according to Eq. (8).

$$f_i = J_{KFEC\_S} \tag{14}$$

Minimization of f_i is the same as minimization of the objective function J_{KFEC_S}, which leads to the optimal partitioning of the image.

3.3 The Proposed Algorithm

The proposed algorithm, PSO-KFECS, takes both advantage of the excellent feature of LHNPSO, in the aspect of optimizing the objective function of kernelized fuzzy entropy clustering with spatial information and the kernel, and the KFEC_S gradient method, in aspect of speeding up convergence.

To make sure that all particles are moving within the search space and avoiding divergent behavior, the position and the velocity are limited as follows:

$$v_{ij}(k+1) = \begin{cases} rand() \cdot v_{\max} & if \quad v_{ij}(k+1) > v_{\max} \\ -rand() \cdot v_{\max} & if \quad v_{ij}(k+1) < -v_{\max} \\ v_{ij}(k+1) & otherwise \end{cases} \tag{15}$$

$$x_{ij}(k+1) = \begin{cases} rand() \cdot \frac{1}{2} \cdot (x_{\max} - x_{\min}) & if \quad x < x_{\min} \quad or \quad x > x_{\max} \\ x_{ij}(k+1) & otherwise \end{cases} \tag{16}$$

Where v_{max} is the largest allowable step size in any dimension; and, $[x_{min}, x_{max}]$ are the bounds of the search space in each dimension. In image clustering, commonly, v_{max} is set to 5 and $[x_{min}, x_{max}]$ are the minimum and maximum of the feature (intensity or gray value) of the image.

Putting all discussions above together, the PSO-KFECS algorithm is shown as follows:

Algorithm 4. PSO-KFECS

Input: Set $k = 1$; Initialize all parameters for LHNPSO algorithm ($c_1, c_2, k_{max}, P, \ldots$); Initialize all parameters for the fitness function in Eq. (8) (C, n, η); Set constraints for the position [x_{min}, x_{max}] and the velocity [$-v_{max}, v_{max}$]; Generate the initial position $\mathbf{X}_i$ using the Halton sequence, the velocity $\mathbf{V}_i$ randomly; Generate randomly the partition matrix **U** for each solution that satisfies Eq. (2); Evaluate f_i according to Eq. (8); Initialize P_{best} with a copy of X_i; and $G_{best} = P_{best}$ while f_s is the minimum

Repeat

  For each particle **do**

    Calculate kernel distance K using Eq. (6)
    Calculate the partition matrix **U** using Eq. (9)
    Calculate the fitness function f_i using Eq. (8)

  Update the P_{best}, G_{best}
  Update the inertia weight w using Eq. (13)
  Update the position $\mathbf{X}_i$ and the velocity $\mathbf{V}_i$ using Eq. (11-12)
  Map position and velocity into search space using Eq. (15-16)

Until the stopping criteria are met or the number of iterations is $k > k_{max}$

Return the cluster centroids **C** and the partition matrix **U**

In this work, the number of non-significant improvements of the fitness function and the maximum number of iterations are used as the stopping criteria of the algorithm. Thus, if the condition $\left\|f_i^{(k+1)} - f_i^{(k)}\right\| < \varepsilon$ is completed k_{stop} times or the condition $k > k_{max}$ is reached, the algorithm is immediately stopped.

4 Experimental Results

This section presents the results of the experimental evaluation of our algorithm. With this aim in view, our algorithm is compared with those from five well-known image clustering algorithms in the literature: FEC [16], KFCM_S2 [18], FLICM [19], PSO-based image clustering algorithms proposed by Orman et al. [11] (PSO_V1) and Wong et al. [29] (PSO_V2). Two image datasets: synthetic images [36], simulated MRI brain images from BrainWeb [37], with different numbers of cluster centroids and levels of corrupting noises, are used to evaluate the performance of the proposed algorithm. All the algorithms are implemented in MATLAB 2014b and executed with a computer with Intel Core i3 1.5 GHz CPU, 4G RAM under Microsoft Windows 7. The values of the parameters of our method are based on conclusions in the relative literature and try-and-error technique. Parameter settings are given in Table 1.

4.1 Quantitative Evaluation

In order to compare the results of different segmentation methods, supervised evaluation methods are used. In supervised evaluation methods, we use Jaccard index [38] and Hausdorff distance [39], because current research [40] reports that they are suitable

Table 1. Setting of specific parameters in PSO-KFECS

Parameters	Values
Population size	40
$c_1 = c_2$	2.0
Degree of fuzzy entropy, n	20
The spatial constraint parameter, η	2.6
The controlling Gaussian kernel parameter, λ	1/π
The number of non-significant improvement, k_{stop}	10
The terminate criterion parameter, ε	0.00001
Maximum number od iterations, k_{max}	100

metrics for the evaluation when there exists outliers with or without small segments, complex boundaries, low densities in the image.

4.1.1 Jaccard Index

This index is an overlap index, which directly compares the segmented image (I_s) and the ground truth image (I_t) by measuring similarity between them. The higher value indicates the better result. Jaccard index is defined as the intersection between segmentations divided by the size of their union, that is

$$JAC(I_s, I_t) = \frac{TP}{TP + FP + FN} \tag{17}$$

Where TP, FP, FN are basic cardinalities of the confusion matrix, namely, the true positives, the false positives, and the false negatives, respectively.

4.1.2 Hausdorff Distance

This is a spatial distance based metric, which measures the dissimilarity between the segmented image and the ground truth image. The lower value indicates the better result. It is defined as follows:

$$HD(I_s, I_t) = \max(h(I_s, I_t), h(I_t, I_s)) \tag{18}$$

Where $h(I_s, I_t)$ is called the directed Hausdorff distance and given by:

$$h(I_s, I_t) = \max_{p_s \in I_s} \min_{p_t \in I_t} \|p_s - p_t\| \tag{19}$$

Where $\|p_s - p_t\|$ is the Euclidean distance between the gray values of pixel p_s in the segmented image and pixel p_t in the ground truth image.

4.2 Experiments on Synthetic Images

To compare the sensitivity of the algorithms to noise, we apply them to 256 × 256 synthetic images [36], which have 4 or 5 regions and corrupted with salt and pepper or

Gaussian noises with different levels. For the salt and pepper noise, the variance of the noise varies from 0.04 to 0.1 with a step of 0.02; for Gaussian noise, the noise variances are in range of [0.004, 0.01] with steps of 0.002.

Figure 1 describes an example of the segmentation results of a synthetic image, including 5 regions corresponding to gray values taken as 1, 61, 121, 181, and 241, corrupted with 0.1 variance of salt and pepper and 0.01 Gaussian noise. From Fig. 1, one can see, visually, that even though the six competitive methods give a coherent segmentation result, the proposed method produces better results than the others.

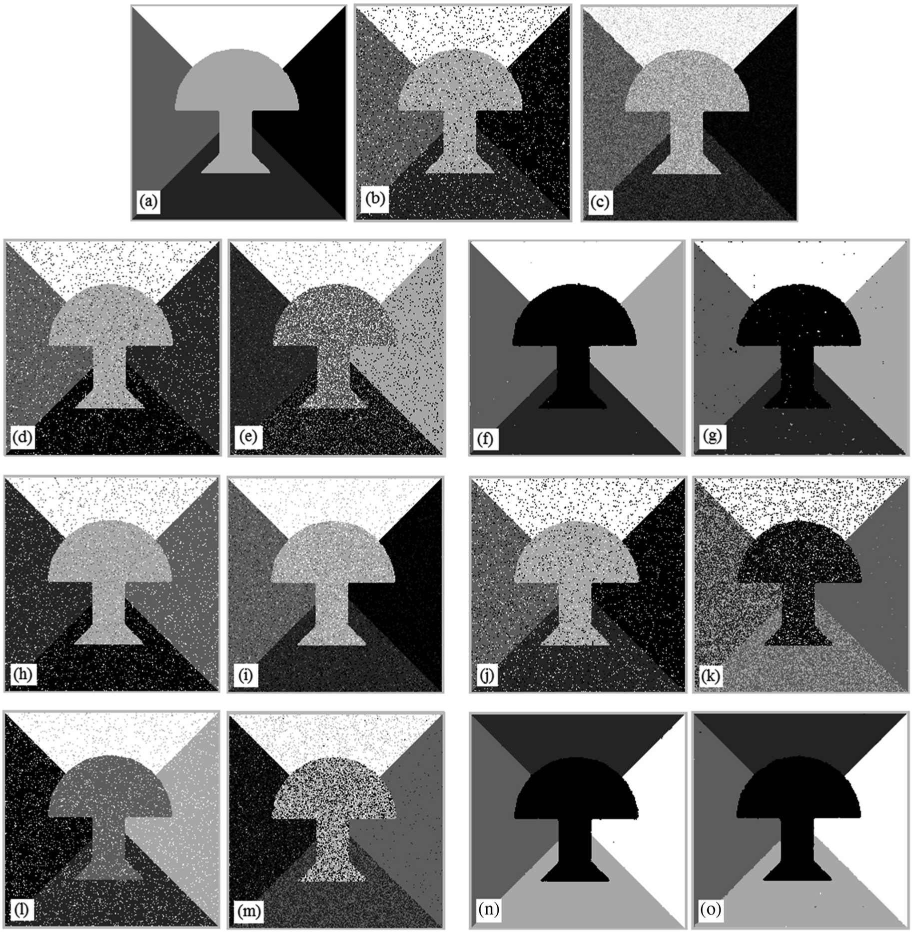

Fig. 1. Segmentation results on synthetic image corrupted by salt and pepper noise (0.1) and Gaussian noise (0.01): (a) original image; (b) salt and pepper noise image; (c) Gaussian noise image; (d, e) FEC results; (f, g) KFCM_S2 results; (h, i) FLICM results; (j, k) PSO_V1 results; (l, m) PSO_V2 results; (n, o) PSO-KFECS results.

Table 2 provides the numerical scores (Eqs. 17 and 18) of the six competitive methods, they are the average of 10 successful program runs. The table shows clearly that the proposed PSO-KFECS algorithm provides superior results. Indeed, the contours of the original images are better reconstructed and the regions are more homogeneous.

Table 2. Segmentation evaluation scores of different methods

Noise type	Metrics	FEC	KFCM_S2	FLICM	PSO_V1	PSO_V2	PSO KFECS
Salt and pepper	*JAC*	0.7318	0.9931	0.7309	0.7325	0.7300	**0.9954**
(0.1)	*HD*	4187	3462	4324	4263	4187	**1660**
Gaussian	*JAC*	0.5105	0.9746	0.6429	0.4765	0.5150	**0.9912**
(0.01)	*HD*	4296	3698	4223	4183	4200	**2980**

4.3 Experiments on Simulated MRI Images

BrainWeb provides a simulated brain database (SBD) that contains a set of realistic MRI data volumes. We have applied the proposed PSO-KFECS and 5 other algorithms on normal brain images, which have characteristics of Mobility T1, slice thickness 1 mm, with different levels of noise (0%, 1%, 3%, 5%, 7%, 9%), and different levels of non-uniformity (0%, 20%, 40%). These images were segmented with 4 cluster centroids: background, cerebral spinal fluid (CSF), gray matter (GM), and white matter (WM).

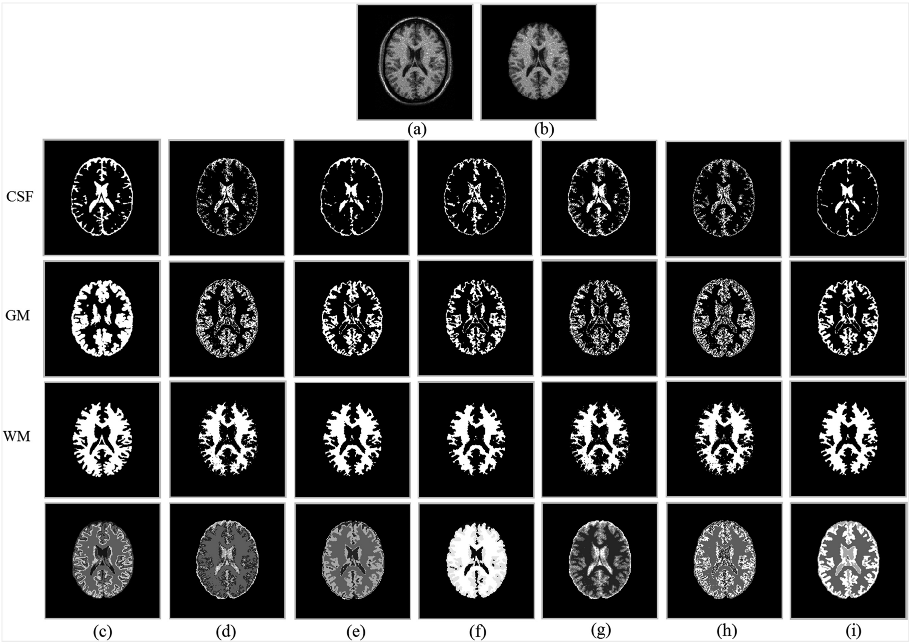

Fig. 2. Original and segmented images by different algorithms: (a) original T1-weighted axial image with 7% noise and 20% intensity of non-uniformity; (b) original image after skull stripping; (c) the ground truth images; (d) FEC results; (e) KFCM_S2 results; (f) FLICM results; (g) PSO_V1 results; (h) PSO_V2 results; (i) PSO-KFECS results.

Figure 2 shows an example of segmentation of simulated brain image with 7% of noise and 20% intensity of non-uniformity. Visually, the comparison of the performance of the same six competitive algorithms is a little bit vague. The quantitative performance evaluation is given in Table 3. In this table, it can be seen that the scores of the proposed algorithm that PSO-KFECS outperforms all competing, only FLICM reveals better for GM with Jaccard index.

Table 3. Segmentation evaluation of the simulated MRI image

Regions	Metrics	FEC	KFCM_S2	FLICM	PSO_V1	PSO_V2	PSO KFECS
CSF	*JAC*	0.8613	0.8978	0.9189	0.8707	0.8957	**0.9297**
	HD	332.6	413.6	229	304.	329.1	**212.6**
GM	*JAC*	0.8112	0.8365	**0.8645**	0.8258	0.8229	0.8549
	HD	264.9	219.4	**205**	215	249.5	**205**
WM	*JAC*	0.8746	0.8869	0.9059	0.8334	0.8584	**0.9210**
	HD	127.7	118.9	113	192.1	171.8	**107.2**
Whole image	*JAC*	0.9388	0.9326	0.9277	0.9114	0.9154	**0.9425**
	HD	263.4	**205**	**205**	259.1	209.3	**205**

5 Conclusion

In this paper, an improved particle swarm optimization with a new fitness function - the kernelized fuzzy entropy clustering with spatial information, for image segmentation - is proposed. Two drawbacks of fuzzy clustering algorithms, which are the trapping of the solution into local minima and the sensitivity to noise and imaging artifacts, have been partially overcome. The experimental results show that our method is more effective in comparison with five competitive methods of the literature. However, there is still much work for us to go further. Specifically, the determination of the parameters: n (degree of fuzzy entropy) and η (controlling parameter of the spatial information) is an open question. In addition, only one criterion (J_{KFECS}) is used to guide the search process of the solution, this may lead to the situation that the solution is a global optimum of the criterion, but it may not be the optimum of the segmentation problem. In addition to the mentioned improvements, we also intend to accelerate the convergence times of our algorithm, by implementing it on multicore computer architecture in order to parallelize the data processing. Indeed, although they are more precise, metaheuristics based algorithms have the drawback of providing more convergence times because they cover more widely the solution search space. Moreover, we plan to apply a multi-objective optimization approach, in order to take benefits of other criteria.

References

1. Gonzalez, R.C., Woods, R.: Digital Image Processing, 3rd edn. Prentice Hall, Englewood Cliffs (2008)
2. Sharma, N., Aggarwal, L.M.: Automated medical image segmentation techniques. J. Med. Phys. **35**(1), 3–14 (2010)

3. Hsu, W., Lee, M.L., Zhang, J.: Image mining: trends and developments. J. Intell. Inf. Syst. **19**(1), 7–23 (2002)
4. Lakshmi, H.C.V., PatiKulakarni, S.: Segmentation algorithm for multiple face detection in color images with skin tone regions using color spaces and edge detection techniques. IJCTE **2**(4), 1793–8210 (2010)
5. Szeliski, R.: Computer Vision: Algorithms and Applications. Springer, London (2011). https://doi.org/10.1007/978-1-84882-935-0
6. Pal, N., Pal, S.: A review on image segmentation techniques. Pattern Recognit. **26**(9), 1277–1294 (1993)
7. Pham, D.L., Xu, C.Y., Prince, J.L.: A survey of current methods in medical image segmentation. Annu. Rev. Biomed. Eng. **2**, 315–337 (2000)
8. Khan, W.: Image segmentation techniques: a survey. J. Image Graph. **1**(4), 166–170 (2013)
9. Taneja, A., Ranjan, P., Ujjlayan, A.: A performance study of image segmentation techniques. In: 4th ICRITO, pp. 1–6 (2015)
10. Freixenet, J., Muñoz, X., Raba, D., Martí, J., Cufí, X.: Yet another survey on image segmentation: region and boundary information integration. In: Heyden, A., Sparr, G., Nielsen, M., Johansen, P. (eds.) ECCV 2002. LNCS, vol. 2352, pp. 408–422. Springer, Heidelberg (2002). https://doi.org/10.1007/3-540-47977-5_27
11. Orman, A.P., Engelbrecht, M., Salman, A.: Particle swarm optimization method for image clustering. Int. J. Pattern Recogn. **19**, 297–321 (2005)
12. Sezgin, M., Sankur, B.: Survey over image thresholding techniques and quantitative performance evaluation. J. Electron. Imaging **13**, 146–148 (2004)
13. Senthilkumaran, N., Rajesh, R.: A study on edge detection methods for image segmentation. In: Proceedings of the International Conferences on Mathematics and Computer Science (ICMCS-2009), vol. 1, pp. 255–259 (2009)
14. Jain, A.K., Murty, M.N., Flynn, P.J.: Data clustering: a review. ACM Comput. Surv. **31**(3), 264–323 (1999)
15. Xu, R., Wunsch, D.: Survey of clustering algorithms. IEEE Trans. Neural. Netw. **16**, 645–678 (2005)
16. Tran, D., Wagner, M.: Fuzzy entropy clustering. In: IEEE International Conference Fuzzy Systems, vol. 1, pp. 152–157 (2000)
17. Bezdek, J.C., Ehrlich, R., Full, W.: FCM: the fuzzy C-means clustering algorithm. Comput. Geosci. **10**(2), 191–203 (1984)
18. Chen, S.C., Zhang, D.Q.: Robust image segmentation using FCM with spatial constraints based on new kernel-induced distance measure. IEEE Trans. Syst. Man. Cybern. Part B Cybern. **34**(4), 1907–1916 (2004)
19. Krinidis, S., Chatzis, V.: A robust fuzzy local information c-means clustering algorithm. IEEE Trans. Image Process. **19**, 1328–1337 (2010)
20. Verma, H., Agrawal, R.K., Kumar, N.: Improved fuzzy entropy clustering algorithm for MRI brain image segmentation. Int. J. Imaging Syst. Technol. **24**(4), 277–283 (2014)
21. Maulik, U.: Medical image segmentation using genetic algorithms. IEEE Trans. Inf. Technol. Biomed. **13**(2), 166–173 (2009)
22. Ouadfel, S., Batouche, M.: An efficient ant algorithm for swarm-based image clustering. J. Comput. Sci. **3**(3), 162–167 (2007)
23. Hassanzadeh, T., Vojodi, H., Moghadam, A.M.E.: An image segmentation approach based on maximum variance intra-cluster method and firefly algorithm. In: 7th International Conference on Natural Computation, pp. 1817–1821 (2011)
24. Nandy, S., Yang, X.S., Sarkar, P.P., Das, A.: Color image segmentation by cuckoo search. Intell. Autom. Soft Comput. **21**(4), 673–685 (2015)

25. Alam, S., Dobbie, G., Koh, Y.S., Riddle, P., Rehman, S.U.: Research on particle swarm optimization based clustering: a systematic review of literature and techniques. Swarm Evol. Comput. **17**, 1–13 (2014)
26. Benaichouche, A.N., Oulhadj, H., Siarry, P.: Improved spatial fuzzy c-means clustering for image segmentation using PSO initialization, Mahalanobis distance and post-segmentation correction. Digit Signal Process. **23**, 1390–1400 (2013)
27. Filho, T.M.S., Pimentel, B.A., Souza, R.M.C.R., Oliveira, A.L.I.: Hybrid methods for fuzzy clustering based on fuzzy c-means and improved particle swarm optimization. Expert Syst. Appl. **42**(17), 6315–6328 (2015)
28. Zhang, Y., Xiong, X., Zhang, Q.: An improved self-adaptive PSO algorithm with detection function for multimodel function optimization problems. Math Probl. Eng. **2013**, 8 (2013). Article ID 716952. http://dx.doi.org/10.1155/2013/716952
29. Wong, M.T., He, X., Yeh, W.C.: Image clustering using particle swarm optimization. In: 2011 IEEE Congress on Evolutionary Computation (CEC), pp. 262–268, June 2011
30. Yang, C., Gao, W., Liu, N., Song, C.: Low-discrepancy sequence initialized particle swarm optimization algorithm with high-order nonlinear time-varying inertia weight. Appl. Soft Comput. **29**, 386–394 (2015)
31. Harrison, K.R., Engelbrecht, A.P., Ombuki-Berman, B.M.: Inertia weight control strategies for particle swarm optimization. Swarm Intell. **10**(4), 267–305 (2016)
32. Zhao, F., Jiao, L., Liu, H.: Kernel generalized fuzzy c-means clustering with spatial information for image segmentation. Digit Signal Process. **23**, 184–199 (2013)
33. Yang, M., Tsai, H.: A Gaussian kernel-based fuzzy c-means algorithm with a spatial bias correction. Pattern Recogn. Lett. **29**(12), 1713–1725 (2008)
34. Kennedy, J., Eberhart, R.C.: Particle swarm optimization. In: IEEE International Conference on Neural Networks, pp. 1942–1948 (1995)
35. Eberhart, R.C., Shi, Y.: Comparing inertia weights and constriction factors in particle swarm optimization. In: IEEE Congress on Evolutionary Computation, San Diego, pp. 84–88 (2000)
36. http://pages.upf.pf/Sebastien.Chabrier/ressources.php
37. BrainWeb: Simulated Brain database (2016). http://brainweb.bic.mni.mcgill.ca/brainweb/
38. Jaccard, P.: The distribution of the flora in the alpine zone. New Phytol. **11**(2), 37–50 (1912)
39. Beauchemin, M., Thomson, K.P.B., Edwards, G.: On the Hausdorff distance used for the evaluation of segmentation results. CJRS **24**(1), 3–8 (1998)
40. Taha, A.A., Hanbury, A.: Metrics for evaluating 3D medical image segmentation: analysis, selection, and tool. BMC Med. Imaging. **15**, 29 (2015)

Author Index